THE PHYSICAL REVIEW

VOLUME 90 *Second Series* NUMBER 1

APRIL 1, 1953

Published for the

AMERICAN PHYSICAL SOCIETY

by the

AMERICAN INSTITUTE OF PHYSICS
Incorporated

LANCASTER, PA., AND NEW YORK, N. Y.

Information for Contributors

Manuscripts

Send manuscripts to S. A. Goudsmit, Brookhaven National Laboratory, Upton, Long Island, New York.

Each article submitted will in general consist of (a) textual material, i.e., all material which is to be set in type, and (b) drawings or photographs from which zinc etchings or copper halftones will be made. Textual material will consist of an abstract, the body of the paper, tabular material, references, and figure captions. All of this material must be in English, typewritten (except mathematical expressions) double spaced with wide margins (for editorial instructions to the printer) on a durable, white paper, preferably letter size. The original copy, not the carbon, should be submitted.

For general style, spellings, abbreviations, and form, recent issues of this journal should be consulted.

The prime requisite is that the copy shall be clear to the typesetter, who is neither a physicist nor a mathematician.

Abstracts

An abstract must accompany each article. It should be adequate as an index and as a summary. As an index, it should give all subjects, major and minor, concerning which new information is presented. As a summary it should give the conclusions of the article and all numerical results of general interest.

Mathematical Expressions

All but the simplest mathematical expressions should be carefully printed in by hand. Be sure to distinguish between capital and small letters. Indicate clearly superscripts and subscripts by inverted carets and carets, respectively. Avoid complicated superscripts and subscripts. Avoid repetition of a complicated expression by representing it by some convenient symbol. Identify in the margin Greek letters and unusual symbols. Use fractional exponents instead of root signs. Use the solidus (/) for fractions wherever its use will save vertical space.

References

References should appear as footnotes, numbered consecutively, and arranged thus:

[1] A. B. Smith, Phys. Rev. 41, 853 (1940).
[2] H. Lamb, *Hydrodynamics* (Cambridge University Press, Cambridge, England, 1940), sixth edition, pp. 573, 645.

Tables

All but the simplest tabular material should be organized in tabular form rather than as a part of the running text. Tables may be typewritten on sheets separate from the running text with indications in the margin of the running text where the table is to be inserted. Each table must have a caption which will make the data in the table intelligible without reference to the text. Avoid complicated column headings; if necessary, use symbols which are explained in the table caption.

Figures

Wherever possible figures should be planned for the width of a column of the *Physical Review* (3 inches). A convenient reduction ratio is about 2:1 or 3:1. The original drawings or photographs should therefore be in general about 6 to 9 inches wide and the lettering and symbols should be large enough on the original that when reduced they shall not be less than about $\frac{1}{16}$ in. (~1.5 mm). If the reduction is 3:1, the original lettering should be not less than $\frac{1}{16}$ in. high.

The process of making zinc etchings or copper halftones is a black and white photographic one. Therefore line drawings must be in *india ink* on white paper or tracing cloth. Coordinate paper is not desirable but if used must be blue lined and the coordinate lines which are to show must be inked over.

Photographs should have maximum black and white contrast.

Plan figures to use space efficiently. Avoid wasting space, particularly at the top or bottom.

Identify on the black or other suitable place each original drawing or photograph with the author's name and the figure number. Figures should be numbered consecutively and their approximate position indicated in the margin of the running text. Figure captions should be typed and included with the manuscript (not as part of the figure).

Avoid round and oval photographs.

Alterations

Take great care that each manuscript is typographically accurate. A limited number of alterations in proof are unavoidable, but the cost of making extensive alterations after the article has been set in type will be charged to the author.

Proof and all correspondence concerning papers in the process of publication should be addressed to the Publication Manager, American Institute of Physics, 57 East 55 Street, New York 22, New York.

THE

PHYSICAL REVIEW

A journal of experimental and theoretical physics established by E. L. Nichols in 1893

VOLUME 90

Second Series

APRIL 1–JUNE 15, 1953

Published for the

AMERICAN PHYSICAL SOCIETY

by the

AMERICAN INSTITUTE OF PHYSICS

Incorporated

THE PHYSICAL REVIEW

A journal of experimental and theoretical physics established by E. L. Nichols in 1893

Published by the American Institute of Physics
for the

AMERICAN PHYSICAL SOCIETY

Officers

President

ENRICO FERMI
Institute for Nuclear Studies
University of Chicago
Chicago 37, Illinois

Vice-President

H. A. BETHE
Cornell University
Ithaca, New York

Secretary

K. K. DARROW
Bell Telephone Laboratories
Office:
Columbia University
New York 27, New York

Treasurer

G. B. PEGRAM
Columbia University
New York 27, New York

Local Secretary
for the Pacific Coast

J. KAPLAN
University of California at Los Angeles
Los Angeles, California

Managing Editor

S. A. GOUDSMIT
Brookhaven National Laboratory
Upton, Long Island
New York

BOARD OF EDITORS

Editor

S. A. GOUDSMIT

Assistant Editor

S. PASTERNACK

Associate Editors

1951–1953	*1952–1954*	*1953–1955*
C. L. CRITCHFIELD	W. P. ALLIS	W. A. FOWLER
M. DEUTSCH	F. G. BRICKWEDDE	KENNETH GREISEN
M. GOLDHABER	W. B. FRETTER	CHARLES KITTEL
T. H. JOHNSON	CONYERS HERRING	R. E. MARSHAK
R. SERBER	H. W. LEVERENZ	W. K. H. PANOFSKY
C. H. TOWNES	ARNOLD NORDSIECK	V. F. WEISSKOPF

Manuscripts for publication should be submitted to S. A. GOUDSMIT, Brookhaven National Laboratory, Upton, Long Island, New York. The authors' institutions are requested to pay a publication charge of $15 per page which, if honored, entitles them to 100 free reprints. Instructions will be sent with galley proofs.

Proof and all correspondence concerning papers in the process of publication should be addressed to the Publication Manager, American Institute of Physics, 57 East 55 Street, New York 22, New York.

Subscription Price

United States and Canada $30.00
Elsewhere $32.00

Back Numbers [1]

Yearly back number rate when complete year is available:
Prior to 1949: **$25.00**
Thereafter: **$33.00**
Single copies: **$3.00** each, prior to July, 1929;
$1.50 each, July, 1929–December, 1941;
$3.00 each, January, 1942–December, 1946;
$1.50 each, thereafter.
General index, 1893–1920: **$4.00**.

Subscriptions, renewals, and orders for back numbers should be addressed to the American Institute of Physics, 57 East 55 Street, New York 22, New York.

Changes of address in the case of members of the American Physical Society should be addressed to the Treasurer; in the case of other subscribers to the American Institute of Physics.

[1] For Series 1 inquire of Physics Department, Cornell University, Ithaca, New York.

The Physical Review is published semi-monthly at Prince and Lemon Streets, Lancaster, Pennsylvania.

Entered as second-class matter March 6, 1947, at the Post Office at Lancaster, Pennsylvania, under the Act of March 3, 1879.

Acceptance for mailing at special rate of postage provided for in paragraph (d-2), section 34.40, P. L. & R. of 1948, authorized January 27, 1933.

THE
PHYSICAL REVIEW

A journal of experimental and theoretical physics established by E. L. Nichols in 1893

SECOND SERIES, VOL. 90, NO. 1 APRIL 1, 1953

The Hyperfine Structure of the $3p\ ^2P_{\frac{1}{2}}$ State of Al^{27}†

HIN LEW AND GÜNTER WESSEL*
Division of Physics, National Research Council, Ottawa, Canada
(Received December 5, 1952)

The hyperfine structure interval of the $3p\ ^2P_{\frac{1}{2}}$ state of Al^{27} has been measured and found to be 1506.14 ±0.05 Mc/sec. From this datum and the known hyperfine structure of the $3p\ ^2P_{\frac{3}{2}}$ state a recalculation of the nuclear electric quadrupole moment, taking into consideration configuration interaction, yields the value $Q=+0.149\times10^{-24}$ cm².

I. INTRODUCTION

PREVIOUS work by Jackson and Kuhn[1] and by Lew[2] on the $3p\ ^2P_{\frac{1}{2}}$ state of Al^{27} yielded values for the hyperfine separation $\Delta\nu$ of 1440±30 Mc/sec and 1500±50 Mc/sec, respectively. Although the latter value was obtained by the atomic beam magnetic resonance method, it was calculated by means of the Breit-Rabi formula from only rough measurements of the so-called low frequency line ($F=3$, $m_F=-2\rightarrow F=3$, $m_F=-3$). Attempts to observe high frequency lines, i.e., those between $F=3$ and $F=2$, were unsuccessful at that time because of difficulties with the radiofrequency oscillator in the region of 1500 Mc/sec. It has been considered worth while to make another attempt to get an accurate value for $\Delta\nu$ by the magnetic resonance method both for the sake of completeness and for the sake of permitting the calculation of a more accurate value of the nuclear electric quadrupole moment. In a recent paper, Koster[3] has shown that in gallium and, by extension, in the other elements of the same column of the periodic table, the hyperfine structure of the $^2P_{\frac{1}{2}}$ state is less perturbed by higher configurations than that of the $^2P_{\frac{3}{2}}$ state. Consequently, a more accurate value of $\langle r^{-3}\rangle$, necessary for the calculation of the nuclear quadrupole moment, is obtainable from the magnetic dipole interaction constant of the $^2P_{\frac{1}{2}}$ state than from that of the $^2P_{\frac{3}{2}}$ state.

II. APPARATUS

The atomic beam apparatus used in this experiment[4] is very similar to the one described by Davis, Nagle, and Zacharias.[5] The two inhomogeneous deflecting magnets have their gradients parallel to each other, and the ribbon which carries the radiofrequency power is oriented so that the magnetic component of the rf field has an appreciable strength only in the direction perpendicular to that of the static field. The method of generation and detection of the aluminum beam is identical with that described by Lew[2] in connection with the measurement of the metastable state of Al, except that a thorium oxide crucible is used instead of one of aluminum oxide. The thorium oxide crucible has been found to have a much longer useful life. The rf power required for the transitions is supplied by a power oscillator using a 2C39 tube with coaxial cavity tuning.[6] Frequencies are measured with a General Radio Type 720-A Heterodyne Frequency Meter in conjunction with a General Radio Type 1110-A Interpolating Frequency Standard. The accuracy of the frequency measuring system is about 1 part in 10^5.

III. RESULTS

The energy levels of an Al^{27} atom with spin 5/2 in the $^2P_{\frac{1}{2}}$ state in the presence of an external field are shown in Fig. 1. All the transitions that are allowed by the selection rules and by the geometrical arrangement

† First reported as an abstract in the Bull. Am. Phys. Soc. **27**, No. 5, 9 (1952).
* National Research Laboratories Postdoctorate Fellow.
[1] D. A. Jackson and H. Kuhn, Proc. Roy. Soc. (London) **A164**, 48 (1938).
[2] H. Lew, Phys. Rev. **76**, 1086 (1949).
[3] G. F. Koster, Phys. Rev. **86**, 148 (1952).
[4] A description of the apparatus will be given in a forthcoming paper by Lew.
[5] Davis, Nagle, and Zacharias, Phys. Rev. **76**, 1068 (1949).
[6] Airborne Instruments Laboratory, Inc., Mineola, New York, Type 124-A Power Oscillator.

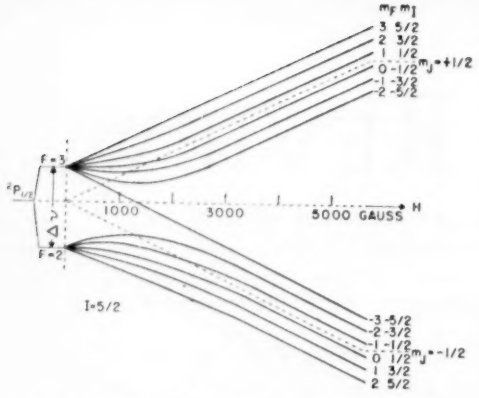

FIG. 1. Energy levels of Al^{27} in the $3p\,^2P_{\frac{1}{2}}$ state in an external magnetic field.

of the magnetic fields have been observed and are shown in Fig. 2. The observed frequencies have been plotted as a function of the external magnetic field. On extrapolating the observations to zero field, we find for the hyperfine separation:

$$\Delta\nu(F=3-F=2)=3a_{\frac{1}{2}}=1506.14\pm0.05 \text{ Mc/sec},$$
$$a_{\frac{1}{2}}=502.05\pm0.02 \text{ Mc/sec}.$$

IV. CALCULATION OF THE NUCLEAR ELECTRIC QUADRUPOLE MOMENT

In calculating the nuclear electric quadrupole moment of Al^{27}, the primary observed quantity used is the electric quadrupole interaction constant b found by Lew[2] in his study of the $^2P_{\frac{1}{2}}$ state,

$$b=18.76\pm0.25 \text{ Mc/sec}.$$

In addition it is necessary to know the quantity $\langle r^{-3}\rangle$ which is the average of the separation between the $3p$ electron and the nucleus calculated for the state $m_J=J$. For hyperfine structure arising from a single p electron, Casimir's relation between the nuclear quadrupole moment and the interaction constant is

$$Q=\frac{5hb}{2e^2\langle r^{-3}\rangle R}, \tag{1}$$

where R is a relativistic correction factor. The quantity $\langle r^{-3}\rangle$ may be evaluated from the magnetic dipole interaction constants $a_{\frac{1}{2}}$ or $a_{\frac{1}{2}}$ of the $^2P_{\frac{1}{2}}$ or $^2P_{\frac{3}{2}}$ states using the well-known relation

$$a_J=-\frac{\mu_0^2 g_I}{h}\frac{2L(L+1)}{J(J+1)}\langle r^{-3}\rangle F_J, \tag{2}$$

where F_J is another relativity correction factor. Using his observed value of $a_{\frac{1}{2}}=94.25$ Mc/sec, Lew found for the quadrupole moment the value $Q=0.155\times10^{-24}$ cm^2 (with relativity correction). If we use the $a_{\frac{1}{2}}$ found in the present work, we get $Q=0.147\times10^{-24}$ cm^2. It is obvious that the disagreement between these values of Q arises from the disagreement between the observed ratio $(a_{\frac{1}{2}}/a_{\frac{1}{2}})$ and the ratio as required by Eq. (2). Experimentally we find

$$(a_{\frac{1}{2}}/a_{\frac{1}{2}})=(502.05/94.25)=5.327, \tag{3a}$$

while from Eq. (2) we should have

$$(a_{\frac{1}{2}}'/a_{\frac{1}{2}}')=5(F_{\frac{1}{2}}/F_{\frac{1}{2}})=5.049, \tag{3b}$$

where we have used relativistic correction factors corresponding to $Z_i=Z-3=10$. As in the cases of Tl and Ga,[3,7] the disagreement is undoubtedly due to a perturbation of the ground configuration by higher configurations. In the case of Ga, Koster has shown that the perturbing configuration is mainly $4s4p5s$. It is to be expected that in Al the main perturbing configuration is correspondingly $3s3p4s$. Since the form of Koster's relations should not depend on the principal quantum number n, his Eq. (16) should hold for Al, but with values for his parameters α_0, α_1, α_2, $s(0)$, $\sigma(0)$ appropriate to Al. In simplified form, these relations may be written

$$a_{\frac{1}{2}}=a_{\frac{1}{2}}'+\epsilon, \quad a_{\frac{1}{2}}=a_{\frac{1}{2}}'-(1-\gamma)\epsilon, \tag{4}$$

where the primed quantities are the magnetic dipole interaction constants in the absence of configuration interaction, involving $\langle r^{-3}\rangle$ for the p electron[8] in accordance with Eq. (2). ϵ and $(1-\gamma)\epsilon$ are correction terms which take into consideration the degree of admixture between configurations as well as the coupling of the $3s3p4s$ states with the nucleus. In Ga, where the observed ratio $(a_{\frac{1}{2}}/a_{\frac{1}{2}})$ exceeds by 30 percent the ratio

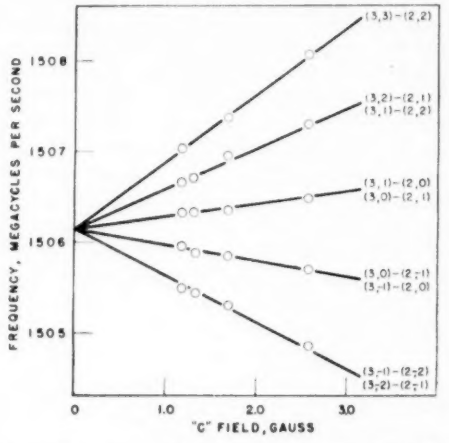

FIG. 2. Observed transitions between levels $F=3$ and $F=2$ of the $3p\,^2P_{\frac{1}{2}}$ state of Al^{27}.

[7] E. Fermi and E. Segrè, Z. Physik **82**, 729 (1933).

[8] It may be noted from Koster's equation (16) that $\langle r^{-3}\rangle$ is in very good approximation the same with or without configuration interaction. The difference between the constants a and a' is mainly due to the influence of the s electrons in the $3s3p4s$ state.

of 5.41 that is expected from Eq. (2), γ can be shown from Koster's figures to be less than one percent. In the case of Al, where the two ratios differ by only five percent, it can be estimated[9] that γ is much smaller than one percent.

Neglecting γ altogether one can evaluate ϵ and $a_{\frac{1}{2}}'$ from Eqs. (3a), (3b), and (4) and obtain

$$\epsilon = 4.30 \text{ Mc/sec}, \quad a_{\frac{1}{2}}' = 497.75 \text{ Mc/sec}.$$

Using Eq. (2), we get

$$\langle r^{-3} \rangle = 8.95 \times 10^{24} \text{ cm}^{-3}.$$

The quadrupole moment of Al then becomes

$$Q = (0.149 \pm 0.002) 10^{-24} \text{ cm}^2.$$

This we shall take as our final value of the quadrupole moment[10] because even if we had not neglected γ but had set it as high as ten percent, a figure which can be safely excluded, the last digit in Q would not be changed.

V. DISCUSSION OF $\langle r^{-3} \rangle$

The value of $\langle r^{-3} \rangle$ for the $3p$ electron given above is probably the most reliable value that can be determined by the various methods at our disposal both because of the fairly reliable theoretical foundations on which it is based and the fairly accurate experimental data. It is of interest to compare this value with that obtainable by other frequently used methods. In Table I are shown values for $\langle r^{-3} \rangle$ calculated in five different ways without relativistic or Sternheimer correction.

In column I is shown the value found above.

In column II, the value is that calculated by the use of Biermann's[11] eigenfunctions and the relation

$$\langle r^{-3} \rangle = \int_0^\infty \frac{1}{r^3} \psi_{3p}^2 r^2 dr \Big/ \int_0^\infty \psi_{3p}^2 r^2 dr.$$

[9] The estimate has been made using Biermann's Al eigenfunctions (reference 11) for the calculation of $\sigma(0)$ and $s(0)$ and assuming that the degree of admixture in Al is about one-fifth that in Ga.

[10] Without Sternheimer correction for induced quadrupole moment [Phys. Rev. **84**, 244 (1951); **86**, 316 (1952)]. This correction factor is 1.005 for Al.

[11] L. Biermann and H. Harting, Z. Astrophys. **22**, 81 (1943); L. Biermann and K. Lübeck, Z. Astrophys. **25**, 325 (1948).

TABLE I. Values of $\langle r^{-3} \rangle$ for the $3p$ electron of the configuration $3s^2 3p$ of Al in units of 10^{24} cm^{-3}, without relativistic or Sternheimer corrections.

I from hfs	II from wave functions	III from fine structure splitting (a) $Z_i = 10.0$	(b) $Z_i = 9.41$	(c) $Z_i = 10.84$
8.95	9.94	8.63	9.18	7.96

In columns III (a), (b), and (c) we give values for $\langle r^{-3} \rangle$ as calculated from the fine structure splitting of the ground configuration according to the relation

$$\delta = (3\mu_0^2/hc) \langle r^{-3} \rangle Z_i = 112.04 \text{ cm}^{-1},$$

in which Z_i has been evaluated in three different ways. Under (a), Z_i has been evaluated, as Koster has done, from the observed effective quantum numbers n^* and the fine structure splittings of the configurations $3s^2 np$, $n = 5, 6, 7$. Under (b) the value of Z_i has been obtained in the same way for $n = 3$ using the method of Crawford and Schawlow[12] for evaluating the Fermi-Segrè correction dn^*/dn. Under (c) the value of Z_i has been calculated by the use of Biermann's eigenfunction and potential for the $3p$ electron in the relation

$$Z_i = -\int_0^\infty \frac{1}{r} \frac{dV}{dr} \psi_{3p}^2 r^2 dr \Big/ \int_0^\infty \frac{1}{r^3} \psi_{3p}^2 r^2 dr.$$

It is interesting to note that the values of $\langle r^{-3} \rangle$ calculated from the Hartree wave functions of Biermann are only ten percent off from our value, while those using Z_i from semi-empirical formulas agree with ours remarkably well in view of the uncertainties in the evaluation of Z_i.

We are very grateful to Dr. P. Brix for many helpful discussions.

[12] M. F. Crawford and A. L. Schawlow, Phys. Rev. **76**, 1310 (1949).

Radiative Correction for the Collision Loss of Heavy Particles

V. Z. JANKUS
Department of Physics, Stanford University, Stanford, California
(Received December 8, 1952)

The correction to the Bethe-Bloch formula for the stopping power of fast heavy particles, due to virtual photons and the emission of real photons, has been computed using the Born approximation for the extreme relativistic case. The fractional correction increases with increasing energy of the incident particle. It is approximately 1 percent when the kinetic energy of the particle is 100 times its rest energy.

RECENTLY Jauch[1] has given an estimate for the correction, due to radiation, to the energy loss of heavy particles passing through matter. This estimate was based upon Schwinger's[2] correction to the elastic cross section due to the emission and re-absorption of virtual photons and the emission of soft real photons.

The purpose of this paper is to present a more complete calculation of the radiative correction which includes also the emission of real photons without restriction as to their energy. The results show that this is a positive correction which increases as the incident energy increases, in the relativistic region, and is quite small even at very high energy. Because of this, the more complicated low energy region is not treated here, and the calculation assumes from the start that we have heavy particles bombarding matter with a velocity $v=\beta c$ very close to that of light.

We shall find the collision loss per unit path length by taking the energy loss per collision, multiplying it by the probability of such a collision, and integrating over all possible collisions. The probability per unit path length of a collision is $n\sigma$, where n is the number of electrons per unit volume and σ is the differential scattering cross section. Since the Bethe-Heitler formula gives the differential bremsstrahlung cross section under the assumption that the scattering center is very massive compared to the particle that is scattered, it is convenient to express the energy loss per collision (in the laboratory system) in terms of quantities proper to the Lorentz frame in which the heavy particle is at rest. A Lorentz transformation will then give the energy loss in the laboratory frame:

$$\begin{aligned}\Delta\mathcal{E}' &= -\gamma[(\mathcal{E}-Mc^2)-\beta q\cos\psi] \\ &\approx \gamma q[\beta\cos\psi-\tfrac{1}{2}q/Mc^2].\end{aligned} \tag{1}$$

Here, $\mathcal{E}$, q, and ψ are the recoil energy, momentum, and direction, respectively, in the rest frame of the incident heavy particle of mass M, and $\gamma^2=1/(1-\beta^2)$.

Let $E_0=E+k$, and

$$q^2=|\mathbf{p}_0-\mathbf{p}-\mathbf{k}|^2=p_0^2+p^2+k^2-2p_0k\cos\theta_0+2pk\cos\theta -2p_0p(\cos\theta_0\cos\theta+\sin\theta_0\sin\theta\cos\phi),$$

where E_0, p_0 are the energy and momentum (expressed in energy units) of the incident electron, E, p those of the scattered electron, k the energy of the emitted photon, θ_0 the angle between photon and incident electron, θ the angle between photon and scattered electron, and ϕ the angle between planes in which θ_0 and θ lie. Then we can write the energy loss,

$$\Delta\mathcal{E}'=\frac{\gamma}{p_0}\left[k(E-p\cos\theta)+\frac{q^2}{2}\left(1-\frac{m\gamma}{M}\right)\right]. \tag{2}$$

We can shorten our integration by splitting the energy loss into two parts:

$$\frac{\gamma}{p_0}k(E-p\cos\theta) \quad\text{and}\quad \frac{\gamma}{p_0}\frac{q^2}{2}\left(1-\frac{m\gamma}{M}\right).$$

For the first part we use Sommerfeld's[3] integration, which gives the differential cross section in terms of k and q, and for the second part we use Bethe's[4] integration.

Sommerfeld[3] gives the differential bremsstrahlung cross section for Coulomb scattering in terms of k and θ_0. However, because of the symmetry of the Bethe-Heitler formula, we can write the differential cross section in terms of k and θ merely by exchanging the symbols with and without subscript zero. Doing this and using our notation, we obtain

$$\frac{Z^2e^4}{137}\frac{dk}{k}\frac{p}{p_0}\sin\theta d\theta\left\{\frac{4\mu^2\sin^2\theta}{(E-p\cos\theta)^4}-\frac{(E_0+E)^2}{E_0E(E-p\cos\theta)^2} +\left[-\frac{\mu^2\sin^2\theta}{(E-p\cos\theta)^4}+\frac{E_0^2+E^2}{E_0E(E-p\cos\theta)^2}\right] \times\log\left(\frac{4E_0^2E^2}{\mu^2k^2}\right)\right\}. \tag{3}$$

If Eq. (3) is multiplied by $(\gamma/p_0)k(E-p\cos\theta)$, the integral of the expression thus obtained converges. After the somewhat tedious term-by-term integration, we obtain as the highest term in the development in

[1] J. M. Jauch, Phys. Rev. **85**, 951 (1952).
[2] J. Schwinger, Phys. Rev. **75**, 899 (1949).
[3] A. Sommerfeld, *Atombau und Spektrallinien* (Friedr. Vieweg and Son, Braunschweig, 1939), p. 551.
[4] H. A. Bethe, Proc. Cambridge Phil. Soc. **30**, 524 (1934).

powers of γ

$$\frac{Z^2e^4}{137\mu}\left[\frac{4}{3}\log^3 2\gamma+\log^2 2\gamma-\left(3+\frac{\pi^2}{2}\right)\log 2\gamma+9+\frac{\pi^2}{3}-\frac{7}{4}\sum_{n=1}^{\infty}\frac{1}{n^3}-\sum_{n=1}^{\infty}\frac{1}{2^n n^3}\right]. \quad (4)$$

To evaluate the contribution of the first term of (2) we can use Bethe's[4] expression for the differential cross section. For $p_0-p-k\ll q\ll E_0$ this is

$$\frac{16Z^2e^4}{137}\frac{dk}{k}\frac{p}{p_0}\frac{dq}{q^3}\left\{\left(\frac{E_0}{E}+\frac{E}{E_0}\right)\frac{q}{2\mu}\frac{\sinh^{-1}(q/2\mu)}{[1+(q/2\mu)^2]^{\frac{1}{2}}}+\frac{\sinh^{-1}(q/2\mu)}{(q/2\mu)[1+(q/2\mu)^2]^{\frac{1}{2}}}-1\right\}. \quad (5)$$

Multiplying (5) by $(\gamma q^2)/(2p_0)$ and integrating over k from $k=k_{\min}$ to $k\approx E_0$ and over q from $q=0$ to $q=Q\gg\mu$ (since values of q of the order p_0-p-k do not contribute in this approximation), we get

$$\frac{8Z^2e^4}{137\mu}\left[\log\frac{E_0}{k_{\min}}\left(\log^2\frac{Q}{\mu}-\log\frac{Q}{\mu}+1\right)-\frac{3}{4}\log^2\frac{Q}{\mu}+\log\frac{Q}{\mu}-1\right]. \quad (6)$$

However, Bethe's formula is not valid for q comparable in magnitude to E_0. For those values of q we are going to use formulas derived by Schiff.[5] He shows that for large recoil momenta we can divide the differential cross section into two parts: one due to the emission of photons close to the direction of the incident electron, another due to the emission of photons close to the direction of the scattered electron. If we take his formulas (2) and (3), make the correction substituting $[\log(2E_0\cos\gamma/\mu)-\frac{1}{2}]$ for $\log(E_0/\mu)$, and then substitute $q/2E$ and $q/2E_0$ for $\cos\gamma$ in (2) and (3), respectively, we find that the differential cross section for large q is the sum of

$$\frac{8Z^2e^4}{137}\frac{dk}{k}\frac{dq}{q^3}\left(1+\frac{E^2}{E_0^2}\right)\left(1-\frac{q^2}{4E^2}\right)\left(\log\frac{q}{\mu}-\frac{1}{2}\log\frac{E_0}{E}\right)$$

and (7)

$$\frac{8Z^2e^4}{137}\frac{dk}{k}\frac{dq}{q^3}\left(1+\frac{E^2}{E_0^2}\right)\left(1-\frac{q^2}{4E_0^2}\right)\left(\log\frac{q}{\mu}-\frac{1}{2}\right),$$

where the first expression is to be taken only if $q<2E$, and the second is valid up to $q=2E_0$. Multiplying (7) by $\gamma q^2/2p_0$, integrating over q and over $k(k_{\min}<k<E_0)$, and neglecting terms that vanish as $k_{\min}/E_0$ or Q/E_0 vanish, we get

$$\frac{8Z^2e^4}{137\mu}\left[\log\frac{E_0}{k_{\min}}\left(\log^2 2\gamma-2\log 2\gamma+2-\log^2\frac{Q}{\mu}+\log\frac{Q}{\mu}-1\right)+\frac{3}{4}\log^2\frac{Q}{\mu}-\left(\frac{1}{8}+\frac{\pi^2}{6}\right)\log\frac{Q}{\mu}-\sum_{n=1}^{\infty}\frac{1}{n^3}+\frac{1}{4}+\frac{\pi^2}{12}\right]. \quad (8)$$

We have to account also for energy loss connected with the emission of virtual photons and of soft real photons. In this case the energy loss is essentially that of the elastic collision

$$\Delta\mathcal{E}'=2\mu\beta^2\gamma^2\sin^2\tfrac{1}{2}\vartheta, \quad (9)$$

where ϑ is the angle of the scattered electron (measured in the meson rest system).

The cross section of such a collision is given by Schwinger.[2] In the extremely relativistic case his formula (1) becomes

$$\delta=\frac{4}{137\pi}\left\{\log\frac{E_0}{k_{\min}}\left[\frac{\lambda^2+\frac{1}{2}}{\lambda(1+\lambda^2)^{\frac{1}{2}}}\sinh^{-1}\lambda-\frac{1}{2}\right]+\frac{-13\lambda^4-8\lambda^2+2}{12\lambda^3(1+\lambda^2)^{\frac{1}{2}}}\sinh^{-1}\lambda-\frac{1}{6}\frac{1}{\lambda^2}+\frac{7}{9}+\phi(\vartheta)\right\}, \quad (10)$$

where $\lambda=(p_0/mc^2)\sin\frac{1}{2}\vartheta\approx\gamma\sin\frac{1}{2}\vartheta$. $\phi(\vartheta)$ is given in the form of a definite integral in reference 2. The additive correction to the differential scattering cross section is $-\delta$ multiplied by the elastic cross section due to Coulomb scattering,[6]

$$\sigma_0(\vartheta)=(\pi Z^2e^4/\gamma^2\mu^2)\cot^3\tfrac{1}{2}\vartheta d\vartheta. \quad (11)$$

Multiplying $-\delta$ with σ_0 and $\Delta\mathcal{E}'$ and integrating over ϑ, we obtain the energy loss due to nearly elastic collisions,

$$\frac{8Z^2e^4}{137\mu}\left[-\log\frac{E_0}{k_{\min}}(\log^2 2\gamma-2\log 2\gamma+2)+\frac{13}{12}\log^2 2\gamma-\frac{95}{36}\log 2\gamma+\frac{829}{216}-\frac{\pi^2}{12}\right]. \quad (12)$$

In performing this integration the most troublesome term is that involving ϕ; it is evaluated exactly by changing the order of the integrations over ϑ and over the variable x of reference 2.

Adding (4), (6), (8), and (12), the division $k_{\min}$ between soft and hard photons cancels out, as it should,

TABLE I. Fractional radiative correction to the Bethe-Block formula.

γ	10	20	50	100	
$\Delta(\%)$	0.27	0.45	0.75	0.95	if $Q=\mu$
$\Delta(\%)$	0.19	0.37	0.66	0.88	if $Q=2E_0$

[4] L. I. Schiff, Phys. Rev. **87**, 750 (1952); in Eq. (4) and the two preceding expressions of this paper, a factor E_0^2 is missing in the denominator.

[6] N. F. Mott and H. S. W. Massey, *The Theory of Atomic Collisions* (Oxford University Press, London, 1949), second edition, p. 80.

and we get for the energy loss due to bremsstrahlung

$$\frac{4Z^2e^4}{137\mu}\left[\frac{1}{3}\log^3 2\gamma+\frac{29}{12}\log^2 2\gamma-\left(\frac{217}{36}+\frac{\pi^2}{8}\right)\log 2\gamma-\left(\frac{\pi^2}{3}-\frac{7}{4}\right)\log\frac{Q}{\mu}+\frac{899}{108}+\frac{\pi^2}{12}-\frac{39}{16}\sum_{n=1}^{\infty}\frac{1}{n^3}-\frac{1}{4}\sum_{n=1}^{\infty}\frac{1}{2^n n^3}\right]. \quad (13)$$

Since energy lost in elastic collisions is given by the Bethe-Bloch formula,[7]

$$-\frac{dw}{dx}=n\frac{4\pi Z^2e^4}{\mu\beta^2}\log\frac{2\mu\beta^2\gamma^2}{I}, \quad (14)$$

we get for the fractional radiative correction for an infinitely heavy particle

$$\Delta=\frac{1}{137\pi\log(2\mu\beta^2\gamma^2/I)}[0.333\log^3 2\gamma+2.42\log^2 2\gamma-7.26\log 2\gamma-1.54\log(Q/\mu)+6.18]. \quad (15)$$

[7] W. Heitler, *The Quantum Theory of Radiation* (Oxford University Press, London, 1944), second edition, p. 218.

Unfortunately, the division Q between small and large momenta does not quite cancel out of the final formula, but Δ depends only logarithmically on Q so that it seems to be reasonable to expect that a reliable result would be obtained by choosing Q somewhere between the extremes $\mu<Q<2E_0$. However, since the Bethe-Heitler formula does not take into account the recoil of the scattering center, formula (15) may be in error when $m\gamma$ is larger than or of the order of M.

Taking collisions of pi-mesons ($M=270m$) with argon atoms as an example, we obtain the values in Table I for the percent radiative correction. The correction is positive, as one would expect, since mesons are losing some additional energy to radiation. Also, the correction is small for mesons of available energy.

Radiation observed in the laboratory should not show a marked anisotropy and the maximum energy of the emitted photons should be of the order of $\frac{1}{2}$ Mev, except for a few hard photons close to the direction of the incident heavy particle.

The author is indebted to Professor L. I. Schiff for suggesting this problem and for his continued interest and advice throughout the solution.

PHYSICAL REVIEW VOLUME 90, NUMBER 1 APRIL 1, 1953

Radiations of Pu^{243}

D. W. Engelkemeir, P. R. Fields, and J. R. Huizenga
Chemistry Division, Argonne National Laboratory, Lemont, Illinois
(Received December 22, 1952)

The radiations of Pu^{243} were studied with beta- and gamma-scintillation spectrometers alone and in coincidence. An incomplete disintegration scheme is deduced which leads to a total beta-disintegration energy of 560 kev. A half-life of 4.98±0.02 hours was observed.

INTRODUCTION

THE radiations of Pu^{243} were first studied[1] by absorption measurements which indicated a maximum beta-energy of 0.5 Mev. O'Kelley and Orth[2] reported a preliminary value of 0.39 Mev for the maximum beta-energy and gammas of 0.095 and 0.12 Mev. The purpose of this research was to determine the total decay energy of Pu^{243}. Therefore, in addition to examining the beta- and gamma-spectra, beta-gamma and gamma-gamma coincidence measurements were undertaken.

SAMPLE PREPARATION

Samples of a nitrate solution of plutonium enriched in Pu^{242} were evaporated to dryness in a quartz tube and irradiated in the thimble of the Argonne Heavy Water Reactor for approximately 15 hours.

Immediately after irradiation the plutonium was purified from all extraneous activity with a resin column, a series of precipitations, and solvent extractions. Several irradiations were made to complete the experiments reported.

APPARATUS

Scintillation spectrometers were employed for the measurement of the beta- and gamma-ray spectra. Thallium-activated sodium iodide crystals $1\frac{1}{4}$ inches in diameter and $\frac{1}{2}$ inch thick were used for gamma-detection, and an anthracene crystal of the same diameter and $\frac{1}{4}$ inch thick was used for the beta-counter. The sodium iodide crystals were sealed in cylindrical 17 ST aluminum cups turned to a thickness of 0.013 inch on the end facing the sample and closed on the other end with a Pyrex window. A similar assembly was used for

[1] Sullivan, Pyle, Studier, Fields, and Manning, Phys. Rev. **83**, 1267 (1951).
[2] G. D. O'Kelley and D. A. Orth, quoted by Thompson, Street, Ghiorso, and Reynolds, Phys. Rev. **84**, 165 (1951).

the anthracene crystal except that the aluminum window was 0.001 inch thick. Short Lucite light pipes coupled the crystals to RCA type 5819 photomultipliers, which were attached to cathode follower preamplifiers. After further amplification the pulses from each detector were fed into a single channel differential pulse-height analyzer (designed by Robert K. Swank of this laboratory) and also into a coincidence circuit having a resolving time, $2T$, of 0.14 microsecond. The outputs of the two analyzers and the coincidence circuit were mixed in a threefold coincidence circuit with a resolving time of about 4 microseconds.

Photopeak widths of 11 percent (full width at half-height) for the 661-kev gamma of Ba^{137} and conversion electron peak widths of 15 percent for the 622-kev Ba^{137} conversion electrons were observed.

GAMMA-SPECTRUM

In order to obtain the gamma-spectrum of Pu^{243} free from interference from the radiations emitted by the alpha-emitting plutonium isotopes in the sample, the spectrum of gammas in coincidence with all betas with energies greater than 100 kev was measured. A beryllium absorber weighing 235 mg/cm² was placed over the gamma-counter. This, added to the 0.013-inch aluminum window covering the crystal, was sufficient to absorb betas with energies less than 0.8 Mev. The 0.001-inch window on the beta-counter was sufficient to absorb the alpha-particles. Samples weighing less than 0.1 mg, spread over an area of 2 cm² on a thin mica sheet, were placed $\frac{1}{8}$ inch from the face of the sodium iodide crystal and $\frac{5}{16}$ inch from the anthracene crystal. Gamma-energy calibration was made with the Ag^{109} gamma, for which the value of 89 kev given by Bradt *et al.*[3] was used rather than 87 kev given by Siegbahn *et al.*[4] since critical absorption measurements by one of us (D.W.E.) have shown that its energy lies between the K absorption edges of lead and bismuth or between 88.2 and 90.6 kev. The gamma-spectrum obtained is shown in Fig. 1, curve A. Prominent peaks at 19 kev and 85 kev are observed, in addition to a low peak at 55 kev which is attributed to the escape of iodine K x-rays following photoelectric absorption of the 85-kev gamma. The peak at 19 kev is probably due to L x-rays of americium. When the coincidence circuit was not used, the spectrum shown in Fig. 1, curve B, was obtained. The only observable difference is the large excess of L x-rays arising from the alpha-emitting plutonium isotopes.

If the entire 19-kev peak in the coincidence spectrum is assumed to be due to L x-rays from the conversion of the 85-kev gamma, the L conversion coefficient may be calculated from the ratio of the areas under the two peaks of curve A, Fig. 1. The observed intensity of the x-rays must be corrected for absorption and for the fluorescence yield. Correction for absorption is complicated by the fact that the L x-rays are distributed over such a wide range of energies.

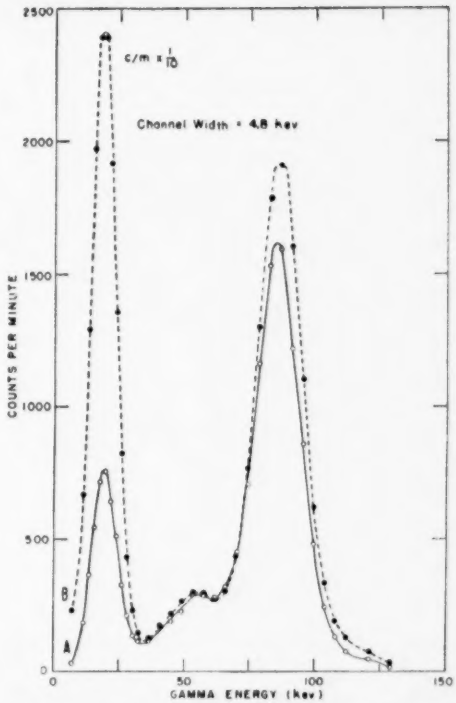

FIG. 1. Gamma-spectrum of Pu^{243}. A. Beta (>100-kev)—gamma coincidences; B. single gamma counts.

In order to correct for absorption the relative intensities of the different L x-ray lines were calculated by assuming that equal amounts of conversion occurred in the three L subshells. The fluorescence yields for the three L subshells were obtained by extrapolating the fluorescence yield and Coster Kronig coefficient data given by Kinsey[5] to $Z=95$. The relative intensities of the x-rays arising from vacancies in each of the L subshells were assumed to be the same as were observed in uranium by Compton and Allison.[6] In calculating the transmission of the x-rays through the absorber it was necessary to calculate the transmission as a function of angle through the absorber and then to integrate over the entire solid angle subtended by the detector (0.40 of 4π). An over-all efficiency of 0.062 was obtained for the number of L x-rays detected per L vacancy.

The efficiency is not very sensitive to assumptions as to the relative amounts of conversion in the three L subshells. The efficiency for the 85-kev gamma was calculated to be 0.38.

After application of these corrections, the ratio of L conversions to unconverted gammas was found to be

[3] Bradt, Gugelot, Huber, Medicus, Preiswerk, Scherrer, and Steffen, Helv. Phys. Acta **20**, 153 (1947).
[4] Siegbahn, Kondaiah, and Johansson, Nature **164**, 405 (1949).
[5] B. B. Kinsey, Can. J. Research **A26**, 404 (1948).
[6] A. H. Compton and S. K. Allison, *X-Rays in Theory and Experiment* (D. Van Nostrand Company, Inc., New York, 1935), pp. 643–645.

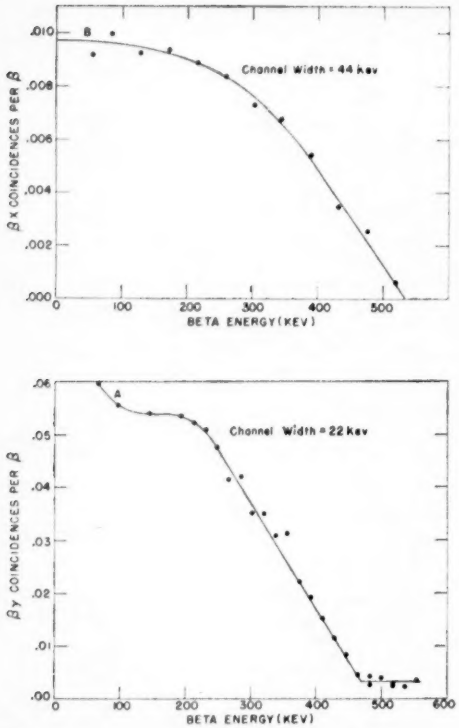

FIG. 2. Coincidences per beta as a function of beta-energy. A. Beta—85-kev gamma coincidences; B. beta—L x-ray coincidences.

1.3. This value is probably reliable to within 30 percent and represents an upper limit to the L conversion coefficient of the 85-kev gamma since some of the x-rays may arise from other transitions.

BETA- AND BETA-GAMMA COINCIDENCE SPECTRA

The total beta-spectrum and the beta-spectrum in coincidence with the 85-kev gamma were measured with the anthracene scintillation spectrometer. The spectrometer was calibrated with the 622-kev conversion electron line of Ba^{137} and was used with a channel width of 22 kev. Alpha-particles from the other plutonium isotopes were absorbed in the 0.001-inch aluminum window to prevent interference with the beta-measurements. The pulse-height selector on the gamma pulse-height analyzer was set to accept only those pulses between 65 kev and 130 kev in height in order to count nearly all of the 85-kev gamma-pulses and to eliminate any x-ray pulses. In Fig. 2, curve A, the number of beta-gamma coincidences per beta is plotted *vs* the beta-energy. The value of $\beta\gamma/\beta$ remains relatively constant up to 200 kev and then drops to a much lower, constant value at 470 kev. This behavior indicates that the 85-kev gamma is coincident with a group of beta-particles having a maximum energy of about 470 kev. The small number of coincidences observed above 470 kev may be due to a slight impurity.

Figure 3 shows the Kurie plots of the total beta-spectrum and of the spectrum in coincidence with the 85-kev gamma. The total beta-spectrum exhibits a continuous curvature which does not permit an accurate estimation of the upper energy limit. The coincidence spectrum does show a fairly straight portion which intercepts the energy axis at 455 kev. To this energy must be added the energy loss in the aluminum absorber,[7] 13 kev, to get the maximum beta-energy of 468 kev. In order to obtain the maximum beta-energy of the total beta-spectrum, the lower energy component was subtracted from the total spectrum in arbitrary amounts until the residual spectrum gave a straight line Kurie plot. In Fig. 3, the observed coincidence spectrum was multiplied by 8 and then subtracted from the total spectrum to give a spectrum having an observed end-point energy of 553 kev which, when corrected for energy loss in the aluminum absorber, gives a maximum beta-energy of 566 kev.[8] If the spectra are assumed to have allowed shapes, this breakdown of the spectrum assigns 60 percent of the betas to the 566-kev branch and 40 percent to the 468-kev branch.

In order to establish whether or not the 566-kev beta-branch is followed by a highly converted transition, beta—L x-ray coincidences were studied as a function of beta-energy. The pulse-height selector associated with the gamma-detector was set to accept only pulses corresponding to gamma-energies between 11 and 27 kev and, thus, counted almost all of the L x-rays and prac-

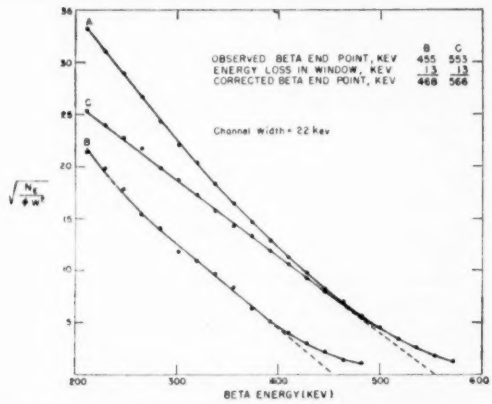

FIG. 3. Kurie plots of Pu^{243} beta-spectra. A. Total beta-spectrum; B. betas in coincidence with 85-kev gamma; C. subtraction of coincidence spectrum from total beta-spectrum.

[7] H. Bethe, *Handbuch der Physik* (Springer-Verlag, Berlin, 1933), Vol. XXIV–1, pp. 519–523.

[8] Multiplication of the coincidence spectrum by eight before subtraction from the total spectrum is equivalent to assuming a detection efficiency of 0.125 for the 87-kev gamma transition, whereas the calculated efficiency, taking into account the conversion coefficient and the fraction of the total 87-kev gamma-spectrum accepted by the analyzer, equals 0.16. The end point of the high energy component is not significantly altered if the subtraction is based upon the calculated detection efficiency.

tically none of the 85-kev gammas. The plot of beta—L x-ray coincidences per beta as a function of beta-energy is shown in Fig. 2, curve B. The steady decrease as the beta-energy is increased indicates clearly that the 566-kev beta is not followed by a gamma-transition highly converted in the L shell. If the 566-kev beta were followed by a gamma-transition completely converted in the L shell, the ratio of $\beta X/\beta$ would be expected to approach a limiting value of 0.06 at high beta-energies. The value of 0.01 observed at low beta-energies is consistent with the assumption that most of the L x-rays are due to conversion of the 85-kev gamma.

Since the 566-kev beta is not in coincidence with the 85-kev gamma and since no other gamma of appreciable intensity is present, the 566-kev beta must represent the total decay energy unless it is followed by a gamma of lower energy than the L binding energies of americium. It is plausible to assume that the 85-kev gamma-transition also proceeds to the ground state of Am^{243} since the sum of the energies of the gamma-transition and the 468-kev beta in coincidence with it equals 553 kev, which is in fair agreement with 566 kev.

GAMMA—85-KEV GAMMA COINCIDENCE SPECTRUM

The spectrum of gammas in coincidence with the 85-kev gamma was measured with two sodium iodide scintillation spectrometers in coincidence. Counter B was $\frac{9}{32}$ inch from the sample and was set to accept pulses from 70 to 89 kev in height. This setting was held fixed and was chosen in order to discriminate against higher energy gammas and at the same time to maintain a high counting efficiency for the 85-kev gamma. An aluminum absorber weighing 713 mg/cm^2 was placed between the sample and counter B. Counter A was $\frac{5}{32}$ inch from the sample and was covered with 71.9 mg/cm^2 of beryllium in addition to the 0.013-inch 17 ST aluminum window in order to absorb the betas. The analyzer for counter A was used with a 5.4-kev channel

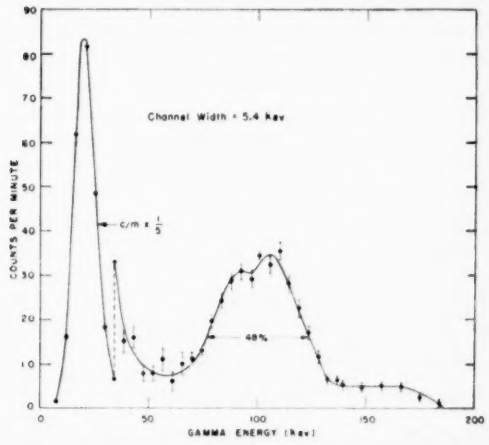

FIG. 4. Pu^{243} 85-kev gamma-gamma coincidence spectrum.

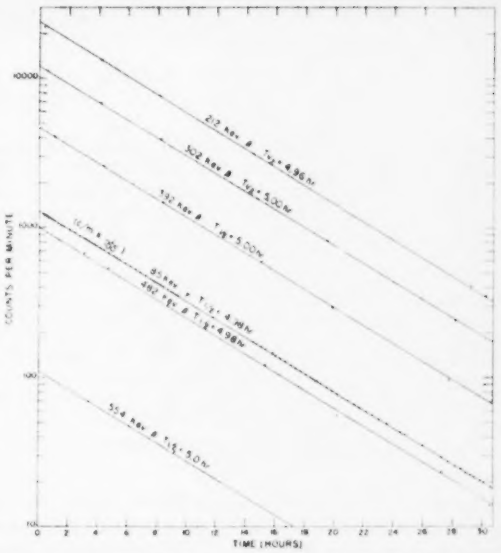

FIG. 5. Decay of the 85-kev gamma and of selected points on the beta-spectrum of Pu^{243}.

whose position was varied to obtain the gamma-spectrum coincident with the gammas detected in counter B.

Figure 4 shows the spectrum obtained. In addition to a prominent line at the position expected for L x-rays, a low intensity broad unresolved peak is obtained at about 100 kev and a low broad continuum extending to 185 kev. The peak at 100 kev must be due to two or more gammas since its width is 48 percent as compared with 25 percent obtained for the 85-kev peak in Fig. 1. The peak shape is consistent with that expected for two gammas of nearly equal intensities with energies of about 92 kev and 107 kev. The high energy shoulder could be caused by a single gamma with an energy of about 160 kev.

If every 85-kev gamma were in coincidence with a completely L converted gamma, the integral number of 85-kev gamma—L x-ray coincidences per 85-kev gamma detected in counter B should equal the detection efficiency of counter A for L vacancies of 0.06 (see section on gamma-spectrum); the observed ratio is 950/48 000 $=0.020$, thus indicating that the 85-kev gamma is in coincidence with L vacancies one-third of the time. Similarly, if every 85-kev gamma were in coincidence with an unconverted 100-kev gamma, the integral number of gamma-gamma coincidences per gamma detected in counter B should be approximately equal to the geometrical efficiency of counter A or 0.38; the observed ratio of 280/48 000$=0.0058$ indicates that very few unconverted gammas with energies of about 100 kev are in coincidence with the 85-kev gamma. It follows from this that the gamma-transitions responsible for the 85-kev gamma—L x-ray coincidences must have high conversion coefficients. Since 566-kev

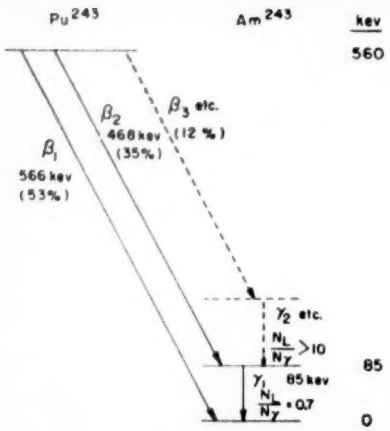

FIG. 6. Proposed decay scheme of Pu^{243}.

beta—L x-ray or gamma-coincidences were not observed, and since an L vacancy accompanies the 85-kev gamma only one-third of the time, these highly converted gamma-transitions must precede the 85-kev gamma. This implies that lower energy beta-groups are present with a total abundance at least one-third as great as that of the 468-kev beta or about 12 percent.

The L conversion coefficient of 1.3 obtained by assuming that all of the L x-rays arise from the conversion of the 85-kev gamma must be corrected for the L x-rays observed to be in coincidence with the 85-kev gamma. Upon making this correction, the conversion coefficient is lowered to 0.72. This value is still an upper limit since L x-rays may be present which are not in coincidence with the 85-kev transition.

HALF-LIFE OF Pu^{243}

The decay curves of the 85-kev gamma and of selected points on both branches of the beta-spectrum of Pu^{243} are shown in Fig. 5. The 85-kev gamma-decay curve was obtained by selecting a channel width great enough to accept almost the entire photopeak so that slight fluctuations in pulse height would not affect the counting rate appreciably. Decay curves of the beta-gamma coincidences and of gamma-gamma coincidences also showed a 5-hour half-life. The best value for the half-life is considered to be 4.98 ± 0.02 hours.

DISCUSSION OF RESULTS

A disintegration scheme which agrees with the experimental observations is shown in Fig. 6. The dotted lines represent transitions which are inferred from the observation of 85-kev—L x-ray coincidences. The transitions marked γ_2, etc., may be any combination of the gammas observed in the gamma-gamma coincidence measurements or some other highly converted gamma which was not observed. It is believed that the total disintegration energy of 560 kev cannot be in error by more than 30 kev. A total disintegration energy of approximately 0.6 Mev is expected on the basis of the following energy cycle, where the alpha-energy of Pu^{243} is estimated as *ca* 4.7 Mev from alpha-decay systematics.

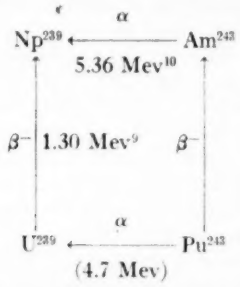

The conversion coefficient of the 85-kev gamma may be compared with the theoretical values calculated by Gellman *et al.*[11] An interpolation of their data for uranium gives values of the total L conversion coefficient of 0.17 for electric dipole, 10 for magnetic dipole, and 30 for electric quadrupole. The observed upper limit of 0.7 indicates that the transition is probably electric dipole. Measurement of the relative intensities of the L conversion electron lines should permit an unambiguous assignment since the relative values of the L_1, L_2, and L_3 conversion coefficients calculated by Gellman *et al.*[11] vary markedly with the kind of transition.

A calculation of the logft values for the two main beta-transitions gives 6.0_8 for the ground-state transition and 5.9_4 for the transitions to the excited state, thus indicating that both transitions are first forbidden with change of parity and $\Delta I=0$ or ±1. This is in agreement with the strong spin-orbit coupling single particle model[12] which predicts for the ground-state transition, $g_{7/2}\rightarrow f_{7/2}$. Possible spin assignments for the first excited state are $f_{5/2}$, $f_{7/2}$, $h_{9/2}$, which would lead to magnetic dipole radiation to the ground state. The most probable assignment to the first excited state on the basis of the single particle model would be $f_{5/2}$. No spin and parity assignments are possible which will allow electric dipole radiations and at the same time assign equal forbiddenness to the two beta-transitions. Further experiments, particularly with magnetic focusing beta-ray spectrometers, will be needed to elucidate the details of the decay scheme.

The authors wish to thank M. S. Freedman for helpful discussions and Gray L. Pyle for assistance in some of the counting.

[9] Huizenga, Magnusson, Freedman, and Wagner, Phys. Rev. **84**, 1264 (1951).
[10] G. T. Seaborg (private communication).
[11] Gellman, Griffith, and Stanley, Phys. Rev. **85**, 944 (1952).
[12] Maria Goeppert Mayer, Phys. Rev. **75**, 1969 (1948); **78**, 16 (1950).

Effects of Radioactive Disintegrations on Inner Electrons of the Atom

J. S. LEVINGER
Louisiana State University, Baton Rouge, Louisiana
(Received November 28, 1952)

The probability that nuclear emission of an alpha- or beta-particle causes ionization of a K or L electron of the atom is calculated by time-dependent perturbation theory using nonrelativistic Coulomb wave functions. Beta-emission (electron or positron) causes an ionization probability of $0.64/Z^2$ and $2.1/Z^2$ per beta in the K and L shells, respectively. (The K shell result agrees with Migdal and Feinberg; the L shell result disagrees with Migdal.) The use of nonrelativistic wave functions causes an appreciable underestimate in the ionization probability for K electrons of heavy atoms. Screening corrections for the use of Coulomb wave functions would increase the ionization probabilities by a factor of 1.4 for K electrons and by a factor of 3 or 4 for L electrons. Migdal's result for dipole electronic transitions caused by nuclear alpha-decay are reduced by a factor 25 (for the case of Po^{210}) because of nuclear recoil. Quadrupole matrix elements such as $(r^{-3})_{n,n'd}$ are evaluated by a new method developed by H. A. Bethe. This method uses the Sommerfeld integral representation for the continuum $n'd$ wave function. Quadrupole transitions are negligible for K electrons, but are the predominant effect for L electrons. The calculated ionization probabilities for Po^{210} are 10^{-7} and 1.1×10^{-4} per alpha in the K and L shells, respectively. For alpha-decay, screening corrections and higher multipole transitions would both increase the ionization probability for L electrons. Madansky and Rasetti's measurements of photons from RaE are consistent with our calculations, but Bruner's measurements on Sc^{44} are not. Grace's interpretation of K x-rays from Po^{210} is consistent with the calculation of this paper, while Barber and Helm's interpretation is not. Rubinson and Bernstein find 8 times the L x-ray yield from Po^{210} we have calculated for Coulomb wave functions.

I. INTRODUCTION

WHEN a radioactive nucleus disintegrates by emission of an alpha- or beta-particle, the radioactive disintegration perturbs the electrons of that atom, and may cause electronic excitation to an unoccupied discrete level, or ionization to the continuum. A hole in an inner electronic shell produced in this manner will be filled either by the emission of a characteristic x-rays, or by the emission of an Auger electron. Similar processes may be caused by other types of nuclear disintegrations: K-capture, neutron emission (or nuclear recoil due to neutron scattering), or fission. The probability of electronic excitation or ionization can be calculated by time-dependent perturbation theory. In this paper we shall calculate the probability of ionization for K or L electrons, for the cases of nuclear beta-decay (electrons or positrons) and nuclear alpha-decay.

We shall not concern ourselves here with calculations of nuclear decay processes involving interaction with the electromagnetic field, such as internal conversion or emission of inner bremsstrahlung. Frequently internal conversion masks the processes that we wish to discuss in this paper, since it may occur with very much higher probability. The emission of inner bremsstrahlung makes more difficult the detection of characteristic x-rays produced in beta-decay.

Recently Madansky and Rasetti[1] and Novey[2] have studied electromagnetic radiation emitted in P^{32} and in RaE beta-decay. The characteristic sulfur x-ray following P^{32} beta-decay is of too low an energy to be detected in this experiment. The RaE measurements show that characteristic K x-rays of Po are less frequent than inner bremsstrahlung: the upper limit for K x-rays is about one photon per 10^4 betas. However, Bruner[3] finds a very much larger yield of negative electrons associated with the positron and K-capture activity of Sc^{44}, in contradiction to the very low negative electron yield found by Porter and Hotz[4] for Fe^{55} (K-capture).

Characteristic lead K, L, and M x-rays associated with the alpha-decay of Po^{210} have been studied by Curie and Joliot,[5] Rubinson and Bernstein,[6] Grace *et al.*,[7] Barber and Helm,[8] and Riou.[9] The observed yields of photons per alpha are: about 10^{-6} for the K shell,[7-9] about 3×10^{-4} for the L shell,[5,6,9] and considerably higher for the M shell.[5] On the other hand, Macklin and Knight[10] found a very much higher yield of L x-rays associated with the alpha-decay of U^{234}.

Calculations of the probability of ionization of K, L, and M electrons in beta- and alpha-decay were first made by Migdal.[11] Migdal treats beta-decay as an example of a sudden perturbation, and alpha-decay as an example of an adiabatic perturbation. Independently Feinberg[12] calculated the effect of beta-decay on K electrons obtaining agreement with Migdal's results based on the sudden change of the nuclear charge. The present author also considered these questions independently some years later,[13] and agreed with the common Migdal-Feinberg result for ionization of K electrons in beta-decay; but there were numerical

[1] L. Madansky and F. Rasetti, Phys. Rev. **83**, 187 (1951); and Phys. Rev. **89**, 679 (1953).
[2] T. B. Novey, Phys. Rev. **86**, 619 (1952) and Phys. Rev. **89**, 672 (1953).
[3] J. A. Bruner, Phys. Rev. **84**, 282 (1951).
[4] F. T. Porter and H. P. Hotz, Phys. Rev. **89**, 903A. 1953.
[5] I. Curie and F. Joliot, J. phys. et radium **2**, 20 (1931).
[6] W. Rubinson and W. Bernstein, Phys. Rev. **86**, 545 (1952).
[7] Grace, Allen, West, and Halban, Proc. Phys. Soc. (London) **A64**, 493 (1951).
[8] W. C. Barber and R. H. Helm, Phys. Rev. **86**, 275 (1952).
[9] M. Riou, J. phys. et radium **13**, 244 (1952).
[10] R. L. Macklin and G. B. Knight, Phys. Rev. **72**, 435 (1947).
[11] A. Migdal, J. Phys. (U.S.S.R.) **4**, 449 (1941).
[12] E. L. Feinberg, J. Phys. (U.S.S.R.) **4**, 424 (1941).
[13] J. S. Levinger, Ph.D. thesis, Cornell University, 1948 (unpublished).

disagreements for the L shell. The ionization probability due to beta-decay has been considered recently by Schwartz,[14] Winther,[15] and Serber and Snyder.[16] Schwartz's numerical results for the L shell ionization probability agree with those given in this paper; he has also extended the calculations to the M shell. Winther calculates the charge distribution of Li^6 recoils from He^6 beta-decay, using helium and lithium atomic wave functions. His results are the same order of magnitude as those of this paper, which apply to hydrogen-like wave functions for inner electron of heavier atoms. Serber and Snyder calculate the average energy expended in ionizing the atom as the change in the electrostatic energy of the nucleus at the center of the electronic charge cloud. Their result of about 100 ev for positron or beta-decay in heavy atoms is larger than the energy expended in ionizing K and L electrons as calculated in this paper. We use their result of excitation energy 2 Rydbergs (27.2 ev) per closed shell to check our calculations of the ionization and excitation for the K shell. Recently Primakoff and Porter[17] have calculated the electron ionization due to K capture.

There was a basic diagreement between the methods used by Migdal and by the present author[13] (the latter being incorrect) in the calculations on effects of alpha-decay. Our present methods for alpha-decay represent a modification and extension of Migdal's work. The dipole transition probability is greatly reduced due to nuclear recoil. The quadrupole transition probability is of great significance for the L shell. Our theoretical results are in order of magnitude agreement with the experimental yields of x-rays.

In Sec. II we discuss the case where the perturbation due to the nuclear decay takes place in a time small compared to the periods of the atomic electrons considered. This is represented in nature by beta-decay. In Sec. III we consider screening corrections to the results of Sec. II, which are based on hydrogenic wave functions. In Sec. IV we discuss the case where the perturbation takes place slowly, i.e., adiabatically, as compared to the periods of the atomic electrons being considered. This case is represented in nature by the alpha-decay of Po, if we consider the K or L electrons. Quadrupole matrix elements such as $(r^{-3})_{1s,n'd}$ are calculated by a new method developed by H. A. Bethe. In Sec. V we estimate the accuracy of our approximations for alpha-decay. In the last section we shall compare our calculations with experimental data.

II. SUDDEN PERTURBATION: BETA-DECAY

When a nucleus of atomic number Z decays by emission of a beta-particle, which has a velocity very much larger than that associated with the orbital electrons, the orbital electrons suddenly find themselves in the field of a nucleus of charge $Z+1$. (For positron decay the change is from Z to $Z-1$.) To simplify our formulas we shall limit ourselves to the case of Z much larger than one, in which case beta and positron emission give very nearly the same result, and will be considered together. The amplitude for an orbital electron initially in state 0 to end in state n due to a sudden perturbation is

$$a_{0n}=\int \psi_n^*(Z+1,r)\psi_0(Z,r)d^3r. \tag{1}$$

Here we explicitly write the atomic number of the nucleus to designate the wave functions before and after the beta-decay.

This formulation was first proposed by Migdal.[11] Feinberg[12] discusses the effects of beta-decay on the orbital electrons in some detail and finds that the "shaking term" corresponding to Eq. (1), is in general much larger than the term for direct collisions. (The latter is analogous to the ionization of an atom by an external fast electron.) He also shows that relativistic effects and exchange effects are small. We shall discuss the approximations in Sec. V; in this section we shall evaluate Eq. (1) using nonrelativistic wave functions for a Coulomb field. In this evaluation we shall repeat some of Migdal's and Feinberg's work, as their papers are not sufficiently well known.

First, let us find an upper limit for the sum of the probability of excitation to all discrete states, and of ionization to the continuum. We shall find the probability $P_{00}=|a_{00}|^2$ that the electron remain in the initial state. The difference $1-P_{00}$ represents the probability of excitation to *all* discrete states, together with ionization to continuum states. It therefore overestimates the probability of losing an electron from state 0, since some transitions to discrete states are forbidden by the Pauli exclusion principle. Still, it gives us an upper limit which is the right order of magnitude. Also it is the starting point for our calculations of screening effects.

For a K electron we have, using hydrogenic wave functions,

$$a_{00}=4Z^{\frac{3}{2}}(Z+1)^{\frac{3}{2}}\int_0^\infty \exp(-Zr)\exp[-(Z+1)r]r^2dr$$

$$=\{[(Z+\tfrac{1}{2})^2-\tfrac{1}{4}]/(Z+\tfrac{1}{2})^2\}^{\frac{3}{2}}\approx 1-3/8Z^2. \tag{2}$$

(The angular integrations give unity. Throughout this paper we use Hartree atomic units,[18] e.g., we measure distances in units of the Bohr radius.) The upper limit for loss of an electron from the $1s$ state is

$$1-|a_{00}|^2=3/4Z^2. \tag{3}$$

We have neglected unity in comparison with Z, so Eq. (3) holds for either beta or positron emission. To find

[14] H. M. Schwartz, J. Chem. Phys. **21**, 45 (1953).
[15] A. Winther, Kgl. Danske Videnskab. Selskab, Mat.-fys. Medd. **27**, 3 (1952).
[16] R. Serber and H. S. Snyder, Phys. Rev. **87**, 152 (1952).
[17] H. Primakoff and E. T. Porter, Phys. Rev. **89**, 903A (1953).
[18] H. A. Bethe, *Handbuch der Physik* (J. Springer, Berlin, 1933), Vol. 24/1, Introduction.

the probability that a hole is produced in the K shell, one considers the perturbation acting separately on each of the two K electrons, and multiplies the above result by 2. (See Feinberg for a detailed justification.)

We have made analogous calculations for the $2s$ and $2p$ electrons of the L shell: we find an upper limit of $2.25/Z^2$ per $2s$ electron, and $1.25/Z^2$ per $2p$ electron.

Let us now calculate the probability that a K electron end up in a continuum state. This will be a lower limit for the production of holes in the K state; and should be a good approximation to it, as the more likely transitions to discrete states are forbidden by the Pauli principle. This calculation can be done in several different equivalent ways; we shall follow the method used by Feinberg.[12] We use an integral representation for the hydrogenic continuum wave functions[19] for an s electron (the angular integrations give the selection rule $\Delta l=0$):

$$R_W=-2Z^{\frac{1}{2}}(2kr)^{-1}(1-e^{-2\pi n'})^{-\frac{1}{2}}(2\pi)^{-1}$$
$$\times\oint e^{-2ikr\xi}(\xi+\tfrac{1}{2})^{-in'-1}(\xi-\tfrac{1}{2})^{in'-1}d\xi. \quad (4)$$

The integral over ξ is taken around a contour that encloses the branch points at $\xi=\frac{1}{2}$ and $\xi=-\frac{1}{2}$.

This wave function is normalized per unit energy. Here

$$n'=Z/k=(E_K/W)^{\frac{1}{2}}. \quad (5)$$

The binding energy of a K electron is, in atomic units ($e^2/a_0=27.2$ ev),

$$E_K=\tfrac{1}{2}Z^2. \quad (6)$$

The positive energy W of the continuum electron is given by

$$W=\tfrac{1}{2}k^2=\tfrac{1}{2}Z^2/n'^2, \quad (7)$$

where k is the wave number.

We use the continuum wave function of Eq. (4) in Eq. (1) for the transition amplitude. [For convenience we use $\psi_0(Z+1,r)$, and $\psi_n{}^*(Z,r)$.]

$$a_{0n'}=NJ, \quad (8)$$

$$N=4Z(1-e^{-2\pi n'})^{-\frac{1}{2}}, \quad (9)$$

$$J=2\pi^{-1}\int\oint e^{-(Z+1)r}e^{-2ikr\xi}(2kr)^{-1}$$
$$\times(\xi+\tfrac{1}{2})^{-in'-1}(\xi-\tfrac{1}{2})^{in'-1}d\xi r^2dr. \quad (10)$$

The double integral J is evaluated as was done by Sommerfeld in calculations of the atomic photoeffect,[20] i.e., we first perform the r integration,

$$\int_0^\infty e^{-\beta r}r dr=1/\beta^2, \quad (11)$$

where

$$\beta=2ik(\xi-in'/2-i/2k). \quad (12)$$

[19] Reference 18, Eq. (4.22). Note that we have corrected a misprint by multiplying by $2^{\frac{1}{2}}$. See Feinberg, reference 12.
[20] Reference 18, Sec. 47; also see reference 12.

The contour for the ξ-integration is transformed to infinity enclosing the pole at $\beta=0$. The result is 2π times the residue at the double pole at $\beta=0$, or $\xi=in'/2+i/2k$.

$$J=(2k)^{-3}\{(\xi^2-\tfrac{1}{4})^{-2}[(\xi-\tfrac{1}{2})/(\xi+\tfrac{1}{2})]^{in'}$$
$$\times(in'-2\xi)\}_{\xi=in'/2+i/2k} \quad (13)$$
$$=2k^{-4}(n'^2+1)^{-2}\exp(-2n'\cot^{-1}n').$$

(Note that we check the orthogonality of $\psi_0(Z)$ and $\psi_{n'}{}^*(Z)$ if we put $\xi=in'/2$ in the $(in'-2\xi)$ term. However, we can use this approximation for ξ in the other terms, and we shall also put $Z+1=Z$ in the term N.) We combine this value for J with the normalization factor of Eq. (9), and square the amplitude, in order to find the transition probability in terms of the energy W of the continuum electron:

$$P(n')dW=2^6Z^{-4}(1-e^{-2\pi n'})^{-1}n'^8(n'^2+1)^{-4}$$
$$\times\exp(-4n'\cot^{-1}n')dW, \quad (14)$$

where the variable n' is given by Eq. (5). The emitted electron is likely to have a value around $n'=1$, or continuum energy $W=$binding energy E_K, as is shown in Fig. 1 where we plot $P(W)$ *vs* W. The probability of ionization to all continuum states is found by numerical integration of Eq. (14), using $dW=-Z^2dn'/n'^3$ [see Eq (7)]. We find

$$P=\int_0^\infty P(n')dW=0.32/Z^2. \quad (15)$$

The probability of ionization as a function of n', and its integral for the ionization probability per K electron per β-decay, is in agreement with the calculations of Migdal and of Feinberg.

The calculations for ionization of $L_{\rm I}$ electrons and $L_{\rm II}$ or $L_{\rm III}$ electrons is performed in an analogous manner. For $L_{\rm I}$ electrons the amplitude is

$$(a_{0n'})_1=N_1J_1, \quad (16)$$

$$N_1=2^{\frac{1}{2}}Z^2(1-e^{-2\pi n'})^{-\frac{1}{2}}, \quad (17)$$

$$J_1=(2\pi)^{-1}(2k)^{-1}\oint\int e^{-\gamma r}[1-\tfrac{1}{2}(Z+1)r]r dr$$
$$\times(\xi+\tfrac{1}{2})^{-in'-1}(\xi-\tfrac{1}{2})^{in'-1}d\xi, \quad (18)$$

$$\gamma=2ik(\xi-in/4-i/4k). \quad (19)$$

The r integration gives a double pole, and a triple pole; the ξ-integration is done by evaluating the residues at these poles. We find for the probability of the transition $2s$ to continuum:

$$P_1(n')dW=2^{11}Z^{-4}(1-e^{-2\pi n'})^{-1}n'^8(3n'^2+4)^2(n'^2+4)^{-6}$$
$$\times\exp[-4n'\cot^{-1}(\tfrac{1}{2}n')]dW. \quad (20)$$

The ionization probability of $0.47/Z^2$ is found from Eq. (20) by numerical integration.

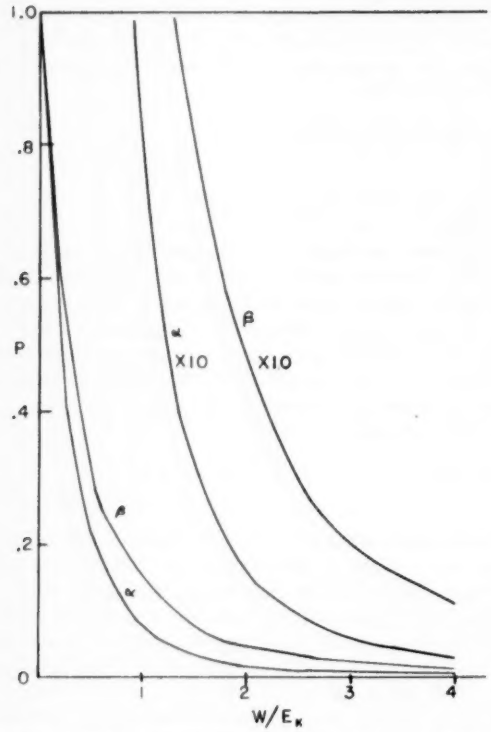

FIG. 1. Calculated energy spectrum for K electrons ionized by beta- or alpha-decay [see Eq. (14) and Eq. (45)]. W is the positive energy of the emitted electron; E_K is the K binding energy. The vertical scale is arbitrary.

For L_{II} or L_{III} electrons the amplitude for a transition to the continuum is

$$(a_{0n'})_2 = N_2 J_2, \tag{21}$$

$$N_2 = Z^3 6^{-\frac{1}{2}}(1-e^{-2\pi n'})^{-\frac{1}{2}}(1+n'^2)^{\frac{1}{2}}, \tag{22}$$

$$J_2 = (2\pi)^{-1}(2k)^{-2}\oint\int e^{-\gamma r} r dr (\xi+\tfrac{1}{2})^{-in'-2}(\xi-\tfrac{1}{2})^{in'-2} d\xi. \tag{23}$$

[Note that here we use a p wave function for the continuum electron. γ is defined by Eq. (19).] The probability for a transition from L_{II} or L_{III} to continuum is

$$P_2(n')dW = 2^{15}3^{-1}Z^{-4}(1-e^{-2\pi n'})^{-1}n'^{10}(n'^2+1) \times (n'^2+4)^{-6}\exp[-4n'\cot^{-1}(\tfrac{1}{2}n')]dW. \tag{24}$$

The ionization probability of $0.21/Z^2$ is found from Eq. (24) by numerical integration.

The results of our calculations for ionization probability by beta or positron decay are collected in Table I where we have neglected unity in comparison with Z. As noted above, we agree with Migdal and Feinberg for the K electron but obtain smaller values than Migdal's for the ionization probability of L electrons. In our thesis[13] we obtained a different result for the L_I electrons. Schwartz's results[14] are in agreement with our present results and extend the calculation to the M shell.

Another type of sudden perturbation is the sudden change of the nuclear velocity: the nucleus suddenly recoils with velocity V in the z direction, owing to neutron emission, or owing to elastic scattering of a neutron. (There is of course a nuclear recoil in beta-decay; but we show below that its effect on the inner electrons is much less than the effect of the nuclear charge change. The nuclear recoil in the case of alpha-decay is considered in the next section.)

Initially the electron has a wave function u_0. After the nucleus recoils, an electron with wave function $u_{n'}$ relative to the nucleus has a wave function $e^{iKz}u_{n'}$ in the laboratory system, where $K=mV/\hbar$ is the wave number of an electron with the nuclear recoil velocity V. The amplitude for a transition from state 0 to state n' is

$$a_{0n'} = \int u_{n'}^* e^{-iKz} u_0 d^3r = -\int u_{n'}^* iKz u_0 d^3r, \tag{25}$$

where in the last expression we have expanded the exponential for K small.[21]

The probability $P_{0n'}$ for a transition is proportional to the square of the dipole moment. This quantity has already been summed over all continuum states.[22] Using these sums, and the appropriate factors for the angular integrations[23] ($\frac{1}{3}$ for transitions from s states to p states), we have for the probabilities summed over all continuum states:

$$\begin{aligned} &P_{1s} = 0.28K^2/Z^2, \quad P_{2s} = 0.90K^2/Z^2, \\ &P_{2p} = 0.69K^2/Z^2, \quad \text{for } m=0, \\ &P_{2p} = 0.48K^2/Z^2, \quad \text{for } m=\pm 1. \end{aligned} \tag{26}$$

The wave number K is expressed in atomic units. It is numerically equal to the nuclear recoil velocity V divided by the characteristic electron velocity $e^2/\hbar$.

In the case of beta-decay, K is very much less than unity, so the yield of vacancies in the K or L shells due to nuclear recoil is very much less than the yield of about $1/Z^2$ due to the nuclear change of charge. Nuclear

TABLE I. Ionization probability in beta-decay.*

	Upper limit	Our calculation	Migdal's calculation
K electron	$0.75/Z^2$	$0.326/Z^2$	$0.32/Z^2$
K shell	$1.5/Z^2$	$0.65/Z^2$	$0.64/Z^2$
L_I electron	$2.25/Z^2$	$0.47/Z^2$	$1.9/Z^2$
L_{II} or L_{III}	$1.25/Z^2$	$0.21/Z^2$	$0.5/Z^2$
L shell	$12/Z^2$	$2.1/Z^2$	$6.8/Z^2$

* The upper limit for ionization of orbital electrons due to beta-decay is given by Eq. (3) and following. The results of our calculations are given in Eqs. (15), (20), and (24), respectively. See reference 11 for Migdal's calculations.

[21] This approach to the problem of nuclear recoil was suggested by R. P. Feynman.
[22] Reference 18, Table XV.
[23] Reference 18, Eq. (39.7).

recoil is of importance in the cases of neutron or alpha emission.

III. APPROXIMATIONS FOR BETA-DECAY

The calculations in the previous section are approximate in three respects: (1) the use of Coulomb wave functions; (2) neglect of relativistic effects, and (3) treatment of beta-decay as a sudden perturbation. In this section we shall correct the first approximation by calculating the screening corrections for Hartree wave functions[24] for Hg. (These functions do not include relativistic effects, or exchange effects.) We shall estimate the errors introduced by the other approximations. We shall also check our calculations by comparison with the average excitation energy calculated by Serber and Snyder.[16]

The probability P_{00} that an electron remain in its initial state when the nuclear charge changes suddenly by one is given in Table I. The results given there are based on Coulomb wave functions, but for K and L electrons they should be reasonably accurate for Hartree wave functions. (For the $1s$ and $2p$ states of Hg there is excellent agreement between Hartree and Coulomb wave functions, provided we use Slater's screening constants to obtain the effective charge[25] for the latter.)

We shall calculate the probability that due to the sudden change of charge the electron be excited from its initial state 0 to some discrete state n. (We are considering a hypothetical atom where the states n are unoccupied, so that the Pauli principle has no effect.) The probability P of ionization to the continuum states is then

$$P=1-P_{00}-\sum_n P_{0n}. \tag{27}$$

While the sum over discrete states n should go to infinity, we find that for Hartree functions we can break off the sum after several terms.

Instead of calculating the matrix element a_{0n} by

$$a_{0n}=\int \psi_n^*(Z+1, r)\psi_0(Z, r)d^3r, \tag{28}$$

we express it in another form:

$$a_{0n}\backsimeq(E_n-E_0)^{-1}\int \psi_n^*(Z, r)\Delta H\psi_0(Z, r)d^3r, \tag{29}$$

where $\Delta H=e^2/r$ is the change of the Hamiltonian due to the sudden beta-decay.[26] E_0 and E_n are the single electron energies estimated using Slater's effective Z.[27] The results of numerical integrations evaluating Eq. (29) for Hartree wave functions for Hg are given in Table II and compared with the matrix elements calculated using Coulomb functions. The first row $1-P_{00}$ gives the results of Table I for Coulomb functions, which should be a good approximation for Hartree functions. The last row P (ionization probability to the continuum) is copied from Table I for Coulomb wave functions. For Hartree functions it is estimated as $P=1-P_{00}-P_{02}-P_{03}-P_{04}-P_{05}$.[28] The screening correction is the ratio of P for Hartree and Coulomb wave functions. The factor $1/Z^2$ (or $1/Z_L^2$ for L electrons) is omitted in Table I. Only the principal quantum number is given in the subscript and 0 means the initial state, e.g., P_{03} means $P_{1s, 3s}$ or $P_{2s, 3s}$ or $P_{2p, 3p}$ for K, L_{I} or L_{II} (or L_{III}) electrons, respectively.

TABLE II. Screening corrections in β-decay for Hg. $1-P_{00}$ is the upper limit for the ionization probability, while P_{01}, P_{02}, etc., are the probabilities of excitation to discrete levels. The ionization probability $P=1-P_{00}-P_{01}-\cdots-P_{05}$. The screening correction is the ratio of P for Hartree functions to P for Coulomb functions.

	K electrons		L_{I}		L_{II} or L_{III}	
	Coulomb	Hartree	Coulomb	Hartree	Coulomb	Hartree
$1-P_{00}$	0.75	~0.75	2.25	~2.25	1.25	~1.25
P_{01}	...	...	0.312	0.28	...	...
P_{02}	0.312	0.24	...	...	...	...
P_{03}	0.059	0.038	1.08	0.47	0.783	0.37
P_{04}	0.022	0.007	0.207	0.060	0.137	0.050
P_{05}						0.006
P	0.326	0.46	0.47	1.44	0.21	0.82
Screening corr.	1.4		3.1		3.9	

This calculation shows that for heavy atoms the screening effects cause an appreciable increase in the ionization probability following β decay: for K electrons the factor is 1.4, while it is 3 or 4 for L electrons.[29]

Screening corrections have been calculated by Reitz[30] for the beta-decay spectrum and for internal conversion coefficients using relativistic wave functions for the atomic field. He did not go to low enough energies to compare in detail with our results above. Thus, for Po he calculated only down to energies of 25 kev, or $W/E_K=0.3$. At this energy screening effects amounted to only 5 percent. Presumably the appreciable fraction of emitted electrons which have a continuum energy less than 0.3 of the K binding energy (see Fig. 1) have quite large screening corrections, so that the screening correction averaged over the electron energy distribution of Fig. 1 amounts to an increase of 40 percent for K electrons of mercury. The large increase in the screening

[24] D. R. Hartree and W. Hartree, Proc. Roy. Soc. (London) **A149**, 210 (1935).

[25] J. C. Slater, *Quantum Theory of Matter* (McGraw-Hill Book Company, Inc., New York, 1951), Appendix 13.

[26] D. Bohm, *Quantum Theory* (Prentice-Hall, Inc., New York, 1951), Sec. 20.6.

[27] Then the energy difference is appreciably greater than that calculated using Coulomb wave functions. If we used the atomic energies for the two different electron states, the energy difference would be appreciably less than that for Coulomb functions, due to the change in the screening of all the other electrons by the one electron making the transition. *Note added in proof:*—We now believe that the above was a poor choice for the energy difference, and gives too large screening corrections.

[28] The P_{05} term is omitted for K and L_{I} electrons.

[29] Screening effects are presumably of great importance in other problems involving the overlap integral of the wave function of an inner electron with that of an electron of low positive energy, e.g., ionization due to alpha-emission (Sec. V); calculation of absorption edges in the atomic photoeffect; or calculation of the stopping power of L electrons.

[30] J. R. Reitz, Phys. Rev. **77**, 10 (1950).

correction for low continuum energies is substantiated by the much larger screening correction for L electrons (3.1 and 3.9) which have in general much lower continuum energy than the electrons emitted from the K shell.

Serber and Snyder's (S.S.) calculation[16] of the average excitation energy of the atom for beta-decay provides a valuable check on our calculations. They calculate the excitation energy of the whole atom as $\Delta E=22.85Z^{2/5}=132$ ev for Hg, using a Fermi-Thomas charge distribution. They also calculate an average excitation energy of 2 Ry$=27.2$ ev per closed electronic shell, assuming hydrogenic wave functions. These results are reached both by calculating the change of the nuclear electric potential energy due to the electronic cloud; and by a direct calculation using sum rules.

Their result of 2 Ry can be checked directly against the average excitation energy for K hydrogenic wave functions, calculated from the second column of Table II. We also need the average positive energy given to a continuum electron: this is determined as $1.03Z^2$ Ry, by numerical integration using Eq. (14) for their energy spectrum. (Also see Fig. 1.) The average excitation energy ΔE for the K shell is

$$\Delta E=2Z^2\text{ Ry}[0.312Z^{-2}(0.75)+0.59Z^{-2}(0.889)+0.022Z^{-2}(0.938)+0.031Z^{-2}(0.97)+0.326Z^{-2}(2.03)]=1.998\text{ Ry}. \quad (30)$$

The numbers in the bracket give the probability times the energy expenditure (factor of Z^2 Ry taken outside) for final states $2s$, $3s$, $4s$, ns ($n>4$), and continuum s, respectively. The agreement with S.S. is within the accuracy of our numerical integration.

Now this calculation neglected the exclusion of transitions to occupied discrete states. The Pauli exclusion principle forbids, for example, a $1s$ to $2s$ transition in which the atom gains energy from the nuclear decay, but it also forbids a $2s$ to $1s$ transition in which the atomic system loses energy to the nuclear decay. The energies involved are exactly equal in magnitude. Thus the excitation energy *for the entire atom* is unaffected by the Pauli principle. However, the Pauli principle causes a smaller excitation energy than 2 Ry for the K shell, and a correspondingly larger excitation energy for the higher shells.[31] (For hydrogen wave functions the excitation energy for the K shell of Hg would be 1.38 Ry.)

Since we have not yet calculated the energy spectrum of continuum electrons for Hartree Hg wave functions, we cannot make a precise comparison between our ΔE and that of S.S. There will in general be a change of the excitation energy of the K shell due to the use of atomic wave functions. This change in wave functions corresponds to a change in the S.S. treatment for closed shells, since they use the virial theorem for a Coulomb field to find the potential energy from the binding energy.

Relativistic effects will be of most importance for K electrons of heavy atoms We have calculated with relativistic Coulomb wave functions the probability P_{00} that an electron remain in the $1s$ state for a change of one in the nuclear charge. The result for the upper limit for the ionization probability is, for $Z\gg1$,

$$1-P_{00}=Z^{-2}[(2\gamma+1)/4+\alpha^2Z^2+\psi'(2\gamma)\alpha^4Z^4]=Z^{-2}(0.70+0.36+0.06)=1.12Z^{-2}, \quad (31)$$

where

$$\gamma=(1-\alpha^2Z^2)^{\frac{1}{2}}, \quad (32)$$

and[32]

$$\psi'(x)=d^2(x!)/dx^2; \quad (33)$$

also $\alpha=e^2/\hbar c$. The numerical result in Eq. (30) is given for lead, $Z=82$, $\gamma=0.80$. Comparing with $1-P_{00}=0.75/Z^2$ for nonrelativistic Coulomb functions [Eq. (3)], we see that for K electrons of lead relativistic corrections might lead to an appreciable increase of the ionization probability. Our work is still preliminary, as we have not yet calculated the probability P of ionization to the continuum. We have shown that relativistic corrections give an upper limit for the ionization probability of $1.12/0.46=2.4$ times that found in Table II for nonrelativistic Hartree wave functions.

In applying the sudden approximation to the case of beta decay, there will be a correction term of order $(v_e/v_b)^2$, where v_e is the velocity of the orbital electron and v_b that of the beta-particle. (See Feinberg's discussion[12] of the relatively low ionization produced by "direct collisions"). The coefficient of this correction term depends on the form of the time rate of change of the Hamiltonian dH/dt [see Eq. (37) in Sec. IV], and this in turn depends on the values of the electron coordinates. For instance, if dH/dt always has the same sign (say positive) we can show that

$$\left|\int_0^\infty (dH/dt)e^{i\omega t}dt\right|_{0n'}\leqslant\left|\int_0^\infty (dH/dt)dt\right|_{0n'}. \quad (34)$$

The right side is proportional to the amplitude for ionization of the n' state for a sudden perturbation. Thus for this case the ionization probability found for the sudden perturbation case sets an upper limit for the ionization probability. But if dH/dt changes sign as t increases (as it does for z positive) it appears that there will be a maximum in the ionization probability as a function of (v_e/v_b) for the velocity of the emitted particle comparable to the velocity of the orbital electrons. Since we then integrate over z, we cannot be sure that Eq. (34) applies.

We should note that since v_b always remains smaller than c, the parameter $v_e/v_b=Z/137n$ is not very much smaller than unity for K electrons of heavy atoms; so

[31] This is analogous to the shift of oscillator strength from one shell to another in dipole transitions in x-ray spectra. See A. H. Compton and S. K. Allison, *X-Rays in Theory and Experiment* (D. Van Nostrand Company, Inc., New York, 1935), p. 551.

[32] E. Jahnke and F. Emde, *Table of Functions* (Dover Publications, New York, 1945), p. 17.

the sudden perturbation treatment will not be very accurate for this case.

In summary, our approximations have in general underestimated the transition probabilities. For K electrons the principal approximation was the use of nonrelativistic wave functions, which may lead to an underestimate of the ionization probability by a factor of 2. For K electrons the screening corrections for the use of Coulomb wave functions lead to an increase of 40 percent in the transition probability. For L electrons screening corrections for Hg give an increase by a factor 3.5. The sudden perturbation calculation should be a fair approximation for the case of beta-decay but becomes poorer for high Z.

IV. ADIABATIC PERTURBATION: ALPHA-DECAY

The alpha-particles from radioactive nuclei travel with a velocity rather smaller than that of the inner orbital electrons (e.g., for Po^{210} the ratio $v_a/v_e=0.087$ for K electrons). The electron velocity $v_e=Z/n$ atomic units for NR Coulomb wave functions, with principal quantum number n; v_a is the velocity of the alpha-particle. Now the alpha-particle is so heavy that it has an extremely small wavelength, so it can be considered as moving through the atom classically, producing a perturbation on the atomic electrons that varies slowly compared with their motions. From the adiabatic theorem we know that a slowly varying perturbation produces very small effects, so we expect to find a very small ionization probability for the K electrons. However, the L electrons have a smaller velocity, so that the perturbation is not so adiabatic, and the transition probability is much larger.

Migdal[11] starts from the formulation of time dependent perturbation theory with perturbation $V(\mathbf{r}, t)$ giving an amplitude for the state n' at infinite time, for the system initially in state 0,

$$a_{n'}=(i\hbar)^{-1}\int_0^\infty V_{0n'}e^{i\omega t}dt$$
$$=(i\hbar)^{-1}[(i\omega)^{-1}e^{i\omega t}V|_0^\infty-\omega^{-2}e^{i\omega t}dV/dt|_0^\infty$$
$$-(i\omega)^{-3}e^{i\omega t}d^2V/dt^2|_0^\infty\cdots]. \quad (35)$$

The last expression is obtained by successive integrations by parts. This type of expansion is useful for a potential which varies slowly with time, so that the higher time derivatives are small. Migdal omits the term $(i\omega)^{-1}e^{i\omega t}V$, without a detailed explanation. This omission is clearer if we use another formulation of time dependent perturbation theory[33] for a Hamiltonian H which is a function of time:

$$\dot{a}_{n'}=\sum_n(a_n/\hbar\omega_{n'n})\left[\exp\left(i\int_0^t\omega_{n'n}dt'\right)\right](dH/dt)_{n'n}. \quad (36)$$

This equation is exact. If the perturbation is small, we can take $a_n(t)=\delta_{n0}$ and we can take $\omega_{n'n}(t')$ and the wave functions $u_n(t)$ and $u_{n'}(t)$ all as time independent. This gives the amplitude after infinite time for the state n'

$$a_{n'}=(\hbar\omega)^{-1}\int_0^\infty e^{i\omega t}(dH/dt)_{0n'}dt$$
$$=(\hbar\omega)^{-1}[(i\omega)^{-1}e^{i\omega t}dH/dt|_0^\infty$$
$$-(i\omega)^{-2}e^{i\omega t}d^2H/dt^2|_0^\infty\cdots]. \quad (37)$$

This expression automatically omits the term involving V (or the change of H), justifying Migdal's omission of this term.[34]

The significant difference between our present calculation and that of Migdal's is that he takes V as the perturbation on the orbital electrons due to the alpha-particle, while we take the Hamiltonian H, which includes both the effect of the alpha-particle and the effect of the nucleus. Migdal uses

$$V=2e^2[x^2+y^2+(z-v_at)^2]^{-\frac{1}{2}}, \quad t\geq 0. \quad (38)$$

For the dipole term he finds

$$-(i\hbar)^{-1}\omega^{-2}e^{i\omega t}dV/dt|_0^\infty$$
$$=-(i\hbar\omega^2)^{-1}2e^2v_ar^{-2}P_1(\cos\theta). \quad (39)$$

Here the alpha-particle moves with velocity v_a along the positive z axis, starting at $t=0$. P_1 is a Legendre polynomial. Since we use the total Hamiltonian H for a nucleus initially of atomic number Z, recoiling with velocity v_n:

$$H=2e^2[x^2+y^2+(z-v_at)^2]^{-\frac{1}{2}}$$
$$+(Z-2)[x^2+y^2+(z+v_nt)^2]^{-\frac{1}{2}}, \quad t\geq 0, \quad (40)$$

we find for the dipole dH/dt term in Eq. (37):

$$(\hbar\omega)^{-1}(i\omega)^{-1}e^{i\omega t}dH/dt|_0^\infty$$
$$=(i\hbar\omega^2)^{-1}[(Z-2)e^2v_n-2e^2v_a]P_1(\cos\theta). \quad (41)$$

The matrix elements of the expression in Eq. (39) or Eq. (41) can be evaluated easily by a trick used by Migdal based on potential energy $V=Ze^2/r$, and Ehrenfest's relations:

$$[r^{-2}P_1(\cos\theta)]_{0n'}=(z/r^3)_{0n'}=[-\partial/\partial z(r^{-1})]_{0n'}$$
$$=m(\dot{z})_{0n'}/Ze^2=(m\omega^2/Ze^2)(z)_{0n'}. \quad (42)$$

The probability of ionization due to alpha-decay is then, according to Migdal,

$$P_a=\sum_{n'}|a_{n'}|^2=(4v_a^2/Z^2)\sum_{n'}|z_{0n'}|^2. \quad (43)$$

We are using Hartree atomic units, so v_a is the alpha-particle velocity in atomic units, and $\hbar$ and m are equal to unity. Now this same sum over continuum states of

[33] L. I. Schiff, *Quantum Mechanics* (McGraw-Hill Book Company, Inc., New York, 1949), Eq. (31.8).

[34] The physical reason for omitting this term is that it corresponds exactly to a sudden change of the Hamiltonian, which does not occur in this case. This term was erroneously included in our calculation for alpha-decay in reference 13.

the squared dipole moment was met above in calculations by sudden perturbation theory of the ionization due to nuclear recoil; and the results for these probabilities, copied from Bethe's Handbuch article, are tabulated in Eq. (26). They are also tabulated in Migdal's Table II, where he includes the factor of 4 for the squared charge of the alpha particle, and also multiplies by the number of $1s$, $2s$, and $2p$ electrons, respectively. To show the relation to the adiabatic theorem, he uses the electron velocity $v_e=Z$ atomic units, so that the ionization probability for dipole transitions per $1s$ electron can be written

$$P_d=4(v_a/v_e)^2(0.28/Z^2), \tag{44}$$

with the coefficients for $2s$ and $2p$ electrons to replace the 0.28 being given in Eq. (26).

However, we use Eq. (41) for dH/dt, and obtain for the ionization probability,[35]

$$P_d=\{[(Z-2)v_n-2v_a]^2/Z^2\}\textstyle\sum_{n'}|z_{0n'}|^2, \tag{45}$$

to replace Migdal's result of Eq. (43). This suggests the definition

$$Zv_z=(Z-2)v_n-2v_a, \tag{46}$$

so that Eq. (45) can be rewritten in a form analogous to Eq. (26), the ionization probability P_d for $1s$ electrons:

$$P_d=v_z^2\textstyle\sum_{n'}|z_{0n'}|^2=0.28v_z^2/Z^2. \tag{47}$$

The physical interpretation of the last two equations is that v_z, as defined in Eq. (46), is the velocity of the *center of charge* of the system composed of alpha-particle with velocity v_a and recoiling nucleus with charge $Z-2$ and velocity v_n in the opposite direction. Further, for the dipole transitions which we are here considering, only the motion of the center of charge is of significance.[36] At time 0, the atomic electrons begin to feel the perturbation of the alpha-particle traveling one way, and the remainder of the charge recoiling in the other direction. Since the electron velocities are large compared to the velocity of separation of alpha and nucleus, the electrons to a first approximation (i.e., the dipole approximation) average out in their motion the fields of alpha and recoiling nucleus, and experience only the sudden change from no motion of the center of charge to motion of the center of charge with velocity v_z; thus Eq. (26) is applicable.

If the alpha-particle and recoiling nucleus had identical charge-to-mass ratios, the center of charge of the system would remain at rest, since the center of mass must do so. Using conservation of momentum, and the definition Eq. (46) we have in the general case:

$$Zv_z=2v_a(A-2Z)/(A-4)=2v_a(0.203). \tag{48}$$

The numerical value 0.203 is for the case Po^{210}; for U^{238} the numerical coefficient is 0.232. Since Zv_z replaces $2v_a$ used by Migdal [Eqs. (43) and (45)], and these quantities enter squared in calculating the ionization probability, we find for this term an ionization probability of $(A-2Z)^2/(A-4)^2=0.04$ that found by Migdal, where the number 0.04 applies to Po^{210}. For K electrons of Po^{210} Migdal finds a probability of 2.5×10^{-6} per alpha, while we find an ionization probability of only 10^{-7} per alpha. (These numbers come from Eq. (47) or (43), using $v_a/v_e=0.087$, as given above.) Since $v_a/v_e\ll1$, Migdal calculated only the dipole term.

We have found that the dipole dH/dt term is greatly reduced due to the nuclear recoil. However, the quadrupole d^2H/dt^2 term of Eq. (37) is changed very little. From Eq. (40),

$$d^2H/dt^2|_0{}^\infty=-2e^2P_2(\cos\theta)r^{-3}[2v_a{}^2+(Z-2)v_n{}^2]. \tag{49}$$

Here, since the small velocity v_n appears squared, the nuclear recoil term can be neglected.

Since the dipole term is made unusually small by the effect of the nuclear recoil, while the quadrupole term is almost unaffected, we see that the type of series Eq. (35) or (37) has the special property that both the dipole and quadrupole terms need to be calculated, but that one can hope to neglect higher multipoles. It turns out that the quadrupole term contains numerical coefficients markedly different from unity, so that it is very small compared to the dipole term for K electrons; but large compared to the dipole term for L electrons. Equation (35) or (37) are actually semiconvergent series, with the general term for the amplitude a_p for

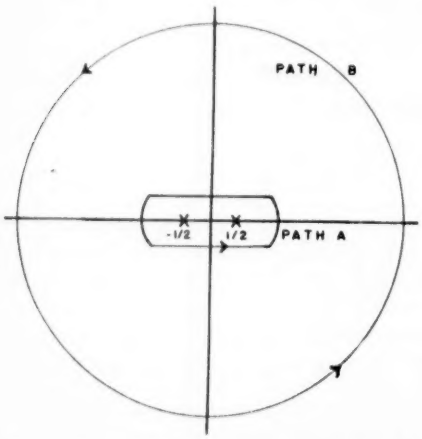

FIG. 2. Contour for Eq. (56). Path A surrounds the branch points at $\xi=\pm\frac{1}{2}$; path B has the large radius ϵ^{-1}.

[35] The shape of the energy spectrum for the emitted electrons is the same as that given by Migdal. It is plotted in Fig. 1, with an arbitrary scale for the ordinate. We see that the emitted K electrons are likely to have a positive energy the order of the K binding energy; but that there are fewer high energy electrons accompanying alpha-decay than beta-decay. Migdal shows that asymptotically the K electrons from alpha-decay fall off as $E^{-9/2}$; while the K electrons from beta-decay fall off as $E^{-7/2}$.

[36] For an analogous use of the concept of the center of charge in the nuclear photoeffect see H. A. Bethe, Revs. Modern Phys. 9, 71 (1937), Secs. 87 to 90. Dr. Bethe suggested use of the concept "center of charge" in our present problem.

the 2^p pole transition being

$$a_p=2e^2[(\hbar\omega)^{-1}(v_a/i\omega)^p r^{-p-1}p!P_p(\cos\theta)]_{0n'}. \quad (50)$$

Successive terms decrease rapidly for the case of K electrons of Po^{210}; but much less rapidly for the L electrons. In this section we shall calculate the quadrupole term for K and L electrons. We discuss the englect of higher terms in the next section.

Migdal's trick of Eq. (42) does not work for the quadrupole term of Eq. (49). Professor Bethe has developed a method to use the same integral representation of the continuum wave functions that we use above[19] for our present matrix element which involves negative powers of r. (The angular integration for $P_2(\cos\theta)$ gives the usual quadrupole selection rules for the angular momentum change, and for allowed transitions gives numerical factors which will be included in our final result.) For K electrons we have transitions to continuum states, with the matrix element

$$(r^{-3})_{1s,\,n'd}=N_3J_3, \quad (51)$$

$$N_3=-4Z^2(n'^2+1)^{\frac{1}{2}}(n'^2+4)^{\frac{1}{2}}(1-e^{-2\pi n'})^{-\frac{1}{2}}, \quad (52)$$

$$J_3=(2k)^{-3}(2\pi)^{-1}\oint\int e^{-\beta_1 r}r^{-4}dr(\xi+\tfrac{1}{2})^{-in'-3}\times(\xi-\tfrac{1}{2})^{in'-3}d\xi, \quad (53)$$

$$\beta_1=2ik(\xi-in'/2). \quad (54)$$

The integration over r is performed first; and since it diverges at the lower limit, we replace this limit by a small number ϵ, and integrate by parts several times:

$$\int_\epsilon^\infty e^{-\beta_1 r}r^{-4}dr=\epsilon^{-3}e^{-\beta_1\epsilon}/3-\epsilon^{-2}\beta_1e^{-\beta_1\epsilon}/6+\epsilon^{-1}\beta_1^2e^{-\beta_1\epsilon}/6-(\beta_1^3/6)\int_\epsilon^\infty e^{-\beta_1 r}r^{-1}dr. \quad (55)$$

Consider any one of the first three terms on the right side, such as $\epsilon^{-3}\exp(-\beta_1\epsilon)/3$. For this term the integral over ξ is

$$I=(3\epsilon^3)^{-1}\oint e^{-\beta_1\epsilon}(\xi+\tfrac{1}{2})^{-in'-3}(\xi-\tfrac{1}{2})^{in'-3}d\xi. \quad (56)$$

The contour integral is to be taken over the path A of Fig. 2, which surrounds the branch points at $\xi=\frac{1}{2}$ and $\xi=-\frac{1}{2}$. This path can be distorted to path B of very large radius without changing the value of the contour integral I. On path B, let $\xi=\epsilon^{-1}e^{i\theta}$, so that $\exp(-\beta_1\epsilon)$ becomes $\exp(-2ike^{i\theta}+kn'\epsilon)$ which is finite. The terms $(\xi+\frac{1}{2})^{-in'-3}(\xi-\frac{1}{2})^{in'-3}$ give a factor of ϵ^6, so that I is proportional to ϵ^3 times an integral of a finite quantity over a path of length $2\pi\epsilon^{-1}$, i.e., I is proportional to ϵ^2 and therefore vanishes as we take the limit ϵ to 0. Similarly the integrals over path B vanish for the second and third terms on the right of Eq. (55). We are then left with the last term, for which we use the asymptotic expression for $\mathrm{Ei}(x)$:

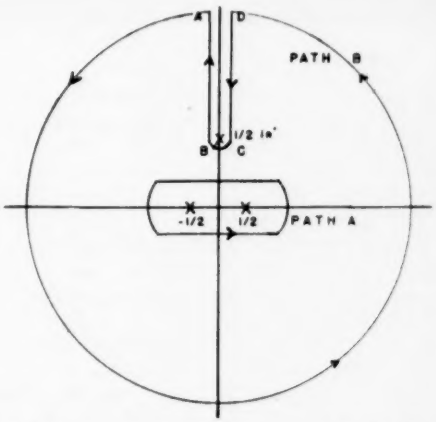

FIG. 3. Contour for Eq. (58). Path A surrounds the branch points at $\xi=\pm\frac{1}{2}$; path B is at infinity except for the portion $ABCD$ surrounding the branch point at $\xi=\frac{1}{2}in'$.

$$(-\beta_1^3/6)\int_\epsilon^\infty e^{-\beta_1 r}r^{-1}dr=(-\beta_1^3/6)(\ln\beta_1+\ln\epsilon+\text{constant}). \quad (57)$$

The terms with $\ln\epsilon$ and constant vanish on integration over ξ by the same argument as above for I. The $\ln\beta_1$ term does not, since it has a branch point at $\beta_1=0$, or $\xi=\frac{1}{2}in'$. The contour integral must be deformed as shown in Fig. 3 in changing from path A to path B, since we must not cross any singularities. Since $\ln\beta_1$ differs by $2\pi i$ on the two linear portions AB and CD, and since the remainder of the contour (at infinity and on the small circle) gives zero, the integral over ξ becomes

$$J_3=(2k)^{-3}i\int_{\frac{1}{2}in'}^{\infty i}(\beta_1^3/6)(\xi+\tfrac{1}{2})^{-in'-3}(\xi-\tfrac{1}{2})^{in'-3}d\xi$$

$$=-(2/3)\int_0^{\cot^{-1}n'}(\cot x-n')^3\sin^4x e^{-2n'x}dx$$

$$=[1-9\exp(-2n'\cot^{-1}n')]/12(n'^2+4). \quad (58)$$

We obtain the second integral on the right using the substitution $\xi=\frac{1}{2}i\cot x$.

We note that Bethe's method of finding the matrix element for negative powers of r for Coulomb wave functions has been checked by calculating the matrix element of $r^{-2}\cos\theta$ and comparing with Eq. (42) for the relation to the matrix element of $r\cos\theta$.

To find the amplitude for transitions to the $n'd$ state, we combine the matrix element $(r^{-3})_{1s,\,n'd}=N_3J_3$ [with N_3 given by Eq. (52) and J_3 by Eq. (58)] with the factor $5^{-\frac{1}{2}}$ from the angular integration of $P_2(\cos\theta)$ between s and d states, and with the factor $4e^2v_a2/\hbar\omega^3$

of Eq. (50). Here it is convenient to use

$$\hbar\omega = E_K + W = \tfrac{1}{2}Z^2 + \tfrac{1}{2}k^2 = \tfrac{1}{2}Z^2 n'^{-2}(n'^2+1). \quad (59)$$

We square the amplitude, multiply by $dW = -Z^2 dn'/n'^3$ and integrate to find the ionization probability for the quadrupole term for K electrons

$$P_q = (2^{10}/45)(v_a/v_e)^4 Z^{-2} \times \int_0^\infty n'^9 [9\exp(-2n'\cot^{-1}n') - 1]^2 \times (n'^2+1)^{-5}(n'^2+4)^{-1}[1-e^{-2\pi n'}]^{-1} dn' = 0.22(v_a/v_e)^4 Z^{-2}. \quad (60)$$

The final result is obtained by numerical integration. We note that the integrand has a sharp peak at $n' \cong 1$, or continuum energy $W \cong$ binding energy E_k.

It is of interest to compare the ionization probability by the quadrupole term with that found for the dipole term in Eq. (47).

$$P_d = (0.203)^2 4 v_a^2 (0.28/Z^2). \quad (61)$$

TABLE III. Ionization probabilities for Po^{210} alpha-decay.[a]

Electron	Equations: Dipole	Equations: Quadrupole	Numerical results: Dipole	Numerical results: Quadrupole
K	$0.28\,(Zv_s/v_K)^2$	$0.22\,(v_a/v_K)^4$	0.00034	0.000013
LI	$0.90\,(Zv_s/v_K)^2$	$86\,(v_a/v_{LI})^4$	0.0011	0.17
LII	$0.55\,(Zv_s/v_K)^2$	$(15+4)(v_a/v_{LII})^4$	0.0007	0.037
$LIII$	$0.55\,(Zv_s/v_K)^2$	$(21+6)(v_a/v_{LIII})^4$	0.0007	0.075

[a] Here v_K, v_{LI}, v_{LII}, and v_{LIII} are the velocities of the K, L_I, L_{II} and L_{III} electrons, respectively, v_a is the alpha-particle velocity; while v_s is the velocity of the center of charge of the system of alpha-particle and recoiling nucleus: see Eq. (46). The table gives probabilities of ionization per electron; and the factor $(1/Z^2)$ is omitted throughout the table.

The ratio

$$P_q/P_d = 0.196(v_a/v_e)^2/(0.203)^2 = 0.036. \quad (62)$$

The use of $(0.203)^2$ applies to the case of Po^{210}, as does the final result using $v_a/v_e = 0.087$. We see that for K electrons the quadrupole term is very much smaller than the dipole term, even though the dipole term is reduced by a factor 25 due to nuclear recoil, while the quadrupole term is unchanged by nuclear recoil. The small numerical factor $0.22/4(0.28) = 0.196$ is of significance in reaching this conclusion; the corresponding numerical factor turns out to be large for the case of ionization of L electrons, and the quadrupole term predominates.

The calculation for the ionization probability of L electrons is carried through in a manner completely analogous to the calculation above for the K electrons, so we will give few details. There are two changes. First putting the binding energy $E_L = \frac{1}{2}Z^2/n^2$, for $n=2$ is a poor approximation, even if we use an effective Z_L as given by Slater. We introduce an empirical parameter θ to fit the experimental data, defined as

$$E_L = \theta Z^2/8. \quad (63)$$

For Po, $\theta = 0.75$ for L_I and K_{II} electrons, and $\theta = 0.63$ for L_{III} electrons. In place of Eq. (59) for K electrons we have then

$$\hbar\omega = E_L + W = \theta Z^2/8 + \tfrac{1}{2}k^2 = (\theta Z^2/8)n'^{-2}(n'^2 + 4/\theta). \quad (64)$$

We will express our final result in terms of the velocity v_L of the L electron, defined as

$$v_L = \tfrac{1}{2}Z\theta^{\frac{1}{2}} \text{ atomic units.} \quad (65)$$

Second, for $2p$ electrons we obtain different results for the angular integrations for the two cases $m=0$ and $m=1$, which must be weighted appropriately.

The quadrupole contribution to ionization probability per L_I electron is

$$P_2 = (2^{11}/45\theta^4)(v_a/v_L)^4 Z^{-2} \times \int_0^\infty \frac{n'^9[A(n')+B(n')]^2 dn'}{(n'^2+4/\theta)^6(n'^2+4)(n'^2+1)(1-e^{-2\pi n'})} = (86/Z^2)(v_a/v_L)^4 \text{ for } \theta = 0.75. \quad (66)$$

Here

$$A(n') = 8n'^2 - 9n' + 4,$$

and

$$B(n') = (-24n'^6 + 153n'^5 + 196n'^4 + 648n'^3 - 1308n'^2 + 144n' + 576)(n'^2+4)^{-2} \times \exp(-2n'\cot^{-1}\tfrac{1}{2}n').$$

We note that the integrand has a maximum at $n' \cong 6$, corresponding to a continuum energy of only $0.15E_L$.*

Quadrupole transitions for $2p$ electrons can be either to $n'p$ or to $n'f$ continuum states. Also, as noted above, we have different results for the angular integrations depending on the value of m for the $2p$ electron, and we have different values of the parameter θ for L_{II} and L_{III} electrons. The probability of a transition to an $n'p$ state for $m=0$ is

$$P_3 = (2^{15}/75\theta^4)(v_a/v_L)^4 Z^{-2} \times \int_0^\infty \frac{n'^{11}[1+3\exp(-2n'\cot^{-1}\tfrac{1}{2}n')]^2 dn'}{(n'^2+4/\theta)^6(n'^2+1)(1-e^{-2\pi n'})}. \quad (67)$$

For L_{II} electrons we have $P_3 = (15/Z^2)(v_a/v_{LII})^4$, while for L_{III} electrons $P_3' = (21/Z^2)(v_a/v_{LIII})^4$.

The probability of a quadrupole transitions from a $2p$ state, with $m=0$, to an $n'f$ state is given by

$$P_4 = (2^{11}/75\theta^4)(v_a/v_L)^4 Z^{-2} \times \int_0^\infty \frac{n'^{11}[A_1(n')+B_1(n')]^2 dn'}{(n'^2+4/\theta)^6(n'^2+1)(n'^2+4)(n'^2+9)(1-e^{-2\pi n'})}, \quad (68)$$

* *Note added in proof:*—We have found an error in this calculation, with the help of J. Scandrett. We should have $A(n') = n'^2+4$ and change the sixth-order polynomial in $B(n')$ to read $(-45n'^6 - 396n'^4 - 1008n'^2 - 576)$. The number 86 in the result is changed to 0.044. This lowers the quadrupole yield for L_I electrons to $8.7\times10^{-5}/Z^2$ (Table III) and lowers the L shell yield to 0.6×10^{-4} (Table IV).

$$A_1(n') = -3n'^2 - 12,$$

$$B_1(n') = (225n'^6 + 2500n'^4 + 38{,}348n'^2 + 3264) \times (n'^2+4)^{-2} \exp(-2n' \cot^{-1}\tfrac{1}{2}n').$$

For L_{II} electrons $P_4 = (3.6/Z^2)(v_a/v_{LII})^4$ while for L_{III} electrons, $P_4' = (6.2/Z^2)(v_a/v_{LIII})^4$. The peak of the integrands in Eqs. (67) and (68) are at n' about 3, or a continuum energy $W \cong 0.6E_L$.

These results for the dipole and quadrupole contributions to the ionization probability are collected in Table III, together with a numerical evaluation for the case of Po^{210}. We have averaged over the results for $m=0$ and $m=1$ cases for the $2p$ electrons. The probabilities are all given omitting the factor $1/Z^2$. The two numbers given for quadrupole transitions for L_{II} and L_{III} electrons are the contributions from transitions to $n'p$ and $n'f$ states, respectively.

In the numerical evaluation we used: the ratio of alpha-velocity to velocity of the K electron, $v_a/v_K = 0.087$ for Po^{210}; the ratio of alpha-velocity to that of the L_I or L_{II} electron, $v_a/v_{LI} = v_a/v_{LII} = 0.21$; the ratio of alpha-velocity to that of the L_{III} electron $v_a/v_{LIII} = 0.23$. v_z is the velocity of the center of charge of alpha and recoiling nucleus; from Eq. (48), $Zv_z/v_a = 0.406$.

In calculating the ionization probabilities we combine the dipole and quadrupole terms; we use the effective charges $Z_K = Z - 0.3$, and $Z_L = Z - 4$; and we also multiply by the number of the electrons in each shell. The resulting ionization probabilities for the different shells are given in Table IV.

As stated above, the very large ratio between ionization yields for L electrons and K electrons is due both to the adiabatic theorem, and to the very different numerical factors in the probabilities for quadrupole transitions: e.g., 15 for $2p$ electrons as compared with 0.22 for $1s$ electrons. The quadrupole transition probability for the L shell is about 100 times the dipole transition probability. While a factor of 25 is accounted for by the decrease of the dipole transition probability due to nuclear recoil, the remaining factor of 4 indicates that the semiconvergent expansion of Eq. (37) may not give accurate results for the value $v_a/v_L = 0.2$ for Po^{210}. The problem of the accuracy of our semiconvergent expansion is discussed further in the next section.

In the above work we have assumed that the alpha-particle was moving along a radius vector from the nucleus: that is, that we were dealing with an s alpha-particle. The imperfect analogy with the internal conversion effect suggests a strong dependence of ionization probability on the alpha-particle angular momentum. This question is considered in some detail in reference 13, where we have shown that the alpha-particle angular momentum has a negligible effect on the ionization probability. Two possible effects are considered: (1) that the classical path of an alpha-particle depends appreciably on its angular momentum relative to the nucleus; and (2) that an alpha-particle of high angular momentum can penetrate the centrifugal barrier more easily if it first gives up some angular momentum to an electron, by ionizing it. The first effect is found to be extremely small. The second effect is also extremely small, since the loss of energy by the alpha-particle in ionizing the electron greatly decreases its rate of penetration through the Coulomb barrier. (This illustrates the difference between internal conversion and the present process of "internal ionization." In internal conversion emission of an electron is a complete substitute for emission of a nuclear gamma, since the emitted electron takes off both the energy difference and the angular momentum difference between the nuclear states. However, in alpha-particle emission, an alpha-particle must still be emitted to change the nuclear Z and A, irregardless of whether an orbital electron is also emitted. The cases of beta or positron emission, or K capture, are similar to that of alpha-emission. The correct analogy for these processes in which particles (alpha, beta, or positron) are emitted from the nucleus is to internal Compton scattering, rather than to internal conversion.)

TABLE IV. Ionization probability for electron shells for Po^{210} alpha-decay.

Electron shell	Ionization probability per alpha
K	0.98×10^{-7}
L_I	0.53×10^{-4}
L_{II}	0.12×10^{-4}
L_{III}	0.47×10^{-4}
L shells	1.1×10^{-4}

V. APPROXIMATIONS IN ALPHA-DECAY

The approximations made in our treatment of the ionization probability of K and L electrons due to alpha-decay are similar to our approximations in the beta-decay treatment. (See Sec. III.) We shall calculate the screening correction for dipole transitions, and estimate the screening correction for quadrupole transitions. We shall also estimate the accuracy of our non-relativistic approximation, and of our semiconvergent expansion.

The screening corrections for dipole transitions can be calculated in a manner rather similar to that of Sec. III. We calculate the dipole matrix elements to discrete states, using Hartree wave functions[24] for Hg. The sum of the squares of all dipole matrix elements r_{0n} can be found from the sum rule,

$$\sum_n (r_{0n})^2 = (r^2)_{00}, \tag{69}$$

where 0 is the initial state, and the sum goes over both discrete and continuum states. The ionization probability is then proportional to $(r^2)_{00}$ minus the sum over the discrete states of the squared dipole matrix elements.

TABLE V. Screening corrections for dipole transitions of K electrons.[a]

Matrix element	Coulomb functions	Hartree for Hg	Hartree-Fock for Cu	Hartree-Fock for A
$(r^2)_{1s,1s}$	3.000	2.980	~3.0	~3.0
$(r_{1s,2p})^2$	1.666	1.525	1.378	1.186
$(r_{1s,3p})^2$	0.267	0.204	0.117	0.067
$(r_{1s,4p})^2$	0.093	0.044	...	...
$(r_{1s,5p})^2$	0.044	0.008	...	...
continuum probability	0.849	1.19	~1.5	~1.7
screening correction		1.4	~1.8	~2.0

[a] The squared matrix elements are given in units of a_0^2/Z^2. The values for Cu and A were calculated by Tuan (reference 37). The value of the continuum probability—i.e., sum of the squared matrix elements over all continuum states—is calculated as $(r^2)_{1s,1s}-(r_{1s,2p})^2-\cdots-(r_{1s,5p})^2$. The screening correction is the ratio of continuum probability for atomic wave functions to that for Coulomb wave functions.

We have made this calculation only for the K electrons, as dipole transitions were found in Sec. IV to be unimportant for higher shells. The results are given in column 3 of Table V. We also include in columns 4 and 5 results for Cu and A, using dipole matrix elements calculated by Tuan[37] for Hartree-Fock wave functions. Column 2 gives the result for Coulomb wave functions.[22]

The screening correction, calculated as the ratio of the ionization probability for atomic wave functions to that for Coulomb wave functions, is 1.4 for Hg, and about 2 for Cu and A. The screening correction for dipole transitions of Hg K electrons is the same as that found in Sec. III for the screening correction in the beta-decay case for the same electrons.

These screening corrections cannot be applied exactly to our calculation of dipole transitions due to alpha-decay, since we originally [Eq. (41)] had the matrix element of $r^{-2}\cos\theta$ which Migdal transformed to a matrix element of $r\cos\theta$, using relations based on there being a Coulomb potential. For the atomic potential the transformation will no longer be exact, but it should be in error by an amount much less than the screening correction of 40 percent.

This method of calculation of screening corrections cannot be applied to quadrupole transitions (which are of interest for the L shell) since we have no sum rule for this case. We can estimate that the screening corrections for quadrupole transitions of L electrons will be somewhat greater than the factor of 3 to 4 found for L electrons in Sec. III for the beta-decay case. Screening corrections became larger for lower energy continuum electrons (e.g., comparison of K and L shells in Sec. III); and the electrons emitted from the L shell in quadrupole transitions [Eqs. (66), (67) and (68)] have somewhat lower energy than those emitted from the L shell in beta-decay [Eqs. (20) and (24)].†

We can make only a tentative estimate on the magnitude of relativistic corrections. Analogies with other processes (ionization by beta-decay, Auger transition rate) suggest a possible increase in the ionization probability of a factor of 2 for K electrons of heavy elements, and a much smaller correction for L electrons.

The accuracy of the adiabatic approximation of expansion into dipole, quadrupole, and higher electric multipole terms is difficult to estimate, since this is a semiconvergent expansion, as noted above. From Eq. (50) the order of magnitude of the ratio of the amplitude for the 2^{p+1} pole to 2^p pole transition is, in the general case,

$$a_{p+1}/a_p=(p+1)v_a/\omega r\cong(p+1)v_a/v_e. \qquad (70)$$

For Po^{210} and L electrons, this gives a_3/a_2 about 0.6; which may be changed quite significantly by numerical factors that occur in calculating matrix elements. [These are omitted in our crude expression Eq. (70).] In an attempt to estimate the accuracy of our semiconvergent expansion we have calculated one of the two octupole transitions for $2p$ electrons, namely $2p$ to $n'd$. We find a transition probability, summed over all continuum states, of $(95/Z^2)\ (v_a/v_{LIII})^6$, which should be compared with the probability for $2p$ to $n'p$ quadrupole (Table III) of $(21/Z^2)(v_a/v_{LIII})^4$. The ratio 4.5 $(v_a/v_{LIII})^2=0.24$ for the case of Po^{210}. Our expansion appears to be quite good for Po^{210} and K electrons; and may be satisfactory within 50 percent accuracy for Po^{210} and L electrons. It seems probable that higher multipole terms, such as the octupole, will increase the transition probability over that calculated for dipole and quadrupole terms alone.

Our summary of corrections to the calculations of ionization probability in alpha-decay is similar to that of Sec. III for the beta-decay case. For K electrons of Po, corrections will increase the probability perhaps by a factor of 2; screening corrections give a 40 percent increase. The expansion of the adiabatic approximation holds quite well. For L electrons of Po, relativistic corrections are small; screening corrections lead to an increase in the ionization probability of somewhat more than a factor of 4; and the expansion of the adiabatic approximation is of uncertain validity.

VI. EXPERIMENTAL RESULTS

Experiments might measure any of three different effects of the ionization of inner electrons due to beta- (or positron) or alpha-decay of the nucleus: (1) the emitted orbital electrons; (2) the characteristic x-rays emitted in filling the holes in the K or L shells; (3) the Auger electrons emitted in competition with the x-ray emission. Very thin, or appropriately diluted sources, must be used to make certain that the effects due to beta- or alpha-decay occur in the same atom, rather than in neighboring atoms. Further, internal conversion of nuclear gammas or emission of inner bremsstrahlung (in beta-decay) may mask or confuse the effects calcu-

[37] T. F. Tuan, M.S. thesis, Louisiana State University, 1952 (unpublished).

† *Note added in proof:*—Preliminary calculations for quadrupole transitions using the atomic wave functions of Ramberg and of Reitz show only a small screening effect, contradicting our estimate above.

lated in this paper. The confusion with internal conversion can best be avoided by choosing sources which emit no nuclear gammas. Also, the line spectrum of electrons from internal conversion could in principle be distinguished from the effects discussed in this paper. The emission of inner bremsstrahlung in beta-decay has been treated carefully theoretically, and recently confirmed in detail by experiment[1,2] so that this effect can be subtracted out.

The first effect listed above has been studied by Bruner[3] for the isotope Sc^{44} which emits positrons, and nuclear gammas and also undergoes K-capture. He used two different magnetic beta-spectrometers to measure the energy spectrum of electrons of energy from 30 to 150 kev emitted from Sc^{44}, and found consistent spectra giving a ratio of electrons/positrons of 4 percent. This high ratio cannot be reconciled with the low yields for the effects calculated in this paper. The yield of K electrons ionized by the sudden perturbation is only $0.64/Z^2$ (increased by perhaps a factor of 2 by screening corrections), and almost all of these are of much smaller energy than that of the electrons measured by Bruner. (See Fig. 1.) He suggests a mechanism of internal conversion of inner bremsstrahlung. This process is very much less probable than Bruner supposes, since the analogy between the internal conversion of nuclear gammas and that of inner bremsstrahlung is poor.[38]

Recently Porter and Hotz[4] have made a cloud-chamber study of electrons from 30 kev to 205 kev accompanying the K capture activity of Fe^{55}. They find an upper limit of 0.6×10^{-6} electron ejected per K capture, in sharp disagreement with Bruner's yield of about 4 percent. Porter and Hotz quote a theoretical prediction[4] of about 10^{-6} for the probability of ejection of an electron in this energy range. This figure is consistent with the work of Migdal,[11] Feinberg[12] and the present author[13] for the effects of beta-decay: the probability of ionization is $0.32/Z^2$; but only 0.4 percent of the ejected electrons from iron have an energy greater than 4.3 times the binding energy, or 30 kev [see Eq. (14) and Fig. 1]. We would then have an ionization probability of 2×10^{-6} per K electron, for beta-decay of Fe. If we treat K capture as another example of a sudden perturbation, the ionization yield per K electron is about half that for beta-decay, since the change in the effective nuclear charge is $1-0.35=0.65$ for K capture instead of one as for beta-decay, and this change enters squared. We then find a yield also about 10^{-6} K electron ejected with energy greater than 30 kev per K capture in Fe^{55}, in agreement with Primakoff and Porter,[17] and not inconsistent with the experiments of Porter and Hotz.‡

Madansky and Rasetti[1] confirmed the theoretical formulas for the spectrum of inner bremsstrahlung from P^{32} and RaE in the 50- to 200-kev range, using a scintillation spectrometer. Their measurement at 90 kev for the RaE case lies above the smooth theoretical curve for inner bremsstrahlung by three experimental errors. If we interpret this deviation as due to K x-rays from Po (the product atom), we find that the K x-rays are roughly 5 percent as abundant as the inner bremsstrahlung of energy greater than 90 kev. Using their figure of 1.6×10^{-3} photon ($E\geq90$ kev) per beta for the inner bremsstrahlung we find an x-ray yield of roughly 8×10^{-5} per beta, with an error of at least a factor of 2. Novey[2] obtains a similar x-ray yield for RaE. This number is in fortuitously good agreement with the theoretical yield $0.64/Z^2=9\times10^{-5}$ (see Table I). (The theoretical yield would be increased by a factor of 2 or more by screening and relativistic corrections.)§

Gray[39] has set an upper limit of 10^{-3} L x-ray per beta by absorption measurements on the photons from RaE. This is consistent with our calculated 3×10^{-4} vacancies in the L shell per beta-emission (see Table I). The L x-ray yield will be somewhat smaller since here the fluorescent yield is appreciably less than unity; but screening effects will more than compensate for this, giving 5×10^{-4} x-ray per beta.

In measurements on characteristic x-rays from beta- or positron-emitters use of a detector with good resolving power is essential to separate the x-rays from the continuous spectrum of inner bremsstrahlung. Ordinary absorption measurements are not good enough and the scintillation spectrometer is just about adequate. Critical absorption techniques or crystal diffraction should prove successful.

Thus for the case of beta- or positron decay, the first two of our three effects have been studied. Bruner's result on the first effect for Sc^{44} is much larger than theoretical results, while Madansky and Rasetti's and Gray's results for the second effect on RaE are not inconsistent with the theoretical calculations.

Many workers have studied the K and L x-rays associated with the alpha-activity of Po^{210}. This isotope emits one nuclear gamma of energy 800 kev and intensity about 1.5×10^{-5} photon per alpha[7-9] which is in coincidence with a correspondingly lower energy alpha.[40] Even a gamma-ray of this low intensity confuses the interpretation of the K x-rays, since some may be due to ionization caused by the alpha-particle, and some due to internal conversion of the nuclear gamma. Since the gamma has much lower intensity than the experimental

[38] See the end of Sec. IV for a discussion of the failure of this analogy. We hazard the guess that Bruner's sources, prepared by evaporation of an aqueous solution, exhibited "clumping"; and that the electrons are principally due to positron-electron scattering in the source.

‡ *Note added in proof:*—Primakoff and Porter include a factor for the correlation of the two K electrons, and also correct a mistake in our calculation that 0.4 percent of the ejected electrons have an energy greater than 30 kev.

§ *Note added in proof:*—Howland and Rubinson (private communication) and Boehm and Wu (Bull. Am. Phys. Soc. **28**, No. 1, 40 (1953)) have both measured the yield of characteristic x-rays associated with S^{35} beta-decay; and the latter group have also observed x-rays from RaE^{210} and Pm^{147}. The measurements are in good agreement with the calculations of this paper.

[39] J. A. Gray, Phys. Rev. **55**, 586 (1939).

[40] S. De Benedetti and G. H. Minton, Phys. Rev. **85**, 944 (1952).

yield of L x-rays, and its internal conversion coefficient is much less than unity, the L x-rays are due almost entirely to ionization by the alpha-particle.

Curie and Joliot[5] observed L and M x-rays from Po, but did not detect K x-rays, due to their low intensity. Zajac *et al.*[41] observed both the 800-kev gammas and x-rays of energy 84 ± 4 kev. Recently Grace *et al.*,[7] Barber and Helm[8] and Riou[9] have identified these x-rays as characteristic K x-rays of lead ($K\alpha$ of 73 kev): the first group used critical absorption techniques, and the second group used energy measurements by a scintillation spectrometer. The K x-rays have an intensity of 1.7×10^{-6} photon per alpha, averaging the results of the last three papers. Correcting for the fluorescent yield, the vacancies in the K shell are 10 percent greater, or 1.9×10^{-6} per alpha. Grace *et al.* believe that the vacancies in the K shell are produced mainly by internal conversion of the 800-kev gamma, while Barber and Helm believe that internal conversion produces only one-third of the K shell vacancies, the remainder or 1.3×10^{-6} per alpha being produced by alpha-particle ionization.

These arguments depend critically on the internal conversion coefficient of the 800-kev gammas. Grace *et al.* measure a conversion coefficient of 0.067 ± 0.017, by counting the number of conversion electrons and the number of gamma-rays. This would assign the majority of the K x-rays to the internal conversion process. Alburger and Friedlander[42] obtained a rough measurement of the internal conversion coefficient by observing with a magnetic beta-spectrometer both the internal conversion electrons and the photoelectrons from an external converter: their result was 0.01 to 0.05. The angular correlation measurements for alpha and gamma of DeBenedetti and Minton[40] show that the 800-kev gamma is electric quadrupole radiation, which according to Rose *et al.*[43] has a calculated internal conversion coefficient in the K shell of 0.01.

In comparison with the above results, we have calculated here 0.10×10^{-6} electron vacancy per alpha, with perhaps a factor of two or three increase for relativistic and screening effects. Migdal's result[11] is 25 times as large as ours, since he does not include the reduction of the dipole transition probability due to nuclear recoil. Grace's results (a small fraction of 1.9×10^{-6}) could agree with our calculation, but Barber and Helm's result of 1.3×10^{-6} is much larger.

An unambiguous separation of the effects of alpha-emission and internal conversion of the nuclear gamma on the K electrons seems quite difficult at the present time. Measurements of electrons in the 50- to 150-kev region, should clarify this issue.[44] One should observe weak lines corresponding to the Auger electrons; and one should also observe a continuous distribution due to the effects of alpha-particle emission. This spectrum could be compared both in intensity and in shape with the theoretical result (Fig. 1).

As noted above, measurements on the L x-rays are not confused by internal conversions of the nuclear gamma[45] of Po^{210}; however, an accurate knowledge of the fluorescent yield for the L shell is necessary for their interpretation. Curie and Joliot[5] measured the L x-rays with an electroscope and determined their energy by absorption measurements. They found a yield of about 4×10^{-4} L x-ray per alpha. Rubinson and Bernstein[6] have recently studied the L x-rays with a proportional counter. They identify them by careful energy measurements as L x-rays and determine the yield as: $L\alpha$, 1.67×10^{-4}; $L\beta$ 1.06×10^{-4}; $L\gamma$ 0.20×10^{-4}; or a total of 2.93×10^{-4} photon per alpha, with an experimental uncertainty of 15 percent. They compare a concentrated and a dilute source to show that the L x-rays are not produced in neighboring atoms. This yield is much greater than our calculated yield of 1.1×10^{-4} L vacancy per alpha using Coulomb wave functions. The calculated yield of L x-rays is appreciably less than this. If, following Rubinson and Bernstein, we use Kinsey's values[46] for the fluorescent yields in the L shell, 1.1×10^{-4} L vacancy distributed among the L_{I}, L_{II}, and L_{III} shells as shown in Table IV gives an L x-ray yield of 0.35×10^{-4}, or only 12 percent of Rubinson and Bernstein's experimental value.[47] Also see Riou[9] who confirms these experimental results. This large difference between calculations and experiment should be attributed to screening corrections and to our use of the semiconvergent expansion into multipoles. As discussed in the previous section, screening corrections increase the calculated yield by at least a factor of 3.5 and higher multipole transitions might also lead to an appreciable increase of the ionization probability for the L electrons.

Macklin and Knight[10] observed x-rays from U^{234} with a yield of roughly one photon per alpha-particle. The photons were identified as L x-rays (of thorium or uranium) by absorption measurements. This x-ray yield is several orders of magnitude greater than the experimental x-ray yield for Po^{210} and is also several orders of magnitude greater than the calculated L x-ray yield due to alpha-emission. Goldhaber and McKeown[48]

[41] Zajac, Broda, and Feather, Proc. Phys. Soc. (London) **A60**, 501 (1948).

[42] D. E. Alburger and S. Friedlander, Phys. Rev. **81**, 523 (1951).

[43] Rose, Goertzel, Spinrad, Harr, and Strong, Phys. Rev. **83**, 79 (1951).

[44] Also H. Halban (private communication) suggests measurements of coincidences between K x-rays and low energy electrons.

[45] But one could make an *ad hoc* assumption of *another* nuclear gamma of energy between the K and L binding energies, which is strongly converted in the L shell. One could make a similar assumption to explain the high yield of K x-rays.

[46] B. B. Kinsey, Can. J. Research **A26**, 404 (1948).

[47] By coincidence, this calculated yield is almost identical with that quoted by Rubinson and Bernstein, based on Migdal's calculations. (Incidentally, we believe Rubinson and Bernstein have misinterpreted Migdal's formula in using $v_e = Ze^2/\hbar n$, rather than as $Ze^2/\hbar$.) *Notes added in proof:*—(1) Correction of our error in the $2s$-$n'd$ calculation lowers the calculated yield to 7 percent of the experimental value. (2) Rubinson (private communication) is now convinced of our interpretation of Migdal's formula. (3) Screening corrections appear to be rather small.

[48] G. Scharff-Goldhaber and M. McKeown, Phys. Rev. **82**, 123 (1951).

studied the radiation from U^{234} with a proportional counter, and identified the 17-kev gammas as L x-rays of thorium. They interpret Teillac's photographic plate measurements[49] of internal conversion electrons (about 0.3 per alpha) as showing the presence of strongly converted gamma-rays of energies from 50 to 90 kev.[50] Recently Bell *et al.*[51] have observed 55-kev gammas from U^{234}, using a scintillation spectrometer. This confirms Goldhaber's interpretation of the L x-ray yield from U^{234}.

In summary, experiments on RaE are consistent with the K x-ray yield for beta-emission calculated in this paper, but do not verify it. Bruner's experiment on Sc^{44} is inconsistent with our calculations. Grace's interpretation that the K x-rays of Po^{210} are mainly due to internal conversion of the 800-kev nuclear gamma is consistent with the calculations of this paper. Barber and Helm's interpretation of 1.3×10^{-6} K vacancy per alpha as due to alpha-emission, is much higher than the yield for NR Coulomb wave functions of 0.1×10^{-6}. Rubinson and Bernstein and Riou's measurements of L x-rays from Po give a yield about 8 times that calculated for Coulomb wave functions, much of the discrepancy being attributed to screening effects. The high x-ray yield from U^{234} is due to internal conversion of a nuclear gamma. The theoretical yields will be increased appreciably by three different corrections: relativistic corrections for the K shell; screening corrections and (for the case of alpha-emission) failure of the adiabatic approximation for the L shell. Due to the provisional nature of some of the present experiments, and the approximate nature of the present calculation, good agreement is not to be expected as yet.

The author is grateful to P. Morrison for his direction of our thesis research on this problem and his continued interest in the problem after that time. He also acknowledges the assistance given by H. A. Bethe, W. Rubinson, D. Bohm, M. Goodrich, H. Halban, L. Madansky, H. M. Schwartz, and J. Wendel in discussions of various aspects of this problem. Much of this work was done at Cornell University; some of the work on screening corrections was done at the University of Wisconsin.

[49] J. Teillac, Compt. rend. **239**, 1056 (1950).
[50] Also see reference 13, p. 35.
[51] Bell, Davis, Francis, and Cassidy, Oak Ridge National Laboratory Progress Report ORNL 1164, 1951 (unpublished).

PHYSICAL REVIEW VOLUME 90, NUMBER 1 APRIL 1, 1953

The Alpha-Particle Induced Phosphorescence of Silver-Activated Sodium Chloride*

C. E. MANDEVILLE AND H. O. ALBRECHT
Bartol Research Foundation of the Franklin Institute, Swarthmore, Pennsylvania
(Received December 16, 1952)

Using as primary excitants ultraviolet light and polonium alpha-particles, the phosphorescent afterglow of the double banded phosphor, silver-activated sodium chloride, has been measured as a function of the time with photosensitive Geiger counters and photomultiplier tubes. The decay curves of the phosphorescent intensity of the two bands can be represented by appreciably different power laws. Decay slopes greater in absolute magnitude than two on a $\log I - \log t$ plot have been frequently observed.

INTRODUCTION

IN several previous communications,[1,2] the writers have discussed the fluorescence and phosphorescence of NaCl-Ag irradiated by nuclear particles. The earlier reports[1,2] constitute mainly an account of how first phosphorescent emission, and later fluorescent pulses, were detected in photosensitive Geiger counters. In the course of qualitative studies of the phosphorescence of the far ultraviolet band as detected with photosensitive Geiger counters, a marked stimulation of the ultraviolet band by long wave light was noted. The soft radiations from the red and green pilot lights on the control panel of the scaling circuit gave rise to a distinct stimulation of the phosphorescent emission. It was immediately suggested[2] that NaCl-Ag might serve as a dosimeter for nuclear radiation, the phosphorescent yield under photostimulation being a measure of dosage received much earlier. However, the present discussion will concern itself mainly with a study of the normal unstimulated phosphorescence induced in samples of NaCl-Ag by alpha-particles and ultraviolet light.

Since the time of the first reports by the writers,[1-3] the study of the phosphorescence of NaCl-Ag has been extended by Furst and Kallmann[4] and by Bittman, Furst, and Kallmann.[5] The light emission has been shown to occur in two bands[2,4] centered, respectively, at 2500A and 4000A. It has also been known for some time that these two bands are emitted when ultraviolet

* Assisted by the joint program of the U. S. Office of Naval Research and the U. S. Atomic Energy Commission.
[1] C. E. Mandeville and H. O. Albrecht, Phys. Rev. **79**, 1010 (1950); **80**, 117, 299, and 300 (1950).
[2] H. O. Albrecht and C. E. Mandeville, Phys. Rev. **81**, 163 (1951); Rev. Sci. Instr. **22**, 855 (1951).
[3] C. E. Mandeville, privately circulated memorandum (September 26, 1950).
[4] M. Furst and H. Kallmann, Phys. Rev. **82**, 964 (1951); **83**, 674 (1951).
[5] Bittman, Furst, and Kallmann, Phys. Rev. **87**, 83 (1952).

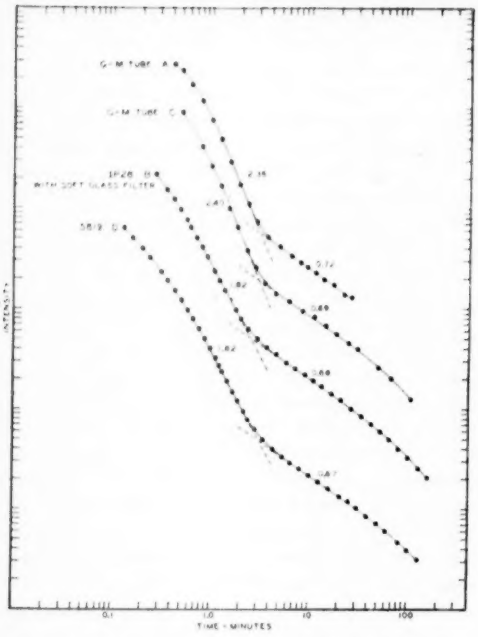

FIG. 1. Phosphorescent decay of NaCl-Ag (Harshaw) irradiated on successive occasions for five seconds at a time by the alpha-particles of polonium. The curves are lettered in chronological order.

light is employed as the primary excitant.[6] A discussion of previous papers on ultraviolet excitation of NaCl-Ag may be found in the aforementioned reference.[6]

PROCEDURE

In the present investigation, the phosphorescence of NaCl-Ag irradiated by alpha-particles and ultraviolet light has been observed, using as detectors photosensitive Geiger counters and photomultiplier tubes RCA-5819 and RCA-1P28. The G-M tubes were constructed with copper cathodes, and the phosphorescent emission was usually introduced through a thin window of Pyrex (3 mg/cm²) or through a side wall of thickness one millimeter, made of Corning 9741 glass. These tubes exhibited a maximum of spectral response at ~2500A with no detectable response whatever above ~3000A. With the strongest phosphorescent sources used, the counting rates of the photosensitive G-M tubes decreased immediately to cosmic ray background when one millimeter of soft glass was inserted before the counter, indicating only response to the ultraviolet of the short wave band. *Thus, measurements with the G-M tubes constituted observation of the decay of the short wave band alone.*[7] The RCA-5819 photomultiplier was utilized for detection of the phosphorescence of the long wave band. Although these tubes are not expected to respond at wavelengths shorter than 3000A, two millimeters of soft glass were interposed between phosphorescent source and phototube as a precautionary measure for elimination of any last vestiges of response to the short wave band. The dc current flowing in the photomultiplier was taken as a measure of the phosphorescent intensity. The current was measured in a fast galvanometer ($T=4$ sec), and measurements were not commenced until several seconds after cessation of irradiation, so that ballistic corrections were small as shown by calculation in terms of the constants of the galvanometer. The deflection of the galvanometer and the readings of a stop watch were photographed simultaneously with a Sept camera. Measurements with an RCA-1P28 photomultiplier tube were also carried out. This detector is sensitive to light emitted in both bands. The decay curve of the combined emission of both bands is of interest for reasons to be discussed later.

The above discussed detectors can, of course, also be used for the detection of "stored light" released by thermostimulation[8] and photostimulation.[9]

In general, the properties of two types of crystals have been investigated. Single crystals of NaCl+1 percent AgCl were obtained from the Harshaw Chemical Company (hereafter referred to as "Harshaw"), and polycrystalline melts of NaCl+0.5 percent AgCl were prepared at the Bartol Research Foundation (hereafter referred to as "Bartol").

RESULTS

The decay of NaCl-Ag (Harshaw), irradiated for five seconds by a source of twenty-five millicuries of polonium alpha-particles, is shown in Fig. 1. For these measurements the same specimen was bombarded repeatedly, under identical conditions; that is, successive decay curves were taken first in the G-M tube, then in a 1P28 tube with filter, again in the G-M tube, and finally in the RCA-5819 photomultiplier tube. The crystal was completely de-excited between bombardments by photostimulation at the conclusion of each decay curve. Because of the response characteristics of the various detectors as discussed in the preceding section, it is evident that curves A and C give the decay of the short wave band and curves B and D that of the long wave band. All of the curves of Fig. 1 exhibit two distinct slopes on the log-log plot.[10] The short wave band has an early slope of $\sim(-2.38)$ followed by a later slope of $\sim(-0.7)$. The long wave band decays initially with a slope of $\sim(-1.83)$ followed by the later

[6] Etzel, Schulman, Ginther, and Claffy, Phys. Rev. **85**, 1063 (1952).

[7] The photosensitivity of the G-M tubes was checked at the beginning and upon completion of each decay curve by means of a standard ultraviolet source. This consisted of an alpha-source bombarding a crystal of fluorite.

[8] H. Friedman and C. P. Glover, Nucleonics **10**, No. 6, 24 (1952).

[9] Kallmann, Furst, and Sidran, Nucleonics **10**, No. 9, 15 (1952).

[10] It is to be observed that at times less than one minute the decay curves are relatively flat, and the slopes have not as yet assumed in absolute magnitude the value of the exponent of the power law which characterizes the decay. A slope equal in magnitude to the exponent is attained when $At\delta \gg 1$ [see Eq. (2) of the text].

slope of $\sim(-0.7)$. From the curves of Fig. 1, several general conclusions can be drawn:

(1) The absolute value of the decay slopes can be considerably larger than two.

(2) At least two trap depths are involved. The steep initial slope represents the depletion of electrons in traps shallower than the traps related to the slope of $\sim(-0.7)$.

(3) The slope of $\sim(-0.7)$ is not the terminal decay slope of the light emission associated with escape of electrons from the deeper traps. It is an earlier slope which is encountered in a transition region such as that described by Mott and Gurney.[11]

(4) The short and long wave bands decay according to differing power laws in the region below $\sim$5 minutes.

A second Harshaw crystal was irradiated by polonium alphas for five seconds at a time, and decay curves were observed with the use of various detectors as shown in Fig. 2. The results are essentially the same as those of Fig. 1, the short wave band decaying with a steeper slope on the log-log plot than does the long wave band. It is to be noted that the slope of curve A is intermediate between the corresponding slopes of curves B and D (the long wave band alone) and curve C (the short wave band). Curve A, obtained with no filter before the 1P28, gives the decay of the combined emission of the two bands. To ascertain whether the slower decay [slope $\sim(-0.7)$] offered any explanation for the differing decay slopes of the two bands, the slower decay was extrapolated to small values of the time and subtracted from the total intensity on the interval 0.5 min$<t<$2 min, t being the time. On this time interval, the slope of the difference curve of curve C became (-3.00) and that of the difference curve of curve D became (-2.16). The apparent difference in the modes of decay was not erased by this operation. The ratio of the slopes remained unchanged. Thus,

$$n_C/n_D = 2.48/1.83 = 3.00/2.16 = 1.35.$$

The decay slopes are thought to have been measured with a probable error of ± 0.05.

The question of whether successive bombardments in some way altered the properties of the crystal come under consideration. The decision was made to observe simultaneously the decay of the two bands resulting from a single irradiation. Accordingly, NaCl-Ag (Bartol) was irradiated for five seconds with polonium alphas. The phosphorescing material was placed between a photosensitive G-M tube and a 1P28 photomultiplier tube. Curves I show the simultaneous decay of the two bands as observed with the 1P28 with filter and with a photosensitive G-M tube. Curves II represent simultaneously observed decay curves using as detectors a G-M tube and the 1P28 without filter. Here again it is clear that the two bands decay with differing power laws and that the decay of the mixture of the two bands has an intermediate slope.[12] It is to be observed that the curves of Fig. 3 assume their maximum negative slopes at times about ten minutes later than do those of Figs. 1 and 2, although the conditions of excitation were identical and the specimen sizes comparable. This difference could be explained by variation of silver content.

DISCUSSION OF RESULTS

Decay slopes greater than two have been previously observed.[13] For example, a slope of -2.09 was reported for ZnS under ultraviolet excitation at 80°C. However, this same decay curve, when examined at a relatively low value of the phosphorescent intensity, begins to exhibit a slope much larger in absolute magnitude than 2. These data are interpreted by Mott and Gurney[11] as evidence for "frozen-in" interstitial ions which serve as luminescence centers.

A similar explanation may also apply to the curves of the present investigation. Let it be assumed that ν interstitial ions are present and that n trapped electrons and n positive holes result from excitation by the alpha-

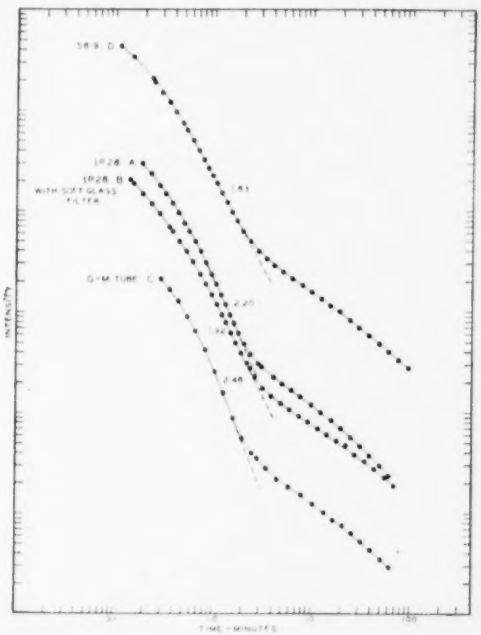

FIG. 2. Phosphorescent decay of NaCl-Ag (Harshaw). The absolute magnitude of the slope of the short wave band observed in the G-M tube is greater than that of the long wave band (5819 and 1P28 with filter). The slope of decay of the two bands combined is intermediate. The curves are lettered chronologically.

[11] N. F. Mott and R. W. Gurney, *Electronic Processes in Ionic Crystals* (Oxford University Press, London, 1948), second edition, p. 215, Fig. 84.

[12] The curves detected in the G-M tubes have been unduly depressed by dead-time loss at times less than one minute. On the interval 1 min$\leq t\leq$5 min where the evaluation of the slope was made, the dead-time loss was negligible.

[13] V. V. Antonov-Romanovsky, Physik. Z. Sowjetunion **7**, 366 (1935).

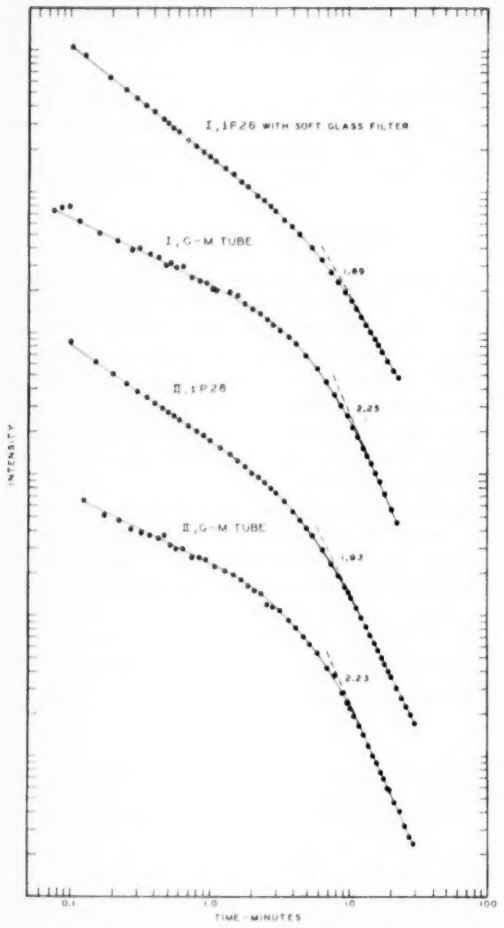

FIG. 3. Phosphorescent afterglow of NaCl-Ag (Bartol) observed simultaneously in G-M tube and photomultiplier.

particles. Then, following Mott and Gurney,[14]

$$dn/dt = -An(n+\nu), \tag{1}$$

where A is a constant. For $n \gg \nu$, the solution of this equation is

$$\frac{dn}{dt} = \left(\frac{dn}{dt}\right)_{t=0} \Big/ (1+An_0t)^2. \tag{2}$$

For $n \ll \nu$, the solution is

$$\frac{dn}{dt} = \left[\left(\frac{dn}{dt}\right)_{t=0}\right] e^{-\nu At}. \tag{3}$$

When the traps are nearly exhausted, at relatively large values of the time, Eq. (1) indicates that a first order process becomes the dominant mode of decay, giving rise through Eq. (3) to slopes on a log-log plot greater than the slope of two which is associated with the normal bimolecular decay of Eq. (2).† For large values of the time, the slope of an exponential process approaches infinity on a log-log plot.

A general conclusion which can be drawn from these measurements is that for a given set of conditions of excitation, the two bands decay according to different power laws. It has been previously shown[6] that the long wave band arises from the presence of paired silver ions in the crystal lattice. It seems, therefore, probable that the trap depth distribution associated with paired silver ions is different from that related to the single silver ions.[15]

ADDITIONAL REMARKS

The decay curves of this paper are representative of about two hundred similar curves which have been recorded in connection with the phosphorescent decay of NaCl-Ag. Although Figs. 1, 2, and 3 refer specifically to the alpha-particle induced phosphorescence, as stated in the introduction, ultraviolet light was also employed as a primary excitant. The decay curves excited by ultraviolet did not differ markedly from those arising from alpha irradiation. Slopes greater in absolute magnitude than two were often encountered.

Although not shown in the accompanying figures, negative slopes having absolute values greater than two were often observed for the decay curves of the long wave band under both ultraviolet and alpha-particle excitation. For one such curve, the "light sum" was calculated for an irradiation with 25 mC of alpha-particles for five seconds. This rough estimate gave a phosphorescence yield in the long wave band of 0.54 photon/alpha on the time interval 5 sec$\leq t \leq \infty$. Taking into account the presence of the short wave band, a total emission of one or two photons per alpha-particle is suggested. In the course of the present measurements, it was estimated that specimens of approximate dimensions 1 cm×1 cm×0.4 cm were irradiated by $\sim 10^9$ alphas to give a light sum of $\sim 10^9$ photons.

The question arose as to whether the long wave band might be sufficiently intense to photostimulate the decay of the short wave band. Two identical crystals of NaCl-Ag were placed adjacent to each other with one millimeter of soft glass intervening. The long wave emission of one seemed to have no effect on the short wave emission of the other.

The writers wish to express their appreciation for the interest and suggestions of Dr. W. F. G. Swann in connection with these measurements. They wish also to acknowledge very helpful commentary by Dr. Raymond T. Ellickson of the University of Oregon.

[14] See reference 11, p. 212.

† An alternative explanation of the large negative slopes may be related to the storage of electrons in deep traps. Equations (1), (2), and (3) would also apply were there no interstitial ions but ν-electrons stored in deep traps and n electrons in shallow traps.

[15] See *Preparation and Characteristics of Solid Luminescent Materials; Cornell Symposium of the American Physical Society* (John Wiley and Sons, Inc., New York, 1948) and remarks by Garlick, Prongsheim, and Maurer, p. 397; also statements by Garlick, paper No. 5, p. 111.

The First Excited States of Even-Even Nuclei

KENNETH W. FORD
Palmer Physical Laboratory, Princeton University, Princeton, New Jersey
(Received December 1, 1952)

The collective model of the nucleus, as expressed in A. Bohr's strong coupling approximation, is applied to the low levels of even-even nuclei. It yields the correct level order of the first few states, and predicts the qualitative regularities of the first excited energy surface which are observed experimentally. The approximation is shown to be much better for two or more extra nucleons than for one, but the first excited energy spacing is sensitive to second-order corrections even for many extra nucleons. Predicted nuclear distortions are larger than is reasonable (a) in the rare earth group, and (b) near doubly magic Pb^{208}. An empirical way to correct for this discrepancy is to diminish the particle-to-surface coupling coefficient.

A simple formula is given for computing an upper limit to the nuclear distortion from the first excited energy of even nuclei. After correction by a single adjustable parameter, this formula yields a fair correlation with quadrupole moments and a better correlation with isotope shifts in the region $50<N<126$. The energy level behavior beyond Pb gives a prediction of quadrupole moment and isotope shift behavior for $N>126$. Certain regularities in the levels of odd-even nuclei are also predicted.

I. INTRODUCTION

THE first excited levels of even-even nuclei (hereafter called simply even nuclei) are known to exhibit regularities in spin and parity,[1,2] and also in energy.[2] A large majority of these levels where spin and parity are known have spin 2, even parity. (There is also a tendency, less marked, for the second excited states of even nuclei to have spin 4, even parity.[1,2]) As a function of mass number A, the energy of the first excited states of even nuclei shows a generally decreasing trend with A, but with large variations around the mean. These variations are strongly correlated with the magic numbers, and show a remarkable regularity as a function of N and Z.[2] Closing a shell in either N or Z brings about a sharp increase in the energy of the first excited state, and closing shells in both N and Z (Ca^{40}, Pb^{208}) a still sharper increase. Those nuclei farthest from any magic number, the rare earths, exhibit anomalously low energies of the first excited state, as do the heaviest elements, around uranium. If the data available for the energy of first excited states of even nuclei are plotted as a function of both N and Z, an energy surface is suggested with sharp spikes at the doubly magic nuclei, sharp ridges along the magic numbers, and broad valleys between the magic numbers.

The predominance of spin-two, even parity first excited levels of even nuclei has received theoretical explanation in terms of the shell model (independent nucleons in spherical well with particle interaction added).[3-5] It is assumed that the first excited level is due to the excitation of a single pair of nucleons. Taking a central attractive force of reasonable range between the nucleons, it is found that the ground state is 0+, as observed; the first excited state is 2+, as usually observed; and the second excited state is 4+, as sometimes observed. The 0–2 energy spacing for the configuration $(j)^2$ is proportional to $(2j+1)$ and equal to about 1.5 Mev for $j=\frac{9}{2}$, a value large compared to most experimental values. The 2–4 spacing for the $(j)^2$ configuration is found to be much smaller than the 0–2 spacing. Experimentally the 0–2 and 2–4 spacings are comparable. De Shalit and Goldhaber[5] argue that the observed regularities in the first excited energies can be explained qualitatively in terms of mixtures of states of excitation of different neutron and proton pairs. The farther one is from a magic number, the more states will be mixed in the first excited level, and the more will that level be lowered due to their interaction, other factors being equal.

The preponderance of spin-two, even parity excited levels receives a simple explanation also in terms of the pure liquid droplet model. On this model, the lowest excited state of collective oscillation is the P_2 ellipsoidal mode, with spin two, even parity. Because of the collective description, however, no explanation of shell structure effects can be given by this model. It gives for the lowest excitation of vibrational energy,

$$E_1=\hbar(C/B)^{\frac{1}{2}}, \tag{1}$$

where

$$C=C_{\text{surface}}+C_{\text{coulomb}}=4\pi r_0^2A^{\frac{2}{3}}\mathcal{O}-(3/10\pi)(Z^2e^2/r_0A^{\frac{1}{3}}) \tag{2}$$

and

$$B=\tfrac{1}{2}\rho_0 r_0^5A^{5/3}=\text{mass coefficient}. \tag{3}$$

Here $\mathcal{O}$ is the nuclear surface tension, given empirically by $4\pi r_0^2\mathcal{O}\cong 15$ Mev. ρ_0 is the density of nuclear matter, and the nuclear radius is assumed to be equal to $r_0A^{\frac{1}{3}}$. For medium and heavy nuclei, where the liquid droplet model is expected to have validity, $C\cong 60$ Mev and does not vary much with A. In this range, therefore,

$$E_1\cong(100/A^{5/6})\text{ Mev}. \tag{4}$$

No such simple law is obeyed. Sharp variations in the empirical E_1 due to shell structure are observed, and the average E_1, as nearly as it can be approximated,

[1] M. Goldhaber and A. W. Sunyar, Phys. Rev. **83**, 906 (1951).
[2] G. Scharff-Goldhaber, Phys. Rev. **87**, 218 (1952).
[3] B. H. Flowers, Phys. Rev. **86**, 254 (1952).
[4] D. Kurath, Phys. Rev. **87**, 218 (1952).
[5] A. De Shalit and M. Goldhaber (to be published).

seems to decrease more rapidly with A than the negative 5/6 power in Eq. (4).

Both the independent particle model of the nucleus and the liquid droplet model are inadequate to explain the observed regularities of the first excited states of even nuclei. Because of the marked shell structure effects, the pure liquid droplet model is especially inappropriate.

The purpose of the present article is to apply the theory of the combined liquid droplet-free particle model, hereafter called the *collective model*, to the problem of the low states of even nuclei. This model has been developed principally by Bohr[6] and by Hill and Wheeler.[7] According to the collective model, the rapid variation of potential near the edge of the nucleus creates a membrane-like surface capable of undergoing oscillation (conventional liquid droplet model) and in addition capable of being distorted by the action of the "free" nucleons within the nucleus into a permanently nonspherical shape. The nonsphericity is important for quadrupole moments. In addition, the nuclear distortion acts back on the particles and strongly affects the interparticle coupling. The nonspherical shape of the nucleus, therefore, will affect a large number of nuclear properties. In particular, magnetic moments[8] and the order of nuclear levels will require an understanding of the nuclear surface effect for their explanation.

In the following sections, Bohr's theory of the collective model is generalized to several extra nucleons and applied in a straightforward way to even nuclei. It is found that the model explains the qualitative regularities of the first excited states but requires modification to give reasonable quantitative values for the energies in the calculable cases near closed shells. The model suggests a relation between the energy of the first excited state of even nuclei and the quadrupole moments of neighboring odd-even nuclei. The regularities in these two quantities are in good qualitative agreement for the heavy nuclei, but the nuclear distortion calculated from excitation energy of even nuclei is considerably larger than the distortion calculated from quadrupole moments.

II. SPIN, PARITY, AND ENERGY OF FIRST EXCITED STATES

A. Bohr Theory for Single Extra Nucleon

Our starting point is the theory of the interaction of extra nucleons with the nuclear surface, as developed by Bohr, especially his strong coupling (of particle to surface) approximation. The direct interaction among the nucleons is neglected. In his treatment of a single extra nucleon outside closed shells, this effect did not enter. We neglect the direct interparticle interaction because it is the aim here to show that the coupling of particles to the nuclear surface—and thereby indirectly to each other—is alone sufficient to account for the general pattern of the low states of even nuclei. Since the interparticle interaction tends to produce the same order of levels as is derived here, its inclusion would serve to reinforce the conclusions on level order derived from the collective model alone. The inclusion of the direct particle interaction in a calculation of the energy of first excited states would greatly complicate the problem and prevent the remarkable result of the collective model—the sensitive dependence of excitation energy on the permanent distortion of the nucleus—from emerging with full clarity.

For ease in treating the case of strong coupling of particle to surface, Bohr develops a Hamiltonian for the nucleus in terms of particle coordinates relative to nuclear axes ($\mathbf{r}'$, σ'), coordinates of distortion relative to nuclear axes (β, γ), and coordinates of the nuclear axes relative to space axes (Euler angles $\theta_1\theta_2\theta_3$). A principal underlying assumption is that the particle motion is so rapid compared to the motion of the nucleus as a whole, that it is a good approximation to treat the particle motion as if the nuclear axes are fixed in space. It is also assumed for convenience that very strong spin-orbit interaction exists, and that j for each particle remains a good quantum number. In fact, the strong surface interaction will break down j-j coupling, and it will be important to consider a finite spin-orbit interaction in problems involving an odd number of particles (e.g., ground-state magnetic moments). For even nuclei, however, the surface-induced pairing effect is so strong that the magnitude of the spin-orbit coupling is probably less important for the behavior of the ground and first excited state than in odd-even nuclei. This point is being investigated in greater detail, but the assumption that j is a good quantum number is retained in the present paper.

The nuclear Hamiltonian is written as the sum of three terms: H_p, particle Hamiltonian; H_s, surface Hamiltonian; and H_{int}, interaction energy averaged over the particle motion. The particle term is

$$H_p = T_p' + V'_{\text{square well}} \text{ (prime denotes variable } \mathbf{r}' \text{ relative to nuclear axes).} \quad (5)$$

Taking the nuclear surface relative to the nuclear axes to be given by

$$R = R_0[1+\textstyle\sum_\mu \alpha_\mu' Y_{2\mu}(\theta', \varphi')], \quad (6)$$

where

$$\alpha_2' = \alpha_{-2}' = (1/\sqrt{2})\beta \sin\gamma, \quad \alpha_1' = \alpha_{-1}' = 0, \quad \alpha_0' = \beta\cos\gamma,$$

we obtain the surface energy in terms of the distortion coordinates β, γ, and the Euler angles defining the nuclear orientation in space:

$$H_s = T_{\text{vib}} + T_{\text{rot}} + V_s. \quad (7)$$

[6] A. Bohr, Kgl. Danske Videnskab, Selskab. Mat. fys. Medd. **26**, No. 14 (1952).
[7] D. Hill and J. A. Wheeler, Phys. Rev. **89**, 1102 (1953).
[8] A. Bohr, Phys. Rev. **81**, 134 (1951).

Surface vibration energy:

$$T_{\text{vib}}=-\frac{\hbar^2}{2B}\left[\frac{1}{\beta^4}\frac{\partial}{\partial\beta}\beta^4\frac{\partial}{\partial\beta}+\frac{1}{\beta^2}\frac{1}{\sin 3\gamma}\frac{\partial}{\partial\gamma}\sin 3\gamma\frac{\partial}{\partial\gamma}\right]. \quad (8)$$

Surface rotational energy:

$$T_{\text{rot}}=\sum_{\kappa=1}^{3}(\hbar^2Q_\kappa^2/2\vartheta_\kappa). \quad (9)$$

Surface potential energy:

$$V_s=\tfrac{1}{2}C\beta^2. \quad (10)$$

B and C are the quantities defined by Eqs. (3) and (2). ϑ_κ is the effective moment of inertia of the nuclear surface about the κ axis and is given by

$$\vartheta_\kappa=4B\beta^2\sin^2[\gamma-(2\pi/3)\kappa]. \quad (11)$$

The component of the rotational angular momentum of the nuclear surface, Q_κ, is given simply by

$$Q_\kappa=I_\kappa-j_\kappa, \quad (12)$$

where I_κ and j_κ are components of the total angular momentum and of the angular momentum of the particle *along the nuclear axes*. The interaction energy, taken to first order in $R-R_0$, is given by

$$H_{\text{int}}=-V_0R_0\delta(r'-R_0)\textstyle\sum_\mu\alpha_\mu'Y_{2\mu}(\theta',\varphi'), \quad (13)$$

where V_0 is the depth of the nuclear potential well. Consistent with the assumption of rapid particle motion relative to nuclear vibration and rotation, this expression is averaged over particle coordinates $r'\theta'\varphi'$ before insertion into the Hamiltonian. It yields

$$\bar{H}^{(1)}{}_{\text{int}}=(nljm|H_{\text{int}}|nljm)=-\beta\cos\gamma(5/\pi)^{\frac{1}{2}}\bar{T}\frac{j(j+1)-3m^2}{4j(j+1)}, \quad (14)$$

where $\bar{T}$ is an energy of the order of magnitude of the particle kinetic energy, which depends on n and l but is here assumed to be a constant. (In the limit of infinite nuclear potential well depth, $\bar{T}$ is exactly the particle kinetic energy.) The matrix elements of Eq. (13) which are diagonal in nlj but off-diagonal in m,

$$\bar{H}^{(2)}{}_{\text{int}}=(nljm_1|H_{\text{int}}|nljm_2)=\beta\sin\gamma(15/\pi)^{\frac{1}{2}}\bar{T}[(j\pm m_1)(j\pm m_1-1)\times(j\mp m_1+1)(j\mp m_1+2)]^{\frac{1}{2}}\delta(m_1,m_2\pm 2), \quad (15)$$

must also be added to the Hamiltonian to account for the mixing of different m's.

Bohr then splits the Hamiltonian into a zero-order part H_0, which commutes with I_3 and j_3, and a perturbing part U, with no diagonal matrix elements in an I_3j_3 representation. These are[9]

$$H_0=H_p+T_{\text{vib}}+\left\{V_s+\left(\frac{\hbar^2}{4\vartheta_1}+\frac{\hbar^2}{4\vartheta_2}\right)[I(I+1)-I_3^2+j(j+1)-j_3^2-(j+\tfrac{1}{2})(I+\tfrac{1}{2})(-1)^{I-j}\delta(\Omega,\tfrac{1}{2})\delta(K,\tfrac{1}{2})]+(\hbar^2/2\vartheta_3)(I_3-j_3)^2+\beta\cos\gamma(5/\pi)^{\frac{1}{2}}\bar{T}\frac{3\Omega^2-j(j+1)}{4j(j+1)}\right\}, \quad (16)$$

and

$$U=U_1+U_2+U_3,$$

$$U_1=(1-D)\left(-\frac{\hbar^2}{\vartheta_1}I_1j_1-\frac{\hbar^2}{\vartheta_2}I_2j_2\right), \quad (17a)$$

where D is the projection operator onto the $j_3I_3(\Omega, K)$ representation,

$$U_2=\left(\frac{\hbar^2}{4\vartheta_1}-\frac{\hbar^2}{4\vartheta_2}+(15/\pi)^{\frac{1}{2}}\frac{\bar{T}\beta\sin\gamma}{4j(j+1)}\right)(j_1^2-j_2^2), \quad (17b)$$

$$U_3=\left(\frac{\hbar^2}{4\vartheta_1}-\frac{\hbar^2}{4\vartheta_2}\right)(I_1^2-I_2^2). \quad (17c)$$

The part of H_0 enclosed in curly brackets, since it contains no derivatives in β, γ, may be regarded as an effective surface potential. It is denoted by $W(\beta,\gamma)$, and the values of β, γ for which W is minimum, by β_1, γ_1. W contains three parts in the following historical order: (1) $V_s=\frac{1}{2}C\beta^2$ = classical liquid droplet surface potential, minimum at $\beta=0$, appropriate for spherically symmetric nuclei; (2) the interaction term H_{int}, linear in β, which displaces the minimum of W to β_1 different from zero, as considered, e.g., by Rainwater[10] and by Feenberg and Hammack;[11] (3) the rotational terms, proportional to $1/\beta^2$, introduced by Bohr to take proper account of the total nuclear dynamics. For extremely strong particle to surface coupling, the rotational terms become negligible and one may revert to the simpler theory which treats the nucleus as stationary in space. Such a limit is not attained in actual nuclei. For rather strong coupling, the rotational terms are smaller than the surface potential V_s or the interaction term H_{int}, but are not negligible. This appears to be the situation for the low levels of most heavy nuclei ($A\gtrsim 150$). The strong coupling approximation is then valid (particle motion rapid relative to nuclear rotation) and the perturbation terms U are found to be small. For larger rotation terms, the strong coupling approximation begins to fail, the amplitude of nuclear oscillation

[9] These expressions are not exactly as given by Bohr, because of the diagonal contribution of Bohr's U_1, pointed out by Davidson and Feenberg (see reference 14).

[10] J. Rainwater, Phys. Rev. **79**, 432 (1950).

[11] E. Feenberg and K. C. Hammack, Phys. Rev. **81**, 285 (1951).

becomes comparable to the mean distortion, and the perturbation terms in U become large. This appears to be the situation for $A \lesssim 75$. In the range $75 < A < 150$, the validity of the strong coupling approximation depends on the number of extra nucleons participating in the distortion. Adding extra nucleons increases the values of $H_{\rm int}$ and V_s, increasing β_1, and thereby decreasing the magnitude of the rotational kinetic energy and of most of the terms in U.

B. Extension to Several Extra Nucleons

The extension of the theory to several extra nucleons is straightforward. The interaction term becomes a sum over the extra particles, and the components of rotational angular momentum are given by

$$Q_s = I_s - j_{as} - j_{bs} - \cdots - j_{ns}.$$

Insisting on I_3, j_{i3}, all i, as good quantum numbers of the zero-order Hamiltonian, we obtain

$$\begin{aligned} H_0 = \textstyle\sum_i H_p^{(i)} + T_{\rm vib} + \Big\{ & \tfrac{1}{2}C\beta^2 + (\hbar^2/2\mathcal{I}_3)(I_3 - \textstyle\sum_i j_{i3})^2 \\ & + \frac{1}{2}\left(\frac{\hbar^2}{2\mathcal{I}_1} + \frac{\hbar^2}{2\mathcal{I}_2}\right)\Big[I(I+1) - I_3^2 + \textstyle\sum_i j_i(j_i+1) - j_{i3}^2 \\ & - \sum_{i \neq m} (j_m - \Omega_m)(j_m + \Omega_m + 1)\delta(j_i, j_m)\delta(\Omega_m, \Omega_i - 1) \\ & - (I + \tfrac{1}{2})(-1)^{I - \sum_i j_i + \frac{1}{2}(n-1)}\delta(K, \tfrac{1}{2}) \\ & \times \textstyle\sum_i (j_i + \frac{1}{2})\delta(\Omega_i, \frac{1}{2})\delta([\Omega_k], [-\Omega_k])\Big] \\ & + (5/\pi)^{\frac{1}{2}}\bar{T}\beta\cos\gamma \textstyle\sum_i \dfrac{3\Omega_i^2 - j_i(j_i+1)}{4j_i(j_i+1)} \Big\}, \end{aligned} \tag{18}$$

where n is the number of extra nucleons, $\delta(j_i, j_m) = 0$ unless the quantum numbers $(nlj)_i = (nlj)_m$, and $\delta([\Omega_k], [-\Omega_k])$ vanishes unless for every particle with quantum numbers $(nlj\Omega)$, except the ith particle, there is another particle with quantum numbers $(nlj, -\Omega)$. Note that for a closed subshell all of the sums over particle quantum numbers vanish. The perturbing Hamiltonian is

$$U = U_0 + U_1 + U_2 + U_3 + U_4.$$

$$U_0 = (1 - D)(\hbar^2/4\mathcal{I}_1 + \hbar^2/4\mathcal{I}_2)\Big(\sum_{i \neq m} j_{i1}j_{m1} + j_{i2}j_{m2}\Big), \tag{19a}$$

where D is the projection operator onto the $I_3 j_{i3}$ representation;

$$U_1 = (1 - D)\Big[-(\hbar^2/\mathcal{I}_1)I_1 \textstyle\sum_i j_{i1} - (\hbar^2/\mathcal{I}_2)I_2 \sum_i j_{i2}\Big]; \tag{19b}$$

$$U_2 = \sum_i \left(\frac{\hbar^2}{4\mathcal{I}_1} - \frac{\hbar^2}{4\mathcal{I}_2} + (15/\pi)^{\frac{1}{2}}\frac{\bar{T}\beta\sin\gamma}{4j_i(j_i+1)}\right)(j_{i1}^2 - j_{i2}^2); \tag{19c}$$

$$U_3 = \tfrac{1}{4}(\hbar^2/\mathcal{I}_1 - \hbar^2/\mathcal{I}_2)(I_1^2 - I_2^2); \tag{19d}$$

$$U_4 = \tfrac{1}{4}(\hbar^2/\mathcal{I}_1 - \hbar^2/\mathcal{I}_2)\Big(\sum_{i \neq m} j_{i1}j_{m1} - j_{i2}j_{m2}\Big). \tag{19e}$$

As before U has no diagonal elements in the I_3, j_{i3} representation. The terms $U_0, \cdots U_4$ are arranged more or less in order of decreasing importance. Matrix elements of angular momenta appearing in U_1, U_2, and U_3 have been given by Bohr.[6] Matrix elements needed for evaluating the effect of U_0 and U_4 are

$$\begin{aligned} &(\Omega_i\Omega_m | j_{i1}j_{m1} + j_{i2}j_{m2} | \Omega_i \pm 1, \Omega_m \mp 1) \\ &\quad = \tfrac{1}{2}[(j_i \pm \Omega_i + 1)(j_i \mp \Omega_i)(j_m \mp \Omega_m + 1)(j_m \pm \Omega_m)]^{\frac{1}{2}}, \\ &(\Omega_i\Omega_m | j_{i1}j_{m1} - j_{i2}j_{m2} | \Omega_i \pm 1, \Omega_m \pm 1) \\ &\quad = \tfrac{1}{2}[(j_i \pm \Omega_i + 1)(j_i \mp \Omega_i)(j_m \pm \Omega_m + 1)(j_m \mp \Omega_m)]^{\frac{1}{2}}. \end{aligned}$$

U_0 connects states for which two particles have Ω_i changed by one, and $\sum_i \Omega_i = \Omega$ is unchanged. U_1 connects states for which one particle has Ω_i changed by one, and K is changed by one. U_2 connects states for which one particle has Ω_i changed by two. U_3 connects states for which K is changed by two. U_4 connects states for which two particles have Ω_i changed by one, and $\sum_i \Omega_i = \Omega$ is changed by two.

In order to get numbers for the energy levels of nuclei on this theory, one further approximation is necessary. The energies will be given by

$$E = W(\beta_1\gamma_1) + E_{\rm particle} + E_\beta + E_\gamma. \tag{20}$$

E_β and E_γ are the energies of the β and γ vibration oscillations about the equilibrium value β_1, γ_1. These can be found approximately by expanding W about β_1, γ_1 to order $(\beta - \beta_1)^2$ and $(\gamma - \gamma_1)^2$, giving a harmonic potential for the vibration levels. Introducing a corresponding approximation in $T_{\rm vib}$, Bohr obtains

$$E_\beta = (2\hbar^2/B\beta_1^2) + \hbar(n_\beta + \tfrac{1}{2})[(\partial^2 W/\partial\beta^2)_{\beta_1\gamma_1}/B]^{\frac{1}{2}}, \tag{21}$$

$$E_\gamma = \hbar(n_\gamma + 1)[(\partial^2 W/\partial\gamma^2)_{\beta_1\gamma_1}/B\beta_1^2]^{\frac{1}{2}}, \tag{22}$$

for the case $\gamma_1 = 0$ or π. For other values of γ_1, to the same approximation, E_β is the same and

$$E_\gamma = \{(9/8)(\hbar^2/B\beta_1^2)\cot^2 3\gamma_1 + \hbar(n_\gamma + \tfrac{1}{2})[(\partial^2 W/\partial\gamma^2)_{\beta_1\gamma_1}/B\beta_1^2]^{\frac{1}{2}}\}.$$

Here n_β and n_γ are integers equal to the number of excitation quanta in the β and γ vibrations. The level spacing of the β and γ vibrations is, in general, large compared to the level spacing of different rotational states. This gives the important result that the rotational energy of the nuclear surface contributes significantly to the ground and low excited states of nuclei, while the vibration levels do not. The previous conclusion that the liquid droplet model cannot take account of shell structure properties is thereby altered completely. According to the collective model, the important contribution of the nuclear surface to low-lying levels comes via rotational energy, but the rotational

energy depends sensitively on the nuclear distortion ($\sim\beta^{-2}$), which in turn is determined by the orbits of the extra nucleons. The collective distortions of the nucleus in this respect, therefore, enhance and multiply shell structure effects, rather than smooth over them. It is found also that the vibrational energies $E_\beta^{(0)}$ and $E_\gamma^{(0)}$ are insensitive to changes in β_1, γ_1, so that the level order and level spacing are given to fair approximation by the potential minimum $W(\beta_1\gamma_1)$ alone. In the calculations described in the next part, W alone was first minimized; then E_β and E_γ were calculated. A more consistent procedure would probably be to find β_1, γ_1 by minimizing the entire energy expression (20). This would yield slightly larger values of the nuclear distortion than minimization of W alone.

Assuming for a moment that the perturbing terms U have a small effect on the solution of the zero-order Hamiltonian H_0, as appears to be the case for heavy nuclei containing several extra nucleons outside closed shells, it is worth while to examine some of the basic qualitative differences between the free particle model alone and the collective model of the nucleus. (1) According to the collective model, a given nuclear state is characterized by more quantum numbers: I, the total angular momentum, and its component M along an axis in space; K, the component of I along the 3-axis of the distorted nucleus; $\Omega_1 \cdots \Omega_n$, the components of the particle angular momenta j_i along the 3-axis of the nucleus, and n_β, n_γ, the degrees of excitation of the surface vibration. J, the total angular momentum of the particles, is *not* a good quantum number; nor is Q, the angular momentum of the nuclear surface. (The term nuclear surface rather than nuclear core is used because the rotation is not a rigid body rotation, but rather the rotation of a surface wave, whose amplitude depends on the distortion of the nucleus, vanishing for a spherical nucleus.) (2) The collective model predicts a larger number of nuclear levels than does the free particle model. (3) According to the collective model, the mechanism of coupling of different nucleons is entirely different from that predicted by the free particle model. The interaction of particles with the nuclear surface may dominate over the direct coupling of particles to each other. Even if j remains a good quantum number, j-j coupling is destroyed. For example, on the independent particle model a state of two particles each of spin 5/2, with net angular momentum zero, contains all m's from $-5/2$ to $+5/2$ in a prescribed combination. According to the collective model, the same two particles can combine to zero net angular momentum with m's (Ω's) $=\pm 5/2$ only. (Inclusion of perturbation terms U mixes in Ω's of $\pm\frac{3}{2}$, $\pm\frac{1}{2}$, but in a proportion unrelated to the unique specification of j-j coupling.) A more detailed discussion of new features of the collective model is given by Hill and Wheeler.[7]

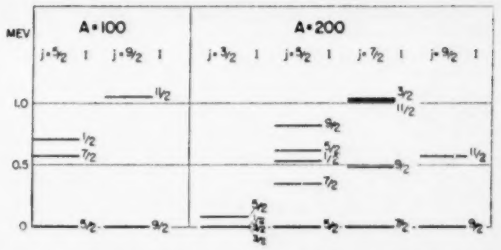

FIG. 1. Predicted energy levels for one extra nucleon outside closed shells. These comprise only those low levels in which the particle states are unchanged. Additional results of detailed calculations with Bohr strong coupling approximation are given in Table III.

C. Numerical Results for Several Examples

Using the Bohr strong coupling approximation, the low-lying levels have been computed for several hypothetical nuclei containing one, two, or four extra particles (of the same nucleon type) outside of a closed shell, with the other nucleon type considered to remain in a closed shell. Only those levels have been treated for which the extra nucleons are not excited to higher single particle levels. This is expected to represent the true situation for the low levels of most even nuclei; but it is not expected to yield the lowest excited states for odd-even nuclei, because of the close spacing of the free particle levels relative to the nuclear rotational levels.

The results for the case of one extra nucleon are given in Fig. 1. The ground state is seen to have spin $I=j$, as already pointed out by Bohr.[8] [For the case $j=\frac{3}{2}$, the ground-state degeneracy in first order will be important for magnetic moments (see reference 14).] The first excited states have spin $j+1$, the second excited excited states, spin $\frac{1}{2}$ or spin $j+2$, and the energy of the first excited state increases with j. This "first excited state" is the lowest excited state with the odd nucleon state unchanged. Lower excited states could appear due to a transition of the odd nucleon to another free particle state, which appears to be the case in most odd-even nuclei.

The Bohr strong coupling picture should give better results for two extra nucleons than for one: First, the high excitation energies of the magic nuclei suggest that pairs of like nucleons are strongly coupled to zero net angular momentum. Therefore, for even nuclei, states due to excitation of nuclear rotational degrees of freedom could lie below levels due to transitions of the extra nucleons among free particle states. Second, the approximation itself is better because of the larger nuclear distortions computed. The results of the computations for two and four extra nucleons are shown in Fig. 2. The computed level order agrees very well with available data. The computed spins for the ground, first excited, and second excited states are 0, 2, 4, with the third excited state being of spin 0, 2, or 6. In one

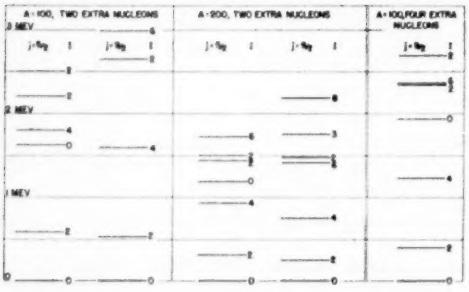

FIG. 2. Predicted energy levels for nuclei with two or four nucleons outside closed shells. Additional results of detailed calculations with Bohr strong coupling approximation are given in Table III.

of the computed cases the level order is 0, 2, 0, 4. The empirical data, which give 0; 2; 4 or 2 as the usual level order, is summarized in Table I, from the recent compilation by Scharff-Goldhaber.[2]

The computed level spacing appears to be of the right order of magnitude, but probably too small. The effect of inclusion of the off-diagonal terms in the Hamiltonian in the strong coupling approximation decreases the computed spacing, as discussed in part *D* of this section. Detailed comparison of theory and experiment for level spacing is possible only in the vicinity of doubly magic Pb^{208}, where the strong coupling approximation should be reasonably good, and where there exist simple examples of even nuclei with only two or four nucleons outside closed shells. Even here, however, the orbital assignments of the extra nucleons are not unambiguous. Table II gives a comparison of observed first excited energies with those calculated "from first principles," using the simplified formula derived in part III, and a nuclear distortion computed by minimizing the effective surface potential W neglecting the rotational terms. For the simplest example, Pb^{206} ($Z=82$, $N=124$), the neutron orbital assignment $(p_{\frac{1}{2}})^{-2}$ gives good agreement with experiment. The assignment $(i_{13/2})^{-2}$ gives considerably too small an energy spacing; the assignment $(p_{\frac{1}{2}})^{-2}$ gives a spherically symmetric nucleus with no low lying rotational state. For Pb^{204}, the neutron assignment $(p_{\frac{1}{2}})^{-2}(i_{13/2})^{-2}$ gives the best agreement with experiment. For Po^{212}, no reasonable assignment gives agreement.

It can be concluded from Table II that the computed nuclear distortions are unreasonably large, and the computed energies therefore too small, on the strong coupling approximation. Halving the particle-to-surface interaction, for example, would lower the values of β to more reasonable magnitude, would bring the energies of Pb^{206} and Pb^{204} into good agreement with the configurations $(i_{13/2})_N^{-2}$ and $(i_{13/2})_N^{-4}$, and would bring the predicted energy for Po^{212} more nearly into agreement with experiment.

Also for many extra nucleons, distortions calculated from first principles are too large. Assuming half-filled shells of $i_{13/2}$ neutrons and $h_{11/2}$ protons, one finds the maximum possible distortion in the rare earth group to be $\beta=1.0$, or three times larger than the largest distortion computed from quadrupole moments. Again a reduction in the particle-to-surface coupling appears to be required. For this case of strong interaction, however, the effect of higher order terms in the interaction energy should also be investigated.

Figure 3 shows the variation in energy of the first excited state and in extra binding energy due to surface coupling for even nuclei filling a hypothetical shell of $j=9/2$ particles. The closed shell energy levels in Fig. 3 and in Table II are computed from Eq. (1). It should be noted that the large energy at double magic Pb^{208} is an important defect of the theory. Two of the three basic parameters of the collective model enter Eq. (1), which should provide an *upper limit* for the excitation energy of doubly magic nuclei. An increase by a factor 4 of the product $(C)(\hbar^2/B)$ is required to secure agreement with experiment for Pb^{208}. A recently determined level[12] of Ca^{40} at 3.8 Mev does agree with the prediction of Eq. (1), however.

TABLE I. Comparison of observed and predicted level order for even nuclei.

State	Predicted spin, collective model, assuming no nucleonic excitation	Observed spin[a]
Ground	0+	0+, no known exceptions
First excited	2+	2+, no known exceptions above $A=75$ among 37 examples
Second excited	4+ (sometimes 0+)	4+, ~40 percent 2+, ~40 percent 0, 1, 3, ~20 percent
Third excited	0+, 2+, or 6+ if second excited is 4+ (4+ if second excited is 0+)	

[a] See reference 2.

The numerical results of the detailed computations using the Bohr strong coupling approximation are given in Table III, for those levels diagrammed in Figs. 1 and 2, and also for higher levels. The higher levels are not included in the figure because they are incomplete, leaving out some levels, especially for the quantum numbers K and Ω unequal, and also because the strong coupling approximation breaks down at the higher excitations. This is indicated by the fact that the rotational energy term W_3 becomes comparable in magnitude to W_1 and $|W_2|$.

The allowed combinations of quantum numbers can be found from the symmetry requirements on the wave function discussed by Bohr. In particular, the wave function must be invariant under a rotation of π about the 2-axis (his R_1 operator) and under a rotation of $\pi/2$ about the 3-axis (his R_2 operator). These operators

[12] J. A. Harvey, Phys. Rev. 88, 162 (1952).

act on an n particle wave function in the $(n_i l_i j_i m_i)$ representation as follows:

$$R_1\chi(\cdots n_i l_i j_i m_i \cdots) = (-1)^{\Sigma_i(j_i+m_i)}\chi(\cdots n_i l_i j_i - m_i \cdots), \quad (23a)$$

$$R_2\chi(\cdots n_i l_i j_i m_i \cdots) = e^{-i(\pi/2)\Sigma_i m_i}\chi(\cdots n_i l_i j_i m_i \cdots). \quad (23b)$$

As a result the wave function must be of the form (replacing m_i by Ω_i),

$$\Psi_M{}^I = \Big(\sum_{\Omega>0,\,K} + \sum_{\Omega=0,\,K\geq 0}\Big)\varphi^I{}_{\Omega,K}(\beta,\gamma) \times[\chi(\cdots j_i, \Omega_i \cdots)D^I{}_{MK}(\theta_i) + (-1)^{I-\Sigma_i j_i}\chi(\cdots j_i, -\Omega_i \cdots)D^I{}_{M,-K}(\theta_i)]. \quad (24)$$

The values of $|K-\Omega|$ are restricted to even integers.

TABLE II. First excited states of selected even nuclei near doubly magic Pb^{208}.

Nucleus	Theoretical Assumed configuration	Distortion, $\beta\cos\gamma$	Energy of first excited state (Mev)	Experimental energy of first excited state (Mev)
$_{82}Pb_{122}$	$[(p_{3/2})^{-4}]_N$	0.0	1.3	
	$[(p_{3/2})^{-2}(p_{1/2})^{-2}]_N$	0.17	0.86	
	$[(p_{3/2})^{-2}(i_{13/2})^{-2}]_N$	0.48	0.10	0.374
	$[(p_{1/2})^{-2}(i_{13/2})^{-2}]_N$	0.33	0.21	
	$[(i_{13/2})^{-4}]_N$	0.50	0.10	
$_{82}Pb_{124}$	$[(p_{1/2})^{-2}]_N$	0.0	1.3	
	$[(p_{3/2})^{-2}]_N$	0.17	0.86	0.803
	$[(i_{13/2})^{-2}]_N$	0.33	0.21	
$_{82}Pb_{126}$	closed shell	0.0	1.3	2.62
$_{82}Pb_{128}$	$[(g_{9/2})^2]_N$	−0.30	0.25	unknown
	$[(d_{5/2})^2]_N$	−0.24	0.40	
$_{82}Pb_{130}$	$[(g_{9/2})^4]_N$	−0.39	0.15	
	$[(g_{9/2})^2(d_{5/2})^2]_N$	−0.52	0.085	unknown
	$[(d_{5/2})^4]_N$	0.23	0.44	
$_{84}Po_{126}$	$[(h_{9/2})^2]_P$	−0.30	0.25	>1(?)
$_{84}Po_{128}$	$[(h_{9/2})^2]_P[(g_{9/2})^2]_N$	−0.58	0.068	0.719
	$[(h_{9/2})^2]_P[(d_{5/2})^2]_N$	−0.52	0.085	

If K and Ω are separately good quantum numbers, as in the first-order approximation used here, then there is only one term in Eq. (24) and further restrictions arise. For an even number of extra nucleons, all of the same n, l, j, and for $\Omega=K=0$, Ψ vanishes for all odd I. These two rules were used to determine the allowed levels in Table III.

D. Validity of the Strong Coupling Approximation

The collective model of the nucleus has two appealing features. First, it contains only a few physical parameters, and none of these are arbitrary. Second, the application of the model through the strong coupling approximation developed by Bohr is relatively easy in first order. The question of the validity of the assumptions on which the whole model is based are therefore most easily approached by means of applications of the model to various examples and comparison with experiment. The more fundamental approach of analysis of the initial assumptions of the model from first principles has been begun by Hill and Wheeler.[7] It is intended here mainly to discuss the question of the validity of the first-order strong coupling approximation relative to the complete Hamiltonian developed by Bohr. Some of the limitations on the complete Hamiltonian are the following: (a) Only the ellipsoidal mode of deformation and vibration is considered. (b) The extra nucleons are taken to have j as a good quantum number. (c) The particle motion is taken to be rapid relative to the motion of the core, and the interaction term is averaged over the particle motion.

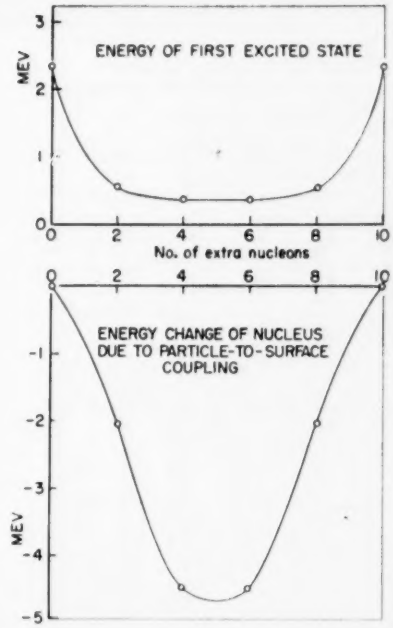

FIG. 3. Energy of first excited state and energy change of nucleus due to surface interaction for highly idealized nuclei. A shell of $j=9/2$ nucleons is assumed to fill while the other group of nucleons remains closed shell. The mass number is taken to be 100. The results at 2 and 4 (same as at 8 and 6) extra nucleons are taken from the strong coupling calculations of Table III and Fig. 2. The results at zero (and at 10) extra nucleons are the weak coupling limit with excitation energy given by Eq. (1) in the text and with no particle-to-surface interaction.

The three parameters which enter the theory are coefficients in the three terms in the effective surface potential W [Eq. (18) and caption of Table III]. The parameter C [Eq. (2)] is the coefficient of the nuclear distortion term, $W_1=\frac{1}{2}C\beta^2$. Using a surface tension energy $4\pi r_0{}^2\mathcal{O}=15.4$ Mev, values of C are obtained as given in Table IV. In the calculations performed at mass numbers 100 and 200, a value $C=65$ Mev was used. It is not certain that the dynamic surface tension is the same as the static surface tension,[7] but approxi-

TABLE III. Summarized results of calculations using Bohr strong coupling approximation.

I = Total angular momentum of nucleus.
Ω_i = Component of nucleon angular momentum along 3-axis of distorted nucleus.
$\Omega = \Sigma_i \Omega_i$.
K = Component of total angular momentum along 3-axis of distorted nucleus.
β_1 = Equilibrium value of distortion parameter.
γ_1 = Equilibrium value of shape parameter.
W_1 = Potential energy of surface deformation = $\frac{1}{2}C\beta^2$.
W_2 = Interaction energy of extra nucleons with nuclear surface ("Rainwater interaction")

$$= (5/\pi)^{\frac{1}{2}} T \beta \cos\gamma \Sigma_i \frac{3\Omega_i^2 - j_i(j_i+1)}{4j_i(j_i+1)}.$$

W_3 = Kinetic energy of surface rotation (diagonal part)

$$= (1/4)(\hbar^2/\mathcal{I}_1 + \hbar^2/\mathcal{I}_2)[I(I+1) - K^2 + \Sigma_i j_i(j_i+1) - \Omega_i^2 - (I+\tfrac{1}{2})(-1)^{I-\Sigma_i j_i + \frac{1}{2}(n-1)} \delta(K, \tfrac{1}{2}) \times \Sigma_i (j_i+\tfrac{1}{2}) \delta(\Omega_i, \tfrac{1}{2}) \delta([\Omega_k], [-\Omega_{k'}]) - \sum_{i \neq m} \delta(j_i, j_m) \delta(\Omega_m, \Omega_i - 1)(j_m - \Omega_m)(j_m + \Omega_m + 1)].$$

$W = W_1 + W_2 + W_3$ = Net effective surface potential energy.
E_β = Zero-point energy of β oscillation.
E_γ = Zero-point energy of γ oscillation.
$E - E_p = W + E_\beta + E_\gamma$ = (net nuclear energy) − (unperturbed particle energy) = diagonal matrix element of Hamiltonian in Bohr strong coupling approximation.
E_{rel} = Nuclear energy normalized to ground state energy = 0.
All energies in Mev.

I	Ω_i	Ω	K	β_1	$\cos\gamma_1$	W_1	W_2	W_3	W	E_β	E_γ	$E-E_p$	E_{rel}
					$A=100$, one extra nucleon, $j=5/2$								
5/2		5/2	5/2	0.2466	−1.0000	1.977	−1.778	1.088	1.287	4.460	2.829	8.576	0.000
7/2		5/2	5/2	0.2971	−1.0000	2.870	−2.142	1.799	2.526	3.726	2.897	9.150	0.574
1/2		1/2	1/2	0.2483	1.0000	2.004	−1.432	1.288	1.860	4.519	2.912	9.291	0.715
5/2		1/2	1/2	0.2646	1.0000	2.275	−1.526	1.512	2.262	4.234	2.931	9.427	0.851
9/2		5/2	5/2	0.3361	−1.0000	3.671	−2.423	2.460	3.708	3.376	2.936	10.021	1.445
3/2		1/2	1/2	0.3176	1.0000	3.278	−1.831	2.362	3.808	3.594	2.980	10.382	1.806
9/2		1/2	1/2	0.3176	1.0000	3.278	−1.831	2.362	3.808	3.594	2.980	10.382	1.806
3/2		3/2	3/2	0.2446	1.0000	1.945	−0.353	1.769	3.361	4.846	3.139	11.347	2.771
5/2		3/2	3/2	0.2755	1.0000	2.466	−0.397	2.267	4.336	4.295	3.147	11.779	3.203
7/2		1/2	1/2	0.3724	1.0000	4.508	−2.148	3.434	5.795	3.204	3.015	12.014	3.438
5/2		1/2	5/2	0.3607	0.8869	4.228	−1.845	3.305	5.688	3.298	3.078	12.065	3.489
7/2		3/2	3/2	0.3061	1.0000	3.045	−0.441	2.825	5.429	3.904	3.154	12.487	3.911
9/2		3/2	3/2	0.3353	1.0000	3.655	−0.484	3.413	6.584	3.627	3.159	13.370	4.794
					$A=100$, one extra nucleon, $j=9/2$								
9/2		9/2	9/2	0.2905	−1.0000	2.744	−2.666	1.411	1.489	3.692	2.795	7.976	0.000
11/2		9/2	9/2	0.3430	−1.0000	3.823	−3.147	2.250	2.926	3.239	2.863	9.028	1.052
1/2		1/2	1/2	0.3270	1.0000	3.475	−2.000	2.475	3.950	3.497	2.973	10.420	2.444
					$A=200$, one extra nucleon, $j=3/2$								
3/2		3/2	3/2	0.1641	−1.0000	0.876	−0.828	0.462	0.509	2.869	1.572	4.951	0.000
3/2		1/2	1/2	0.1642	1.0000	0.876	−0.829	0.462	0.509	2.869	1.572	4.951	0.000
1/2		1/2	1/2	0.1898	1.0000	1.170	−0.958	0.691	0.904	2.442	1.605	4.951	0.000
5/2		3/2	3/2	0.2019	−1.0000	1.324	−1.019	0.815	1.120	2.295	1.617	5.033	0.082
7/2		1/2	1/2	0.2163	1.0000	1.521	−1.092	0.975	1.405	2.152	1.630	5.186	0.235
7/2		3/2	3/2	0.2317	−1.0000	1.744	−1.169	1.160	1.735	2.029	1.641	5.405	0.454
5/2		1/2	1/2	0.2413	1.0000	1.892	−1.218	1.283	1.958	1.964	1.648	5.569	0.618
9/2		3/2	3/2	0.2574	−1.0000	2.153	−1.299	1.503	2.358	1.871	1.658	5.886	0.935
9/2		1/2	1/2	0.2857	1.0000	2.653	−1.442	1.932	3.143	1.745	1.672	6.561	1.610
					$A=200$, one extra nucleon, $j=5/2$								
5/2		5/2	5/2	0.1959	−1.0000	1.247	−1.412	0.541	0.376	2.263	1.523	4.162	0.000
7/2		5/2	5/2	0.2326	−1.0000	1.759	−1.677	0.920	1.002	1.940	1.570	4.512	0.350
1/2		1/2	1/2	0.1939	1.0000	1.222	−1.118	0.662	0.766	2.356	1.580	4.702	0.540
5/2		1/2	1/2	0.2058	1.0000	1.377	−1.187	0.784	0.973	2.222	1.593	4.789	0.627
9/2		5/2	5/2	0.2613	−1.0000	2.218	−1.883	1.276	1.612	1.780	1.597	4.988	0.826
1/2		5/2	1/2	0.2432	−0.8453	1.922	−1.482	1.182	1.622	1.915	1.558	5.095	0.933
3/2		1/2	1/2	0.2450	1.0000	1.951	−1.413	1.244	1.782	1.915	1.628	5.326	1.164
9/2		1/2	1/2	0.2450	1.0000	1.951	−1.413	1.244	1.782	1.915	1.628	5.326	1.164
7/2		1/2	1/2	0.2857	1.0000	2.654	−1.648	1.830	2.835	1.724	1.654	6.213	2.051
3/2		3/2	3/2	0.1846	1.0000	1.107	−0.266	0.974	1.816	2.675	1.744	6.235	2.073
5/2		1/2	5/2	0.2762	0.8899	2.480	−1.418	1.771	2.833	1.780	1.669	6.283	2.121
5/2		3/2	3/2	0.2076	1.0000	1.401	−0.299	1.251	2.353	2.375	1.750	6.479	2.317
7/2		3/2	3/2	0.2306	1.0000	1.728	−0.332	1.561	2.957	2.162	1.755	6.874	2.712
9/2		3/2	3/2	0.2524	1.0000	2.071	−0.364	1.889	3.596	2.011	1.759	7.366	3.204
					$A=200$, one extra nucleon, $j=7/2$								
7/2		7/2	7/2	0.2169	−1.0000	1.530	−1.825	0.617	0.322	2.004	1.507	3.833	0.000
9/2		7/2	7/2	0.2540	−1.0000	2.097	−2.136	1.029	0.990	1.772	1.553	4.315	0.482
11/2		7/2	7/2	0.2824	−1.0000	2.592	−2.375	1.405	1.622	1.655	1.580	4.857	1.024
3/2		1/2	1/2	0.2216	1.0000	1.595	−1.331	0.930	1.194	2.069	1.601	4.864	1.031
3/2		7/2	3/2	0.2631	−0.8694	2.250	−1.924	1.288	1.614	1.768	1.524	4.906	1.073
7/2		1/2	1/2	0.2368	1.0000	1.822	−1.422	1.111	1.510	1.958	1.614	5.082	1.249

TABLE III.—(*Continued*).

I	Ω_1	Ω_2	Ω	K	β_1	$\cos\gamma_1$	W_1	W_2	W_3	W	E_β	E_γ	$E-E_0$	E_{rel}
					$A=200$, one extra nucleon, $j=7/2$—(*Continued*)									
1/2			1/2	1/2	0.2520	1.0000	2.064	−1.514	1.307	1.857	1.867	1.626	5.350	1.517
11/2			1/2	1/2	0.2692	1.0000	2.355	−1.617	1.546	2.284	1.784	1.637	5.705	1.872
3/2			3/2	3/2	0.2246	1.0000	1.639	−0.809	1.234	2.064	2.136	1.684	5.884	2.051
5/2			1/2	1/2	0.2870	1.0000	2.676	−1.724	1.814	2.767	1.713	1.648	6.127	2.294
5/2			3/2	3/2	0.2401	1.0000	1.873	−0.865	1.440	2.448	2.021	1.692	6.161	2.328
5/2			5/2	5/2	0.2026	−1.0000	1.335	−0.243	1.213	2.304	2.441	1.758	6.502	2.669
7/2			3/2	3/2	0.2576	1.0000	2.154	−0.928	1.690	2.917	1.916	1.699	6.532	2.699
7/2			5/2	5/2	0.2267	−1.0000	1.670	−0.272	1.534	2.932	2.201	1.762	6.896	3.063
9/2			3/2	3/2	0.2754	1.0000	2.466	−0.993	1.969	3.442	1.829	1.706	6.977	3.144
9/2			1/2	1/2	0.3220	1.0000	3.369	−1.934	2.401	3.837	1.607	1.665	7.109	3.276
9/2			5/2	5/2	0.2493	−1.0000	2.020	−0.299	1.870	3.590	2.038	1.765	7.393	3.560
11/2			3/2	3/2	0.2933	1.0000	2.796	−1.057	2.267	4.006	1.757	1.712	7.475	3.642
11/2			5/2	5/2	0.2704	−1.0000	2.376	−0.325	2.214	4.265	1.920	1.768	7.953	4.120
					$A=200$, one extra nucleon, $j=9/2$									
9/2			9/2	9/2	0.2325	−1.0000	1.757	−2.134	0.691	0.315	1.860	1.501	3.676	0.000
11/2			9/2	9/2	0.2704	−1.0000	2.376	−2.481	1.135	1.031	1.674	1.546	4.251	0.575
1/2			1/2	1/2	0.2526	1.0000	2.073	−1.545	1.301	1.829	1.861	1.623	5.313	1.637
					$A=100$, two extra nucleons, $j=5/2$									
0	5/2	−5/2	0	0	0.2984	−1.0000	2.894	−4.303	0.743	−0.665	3.294	2.547	5.176	0.000
2	5/2	−5/2	0	0	0.3379	−1.0000	3.711	−4.872	1.275	0.114	3.009	2.633	5.757	0.581
0	1/2	−1/2	0	0	0.2992	1.0000	2.908	−3.450	1.183	0.641	3.467	2.695	6.803	1.627
4	5/2	−5/2	0	0	0.3915	−1.0000	4.981	−5.644	2.159	1.495	2.759	2.720	6.974	1.798
2	1/2	−1/2	0	0	0.3325	1.0000	3.593	−3.835	1.676	1.434	3.196	2.751	7.381	2.205
2	5/2	−5/2	0	2	0.3839	−0.8893	4.789	−4.922	2.328	2.196	2.859	2.619	7.673	2.497
6	5/2	−5/2	0	0	0.4426	−1.0000	6.366	−6.381	3.175	3.160	2.605	2.781	8.547	3.371
4	1/2	−1/2	0	0	0.3820	1.0000	4.742	−4.406	2.539	2.876	2.922	2.815	8.613	3.437
2	3/2	1/2	2	2	0.2792	1.0000	2.534	−2.013	1.528	2.049	3.940	2.876	8.865	3.689
4	5/2	3/2	4	4	0.2646	−1.0000	2.275	−1.526	1.512	2.262	4.234	2.931	9.427	4.251
1	3/2	−1/2	1	1	0.3165	1.0000	3.255	−2.281	2.114	3.088	3.536	2.918	9.542	4.366
1	5/2	−3/2	1	1	0.2781	−1.0000	2.513	−1.604	1.711	2.621	4.035	2.945	9.601	4.425
2	3/2	−1/2	1	1	0.3325	1.0000	3.593	−2.397	2.394	3.590	3.404	2.933	9.926	4.750
2	5/2	−3/2	1	1	0.2999	−1.0000	2.924	−1.730	2.059	3.253	3.769	2.966	9.988	4.812
6	1/2	−1/2	0	0	0.4313	1.0000	6.045	−4.974	3.558	4.628	2.743	2.863	10.234	5.058
8	5/2	−5/2	0	0	0.4893	−1.0000	7.783	−7.055	4.255	4.982	2.509	2.825	10.317	5.141
5	5/2	3/2	4	4	0.3176	−1.0000	3.278	−1.831	2.362	3.808	3.594	2.980	10.382	5.206
0	3/2	−3/2	0	0	0.2815	1.0000	2.576	−0.812	2.170	3.935	4.137	3.084	11.155	5.979
2	3/2	−3/2	0	0	0.3083	1.0000	3.089	−0.889	2.645	4.845	3.816	3.095	11.757	6.581
2	5/2	−1/2	2	2	0.2755	−1.0000	2.466	−0.397	2.267	4.336	4.295	3.147	11.779	6.603
3	5/2	1/2	3	3	0.2805	−1.0000	2.557	−0.404	2.355	4.507	4.222	3.149	11.878	6.702
					$A=100$, two extra nucleons, $j=9/2$									
0	9/2	−9/2	0	0	0.3605	−1.0000	4.224	−6.615	0.916	−1.475	2.681	2.506	3.712	0.000
2	9/2	−9/2	0	0	0.3874	−1.0000	4.877	−7.108	1.323	−0.909	2.588	2.561	4.241	0.529
4	9/2	−9/2	0	0	0.4304	−1.0000	6.021	−7.898	2.071	0.194	2.477	2.634	5.305	1.593
2	9/2	−9/2	0	2	0.4306	−0.9114	6.027	−7.202	2.426	1.251	2.544	2.565	6.360	2.648
6	9/2	−9/2	0	0	0.4755	−1.0000	7.348	−8.725	2.985	1.608	2.394	2.694	6.696	2.984
3	9/2	−9/2	0	2	0.4527	−0.9215	6.659	−7.655	2.832	1.837	2.489	2.645	6.970	3.258
8	9/2	7/2	8	8	0.3458	−1.0000	3.886	−4.230	1.771	1.427	3.076	2.741	7.243	3.531
1	9/2	−7/2	1	1	0.3538	−1.0000	4.067	−4.328	1.903	1.643	3.030	2.752	7.426	3.714
0	1/2	−1/2	0	0	0.3744	1.0000	4.556	−4.580	2.266	2.241	2.926	2.780	7.947	4.235
2	1/2	−1/2	0	0	0.3916	1.0000	4.984	−4.791	2.589	2.782	2.852	2.800	8.435	4.723
4	1/2	−1/2	0	0	0.4237	1.0000	5.835	−5.183	3.243	3.895	2.740	2.834	9.468	5.756
2	9/2	−5/2	2	2	0.3517	−1.0000	4.019	−2.689	2.675	4.006	3.250	2.932	10.188	6.476
1	3/2	−1/2	1	1	0.4230	1.0000	5.814	−4.528	3.551	4.837	2.799	2.883	10.520	6.808
0	7/2	−7/2	0	0	0.3441	−1.0000	3.847	−2.104	2.795	4.538	3.367	2.985	10.889	7.177
					$A=200$, two extra nucleons, $j=5/2$									
0	5/2	−5/2	0	0	0.2587	−1.0000	2.175	−3.730	0.310	−1.245	1.504	1.360	1.619	0.000
2	5/2	−5/2	0	0	0.2835	−1.0000	2.612	−4.087	0.568	−0.907	1.437	1.404	1.934	0.315
4	5/2	−5/2	0	0	0.3196	−1.0000	3.320	−4.608	1.016	−0.273	1.368	1.454	2.550	0.931
0	1/2	−1/2	0	0	0.2460	1.0000	1.967	−2.838	0.548	−0.322	1.685	1.439	2.801	1.182
2	5/2	−5/2	0	2	0.3131	−0.9035	3.187	−4.079	1.147	0.255	1.425	1.377	3.057	1.438
2	1/2	−1/2	0	0	0.2691	1.0000	2.354	−3.104	0.802	0.052	1.592	1.473	3.117	1.498
6	5/2	−5/2	0	0	0.3554	−1.0000	4.106	−5.125	1.544	0.525	1.322	1.492	3.340	1.721
4	1/2	−1/2	0	0	0.3043	1.0000	3.010	−3.510	1.255	0.754	1.492	1.514	3.761	2.142
8	5/2	−5/2	0	0	0.3889	−1.0000	4.916	−5.608	2.112	1.421	1.292	1.521	4.234	2.615
2	3/2	1/2	2	2	0.2195	1.0000	1.566	−1.583	0.775	0.759	2.036	1.555	4.350	2.731
6	1/2	−1/2	0	0	0.3400	1.0000	3.756	−3.921	1.795	1.630	1.423	1.547	4.600	2.981
3	3/2	1/2	2	2	0.2435	1.0000	1.927	−1.756	1.050	1.222	1.872	1.581	4.675	3.056

TABLE III.—(*Continued*).

I	Ω_1		Ω_2		Ω	K	β_1	$\cos\gamma_1$	W_1	W_2	W_3	W	E_β	E_γ	$E-E_0$	E_{rel}
								$A=200$, two extra nucleons, $j=5/2$—(*Continued*)								
1	3/2	−1/2			1	1	0.2468	1.0000	1.980	−1.779	1.090	1.291	1.853	1.584	4.728	3.109
4	5/2	3/2			4	4	0.2058	−1.0000	1.377	−1.187	0.784	0.973	2.222	1.593	4.789	3.170
1	5/2	−3/2			1	1	0.2158	−1.0000	1.513	−1.245	0.891	1.160	2.127	1.604	4.891	3.272
2	3/2	−1/2			1	1	0.2586	1.0000	2.173	−1.864	1.241	1.550	1.793	1.595	4.937	3.318
2	5/2	−3/2			1	1	0.2320	−1.0000	1.749	−1.338	1.080	1.491	1.999	1.618	5.109	3.490
3	3/2	−1/2			1	1	0.2734	1.0000	2.429	−1.971	1.444	1.902	1.727	1.606	5.236	3.617
5	5/2	3/2			4	4	0.2450	−1.0000	1.951	−1.413	1.244	1.782	1.915	1.628	5.326	3.707
3	5/2	−3/2			1	1	0.2507	−1.0000	2.043	−1.446	1.320	1.917	1.883	1.632	5.432	3.813
0	3/2	−3/2			0	0	0.2139	1.0000	1.487	−0.617	1.179	2.049	2.257	1.703	6.010	4.391
2	3/2	−3/2			0	0	0.2339	1.0000	1.778	−0.675	1.441	2.545	2.088	1.712	6.345	4.726
2	5/2	−1/2			2	2	0.2076	−1.0000	1.401	−0.299	1.251	2.353	2.375	1.750	6.479	4.860
3	5/2	1/2			3	3	0.2114	−1.0000	1.452	−0.305	1.300	2.448	2.335	1.751	6.534	4.915
3	5/2	−1/2			2	2	0.2277	−1.0000	1.685	−0.328	1.521	2.878	2.185	1.755	6.818	5.199
4	5/2	1/2			3	3	0.2360	−1.0000	1.810	−0.340	1.640	3.109	2.121	1.756	6.986	5.367
4	3/2	−3/2			0	0	0.2666	1.0000	2.311	−0.769	1.926	3.468	1.891	1.723	7.081	5.462
								$A=200$, two extra nucleons, $j=9/2$								
0	9/2	−9/2			0	0	0.3180	−1.0000	3.287	−5.836	0.369	−2.179	1.228	1.342	0.390	0.000
2	9/2	−9/2			0	0	0.3338	−1.0000	3.621	−6.125	0.559	−1.945	1.216	1.367	0.638	0.248
4	9/2	−9/2			0	0	0.3610	−1.0000	4.236	−6.625	0.923	−1.465	1.200	1.404	1.139	0.749
6	9/2	−9/2			0	0	0.3911	−1.0000	4.972	−7.177	1.383	−0.822	1.187	1.438	1.804	1.414
2	9/2	−9/2			0	2	0.3606	−0.9267	4.227	−6.133	1.160	−0.745	1.242	1.366	1.863	1.473
3	9/2	−9/2			0	2	0.3749	−0.9334	4.568	−6.421	1.357	−0.497	1.229	1.407	2.139	1.749
8	9/2	−9/2			0	0	0.4210	−1.0000	5.759	−7.725	1.897	−0.068	1.178	1.467	2.576	2.186
8	9/2	7/2			8	8	0.2806	−1.0000	2.560	−3.433	0.843	−0.030	1.529	1.467	2.966	2.576
1	9/2	−7/2			1	1	0.2862	−1.0000	2.663	−3.501	0.912	0.073	1.514	1.474	3.060	2.670
0	1/2	−1/2			0	0	0.3008	1.0000	2.941	−3.680	1.101	0.362	1.477	1.491	3.330	2.940
0	9/2	−9/2			0	0	0.4496	−1.0000	6.568	−8.249	2.444	0.763	1.172	1.490	3.424	3.034
2	1/2	−1/2			0	0	0.3131	1.0000	3.185	−3.830	1.270	0.626	1.451	1.505	3.581	3.191
9	9/2	7/2			8	8	0.3203	−1.0000	3.334	−3.918	1.375	0.791	1.437	1.512	3.740	3.350
2	3/2	1/2			2	2	0.2924	1.0000	2.778	−3.130	1.214	0.862	1.549	1.525	3.937	3.547
4	1/2	−1/2			0	0	0.3361	1.0000	3.672	−4.112	1.616	1.176	1.410	1.527	4.113	3.723
3	3/2	1/2			2	2	0.3047	1.0000	3.017	−3.261	1.386	1.142	1.518	1.537	4.196	3.806
6	1/2	−1/2			0	0	0.3636	1.0000	4.296	−4.448	2.072	1.920	1.372	1.549	4.841	4.451
1	3/2	−1/2			1	1	0.3321	1.0000	3.584	−3.555	1.806	1.836	1.460	1.560	4.856	4.466
2	9/2	−5/2			2	2	0.2736	−1.0000	2.432	−2.092	1.386	1.727	1.713	1.594	5.034	4.644
7	9/2	5/2			7	7	0.2843	−1.0000	2.627	−2.174	1.540	1.993	1.673	1.602	5.268	4.878
0	3/2	−3/2			0	0	0.3187	1.0000	3.301	−2.924	1.839	2.216	1.530	1.587	5.333	4.943
0	7/2	−7/2			0	0	0.2652	−1.0000	2.286	−1.622	1.475	2.139	1.798	1.632	5.568	5.178
2	7/2	−7/2			0	0	0.2781	−1.0000	2.514	−1.701	1.663	2.476	1.743	1.640	5.859	5.469
1	5/2	−3/2			1	1	0.2976	1.0000	2.878	−1.820	1.968	3.026	1.673	1.651	6.350	5.960
4	7/2	−7/2			0	0	0.3022	−1.0000	2.969	−1.849	2.044	3.165	1.659	1.653	6.477	6.087
6	7/2	5/2			6	6	0.2337	−1.0000	1.775	−0.357	1.596	3.013	2.135	1.753	6.902	6.512
0	5/2	−5/2			0	0	0.2748	1.0000	2.454	−0.840	2.034	3.647	1.847	1.720	7.215	6.825
1	7/2	−5/2			1	1	0.2589	−1.0000	2.179	−0.396	1.981	3.764	1.971	1.758	7.493	7.103
								$A=100$, four extra nucleons, $j=9/2$								
0	9/2	7/2	−7/2	−9/2	0	0	0.4486	−1.0000	6.540	−10.975	1.052	−3.383	2.172	2.448	1.237	0.000
2	9/2	7/2	−7/2	−9/2	0	0	0.4653	−1.0000	7.037	−11.385	1.345	−3.003	2.158	2.479	1.634	0.397
4	9/2	7/2	−7/2	−9/2	0	0	0.4963	−1.0000	8.006	−12.143	1.934	−2.203	2.136	2.531	2.464	1.227
0	3/2	1/2	−1/2	−3/2	0	0	0.4340	1.0000	6.121	−9.291	1.476	−1.694	2.334	2.531	3.171	1.934
2	3/2	1/2	−1/2	−3/2	0	0	0.4500	1.0000	6.581	−9.634	1.764	−1.288	2.310	2.558	3.580	2.343
6	9/2	7/2	−7/2	−9/2	0	0	0.5327	−1.0000	9.221	−13.033	2.705	−1.106	2.117	2.584	3.595	2.358
2	9/2	7/2	−7/2	−9/2	0	2	0.5033	−0.9342	8.232	−11.504	2.480	−0.792	2.194	2.523	3.926	2.689
4	3/2	1/2	−1/2	−3/2	0	0	0.4802	1.0000	7.493	−10.279	2.353	−0.433	2.272	2.604	4.443	3.206
1	9/2	7/2	−5/2	−9/2	1	1	0.4494	−1.0000	6.564	−8.934	2.097	−0.273	2.376	2.610	4.712	3.475
8	9/2	7/2	−7/2	−9/2	0	0	0.5699	−1.0000	10.557	−13.945	3.585	0.198	2.103	2.629	4.930	3.693
2	9/2	7/2	−5/2	−9/2	1	1	0.4583	−1.0000	6.823	−9.109	2.269	−0.016	2.362	2.622	4.968	3.731
8	9/2	7/2	5/2	−5/2	8	8	0.3917	−1.0000	4.988	−3.594	3.191	4.584	2.975	2.909	10.468	9.231
1	9/2	5/2	−5/2	−7/2	1	1	0.3963	−1.0000	5.104	−3.636	3.286	4.754	2.956	2.913	10.623	9.386

mately the same value as used here has been used with success in the theory of fission.[13]

The parameter B [Eq. (3)] enters the coefficient of the rotational energy term W_3 [Eq. (18) and caption of Table III]. It is proportional to the moment of inertia of the nucleus and determines through ϑ_4 the mass involved in the collective nuclear rotation. B is also contained in nearly every off-diagonal term [Eqs. (19)], so that the validity of the approximation depends on the size of B. Since $B\sim A^{5/3}$, the strong coupling approximation improves rapidly with increasing A. The values of $\hbar^2/B$ used in the calculations at $A=100$ and 200 are given in Table IV.

[13] N. Bohr and J. A. Wheeler, Phys. Rev. **56**, 426 (1939).

The parameter $\bar{T}$ (same as Bohr's $k/2$) appears in the interaction term W_2 [Eq. (14)]. From the averaging process of the first-order Rainwater interaction term, $\bar{T}$ is defined by

$$\bar{T}=\tfrac{1}{2}V_0R_0^3|\rho_{nl}(R_0)|^2, \tag{25}$$

where $\rho_{nl}(R_0)$ is the value of the radial part of the particle wave function at the edge of the nuclear well, R_0 is the radius of the well, and V_0 the depth of the well. In the limit of a deep well, $\bar{T}$ approaches particle kinetic energy. For a nuclear well, Feenberg and Hammack[11] estimate that $\bar{T}$ is reduced by about 25 percent from its deep well value. It is at any rate a rather uncertain quantity. In the calculations described here, $\bar{T}$ was taken to be constant and equal to 20 Mev.

A simple method for a first check of the validity of the strong coupling approximation has been suggested by Davidson and Feenberg.[14] This is a comparison of the calculated diagonal matrix element of the Hamiltonian in first order (the $E-E_p$ of Table III) with the zero-order energy, $(E-E_p)_0=(5/2)\hbar\omega$, the zero-point energy of the lowest mode of surface vibration. The energy $\hbar\omega$ is given by Eq. (1). This comparison is shown in Table V, where it is seen that for one extra particle the ground-state energy (surface energy+interaction energy) is increased in first order, while for two or more extra particles the energy is lowered in first order. It can be concluded, therefore, that the strong coupling approximation is probably poor for only one extra nucleon outside closed shells and that it is perhaps good for two or more extra nucleons. The fact that the energy is raised in first order does not prove that the approximation is useless. Level order might be given correctly, for example, although level spacing would be greatly in error.*

The off-diagonal terms [Eqs. (19)] contain largely terms from the surface rotational energy. A criterion of validity of the approximation should therefore be that the rotational terms which are included, W_3, are small compared to the surface distortion energy, W_1, and the interaction energy, W_2; i.e., $W_3\ll W_1$ or $|W_2|$. For the most favorable one-particle case treated, $A=200$, $j=9/2$, W_3 is about $\frac{1}{3}$ of W_1 or $|W_2|$ in the ground state. W_3 becomes relatively larger for the excited states. For two extra particles at the same A and j, however, W_3 is about 1/9 of W_1 and $\frac{1}{16}$ of $|W_2|$. The approximation for two extra particles appears definitely better than for one by this criterion. A corollary to the rule that W_3 should be relatively small is the rule that the equilibrium deformation β should not be greatly altered by the inclusion of the rotation terms in W. Calling β_{static} the equilibrium β calculated from W_1+W_2 only, it is found that the inclusion of the rotation greatly increases this value for one extra nucleon, but increases it only slightly for two extra nucleons.

TABLE IV. Energy parameters of liquid droplet model. A = mass number; C and B defined by Eqs. (2) and (3) in text.

A	C (Mev)	$\hbar^2/B$ (Mev)
10	21.2	
30	41.5	
50	54.0	0.251
75	62.5	
100	65.6	0.0794
150	69.6	
200	62.9	0.0249
240	56.3	

TABLE V. Ground state energies in zero order, and in first-order strong coupling approximation. Zero-order energy, $E^{(0)}=(5/2)\hbar\omega$ = zero-point vibrational energy about spherical equilibrium position. First-order energy, $E^{(1)}$ = surface energy + interaction energy in strong coupling approximation. Energies are given in Mev.

No. of extra nucleons	$A=100$, $E^{(0)}=5.75$ Mev			$A=200$, $E^{(0)}=3.14$ Mev		
	j	$E^{(1)}$	$E^{(1)}-E^{(0)}$	j	$E^{(1)}$	$E^{(1)}-E^{(0)}$
1				3/2	4.92	+1.78
	5/2	8.58	+2.85	5/2	4.16	+1.02
				7/2	3.83	+0.69
	9/2	7.98	+2.25	9/2	3.68	+0.54
2	5/2	5.18	−0.55	5/2	1.62	−1.52
	9/2	3.71	−2.02	9/2	0.39	−2.75
4	9/2	1.24	−4.49			
6	9/2	1.24	−4.49			
8	9/2	3.71	−2.02			

Some data indicative of the validity of the approximation are collected in Table VI. It is clear that the approximation is considerably better for two extra nucleons than for one. For the particular two-particle case listed in Table VI, the effect of U_0 on the three lowest $I=0$ states, at 0, 1.18, and 4.39 Mev, was calculated in more detail. The ground state $(5/2, -5/2)$ was shifted downward by 0.02 Mev, the state $[(\frac{1}{2}, -\frac{1}{2})$ etc. $\cdots]$ was shifted down by 0.08 Mev, and the state $(\frac{3}{2}, -\frac{3}{2})$ was shifted up to 0.10 Mev. The perturbation U_0 mixed into the ground state only 0.6 percent of the state $(\frac{1}{2}, -\frac{1}{2})$ and less than 0.1 percent of the state $(\frac{3}{2}, -\frac{3}{2})$, a negligible effect. The result would not be so favorable at $A=100$, where $\hbar^2/B$ is three times greater than at $A=200$, and the off-diagonal matrix elements are greater by about the same factor.

The situation with the distance to the first excited state is not so favorable, however. Since the level spacing depends principally on the rotation term W_3, it is also small compared to W_1 and $|W_2|$ and is likely to be strongly affected by the off-diagonal terms. This idea was tested by first-order perturbation calculations on the lowest two states of each of the two and four extra particle cases shown in Fig. 2. U_0 mixes the lowest two states with a higher pair of levels with spin 0 and 2 and about the same separation. Therefore, it has the effect to lower the ground and first excited states by about the same amount and not alter their spacing appreciably. U_2 and U_4 behave like U_0 in this

[14] J. Davidson and E. Feenberg, Phys. Rev. **89**, 856 (1953).

* A. Bohr and B. Mottelson (private communication) find that improved expressions for E_β and E_γ lead to a lowering of the energy also for one extra nucleon.

TABLE VI. Validity of the strong coupling approximation (all energies in Mev).

		$A=100$, one extra particle, $j=5/2$	$A=200$, one extra particle, $j=5/2$	$A=200$, two extra particles, $j=5/2$
Ground state	W_1	1.98	1.25	2.18
	W_2	−1.78	−1.41	−3.73
	W_3	1.09	0.54	0.31
Total zero-order energy		5.73	3.14	3.14
Total first-order energy		8.58	4.16	1.62
Approx. spacing of lowest levels connected by off-diagonal terms		1.0	0.7	1.7
Rough average values of off-diagonal terms between lowest connected states	$\bar{U}_0$	—	—	0.5
	$\bar{U}_1$	1.0	0.3	0.2
	$\bar{U}_2$	0.3	<0.3	$\ll 2.0$
	$\bar{U}_3$	$\ll 0.3$	<0.08	<0.05
	$\bar{U}_4$	—	—	<0.05
β_{static}		0.111	0.111	0.222
β_1		0.247	0.196	0.259

respect, and are smaller. U_1 and U_3, however, connect the first excited level with a higher excited level of spin 2, but have no nonvanishing matrix elements with the ground state. U_1 and U_3, therefore, act to lower the first excited energy and decrease the spacing of the lowest two states. The effect is very appreciable, as shown in Table VII. The energy spacing is diminished by 15 percent to 30 percent. The shift is small compared to the spacing of the levels mixed (so that the wave functions do not mix to a large extent), but it is an appreciable fraction of the lowest level spacing. In considering the validity of the approximation, therefore, it is important to refer to the particular nuclear properties of interest.

The computed distortions in the first-order strong coupling approximation are too large, because the coefficient of β in the interaction term W_2 is maximized by the ground-state quantum numbers Ω_i. For *any* admixture of other Ω_i, the coefficient will be decreased, and the computed equilibrium distortion, therefore, will be decreased.

It can be concluded that explicit calculation with the strong coupling approximation *should* be valid for several extra nucleons and for $A \gtrsim 100$. In addition, the ideas of the strong coupling model, e.g., that nuclear distortion plays an important role in even nuclei, should be valid after the strong coupling approximation in first order breaks down. A distortion $\beta \gtrsim 0.2$ appears to be necessary for the validity of the approximation in first order.

III. CORRELATION OF EXCITATION ENERGY WITH QUADRUPOLE MOMENTS

Both the first excited energies of even nuclei and the quadrupole moments (largely of odd-even nuclei) are known to exhibit a regular behavior as a function of N and Z, each with marked shell structure effects. The collective model discussed above predicts that the first excited energy of even nuclei depends principally on the equilibrium value of the nuclear distortion, provided the distortion is large enough. Likewise quadrupole moments, especially the large moments, are most easily interpreted in terms of a distorted nucleus. Because of the observed regularities in both of these quantities, it is natural to test the idea of the collective model and the idea that the nuclear distortion is a reasonably smooth function of N and Z for all nuclei by attempting to correlate the known quadrupole moments with the known first excited energies of even nuclei.

In order to carry out this correlation, we develop highly simplified formulas for these two quantities in terms of the nuclear distortion. On the basis of the detailed calculations summarized in Table III, the following assumptions and simplifications are made for the even nuclei. The distortion parameters β_1, γ_1 are taken to be the same in the ground and first excited state. In fact, β_1 is somewhat larger for the first excited level. The zero-point vibration energies E_β and E_γ are taken to be the same in ground and first excited state. The quantum numbers of the ground state are taken to be $K=\Omega=0$, $I=0$, and of the first excited state, $K=\Omega=0$, $I=2$. The extra nucleon states are assumed the same for ground and first excited state. As a result of these simplifications, only the rotation term W_3 differs between the ground and first excited states. The first excited energy is, therefore,

$$E_1=\frac{1}{16}\frac{\hbar^2}{B\beta_1^2}\left(\frac{1}{\sin^2(\gamma_1-2\pi/3)}+\frac{1}{\sin^2(\gamma_1-2\pi/3)}\right)$$
$$\times\{[I(I+1)-K^2$$
$$+f(\text{particle quantum numbers})]_1$$
$$-[I(I+1)-K^2$$
$$+f(\text{particle quantum numbers})]_0\}. \quad (26)$$

Inserting the values $\gamma_1=0$ or π, $I_1=2$, $I_0=0$, $K_1=K_0=0$, $\hbar^2/B=171/A^{5/3}$ Mev, and f_1 (particle quantum

TABLE VII. First-order corrections to detailed calculations.

Example	First excited energy in first order (Mev)	Shift due to U_1+U_4 (Mev)	Energy in second order	Percent decrease
$A=100$, two extra nucleons, $j=5/2$	0.581	−0.119	0.462	20
$A=100$, two extra nucleons, $j=9/2$	0.529	−0.161	0.368	30
$A=200$, two extra nucleons, $j=5/2$	0.315	−0.042	0.273	13
$A=200$, two extra nucleons, $j=9/2$	0.248	−0.039	0.209	16
$A=100$, four extra nucleons, $j=9/2$	0.397	−0.064	0.333	16

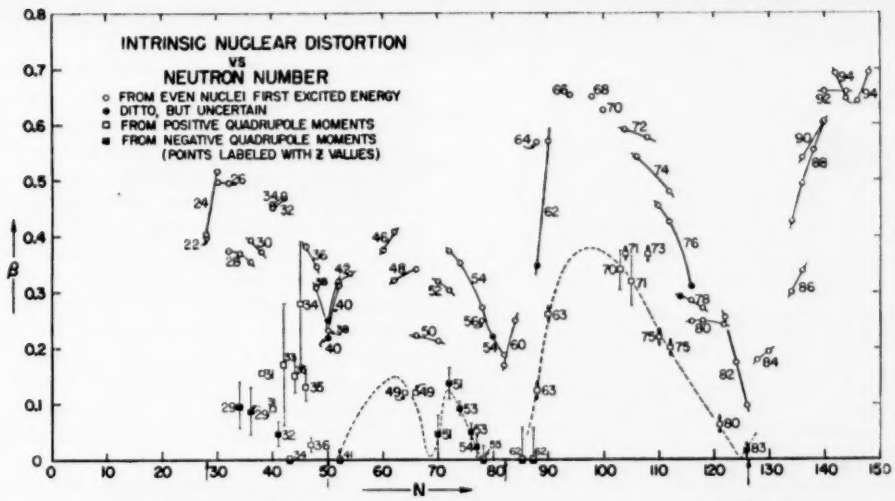

FIG. 4. Correlation of even nuclei first excited levels with quadrupole moments. The circled points are computed from Eq. (30a) in the text and represent upper limits to the nuclear distortion as computed from energy levels. The least accurate points are those near the maxima at $N=100$ and $N=145$, because here the energies are minimum and are least well known. The squared points are computed from quadrupole moments. Experimental errors are indicated on those points where they are known (to this author). Vertical arrows indicate unknown experimental errors. The distortions computed from quadrupole moments are seen to exhibit a regular behavior vs N only for $N>50$. If (a) the interpretation of the nature of the first excited states of even nuclei is correct, (b) quadrupole moments give a correct indication of the magnitude of the nuclear distortion, and (c) neighboring even-even and odd-even nuclei have comparable distortions, then Eq. (30a) overestimates the nuclear distortion by a factor of about 1.7 for large distortions and by very much more for small distortions. The factor of 1.7 is reasonable within the framework of the strong coupling approximation; factors much greater than 2 are not.

numbers) $=f_0$ (particle quantum numbers), one gets

$$E_1=\hbar^2/B\beta_1^2=171/A^{5/3}\beta_1^2 \text{ Mev}. \tag{27}$$

In order to get an equally simple formula for the quadrupole moment, it is assumed that the nuclear charge is uniformly distributed over a cylindrically symmetric ellipsoid, i.e., that the contribution to Q from the nonspherical distribution of extra nucleons is small compared to the contribution from the distorted core. For a stationary ellipsoid one obtains to first order in β,

$$Q_{\text{stat}}=(2/5)ZR_0^2(3/2)(5/\pi)^{\frac{1}{2}}\beta\cos\gamma. \tag{28a}$$

A distortion β corresponds to a fractional extension of the radius along the symmetry axis of the ellipsoid of $\frac{1}{2}(5/\pi)^{\frac{1}{2}}\beta\cos\gamma=0.631\beta\cos\gamma$ and a fractional extension perpendicular to the symmetry axis of

$$-(1/4)(5/\pi)^{\frac{1}{2}}\beta\cos\gamma=-0.315\beta\cos\gamma.$$

Positive $\cos\gamma$ corresponds to the cigar shape (prolate) and negative $\cos\gamma$ to the pancake shape (oblate). Putting the undistorted nuclear radius $R_0=1.40\times10^{-13}A^{\frac{1}{3}}$ cm, we have

$$Q_{\text{stat}}=0.0148ZA^{\frac{2}{3}}\beta\cos\gamma. \tag{28b}$$

Because of the quantum-mechanical fluctuations in the direction of $\mathbf{I}$, the expectation value of Q is reduced[8] by the factor $I(2I-1)/[(I+1)(2I+3)]$. Therefore, one obtains finally

$$Q_{\text{obs}}=0.0148ZA^{\frac{2}{3}}\frac{I(2I-1)}{(I+1)(2I+3)}\beta\cos\gamma. \tag{29}$$

Formulas (27) and (29) are inverted to define nuclear distortions:

$$|\tilde{\beta}|=\frac{13.1}{A^{5/6}[E_1(\text{Mev})]^{\frac{1}{2}}}, \tag{30a}$$

$$\beta_Q=\frac{67.5}{ZA^{\frac{2}{3}}}\frac{(I+1)(2I+3)}{I(2I-1)}Q_{\text{obs}}(\text{barns}). \tag{30b}$$

If it is assumed that the total quadrupole moment is the sum of a moment due to the distorted core plus a moment due to the nonspherical distribution of extra protons outside closed shells, then β_Q may be too large or too small depending on whether these two moments have the same or opposite sign. (Note that β_Q has the sign of Q, whereas the β in Bohr's theory is intrinsically positive.)

The distortion $|\tilde{\beta}|$ computed from the energy levels is always too large, and in general very much too large: First, within the first-order approximation, Eq. (30a) is an oversimplification, and it can be shown that $|\tilde{\beta}|>\beta$ (first excited state) $>\beta$ (ground state). When the strong coupling approximation is very good, and β

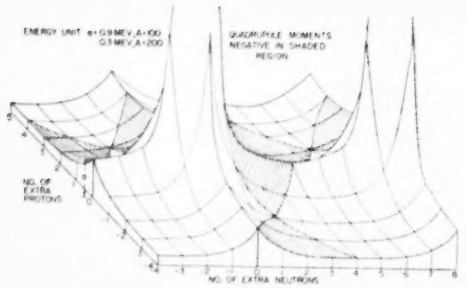

FIG. 5. Energy surface of first excited states of even nuclei for idealized nuclei. Shells for both neutrons and protons are assumed to consist of states of $j=7/2$ only. The nuclear distortion is computed in the strong coupling limit ignoring the rotational energy term in W. The excitation energy is computed in the same limit by means of Eq. (30a) in the text. The lines separating the shaded and unshaded regions are loci of equal energy of the prolate and oblate forms of nuclear distortion. The strong coupling limit used is not even approximately valid at the double magic nuclei, where it yields infinite spikes. The opposite limit of weak coupling yields a finite maximum at the double magic nuclei given by Eq. (1). This maximum varies approximately as $A^{-5/6}$, while the energy surface plotted varies as $A^{-5/3}$. The empirical energy surface (Scharff-Goldhaber) shows a similar behavior, with spikes at the double magic nuclei and ridges along the magic numbers.

is large, then $|\tilde{\beta}|$ is larger than β (ground state) by only a few percent. When the strong coupling approximation is barely valid, i.e., W_3 is comparable to W_1 and $|W_2|$, $|\tilde{\beta}|$ may be too large by up to a factor two. Next, the second-order corrections, as indicated in Table VII, will act to lower the numerator of Eq. (30a). For a 30 percent decrease in energy spacing due to second-order terms, Eq. (30a) will overestimate β by 20 percent. An approximate formula taking into account the effect of U_1 only is

$$|\tilde{\beta}| = \frac{13.1}{A^{5/6}[E_1(\text{Mev})]^{\frac{1}{2}}}[1-(j+\bar{\Omega})(j-\bar{\Omega}+1)/3\Gamma]^{\frac{1}{2}}. \quad (31)$$

U_1 connects states with *one* Ω_i differing by one, other quantum numbers unchanged. $\bar{\Omega}$ above is the larger of the two different Ω_i; j is associated with that particle whose Ω is changed. Γ is the ratio of the energy spacing of the connected states to the energy spacing of the ground and first excited states. For example, for $j=\bar{\Omega}=5/2$, $\Gamma=5$, Eq. (31) gives a value smaller than Eq. (30a) by 19 percent. Finally, the admixture of states of $K=1$ or 2 to the first excited state ($K=0$) will lower $|\tilde{\beta}|$, since the numerator of Eq. (30a) contains effectively $[I(I+1)-K^2]^{\frac{1}{2}}$.

Unfortunately, no simple or calculable expressions exist for applying these three corrections to Eq. (30a) for nuclei in general. We are forced, therefore, to use Eq. (30a) for the correlation, but with the anticipation that it will yield values of $|\tilde{\beta}|$ considerably too large by roughly 10 to 50 percent if the strong coupling picture is valid; by more if it is not. For any detailed calculation on specific nuclei, this rough formula would, of course, have to be improved.

Figure 4 gives the computed distortions $|\beta_Q|$ and $|\tilde{\beta}|$ *vs* neutron number N for known quadrupole moments and first excited states of even nuclei beyond $N=28$. The first evident feature is that $|\tilde{\beta}|$ is everywhere considerably greater than $|\beta_Q|$, as expected. It is larger by nearly a factor two at the maximum. The two sets of data represented in Fig. 4 show qualitative similarities, however. Just beyond neutron number 82, both curves rise precipitously, reaching a maximum at the same place, as nearly as can be guessed, and falling more slowly to minima at neutron number 126. The neutron shell 50 to 82 is more confused because the line of stable nuclei crosses proton number 50 in this shell. Curves of $|\tilde{\beta}|$ *vs* N join smoothly points for $Z=50$, for $Z=50\pm2$, and for $Z=50\pm4$, with a sharp decrease at proton number 50 as well as at neutron magic numbers. This behavior fits the simple ideas of the collective model (Fig. 5). In the same region $|\beta_Q|$ appears to have two maxima and to reach zero between. A possible explanation for this is offered schematically in Fig. 6. The collective model predicts a change in the sign of Q in the middle of a shell where the distortion is large. At this point the prolate and oblate forms are of

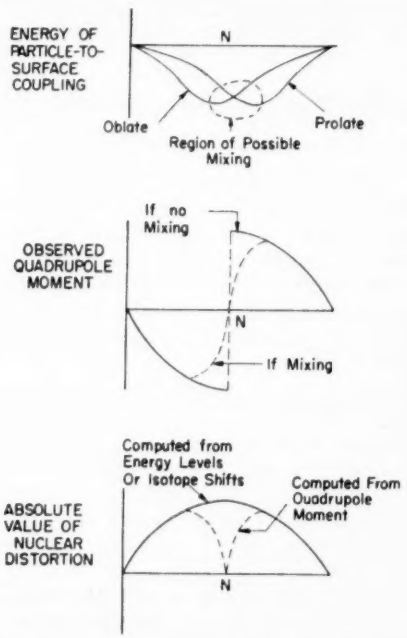

FIG. 6. Prolate-oblate crossover in nuclei. The diagrams show schematically how a mixing of the prolate and oblate forms of distortion in the region where these are of nearly equal energy could yield small quadrupole moments despite a large intrinsic distortion. Such a mixing requires an interaction between states of different Ω_i. This interaction is afforded in the strong coupling theory by the off-diagonal terms U_0, U_2 and U_4, Eqs. (19). Also a breakdown of the approximation that the particle motion can be treated relative to the ellipsoid axes would permit such mixing.

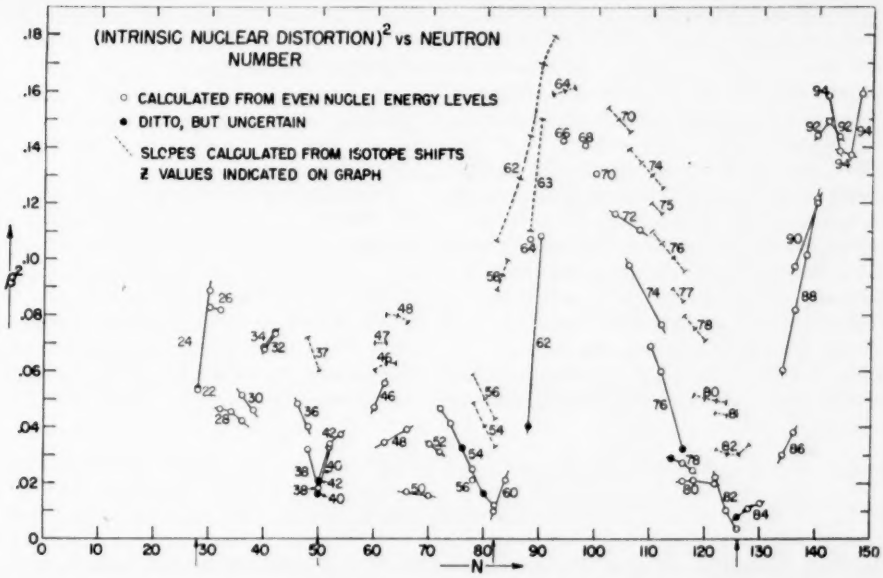

FIG. 7. Correlation of even nuclei energy levels with isotope shifts. β^2 is taken to be $\frac{1}{4}|\tilde{\beta}|^2$ in order to bring the maximum distortions calculated from energy levels and from quadrupole moments into agreement. The solid lines connect computed distortions for isotopes of the same element. The dashed lines represent the slope $[d(\beta^2)/dN]_Z$ taken from isotope shifts. The positions vertically of the dashed lines on the graph are meaningless —only the slopes are to be compared. A single adjustable parameter in the isotope shift data fitted at Pb^{208} brings all the slopes into agreement except in the region below $N=65$, where the isotope shift slopes are slightly too small, i.e., too negative. (The fluctuations of the energy level points at $Z=92$ and 94 are probably not significant. These correspond to energy levels around 40 kev which are not accurately known. The curves β^2 *vs* N appear to be reaching another maximum in this region.)

equal energy and the simple model predicts an abrupt change from one shape to the other. If the nuclear ground state in this region is a mixture of the nearly equal energy prolate and oblate forms, a very small *measured* quadrupole moment will result, while the intrinsic distortion, as measured, for example, by the energy levels, will remain large.

Wilets has suggested that nuclear distortion may account for the regularities[15] in the isotope shift anomalies. Isotope shifts could throw light on the prolate-oblate crossover question discussed above and on the question whether even nuclei distortions may be larger than odd-even distortions. An analysis which will be published elsewhere[16] shows that the isotope shift anomalies are best explained in terms of a distortion with a *shape vs* N and Z derived from energy levels of even nuclei but with a lower *magnitude* corresponding to that found from quadrupole moments.

The energy level—isotope shift correlation is shown in Fig. 7, in which the values of $|\tilde{\beta}|^2$ found from energy levels are arbitrarily reduced by a factor of three everywhere to bring them into agreement with the quadrupole moments at their maximum. The isotope shift data are also altered with a single adjustable parameter chosen to make the anomaly positive at $Pb^{210-208}$ and negative at $Pb^{208-206}$. The isotope shifts yield only the slope $[d(\beta^2)/dN]_Z$, and the magnitude of the line segments plotted are meaningless. The slopes, however, show a generally reasonable agreement with the trend of points calculated from energy levels. Especially to be noted are the large positive slopes just beyond $N=82$ and the smaller negative slopes below $N=126$, as were observed also in the quadrupole moment data.

On the basis of the results shown in Fig. 1, certain regularities in the low levels of odd-even nuclei can also be predicted. With each low-lying single particle level of spin $I=j$ should be associated a level of spin $I=j+1$, same parity, higher by the order of magnitude of neighboring even-even first excited energies. To the same approximation as Eq. (27), the energy difference of these level pairs is given by

$$\Delta E_{j+1,j}=\frac{\hbar^2}{B\beta_1^2}\left(\frac{2j+2}{6}\right). \tag{32}$$

IV. CONCLUSIONS

The successes of the collective model as applied to the low states of even nuclei are (a) the order of levels for the first few levels agrees with experiment; (b) the spacing of the 0+–2+ and 2+–4+ levels are comparable, as observed experimentally; (c) the first

[15] P. Brix and H. Kopfermann, Phys. Rev. **85**, 1050 (1952).
[16] Wilets, Hill, and Ford (to be published).

excited energy surface has the same qualitative features as the experimental energy surface (see Fig. 5); and (d) details of the shape of the curve of distortion *vs* N in the neutron shell 82 to 126 as calculated from energy levels agree with the curves found from quadrupole moments and from isotope shifts.

The serious defects of the model is that nuclear distortions calculated from first principles appear to be larger than is reasonable, implying that the particle-to-surface interaction may be weaker than is assumed. Because Eq. (30a) gives only an upper limit to β, the large distortions calculated from even nuclei energy levels do not necessarily speak against the validity of the strong coupling approximation. The required correction of nearly a factor two is larger than expected, however, for the case that the strong coupling approximation is valid (for wave functions) in first order. The very high first excited state of Pb is also a particular defect of the theory.

On the basis of Figs. 4 and 7, large quadrupole moments (5–8 barns) are predicted near uranium, and large isotope shifts (about twice the theoretical value) are predicted near radium.

I am indebted to Professor E. Feenberg and Dr. A. De Shalit, Dr. G. Scharff-Goldhaber, and Dr. M. Goldhaber, for helpful comments and suggestions; to G. Scharff-Goldhaber for supplying a summary of even nuclei energy levels in advance of publication and to Dr. L. Wilets for information on isotope shifts. Especially it is a pleasure to acknowledge my indebtedness to Professor J. A. Wheeler for many stimulating and valuable discussions.

PHYSICAL REVIEW VOLUME 90, NUMBER 1 APRIL 1, 1953

Cosmic-Ray Neutron Production in Elements as a Function of Latitude and Altitude*

J. A. Simpson and R. B. Uretz
Institute for Nuclear Studies, University of Chicago, Chicago, Illinois
(Received November 17, 1952)

The relative rates of local neutron production in Al, Cu, Sn, and Pb were obtained at geomagnetic latitudes $\lambda = 40°$ and 54° at atmospheric depth 312 g-cm^{-2} (30 000 ft pressure altitude). The latitude and altitude dependence of local neutron production in carbon and lead were measured in the latitude interval 0°–54° with pile geometries containing BF_3 proportional counters. From these observations several results were obtained:

1. The relative neutron multiplicities in elements were measured and found to be in good agreement with reported low altitude observations.
2. A neutron transition maximum in lead at ~20 g-cm^{-2} Pb was obtained at 33 000 ft pressure altitude.
3. The absorption mean free path for the neutron producing radiation in lead was 350 g-cm^{-2}.
4. An anomalous air absorption mean free path for the nucleonic component has been found for measurements derived from local neutron production in lead at $\lambda \gtrsim 40°$.
5. Aside from the absorption anomaly in elements of high atomic weight A, local neutron production in elements of high A as a function of λ is in fair agreement with the free air neutron latitude effect.
6. Local production in carbon as a function of λ and altitude is in agreement with corresponding free air neutron measurements.

I. INTRODUCTION

THE production and development of the intermediate and low energy portion of the nucleonic component has been studied by observing nuclear disintegrations and neutrons as a function of both altitude and latitude. The behavior of this low energy component may also be explored by determining the properties of nuclear disintegrations produced in a local mass absorber by incident nucleons. We shall define this process as local nuclear disintegration production. These local disintegrations principally yield neutrons, protons, and alpha-particles, i.e., disintegration products. Within a large local absorber mass the charged particles of low energy disappear by ionization energy loss and are not readily detected outside the local mass. The disintegration neutrons, however, escape from the local mass and may be detected. We define the observed neutron production as local neutron production.

In this paper we describe measurements of local neutron production in the elements C, Al, Cu, Sn, and Pb as a function of geomagnetic latitude and as a function of altitude in the range of atmospheric depths 200 to 600 g-cm^{-2}. From these measurements we determine the average neutron multiplicity from low energy nuclear disintegrations. The measurements were obtained in a series of aircraft flights from January, 1948 through November, 1949.

Local neutron production has been extensively investigated at sea level and mountain altitudes by the Cornell University and Yale groups for carbon and lead close to the latitudes $\lambda = 50 - 52°$N. Neutron produc-

* Work initiated under U. S. Office of Naval Research contract and continued with assistance of Office of Scientific Research, A.R.D.C., U. S. Air Force.

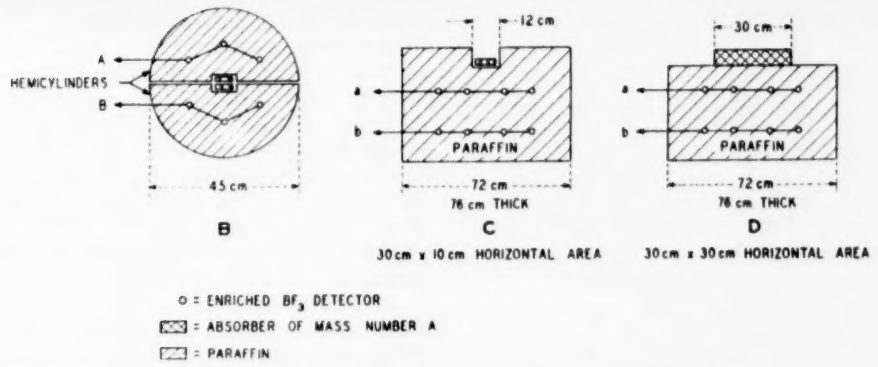

FIG. 1. Pile geometries of local neutron producer with paraffin moderator. These geometries were carried by B-29 aircraft from geomagnetic latitude 0° to 65°N. All measurements were obtained in spring and summer months 1948 and 1949.

tion and neutron multiplicity from high energy incident nucleons have been measured in lead.[1] The neutron producing event was selected by the requirement that the incoming nucleon produce not only the fast neutrons but also one or more charged particles capable of penetrating several grams of lead and paraffin. Hence, these measurements were of high energy processes. Measurements of neutron production and multiplicity have also been obtained for disintegrations in lead and carbon due to the entire incident radiation[2,3] with no requirement that a disintegration produce high energy charged particles. Thus, the detected neutrons are not related in time by the apparatus to specific incident particles. Neutrons detected under these conditions were called incoherent neutrons, and we shall also adopt this definition.

The measurements we report in this paper are for the total incoherent local neutron production in elements; hence, the production is due to the total incident radiations. Some preliminary results of our measurements have already been reported.[4] Although we do not consider these measurements as the best that could be obtained, principally because of limitations of aircraft facilities, we have decided to publish them because they remain the only known measurements of this kind at high altitude, and we have found these results useful for interpreting the intensity variations of the nucleonic component and their relationship to primary intensity variations.

II. DETECTOR GEOMETRY AND EXPERIMENTAL PROCEDURES

The neutrons from mass absorbers are reduced in energy by collisions in a local paraffin moderator before being detected by boron trifluoride proportional counters. The geometrical arrangements of masses for neutron production and the paraffin moderator are called pile geometries and are shown in Fig. 1. These pile structures were mounted in the aircraft cabin so that the incident radiation passed through less than 1 g-cm^{-2} of cabin wall. A radium beryllium source of neutrons was used to periodically check the efficiency of the neutron detecting system. The absorbers were pure elements and were analyzed for possible impurities having high neutron capture cross sections.

Principally because of uncertainties in the determination of the absolute efficiencies of the pile geometries shown in Fig. 1, we shall report all our measurements as *relative* neutron production rates. Each measurement of local neutron production in the absorber is a difference measurement; i.e., the difference between the counting rate observed in the geometry *with* and *without* the selected absorber.

The piles were airborne at geomagnetic latitudes 0°, 40°, and 54°N. Details on the method of determining latitude and pressure altitude have been described in earlier papers.[5]

Since large changes of intensity of the order of 5–30 percent may occur in the nucleonic component with time,[5] the data on relative local neutron production were corrected for temporal intensity changes by monitoring the neutron intensity in the atmosphere wherever possible.

It is clear that the measured neutron production rate of a unit mass of absorber at the top of the absorber in a pile geometry may be different from a unit mass on the bottom of the absorber because of (a) the difference in solid angles subtended by a unit mass in these positions, (b) neutron scattering and end effects, (c) star-producing radiation directed upward from the paraffin moderator, and (d) absorption of the incident radiation in the absorber. In measurements of this type a local producer always subtends a large solid angle of the moderating paraffin block. If star-producing radiation

[1] Cocconi, Tongiorgi, and Widgoff, Phys. Rev. **79**, 768 (1950).
[2] V. Tongiorgi, Phys. Rev. **76**, 517 (1949).
[3] C. G. Montgomery and A. R. Tobey, Phys. Rev. **76**, 1478 (1949).
[4] J. Simpson, Proc. Echo Lake Cosmic Ray Symposium, U. S. Office of Naval Research, p. 252 (1949); Simpson, Baldwin, and Molner, Phys. Rev. **77**, 751 (1950).
[5] J. Simpson, Phys. Rev. **83**, 1175 (1951).

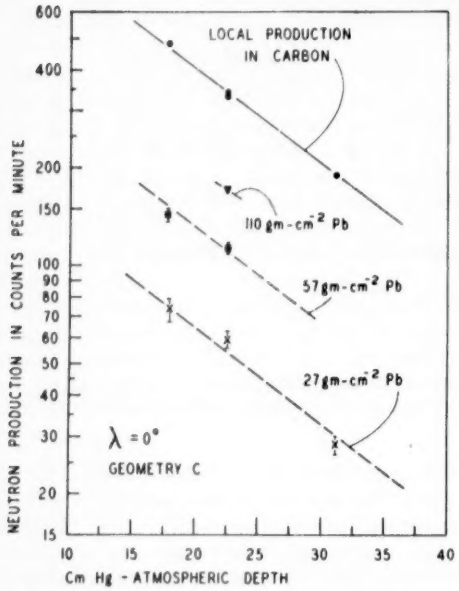

FIG. 2. Local neutron production at the geomagnetic equator as a function of atmospheric depth.

passes upward from the paraffin block because of high energy interactions in the paraffin, it is possible to increase the nuclear disintegration rate in the local producer when it is placed over the paraffin. The contribution of this process to our observed production rates has not been investigated because it appears to be a very small effect[6,7] for paraffin except possibly with absorber thicknesses the order of 7–10 g-cm^{-2} or less. Any contribution of this type has been included in the experimental correction curves for all absorber thicknesses in the four geometries. A typical correction curve, which will be described in detail later, is shown in Fig. 6.

Since the average neutron energy from light element disintegrations is higher than the average neutron energy from heavy nuclei,[8] the dependence of the geometry efficiency on neutron energy was estimated by comparing the relative counting ratio in counter banks *a* and *b* in geometry *D*. This ratio appeared insensitive to the atomic weight of the absorber; hence, counter bank *a* was used for all the measurements reported in this paper.

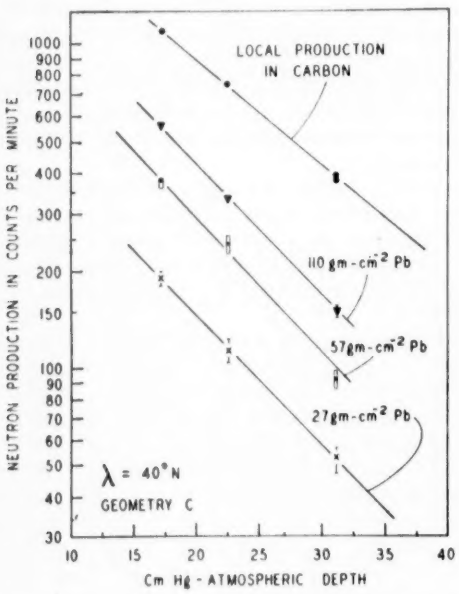

FIG. 3. Local neutron production at geomagnetic latitude 40°N as a function of atmospheric depth.

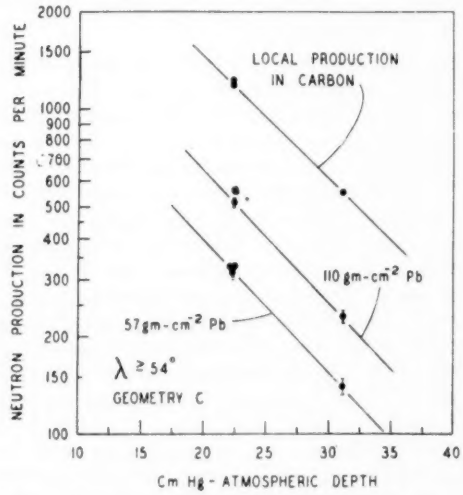

FIG. 4. Local neutron production at geomagnetic latitude 54°N as a function of atmospheric depth.

III. LATITUDE AND ALTITUDE DEPENDENCE OF LOCAL NEUTRON PRODUCTION IN CARBON AND LEAD

A. Relative Local Production Measurements

To determine the air absorption mean free path, *L*, of the radiation which generates the local neutrons in lead and carbon, we measure the local neutron production rate in a geometry as a function of altitude at $\lambda = 0°$, 40°, and 54°N. Geometry *C* was used for these measurements with lead thicknesses of 27, 57, and 110 g-cm^{-2}. For the measurements of $L(\lambda)$ no geometrical correction for lead thickness is required since the correction is a constant factor for all latitudes and altitudes. The results are given in Figs. 2, 3, and 4 for 0°, 40°, and 54° geomagnetic latitude, respectively. Assum-

[6] For star production above lead, see Malaspina, Merlin, Provacci, and Rostagni, Nuovo cimento **7**, 145 (1950).
[7] S. B. Treiman and W. Fonger, Phys. Rev. **85**, 364 (1951).
[8] D. M. Skyrme and W. S. C. Williams, Phil. Mag. **42**, 1187 (1951).

ing for the equilibrium altitude region a curve of the form $I = I_0 e^{-x/L}$, where x = atmospheric depth in g-cm^{-2}, values for L have been computed for Table I and compared with measurements from both fast neutron production in the free atmosphere and nuclear disintegrations in pulse ion chambers for corresponding latitudes. The latitude dependence at atmospheric depth 312 g-cm^{-2} (30 000 ft) is given in Table II for local production measurements.

By covering all BF_3 detectors in the piles of Fig. 1 with cadmium we determine the extent to which charged particles and showers produced in the lead absorber could contribute to the observed counting rates. The results using piles C and D are given in Table III. We observe that the total counting rate for cadmium covered counters is ~3 percent of the observed rate with 110 g-cm^{-2} thick lead as a local neutron producer in geometry C. A similar result at higher altitude is found for geometry D; hence, most of the residual ~3 percent background must be due to local star production in the proportional counters and to neutrons which penetrate the cadmium shields. These results are in agreement with earlier, more extensive measurements of detector background, which indicated that interference by recoils and showers is a small effect, probably representing less than 1 percent of the observed neutron counting rates in the piles.[5]

TABLE I. The air absorption mean free path, L, of the neutron-producing radiation as measured by local neutron production in lead and carbon.

Geomagnetic latitude λ	Local fast neutron producer—geometry C	L as measured by local production	L as measured by free air neutron production[a]	L as measured by local star production[b]
0°	Carbon	200	212±4	220
	Lead (57 g-cm^{-2} thick)	200		
	Lead (27 g-cm^{-2} thick)	202		
40°N	Carbon	183	181±3	174–160
	Lead (110 g-cm^{-2} thick)	148		
	Lead (57 g-cm^{-2} thick)	140		
	Lead (27 g-cm^{-2} thick)	147		
54°N	Carbon	157	157±2	164
	Lead (110 g-cm^{-2} thick)	143		
	Lead (57 g-cm^{-2} thick)	145		

[a] See reference 5.
[b] See reference 11.

B. The Mean Free Path Anomaly

We obtain an anomalous effect at latitudes 40° and 54° for measurements of the mfp of the neutron producing radiation in air if the measurement is obtained with a local lead absorber; namely, the mfp is ~20 percent lower at 40° for local production in lead than for either the local production in carbon or for free air neutron production as shown in Table I. We have repeated our measurements at 40° to verify these results. Although we have no clear explanation for this effect, we wish to consider a tentative interpretation of the phenomenon.

TABLE II. Geomagnetic latitude factors for the local production of fast neutrons at an atmospheric depth of 312 g-cm^{-2} (30 000 ft pressure altitude).

Local neutron producer—geometry C	$\frac{I_{40°}}{I_{0°}}$	$\frac{I_{54°}}{I_{40°}}$	$\frac{I_{54°}}{I_{0°}}$	Time of measurement
Carbon (paraffin)	2.2	1.6	3.7	April-August 1949
Lead, 27 g-cm^{-2} thick	2.1	···	···	April-August 1949
Lead, 57 g-cm^{-2} thick	2.1	1.4	3.5	April-August 1949
Lead, 110 g-cm^{-2} thick	2.0	1.5	3.5	April-August 1949
Local neutron producer—geometry B				
Carbon	···	···	3.3	June 1948

[a] Note: These latitude ratios vary with time (reference 5) and, hence, should be considered as approximately correct for a time averaged period of ~1 month.

In the region of $\lambda \approx 40°$ for atmospheric depths $200 < x < 600$ g-cm^{-2} it is known that the nucleons incident on a local absorber have an *average* energy in the range 100–500 Mev. Further, Treiman[9] has recently shown that for latitudes $\lambda \lesssim 43°$N an appreciable contribution to the neutron production in the atmosphere is obtained from the break-up of primary alpha-particles and heavier nuclei. In the region of 40° these break-up nucleons have a low average energy.

We now consider reported measurements of total and absorption cross sections for neutrons in the energy range ~80 to 300 Mev. The measurements of DeJuren, and DeJuren and Moyer[10] indicate that these cross sections for carbon and lead *decrease* with increasing energy in the region of 80–100 Mev with σ(carbon) decreasing by a much larger factor than σ(Pb). Both σ_C and σ_{Pb} become flat in the region $E \gtrsim 220$ Mev. If we assume (1) that the average nucleon energy in the atmosphere increases slowly with increasing altitude, and (2) that the nucleons incident on the

TABLE III. Evidence that charged particles and showers from the lead absorbers do not register in geometry C. (Position of measurement: $\lambda = 40°$N; altitude = 30 000; 19 May 1949).

I	Geometry C	Events/minute
1.	Local production in carbon (paraffin)	750±9
2.	Local production in carbon plus 110 g-cm^{-2} thick lead absorber	1090 = 750 + 340
3.	Local production in carbon; all BF_3 counters covered with cadmium 0.04 in. thick	32.4±0.9
4.	Local production in carbon plus 110 g-cm^{-2} thick lead absorber; counters cadmium covered	34.3±0.9
II	Geometry D at 37 000′	Events/minute
1.	Local production in carbon	1880±13
2.	Local production in carbon; All BF_3 counters covered with cadmium	52±1.8
3.	Local production in carbon plus 14 g-cm^{-2} lead; cadmium covered counters	55±2.6

[9] S. B. Treiman, Phys. Rev. **86**, 917 (1952).
[10] J. DeJuren, Phys. Rev. **80**, 27, 132 (1950); J. DeJuren and B. J. Moyer, Phys. Rev. **81**, 919 (1951); also Taylor, Pickavance, Cassels, and Randle, Phil. Mag. **42**, 328 (1951).

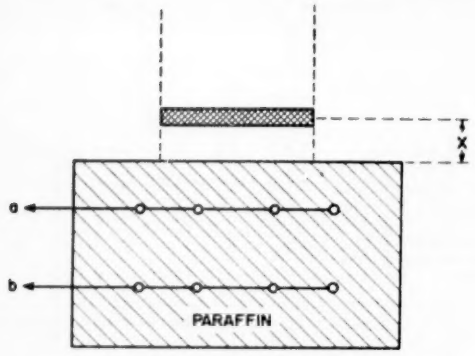

FIG. 5. Geometry used to determine dependence of local neutron counting rate upon the position of the local producer. By changing X the correction curves shown in Figs. 6 and 7 are obtained.

local production geometry have an average energy of ~100–300 Mev, then the local neutron production rate in lead will *increase* relative to the neutron production rate in carbon as the altitude of observation is increased. Thus, calculations of the mfp, L, of the neutron producing radiation in air obtained from local production in carbon and lead will give $L_C > L_{Pb}$. The sign of this effect is correct, but since the exact incident nucleon energy distribution is unknown, we cannot determine whether or not the magnitude of the effect is correct.

We note that measurements of L using the star production in brass and argon from pulse ion chamber measurements also demonstrates this anomalous effect.[11] From the above arguments we conclude that a measurement of L near 40° by a determination of star production in photographic emulsions should yield values which are significantly *lower* than free atmosphere measurements, since a large fraction of the stars are produced in the heavy nuclei of the emulsion.

IV. LOCAL NEUTRON PRODUCTION AS A FUNCTION OF ATOMIC WEIGHT AND LATITUDE

To compute the relative local neutron production per unit mass for nucleonic component absorbers of different thicknesses we must know the change of neutron detection "efficiency" in the geometry and neutron scattering as a function of vertical position of the local absorber above the geometry. A correction curve which includes these factors was obtained by measuring at high altitude the *observed* local production from a thin lead plate as a function of its vertical displacement X above the paraffin moderator, see Fig. 5. The results for pile geometries "C" and "D" are shown in Figs. 6 and 7, respectively. G_x is the fractional loss of observed production in a thin horizontal layer of local absorber at elevation X above the paraffin geometry.

With these curves we compare the neutron production rate of local masses of different thicknesses. In general, it was necessary to increase the thickness of the low atomic weight absorbers in order to achieve the same magnitude of count rates among the Al, Cu, Sn, and Pb absorbers. All measurements of relative neutron production per unit mass among the Al, Cu, Sn, and Pb absorbers were corrected in this manner and, tabulated in Table IV. The measurements at 55° and 40° were obtained at different times and no corrections for temporal changes of cosmic-ray intensity were attempted. However, it is clear that the neutron production per unit absorber mass displays a *latitude* dependence which is, within the experimental errors, independent of atomic weight.

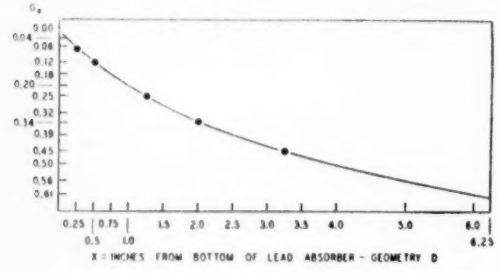

FIG. 6. Correction curve for position of local neutron producer in geometry D (see Figs. 1 and 5).

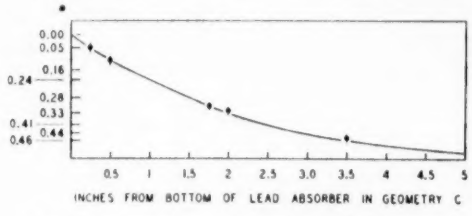

FIG. 7. Correction curve for position of local neutron producer in geometry C (see Figs. 1 and 5).

An estimate of the average neutron multiplicity, ν, from nuclear disintegrations in the absorbers as a function of the atomic weight, A, of the nucleus may be obtained if we make three assumptions:

First, we assume that for these low energy processes each incoming nucleon which interacts with absorber nuclei generates only one low energy nuclear disintegration, i.e., no products of the disintegration produce secondary disintegrations. For measurements of the kind reported here, namely, incoherent neutron production rates, a decision on this question may be obtained from the data on locally produced nuclear disintegrations in ion chambers.[11] We find that the frequency of nuclear disintegrations decreases exponentially with increasing size of the disintegrations and that the slope of the frequency *vs* energy curve for the disintegrations does not change appreciably with geomagnetic latitude. Since on the average only the more energetic disintegrations produce pions or nucleons of

[11] Simpson, Baldwin, and Uretz, Phys. Rev. 84, 332 (1951).

sufficient energy for additional star production,[12] we see that by far the greatest contribution to the local star production rate must come from low energy stars. Hence, we conclude that when a high energy nucleon enters a local absorber and produces a nuclear disintegration the process will not, in general, lead to additional disintegrations within the absorber.

Quantitative data on this question have been obtained by Cocconi *et al.*[1] at mountain altitudes which show that for neutron production in lead the average neutron multiplicity in a disintegration process remains constant up to at least 22 g-cm^{-2} lead thickness for incident high energy charged particles, and that for incoherent neutrons this multiplicity is approximately unchanged for even greater lead thicknesses. The above evidence indicates that the incoherent neutron production in local masses has its origin in small star production. Consequently, it is not surprising to find in the equilibrium portion of the atmosphere that the altitude dependence of local neutron production in lead and carbon, except for the lead anomaly, are similar to local star production as shown in Tables I and II. Thus, we assume that single nuclear interactions con-

TABLE IV. Local production of fast neutrons in elements at $\lambda=55°$ and $\lambda=40°$; 30 000 ft pressure altitude.

Nuclear mass number A of absorber	Geomagnetic latitude	*Relative* neutron production rates per gram of absorber	Geomagnetic latitude	*Relative* neutron production rates per gram of absorber
208 (Pb)	55°N	1.70×10^{-2}	40°N	1.35×10^{-2}
119 (Sn)		1.30×10^{-2}		1.0×10^{-2}
64 (Cu)		1.1×10^{-2}		0.7×10^{-2}
27 (Al)		0.7×10^{-2}		

stitute the predominant process in local absorbers provided absorber thicknesses are used which are <0.5 of the absorption mfp of the incident radiation in the absorber.

Second, we assume that the nucleon interaction with the nucleus has a geometrical cross section, $\sigma \propto A^{\frac{2}{3}}$. This is only approximately true since for nucleons incident on nuclei in the hundreds of Mev energy range the nuclei are partially transparent and, hence, the cross sections are less than geometrical.

Third, it is assumed that, although the average energy of the disintegration product neutrons decreases with increasing atomic weight of the parent nucleus, the efficiency for detection is unchanged. This assumption appears to be fairly satisfactory on the basis of measurements of neutron intensity in the upper and lower horizontal set of BF_3 counters in geometry "*D*" for various elements. Also this question has been investigated by Cocconi, *et al.*[1]

With these three assumptions we may determine the relative neutron production rate P per gram in an absorber of atomic weight A and density ρ as follows:

$$\sigma = KA^{\frac{2}{3}},$$

and the production rate of neutrons per unit volume per incident particle $=\sigma(\rho/A)\bar{\nu}$, where $\bar{\nu}$ is the average neutron multiplicity per disintegration. Then, the total production rate $=\sigma(\rho V/A)\bar{\nu}=\sigma(m/A)\bar{\nu}$, where V and m are the volume and mass of the absorber, respectively. Hence, the observed production rate/g of absorber $=P=K'\sigma\bar{\nu}/A=K'K\bar{\nu}/A^{\frac{1}{3}}=K'K\bar{\nu}A^{-\frac{1}{3}}$, where K' is a factor which includes the efficiency of the pile for detection of a disintegration product neutron. If we call $A^{-\frac{1}{3}}=\eta$, then $dP/d\eta=K'K\bar{\nu}$. Hence, the *ratio* of neutron multiplicities from two elements may be determined from the slope of the curve P *vs* $A^{-\frac{1}{3}}$, which is shown in Fig. 8. For example, the ratio $\bar{\nu}(\text{lead})/\bar{\nu}(\text{aluminum})=11/2.4=4.6$, and extrapolating the curve to carbon, $\bar{\nu}(\text{lead})/\bar{\nu}(\text{carbon})\approx 11$. These values appear to be in fair agreement with the measurements of Tongiorgi[2] at mountain altitudes for the incoherent neutrons from low energy processes. The production rates per gram at mountain and sea level altitudes in carbon and lead were determined by Montgomery and Tobey[3] as $P_{Pb}/P_C\approx 2.6$. The corresponding ratio from Fig. 8 by extrapolation is $P_{Pb}/P_C=3$. Thus, with the assumption of $\sigma=KA^{\frac{2}{3}}$ for the cross section, we find that the multiplicity of disintegration product neutrons increases rapidly with atomic weight of the parent nucleus. These calculations of multiplicity may be in error by as much as a factor of two, but the relative multiplicities are probably not in error by more than 25 percent.

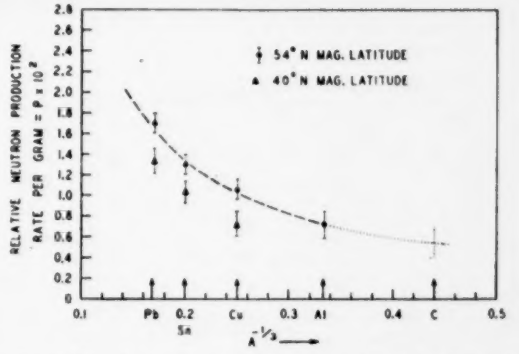

FIG. 8. Local neutron production as a function of atomic weight A. The upper curve is for $\lambda=54°$ and the lower points are for $\lambda=40°$.

V. THE TRANSITION MAXIMUM IN LEAD AND THE ABSORPTION OF THE NUCLEONIC COMPONENT IN LEAD

The nuclear absorption of the neutron producing radiation may be obtained for lead at high altitude by measuring the change of local neutron production in a thin lead absorber when covered with additional lead absorbers. The arrangement of absorbers is shown in Fig. 9; each plate is 1.27 cm thick. We use the bottom

[12] Camerini, Fowler, Lock, and Muirhead, Phil. Mag. **41**, 415 (1950).

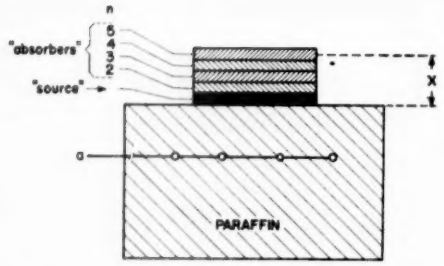

FIG. 9. Arrangement of lead absorber plates used to determine the neutron transition effect in lead and the absorption mean free path in lead for nucleons. The plate $n=1$ is called the neutron "source."

plate of the stack of absorbers as the "source" of neutrons and consider all the plates above it as absorbers of the neutron producing radiation. Since both the "source" plate and the absorber plates produce neutrons, a difference measurement for each increasing number of absorber plates is required to determine the neutron production rate which arises from the "source" plate alone. These measurements are corrected for geometry and neutron scattering by means of the correction curve in Fig. 6. All plates were 30×30 cm in horizontal cross section on pile *D*. Plates of this size avoid serious errors due to oblique incidence of the nucleons.

Again we assume that only single interactions occur in the "source" or absorber plates. We compute the true counting rate, C_T, due to the "source" layer of mass M_n in the presence of the absorber, where n is the number of 1.27 cm thick plates stacked on the geometry. Call the measured counting rate R_n for a stack of n plates. The fractional correction for the nth plate is G_n obtained from Fig. 6. If the "source" plate is called $n=1$ with mass M_1, and with a corrected neutron production rate P_1 per g mass, then the true counting rate for the "source" layer covered with $n-1$ plates is

$$C_T=[1+G_1][R_n-\{(1-G_n)P_1M_1+(1-G_{n-1})P_2M_2 +\cdots+(1-G_2)P_{n-1}M_{n-1}\}].$$

This expression takes into account any transition effect which may occur in the $n-1$ plates.

The values of C_T as a function of lead absorber thickness in g-cm^{-2} have been plotted in Fig. 9 for measurements at 33 000 ft pressure altitude at $\lambda=40°$N. The exponential absorption of the nucleons producing the neutrons in lead as derived from the tail of the absorption curve is 350 ± 40 g-cm^{-2} Pb.

A small neutron "transition" effect in lead is observed with a maximum near 15 g-cm^{-2}. The recent measurements by Treiman and Fonger[7] near sea level in Chicago using an improved geometry indicate that this transition effect is not strongly altitude-dependent. Hence, the transition effect is probably a characteristic of the low energy nucleonic component. Similar transition maxima have been found at high altitudes for the nuclear disintegration intensity observed in photographic emulsions.[13]

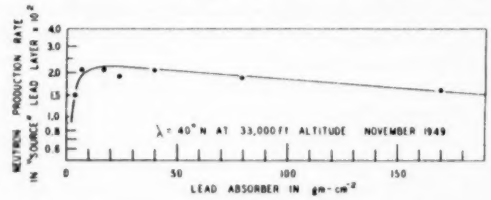

FIG. 10. The neutron transition effect in lead and the exponential absorption of the neutron producing radiation in lead. The "transition" maximum occurs at 15–20 g-cm^{-2} Pb. The absorption mean free path in lead is 350 ± 40 g-cm^{-2}.

The authors wish to thank Messrs. E. Hungerford and S. Molner for their assistance with these measurements and express appreciation for the skillful flying of the B-29 by the U. S. Air Force group under the command of Major W. Gustafson.

[13] Freier, Ney, and Oppenheimer, Phys. Rev. **75**, 1451 (1949); J. J. Lord and M. Schein, Phys. Rev. **75**, 1956 (1949); M. Shapiro and A. Gabrysh, Phys. Rev. **84**, 160 (1951).

Excitation of Molecular Rotation-Vibration by Electron Impact

PHILIP M. MORSE
Massachusetts Institute of Technology, Cambridge, Massachusetts
(Received December 19, 1952)

The integral equation for the scattering of an electron from a symmetric diatomic molecule is solved approximately to obtain the effective interaction integral between the electron and the molecular vibration-rotation, neglecting polarization and exchange. This interaction depends on the difference of phase of the incident wave function between the two nuclear centers and thus on the momentary direction and magnitude of the internuclear radius vector. From this interaction function the effective cross sections for rotation-vibration excitation are computed and, by various sum rules, a closed formula for mean loss of energy of the electron to molecular rotation-vibration is obtained. This is compared with the corresponding loss of energy of the rebounding electron to the motion of the center of gravity of the molecule. These two quantities are shown to be the same order of magnitude, their ratio changing from $\frac{1}{3}$, for very small equilibrium internuclear distance, to 1, for very large internuclear distance.

I. INTRODUCTION

THE scattering of an electron from a potential field $V(r)$ is described by a solution of the integral equation,[1]

$$\psi(\mathbf{r})=e^{ik\mathbf{a}_i\cdot\mathbf{r}}-\frac{2m}{h^2}\int\frac{e^{ik|\mathbf{r}-\mathbf{r}'|}}{4\pi|\mathbf{r}-\mathbf{r}'|}V(\mathbf{r}')\psi(\mathbf{r}')dv', \quad (1)$$

where $k=(mv/h)$, v being the incident electronic speed, where $\mathbf{k}_i=k\mathbf{a}_i$, $\mathbf{a}_i$ being a unit vector in the incident direction, and where $\mathbf{r}$ is the radius vector giving the position of the electron. To obtain the scattered wave we obtain the asymptotic form[2] for,

$$\psi(\mathbf{r})\rightarrow e^{i\mathbf{k}_i\cdot\mathbf{r}}+(e^{ikr}/r)f(\vartheta),$$
$$f(\vartheta)=-\frac{m}{2\pi h^2}\int e^{-i\mathbf{k}_s\cdot\mathbf{r}'}V(\mathbf{r}')\psi(\mathbf{r}')dv', \quad (2)$$

where $f(\vartheta)$ is the angle-distribution factor for the scattered wave, from which we obtain the cross section for scattering; $\mathbf{k}_s=k\mathbf{a}_s$, where $\mathbf{a}_s$ is a unit vector in the direction of the scattered electron. If ψ is known exactly Eq. (2) is an exact expression and $|f|^2$ will produce exact expressions for the differential and total cross sections for elastic scattering from the potential V.

If now the potential field of a symmetric diatomic molecule may be broken into two equal parts, each centered about a nucleus,

$$V(\mathbf{r})\simeq U(\mathbf{r}-\tfrac{1}{2}\mathbf{R})+U(\mathbf{r}+\tfrac{1}{2}\mathbf{R}), \quad (3)$$

where $\mathbf{R}$ is the internuclear radius vector, then, to the approximation for which this separation is valid, Eq. (2) may be further simplified. For example, we may show that, to a fairly good approximation, the two integrals about the two nuclei differ only by a phase factor, and that

$$f(\vartheta)\simeq 2f_a(\vartheta)\cos[\tfrac{1}{2}(\mathbf{k}_i-\mathbf{k}_s)\cdot\mathbf{R}], \quad (4)$$

where

$$f_a(\vartheta)\simeq e^{-\frac{1}{2}i\mathbf{k}_i\cdot\mathbf{R}}\left(\frac{m}{2\pi h^2}\right)\int e^{-i\mathbf{k}_s\cdot\mathbf{r}'}U(\mathbf{r}')\psi(\mathbf{r}'+\tfrac{1}{2}\mathbf{R})dv'$$
$$\simeq e^{\frac{1}{2}i\mathbf{k}_i\cdot\mathbf{R}}\left(\frac{m}{2\pi h^2}\right)\int e^{-i\mathbf{k}_s\cdot\mathbf{r}'}U(\mathbf{r}')\psi(\mathbf{r}'-\tfrac{1}{2}\mathbf{R})dv'.$$

It may be shown[3] that Eq. (4) is a good approximation even when the Born approximation ($\psi\simeq e^{i\mathbf{k}_i\cdot\mathbf{r}}$) is not valid, and that, when an appropriate $f_a(\vartheta)$ is used, it appears to correspond fairly satisfactorily with experimental results. It is, of course, completely analogous to the formulas for x-ray scattering.

II. INTERACTION WITH EXCITATION-ROTATION

The foregoing is, of course, well-known and is included here only for reference and comparison with the following. Its chief defect is the fact that the molecule is not simply a potential field but is a system which may absorb energy from the incident electron. To take this into account we express the wave function for the N molecular electrons plus the two nuclei as

$$\psi_{\nu,n}=u_\nu(\mathbf{r}_1,\cdots,\mathbf{r}_N)\chi_n(\mathbf{R}), \quad (5)$$

where u_ν is the electronic factor, referred to the nuclei as momentarily fixed and χ is the nuclear part, referred to the molecular center of mass; ν is the electronic quantum numbers, and $n=(n,l,m)$ are the quantum numbers for nuclear motion. This function is a solution of $H_m\psi=E_{\nu,n}\psi$, where H_m is the energy operator for the target molecule.

The equation for the molecule plus incident electron is

$$\left[H_m-\frac{\hbar^2}{2m}\nabla^2+V_m(\mathbf{r},\mathbf{r}_1,\cdots,\mathbf{r}_N,\mathbf{R})\right]\Psi$$
$$=\left(E_{0,0}-\frac{\hbar^2k_0^2}{2m}\right)\Psi, \quad (6)$$

[1] N. F. Mott and H. S. W. Massey, *Theory of Atomic Collisions* (Clarendon Press, Oxford, 1949), second edition, p. 116.
[2] See reference 1, Chap. II.
[3] H. S. W. Massey and E. H. S. Burhop, *Electronic and Ionic Impact Phenomena* (Oxford University Press, London, 1952), Chap. IV.

where $E_{0,0}$ is the energy for the initial state, k_0 is $\hbar$ times the initial momentum of the incident electron, $\mathbf{r}$ is the incident electronic position and where V_m is the interaction potential between the incident electron and each electron and nucleus of the molecule. This is equivalent to the integral equation,

$$\Psi(\mathbf{r}, \mathbf{r}_1, \cdots, \mathbf{r}_N, \mathbf{R}) = \psi_0 e^{ik_0\cdot r} - \frac{2m}{\hbar^2}\sum_{\nu,n}\psi_{\nu,n}\int\cdots\int\frac{\exp(ik_{\nu,n}|\mathbf{r}-\mathbf{r}'|)}{4\pi|\mathbf{r}-\mathbf{r}'|} \times\bar{\psi}_{\nu,n}V_m(\mathbf{r}', \cdots, \mathbf{R}') \cdot\Psi(\mathbf{r}', \mathbf{r}_1', \cdots, \mathbf{r}_N', \mathbf{R}')dv'dv_1'\cdots dv_N'dV', \quad (7)$$

where dV is the volume element $R^2dR\sin\alpha d\alpha d\beta$ for the internuclear coordinates with respect to the center of mass of the molecule.

If we neglect polarization and exchange effects, the larger part of Ψ, which corresponds to no excitation of the molecule, will have the form $\psi(\mathbf{r})u_0\chi_0$, where ψ is a solution of an equation like (1) and $u_0\chi_0$ is the ground-state wave function for the molecule as defined in Eq. (5). Neglecting cross terms in the sum above, we obtain for the asymptotic form for the part of Ψ corresponding to no electronic excitation,

$$\psi_0 e^{ik_0\cdot r} + \sum_n u_0\chi_n f_n(\vartheta)\exp(ik_n r)/r$$

$$f_n(\vartheta) \simeq \frac{m}{2\pi\hbar^2}\int dV'\bar{\chi}_n\chi_0\left[\int\cdots\int|u_0|^2 \times V_m e^{-ik_n\cdot r}\psi(\mathbf{r}')dv'\cdots dv_N'\right]. \quad (8)$$

The integral in square brackets in the expression for f_n is quite analogous to that in Eq. (2). The integration over the molecular electronic coordinates produces the average potential of the incident electron with respect to the molecule in the ground state electronically, when the internuclear radius vector is $\mathbf{R}'$.

This average potential can be approximately split into two parts, each centered around one nucleus, as in Eq. (3):

$$\int\cdots\int V_m|u_0|^2dv_1'\cdots dv_N' \simeq U(\mathbf{r}-\tfrac{1}{2}\mathbf{R}) + U(\mathbf{r}+\tfrac{1}{2}\mathbf{R}),$$

where the form of $U(\mathbf{r})$ is more or less independent of $\mathbf{R}$. Consequently the whole integral in the brackets in the expression for $f_n(\vartheta)$ is, approximately [see discussion of Eq. (4)],

$$2f_a(\vartheta)\cos[\tfrac{1}{2}(\mathbf{k}_0-\mathbf{k}_n)\cdot\mathbf{R}'],$$

where f_a is an angle-distribution factor approximately equal to that for one of the constituent atoms of the molecule, $\mathbf{k}_0$ is a vector of magnitude $(mv/\hbar)$ directed along the z axis (incident beam), and $\mathbf{k}_n$ is a vector representing the scattered beam, at polar angles ϑ, φ with respect to the z axis, of magnitude k_n such that

$$k_n^2 = k_0^2 - (2m/\hbar^2)(E_{0,0}-E_{0,n}). \quad (9)$$

The internuclear vector $\mathbf{R}'$ has magnitude R' and polar angles α and β.

We may consequently write the angle-distribution factor $f_n(\vartheta)$, giving the amplitude of the beam scattered after exciting the vibration-rotation states of the molecule from the lowest state ($n=0$) to that represented by quantum number n with no corresponding electronic excitation, as

$$f_n(\vartheta) \simeq 2f_a(\vartheta)\int\cos(\tfrac{1}{2}\mathfrak{y}_n\cdot\mathbf{R}')\bar{\chi}_n(\mathbf{R}')\chi_0(\mathbf{R}')dV', \quad (10)$$

where the vector $\mathfrak{y}_n = \mathbf{k}_0 - \mathbf{k}_n$ has a magnitude approximately equal to $(2mv/\hbar)\sin(\frac{1}{2}\vartheta)$, as long as $(E_{0,0}-E_{0,n}) \ll (2mv^2)\sin^2(\frac{1}{2}\vartheta)$. To this approximation, therefore, the interaction between the incoming electron and the vibration-rotation states of the molecule is produced by the phase difference of the incident electronic wave function at the two nuclei, as indicated by the cosine term. If the discussion of Massey and Burhop[3] is valid, then it should be expected that this interaction term would be predominant, and would be larger than any interaction term depending on the polarization of the molecule by the incoming electron.

III. EXCITATION PROBABILITIES

If the classical vibration frequency of the diatomic molecule is ω and if the equilibrium separation between the two nuclei is R_0, the allowed vibration-rotation energies and corresponding internuclear wave functions are, approximately,

$$E_{0,n} \simeq \epsilon_{n,l} = E_{0,0} + h\omega n + (h^2/MR_0^2)l(l+1), \quad (11)$$
$$\chi_n(\mathbf{R}) \simeq C_n e^{im\beta}P_l^m(\cos\alpha)\exp(-\tfrac{1}{2}b^2x^2)H_n(bx)/(R_0+x),$$

where $R = R_0 + x$, M is the mass of each nucleus, $b^2 = M\omega/2\hbar$, n stands for the trio of integers n, l, m wherever it is not necessary to write out all three, where H_n is the nth Hermite polynomial, and where the normalizing factor C_n is given by

$$C_n^2 = \frac{2l+1}{4\pi}\frac{(l-m)!}{(l+m)!}\frac{b/\sqrt{\pi}}{n!2^n}.$$

In general, the spacing of the rotational levels, dependent on l, is smaller than the spacing of the vibrational levels, dependent on n (i.e., usually $MR_0^2\omega \gg \hbar$). When this is true $bR_0 \gg 1$, so that $\lim(R\chi)(R\to 0)$ is a negligibly small quantity.

For ease in computation we can take the polar axis for χ to point along $\mathfrak{y}_n$, thus eliminating the unimportant quantum number m. The probability that the incident electron is scattered into the solid angle $d\Omega$ at an angle ϑ to the incident direction, leaving the mole-

cule with no electronic excitation but in the final rotation-vibration state characterized by the numbers l and n (initially $n=l=0$), is then

$$\sigma_{nl}(\vartheta)d\Omega \simeq (k_{nl}/k_0)|f_{nl}(\vartheta)|^2 d\Omega,$$

where

$$|f_{nl}|^2=\left(\frac{2l+1}{\pi n!2^n}\right)|f_a|^2\int_{-\infty}^{\infty}\exp(-b^2u^2)H_n(bu)d(bu)$$
$$\times\int_{-\infty}^{\infty}\exp(-b^2v^2)H_n(bv)d(bv)$$
$$\times\int_{-1}^{1}P_l(y)\cos[\tfrac{1}{2}\mu_n(R_0+u)y]dy$$
$$\times\int_{-1}^{1}P_l(z)\cos[\tfrac{1}{2}\mu_n(R_0+v)z]dz, \quad (12)$$

where we have extended the integration over u and v to $-\infty$, which is allowable as long as $bR_0\gg 1$ as mentioned above.

The differential cross section σ_{00}, for no excitation (purely elastic) is then

$$\sigma_{00}\simeq|f_a|^2\left[\int_{-1}^{1}\exp(-\mu_0^2y^2/16b^2)\cos(\tfrac{1}{2}\mu_0R_0y)dy\right]^2. \quad (13)$$

The maximum value of μ_0 is $2k_0=(2mv/\hbar)$. Therefore the maximum value of the ratio $(\mu_0/16b^2)$ is $(m/M)\times(\frac{1}{2}mv^2/\hbar\omega)$ and unless the initial kinetic energy of the incident electron is smaller than the spacing between vibrational levels, the exponential factor is practically unity and

$$\sigma_{00}\simeq 4|f_a|^2(2/\mu_0R_0)^2\sin^2(\tfrac{1}{2}\mu_0R_0), \quad (14)$$

where $\mu_0=(2mv/\hbar)\sin(\frac{1}{2}\vartheta)$. This is the result we would have obtained if we had averaged the f given in Eq. (4) over all orientations of **R** and then squared the result.

If the incident electronic kinetic energy is sufficiently larger than the vibrational spacing, the effect of the rotational energies on the magnitude of μ_n is negligible and we can sum σ_{nl} over l to obtain the total cross section for molecular transition from vibrational state 0 to state n for any possible final rotational state. We use the formula

$$\sum_l \tfrac{1}{2}(2l+1)P_l(y)P_l(z)=\delta(y-z) \quad (15)$$

to enable us to integrate over z in Eq. (12). Moreover we can use the formula

$$e^{izs}=\exp(-\tfrac{1}{4}x^2)\sum_{n=0}^{\infty}(ix)^nH_n(z)/2^nn! \quad (16)$$

to enable us to expand the cosine factors in Eq. (12) and thence to integrate over u and v, eventually obtaining

$$\sigma_n\simeq(k_n/k_0)\sum_l|f_{nl}|^2$$
$$\simeq\frac{k_n|f_a|^2}{k_02^nn!}\int_{-1}^{1}[1\pm\cos(\mu_nR_0z)]$$
$$\times\exp(-\mu_n^2z^2/8b^2)(\mu_nz/2b)^{2n}dz, \quad (17)$$

where the plus sign is used if n is even, the minus sign if n is an odd integer. If $(\mu_n/4b)^2\ll 1$ these integrals may be easily computed; the one for $n=0$ is much larger than the rest in that case.

Finally, if the kinetic energy of the incoming electron is large enough compared to the vibrational spacing so that $k_n\simeq k_0$ for the first ten or twenty vibrational levels, we can sum σ_n over n to obtain the total probability of scattering at an angle ϑ with any amount of vibration-rotation excited,

$$\sigma_{re}\simeq\sum_n\sigma_n\simeq\sum_n|f_n|^2.$$

Here we can use the formula for Hermite polynomials,

$$\sum_{n=0}^{\infty}(1/\pi^{\frac{1}{2}}2^nn!)\exp[-\tfrac{1}{2}(u^2+v^2)]H_n(u)H_n(v)=\delta(u-v), \quad (18)$$

and sum Eq. (12) over both l and n, obtaining

$$\sigma_{re}\simeq 2|f_a|^2\{1+[\sin(\mu_0R_0)/\mu_0R_0]\}, \quad (19)$$

which is to be compared with Eq. (14). This result is obtained by averaging the square of the f of Eq. (4) over all orientations of R. This does not fall off as rapidly as μR increases (ϑ increases), indicating that the large-deflection scattering is more likely to produce vibration-rotation, which is not surprising.

IV. MEAN LOSS OF ENERGY

Finally, when the incoming electron's kinetic energy is large compared with the rotational level spacing we can compute the mean loss of energy, from the electron which has been deflected by an angle ϑ, to rotation-vibration energy of the molecule. This is, of course, the weighted sum of the various allowed energies, $\sum\sigma_{nl}(\epsilon_{nl}-\epsilon_{00})$, divided by the sum of the probabilities $\sum\sigma_{nl}=\sigma_{re}$.

The term $(\epsilon_{nl}-\epsilon_{00})$ [see Eq. (11)] has two terms, one dependent on n, the other on l. For the terms involving n in the series we use the sum rule for spherical harmonics, Eq. (15), together with Eqs. (12) and (16),

$$\sum_{nl}\hbar\omega n|f_{nl}|^2$$
$$=\hbar\omega|f_a|^2\int_{-1}^{1}\exp[-\mu_0^2z^2/8b^2]$$
$$\cdot\sum_{n=1}^{\infty}\frac{1}{(n-1)!}\left(\frac{\mu_0^2z^2}{8b^2}\right)^n[1+(-1)^n\cos(\mu_0R_0z)]dz$$
$$=2\hbar\omega|f_a|^2\left(\frac{\mu_0^2}{8b^2}\right)\int_0^1 z^2\left[1+\exp\left(-\frac{\mu_0^2z^2}{4b^2}\right)\right.$$
$$\left.\times\cos(\mu_0R_0z)\right]dz. \quad (20)$$

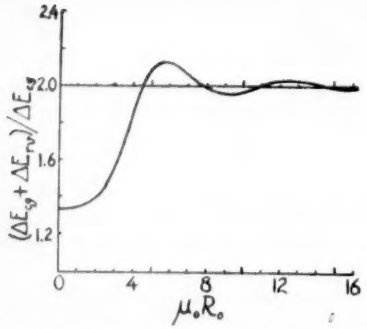

FIG. 1. Ratio between total energy lost to rotation-vibration-translation and energy lost to translation of molecule, as function of $\mu_0 R_0=(2mvR_0/\hbar)\sin(\frac{1}{2}\vartheta)$.

For the terms involving l in the series we use Eq. (18) and a modification of Eq. (15) based on the equation for the Legendre polynomials:

$$\int_{-1}^{1}\sum_l \tfrac{1}{2}(2l+1)l(l+1)P_l(z)P_l(z')F(z')dz' = \frac{d}{dz}\left[(1-z^2)\frac{d}{dz}F(z)\right]$$

for any continuous, integrable $F(z)$. The result is

$$\sum_{nl}\left(\frac{\hbar^2}{MR_0^2}\right)l(l+1)|f_{nl}|^2 = \left(\frac{\hbar^2\mu_0^2}{2M}\right)|f_a|^2\int_0^1 \sin^2(\tfrac{1}{2}\mu_0 R_0 z)(1-z^2)dz \qquad (21)$$

$$=\frac{4}{3}|f_a|^2\frac{m}{M}(\tfrac{1}{2}mv^2)(1-\cos\vartheta)[1-j_0(\mu_0R_0)-j_2(\mu_0R_0)],$$

where $j_n(\omega)$ is the spherical Bessel function $(\pi/2\omega)^{\frac{1}{2}}\times J_{n+\frac{1}{2}}(\omega)$ and where $\mu_0=2(mv/\hbar)\sin(\frac{1}{2}\vartheta)$.

When the incident electronic kinetic energy ($\frac{1}{2}mv^2$) is not small compared with the spacing of the vibrational levels [see discussion of Eq. (13)] the exponential in Eq. (20) may be set equal to unity and the sum for the vibrational levels becomes

$$\sum_{nl}\hbar\omega n|f_{nl}|^2\simeq\tfrac{2}{3}|f_a|^2\frac{m}{M}(\tfrac{1}{2}mv^2)(1-\cos\vartheta)\cdot[1+j_0(\mu_0R_0)-2j_2(\mu_0R_0)]. \qquad (22)$$

We note that when the equilibrium spacing between molecular nuclei, R_0, is small enough so that $\mu_0R_0\ll1$ then the amount of energy given up by the electron to rotational energy becomes small compared to that donated to vibrational energy, but that when $\mu_0R_0\gg1$ twice as much energy is given up to the rotational motion as to the vibrational. This is to be expected because rotational motion represents two degrees of freedom, vibrational motion only one.

Finally, when the incident electron kinetic energy is large compared to $\hbar\omega$, the average loss of energy to rotation-vibration is the sums of Eqs. (21) and (22) divided by the sum of $|f_{nl}|^2$ given in Eq. (19):

$$(\Delta E)_{rv}\simeq\frac{m}{M}(\tfrac{1}{2}mv^2)(1-\cos\vartheta)\times\left[\frac{1-\frac{1}{3}j_0(\mu_0R_0)-(4/3)j_2(\mu_0R_0)}{1+j_0(\mu_0R_0)}\right]. \qquad (23)$$

Classical mechanics indicates that, when $m\ll M$, the energy lost to motion of the center of gravity of a molecule of total mass $2M$, by an electron which is deflected by an angle ϑ by the impact, is

$$(\Delta E)_{cg}\simeq(m/M)(\tfrac{1}{2}mv^2)(1-\cos\vartheta). \qquad (24)$$

We therefore see that the total energy lost by the electron to the molecule, when its initial energy is small compared to the molecular electronic excitation energy but large compared to the vibration-rotation energies varies from $(4/3)(\Delta E)_{cg}$ to $2(\Delta E)_{cg}$ as $\mu_0R_0=(2mvR_0/\hbar)\times\sin(\frac{1}{2}\vartheta)$ goes from zero to values much larger than unity. The limiting factor 2 corresponds to the energy the electron would lose if the two nuclei were not bound together and the electron struck one nucleus, independent of the other. The limiting factor 4/3 indicates that, for small R_0, of the six degrees of freedom the three corresponding to the motion of the center of gravity and the one corresponding to vibration are excited, but not the two corresponding to rotation; for large R_0 the factor is 2, all six degrees of freedom are excited. The behavior of this ratio of total energy lost to the molecule, $\Delta E=(\Delta E)_{cg}+(\Delta E)_{rv}$ to the energy lost to motion of the center of gravity, $(\Delta E)_{cg}$, for intermediate values of (μ_0R_0), is given in Fig. 1.

When the incident electronic kinetic energy is small compared to $\hbar\omega$ only the rotational energies may be excited and the mean energy lost, in addition to $(\Delta E)_{cg}$, is

$$(\Delta E)_{rv}\simeq\frac{2}{3}\frac{m}{M}(\tfrac{1}{2}mv^2)(1-\cos\vartheta)\times\left[\frac{1-j_0(\mu_0R_0)-j_2(\mu_0R_0)}{1+j_0(\mu_0R_0)}\right]. \qquad (25)$$

For intermediate values of electronic energy the sum of $\hbar\omega n\sigma_n$ in the expression for ΔE must use Eq. (17) and be computed term by term.

These results indicate that the amount of energy lost to rotation-vibration of a gas molecule by a free electron is of the same order of magnitude as that lost to moving its center of mass, the ratio going from unity, for very slow electrons to two for faster ones and that appre-

ciably larger amounts of energy are not lost until the electronic energy is large enough to excite the molecular electrons. This conclusion is probably a correct one, though the results worked out here do not include the effects of polarization. Inclusion of polarization is unlikely to change the vibration-rotation cross sections by a very large factor; it is more likely to affect the cross sections for electronic excitation, which appear for incident energies larger than those considered here. There is no indication of any sharp-peaked resonance effect in the energy region considered, nor, indeed, should one have been expected.

PHYSICAL REVIEW VOLUME 90, NUMBER 1 APRIL 1, 1953

Magnetic Structure Transitions*†

J. SAMUEL SMART
United States Naval Ordnance Laboratory, White Oak, Maryland
(Received December 8, 1952)

The problem of magnetic phase transitions between ferromagnetism and antiferromagnetism, or between two different kinds of antiferromagnetic arrangement, is treated by a molecular field approach. It is shown that such transitions may occur if the molecular field coefficients vary with temperature; if they do occur, they will be of first order. The theoretical results agree qualitatively with the experimental results of Guillaud and Serres on MnAs.

THE Weiss molecular field treatment of ferromagnetism and antiferromagnetism has recently modified to include both first and second nearest neighbor interactions with all four combinations of signs.[1-3] One of the results of these investigations is that there are, in general, at least three possible types of magnetic ordering for a given magnetic lattice. They are ferromagnetic ordering and two types of antiferromagnetic ordering, one favoring antiferromagnetic arrangement of nearest neighbors and the second favoring antiferromagnetic arrangement of second nearest neighbors. The type of ordering which will actually occur is that with the highest Curie temperature and is determined by the signs and relative magnitudes of the interactions. In some instances, there is a critical value for the ratio γ_2/γ_1 (the Weiss field coefficients for first and second nearest neighbor interactions) such that the orderings on either side of this critical value are of different kinds. This result suggests that, in addition to the usual Curie temperature transitions, there may sometimes occur transitions in which the magnetic ordering changes from one kind to another. Moreover, there is excellent experimental evidence, owing to Guillaud[4] and Serres,[5] that transitions from a ferromagnetic to an antiferromagnetic arrangement occur in MnAs and MnBi. The purpose of this paper is to develop a simple theoretical model for such transitions. Garrett[6] and Ziman[7] have recently discussed the problem of phase transitions from an antiferromagnetic to a "ferromagnetic" state produced by a strong magnetic field. We shall discuss here, using a model similar to Garrett's, the possibility of changes in the type of magnetic ordering in zero applied field.

PROPERTIES OF A NORMAL FERROMAGNET OR ANTIFERROMAGNET

For simplicity, we consider a system of N atoms whose magnetic moments are due to a single unpaired spin on each atom. Let the atoms be arranged on a lattice which may be divided into n sublattices in such a way that a given atom has neither first nor second nearest neighbors on its own sublattice and only one kind of neighbors on any other sublattice. Let γ_1 and γ_2 be the Weiss field coefficients for first and second nearest neighbor interactions. If we assume, as is usual, that the molecular field is an approximation to the effects of exchange coupling, then the γ_i are given by

$$\gamma_i = 2Z_i|J_i|/g\beta, \quad i=1, 2, \tag{1}$$

where Z_i is the number of ith nearest neighbors and J_i is the exchange interaction between electrons on ith neighbors; β is the Bohr magneton and g the gyromagnetic ratio of the electron. Then the molecular field $\mathbf{H}_{jk}$ acting on an atom on the jth sublattice due to its neighbors on the kth sublattice is

$$\mathbf{H}_{jk} = \epsilon_{jk}\gamma_{jk}\mathbf{S}_k, \tag{2}$$

where ϵ_{jk} is $+1$ or -1 depending on whether the $j-k$ interaction is ferromagnetic or antiferromagnetic, γ_{jk} is

* Supported in part by the U. S. Office of Naval Research.
† A preliminary account of this work was given at the Washington Conference on Magnetism, September, 1952, and is being published in the Reviews of Modern Physics.
[1] L. Néel, Ann. phys. **3**, 137 (1948).
[2] P. W. Anderson, Phys. Rev. **79**, 705 (1950).
[3] J. S. Smart, Phys. Rev. **86**, 968 (1952).
[4] C. Guillaud, J. phys. et radium **12**, 223 (1951), and other references given there.
[5] A. Serres, J. phys. et radium **5**, 146 (1947).
[6] C. G. B. Garrett, J. Chem. Phys. **19**, 1154 (1951).
[7] J. M. Ziman, Proc. Phys. Soc. (London) **A64**, 1108 (1951).

either γ_1 or γ_2 (or some simple fraction thereof) and $\mathbf{S}_k$ is the average spin per atom on the kth sublattice.

We shall define a normal ferromagnet (or antiferromagnet) as one in which γ_1 and γ_2 are independent of temperature. The theoretical magnetic and thermodynamic properties of such a material are well known; the remainder of this section is devoted to listing some of these properties for comparison with results to be obtained later in this paper. First of all, the Weiss-Langevin equation of state for the material takes the form

$$\sigma_j=\sigma=\tanh(\sigma/\tau) \tag{3a}$$

and

$$\sigma_j=\eta_{jk}\sigma_k, \quad j,k=1,2,\cdots,n, \tag{3b}$$

where σ_j is the reduced magnetization of the jth sublattice and $\tau=T/T_c$. The η_{jk} are either $+1$ or -1; different sets of the η_{jk} obviously describe different kinds of magnetic ordering. The explicit expression for the Curie temperature corresponding to a given set of η_{jk} is

$$T_c=(g\beta/4k)\sum_{k\neq j}^{n}\eta_{jk}\epsilon_{jk}\gamma_{jk}. \tag{4}$$

Values of T_c for body-centered cubic and face-centered cubic lattices for various types of ordering are given in reference 3.

For a reduced magnetization σ_j, there are $(N/n)\times(1+\sigma_j)$ spins aligned in one direction and $(N/n)(1-\sigma_j)$ spins aligned in the other direction on the jth sublattice. Then the entropy of the entire sample is

$$S=k\ln\prod_{j=1}^{n}\frac{(N/n)!}{[(N/n)(1+\sigma_j)]![(N/n)(1-\sigma_j)]!}. \tag{5}$$

We note that this expression is an even function of σ_j; in other words, the entropy is unchanged if the directions of all the spins on a given sublattice are reversed. This result enables us to classify the types of transitions which may occur. If some of the sublattices merely reverse their directions of magnetization without changing σ, then the transition occurs without change in entropy and is a second order phase transition. On the other hand, if the reduced magnetizations of the sublattices are changed as well as their directions, the transition will in general be of the first order.

By use of Stirling's approximation and Eq. (3b), the expression for the entropy may be reduced to a form more convenient for calculation.

$$S=Nk[\ln 2-\tfrac{1}{2}\ln(1-\sigma^2)-\sigma\tanh^{-1}\sigma]. \tag{6}$$

The Gibbs free energy in zero applied magnetic field may be obtained from the differential relation

$$dG=-SdT, \tag{7}$$

and we find, by integrating (7),

$$G(T)=Nk\left[-T\ln 2+\tfrac{1}{2}T_c\left(\sigma^2+\frac{\sigma\ln(1-\sigma^2)}{\tanh^{-1}\sigma}\right)\right], \tag{8}$$

if we set $G(T_c)=-NkTc\ln 2$. (This is equivalent to setting the internal energy, U, equal to zero when $\sigma=0$.) The function of σ in Eq. (8) is zero for $\sigma=0$ and decreases monotonically for increasing σ (or decreasing T). Thus that type of ordering which has the highest Curie temperature will have the lowest Gibbs free energy for all temperatures below its Curie point. Consequently, there will be no transitions from one type of ordering to another for a normal material, or as long as the equations of state have the form of Eqs. (3).

EFFECTS OF TEMPERATURE VARIATION OF THE WEISS FIELD COEFFICIENTS

We have seen that magnetic structure transitions do not occur in a normal ferromagnet or antiferromagnet. A possible explanation of the fact that such transitions apparently do occur in nature is that the Weiss field coefficients, γ_1 and γ_2, actually vary with temperature. Thus, if a material has a value of γ_2/γ_1 near the critical ratio for some given temperature, a change in temperature may shift the ratio across the critical value and thus produce a transition. There are a number of reasons why γ_1 and γ_2 may be expected to be temperature-dependent but perhaps the simplest is that the exchange integrals, J_i, are expected to depend sensitively on the interatomic separation which of course varies with temperature. This point has been especially emphasized by Néel.[8] We shall assume a simple linear variation of the form

$$\gamma_i=\gamma_{i0}(1+\alpha_i T), \quad i=1,2. \tag{9}$$

Thus the molecular fields, as defined by Eq. (2), now have a temperature variation over and above that resulting from the spontaneous magnetization. This leads to a new form for the equation of state:

$$\sigma_j=\sigma=\tanh\left(\frac{1+\lambda\tau}{\tau}\sigma\right). \tag{10}$$

with $\sigma_j=\eta_{jk}\sigma_k$ as before. In this equation $\tau=T/T_c^0$, where T_c^0 is the Curie temperature for $\alpha_1=\alpha_2=0$. The temperature coefficient λ is a function of the γ_{i0} and α_i whose exact form depends on both the type of lattice and the type of ordering occurring. We have

$$\lambda=(g\beta/4k)\sum_{k\neq j}^{n}\eta_{jk}\epsilon_{jk}\gamma_{jk}(\alpha_{jk}. \tag{11}$$

One effect of the temperature dependence of the γ_i is to distort the normal $\sigma-\tau$ curve obtained for $\alpha_1=\alpha_2=0$. An example of this distortion is shown in Fig. 1 for the special case $\lambda=-0.23$. The new Curie temperature is given by

$$T_c=T_c^0/(1-\lambda). \tag{12}$$

The entropy is of course the same function of σ as it was for the normal case. The calculation of the Gibbs

[8] L. Néel, Ann. phys. 8, 237 (1937).

free energy from the differential relation is somewhat more difficult than for the normal case because of the more complicated relationship between σ and τ. We were unable to integrate the expression exactly; however, it can be written as

$$G(T)=Nk\left[-T\ln 2+\tfrac{1}{2}T_c^0\left\{\frac{\sigma^2\tanh^{-1}\sigma+\sigma\ln(1-\sigma^2)}{\tanh^{-1}\sigma-\lambda\sigma}+\lambda\int_{\tau_c}^{\tau}\sigma^2 d\tau\right\}\right], \quad (13)$$

with $\tau_c=T_c/T_c^0$.

Now let us consider two possible types of magnetic ordering, which we designate by A and B, for a particular system. First of all, it is important to note that though γ_{10}, γ_{20}, α_1, and α_2 are the same for the A and B states, the temperature coefficients λ_A and λ_B are unequal since they are different functions of the first four quantities. It is this difference which makes the ordering transitions possible.

We assume that the A state has the highest actual Curie temperature. Then for temperatures just below T_{CA}, $G_A<G_B$, and the A ordering will obtain. Evidently the condition that a magnetic structure transition occurs is

$$G_B(0)<G_A(0), \quad (14a)$$

or, with the use of Eq. (11),

$$\lambda_A T_{CA}^0\int_0^{\tau_{CA}}\sigma_A^2 d\tau_A-\lambda_B T_{CB}^0\int_0^{\tau_{CB}}\sigma_B^2 d\tau_B<T_{CB}^0-T_{CA}^0, \quad (14b)$$

where $\tau_A=T/T_{CA}^0$ and $\tau_B=T/T_{CB}^0$.

It is not immediately obvious whether such transitions would be first or second order. However, we note that the temperature at which $\sigma_A=\sigma_B$ is given by

$$(1+\lambda_A\tau_A)\tau_A^{-1}=(1+\lambda_B\tau_B)\tau_B^{-1},$$

or

$$T_s=(T_{CA}^0-T_{CB}^0)/(\lambda_B-\lambda_A). \quad (15)$$

Inspection of Eq. (13) shows that in general $G_A(T_s)\neq G_B(T_s)$. Consequently if Eq. (14) is satisfied and a transition does occur it will be a first-order transition.

So far all of the discussion has been for zero applied field. The effect of an external magnetic field is twofold; first, it adds a term of the order of magnitude of $-MH$ to the Gibbs free energy where M is the total magnetization of the sample; second, it alters the σ_j so that $\sigma_j=\eta_{jk}\sigma_k$ no longer holds and thus changes the form of Eq. (13). For materials with Curie temperatures of 100°K or above, these effects are relatively small, except for ferromagnetic states where the $-MH$ term may make an appreciable contribution to the Gibbs free energy. In particular, without attempting any detailed calculations, it can be said that an external magnetic field may produce an appreciable shift in transition temperatures in cases where one of the states is ferromagnetic.

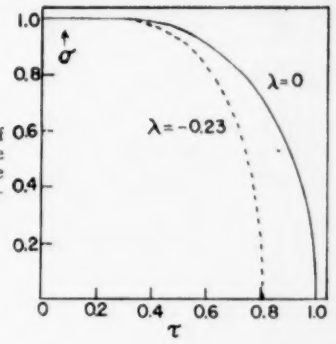

FIG. 1. Distortion of the normal $\sigma-\tau$ curve owing to temperature variation of the molecular field coefficients.

The other changes in the Gibbs free energy produced by application of an external field will be important in cases where the Curie temperatures are extremely low. We shall not, however, discuss these effects any further here.

COMPARISON WITH EXPERIMENTAL DATA

In this section we first review briefly the experimental data on the compounds MnAs and MnBi, most of which is due to Guillaud[4] and Serres.[5] MnAs and MnBi both crystallize in the NiAs structure; the magnetic lattice is a hexagonal layer arrangement. Both compounds are ferromagnetic at low temperatures with saturation magnetizations corresponding to about 3.5β per Mn atom. When MnAs is heated to about 318°K, its magnetization drops suddenly from $0.64\,M_0$ to zero; when the material is cooled, the magnetization reappears at 305°K. Above 350°K the paramagnetic susceptibility increases gradually with temperature to 395°K; above this latter temperature, the susceptibility begins to fall off, following the relation $\chi=C/(T-\theta)$ with $\theta=+285$°K and C corresponding to a moment of 3.7β per Mn atom. The interpretation of these results, which are shown in Fig. 2, is that MnAs undergoes a transition from a ferromagnetic to an antiferromagnetic state at 318°K and that the antiferromagnetic Curie temperature is at 395°K. No susceptibility data has been obtained on MnBi but it has a similar discontinuity in the magnetization at 630°K; Guillaud has reported a specific heat anomaly at 720°K which might indicate an antiferromagnetic Curie temperature.

In both compounds, the low temperature transition seems to be of first order as there is a latent heat observed in each case along with a volume change of 3 percent for MnAs and 4.5 percent for MnBi. MnAs contracts along the a axis and MnBi along the c axis upon being heated through the transition temperature. If the suggestions of Smart and Greenwald[9] concerning crystal structure changes in other antiferromagnetic

[9] J. S. Smart and S. Greenwald, Phys. Rev. 82, 113 (1951).

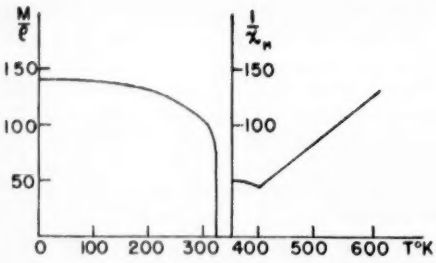

FIG. 2. Magnetization and reciprocal susceptibility of MnAs as a function of temperature (from Guillaud and Serres).

materials are used as a guide, these results indicate that the antiferromagnetic ordering in MnBi consists in having the spin directions alternate from layer to layer in the hexagonal layer arrangement. On the other hand, the change in a axes for MnAs suggests that its magnetic structure may be an arrangement whereby the spin direction alternate in planes parallel to the c axis. In this case, the symmetry should be deformed to something lower than that of the hexagonal layer structure, but this effect might not be detectable unless an apparatus of high resolution was used. Figure 3 shows the two types of magnetic ordering suggested above.

The theoretical model used here is much too simple to try to obtain any quantitative agreement between calculated and observed magnetic and thermal changes in MnAs. For example, the theory would never allow any changes in volume, since we have assumed only a pure magnetic material. Also, the crystal structure indicates that third nearest neighbor interactions may be as important as first and second; if this were so, it would complicate the analysis considerably.

However, there seems to be good qualitative agreement between the theory and the experimental results. First of all, the transitions are first-order transitions, as has been mentioned previously. Second, numerical calculations show that the values of α_1 and α_2 required to give the observed transitions is of the order of magnitude of 10^{-4}/°K. This value is in good agreement with estimates (made by Néel[5]) based on other considerations. Also, Guillaud's data[4] shows a variation of transition temperature with applied field which seems to be of the right order of magnitude.

Finally, there is some supporting evidence from the magnetic susceptibility data. The θ/T_c ratio for MnAs is $+0.7$, all other known antiferromagnets have a negative θ/T_c. This unique behavior can be understood however if it is assumed that the transition from ferromagnetism to antiferromagnetism is caused by temperature variation of the molecular field coefficients. First of all, in the ferromagnetic state, the material will have $\theta/T_c=+1$. If the Curie temperature of the antiferromagnetic state now becomes slightly higher because of changes in γ_1 and γ_2 and a transition occurs, the corresponding θ/T_c should be slightly less than $+1$ as is observed.

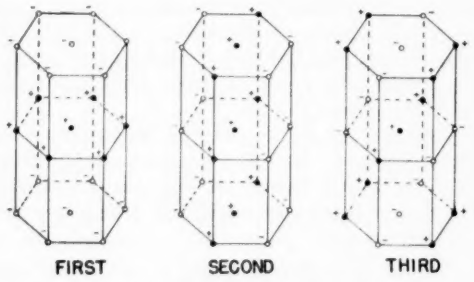

FIG. 3. Possible types of magnetic ordering for the hexagonal layer lattice.

We may also expect that transitions between two different kinds of antiferromagnetic ordering will occur in some cases. There is no definite experimental evidence for such transitions, although the susceptibility and crystal structure anomalies observed[10] in FeS suggest something of the sort. Neutron diffraction experiments would probably be required to determine whether the low temperature transition in FeS is really a magnetic structure transition or whether it is some other effect such as a change in direction of the antiferromagnetic axes.

The author is greatly indebted to various members of the Solid State Division for discussions of this problem.

[10] H. Haraldsen, Z. anorg. u. allgem. Chem. **246**, 169, 175 (1941).

The Effect of Temperature on the Duration of the $^3P_2$ Metastable Level of Neon*

F. A. GRANT AND A. D. KRUMBEIN
Department of Physics, University of Maryland, College Park, Maryland

(Received July 17, 1952)

Using the light absorption method, the duration of the $^3P_2$ metastable level of neon has been measured as a function of pressure at the temperatures of boiling water, ice, dry ice-alcohol, and liquid nitrogen. At pressures below 1 mm of mercury departure from Zemansky's formula is found only at the temperature of liquid nitrogen, while at pressures above 2 mm departures are found at all temperatures.

INTRODUCTION

USING previously described techniques,[1] the duration of the $^3P_2$ metastable neon level has been measured as a function of pressure and temperature. Light from a pulsed neon glow discharge tube *E* (Fig. 1) traverses a second neon filled discharge tube *A*, of which the afterglow is to be investigated. The monochromator rejects all radiation except the 5945A line, which is incident on the 931-A photomultiplier tube and the voltage output is displayed on a cathode-ray tube screen. The absorption of this radiation is a measure of the population of the $^3P_2$ metastable neon level.

In the present investigation, the repetition frequency of the *E* tube discharge was varied from 800 cycles per second for the long lifetimes to 3000 cycles per second for the shorter lifetimes. The pulse duration was 20 microseconds. The repetition frequency of the *A* tube discharge was varied from 20 cycles per second to about 100 cycles per second, and the pulse duration was one millisecond. The absorption of the *E* tube light pulses was measured during the afterglow of the *A* tube discharge.

PRESSURE MEASUREMENT

The pressure of the neon in the *A* tube was measured with a manometer (Fig. 2) containing Octoil-S oil, which had been freed of dissolved gases by boiling under vacuum. By direct comparison with a mercury manometer, and by measurement of densities, it was determined that 1 mm of mercury is equivalent to 15 mm of Octoil-S.

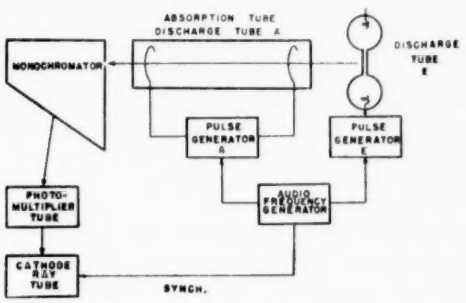

FIG. 1. Block diagram of electrical and optical systems.

TEMPERATURE CONTROL

The Pyrex discharge tube *A* (Fig. 3) consisted of a central discharge tube 48 mm i.d. and 108 cm long, surrounded by a Pyrex jacket in which the temperature-control medium was placed. Boiling water, ice, and a dry ice-alcohol bath were successively placed in the jacket. However, to reduce the rate of evaporation and to prevent the frosting of the end windows, the whole tube was placed in an evacuated brass chamber with plane windows (Fig. 4) when liquid nitrogen was used.

GAS PURITY

The gas used was "mass spectroscopically pure" neon supplied by the Linde Air Products Company. After the introduction of neon gas into the discharge tube, the tungsten electrodes were heated to incandescence and the tube was evacuated and filled repeatedly until all trace of the H_α line had been removed from the spectrum. It was found that the action of the discharge was very effective in removing impurities, with the exception of the noble gases such as argon. The consistency of the results obtained with different samples of the gas indicated that removable impurities had been reduced to a negligible concentration. Using a spectroscopic method, the neon used was analyzed in this laboratory and found to contain 0.008 percent argon.

ABSORPTION MEASUREMENTS

The signal-to-noise ratio was approximately 30, so that it was feasible to measure the absorption (repre-

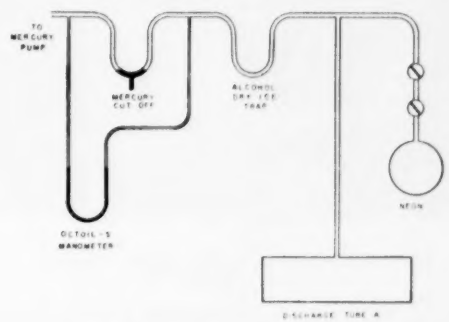

FIG. 2. Pumping and gas filling system.

* Supported by the Bureau of Ships.
[1] F. A. Grant, Can. J. Research **A28**, 339 (1950).

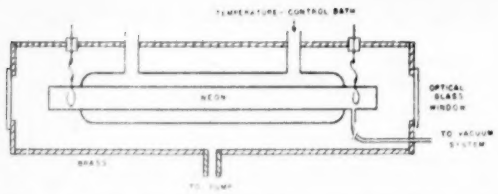

FIG. 3. Absorption discharge tube and vacuum chamber required to reduce evaporation of liquid nitrogen.

sented by the letter A in the following paragraph) visually from the screen of the cathode-ray tube.

DETERMINATION OF THE MEAN LIFE

The quantity $\log\log[1/(1-A)]$ was plotted as a function of time. After a short interval, the behavior of this function is linear and the mean life of the $^3P_2$ level is inversely proportional to the slope of the curve. As explained previously,[1] the resulting mean life was then reduced by six percent to correct for the fact that α, defined as (breadth of emission line)/(breadth of absorption line), is not zero. The value of α at room temperature was assumed to be 1.5, but further investigation will be made to determine its value when the emission tube is at room temperature and the absorption tube is at the temperature of liquid nitrogen.

EXPERIMENTAL RESULTS

Every point in Fig. 5 is the mean of at least three determinations of the mean life. Readings were taken at pressures chosen at random, and each curve represents the results of runs made on several different days with different samples of gas.

TREATMENT OF EXPERIMENTAL DATA

If the relation between T and p were of the form[2]

$$1/T=(B/p)+Cp, \qquad (1)$$

where T = the mean life in seconds, p = the pressure in millimeters of mercury, B = a constant determined by the temperature and the geometry of the discharge tube, and C = a constant independent of the geometry of the apparatus, a plot of $\log T$ *vs* $\log p$ would be a symmetrical curve concave downward, asymptotic to straight lines of slope $+1$ and -1. The first term on the right-hand side of Eq. (1) represents the diffusion of metastable atoms to the walls of the discharge tube, the second term the destruction of metastable atoms in the volume of the gas. An inspection of Fig. 5 shows that at the higher temperatures the curves are indeed asymptotic to straight lines of slope $+1$ and that the B/P term appears to be justified. However, none of the curves appears to be asymptotic to straight lines of slope -1 at higher pressures. That is, the volume destruction of metastable atoms cannot be represented by a single term of the type Cp. Measurements made in this laboratory on the effect of traces of argon in neon

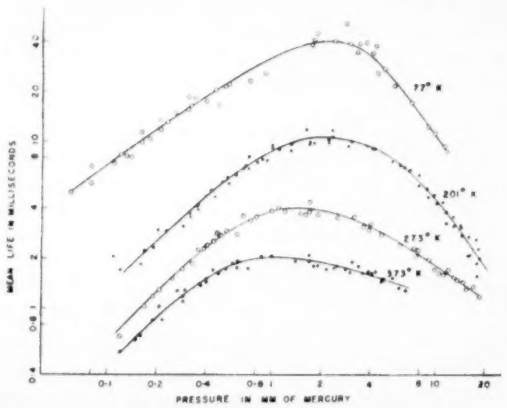

FIG. 5. Mean life of the $^3P_2$ metastable neon level as a function of pressure at various temperatures.

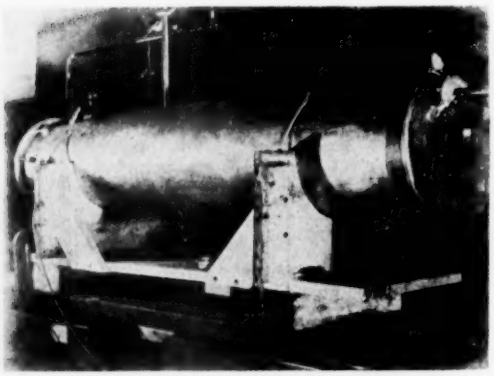

FIG. 4. Photograph of vacuum chamber enclosing absorption discharge tube.

indicate that the effect of this impurity is to introduce an additional term of the type $C'p$ into Eq. (1), so that the behavior described is not attributable to traces of argon (0.008 percent) present in the neon.

It is possible that the departure of the 77°K curve from slope $+1$ at low pressures is due to pressure broadening or to a loss of metastable atoms resulting from "forbidden" radiation. A natural mean life of 0.06 second could account for the observed effect. Holstein[3] has estimated that the mean lives of the $^3P_2$ metastable levels of the noble gases lie in the range 0.01 to 1 second.

It is shown elsewhere[1] that a decrease in the breadth of the absorption line results in an apparent increase in the mean life. Hence at low temperatures and pressures, where the absorption line width is narrowest (and α is greatest), it is possible that the plotted values of the

[2] A. C. G. Mitchell and M. W. Zemansky, *Resonance Radiation and Excited Atoms* (Cambridge University Press, Cambridge, 1934).

[3] T. Holstein, Westinghouse Research Laboratories Report R-94411-9-A (unpublished).

mean lives are too great (Fig. 5), thereby reducing the slope of the curve below $+1$.

The effect of pressure broadening would be to reduce the value of α at higher pressures, and the corresponding error becomes progressively smaller. It is considered unlikely that the slope -2 of the 77°K curve at higher pressures is attributable to this effect. Moreover, the departure of the 373° and 273° curves from slope -1 is in the wrong direction to be explained by this effect.

DIFFUSION COEFFICIENTS OF METASTABLE NEON ATOMS

The diffusion coefficient D_m for metastable atoms in the parent gas can be calculated[2] using the formula

$$\frac{B}{p}=\left(\frac{5.81}{a^2}+\frac{\pi^2}{L^2}\right)D_m,$$

TABLE I. Diffusion coefficients calculated from data of Fig. 5.

Reference	Temperature °K	B	$D_m p$	$D_m p(300/T)^{\frac{1}{2}}$
	373	190	173±35	125±25
	273	160	145±30	167±30
	201	88	80±15	145±30
	77	15.5	14.1±3	108±20
Grant[a]	303[d]		127±20	125±20
Molnar[b]	298		120±10	120±10
Biondi[c]	300		200±20	200±20
Phelps and Molnar[c]	300		150±30	150±30

[a] See reference 4.
[b] See reference 5.
[c] See reference 6.
[d] $B=66\pm10$ with discharge tube 6.7 cm diameter.

in which a is the discharge tube radius and L the discharge tube length in centimeters. The length of the discharge tube is much greater than the radius, so that

$$D_m p=a^2B/5.81.$$

In Table I, the values of B obtained from the data of Fig. 5 have been listed.[4–6] In the values of the third column appear the values of $D_m p$ calculated therefrom, together with the values obtained by Molnar, Biondi, and by Phelps and Molnar. Following Mitchell and Zemansky,[2] D_m is assumed to vary as the three-halves power of the absolute temperature. In the fourth column of the table, the values of $D_m p(300/T)^{\frac{1}{2}}$ have been tabulated. The variation of this quantity with temperature does not appear to be significant.

THE VOLUME LOSS OF METASTABLE ATOMS

The quantity $G=(1/T-B/p)$ has been plotted as a function of pressure in Fig. 6. Since the term B/p represents the diffusion loss, G represents the volume loss of metastable atoms. This quantity appears to vary as a fractional power of the pressure except at

[4] F. A. Grant, Phys. Rev. **84**, 844 (1951).
[5] J. P. Molnar, Phys. Rev. **83**, 945 (1951).
[6] M. A. Biondi, Phys. Rev. **82**, 454 (1951).

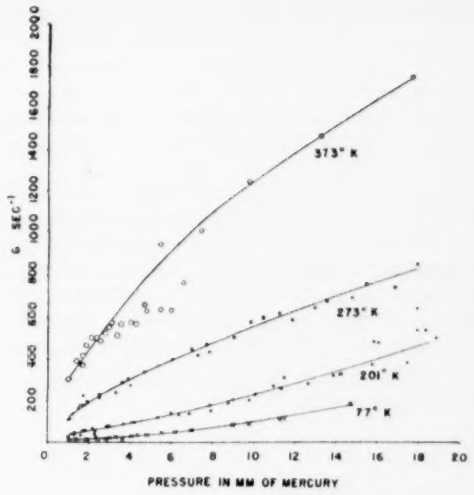

FIG. 6. The volume destruction term G plotted as a function of pressure.

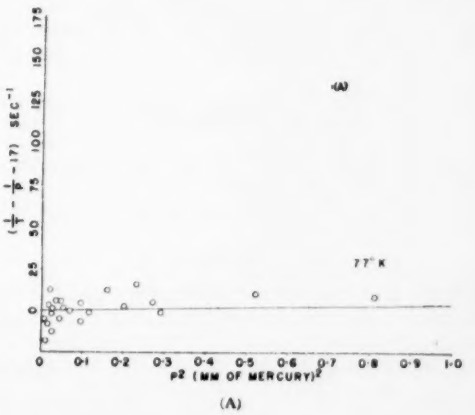

(A)

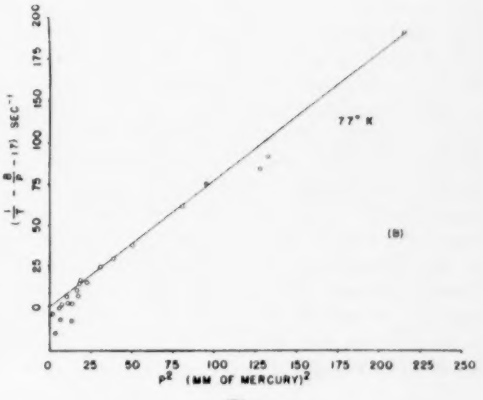

(B)

FIG. 7. $(G-17)$ plotted as a function of p^2, for 77°K. (A) $p<1$ mm Hg; (B) $p>1$ mm Hg.

77°K. In Fig. 7, G at 77°K has been plotted against p^2 and appears to be a linear function of p^2. In order to make the curve meet the origin, the constant 17 sec^{-1} has been subtracted from G. The possibility that this constant term represents the loss of metastable atoms resulting from "forbidden" radiation has been discussed above.

Molnar[7] has pointed out that "since rates of electron diffusion or recombination depend on gas temperature in a not very sensitive way, it may be possible to separate the destructive effects of these particles from those of the neutral atoms by careful measurements of G as a function of temperature and pressure." Since the $^3P_2$ metastable level is 0.05 ev lower than the radiating $^3P_1$ level, the probability of this transition, on the other hand, should be highly dependent on the kinetic energy of the colliding particles, i.e., on the gas temperature.

According to this interpretation, we should expect that the dominant process at 77°K is not destruction of metastables by collisions with normal atoms. Inspection of the experimental results (Fig. 5) leads us to believe that the less temperature-sensitive process introduces into G a term proportional to p^2. The shape of the curves suggests that if measurements were made at pressures above 20 mm of mercury, this process would probably be the dominant one at all the temperatures considered.

The authors wish to thank Professor R. D. Myers for much stimulating discussion of the results obtained in this research.

[7] J. P. Molnar, Bell Telephone Laboratories Report 38140 (July 18, 1950) (unpublished).

PHYSICAL REVIEW VOLUME 90, NUMBER 1 APRIL 1, 1953

The Photodisintegration of the Deuteron

LAMEK HULTHÉN AND BENGT C. H. NAGEL
Royal Institute of Technology, Stockholm, Sweden

(Received December 3, 1952)

The photomagnetic and photoelectric cross sections have been calculated for γ-energies from threshold (2.23 Mev) up to 20 Mev, using a central Yukawa potential with the same range (i.e., meson mass) in the ^1S and ^3S states and no interaction in the ^3P state. Exchange and quadrupole effects have been neglected. Results are given for three ranges, equivalent to meson masses 199, 256, and 298.5, and are compared with recent measurements.

In the last section a comparison is made with the results obtained by the effective range method.

I. INTRODUCTION

IN two previous papers[1,2] by Hansson and one of the present authors, theoretical values of the photo cross sections were given for a few γ-energies (2.52, 2.62, 2.76, and 6.20 Mev). We have found it desirable to extend these calculations to the whole region of small and moderate energies, at the same time trying to improve the accuracy. On the other hand, the underlying theoretical assumptions have been simplified in some respects. Thus we have neglected the influence of the charge exchange on the photomagnetic cross section σ_m, mainly because it is difficult to find an unambiguous basis for treating this effect. It should also be pointed out that the effect has been calculated in the case of the Møller-Rosenfeld theory where it turned out to be insignificant.[1,3] Moreover, we have carried out the present calculations of the photoelectric cross section σ_e on the assumption that no interaction exists in the ^3P state. The earlier results[1,2] indicate that σ_e is not very sensitive to variations of the ^3P interaction within plausible limits. A closer study of this point is deferred to a forthcoming paper by Hansson.

[1] I. F. E. Hansson and L. Hulthén, Phys. Rev. **76**, 1163 (1949).
[2] I. F. E. Hansson, Phys. Rev. **79**, 909 (1950).
[3] See also B. C. H. Nagel and S. G. Nilsson, Transactions of the Royal Institute of Technology (to be published).

Thus we have assumed the following interactions:

$$\begin{aligned} &^1S: \quad V(r) = -{}^1B \cdot e^{-\kappa r}/r, \\ &^3S: \quad V(r) = -{}^3B \cdot e^{-\kappa r}/r, \\ &^3P: \quad V(r) = 0, \\ &\kappa = M_m c/\hbar, \quad M_m \text{ meson mass.} \end{aligned} \tag{1}$$

The calculations have been carried out for three different ranges $1/\kappa$, corresponding to meson masses 199.0, 255.8, and 298.5 M_e (electron mass). In each case ^3B has been determined from the deuteron binding energy $|E_0|$, for which we have accepted the value 2.23 Mev. ^1B is then fixed by the epithermal neutron-proton scattering cross section $\sigma_0 = 20.36$ barns, taking into account that the ^1S state is virtual.

II. CALCULATION OF THE EIGENFUNCTIONS

Introducing dimensionless quantities, the Schrödinger equation of an S state can be reduced to the following form, $\phi(x)$ being proportional to r times the radial part $\psi(r)$ of the wave function:

$$d^2\phi/dx^2 + \left(a + b\frac{e^{-x}}{x}\right)\phi = 0, \tag{2}$$

where $x = \kappa r$, $a = M(E/\hbar^2\kappa^2)$, $M = \frac{1}{2}(M_n + M_p)$, ($E$ = en-

TABLE I. Approximate ground-state functions for three different meson masses M_m/M_e. The symbols used are explained in the text.

$(-a_0)^{\frac{1}{2}}$	^3b	h_1	h_2	h_3	C	$(1/\kappa)\times10^{+13}$ (cm)	M_m/M_e	^1b
0.45	2.6629	0.63898	−0.10108	0.06347	1.37296	1.9408	199.0	1.5071
0.35	2.4490	0.63657	−0.11379	0.06877	1.13166	1.5095	255.8	1.5436
0.30	2.3413	0.63514	−0.12084	0.07181	1.01048	1.2939	298.5	1.5624

ergy in the center-of-mass system, M_n = neutron mass, M_p = proton mass), and $b=MB/\hbar^2\kappa$.

For the eigenfunction of the ground state we have used the results of Hulthén and Laurikainen.[4] Taking

$$\phi_0(x)=C\exp[-(-a_0)^{\frac{1}{2}}x](1-e^{-x})\times(1+h_1e^{-x}+h_2e^{-2x}+h_3e^{-3x}),\qquad \int_0^\infty\phi_0^2dx=1, \tag{3}$$

we get the values of the parameters given in Table I.

The eigenfunctions of the continuous ^1S spectrum have been obtained by the method described by Hulthén.[5] The form of the trial function is

$$\phi_1(x)=\sin(a^{\frac{1}{2}}x+\eta)-\sin\eta[e^{-x}+(1-e^{-x})\times(c_1e^{-x}+c_2e^{-2x}+c_3e^{-3x})], \tag{4}$$

η being the asymptotic phase. Thus ϕ_1 is normalized to amplitude 1 for $x\to\infty$. The ^1b values are found in Table I.

The approximate solutions (4) are given in Table II for some values of $a^{\frac{1}{2}}$. A more detailed account of these calculations is given by Hulthén and Skavlem.[6]

We also write down the eigenfunction of the ^3P state, corresponding to interaction zero,

$$\phi_2(x)=\frac{\sin(a^{\frac{1}{2}}x)}{a^{\frac{1}{2}}x}-\cos(a^{\frac{1}{2}}x). \tag{5}$$

III. FORMULAS FOR THE CROSS SECTIONS

Using the preceding notations, the cross section for the photoelectric dipole transition from the ground state to a ^3P state can be expressed as follows:

$$\sigma_e=\frac{\pi}{3}\frac{e^2}{\hbar c}\left(\frac{M_n}{M_m}\right)^2\frac{1}{\kappa^2}\frac{h\nu}{Mc^2}\frac{1}{a^{\frac{1}{2}}}J_e^2,\qquad J_e=\int_0^\infty\phi_0(x)\phi_2(x)x\,dx, \tag{6}$$

a being connected with the γ-energy $h\nu$ and the binding energy $|E_0|$ in the following way:

$$a=\frac{M}{\hbar^2\kappa^2}\left(h\nu-|E_0|-\frac{(h\nu)^2}{4Mc^2}\right); \tag{7}$$

the last term (the Doppler effect) is negligible in the energy region considered here.

The corresponding expression for the photomagnetic cross section ($^3S\to{}^1S$) is

$$\sigma_m=\frac{\pi}{3}\frac{e^2}{\hbar c}(\mu_p-\mu_n)^2\left(\frac{M}{M_p}\right)^2\frac{1}{\kappa^2}\frac{h\nu}{Mc^2}\frac{1}{a^{\frac{1}{2}}}J_m^2,\qquad J_m=\int_0^\infty\phi_0(x)\phi_1(x)dx, \tag{8}$$

where μ_p and μ_n are the magnetic moments of proton and neutron, respectively, expressed in nuclear magnetons ($e\hbar/2M_pc$): $\mu_p=2.7928$, $\mu_n=-1.9131$.

In each case J_m has been obtained for the proper ^1b value (Table I) by quadratic interpolation between the J_m values corresponding to the b's of Table II.

IV. A METHOD FOR IMPROVING THE VALUES OF THE MATRIX ELEMENTS

In order to get an idea of the accuracy of the matrix elements, we carried out the calculation in a few cases, using approximate eigenfunctions with one, two, and three parameters, respectively.

By way of illustration, take the case of the photoelectric matrix element J_e for $h\nu=4.46$ Mev and $M_m=298.5M_e$ [$(-a_0)^{\frac{1}{2}}=0.3$, $a^{\frac{1}{2}}=0.3$]. Table III gives

TABLE II. Approximate ^1S state eigenfunctions. The symbols used are explained in the text.

b	$a^{\frac{1}{2}}$	c_1	c_2	c_3	$\cot\eta$
1.50	→0	−0.5430	0.1864	−0.0995	$0.086117/(a)^{\frac{1}{2}}$
1.55	→0	−0.5673	0.1899	−0.1026	$0.060676/(a)^{\frac{1}{2}}$
1.60	→0	−0.5922	0.1930	−0.1056	$0.036455/(a)^{\frac{1}{2}}$
1.50	0.1	−0.5645	0.2081	−0.1108	0.98346
1.55	0.1	−0.5887	0.2113	−0.1138	0.72404
1.60	0.1	−0.6134	0.2135	−0.1162	0.47707
1.50	0.2	−0.6245	0.2668	−0.1408	0.67102
1.55	0.2	−0.6481	0.2679	−0.1426	0.53399
1.60	0.2	−0.6723	0.2686	−0.1442	0.40356
1.50	0.3	−0.7119	0.3458	−0.1795	0.68863
1.55	0.3	−0.7349	0.3445	−0.1799	0.53953
1.60	0.3	−0.7584	0.3426	−0.1802	0.44524
1.50	0.4	−0.8147	0.4283	−0.2168	0.66982
1.55	0.4	−0.8363	0.4223	−0.2145	0.58786
1.60	0.4	−0.8588	0.4172	−0.2130	0.50990
1.50	0.5	−0.9201	0.4924	−0.2389	0.72164
1.55	0.5	−0.9416	0.4857	−0.2368	0.64872
1.60	0.5	−0.9632	0.4777	−0.2340	0.57941

[4] L. Hulthén and K. V. Laurikainen, Revs. Modern Phys. **23**, 1 (1951).
[5] L. Hulthén, Arkiv Mat. Astron. Fysik **A35**, No. 25 (1948).
[6] L. Hulthén and S. Skavlem, Phys. Rev. **87**, 297 (1952).

TABLE III. Ground-state functions with one, two, and three parameters [Eq. (3)] and corresponding photoelectric matrix elements $(J_e)_n$. $(-a_0)^{\frac{1}{2}}=0.3$; $(a)^{\frac{1}{2}}=0.3$; $^3b=2.3413$.

n	h_1	h_2	h_3	C_n	C_n/C_3	$(J_e)_n$	$(J_e)_n/(J_e)_3$	I_∞
1	0.57430	...	...	1.01535	1.00482	5.61265	1.00435	0.98963
2	0.59356	−0.01953	...	1.01333	1.00282	5.60238	1.00251	0.99240
3	0.63414	−0.12084	0.07181	1.01048	1.00000	5.58833	1.00000	0.99596
		Extrapolated to $I_\infty=1$		1.00745	0.99700	5.5730	0.99725	1.00000

the values of the parameters obtained by Hulthén and Laurikainen[4] and the corresponding J_e. I_∞ is an integral, defined by[7]

$$I_\infty=\frac{^3b}{C(-a_0)^{\frac{1}{2}}}\int_0^\infty \sinh[(-a_0)^{\frac{1}{2}}x]\frac{e^{-x}}{x}\phi_0(x)dx. \quad (9)$$

This quantity would equal 1 if $\phi_0(x)$ were exact;[8] the deviation from 1 gives an idea of the accuracy of $\phi_0(x)$ preferably at large and moderate x.

Table III indicates a correlation between J_e and the normalization constant $C(=C_n)$. This is not surprising; for small and moderate energies J_e is largely determined by the asymptotic behavior of $\phi_0(x)$, that is $C\exp[-(-a_0)^{\frac{1}{2}}x]$. This, however, does not help us so much, since we do not know the correct value of C, corresponding to an infinite number of parameters. But there is also reason to expect a correlation of C with I_∞. C is determined from the parameters h_ν by the condition [see Eq. (3)]

$$I_N=\int_0^\infty\left(\frac{\phi_0(x)}{C}\right)^2dx=\frac{1}{C^2};$$

and, plotting I_N or C against I_∞, we get a fairly straight line. Extrapolating to $I_\infty=1$, we obtain a C value, which

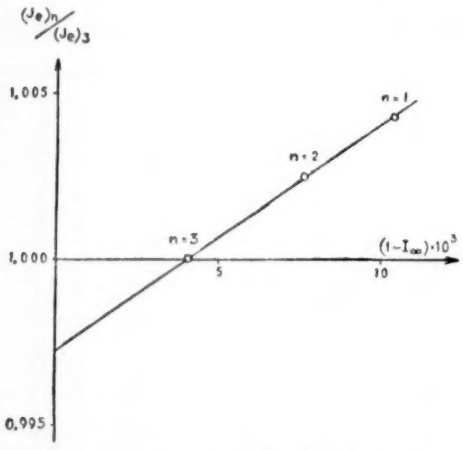

FIG. 1. Correction of the photoelectric matrix element.

should represent the asymptotic behavior of $\phi_0(x)$ more correctly, $C_{\text{extr}}=1.00745$. This would give us a possibility to improve J_e, but we prefer to do this by plotting J_e directly against I_∞ (see Fig. 1). Extrapolation to $I_\infty=1$ gives $(J_e)_{\text{extr}}=0.9972_5\cdot(J_e)_3=5.5730$. The correction factors were calculated in this way for a few instances, most of which are given in Table IV. In other cases the correction factors can be obtained by linear interpolation.

The same procedure can be applied to the integral J_m as far as the error arising from $\phi_0(x)$ is concerned. It is also possible to correct for the uncertainty from $\phi_1(x)$ in a similar way, by plotting J_m, calculated with one, two, and three parameters c_ν [Eq. (4)] and three parameters h_ν in $\phi_0(x)$ against the integral

$$\rho_1=\frac{^1b\cdot\int_0^\infty \sin(a^{\frac{1}{2}}x)\cdot\frac{e^{-x}}{x}\phi_1(x)dx}{a^{\frac{1}{2}}\sin\eta}, \quad (10)$$

which would equal 1 for an exact solution $\phi_1(x)$.[9] An example is given in Table V. [For $\phi_0(x)$ see Table I.]

Since the corrections turn out to be small, it seems safe to assume that the errors due to $\phi_0(x)$ and $\phi_1(x)$ add linearly. The total correction thus obtained is given in Table VI for a few cases.

TABLE IV. Correction factors for the photoelectric matrix element J_e. To obtain an improved J_e value, multiply $(J_e)_3$ [three parameters in $\phi_0(x)$] by the correction factor given below.

	h_ν (in Mev)				
$(-a_0)^{\frac{1}{2}}$	2.23	4.46	6.14	10.00	15.00
0.30	0.9970	0.9973	0.9975	0.9977	0.9986
0.45	0.9962	0.9968	0.9975	0.9994	1.0000

TABLE V. ^1S state eigenfunctions with one, two, and three parameters and corresponding photomagnetic matrix element $(J_m)_n$. $(-a_0)^{\frac{1}{2}}=0.45$; $^1b=1.5$; $a=0$.

n	c_1	c_2	c_3	$a^{\frac{1}{2}}\cot\eta$	ρ_1	$\frac{J_m}{(a)^{\frac{1}{2}}}$	$\frac{(J_m)_n}{(J_m)_3}$
1	−0.4633	...	...	0.086200	0.9951	29.359	0.99594
2	−0.5074	0.0644	...	0.086134	0.9980	29.444	0.99884
3	−0.5430	0.1864	−0.0995	0.086117	0.9991	29.478	1.00000
				Extrapolated to $\rho_1=1$		29.505	1.0009

[7] In the corresponding formula (22) of reference 4, h_ν should be replaced by h_ν/h_0.

[8] L. Hulthén, Kgl. Fysiograf. Sällskap. Lund, Förh. **15**, No. 22 (1945).

[9] L. Hulthén, Kgl. Fysiograf. Sällskap. Lund, Förh. **14**, No. 8 (1944).

TABLE VI. Correction factors for the photomagnetic matrix element J_m. To obtain an improved J_m value, multiply $(J_m)_3$ [three parameters in $\phi_0(x)$ as well as in $\phi_1(x)$] by the correction factor given below.

$(-a_0)^{\frac{1}{2}}$	$h\nu$ (in Mev) 2.23	2.34	2.48
0.30	0.9993	...	0.9995
0.45	0.9994	0.9996	...

V. RESULTING CROSS SECTIONS

The resulting values for σ_m, σ_e, etc., are given in Tables VII to X.[10] The remaining uncertainty resulting from errors in the eigenfunctions is believed not to exceed one or two parts in a thousand.

For the sake of completeness we also include, in Table X, the results of earlier calculations[3,11] of the neutron-proton capture cross section σ_c.

Figures 2–6 give the results in graphical form. In the graphs for σ and σ_m/σ_e, the theoretical curves are compared with some recent experimental results. These experimental values are also given in the captions of the figures together with the corresponding theoretical values, interpolated to a meson mass $286.4M_e$. This meson mass is fixed by the coherent scattering amplitude $f=-3.78\times10^{-13}$ cm[12] (see Sec. VIIIA).

TABLE VII. Resulting photo cross sections, $(-a_0)^{\frac{1}{2}}=0.30$; $M_m/M_e=298.5$. Cross sections are given in units of 10^{-28} cm². $\sigma=\sigma_m+\sigma_e$. Figures in brackets indicate uncertain interpolation.

$a^{\frac{1}{2}}$	$h\nu$ (Mev)	σ_m	σ_e	σ	σ_m/σ_e
0.01	2.232	(2.13)	0.007	2.14	300
0.02	2.240	(3.80)	0.056	3.86	68
0.03	2.252	(4.83)	0.186	5.02	26
0.04	2.270	(5.33)	0.432	5.76	12.3
0.05	2.292	5.440	0.819	6.26	6.640
0.06	2.319	5.315	1.366	6.68	3.890
0.08	2.389	4.769	2.964	7.73	1.609
0.10	2.478	4.131	5.185	9.32	0.7967
0.12	2.587	3.542	7.873	11.41	0.4498
0.14	2.716	3.034	10.804	13.84	0.2808
0.15	2.788	2.811	12.284	15.10	0.2288
0.16	2.864	2.606	13.740	16.35	0.1897
0.18	3.033	2.247	16.473	18.72	0.1364
0.20	3.221	1.946	18.853	20.80	0.1032
0.25	3.779	1.385	22.777	24.16	0.0608
0.30	4.460	1.011	23.883	24.89	0.0423
0.35	5.265	0.756	22.977	23.73	0.0329
0.40	6.195	0.578	20.976	21.55	0.0276
0.45	7.248	0.451	18.553	19.00	0.0243
0.50	8.425	0.357	16.104	16.46	0.0221
0.55	9.725	0.287	13.829	14.12	0.0208
0.60	11.150	0.234	11.810	12.04	0.0198
0.65	12.699	0.193	10.064	10.26	0.0191
0.70	14.371	0.161	8.573	8.73	0.0187
0.75	16.168	0.136	7.311	7.45	0.0186
0.80	18.088	0.116	6.246	6.36	0.0186
0.90	22.300	0.082	4.591	4.67	0.0179
1.00	27.008	0.062	3.411	3.47	0.0182

TABLE VIII. Resulting photo cross sections. $(-a_0)^{\frac{1}{2}}=0.35$; $M_m/M_e=255.8$. Cross sections are given in units of 10^{-28} cm². $\sigma=\sigma_m+\sigma_e$. Figures in brackets indicate uncertain interpolation.

$a^{\frac{1}{2}}$	$h\nu$ (Mev)	σ_m	σ_e	σ	σ_m/σ_e
0.01	2.232	(1.77)	0.005	1.78	370
0.02	2.237	(3.28)	0.038	3.32	86
0.03	2.246	(4.37)	0.127	4.50	34
0.04	2.259	(5.03)	0.296	5.33	17.0
0.05	2.276	5.332	0.566	5.90	9.428
0.06	2.296	5.371	0.952	6.32	5.643
0.07	2.319	5.258	1.466	6.72	3.588
0.08	2.347	5.052	2.112	7.16	2.392
0.10	2.412	4.530	3.797	8.33	1.193
0.12	2.492	3.991	5.947	9.94	0.6711
0.14	2.587	3.499	8.442	11.94	0.4144
0.15	2.640	3.275	9.771	13.05	0.3352
0.16	2.696	3.067	11.127	14.19	0.2757
0.18	2.820	2.695	13.840	16.53	0.1947
0.20	2.958	2.374	16.435	18.81	0.1444
0.25	3.368	1.755	21.717	23.47	0.0808
0.30	3.868	1.325	24.704	26.03	0.0536
0.35	4.460	1.018	25.517	26.53	0.0399
0.40	5.143	0.798	24.754	25.55	0.0322
0.45	5.916	0.635	23.042	23.68	0.0275
0.50	6.781	0.511	20.869	21.38	0.0245
0.55	7.737	0.417	18.569	18.99	0.0225
0.60	8.784	0.344	16.339	16.68	0.0211
0.65	9.921	0.286	14.277	14.56	0.0201
0.70	11.150	0.241	12.428	12.67	0.0194
0.75	12.470	0.206	10.797	11.00	0.0191
0.80	13.881	0.176	9.375	9.55	0.0188
0.90	16.976	0.128	7.078	7.21	0.0181
1.00	20.434	0.097	5.364	5.46	0.0182

TABLE IX. Resulting photo cross sections. $(-a_0)^{\frac{1}{2}}=0.45$; $M_m/M_e=199.0$. Cross sections are given in units of 10^{-28} cm². $\sigma=\sigma_m+\sigma_e$. Figures in brackets indicate uncertain interpolation.

$a^{\frac{1}{2}}$	$h\nu$ (Mev)	σ_m	σ_e	σ	σ_m/σ_e
0.01	2.231	(1.30)	0.003	1.31	510
0.02	2.234	(2.59)	0.021	2.62	127
0.03	2.240	(3.63)	0.069	3.70	53
0.04	2.248	(4.37)	0.161	4.53	27.1
0.05	2.258	4.860	0.310	5.17	15.66
0.06	2.270	5.126	0.528	5.65	9.715
0.08	2.300	5.200	1.201	6.40	4.331
0.10	2.340	4.945	2.227	7.17	2.220
0.12	2.389	4.564	3.619	8.18	1.261
0.14	2.446	4.156	5.350	9.51	0.7768
0.15	2.478	3.956	6.328	10.28	0.6253
0.16	2.512	3.764	7.369	11.13	0.5108
0.18	2.587	3.405	9.602	13.01	0.3546
0.20	2.671	3.081	11.964	15.04	0.2575
0.25	2.918	2.412	17.872	20.28	0.1350
0.30	3.221	1.921	22.911	24.83	0.0838
0.35	3.579	1.547	26.437	27.98	0.0585
0.40	3.992	1.261	28.329	29.59	0.0445
0.45	4.460	1.039	28.787	29.83	0.0361
0.50	4.983	0.864	28.160	29.02	0.0307
0.55	5.561	0.725	26.793	27.52	0.0271
0.60	6.195	0.613	24.983	25.60	0.0246
0.65	6.883	0.522	22.964	23.49	0.0227
0.70	7.626	0.447	20.885	21.33	0.0214
0.75	8.425	0.385	18.854	19.24	0.0204
0.80	9.278	0.333	16.928	17.26	0.0197
0.90	11.150	0.254	13.503	13.76	0.0188
1.00	13.243	0.197	10.698	10.90	0.0185

[10] For the fundamental constants entering into Eqs. (6)–(8) we have used the following figures: $\hbar c/e^2=137.04$; $Mc^2=938.8$ Mev; $M_n/M_p=1.00138$; $h=6.6237\times10^{-27}$ erg; $M_p/M_e=1836.0$. The deviations of these values from those given by J. A. Bearden and H. M. Watts, Phys. Rev. **81**, 73 (1951) are insignificant in this connection.

[11] L. Hulthén, Phys. Rev. **79**, 166 (1950).

[12] Ringo, Burgy, and Hughes, Phys. Rev. **82**, 344 (1951).

TABLE X. Neutron-proton capture cross section σ_c at a neutron velocity of 2.2×10^8 cm/sec, $|E_0|=2.23$ Mev.

M_m/M_e	σ_c (barns)
200	0.3013
300	0.3089
286.4	0.3079

VI. ANGULAR DISTRIBUTION IN THE LABORATORY SYSTEM

If the values of σ_m/σ_e are to be compared with results obtained from measurements on the angular distribution of photoneutrons (or protons), the influence of the γ-ray momentum must normally be taken into account. Let θ be the angle between the directions of the photoneutron and the incident γ-ray, respectively, in the laboratory system (deuteron initially at rest). Simple geometrical considerations then give the following differential cross section $\sigma(\theta)$ in the laboratory system:

$$\sigma(\theta)d\Omega=(\sigma_m+\tfrac{3}{2}\sigma_e\sin^2\theta f(\theta))\times(1-\alpha^2\sin^2\theta)^{-\frac{1}{2}}f(\theta)d\Omega/4\pi,$$
$$f(\theta)=1+2\alpha\cos\theta(1-\alpha^2\sin^2\theta)^{\frac{1}{2}}+\alpha^2(\cos^2\theta-\sin^2\theta), \quad (11)$$
$$\alpha=\bar{v}/v_n.$$

Here $\bar{v}$ is the velocity of the center of mass of the neutron and proton in the laboratory system and v_n is the velocity of the neutron relative to the center of mass; thus,

$$\frac{\bar{v}}{v_n}=\frac{h\nu}{2[(MM_p/M_n)c^2\{h\nu-|E_0|-(h\nu)^2/4Mc^2\}]^{\frac{1}{2}}}, \quad (12)$$

where M_n and M_p denote the masses of the neutron and proton, respectively.

VII. DISCUSSION

For a comparison with experimental results we refer to Figs. 4–6. The most accurate determinations of the total cross section at γ-energies above 4 Mev seem to favor a meson mass between 250 and 300. There is, however, a certain discrepancy at lower energies which is brought out by Fig. 5. Taking the measurements of Halban and Siegbahn and collaborators,[13] we see not only that the most probable theoretical cross sections fall short of the experimental values but also that the energy dependence is rather different. The results of Snell, Barker, and Sternberg (see caption of Fig. 4, reference b) show the same trend of the cross section

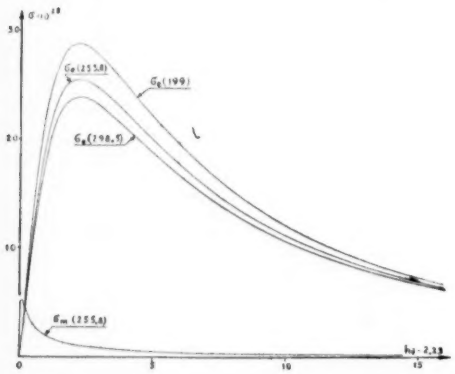

FIG. 2. The photoelectric cross section as a function of excess energy $h\nu-2.23$. Three meson masses.

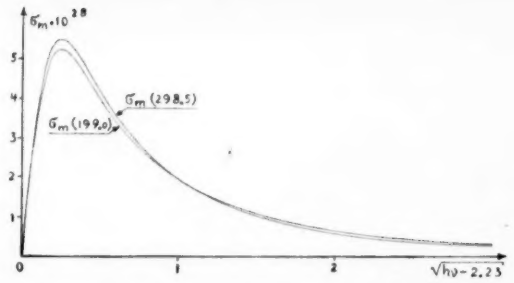

FIG. 3. The photomagnetic cross section as a function of $(h\nu-2.23)^{\frac{1}{2}}$. Two meson masses.

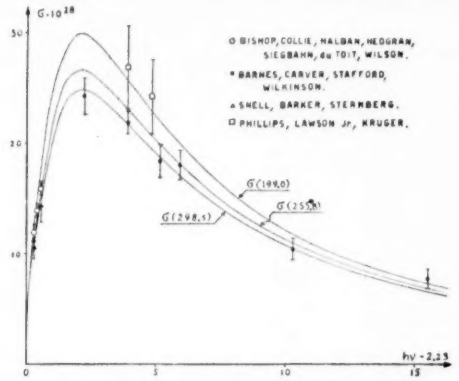

FIG. 4. The total photo cross section as a function of excess energy $h\nu-2.23$. Three meson masses. The following table lists the experimental results and the comparison with the theoretical results for a meson mass $M_m/M_e=286.4$.

$h\nu$ (Mev)	σ_{exp} (10^{-28} cm^2)	Ref.	σ_{theor} (10^{-28} cm^2)	Ratio $\sigma_{exp}/\sigma_{theor}$
2.504	11.9 ±0.8	a	9.92	1.20 ±0.08
	10.6(±1.1)	b		
2.618	13.9 ±0.6	a	12.18	1.14 ±0.05
2.757	15.9 ±0.6	a	14.80	1.07 ±0.04
	14.3 ±1.1	b		
4.45 ±0.04	24.3 ±1.7	c	25.36	
6.14 ±0.01	21.9 ±1.0	c	22.09	
	26.9 ±3.8	d		
7.0	24.2 ±3.4	d	19.91	
7.39 ±0.15	18.4 ±1.5	c	19.01	
8.14 ±0.08	18.0 ±1.3	c	17.33	
12.50 ±0.21	10.4 ±1.0	c	10.61	
17.6 ±0.2	7.7 ±0.9	c	6.68	

[a] See reference 13.
[b] Snell, Barker, and Sternberg, Phys. Rev. **80**, 637 (1950).
[c] Barnes, Carver, Stafford, and Wilkinson, Phys. Rev. **86**, 359 (1952).
[d] Phillips, Lawson, and Kruger, Phys. Rev. **80**, 326 (1950).

[13] Bishop, Collie, Halban, Hedgran, Siegbahn, Du Toit, and Wilson, Phys. Rev. **80**, 211 (1950).

increasing more slowly with energy than is predicted by theory. This tendency was already observed by Halban and Siegbahn and collaborators (see especially their Table IX and Discussion). They also indicated that a better agreement would be obtained if the theoretical photomagnetic cross section were increased, for example, by charge exchange. On the other hand, differences, if any, between later experiments by Bishop, Beghian, and Halban on the angular distribution of photoprotons and the present theoretical values of σ_m/σ_e (see caption of Fig. 6) rather point in the opposite direction. An increase of the theoretical σ_m, sufficient to give agreement with the measured total cross sections, would lead to a definite discrepancy in the angular distribution. Thus, although the experiments discussed here seem very accurate, they do not allow more definite theoretical conclusions.

VIII. THE EFFECTIVE RANGE AND THE PHOTO CROSS SECTIONS

The concept of effective range, originally introduced in the theory of low energy scattering,[14,15] has also been used in the theory of photodisintegration.[16–18] It appears, however, that the accuracy of the resulting cross sections will not be quite satisfactory, unless the effect of the potential shape is taken into account. In particular this applies to the Yukawa potential. Salpeter[17] has already given a thorough general discussion of the shape effects, and it may be of some interest to compare his results for the Yukawa potential with ours.

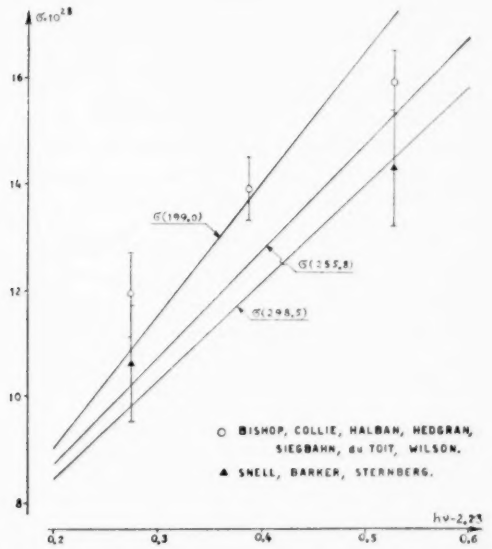

FIG. 5. The total photo cross section as a function of excess energy $h\nu-2.23$ in the interval 0.2–0.6 Mev. Three meson masses.

[14] J. M. Blatt and J. D. Jackson, Phys. Rev. **76**, 18 (1949).
[15] H. A. Bethe, Phys. Rev. **76**, 38 (1949).
[16] H. A. Bethe and C. Longmire, Phys. Rev. **77**, 647 (1950).
[17] E. E. Salpeter, Phys. Rev. **82**, 60 (1951).
[18] D. H. Wilkinson, Phys. Rev. **86**, 373 (1952).

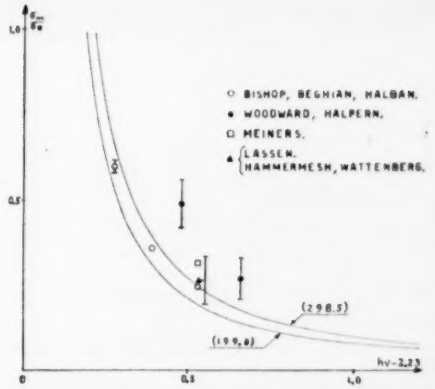

FIG. 6. The ratio of photomagnetic to photoelectric cross section as a function of excess energy $h\nu-2.23$. Two meson masses. The following table lists the experimental results and the comparison with the theoretical results for a meson mass $M_m/M_e=286.4$.

$h\nu$ (Mev)	$(\sigma_m/\sigma_e)_{\text{exp}}$	Ref.	$(\sigma_m/\sigma_e)_{\text{theor}}$
2.504	0.600 ±0.02	a	0.664
2.618	0.360 ±0.008	a	0.386
2.71	0.49 ±0.07	b	0.279
2.757	0.247 ±0.007	a	0.243
	0.317 ±0.012	c	
	0.265 ±0.065	d	
	0.265 ±0.07	e	
2.89	0.27 ±0.06	b	0.176

The result given in reference e has been corrected for γ-ray momentum.

[a] Bishop, Beghian, and Halban, Phys. Rev. **83**, 1052 (1951).
[b] W. M. Woodward and I. Halpern, Phys. Rev. **76**, 107 (1949).
[c] E. P. Meiners, Jr., Phys. Rev. **76**, 259 (1949).
[d] N. O. Lassen, Phys. Rev. **75**, 1099 (1949).
[e] B. Hammermesh and A. Wattenberg, Phys. Rev. **76**, 1408 (1949).

A. Different Integrals Related to the Triplet Effective Range

To begin with, we compute the various integrals $\rho(E_1, E_2)$ (the notation is that of reference 15) for the Yukawa potential. Having fixed the deuteron binding energy and chosen a meson mass, corresponding to a suitable value of $(-a_0)^{\frac{1}{2}}$ [see Eqs. (2) and (3)], we obtain the binding parameter b and the ground state eigenfunction from the tables of Hulthén and Laurikainen[4] (see also Table I above). $\rho(-\epsilon, -\epsilon)$ is then obtained from

$$\rho(-\epsilon, -\epsilon)=1/\kappa[(-a_0)^{-\frac{1}{2}}-2C^{-2}].$$

The normalization constant C [Eq. (3)] has been corrected according to Sec. IV above, which means that the error in $\rho(-\epsilon, -\epsilon)$ does not exceed a few parts in a thousand. The triplet scattering length a_t and effective range $r_t=\rho(0, 0)$ are obtained from Table XII of Hulthén and Skavlem.[6] $\rho(0, -\epsilon)$ is given by

$$\rho(0, -\epsilon)=\frac{2}{\kappa(-a_0)^{\frac{1}{2}}}\left(1-\frac{1}{\kappa a_t(-a_0)^{\frac{1}{2}}}\right).$$

TABLE XI. Triplet-scattering length a_t and different integrals related to the triplet-effective range as functions of meson mass. $\epsilon=|E_0|=2.23$ Mev; a_t and ρ in 10^{-13} cm.

$(-a_0)^{\frac{1}{2}}$	M_m/M_e	a_t	$\rho(-\epsilon,-\epsilon)$	$\rho(0,-\epsilon)$	$\rho(0,0)$	$\rho(0,2.5)$	$\rho(0,5)$
0.25	358.2	5.227	1.564	1.510	1.461	1.418	1.385
0.30	298.5	5.350	1.763	1.674	1.599	1.542	1.498
0.35	255.8	5.453	1.940	1.804	1.705	1.633	1.582
0.40	223.9	5.533	2.096	1.904	1.778	1.698	1.644
0.45	199.0	5.589	2.237	1.971	1.823	1.747	1.690
0.3126	286.4	5.377	1.810	1.709	1.629	1.567	1.521

For positive energies $\rho(0, E)$ has been calculated from the formula

$$k\cot\eta=-1/a_t+\tfrac{1}{2}\rho(0,E)k^2,$$

using the asymptotic phases η given by Hulthén and Skavlem. E denotes the energy in Mev in the center-of-mass system: thus $\rho(0, 2.5)$ corresponds to Salpeter's $\rho(0, 5)$. The resulting ρ-values are given in Table XI for six different meson masses. The figures of the last row (interpolated) correspond to the empirical value of $a_t=(5.377\pm0.021)\times10^{-13}$ cm, obtained from $\sigma_0=20.36\pm0.10$ barns, f (coherent scattering amplitude) $=(-3.78\pm0.02)\times10^{-13}$ cm, which gives a meson mass 286 ± 9, assuming $|E_0|=2.230\pm0.004$ Mev. We then have $\rho(0,-\epsilon)=(1.709\pm0.028)\times10^{-13}$ cm (probable error). Thus the uncertainty in the empirical value of $\rho(0,-\epsilon)$ is smaller than the difference between $\rho(0,0)$, $\rho(0,-\epsilon)$, and $\rho(-\epsilon,-\epsilon)$. We also note that the linear dependence of $\rho(E_1, E_2)$ on (E_1+E_2), assumed by Salpeter,[17] is valid only for rather small energies. For example, taking the figures of the last row in Table XI, we need the quadratic formula,

$$\rho(0,E)=\rho(0,0)-0.068\frac{E}{|E_0|}+0.012\left(\frac{E}{|E_0|}\right)^2,$$

to account for the three values $\rho(0,-\epsilon)$, $\rho(0,0)$, and $\rho(0, 2.5)$.

B. The Photoelectric Cross Section

The photoelectric cross section may be written[18]

$$\sigma_e=\sigma_{e0}[1-\gamma\rho(-\epsilon,-\epsilon)]^{-1}F^2,$$

$$\sigma_{e0}=\frac{8\pi}{3}\frac{e^2}{\hbar c}\left(\frac{M_n}{M}\right)^2\frac{\hbar^2}{M}\frac{|E_0|^{\frac{1}{2}}(h\nu-|E_0|)^{\frac{3}{2}}}{(h\nu)^3}.$$

σ_{e0} is the expression of Bethe and Peierls, where the ground state wave function is assumed to be $2\gamma^{\frac{1}{2}}e^{-\gamma r}$,

TABLE XII. Parameter E_1 in the correction factor F as a function of meson mass, E_1 in Mev.

$(-a_0)^{\frac{1}{2}}$	M_m/M_e	E_1
0.30	298.5	48.74
0.35	255.8	37.89
0.40	223.9	30.72
0.45	199.0	25.57

TABLE XIII. Correction factor F^2 as a function of energy for two meson masses.

$h\nu$ (Mev)	F^2 $M_m/M_e=298.5$	$M_m/M_e=255.8$
2.23	0.9976	0.9960
4.0	0.9927	0.9884
6.0	0.9847	0.9762
8.0	0.9747	0.9615
10.0	0.9632	0.9450
12.0	0.9507	0.9273
14.0	0.9377	0.9098
16.0	0.9237	0.8912

$\gamma=(M|E_0|/\hbar^2)^{\frac{1}{2}}$. The main error in σ_{e0} is due to the wrong normalization; this is corrected by the factor $[1-\gamma\rho(-\epsilon,-\epsilon)]^{-1}$, while F^2 accounts for the difference between the correct eigenfunction and its asymptotic form. F and $\rho(-\epsilon,-\epsilon)$ depend on the potential shape, F on the energy as well. If $\rho(0,-\epsilon)$ is substituted for $\rho(-\epsilon,-\epsilon)$, as is done in reference 16, the value of σ_e decreases by 4 percent in the case of a Yukawa potential with meson mass 286.

F can be computed as the ratio of the matrix element J_e [Eq. (6)] to a corresponding expression $(J_e)_{\text{asymptotic}}$, where the ground-state function $\phi_0(x)$ has been replaced by its asymptotic form. It appears that F can be accurately[19] represented by the formula

$$F=1-0.640(h\nu/(E_1+h\nu))^2,$$

where E_1 depends on the meson mass [compare the expression of F for the Hulthén potential, reference 18, Eq. (3)]. E_1 is given for different meson masses in Table XII, while Table XIII contains F^2 for a few meson masses and some energies from threshold up to 16 Mev. From Table XIII we conclude that the shape-dependent version of the effective range theory is rather accurate, giving σ_e with an error less than 2 percent up to γ-energies about 6 Mev, if we keep to ranges corresponding to a meson mass above 275 M_e.

C. The Photomagnetic Cross Section

In all calculations of the photomagnetic cross section σ_m based on the effective range theory, the authors have started from the experimental value of σ_c, the capture cross section. On the other hand, in the presentation given above both quantities σ_m and σ_c were calculated

TABLE XIV. Singlet scattering length a_s and different integrals related to the singlet effective range as functions of meson mass. a_s and ρ in 10^{-13} cm.

M_m/M_e	a_s	$\rho(0,0)$	$\rho(0,2.5)$	$\rho(0,5)$
298.5	−23.710	3.023	2.865	2.747
255.8	−23.636	3.582	3.346	3.175
199.0	−23.543	4.749	4.290	3.995
286.4	−23.690	3.162	2.987	2.856

[19] The deviations between F obtained from this formula and F calculated directly do not exceed 0.0005 in the energy interval up to 16 Mev for meson masses 298.5 and 255.8 M_e.

theoretically. Therefore, a direct comparison of the numerical results for σ_m would not tell us so much about the effective range approximation itself.

To get an idea of its accuracy we have first computed the integral $\rho(0, E)$ connected with the singlet state [$\rho(0, 0) = r_s$, the singlet effective range] for a few meson masses and energies. The procedure has already been indicated in Sec. VIIIA, and the results are found in Table XIV.

Secondly, we have calculated the integral D introduced by Bethe and Longmire[16] [Eq. (25)] for various meson masses and energies, using our approximate eigenphases and eigenfunctions. It appears that D can be accurately represented by a linear function of energy up to 5–6 Mev, the variation with energy being small. The results are given in Table XV, together with an interpolation to meson mass 286. For comparison Table XV also includes the D values obtained from the

TABLE XV. The integral D and some approximations to D (see the text) as functions of meson mass. D, D_{BL}, and D_S in 10^{-13} cm. Energy E in Mev.

M_m/M_e	D	D_{BL}	D_S
298.5	$1.120(1-0.0071E)$	1.174	1.113
255.8	$1.265(1-0.0083E)$	1.347	1.230
199.0	$1.530(1-0.0103E)$	1.680	1.413
286.4	$1.158(1-0.0074E)$	1.218	1.145

approximate formula of Bethe and Longmire

$$D_{BL} = \tfrac{1}{4}[r_s + \rho(0, -\epsilon)],$$

and of Salpeter

$$D_S = 0.686 + 0.146 r_s + 0.57[\rho(0, -\epsilon) - 1.720] - 0.09[\rho(0, -\epsilon) - 1.720] r_s, \text{ in units } 10^{-13} \text{ cm}.$$

Finally, we have calculated σ_m by the effective range formula given by Salpeter[17] [Eqs. (22)–(24b)],[20] using the same value for r_s[$= \rho(0, 0)$, Table XIV] but different values of D[D_{BL}, D_S, and D for energy zero, according to Table XV]. The approximation common to these three cases is not only that D is considered

[20] Of course we have other numerical constants in (23) than Salpeter. In (24a) there is a misprint: the expression in the first brackets should be squared.

TABLE XVI. Photomagnetic cross section σ_m calculated according to different effective range versions and values interpolated from Tables VII to VIII.

		$\sigma_m(10^{-28}$ cm)			
		Effective range			Interpolated from Tables VII–VIII
M_m/M_e	$h\nu$ (Mev)	Bethe-Longmire	Salpeter	Improved	
298.5	2.504	3.722	3.988	3.971	3.971
	2.757	2.706	2.908	2.895	2.902
	6.14	0.540	0.602	0.597	0.587
255.8	2.504	3.627	3.995	3.916	3.921
	2.757	2.641	2.926	2.863	2.872
	6.14	0.544	0.642	0.617	0.599

independent of energy but also that $k \cot\eta$ is replaced by $-1/a_s + \frac{1}{2} r_s k^2$. Besides, in the BL version we have found it most consistent to use $\rho(0, -\epsilon)$ instead of $\rho(-\epsilon, -\epsilon)$ in the normalization factor. In Table XVI the results are compared with the σ_m values interpolated from our Tables VII and VIII. The difference between the S version and the improved result is due only to the different D values used.

The conclusion is that the shape-dependent effective range approximation can give rather accurate results for σ_m in the most interesting region (up to 6 Mev), provided the calculations are based on an accurate knowledge of the ground state as well as the singlet state of zero energy.

In the present paper no attempt has been made to estimate the influence of noncentral forces. The preliminary discussion of Bethe and Longmire[16] indicates that the influence on the photo cross sections will not be considerable. However, we feel that the increasing accuracy of the experiments may soon make a more detailed study worth while, and we hope that the calculations on the neutron-proton problem with tensor forces which are in progress at this institute will enable us to return to the question on a later occasion.

We are indebted to Mr. Vilhelms Grinvalds for carrying out the greater part of the numerical work. Financial support from the Swedish Atomic Energy Committee and the Swedish State Council of Technical Research is gratefully acknowledged.

Electronic Transitions in the Luminescence of Zinc Sulfide Phosphors

RICHARD H. BUBE
RCA Laboratories Division, Radio Corporation of America, Princeton, New Jersey
(Received December 22, 1952)

The electronic transitions involved in the processes of (1) absorption, (2) excitation, (3) emission, (4) trapping, and (5) photoconductivity, at room temperature, have been measured for zinc sulfide phosphors, without added impurity, and with silver, copper, and manganese impurity.

Three types of excitation transitions are found: (1) from the filled band to the conduction band, (2) from an impurity level above the filled band to the conduction band, and (3) from a ground-state level to an excited-state level of an impurity ion. The first two transitions result in trapping and photoconductivity; the third does not.

Emission transitions occur from a level below the bottom of the conduction band to a level above the filled band.

The same five major trap depths are common to all zinc sulfide phosphors regardless of the nature of the impurity. Optical trap emptying by visible light, like thermal trap emptying, involves a process of stimulation in which trapped electrons are raised into the conduction band before returning to luminescence centers to produce emission.

A tentative energy-level diagram is constructed from the data obtained.

INTRODUCTION

ONE of the primary goals in the understanding of luminescence is the description of luminescence phenomena in terms of an energy-level diagram. This description involves the determination of the location of energy levels, and the identification of transitions between energy levels. The required information for such a description can be largely obtained from measurements of absorption, excitation, emission, trapping, and photoconductivity.

(1) Measurements of absorption allow the determination of the width of the forbidden gap between filled and conduction bands. (2) A correlation of measurements of absorption and excitation allow the determination of the magnitude of the excitation transition. If trapping and photoconductivity result from excitation, the termination of the excitation transition may be identified as the conduction band. If excitation does not produce trapping and photoconductivity, the termination of the excitation transition is probably an excited state of the activator ion or complex. (3) Measurements of emission give the magnitude of the emission transitions. Location of the levels involved in the emission transition may be obtained from measurements of emission intensity as a function of temperature. (4) Glow curve measurements give the data from which the location of the trapping levels may be determined.

Many types of such measurements have been previously reported, both for ZnS phosphors and for other luminescent materials. Various transitions in ZnS phosphors have been studied by Kroeger,[1,2] Garlick,[3–5] Klick,[6] Piper and Williams,[7] and Klasens.[8] Similar studies with the same purpose have been reported for CdS by Klick[9] and Broser and Warminsky.[10] Theoretical studies on the development of energy band diagrams for phosphors have recently been reported by Klick[11] and Williams.[12,13]

It is the purpose of this paper to present a summary of measurements, of the different types enumerated above, obtained with a series of ZnS phosphors prepared from the same pure material and prepared under identical conditions. This procedure allows a distinction to be made between effects which are essentially due to changes in impurity, and other effects which are caused by variations in preparation technique.

The results presented here (1) confirm many previously reported observations, and (2) provide additional quantitative data on these and other related phenomena.

EXPERIMENTAL

Most of the measurements described in this paper have been made with (1) hex.-ZnS phosphor prepared without additives; (2) hex.-ZnS, [NaCl(2)];[14] (3) hex.-ZnS:Ag(0.01), [NaCl(2)]; (4) hex.-ZnS:Cu(0.01), [NaCl(2)]; and (5) hex.-ZnS:Mn(0.01), [NaCl(2)]. These phosphors were prepared[15] from triply-purified ZnS, for which spectrographic analysis[16] showed the

[1] F. A. Kroeger, *Luminescence in Solids Containing Manganese* (Van Campen, Amsterdam, 1940), pp. 44–57.
[2] F. A. Kroeger and J. A. M. Dikhoff, J. Electrochem. Soc. **99**, 144 (1952).
[3] G. F. J. Garlick and A. F. Gibson, Nature **161**, 359 (1948).
[4] G. F. J. Garlick and A. F. Gibson, J. Opt. Soc. Am. **39**, 935 (1949).
[5] G. F. J. Garlick and D. E. Mason, J. Electrochem. Soc. **96**, 90 (1949).
[6] C. C. Klick, J. Opt. Soc. Am. **41**, 816 (1951).
[7] W. W. Piper and F. E. Williams, Phys. Rev. **86**, 659 (1952).
[8] Klasens, Ramsden, and Quantie, J. Opt. Soc. Am. **38**, 60 (1948).
[9] C. C. Klick, Phys. Rev. **86**, 659 (1952).
[10] I. Broser and R. Warminsky, Ann. Physik **7**, 289 (1950).
[11] C. C. Klick, Phys. Rev. **85**, 154 (1952).
[12] F. E. Williams, J. Chem. Phys. **19**, 457 (1951).
[13] S. Roberts and F. E. Williams, J. Opt. Soc. Am. **40**, 516 (1950).
[14] Proportions of additives are given in weight percent throughout the paper.
[15] Phosphors prepared by P. R. Celmer.
[16] Spectrographic analysis by S. Larach.

absence of all cation impurities, except for faint traces of Mg and Na. In particular, the analysis showed that Cu was absent, at least for proportions greater than 10^{-6} percent. All of these phosphors were prepared by heating in covered crucibles in air for five minutes at 1250°C. After heating and cooling, the core of each sample was washed with triple-distilled water before being used for measurement.

In addition to these phosphors, a hex.-ZnS:Cu(0.03), [NaCl(2)]; a hex.-ZnS:Mn(1.0), [NaCl(2)]; and a hex.-ZnS:Mn(1.0) phosphor were prepared under similar conditions for use where a higher proportion of impurity was necessary.[17] For the ZnS:Mn phosphor prepared with chloride, the Mn was added as the chloride; for the ZnS:Mn phosphor prepared without chloride, the Mn was added as the nitrate.

For future reference in the remainder of this paper, it will be assumed that the phosphor under discussion has been prepared with chloride unless the absence of chloride in the preparation is specifically mentioned.

Because of the number of different types of measurements that were used in this study, the experimental technique will be described in the same section as the experimental results. Excitation sources were as follows: a 250-watt GE Purple-X lamp for Fig. 1(c); a 100-watt C-H4 mercury spot-projector lamp with Corning 5860 filter (3.2–3.9 ev) for Fig. 3(a), Fig. 4, and Fig. 6; an 8-volt miniature lamp, GE 1183, without filters for Fig. 1(a) and 1(b), and with the Corning 5860 or Farrand filters (half-width of about 0.04 ev at 5000A, and 0.07 ev at 4000A) for Fig. 3(b), Fig. 5, Fig. 7, Fig. 10, Fig. 11, and the data of Table VI.

RESULTS

Absorption

Measurements of absorption were made by measuring the diffuse reflectivity from a layer of phosphor with an effectively infinite thickness. In order to detect the absorption in spectral regions where the absorption was low, e.g., the fine structure caused by impurity absorption in ZnS:Mn, a method was used, utilizing an integrating sphere of $MgCO_3$, in which the incident radiation was reflected at least twice from the sample before detection. The intensity of the reflected light was measured with a recording grating spectroradiometer, designed and constructed by Shrader, which will be described in another publication.

Figure 1 shows the reflectivity curves obtained at room temperature with the ZnS phosphors of this study. In order to obtain impurity absorption effects for the ZnS:Mn phosphor comparable in magnitude to those found for the ZnS:Ag(0.01) and ZnS:Cu(0.01) phosphors, it is necessary to use an impurity proportion

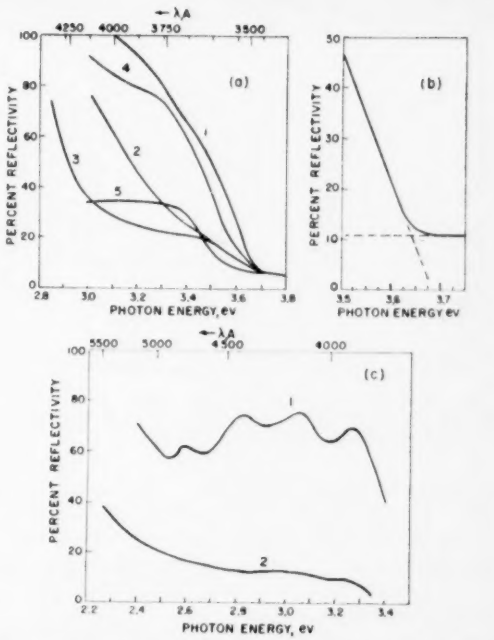

FIG. 1. Diffuse reflectivity spectra of ZnS phosphors. (a) Obtained with single reflection. (1) ZnS; (2) ZnS:Ag(0.01); (3) ZnS:Cu(0.01); (4) ZnS:Mn(1.0); (5) ZnS:Mn(1.0), no chloride. (b) Obtained with single reflection. ZnS. (c) Obtained with multiple reflection. (1) ZnS:Mn(1.0); (2) ZnS:Mn(1.0), no chloride.

100 times as large; measurements were made with ZnS:Mn(1.0) phosphor.

Table I presents a summary of the absorption data obtainable from these curves. The location of the absorption edge for the hex.-ZnS phosphor at 3.64 ev is in good agreement with the value of 3.67±0.03 ev reported by Piper and Williams[7] for single crystals of ZnS, and with the values of 3.70 ev and 3.55 ev reported for ZnS phosphors prepared with the exclusion of oxygen and with 1 percent ZnO, respectively, by Kroeger and Dikhoff.[2]

In addition to the host-crystal absorption, there are absorption bands associated with the Ag, Cu, and Mn impurities. A pronounced difference in absorption is found with the ZnS:Mn(1.0) phosphor depending on whether chloride is present in the preparation.

Excitation

The excitation spectra of the ZnS phosphors of this study were measured with the assistance of DeVore using the monochromator arrangement previously described by him.[18] The luminescence emission was detected with a 1P21 phototube through suitable filters.

Figure 2 shows the excitation spectra obtained in this manner at room temperature, and a summary of the

[17] The proportion of Cu in the ZnS:Cu phosphors of this study was less than that required to produce the blue emission associated with a Cu proportion higher than 0.03 percent.

[18] H. B. DeVore and J. W. Dewdney, Phys. Rev. **83**, 805 (1951).

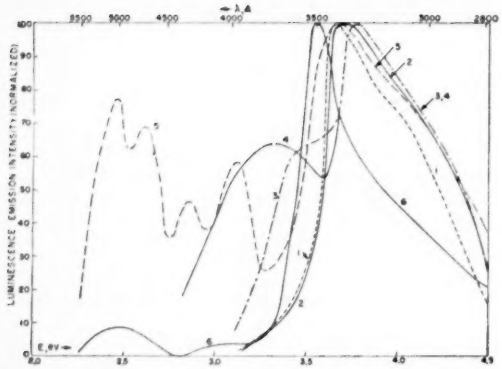

FIG. 2. Excitation spectra of ZnS phosphors. (1) ZnS, no chloride; (2) ZnS; (3) ZnS:Ag(0.01); (4) ZnS:Cu(0.03); (5) ZnS:Mn(1.0); (6) ZnS:Mn(1.0), no chloride.

excitation data is given in Table I, where it is compared with the absorption data. Each phosphor has an excitation peak at about the same energy as the absorption edge. In addition, each absorption peak due to an impurity has a corresponding excitation peak at approximately the same energy.

Although the absorption for the ZnS:Mn phosphor prepared without chloride is greater in the energy range from 2.0 to 3.5 ev than the absorption for the ZnS:Mn phosphor prepared with chloride, the excitation spectra show that the excitation process is much less efficient in the phosphor prepared without chloride. These observations are similar to previously reported results: (1) the presence of chloride in the preparation was found to decrease the absorption of ZnS phosphor,[19] and (2) the presence of gallium in the preparation was found to increase the luminescence efficiency of ZnS:Cu and ZnS:Mn phosphors, prepared in H_2S, for photoexcitation.[20]

Emission

The emission spectra for the ZnS phosphors of this study at room temperature, as measured with an automatic recording spectroraiodmeter,[21] are given in Fig. 3(a). Table II presents a summary of the energies for peak emission intensity and of the half-widths of the emission spectra.

TABLE I. A summary of absorption and excitation data.

Phosphor	Process associated with	Absorption edge or max. ev	Excitation max. ev
ZnS	Host crystal	3.64	3.70
ZnS:Ag(0.01)	Host crystal	3.69	3.77
ZnS:Ag(0.01)	Ag impurity	3.50*	3.42
ZnS:Cu(0.01)	Host crystal	3.69	3.77
ZnS:Cu(0.01)	Cu impurity	3.18*	3.30
ZnS:Mn(1.0)	Host crystal	3.64	3.65
ZnS:Mn(1.0)	Mn impurity	3.18	3.12
		2.92	2.87
		2.67	2.60
		2.52	2.45
ZnS:Mn(1.0) (No chloride)	Host crystal	3.57	3.55

* Values obtained by taking ratios of reflectivity of ZnS:Ag and ZnS:Cu to the reflectivity of ZnS phosphor.

[19] R. H. Bube, J. Chem. Phys. **20**, 708 (1952).
[20] R. H. Bube and S. Larach, J. Chem. Phys. **21**, 5 (1953).

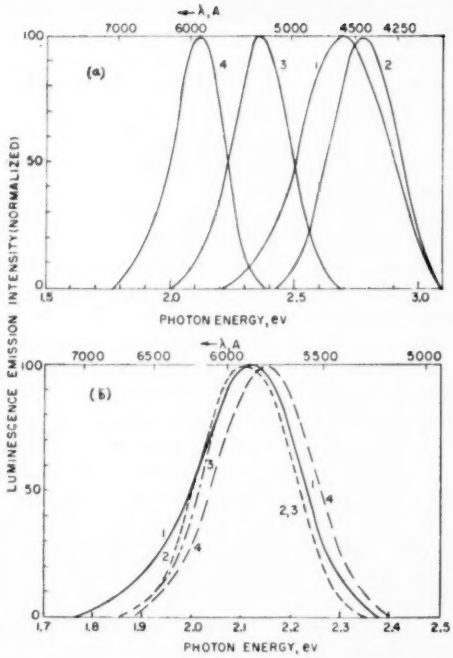

FIG. 3. Emission spectra of ZnS phosphors. (a) Excitation by ultraviolet of energy 3.2–3.9 ev. (1) ZnS; (2) ZnS:Ag(0.01); (3) ZnS:Cu(0.01); (4) ZnS:Mn(1.0). (b) Excitation of ZnS:Mn(1.0) with various excitation energies. (1) 3.2–3.9 ev; (2) 3.18 ev; (3) 2.87 ev; (4) 2.48 ev.

Essentially the same emission spectrum is obtained for the ZnS phosphors regardless of whether the excitation energy is absorbed by the host crystal or by the activator. In particular, the emission spectra for ZnS:Mn(1.0) phosphor obtained for different excitation energies are given in Fig. 3(b). The principal difference between the spectra is that a secondary emission band with peak at 1.85 ev (not resolved in Fig. 3(b), but clearly resolved in other measurements), found for ultraviolet excitation in the host-crystal absorption band, is absent for excitation in the activator bands, as it is also for cathode-ray excitation.

TABLE II. Summary of peak emission energies and half-widths.

Phosphor	Emission associated with	Energy for peak emission, ev	Emission half-width, ev
ZnS	Perturbed S	2.68	0.40
ZnS:Ag(0.01)	Ag impurity	2.77	0.31
ZnS:Cu(0.01)	Cu impurity	2.35	0.27
ZnS:Mn(1.0)	Mn impurity	2.12	0.23

[21] V. K. Zworykin, J. Opt. Soc. Am. **29**, 84 (1939).

TABLE III. Relative peak emission intensities of ZnS:Mn phosphors.

Crystal structure	% Mn	2% NaCl	Ultraviolet (3.2–3.9 ev) excitation[a] Blue (host-crystal) emission	Ultraviolet (3.2–3.9 ev) excitation[a] Orange (Mn) emission	6-kv cathode-ray excitation[b] Blue (host-crystal) emission	6-kv cathode-ray excitation[b] Orange (Mn) emission
cubic	0.01	Yes	122	0	134	0
cubic	0.01	No	0	0	0	5
hexagonal	0.01	Yes	48	0	75	0
hexagonal	0.01	No	22	0	48	0
cubic	0.1	Yes	43	4.7	27	0
cubic	0.1	No	0	0	0	27
hexagonal	0.1	Yes	12	14	12	0
hexagonal	0.1	No	3.4	3.4	2.5	1.2
cubic	1.0	Yes	0	36	0	1.6
cubic	1.0	No	0	2.6	0	21
hexagonal	1.0	Yes	0	70	0	9.3
hexagonal	1.0	No	0	17	0	7.5
cubic	10.0	Yes	0	50	0	2.5
cubic	10.0	No	0	0	0	1.4
hexagonal	10.0	Yes	0	3.4	0	0
hexagonal	10.0	No	0	2.5	0	0

[a] hex.-ZnS:Ag(0.02):Cu(0.01), (RCA 33Z22A), standard equal to 100 for ultraviolet excitation.
[b] hex.-Zn_2SiO_4:Mn(0.3), (RCA 33W2A), standard equal to 100 for cathode-ray excitation

ZnS, ZnS:Ag, and ZnS:Cu phosphors are much more efficient for both ultraviolet and cathode-ray excitation if they are prepared with halide, particularly for low preparation temperatures. ZnS:Mn phosphors are, in general, more efficient for photoexcitation if prepared with halide (an especially prominent effect for excitation in the activator bands, as shown in Fig. 2), and more efficient for cathode-ray excitation if prepared without halide.[22] Table III compares the peak emission intensity of various ZnS:Mn phosphors to demonstrate these effects quantitatively.

Although cubic ZnS, ZnS:Ag and ZnS:Cu phosphors have their emission maximum at a lower energy than the corresponding hexagonal phosphors, the emission maximum for ZnS:Mn phosphors is independent of crystal structure. The location of the emission for ZnS:Mn phosphors is also independent of the presence or absence of halide in the preparation, and of the type of excitation. Among all the phosphors listed in Table III, the location of the emission maximum varies by only 0.05 ev, and by only 0.02 ev if similar cubic and hexagonal phosphors are compared.

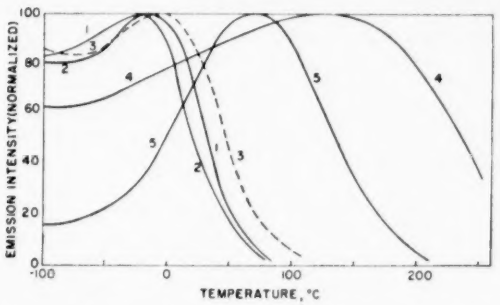

FIG. 4. Luminescence emission intensity as a function of operating temperature for ultraviolet excitation, 3.2–3.9 ev. (1) ZnS, no chloride; (2) ZnS; (3) ZnS:Ag(0.01); (4) ZnS:Cu(0.01); (5) Orange band of ZnS:Mn(0.01).

[22] H. W. Leverenz, *An Introduction to Luminescence of Solids* (John Wiley and Sons, Inc., New York, 1950), p. 89.

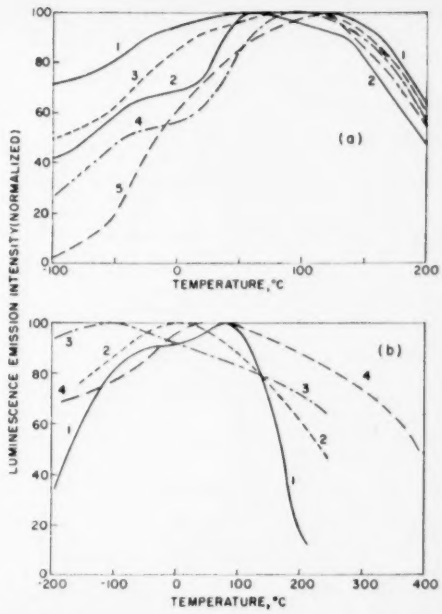

FIG. 5. (a) Luminescence emission intensity as a function of operating temperature for ZnS:Cu(0.01) for various excitation energies. (1) 3.2–3.9 ev; (2) 3.18 ev; (3) 2.97 ev; (4) 2.87 ev; (5) 2.75 ev. (b) Luminescence emission intensity as a function of operating temperature for ZnS:Mn(1.0) for various excitation energies. (1) 3.2–3.9 ev; (2) 3.18 ev; (3) 2.87 ev; (4) 2.48 ev.

The variation of emission intensity with operating temperature for the ZnS phosphors of this study are given in Figs. 4 and 5. Table IV lists the temperatures for which maximum emission intensity occurs, and the

TABLE IV. Summary of data on variation of emission intensity with operating temperature.

Phosphors	Excitation by, ev	Temp. of int. max. °C	Temp. for int. of 80% max. °C
ZnS (No chloride)	3.2–3.9	−20	16
ZnS	3.2–3.9	−20	4
ZnS:Ag(0.01)	3.2–3.9	−5	27
ZnS:Cu(0.01)	3.2–3.9	120	199
ZnS:Mn(0.01) (Orange band)	3.2–3.9	70	107
ZnS:Cu(0.01)	3.17	(140)	151
	2.98	100	172
	2.87	100	168
	2.76	120	160
ZnS:Mn(1.0)	3.2–3.9	80	118
	3.17	0	118
	2.87	−100	112
	2.48	80	246

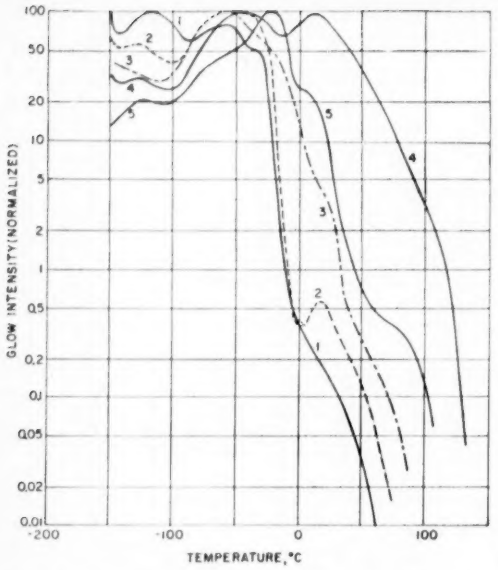

FIG. 6. Glow curves for ZnS phosphors after excitation at −160°C with ultraviolet, 3.2–3.9 ev. (1) ZnS, no chloride; (2) ZnS; (3) ZnS:Ag(0.01); (4) ZnS:Cu(0.01); (5) Orange band of ZnS:Mn(0.01).

temperature for which the intensity has decreased to 80 percent of the maximum.

Figure 5 shows the variation of emission intensity with operating temperature for the ZnS:Cu(0.01) and ZnS:Mn(1.0) phosphors for various excitation energies. The curves of Fig. 5(a) below the temperature breakpoint, and curve 1 of Fig. 5(b) below 0°C, may not be considered accurate indications of the variation of emission intensity at these temperatures, since the temperature was raised at a rate which probably did not allow complete equilibrium to be established between low intensity excitation and trapping processes. The significant result, however, is that the temperature breakpoint and the decrease of intensity beyond the breakpoint is relatively independent of the excitation energy for ZnS:Cu, but very dependent on the excitation energy for ZnS:Mn.

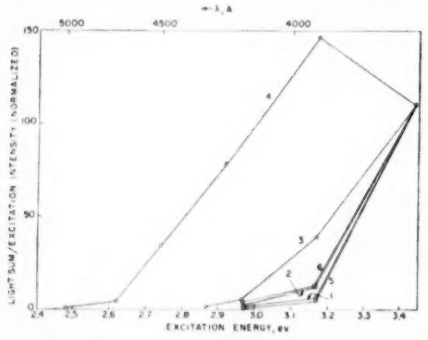

FIG. 7. Light sums corrected for excitation intensity, measured with thermal stimulation, for ZnS phosphors, as a function of excitation energy. (1) ZnS, no chloride; (2) ZnS; (3) ZnS:Ag(0.01); (4) ZnS:Cu(0.01); (5) ZnS:Mn(0.01); (6) ZnS:Mn(1.0).

Trapping

The variation of trap distribution with impurity for the series of ZnS phosphors was obtained with measurements of glow curves using the apparatus described in past publications.[23] The glow curves of Fig. 6 show that there are five major glow peaks which are common to all the ZnS phosphors regardless of the impurity. Since these phosphors were prepared in an atmosphere containing oxygen, the effects of oxygen as reported by Kroeger and Dikhoff[2] may be expected. The results presented here show that trap depths are characteristic of defects in the ZnS host crystal. Kroeger and Dikhoff suggest that at least the four deepest trap depths are in some way associated with incorporated oxygen. Previous work by the author[19,23] has suggested a correlation between traps and omission defects, the formation of which may be oxygen dependent.

The five glow peaks are located at about −120°, −60°, −25°, 15°, and 90°C. The principal reason for the deep traps being more prominent in the Cu and Mn phosphors than in the others is probably simply the higher luminescence efficiency of the Cu and Mn phosphors at these temperatures.

TABLE V. Time constant as a function of temperature and excitation energy for ZnS:Mn(1.0) phosphor.

Temperature, °C	Time constant, millisec			
	3.2–3.9 ev	3.18 ev	2.87 ev	2.48 ev
−150	400	1.4	1.8	2.3
25	9.2	1.5	1.6	2.3
100	4.0	1.8	1.7	2.6

The number of traps which are filled in a given length of time is a function of the excitation energy. The light sums, corrected for differences in excitation intensity with energy, are plotted in Fig. 7 as obtained from glow curves. Light sums for each phosphor are relative to the light sum obtained for excitation with the 5860 filter (which is set equal to 100 and plotted at 3.44 ev, the peak of the 5860 filter transmission). A comparison of the results with Fig. 2 shows that excitation in the Cu and Ag impurity bands produces trapping, whereas excitation in the Mn impurity band does not.

As an additional check on the difference between excitation in the host-crystal region and excitation in the impurity bands of ZnS:Mn phosphor, the time constant of the decay of phosphorescence emission was measured as a function of temperature for these different types of excitation. Table V summarizes the results for the ZnS:Mn(1.0) phosphor. The time constant was measured as the reciprocal of the frequency for which the percent modulation of the emission with chopped-

[22] R. H. Bube, Phys. Rev **80**, 655 (1950).

light excitation was down to $100/e$. Because of the difficulty in separating the exciting light and the emitted light for the lower energy excitations, values of the time constant should probably be considered to have a possible error as high as 25 percent for these excitations. The results indicate the complete absence of trapping for temperatures at least below 100°C for excitation in the Mn bands, whereas trapping is found over this temperature range for excitation in the host-crystal band.

Although no change in trap depths was previously detected for ZnS:Cu phosphors as a function of Cu proportion up to 0.3 percent Cu,[23] a change in trap depths with Mn proportion is found for the ZnS:Mn phosphors, where glow curves may be obtained for 10 percent Mn. Figure 8 shows the variation of glow peak location for the four shallowest trap depths as a function of Mn proportion. The decrease in trap depth is about 0.1 ev for a change in Mn proportion from 0.001 percent to 10.0 percent.

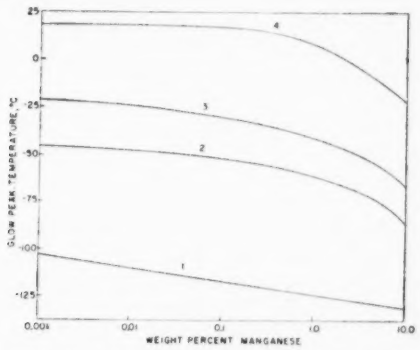

FIG. 8. Variation of location of glow peak with proportion of Mn in ZnS:Mn phosphors for four different trap depths.

The presence of retrapping in the course of the glow curve measurement has been found for ZnS:Mn phosphors, in a similar way to its occurrence for ZnS:Cu phosphors.[23] Figure 9(b) gives the relative intensities of the glow peaks at −60°, −25°, and 15°C compared to the intensity of the glow peak at −120°C, as a function of the percent of the total number of traps which are filled at the beginning of the glow curve measurement, as measured with ZnS:Mn(0.01). The variation in these relative intensities is caused by the retrapping of electrons, freed from shallow traps in the course of the glow curve measurement, by empty deeper traps. The result is that high temperature glow peaks are most prominent relative to glow peaks at lower temperatures, for excitation conditions such that few electrons are initially trapped.

Figure 9(a) shows another effect for ZnS:Mn(0.01) phosphor which is dependent on the number of electrons trapped before the start of the glow curve measurement: the ratio of blue emission (host-crystal) intensity in the glow curve to the orange emission (Mn) intensity.

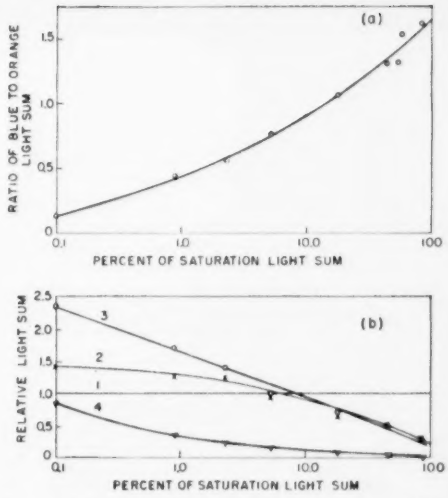

FIG. 9. (a) Variation of the ratio of blue to orange thermally-stimulated light sum of ZnS:Mn(0.01) with the percent of the saturation light sum. (b) The light sum of glow peaks at −60°C, curve (2); −25°C, curve (3); and 15°C, curve (4); relative to the glow peak at −120°C, curve (1); as a function of the percent of saturation light sum.

Light which does not produce trapping may be used to remove electrons from traps to which they have been excited by previous irradiation. Table VI presents a summary of the percent of traps emptied in a ten-minute interval by light of various energies, but of equal intensity, for the phosphors of this study. The process of trap emptying is relatively independent of impurity or irradiating energy over the range studied.

In order to investigate the nature of the transition involved in the optical emptying of traps, the optically-stimulated light sum obtained by irradiation by 2.00 ev light at −160°C (after all traps had been filled by ultraviolet excitation) was compared with the difference in thermally-stimulated light sums for the case in which a glow curve was measured without previous 2.00-ev irradiation, and the case in which the glow curve was measured after irradiation. The data presented in Fig. 10 shows that at least 70 percent of the electrons optically freed from traps undergo radiative transitions. From Fig. 10(b) it is seen that the glow intensity for very shallow traps is greater for the curve obtained after irradiation. This is true in general, also for trap-emptying measurements with higher energy

TABLE VI. Summary of trap emptying as a function of impurity and irradiating energy.

Phosphor	Percent of traps emptied in a 10-minute irradiation			
	3.18 ev	2.87 ev	2.43 ev	2.00 ev
ZnS	32	52	46	29
ZnS:Ag(0.01)	20	46	48	25
ZnS:Cu(0.01)	...	...	42	8
ZnS:Mn(0.01)	36	31	23	35

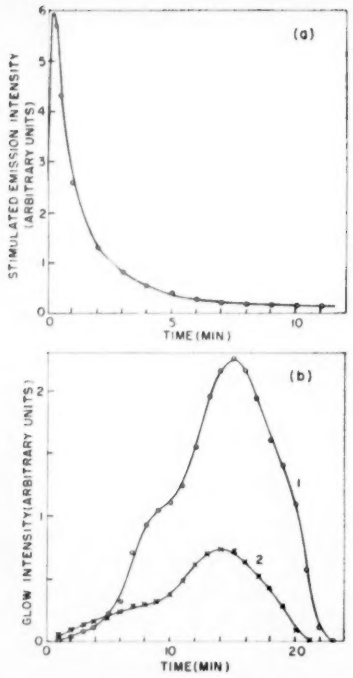

FIG. 10. (a) The photostimulated emission of ZnS phosphor at −160°C, after trap-filling with excitation energies 3.2–3.9 ev, for irradiation with light of energy 2.00 ev. (b) (1) Glow curve obtained for ZnS phosphor after 5 minutes of excitation followed by 15 minutes of decay; (2) glow curve obtained after 5 minutes of excitation followed by 15 minutes of irradiation with light of energy 2.00 ev.

irradiating light. The effect is caused by the retrapping in shallow traps of electrons optically freed from deeper traps.

Photoconductivity

The photoconductivity of the series of ZnS phosphors was measured at room temperature as a function of excitation energy. A photoconductivity cell was made by painting a thin paste of phosphor powder in castor oil over a conducting transparent coating on glass. A copper weight, resting on top of the paste, was the second electrode. A comparison of the results shown in Fig. 11 with Fig. 7 and Fig. 2, indicates that excitation in the Ag and Cu impurity bands produces photoconductivity as well as trapping, whereas excitation in the Mn impurity bands produces neither photoconductivity nor trapping.

DISCUSSION

Absorption and Excitation Processes

The following conclusions may be drawn from the above data as far as the excitation processes are concerned:

(1) Excitation of the host-crystal emission in ZnS phosphors is the result of an excitation transition from the top of the filled band to the bottom of the conduction band. The excitation process is most efficient when the excitation energy is about the same as the energy of the forbidden gap, but excitation still occurs for larger excitation energies, being about 20 percent of its maximum efficiency for an excitation energy 1 ev larger than the forbidden gap for all the phosphors prepared with halide. The decrease in excitation efficiency for excitation energies larger than the forbidden gap may be attributed to an increased host-crystal absorption, resulting in dense excitation of surface layers with only a small number of active centers. For excitation energies less than the forbidden gap, the excitation efficiency falls off much more rapidly, being decreased to 20 percent of the maximum for an excitation energy of about 0.15 ev less than the forbidden gap. Excitation produces both trapping and photoconductivity.

(2) Excitation of the emission of ZnS:Ag phosphors can occur either by a transition from the filled band to the conduction band, if the excitation energy is greater than about 3.50 ev, or by direct excitation from the Ag level to the conduction band for excitation by lower energy. The unexcited Ag level is located at about 0.22 ev above the top of the filled band. For both types of excitation transitions, trapping and photoconductivity result. Excitation of Ag centers for the transition from filled band to conduction band is probably associated with the migration of holes in the filled band to Ag centers.

(3) Excitation of the emission of ZnS:Cu phosphors is similar to that described for ZnS:Ag phosphors. The unexcited Cu level is located at about 0.34 ev above the top of the filled band. Trapping and photoconductivity occur for excitation absorbed by the host crystal and for excitation absorbed by Cu centers themselves. Excitation of Cu centers for the transition from filled band to conduction band is probably also associated with the migration of holes to Cu centers.

(4) Excitation of the emission of ZnS:Mn phosphors can occur either by a transition from the filled band to the conduction band, exactly as in the case of ZnS:Ag and ZnS:Cu phosphors, or by a transition to any one of four excited states of the Mn ion.

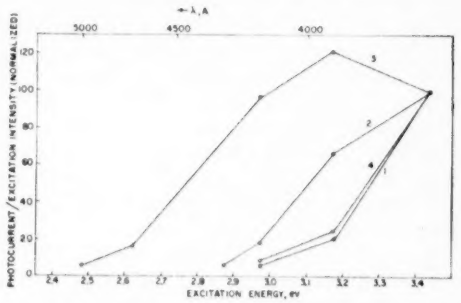

FIG. 11. Photocurrent, corrected for excitation intensity, for ZnS phosphors as a function of excitation energy. (1) ZnS; (2) ZnS:Ag(0.01); (3) ZnS:Cu(0.01); (4) ZnS:Mn(1.0).

The principal problem preventing the complete explanation of the excitation of ZnS:Mn phosphors is that involving the existence of a level associated with the Mn impurity within the forbidden gap.

That such a level may not exist is suggested by the following evidence. (1) No indication is found of an absorption or an excitation from such a level to the conduction band, resulting in trapping and photoconductivity, such as was found for the ZnS:Ag and ZnS:Cu phosphors. (2) The variation of the emission intensity with operating temperature is different for excitation absorbed by the host crystal and excitation absorbed by the Mn centers directly; a difference which does not occur in ZnS:Ag and ZnS:Cu phosphors.

On the other hand, there are a number of phenomena common to ZnS:Ag, ZnS:Cu, and ZnS:Mn phosphors, which are explained for the ZnS:Ag and ZnS:Cu phosphors in terms of hole migration to a level in the forbidden gap. (1) The relative intensity of blue and orange emission bands in a ZnS:Mn phosphor with a low Mn proportion (so that the blue host-crystal emission is still observed), is a function of the excitation intensity, higher excitation intensities making the blue emission more prominent. (2) Mn centers are excited by absorption of energy by the host crystal. (3) The orange emission associated with Mn centers increases in intensity over the temperature range for which the blue emission is decreasing. (4) The ratio of blue to orange intensity in the decay and in the glow-curve is much less than in the emission during excitation.

Although it may be possible to construct formal models to reconcile some of these observations, the lack of more positive evidence makes a hypothetical suggestion at this point of questionable value.

Emission Processes

The fact that the energy of the emitted radiation is considerably smaller than the excitation energy used to product it, shows that a readjustment of levels occurs as a result of the excitation process. Two energy-level diagrams are needed, therefore, to describe the luminescence processes; one for the location of levels before excitation, and another for the location of levels during excitation.

A method has been proposed by Klasens[24,25] by which the energy difference between the top of the filled band and the ground-state level of the excited center may be calculated from the variation of emission intensity with temperature during excitation. This method is based on the assumption that the cause of the decrease of efficiency at high temperatures is a filling of excited centers by the thermal raising of electrons from the filled band to the centers. (Another mechanism, which results in an equation between the efficiency and the temperature of exactly the same form, is the thermal raising of electrons from the level from which the emission transition would be made, into the conduction band before such a transition has occurred. The application of this mechanism will be ruled out as a result of the following discussion.)

TABLE VII. Location of energy levels for excited centers.

Phosphor	E^*[a]	E^{**}[b]
ZnS	0.55 ev	0.41 ev
ZnS:Ag(0.01)	0.55	0.32
ZnS:Cu(0.01)	0.95	0.34
ZnS:Mn(1.0)		
Host-crystal excitation	0.60	
Mn excitation	0.37	

[a] Energy difference between the ground-state level of the excited center and the top of the filled band; values reported by Garlick and Gibson (reference 4).

[b] Energy difference between the excited-state level of the excited center and the bottom of the conduction band; calculated for room temperature assuming a negligible change in the value of E^* between the temperature of the breakpoint and room temperature.

According to the formulation by Klasens, the efficiency, E, is expressible in terms of the activation energy, E^*, for the temperature-quenching process, and the absolute temperature, T, according to the equation:

$$E=1/[1+C\exp(-E^*/kT)] \quad (1)$$

The quantity C is expressible in terms of the ratio:

$$C=F/(s\nu J)^1, \quad (2)$$

where F is the frequency-factor of the temperature-quenching transition, s is the capture cross section for the luminescence center, v is the electron velocity, and J is the number of excitations per second per cm^3.

Garlick and Gibson[4] have used this equation to calculate E^* for ZnS, ZnS:Ag, ZnS:Cu, and ZnS:Mn phosphors by plotting $\ln(1/E-1)$ as a function of $1/T$ for the portion of the E *vs* T curve past the breakpoint. The values which they have reported are given in Table VII. There is good independent evidence which supports these values, at least in the case of the ZnS:Cu phosphor. The measurement of the decay of ZnS:Cu phosphor at high temperatures shows that for long decay times, an exponential decay is found, the slope of which is temperature dependent.[23] From the variation of the slope with temperature, a value of E^* of 1.0 ev and a value of F of 3×10^{10} sec^{-1} were calculated. Schoen[26] has pointed out that the rate-controlling step in this process is very probably a raising of electrons from the filled band to the excited activator levels. It has also been reported that the stimulation spectrum of ZnS:Cu phosphors contains a peak associated with the Cu at 1.3 microns (0.95 ev),[5,27] and that the ratio of blue (host-crystal) to green (Cu) emission intensity during the decay becomes much larger during stimulated decay than during normal decay.[28] These results favor a value of $E^*=0.95$ ev and $F=10^{10}$ sec^{-1} for the

[24] H. A. Klasens, Nature **158**, 306 (1946).
[25] H. A. Klasens and M. E. Wise, J. Opt. Soc. Am. **38**, 226 (1948).
[26] M. Schoen, Z. Naturwiss. **38**, 235 (1951).
[27] E. F. Daly, Proc. Roy. Soc. (London) **196**, 554 (1949).
[28] R. H. Rube, Phys. Rev. **80**, 764 (1950).

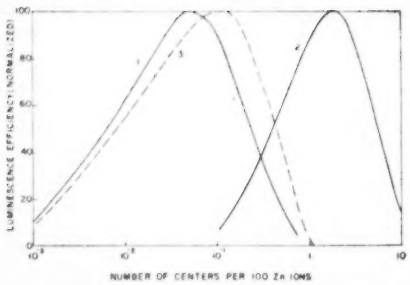

FIG. 12. The luminescence efficiency of (1) ZnS:Cu phosphors and (2) ZnS:Mn phosphors as a function of impurity proportion, assuming that a center is associated with each impurity ion; and (3) the luminescence efficiency of ZnS:Mn phosphors as a function of impurity proportion, assuming that a center is associated with each pair of Mn ions.

temperature-quenching transition in ZnS:Cu phosphors.

Using the values of E^* as reported by Garlick and Gibson, and assuming that F is of the order of 10^{10} sec^{-1} for ZnS and ZnS:Ag as well as for ZnS:Cu, the data of Fig. 4 may be used to calculate the capture cross section for the luminescence centers. (The method used by Garlick and Gibson to calculate E^*, being very dependent on the exact shape of the E *vs* T curve, is not applicable to the data of Figs. 4 and 5, which were obtained with nonmonochromatic excitation and with a thick sample. The location of the temperature breakpoint is a more simply determinable quantity.) The capture cross section is calculated by inserting into Eq. (1) the value of T for which E is 80 percent of its maximum value, as given in Table IV, known values of E^* and F, and an estimated value of J. Measurements with a CsSb cell gave a value of 5×10^{14} photons per second incident on the sample which had an area of 6 cm^2. If it is assumed that the ultraviolet penetrates about 10^{-4} cm, the value of $J=10^{18}$ excitations per second per cm^3 is obtained. The value of s is found to be about 10^{-24} cm^2, approximately the same for ZnS, ZnS:Ag, and ZnS:Cu. This value is much smaller than the atomic cross section, but is of about the order of magnitude of cross sections calculated from measurements of photoconductivity on many different materials, such as PbS, CdS, and ZnS, as summarized by Rose.[29]

The ratio of the frequency-factor for transitions out of a given energy level, and the cross section for capture into that energy level, is a constant at a given temperature. Mott and Gurney[30] have calculated this ratio:

$$F/s=2(6)^{\frac{1}{2}}(\pi)^{\frac{1}{2}}mh^{-3}(kT)^2, \qquad (3)$$

which for room temperature gives a value of 1.5×10^{26}. Rose[29] has shown how this same value for the ratio may be obtained by simple considerations involving the Fermi-limit concept. The value of s calculated above is for capture into the excited-state energy level of the excited center lying below the bottom of the conduction band. The frequency-factor for thermal excitation from this level to the conduction band may then be calculated to be about 10^2 sec^{-1}. This very low value of the frequency-factor, compared to the value of 10^{10} sec^{-1} found for thermal excitation from the filled band, is possibly explainable in terms of a difference in coupling between isolated impurity ions and the crystal vibrations, and host-crystal ions and the crystal vibrations.

The capture cross section of a hole in the filled band for an electron is found to be 10^{-16} cm^2 by calculation from Eq. (3), or about the order of magnitude of the atomic cross section.

The discussion of the temperature-quenching process thus far has assumed that the transition involved is that from the filled band to excited centers. Garlick and Gibson, however, have suggested that the activation energies they measured are for the thermal excitation from excited-state level into the conduction band. That the latter process can have no effect in the observed process of temperature-quenching may be shown in the following way. Measurements of Strange and Henderson[31] have shown that the initial decay in ZnS phosphors has a time constant of at most about 10^{-5} sec. If the probability of a transition from the excited-state level into the conduction band is calculated at temperatures near the observed temperature breakpoint, for the E^* of Garlick and Gibson and $F=10^{10}$ sec^{-1}, it is found that the probability of such transitions is of the order of one per sec, or a factor 10^5

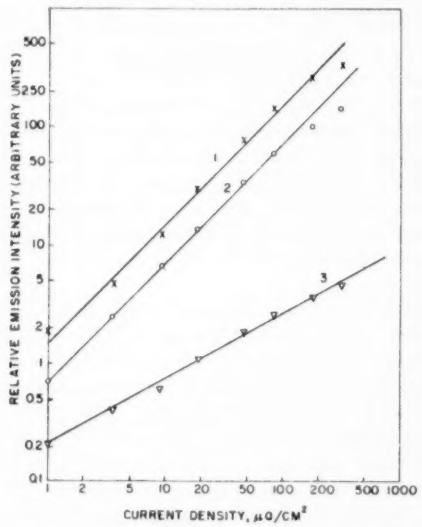

FIG. 13. The relative cathodoluminescence emission intensity of (1) ZnS:Ag(0.01); (2) ZnS:Cu(0.01); and (3) ZnS:Mn(1.0); as a function of current density for 4-kv cathode-ray excitation.

[29] A. Rose, RCA Rev. **12**, 362 (1951).

[30] N. F. Mott and R. W. Gurney, *Electronic Processes in Ionic Crystals* (Oxford University Press, London, 1940), p. 108.

[31] J. W. Strange and S. T. Henderson, Proc. Phys. Soc. (London) **58**, 369 (1946).

times smaller than would be necessary to make the raising of an electron in the excited-state level into the conduction band more probable than the return of the electron to the ground state with radiation.

For ZnS, ZnS:Ag, and ZnS:Cu phosphors, the ground-state level of the center was raised relative to the filled band as a result of excitation. The explanation of the effect of excitation on the levels of ZnS:Mn phosphor is made much more complicated by the fact that the value of E^* determined for ZnS:Mn is dependent on whether the excitation is absorbed by the host crystal or by the Mn centers directly. Values reported by Garlick and Gibson are included in Table VII.

One of the outstanding characteristics of ZnS:Mn phosphors is that the luminescence properties of ZnS:Mn(1.0) are comparable to properties obtained with ZnS:Ag or ZnS:Cu phosphors with only 0.01 percent impurity. It is reasonable to believe that there are the same number of active centers in ZnS:Mn and ZnS:Ag or ZnS:Cu phosphors with equal emission intensity. Leverenz,[32] for example, has reported that the saturation characteristics of ZnS:Mn(1.0) are quite different from those of Zn_2SiO_4:Mn(1.0), but are similar to those of ZnS:Ag(0.01) or ZnS:Cu(0.01). Figure 12 shows the variation of luminescence efficiency as a function of the impurity proportion of ZnS:Cu and ZnS:Mn phosphors. An explanation is required that will not only indicate why a certain fraction of the Mn ions incorporated do not act as effective centers, but which will also indicate why this fraction varies in an apparently irregular way experimentally found as a function of Mn proportion. The simple assumption that centers in ZnS:Mn phosphors are associated, not with isolated Mn ions, but with pairs of Mn ions, is able to furnish such an explanation to a first approximation, as is demonstrated by the dashed curve 3 of Fig. 12. Calculations of the number of pairs as a function of Mn proportion was obtained from the probability curves based on a random distribution of Mn ions, published by Leverenz.[33]

The fundamental difference between ZnS:Mn and ZnS:Ag or ZnS:Cu phosphors may also be demonstrated by measuring the luminescence emission intensity as a function of current density for 4-kv cathode-ray excitation below saturation. The results shown in Fig. 13 indicate that the emission intensity for ZnS:Ag and ZnS:Cu varies very closely to linearly with current density, but the emission intensity of the ZnS:Mn phosphor increases as the square-root of the current density. The square-root relationship indicates that the probability of exciting centers decreases as the number of excited centers increases, even below normal saturation, for ZnS:Mn.

[32] See reference 22, p. 359.
[33] See reference 22, p. 478.

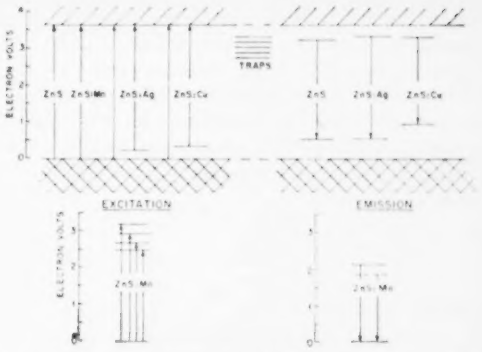

FIG. 14. A tentative energy-level diagram for the excitation and emission transitions in ZnS phosphors. Impurity levels for the ZnS:Mn phosphor are presented separately because of uncertainty about the nature or existence of the ground-state level in the forbidden gap, as discussed in the text.

Trapping Processes

Trapping in ZnS phosphors occurs for excitation transitions which raise an electron into the conduction band with accompanying photoconductivity.

Traps are characteristic of defects in the host crystal. Differences in impurity may change the relative distribution of traps of different depths to some extent, but not the trap depths themselves, except, as in the case of high proportions of Mn, when crystal spacings are altered.

Optical stimulation of trapped electrons with visible light raises the electrons from traps into the conduction band. Evidence for this conclusion is that (1) a large proportion of the freed electrons return to centers with normal luminescence emission, (2) electrons raised from deep traps by optical stimulation are retrapped by empty shallow traps, and (3) the effectiveness of trap-emptying is independent of impurity or irradiating energy.

Retrapping occurs whenever the number of empty traps becomes appreciable. Cases are found both for retrapping by deep traps of electrons freed from shallow traps, as in the case of the glow curve experiment, and for retrapping by shallow traps of electrons freed from deep traps, as in the case of optical stimulation. The retrapping process involves a raising of electrons to the conduction band, and is not the result of simple transitions between trapping levels.

No direct evidence has been found with these phosphors for transitions directly from trapping levels to the filled band.

SUMMARY

A tentative energy-level diagram for the excitation and emission processes in ZnS phosphors at room temperature is given in Fig. 14 for ZnS, ZnS:Ag, ZnS:Cu, and ZnS:Mn phosphors. Trapping levels are

included at the trap depths obtained by assuming a frequency-factor for trap-emptying of 10^{10} sec^{-1}. Energy levels for the impurity-associated excitation and emission processes of ZnS:Mn phosphors are included below the band diagrams for the other ZnS phosphors, because of the uncertainty of the nature or even the existence of a real energy level for the Mn in the forbidden gap.

The next logical extension of these measurements is the determination of the variation in electronic transitions with temperature.

The author wishes to express his thanks to Dr. R. E. Shrader for his assistance in obtaining measurements of absorption, to Dr. H. B. DeVore for his assistance in obtaining measurements of excitation, and to Dr. A. Rose for helpful discussions.

PHYSICAL REVIEW VOLUME 90, NUMBER 1 APRIL 1, 1953

The Zeeman Effect in the Spectra of Tellurium

J. B. GREEN* AND R. A. LORING†
Mendenhall Laboratory of Physics, Ohio State University, Columbus, Ohio
(Received December 3, 1952)

Over one hundred lines of tellurium have been investigated in fields of approximately 36 000 gauss; g values have been established for Te I, Te II, Te III, and from one line of Te IV. Classifications already published for many of these lines are in general agreement with the Zeeman patterns given in this report. Some previously indefinite assignments of j values are established.

THE experimental data on which this paper is based were taken during the summer of 1936 on the 21-foot concave grating spectrograph which was then in existence at the Mendenhall Laboratory of Physics.

The method of excitation of the tellurium was the same as that described for the excitation of the spectra of arsenic.[1,2]

TELLURIUM I

The first classification of the arc spectrum of tellurium was given by McLennan[3] and his co-workers and was later extended by Bartelt,[4] but no Zeeman effects have ever been published.

TABLE I. Zeeman effect for tellurium I.

Wavelength	Classification		Zeeman pattern	g_1	g_2
2383.27	$p^4\,{}^3P_0-6s({}^4S)\,{}^5S_1$		(0) 1.90	···	1.90
2385.78	${}^3P_1-$	${}^5S_1$	(0.40) 1.49 1.90	1.49	1.90
2530.73	${}^3P_1-$	${}^5S_2$	(0) (0.47) 1.96 2.47	1.49	1.98
2769.65	${}^1D_2-$	${}^3S_1$	0 0.94	?	?
2858.28			(0) 1.10		
3175.13	$^1S_0-5d({}^4S)\,{}^3D_1$		(0) 1.39	···	1.39

Six lines of this spectrum were observed, five classified and one unclassified. Table I gives the results, together with the g values garnered therefrom. The classifications are those of Bartelt.[4] The line λ2770 is a fuzzy triplet, and if we omit the usual designation for polarization (there is no information on polarization), the pattern is consistent with the g value, 1.03, calculated for the $^1D_2$ level on the basis of the structure of the p^4 configuration. The pattern of λ2858 yields no clue to its classification. In view of the g value for the $j=1$ level of λ3175, it seems inappropriate to assign LS classification to this level.

TABLE II. g values for tellurium II.

Even terms				Odd terms			
Level j	g value	Accuracy	Mack	Level j	g value	Accuracy	Mack
71 5/2	1.60	c	1.70	93°1/2	0.79	a	···
74 3/2	1.67	b	1.78	96°3/2	1.33	a	1.3
76 1/2	2.62_5	a	2.71	99°3/2	1.25_5	a	1.30
78 1/2	2.25	a	2.4	100°5/2	1.36_5	b	1.39
81 3/2	1.08	a	1.12	101°3/2	1.30	a	1.30
82 3/2	1.44	a	1.42	101°1/2	2.33_5	a	2.29
83 1/2	1.02	b	1.07	102°5/2	1.35	b	1.33
85 5/2	1.35 or 0.95	c	···	103°7/2	1.34	c	1.36
85 3/2	0.86	b	0.8	103°3/2	1.72	a	1.74
85'5/2	1.47	b	1.49	105°3/2	1.20	b	1.18
86 3/2	0.93	a	0.99	105°5/2	1.27_5	a	1.29
87 5/2	1.13	b	···	106°1/2	0.81	c	···
88 3/2	1.12	c	1.14	107°5/2	1.15	d	···
117 3/2	1.62	c	···	112°3/2	1.10	c	1.12
120 5/2	1.57	c	···	112°5/2	1.33	c	···
124 5/2	1.27	c	1.27				
121'3/2	0.89	c	1.24				
123 7/2	1.28	d	1.24				

* Now at Operations Research Office, The Johns Hopkins University, Baltimore, Maryland.
† Deceased.
[1] J. B. Green and W. M. Barrows, Jr., Phys. Rev. **47**, 131 (1935).
[2] A word of caution should be inserted here. Tellurium, after it comes in contact with the skin, is readily absorbed by the body. It is then eliminated very slowly by means of perspiration which gets on the clothing of the unfortunate victim, or by means of expiration. The result is an aura of concentrated garlic which seems to persist for several months after only one short exposure.
[3] J. C. McLennan *et al.*, Phil. Mag. **4**, 486 (1927).
[4] O. Bartelt, Z. Physik **88**, 522 (1934).

TABLE III. Zeeman effect for Te II.[a]

Wavelength	Pattern	Classification	g_1	g_1	Remarks
2711.61	(0) 0.97				
2858.29	(0) 1.10				
2868.86	(0) 0.98				
2895.49	(0) 1.10				
3017.51	(0) 1.50				
3047.00	(0) 1.21				
3073.43	(0) 0.85				
3256.81	(0) 1.12				
3329.25	(0) 1.90	$71_{5/2}-101^{\circ}{}_{3/2}$	1.65	(1.30)	
3362.83	(0) 1.01				
3406.77	(0) 1.13				
3442.22	(0) 1.70	$74_{3/2}-103^{\circ}{}_{3/2}$	1.70	1.70	
3456.84	(0.42) 1.47	$71_{5/2}-100^{\circ}{}_{5/2}$	1.56	1.38	
3497.93	(0) 1.10				
3521.07	(0) 1.94	$71_{5/2}-99^{\circ}{}_{3/2}$	1.65	(1.26)	
3617.55	(0.45) **1.29** 2.15	$76_{1/2}-103^{\circ}{}_{3/2}$	2.61	1.73	
3654.36	(0) 0.84				
3797.18	(···) (**0.57**) 1.10 **1.48** 1.88	$74_{3/2}-101^{\circ}{}_{3/2}$	1.67	1.29	
3918.50	(0.23) 0.99	$86_{3/2}-112^{\circ}{}_{3/2}$	0.91	1.07	
3936.21	(0.39) 1.88	$1/2\rightarrow 1/2$	1.49	2.27	
3947.93	(0.47) ···	$\Delta j=0$			
3975.90	(0.46) 1.23	$87_{5/2}-112^{\circ}{}_{5/2}$	1.13	1.33	
4006.50	looks like $5/2\rightarrow 3/2$	$(71_{5/2}-96^{\circ}{}_{3/2})$?	1.77	1.62?	Inconsistent pattern
4011.68	(0.66) ··· **1.96**	$76_{1/2}-101^{\circ}{}_{3/2}$	2.64	1.32	
4048.89	(···) (0.67) 1.48 1.89	$74_{3/2}-99^{\circ}{}_{3/2}$	1.69	1.26	
4169.77	(0) 0.93				
4261.08	(0) 1.12	$93^{\circ}{}_{1/2}-117_{3/2}$			Inconsistent pattern
4364.02	(0.45) very fuzzy	$85_{5/2}-107^{\circ}{}_{5/2}$	1.35 0.95	(1.15)	
4434.96	(0) 0.93	$83_{1/2}-106^{\circ}{}_{1/2}$	(1.02)	0.84	
4478.33	(0) 1.31	$102^{\circ}{}_{5/2}-124_{5/2}$	(1.35)	1.27	
4557.84	(0.54) 1.09	$99^{\circ}{}_{3/2}-121'{}_{3/2}$	1.29	0.89	
4602.57	(0) 0.92				
4641.19	(0.34) **1.40** 2.00 looks like $1/2\rightarrow 3/2$	$(103^{\circ}{}_{7/2}-124_{5/2})$?	2.36	1.72	Improper classification?
4654.38	(0) 1.11				
4664.34	(0) 1.26				
4686.95	(0) 1.19	$102^{\circ}{}_{5/2}-123_{7/2}$	(1.35)	1.28	
4706.53	(0) 1.27				
4729.83	(0.63) 1.74	$78_{1/2}-99^{\circ}{}_{3/2}$	2.22	1.26	
4738.67	(0) 1.02				
4769.73	(0) 0.89	$85_{3/2}-106^{\circ}{}_{1/2}$	(0.86)	0.80	
4784.85	(···) (**0.47**) ··· **1.13** 1.42	$3/2\rightarrow 3/2$	1.27	0.99	
4831.30	(0) 1.09				
4842.88	(0) 1.39				
4864.10	(0) 1.14	$87_{5/2}-107^{\circ}{}_{5/2}$	[1.13]	1.15	
4866.22	(0) 1.14	$118'-97^{\circ}{}_{1/2}$			
4875.53	(0) 1.14	$100^{\circ}{}_{5/2}-120_{5/2}$			Inconsistent pattern
4885.22	(0) 1.07				
4893.58	(0) 1.47	$81_{3/2}-102^{\circ}{}_{5/2}$			(0) 1.55 calc
4894.94	(**0.21**) (0.63) ··· 1.09 1.48 **1.89**	$85_{3/2}-105^{\circ}{}_{5/2}$	0.86	1.27	
5000.87	(0.47) 1.37	$85'_{5/2}-105^{\circ}{}_{5/2}$	1.47	1.27	
5037.97	(0.66) 1.92	$76_{1/2}-96^{\circ}{}_{3/2}$	2.65	1.33	
5130.99	(0.14) **0.82** ···	$3/2\rightarrow 1/2$	0.97	1.25	
5133.23	[0.56]	$81_{3/2}-101^{\circ}{}_{1/2}$			Mixed polarization
5149.90	(0) 1.20				
5164.00	(0) 0.97	$86_{3/2}-106^{\circ}{}_{1/2}$	(0.93)	0.78	
5172.99	(0.27) 1.20	$81_{3/2}-101^{\circ}{}_{3/2}$	1.10	1.29	
5238.07	(0.45) ··· **2.15**	$74_{3/2}-93^{\circ}{}_{1/2}$	1.70	0.80	
5256.36	(0) 1.25				
5300.67	(0) 1.05				
5304.99	(0.69) 1.45	$3/2\rightarrow 3/2$	1.69	1.20	
5311.07	(**0.18**) (0.54) ··· 1.13 1.47 **1.80**	$86_{3/2}-105^{\circ}{}_{5/2}$	0.93	1.28	
5366.91	(0.45) **0.99** 1.87	$82_{3/2}-101^{\circ}{}_{1/2}$	1.44	2.34	
5410.41	(0.19) 1.38	$82_{3/2}-101^{\circ}{}_{3/2}$	1.44	1.31	
5449.82	(**0.16**) (0.40) **1.08** 1.32 ··· ···	$85'_{5/2}-103^{\circ}{}_{3/2}$	1.47	1.73	
5465.17	(0.45) (1.47)	$102^{\circ}{}_{5/2}-120_{5/2}$	1.37	1.57	
5479.13	(···) **0.41** (0.77) **1.07** 1.345	$86_{3/2}-105^{\circ}{}_{3/2}$	0.93	1.20	

TABLE III.—(*Continued*).

Wavelength	Pattern	Classification	g_1	g_2	Remarks
5488.07	(**0.15**) (0.44) 1.25 1.51 **1.80**	$81_{3/2}-100°_{5/2}$	1.07	1.36	
5576.40	(0) 1.07				
5618.47	(0.64) 1.69	$83_{1/2}-101°_{1/2}$	1.05	2.33	
5630.66	(0.52) 1.43	$99°_{3/2}-117_{3/2}$	1.24	1.62	
5649.30	(0.45) **0.87** 1.80	$78_{1/2}-96°_{3/2}$	2.24	1.33	
5651.51	(0.18) 1.17	$81_{3/2}-99°_{3/2}$	1.10	1.24	
5655.15	(0.92) 1.70	$76_{1/2}-93°_{1/2}$	2.62	0.79	
5666.26	(0.16) 1.17 **1.45**	$83_{1/2}-101°_{3/2}$	0.99	1.29	
5708.07	(0) 1.19	$85'_{5/2}-103°_{7/2}$	(1.45_6)	1.34	
5741.66	(0) 1.41				
5755.87	(0) 1.36	$82_{3/2}-100°_{5/2}$			(0) 1.31 calc
5765.25	(0) 1.12				
5851.09	(0.14) 1.21	3/2→3/2	1.16	1.26	
5936.21	(0.27) 1.34	$82_{3/2}-99°_{3/2}$	1.44	1.24	
5972.64	(0) 1.44				
5974.70	(0.33) 1.40	$85'_{5/2}-102°_{5/2}$	1.47	1.33	
5993.94	(0.42) 0.88	$120_{5/2}-103°_{3/2}$			
6014.64	(0) 1.41				
6230.80	(0) 1.16	$88_{3/2}-105°_{3/2}$	1.12	(1.20)	
6245.61	(0) 1.34	$83_{1/2}-99°_{3/2}$			(0) 1.315 calc
6437.06	(0.75) 1.53	$78_{1/2}-93°_{1/2}$	2.28	0.79	

[a] Boldface numbers denote the strongest components.

TELLURIUM II

Wavelengths of tellurium II lines have been published by Bloch and Bloch,[5] and a classification has been presented by Rao and Sastry,[6] but the classifications given for several lines are not consistent with the Zeeman effect data given in this paper. More recently, Mack and his co-workers[7] have given a more complete classification which fits the observed Zeeman patterns in most cases. While most of the g values in Table II are in general agreement with those given by Mack, there are some significant differences and some additions. The j values of 93° and 112°3/2, 5/2 are definitely established as 1/2 and 5/2, respectively.

Table III is a summary of those lines attributed by Bloch and Bloch[5] to Te II whose Zeeman patterns were measured. Classifications are those of Mack.[7] Table II is a summary of the g values derived from Table III.

TABLE IV. Zeeman effect for tellurium III.

Wavelength	Classification	Zeeman pattern	g_1	g_2
5537.87	$6s\ ^1P_1 - 6p\ ^3P_0$	(0) 1.00	1.00	···
5326.80	$5d\ ^3D_3 - 6p\ ^3P_2$	(0) 1.28	1.35	(1.43)
4876.63	$5d\ ^3P_1 - 6p\ ^3S_1$	(0) 1.14	(1.26)	1.02
4783.30	$6s\ ^3P_1 - 6p\ ^1P_1$	[0.69] 1.37	1.37	(0.76)
4725.69	$6s\ ^3P_0 - 6p\ ^1P_1$	(0) 0.76	···	0.76
4355.70	$5d\ ^3P_2 - 6p\ ^3P_2$	(0.14) 1.39	1.35	1.43
4302.12	$5d\ ^3P_2 - 6p\ ^3D_3$	(0) 1.22	(1.34)	1.28
4122.80	$6s\ ^3P_2 - 6p\ ^3P_2$	(0) 1.36	1.28	(1.43)
4074.88	$6s\ ^3P_2 - 6p\ ^3D_3$	(0) 1.28	1.29	(1.28)
4062.01	$6s\ ^3P_1 - 6p\ ^3D_2$	(0) 1.05	(1.37)	1.16
4054.89	$6s\ ^3P_0 - 6p\ ^3D_1$	(0) 1.24	···	1.24
3984.42	$5d\ ^3P_2 - 6p\ ^3P_1$	(0) (0.42) **0.91** 1.34	1.34	1.76
3968.42	$5d\ ^3P_1 - 6p\ ^1D_2$	(0) 1.08	1.26	(1.14)
3841.60	$5d\ ^3F_3 - 6p\ ^3D_2$	(0) 0.97	1.07	(1.16)
3550.64	$5p^3\ ^1D_2 - 6p\ ^1P_1$	(0) (0.54) ··· ··· **1.67**	1.13	0.59
3474.67	$6s\ ^1P_1 - 6p\ ^1D_2$	(0) 1.21	(1.00)	1.14
3455.59	$6p\ ^3P_0 - 6d\ ^3P_1$	(0) 1.43	···	1.43

TELLURIUM III

Seventeen lines of Te III, classified by Krishnamurty and Rao[8] and Rao,[9] were measured. These are listed in Table IV. The classification given by Krishnamurty[10] for the line λ3984 is favored by the Zeeman effect. The classification given for λ4876 is questionable. The pattern should probably have been resolvable with the calculated g values. Parentheses indicate g values assumed from measurements of other lines.

TELLURIUM IV

Only one line classified by Rao[9] as belonging to Te IV was found on our plates. This line is λ3585.27, $^2S_{\frac{1}{2}} \rightarrow {}^2P_{\frac{1}{2}}$, (0.68) 1.34. The classification is in agreement with the Zeeman pattern.

[5] L. Bloch and E. Bloch, Ann. phys. **13** 233 (1930).
[6] K. R. Rao and M. G. Sastry, Indian J. Phys. **14**, 423 (1940).
[7] Mack, Murakawa, Ross, Pick, and van den Bosch, Phys. Rev. **83**, 654 (1951).
[8] S. G. Krishnamurty and K. R. Rao, Proc. Roy. Soc. (London) **A158**, 562 (1937).
[9] K. R. Rao, Proc. Roy. Soc. (London) **A133**, 220 (1931).
[10] S. G. Krishnamurty, Proc. Roy. Soc. (London) **A151**, 178 (1935).

Effects of Departures from the Single Particle Model on Nuclear Magnetic Moments*

A. DE-SHALIT†
Palmer Physical Laboratory, Princeton University, Princeton, New Jersey
(Received June 23, 1952; revised manuscript received December 9, 1952)

Departures from the single particle model (SPM) are considered, in which the SPM wave function is mixed with others representing states for which the core no longer has zero angular momentum. It is found that under certain restrictions an experimentally established relation exists between the deviations of odd-N nuclei from the Schmidt lines and those of odd-Z nuclei.

INTRODUCTION

IT was observed long ago that magnetic moments of odd-A nuclei, when divided into two groups according to whether Z or N is odd, show a striking regularity. Schmidt[1] has pointed out that this regularity can be approximately predicted on the basis of a model which assumes that for odd-A nuclei the magnetic moment is due to one single nucleon only, the rest of the nucleus being so coupled as to give a vanishing total magnetic moment.

Recent developments in the theory of nuclear structure have given further support to the original idea of Schmidt. The big pairing energy[2] which tends to couple pairs of equivalent nucleons to a resultant angular momentum zero lends strong support to the assumption that the ground state is formed by coupling the odd nucleon to the spherically symmetric core. The regularities found among the nuclear spins of the ground states also support this interpretation.

The Schmidt lines on which the magnetic moments should lie when plotted against the nuclear spins represent, however, only an approximation to the experimental data. As is well known, nearly all magnetic moments deviate from them, in some cases quite considerably. These deviations, however, show some regularities which suggest that they should be considered more closely. Most important is the fact that, with very few exceptions among the lightest nuclei, all magnetic moments lie between the Schmidt lines. Thus any attempt to explain the deviation should at least agree with this qualitative observation.

Further, on the above Schmidt diagram "forbidden zones" are observed, both for odd-Z and odd-N nuclei, lying more or less midway between the two Schmidt lines and separating the two groups of magnetic moments which correspond to $j=l+\frac{1}{2}$ and $j=l-\frac{1}{2}$. It should be noted in this connection that the apparent appearance of this forbidden region in the case of odd-N nuclei may very well be due to experimental difficulties. In fact, in this case only small magnetic moments are covered by the forbidden zone (see Fig. 2), and as an odd-N nucleus is usually a comparatively low abundant isotope among many abundant even-even isotopes of the same element, its magnetic moment, if small, can easily escape observation.

Other regularities concern the relative deviation of related nuclei. Thus in the case of nuclei differing by two neutrons or two protons and having the same total and orbital angular momenta—the heavier one almost always lies nearer to the Schmidt line.[3,4] Also the deviations of odd-Z nuclei are bigger than those of odd-N' nuclei if $Z=N'$.

Many attempts have been made to explain the deviations of magnetic moments from the Schmidt lines.[4] The present note is concerned with the extent to which simple departures from the single particle model may explain the observed regularities in the deviations.

THE CORE EFFECTS

Let us assume that there are n nucleons involved in the formation of the ground state under consideration and that each of them has an angular momentum $\mathbf{j}_k$ (we confine ourselves to jj coupling), and magnetic dipole $\boldsymbol{\mu}_k=g_k\mathbf{j}_k$. The total magnetic dipole will then be

$$\boldsymbol{\mu}=\sum\boldsymbol{\mu}_k=\sum g_k\mathbf{j}_k.$$

It is easily verified that $\boldsymbol{\mu}$ satisfies the following commutation relations with $\mathbf{J}=\sum\mathbf{j}_k$:

$$[\mu_x, J_x]=0, \quad [\mu_x, J_y]=i\hbar\mu_z, \quad [\mu_x, J_z]=-i\hbar\mu_y, \quad \text{etc.},$$

and therefore the average value of $\boldsymbol{\mu}$ in the state $(j_1, j_2, \cdots, j_n, J, M)$ characterized by the eigenvalues of $j_1^2, j_2^2, \cdots, j_n^2, J^2$ and J_z is

$$\langle\boldsymbol{\mu}\rangle=\langle\mathbf{J}\rangle\frac{1}{J(J+1)}\sum g_k\langle(\mathbf{j}_k\cdot\mathbf{J})\rangle,$$

or, in terms of the total g factor,

$$g=\frac{1}{J(J+1)}\sum g_k\,\langle(\mathbf{j}_k\cdot\mathbf{J})\rangle. \tag{1}$$

This is the well-known Landé formula, which in the

* This work was supported by the U. S. Atomic Energy Commission and the Higgins Scientific Trust Fund.
† Now at the Physics Department, Massachusetts Institute of Technology, Cambridge, Massachusetts.
[1] T. Schmidt, Z. Physik **106**, 358 (1937).
[2] M. Mayer, Phys. Rev. **78**, 16 (1950).
[3] A. de-Shalit, Phys. Rev. **80**, 103 (1950).
[4] A. Russek and L. Spruch, Phys. Rev **87**, 1111 (1952).

TABLE I. A comparison of deviations of similar odd-Z and odd-N nuclei from the Schmidt limits.

Odd-Z nucleus	μ	Δg_P	Odd nucleon state	Odd-N nucleus	μ	Δg_N	$\Delta g_P : \Delta g_N$
$_5B^{11}$	2.6886	1.104	$p_{3/2}$	$_4Be_7^5$	−1.1776	0.7359	1.50
$_{13}Al_{14}^{27}$	3.639	1.153	$d_{5/2}$	$_{12}Mg_{13}^{25}$	−0.96	0.95	1.21
$_{17}Cl_{18}^{35}$	0.8210	0.697	$d_{3/2}$	$_{16}S_{17}^{33}$	0.64292	0.5052	1.38
$_{17}Cl_{20}^{37}$	0.683	0.559	$d_{3/2}$	$_{16}S_{17}^{33}$	0.64292	0.5052	1.11
$_{37}Rb_{48}^{85}$	1.349	0.487	$f_{5/2}$	$_{30}Zn_{37}^{67}$	0.90	0.46	1.05
$_{49}In_{64}^{113}$	5.460	1.333	$g_{9/2}$	$_{38}Sr_{49}^{87}$	−1.10	0.81	1.64
$_{49}In_{66}^{115}$	5.475	1.318	$g_{9/2}$	$_{38}Sr_{49}^{87}$	−1.10	0.81	1.62
$_{51}Sb_{70}^{121}$	3.70	1.09	$d_{5/2}$	$_{40}Zr_{51}^{91}$	−1.10	0.81	1.35

case $n=2$ takes the form

$$g=\tfrac{1}{2}(g_1+g_2)+(g_1-g_2)\frac{j_1(j_1+1)-j_2(j_2+1)}{2J(J+1)}. \quad (1a)$$

One also sees from this formula that if the g factors of all the nucleons involved are equal to each other, they are also equal to the g factor of the combined angular momentum. In particular, the g factor of any state of equivalent nucleons is equal to that of the correspond-single particle state.

The evaluation of the scalar products $(\mathbf{j}_k\cdot\mathbf{J})$ in (1) for $n>2$ is generally impossible without further assumptions on the way in which the angular momenta are coupled. In a final form of the theory such "assumptions", or "coupling schemes" as they are called, should result from the type and form of the forces between the nucleons, but with the present state of the theory of nuclear forces this can hardly be expected to yield reasonable results.

The experimental data of nuclear spectroscopy seem to indicate that one should first couple among themselves the angular momenta of the protons and the neutrons separately, and the two resulting angular momenta should then be coupled to give the total nuclear spin. This suggests that in introducing departures from the SPM, we do so first for the odd group of particles in the nucleus, leaving the even group in its state of spherical symmetry. Thus the g_k's in Eq. (1) will all refer to nucleons of the same charge character. Now the g factor of a single nucleon can be written in the form,

$$g_k=g_l+(g_s-g_l)\epsilon_k/(2k+1),\ (\epsilon_k=\pm1 \text{ for } j_k=l_k\pm\tfrac{1}{2}), \quad (2)$$

where g_l and g_s are the orbital and spin g factors, respectively, and depend only on the charge of the nucleon. (For protons $g_l=1$, $g_s\approx5.6$; for neutrons $g_l=0$, $g_s\approx-3.8$.) Introducing (2) into (1) we now obtain:

$$g=g_l+(g_s-g_l)\frac{1}{J(J+1)}\sum\frac{\epsilon_k}{2l_k+1}\langle(\mathbf{j}_k\cdot\mathbf{J})\rangle. \quad (3)$$

As the Schmidt value of the g factor, g_0, is given by a formula similar to (2), we see that the deviation from the Schmidt line for the state considered will be

$$\Delta g=g-g_0=(g_s-g_l)\left\{\frac{1}{J(J+1)}\sum\frac{\epsilon_k}{2l_k+1}\times\langle(\mathbf{j}_k\cdot\mathbf{J})\rangle-\frac{\epsilon_0}{2l_0+1}\right\}; \quad (4)$$

($j_0=J$ is the angular momentum of the odd nucleon).

In Eq. (4) we have separated the two factors which influence the magnetic moment of a certain combination of angular momenta, namely, the electromagnetic properties of the nucleons involved and the way in which the configuration is constructed from its nucleons' angular momenta. We might expect that the latter will be the same whether the odd group consists of protons

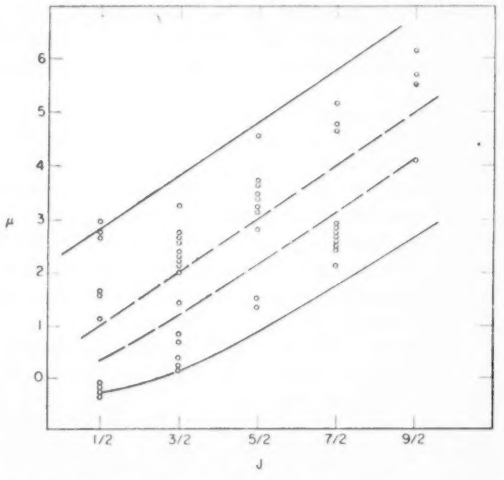

FIG. 1. Magnetic moments (in nuclear magnetons) of odd-Z nuclei plotted against nuclear spin. Full lines are the Schmidt limits; broken lines are limits of the forbidden-zone (taken to be Dirac lines in this case).

or of neutrons (provided, of course, their number and angular momenta are the same). The electromagnetic factor (g_s-g_l) is, however, different. We therefore get for the ratio of the deviations of such similar nuclei from the Schmidt lines the value,

$$|\Delta g_P|/|\Delta g_N|=|g_s^P-g_l^P|/|g_s^N-g_l^N|\approx1.20.\ddagger$$

Thus the bigger deviation of odd-Z nuclei from the Schmidt lines is correctly predicted, as can be seen from Table I.

Another way to check the validity of this approximation is the following: As was mentioned in the introduction, forbidden zones are observed both for odd-Z

‡ *Note added in proof:*—It was pointed out to me by Professor E. Feenberg that this result remains valid for any coupling scheme provided one assumes, as is done here, that the contributions to the angular momentum come only from nucleons of the same charge as that of the odd one.

nuclei as well as for odd-N nuclei; if the above approximation is a good one, the widths of the allowed zones should be in the ratio of 1.20 to one. Figure 1 shows the Schmidt diagram for odd-Z nuclei; the limits of the forbidden zones are taken to be the Dirac lines.[5] Figure 2 shows the Schmidt diagram for odd-N nuclei; the limits of the forbidden zone in this case were obtained from those of the proton case by the above procedure. The agreement is strikingly good.

Equation (4) as it stands does not determine the sign of the deviation. To arrive at this we should make further assumptions on the way in which the real wave function of the ground state is different from that of the SPM. A suggestion may be based on the following consideration.

If the single particle approximation is valid, the bare core of an odd nucleus A should resemble very much the even nucleus A-1. We know that the ground state of an even nucleus has angular momentum zero, positive

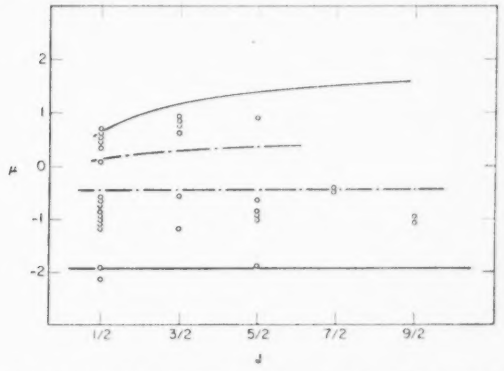

FIG. 2. Magnetic moments of odd-N nuclei plotted against nuclear spin. Full lines are the Schmidt limits; broken lines are limits of the forbidden zone deduced from the corresponding limits in Fig. 1.

parity, and that the first excited state nearly always has angular momentum 2, positive parity, indicating that it is very probably an excited state of a configuration of an even number of equivalent nucleons from the core. It is thus natural to assume that the single-particle wave function of the ground state is mixed with the wave function of that state in which the odd nucleon combines with the first excited state of the core. The fact that both the ground state as well as the first excited state of the core have the same parity makes such a mixture possible.

Using the Landé formula (1a) for evaluating the g factor of the state in which the core has angular momentum j_c, and the total angular momentum J is equal to that of the odd particle j_o we obtain

$$g=g_o-(g_o-g_c)\frac{j_c(j_c+1)}{j_o(j_o+1)}. \qquad (5)$$

[5] F. Bloch, Phys. Rev. **83**, 839 (1951); A. de-Shalit, Helv. Phys. Acta **24**, 296 (1951).

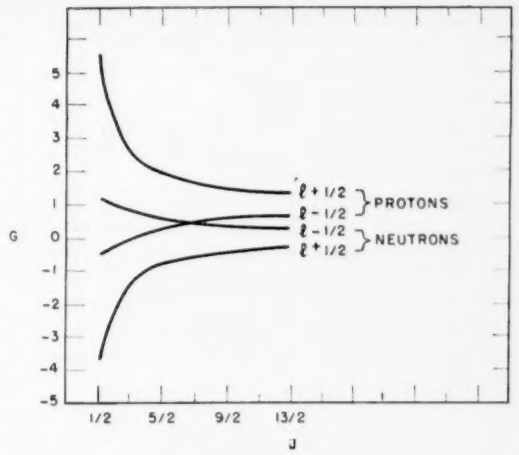

FIG. 3. g factors of single nucleons as a function of total angular momentum.

As the excited state of the core is assumed to be formed by equivalent nucleons, g_c should be set equal to the g factor of one of these nucleons. Figure 3 shows the dependence of the g factor of a single nucleon on its total angular momentum. An inspection of this graph immediately shows that Eq. (5) will give the observed direction of deviation from the Schmidt lines provided the many-particles configurations are formed by combining an $l\pm\frac{1}{2}$ odd nucleon with excited states of either $l'\mp\frac{1}{2}$ pairs or with excited $l''\pm\frac{1}{2}$ pairs where $l''>l$. (By $l\pm\frac{1}{2}$ particle we mean a particle in a state of total angular momentum j and parity $(-1)^{j\mp\frac{1}{2}}$, etc.)

It is evident that if one wants to explain the deviations of magnetic moments from the Schmidt lines by means of mixing single-particle states with many-particle states, some sort of a selection rule should be invented to take account of the fact that the experimental points always lie between the Schmidt lines, and the above restriction represents one possibility. It is interesting to note, however, that this rule seems to be quite reasonable when we inspect the detailed structure of the shells as proposed by Mayer[2] and by Jensen.[6] In fact one may expect that the main contribution to the deviation would come from the "last" pair of nucleons added to the core. Very often this last pair is formed in a state of high angular momentum ($g_{9/2}$, $h_{11/2}$, $i_{13/2}$, etc.) making the situation in favor of the second alternative of the above rule. One also finds that in most of the cases $l\pm\frac{1}{2}$ states have $l'\mp\frac{1}{2}$ states as their neighbors, in which case the first alternative of the rule applies.

DISCUSSION

We have completely ignored the contribution of exchange currents to the observed magnetic moments. This is certainly unjustified.[4] It is, however, still

[6] Haxel, Jensen, and Suess, Phys. Rev. **75**, 1766 (1949).

questionable how important their contribution is. On the one hand, the fact that the proton forbidden zone has as its limits the Dirac lines strongly supports the use of a quenching mechanism to explain the deviations from the Schmidt lines,[7] but the occurrence of a forbidden zone for the neutrons raises the question whether this coincidence is not accidental.

It was once suggested that the direction of deviation of the magnetic moments be explained by a mixture of an $l\pm\frac{1}{2}$ state with an $l'\mp\frac{1}{2}$ one. This interpretation has been rejected because of the difference in parity of these two states. The present note somewhat revives these ideas, the parity difficulty being overcome by involving pairs in the admixture. In this respect it is similar to the somewhat less explicit work of Davidson.[8] Although some arguments were given in favor of our rule for the formation of the many-particle configuration stated above, this rule should still be considered as somewhat arbitrary.

The case of nuclei with nuclear spin $\frac{1}{2}$ deserves special mention. Only such a state of the core can affect its magnetic moment which has a total angular momentum 1. States of that angular momentum are rather rare among the known spectra of even-even nuclei and probably need a comparatively higher energy to be excited. There is, however, no indication of a better agreement with the Schmidt limits for spin $\frac{1}{2}$ nuclei. The question is thus left open.

[7] H. Miyazawa, Prog. Theoret. Phys. **6**, 801 (1951).

[8] J. P. Davidson, Phys. Rev. **85**, 432 (1952).

PHYSICAL REVIEW VOLUME 90, NUMBER 1 APRIL 1, 1953

A Search for Penetrating Showers from Hydrogen at Sea Level Using a Cloud Chamber*

ALBERT B. WEAVER†
Department of Physics, University of Chicago, Chicago, Illinois
(Received December 16, 1952)

The extent to which multiple production of π-mesons takes place in local sea-level penetrating showers was studied with a counter controlled cloud chamber in a magnetic field. The rates at which penetrating showers occur under carbon, aluminum, and lead were determined and a search was made for them under liquid hydrogen. In a total operating time of 626 hours with an average thickness of 2.28 g/cm² of liquid hydrogen above the chamber, no penetrating showers were found which could have originated in the hydrogen. On the basis of the rates at which such showers occur in heavier materials and the number of them formed in the material of the Dewar while operating with hydrogen, one would have expected to detect a minimum of 6 showers from the hydrogen if the cross section for the production of penetrating showers were the geometric area of the nucleus (taken as 6×10^{-26} cm² for hydrogen). It can then be concluded that the majority of sea-level local penetrating showers detected below heavy materials by an apparatus of this kind can be attributed mainly to plural production.

From momentum measurements in the magnetic field, the minimum value which can be assigned to the momentum of the incident nucleons which causes the average penetrating shower detected with this apparatus was estimated at 6 Bev/c. It follows that the multiple production of charged mesons in a single nucleon-proton collision at about 6 Bev probably does not occur in more than 15 percent of the cases.

The ratios of the rates at which penetrating showers were detected under C, Al, and Pb were proportional to the geometric area of the nuclei within statistical limits.

An event found in the hydrogen which is very similar in appearance to the μ-meson interaction first observed by Braddick and Hensby is discussed. A photograph of a nuclear collision in lead is described in which very little energy is transferred to the lead nucleus although the incident particle has a momentum estimated to be 40 Bev/c.

I. INTRODUCTION

ONE of the more direct ways to study high energy nuclear interactions of fundamental particles is by means of cloud-chamber observations on local penetrating showers. There have been many cloud-chamber studies of these events at various altitudes and issuing from a wide variety of materials.[1–11] At sea level, practically all such showers are believed to be caused by the collision of very high energy nucleons with atomic nuclei.[12] The resulting penetrating showers have a complex character in general which Janossy suggested is due to successive collisions in the same nucleus (so-called plural production of mesons).[13] A large positive excess among the penetrating particles in local sea-level penetrating showers has been established[8,14] which is interpreted to indicate the presence

* Assisted by the joint program of the U. S. Office of Naval Research and the U. S. Atomic Energy Commission.

† Now at the University of Washington, Seattle, Washington.

[1] Watase, Miyake, and Suga (private communication to Marcel Schein).

[2] W. B. Fretter, Phys. Rev. **80**, 921 (1950).

[3] Chang, del Castillo, and Grodzins, Phys. Rev. **84**, 582 (1951).

[4] B. P. Gregory and J. H. Tinlot, Phys. Rev. **81**, 667 (1951).

[5] J. R. Green, Phys. Rev. **80**, 832 (1950).

[6] A. J. Hartzler, Phys. Rev. **82**, 359 (1951).

[7] M. Gottlieb, Phys. Rev. **82**, 349 (1951).

[8] K. H. Barker and C. C. Butler, Proc. Phys. Soc. (London) **A64**, 4 (1951).

[9] W. W. Brown and A. S. McKay, Phys. Rev. **77**, 342 (1950).

[10] Froehlich, Harth, and Sitte, Phys. Rev. **87**, 504 (1952).

[11] Walker, Duller, and Sorrels, Phys. Rev. **86**, 865 (1952).

[12] G. D. Rochester, Proc. Roy. Soc. (London) **A187**, 464 (1946).

[13] L. Janossy, Phys. Rev. **64**, 345 (1943).

[14] Butler, Rosser, and Barker, Proc. Phys. Soc. (London) **A63**, 145 (1950).

of a large proportion of protons among the secondaries. This seems to show that at the energies involved in the majority of these showers, most of them are due to plural processes.

Heisenberg has suggested that more than one meson can be created in a single nucleon-nucleon interaction,[15] and considerable evidence for the existence of multiple production has been obtained at extremely high energies in photographic emulsions.[16] Recently, a penetrating shower with four secondaries has been found in hydrogen in a high pressure cloud chamber,[1] and penetrating showers have been observed from lithium[2] and beryllium[3] in multiple plate cloud chambers. It is not clear, however, that these showers occurred at the same energies and with the same frequency as do the majority of sea-level penetrating showers in heavier elements.

It seems important, then, to study the cross section for penetrating showers in nucleon-nucleon collisions by using a hydrogen target. If multiple production is probable at the energies at which the main fraction of sea-level penetrating showers occur, it would be expected that penetrating showers would also occur in hydrogen with comparable frequency. On the other hand, if such penetrating showers in heavy elements are due to the ejection of high energy nucleons and the plural production of mesons, the cross section for showers in hydrogen should be extremely small. If both plural and multiple production play a role at these energies, showers should occur in hydrogen but their frequency and character should be radically different than in heavier elements since in hydrogen plural production of mesons could not occur and since at most two protons could be emitted.

For this purpose an experiment was carried out in which a Dewar containing liquid hydrogen was mounted above a counter controlled cloud chamber. To make a comparison, lead, aluminum, and carbon were also used as targets for the production of penetrating showers.

Any particle which could traverse a two-centimeter lead plate mounted in the center of the cloud chamber without multiplication or scattering through an angle greater than 5° was classed as a penetrating particle. If the momentum of the particle could be determined to be over 1 Bev/c, the requirement that the scattering be under 5° was dropped. A penetrating shower was defined as at least two penetrating particles accompanied either by one or more heavily ionizing particles or by a cascade component or both. This is the criterion used by Butler, Rosser, and Barker with a somewhat similar cloud chamber operated under a lead target.[14]

[15] W. Heisenberg, Z. Physik **101**, 533 (1936).

[16] Lord, Fainberg, and Schein, Phys. Rev. **81**, 313 (1951), **80**, 970 (1950); Kaplon, Peters, and Ritson, Phys. Rev. **85**, 900 (1952); Camerini, Fowler, Lock, and Muirhead, Phil. Mag. **41**, 413 (1950); E. Pickup and L. Voyvodic, Phys. Rev. **82**, 265 (1951); M. Teucher, Naturwiss. **37**, 260 (1950); Hopper, Biswas, and Derby, Phys. Rev. **84**, 457 (1951); L. S. Osborne, Phys. Rev. **81**, 239 (1951); W. Heisenberg, Naturwiss. **39**, 69 (1952).

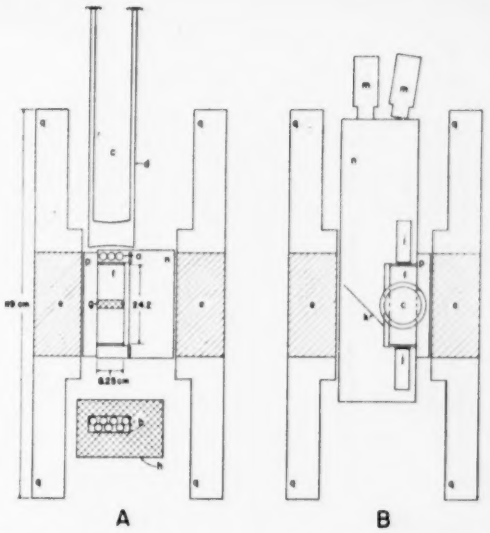

FIG. 1. Side view (A) and top view (B) of the apparatus with the hydrogen Dewar in place and using control 2. a, upper counter tray; b, lower tray; c, hydrogen; d, hydrogen Dewar; e, magnet pole-pieces; f, cloud chamber; g, lead plate; h, lead shield; j, flash lamp housings; k, mirror; m, cameras; n, light-tight aluminum box; p, back chamber of the cloud chamber; q, magnet coil housings.

Any event which could be recognized as part of an extensive shower was not considered. It should be added that the counter control imposed another condition on the showers which were studied—that at least one particle issuing from the target block was able to penetrate 56 g/cm² of lead (h, Fig. 1). This required a minimum momentum of 620 Mev/c for a proton and 150 Mev/c for a meson.

The cloud chamber was placed in a large electromagnet, but since the heat exchanger was shared with a small cyclotron, the magnet could not be operated part of the time and a number of pictures were obtained without a magnetic field.

II. THE APPARATUS

The arrangement of the apparatus used in this work is shown schematically in Fig. 1.

The electromagnet had pole faces (e in Fig. 1) 30.5 cm in diameter and was operated with an air gap of 28 cm during part of the experiment and of 33 cm during the remainder. It was oil cooled and was capable of producing a field of 9270 oersteds with the smaller gap and of 8500 with the larger, without a temperature rise sufficient to disturb the operation of the cloud chamber. At a distance of 5 cm from the axis of the cloud chamber, the field was 1.8 percent lower. By examining the negatives of cloud-chamber pictures under a low power microscope, track curvatures could be determined up to about 16 meters on most tracks, which corresponded to a momentum of about 4 Bev/c. On very

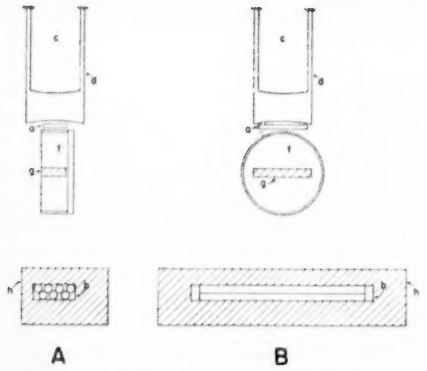

FIG. 2. Side view (*A*) and front view (*B*), of the counter control. *a*, tray *a*; *b*, tray *b*; *c*, hydrogen; *d*, Dewar; *f*, cloud chamber; *g*, lead plate; *h*, lead shield.

sharp long tracks, curvatures could be measured to about 30 meters, corresponding to about 8 Bev/*c*.

The chamber (*f* in Fig. 1) was cylindrical in shape with a diameter of 25 cm and a useful depth of 6 cm. A lead plate 2 cm thick (*g*) was mounted in the center of the chamber. A mirror (*k*) was mounted at an angle of 45° with the axis of the chamber and stereoscopic pictures were taken with the two cameras (*m*).

On the basis of the results obtained with Geiger counters[17] it was not anticipated that events in hydrogen would exhibit high multiplicities except at very high energies. For this reason, the counter control was designed to discriminate as little as possible against events in which few particles are present. Three counter arrangements were used which were approximately equally effective in the rate at which they produced pictures of penetrating showers. They will be designated as controls 1, 2, and 3, respectively.

In the arrangement of control 1, tray *a* of Fig. 2 consisted of 12 counters 1.2 cm in diameter with the axis of the counters parallel to that of the chamber. A tray of 7 counters 2.5 cm in diameter (tray *b*), shielded by lead (*h*) against electron showers, was placed below the chamber. A coincidence between a selected minimum number of counters in tray *a* and any counter in tray *b* tripped the chamber. The minimum number of counters in tray *a* required was controlled by the bias setting of a discriminator circuit so that it could be varied as desired. While using control 1, the required minimum was set at any 3, since this setting gave a higher ratio of operating time (the time during which the apparatus would respond to a coincidence) to dead time than a setting of 2. The dead time of the chamber after a count is 1 minute and the ratio of operating to dead time was 15:1. The lead shielding (*h*) around tray *b* (7.5 cm thick on the bottom, 4 cm thick on one side, and 10 cm thick elsewhere) was used to reduce the frequency of low energy air showers and local electron showers which actuated the chamber. The material in the magnet and the field of the magnet also tended to reduce the number of counts resulting from this type of activity.

Since no events emanating from the hydrogen were observed in 104 hours operating time with control 1, control 2 was adopted. In this arrangement, tray *a* (Fig. 2) consisted of 3 counters 2.5 cm in diameter, mounted with axis at right angles to the axis of the chamber. To make it possible to register only two particle events, any 2 of these in coincidence with any one counter of tray *b* was required to operate the chamber. To further reduce the control discrimination against low energy events, the amount of lead above tray *b* was changed to 5 cm. These measures reduced the ratio of operating time to dead time to about 9 to 1 and did not appreciably affect the rate at which penetrating showers were registered. The resolving time of the circuits was about 4 microseconds so that very few accidentals were expected, although only 3 counters in all were required to operate the chamber.

Control 3 was adopted to further reduce the distance

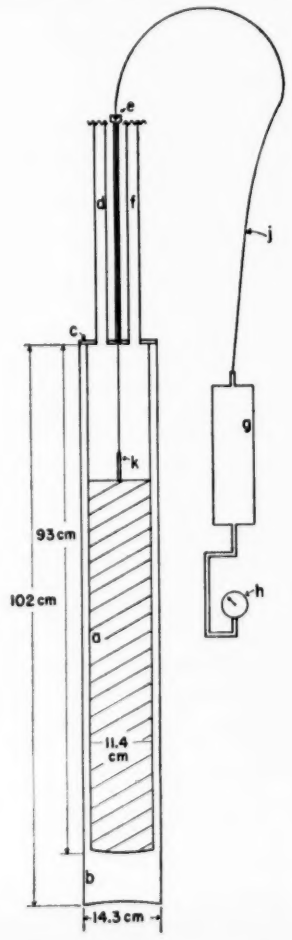

FIG. 3. Liquid hydrogen Dewar. *a*, liquid hydrogen; *b*, bottom evacuated space, containing carbon; *c*, Dewar cover; *d*, exhaust tube for the evaporating hydrogen; *f*, filling tube; *e*, gasket; *g*, hydrogen tank; *h*, pressure gauge; *j*, capillary tube; *k*, bulb.

[17] M. Vidale and M. Schein, Phys. Rev. **84**, 593 (1951).

between the Dewar and the chamber and to register more collimated events. Tray *a* in this case consisted of six 1.2-cm diameter counters mounted with axis perpendicular to the axis of the cloud chamber. Any two of them in coincidence with one in tray *b* would operate the chamber.

While operating with controls 1 and 2, the liquid hydrogen was contained in a cylindrical Dewar (Figs. 1 and 3) of 11.3-cm inside diameter and 91.4-cm inside height. While control 1 was used, this Dewar was placed inside a larger Dewar containing liquid nitrogen. When control 2 was adopted, the nitrogen Dewar was omitted in order to place the hydrogen as close as possible to the chamber. Dispensing with the liquid nitrogen considerably increased the evaporation rate of the hydrogen. The liquid hydrogen target remained over 2 g/cm² thick for 100 hours with the liquid nitrogen present and for only 25 hours without it. While operating with control 3, a Dewar of 15.2-cm inner diameter and 143.5-cm inner height was adopted in order to increase the solid angle subtended by the Dewar as seen from the cloud chamber.

The height of the hydrogen column was measured with a hydrogen thermometer as shown in Fig. 3. The bulb (*k*) inside the Dewar was connected by a flexible capillary tube (*j*) to a pressure gauge (*h*) and a tank (*g*) which acted as a hydrogen reservoir. The bulb could be lowered until it touched the surface of the liquid hydrogen by sliding the tube (*j*) through a Teflon gasket (*e*). At this point, the gauge registered a sharp decrease in pressure.

Because of the construction of the Dewars, the chamber, and the magnet, it was not possible to reduce the distance between the bottom of the hydrogen column and the top of the visible part of the chamber to less than 26.7 cm with control 1, 14 cm with control 2, or 11.3 cm with control 3. A large part of this distance was due to the fact that each of the Dewars was about 9 cm thick from the bottom of the inside shell to the base. This space was occupied by a copper reflector and a layer of about 2.2 g/cm² of carbon to adsorb residual gases in the evacuated space at low temperatures. A Dewar which largely eliminated this space was obtained but could not be used because of leaks.

When the carbon, aluminum, and lead were used as targets for generating penetrating showers, they could be placed somewhat closer to the chamber, 5 cm above using control 2 and 8.17 cm using control 1.

To determine the position of the tracks sufficiently accurately so that the point of origin of the showers above the chamber could be found, the negatives of the pictures were reprojected in the original cameras, and they were also studied with a low power microscope with a micrometer stage. The second method, while more tedious, proved to be more accurate. It was found by photographing thin wires and by measuring very energetic tracks that the distortion of the lenses was less than the uncertainty with which the center of a good track could be determined. The position of the smallest clusters of droplets along a sharp track could be measured to ± 1 micron on the negative, corresponding to about ± 10 microns in the position of the track in space. The distortions introduced by imperfections in the lenses were less than this. The positions of the tracks were measured relative to a centimeter scale in the front of the chamber. A wire in the back of the chamber served to check apparent distances. Corrections were made for the gas motion in the chamber by assuming that the motion of any small volume of the gas was parallel to the axis of the chamber by an amount of 8 percent (the expansion ratio) of its perpendicular distance from the front glass plate. Corrections were also made for the refraction of the front glass plate but these corrections were small.

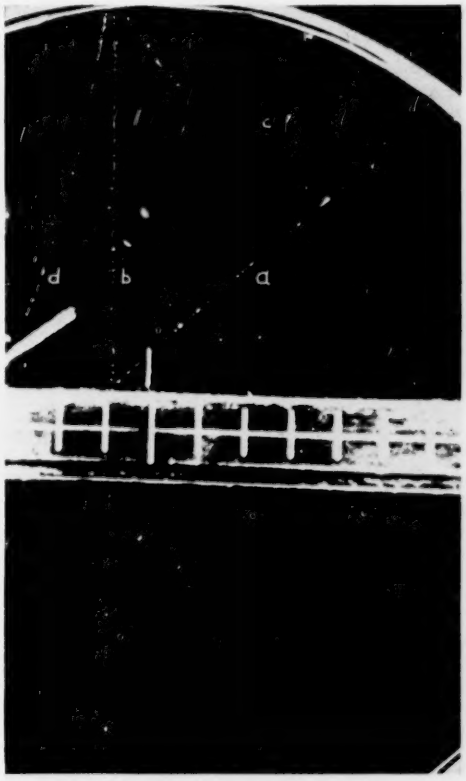

FIG. 4. Star formed in the lead plate of the chamber by a very high energy particle.

III. DISCUSSION OF EVENTS

Figure 4 is an unusual event in which a very energetic particle (track *b*) forms a star in the upper part of the lead plate but loses only a small fraction of its energy in doing so. Track *a* is about four times minimum ionization and its curvature is that of a positively charged particle of momentum 300 Mev/*c*. These facts

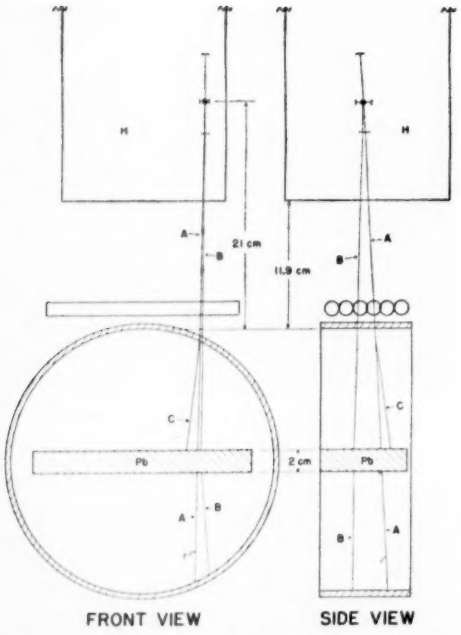

FIG. 5. Schematic drawing of an event in which two penetrating particles trace back to a point in the hydrogen. The estimated accuracy in the location of the junction point is indicated. An energetic δ-ray is visible from track A in the lower part of the chamber.

indicate that it is a proton. Although the star occurs in the well illuminated part of the chamber, no tracks other than a and b can be seen issuing from it. Track b is deviated 0.55° (in the plane of the picture) on traversing the lead. That this is the result of the star formation and is not due to small angle scattering[18] is evidenced by the fact that its radius of curvature under the lead is too large to measure which means the momentum is greater than 4 Bev/c. Track c is an electron, and the two tracks at d are positrons which appear to accompany track b. When the picture was taken, 110 g/cm^2 of lead was above the chamber and the cascade radiation was probably formed in this lead by b or possibly by other particles which do not appear in the picture.

If one assumes that the small energy transfer is due to the possibility that particle b only grazed the nucleus, imparting some momentum to a peripheral nucleon which then caused the star, the momentum of b can be found from the assumed energy of the star.[6] The minimum energy which could have been given to the star by track b is the energy of the visible proton, a, which is 44 Mev. The minimum momentum of b under this assumption is 31 Bev/c. A more probable momentum would be 45 Bev/c, corresponding to an assumed energy for the star of 90 Mev, which allows for neutral particles and fragments which do not escape from the lead.

It is very unlikely that track b is the result of an interaction in the 110 g/cm^2 of lead above the chamber since, if this were the case, a large penetrating shower would accompany it instead of the small amount of cascade radiation actually seen.

High energy collisions with small energy transfers have been observed in photographic emulsions[19] and in multiplate cloud chambers,[6] but they are rare.[6,7,11] The average number of penetrating tracks formed in gold by a 30-Bev primary is 7 and by a 60-Bev particle, 11.[6]

Figure 5 is a drawing of an event which took place in the hydrogen. The corresponding cloud chamber picture is shown in Fig. 6. It occurred while using control 3 and with no magnetic field. Tracks a and b trace to a point in the hydrogen 21 $^{+4.5}_{-3.0}$ cm above the visible part of the chamber. The three tracks are at minimum ionization. Track a is scattered through a projected angle of 0.3° in the 2-cm lead plate. If this deviation is due to multiple scattering, its most probable momentum is 6 Bev/c. Track c meets a at a point in the glass of the chamber and can be interpreted as a knock-on electron. It makes an angle of 10° with a which, if it were a knock-on, from conservation of momentum and energy, would correspond to a momentum of 30 Mev/c if a is a meson, or about 5 Mev/c if a is a proton of momentum 6 Bev/c. As would be expected for an electron in this energy range, it does not penetrate the lead plate.[20]

Track b makes an angle of 4.3±0.8° with a. It is scattered in the lead plate through a projected angle of 5.4±0.2° with its original direction. If this deviation were due to multiple scattering, the most probable momentum of b would be 300 Mev/c (or 590 Mev/c if b were the track of a proton, but in this case, the ionization rules out a proton of this low a momentum).

A number of pairs of penetrating particles which make an angle of a few degrees with each other has been seen during the course of this experiment. Most of them were apparently formed in the carbon or lead targets, but one has been found which traces back to the Dewar walls.

In cloud-chamber pictures taken underground, Braddick and Hensby and others[21] have found a number of penetrating pairs very similar to that described above. These investigators conclude that the initiating particle in the events which they have studied is a μ-meson, that the secondary is probably a μ- or π-meson

[18] J. G. Wilson, Proc. Roy. Soc. (London) **A174**, 73 (1940).

[19] Lord, Schein, and Vidale, Phys. Rev. **76**, 321 (1949).

[20] Niels Arley, *On the Theory of Stochastic Processes and their Application to the Theory of Cosmic Radiation* (G.E.C. Gads Forlag, Copenhagen, 1943; 2nd ed. John Wiley and Sons, Inc., New York, 1949); R. R. Wilson, Phys. Rev. **86**, 261 (1952).

[21] H. J. J. Braddick and G. S. Hensby, Nature **144**, 1012 (1939); Braddick, Nash, and Wolfendale, Phil. Mag. **42**, 1277 (1951); E. P. George and P. T. Trent, Nature **164**, 838 (1949); E. P. George (private communication).

of mean energy 1 Bev, and that the cross section for the process is about 5×10^{-29} cm^2/nucleon for lead and of the same order of magnitude for sandstone.[22] A cross section of this magnitude is estimated to be consistent with the observation of such an event in hydrogen during the operating time of this experiment.

If, however, one assumes that this event is not of the same type as those found by Braddick and Hensby, several alternative interpretations should be considered.

The first is elastic scattering of a meson or a proton on a proton in the hydrogen. From conservation of momentum and energy, the equation for the angle θ, between two particles in the laboratory system of reference after one has collided with the other, is

$$\cos\theta=(E_0-m_0c^2)(E_1-m_0c^2)/p_0p_1c^2.$$

E_0 is the energy after collision (including rest mass) of the particle originally at rest, m_0 is its mass, and p_0 its momentum after collision. The corresponding quantities for the incident particle are given the subscript 1. It is apparent from this equation that if, as in this case, m_0 is equal to or larger than the rest mass of the incoming particle, θ cannot be as small as 4.3° unless both particles are of extremely high energy, which is certainly not the case because of their scattering in the lead. The angles and energies are also inconsistent with the hypothesis that a and b are an electron pair, as is also apparent from the fact that both particles penetrate 2 cm of lead.

If we consider the possibility that track a is a μ-meson and b a knock-on electron, the relation between the angle, θ, between a and b and the momentum of b is

$$P_b=\frac{\cos\theta}{\sin^2\theta}\ \text{Mev}/c,$$

provided $\theta\geqslant4°$ and the momentum of the meson $\geqslant5$ Bev/c. This equation follows from the conservation of momentum and energy. Taking into account the probable uncertainty in θ due to the multiple scattering experienced by track b in the material (0.3 radiation length) between the point where a and b meet and the interior of the cloud chamber, the momentum of b is probably between 200 and 400 Mev/c. The cross section per atom for a knock-on of energy ϵE formed by a meson of energy E and spin $\frac{1}{2}$[23] is

$$\sigma(E,\epsilon)d\epsilon=1.6\times10^{-32}\frac{2\pi Z}{\alpha}\frac{\mu}{m}\frac{\mu c^2}{E}\frac{d\epsilon}{\epsilon^2}\left(1-\frac{\epsilon}{\epsilon_m}+\frac{\epsilon^2}{2}\right)\ \text{cm}^2,$$

$$E\leqslant500\ \text{Bev},$$

where Z is the charge of the atom struck, α the fine structure constant, μ the meson mass, m the electron mass, and ϵ_m the maximum fractional energy transfer possible,

$$\epsilon_m\sim E/(E+10),$$

if E is expressed in Bev. The cross section for producing an electron in the energy range w_1 to w_2 is then (if all energies are expressed in Bev):

$$\sigma(E,w_1,w_2)=2.76\times10^{-28}Z\left\{\left(\frac{1}{w_1}-\frac{1}{w_2}\right)-\frac{E+10}{\epsilon^2}\ln\frac{w_2}{w_1}+\frac{1}{2E^2}(w_2-w_1)\right\}\ \text{cm}^2,$$

$$E\leqslant500,\quad w_1<w_2\leqslant E^2/(E+10).$$

From this expression, the cross section for the production of a knock-on electron of more than 300-Mev energy by a 6-Bev μ-meson is 5.6×10^{-26} cm^2/hydrogen atom. Before this cross section is compared with that for the μ-meson interaction described by Braddick, however, it must be multiplied by the probability that an electron of about 300-Mev energy would traverse the lead plate without any interaction other than multiple scattering (which would account for the total scattering angle at this energy). The work of Arley

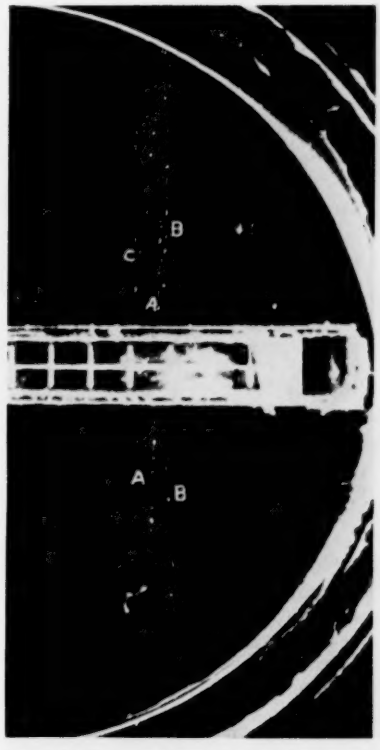

FIG. 6. Front camera view of event sketched in Fig. 5.

[22] According to recent counter experiments of Amaldi, Castagnoli, Gigli, and Sciuti, however, the cross section for this type of event is 6×10^{-30} cm^2/nucleon (private communication to Marcel Schein).

[23] H. C. Corben and J. Schwinger, Phys. Rev. **58**, 953 (1940); R. F. Christy and S. Kusaka, Phys. Rev. **59**, 416 (1941).

and of Wilson[20] shows that the probability of an electron of 300-Mev momentum appearing below the lead as a single particle is about 15 percent. The probability of the scattering angle being small must, however, be much lower than this. Neddermeyer and Anderson[24] using a platinum plate equivalent to 1.96 cm of lead in a cloud chamber found that the energy loss in the platinum was 80 to 100 percent in 14 out of 17 cases and was as low as 50 percent in only one case for particles whose energy was under 500 Mev and which were either accompanied by other particles on entering the chamber, or which produced other particles in the platinum. In the present instance, track *b* traverses a total of 4.2 radiation lengths so that the probability that it would undergo no relatively large scale energy losses if it is an electron might be expected to be about $1\frac{1}{2}$ percent ($e^{-4.2}$). It is concluded that the cross section for a knock-on which would have the appearance of Fig. 5 is about $0.015\times5.6\times10^{-28}=8\times10^{-30}$ cm^2/hydrogen atom.

It is also possible that the tracks in Fig. 5 issued from a nucleon-proton collision in which a single π-meson was produced. The probability that this is the case cannot be estimated without making some assumptions concerning the interactions. In Fermi's theory[25] the assumption is made that the probability of an allowable state is proportional to its statistical weight. An estimate was made under this assumption and the assumptions that at the energies involved here the total cross section for single meson production is geometric[26] and that the conservation of angular momentum does not greatly alter the angular distribution from that of a central collision. With these assumptions, it was found that the probability of a single meson production event in which two secondary charged particles are emitted within an angle as small as 4.3° is less than 5 percent of the probability of a μ-meson interaction of this appearance, assuming it occurred with the cross section given by Braddick. In this estimate, the nucleon spectrum was assumed to be twice the proton spectrum given by Mylroi and Wilson[27] since the number of neutron produced penetrating showers at sea level is approximately equal to the number of proton produced showers.[28] The μ-meson spectrum used was that given by Rossi.[29]

TABLE I. Rates at which penetrating showers were registered under cabon, aluminum, and lead.

Material	Thickness (g/cm^2)	Rate (showers/hour)
Carbon	57.3	0.09±0.02
Aluminum	92.5	0.07±0.03
Lead	168	0.07±0.02

The fact that no example of single meson production in the hydrogen was detected (with the possible exception of the event of Fig. 5) is consistent with considerations of the type outlined above.

IV. PENETRATING SHOWERS UNDER CARBON, ALUMINUM, AND LEAD

The rates at which penetrating showers were registered under carbon, aluminum, and lead are shown in Table I. The rates are given on the basis of the operating time, which excludes the dead time of the chamber. The statistical standard deviations are given for these rates.

Butler, Rosser, and Barker[14] employed an apparatus similar to that used in this work and defined a penetrating shower in the same way. From the data which they reported, using a lead absorber above the chamber, their counting rate was 0.09±0.01, which is consistent with the figures given above, although the geometries, counter controls, and chamber sizes were somewhat different in the two cases.

Although the observations on heavier elements were made primarily to estimate the average energy of the penetrating showers and to establish the efficiency of the apparatus in detecting penetrating showers, and the counting rate to be expected, some other inferences can be made. A comparison of the counting rates in the three materials (the thickness of each of which is approximately one geometrical nuclear mean free path for collision) shows that they are equal within the limits set by the statistics. This is in agreement with recent results.[4,30]

In the case of 23 percent of the penetrating showers found under lead, γ-rays formed at least one electron shower in the lead plate in the center of the chamber, and in the case of 11 percent, at least two. In carbon the corresponding figures are 42 percent and 31 percent. This is evidence that γ-rays are formed in these showers which are not as likely to escape from the lead block as from the carbon.

From the nucleon flux and the frequency of the showers shown in Table I, it is possible to make a rough estimate of their energy, assuming that the variation of the cross section for the production of a penetrating shower with the momentum of the incident particle can be approximated by a step function, i.e., that it is zero below a certain critical momentum, p_m, and geometric above it. In a manner similar to that which will be outlined in Sec. V, this was done. The lower limit estimated for p_m was 4 Bev/c.

That there can be no appreciable contribution to the

[24] S. H. Neddermeyer and C. D. Anderson, Phys. Rev. **51**, 884 (1937).
[25] E. Fermi, Prog. Theor. Phys. **5**, 570 (1950).
[26] Camerini, Davies, Fowler, Franzinetti, Muirhead, Lock, Perkins, and Yekutieli, Phil. Mag. **48**, 1261 (1951).
[27] M. G. Mylroi and J. G. Wilson, Proc. Phys. Soc. (London) **A64**, 404 (1951).
[28] L. Janossy and G. D. Rochester, Proc. Roy. Soc. (London) **A182**, 180 (1943).
[29] B. Rossi, Revs. Modern Phys. **20**, 537 (1948).
[30] L. Mezzetti and R. Querzoli, Phys. Rev. **79**, 168 (1950); E. P. George and A. C. Jason, Proc. Phys. Soc. (London) **A63**, 1081 (1950).

number of penetrating showers by impinging nucleons of momentum below a few Bev/c is also indicated by the fact that the rates of penetrating showers in smaller thicknesses of material can be correctly estimated by the use of the rates given in Table I by assuming the probability of a shower is proportional to $(1-e^{-x/\lambda})$. A proton must have a momentum of about 900 Mev/c to penetrate any of the three blocks of material employed in finding these rates. Consequently, if incident nucleons of momentum not much greater than 1 Bev/c contributed appreciably to the number of penetrating showers, the rates at which these showers were detected under thinner targets should be proportionately higher than the rates one would expect on the basis of the thick target results of Table I. This is not the case. As shown in Sec. V, the number of penetrating showers formed in the bottom of the Dewar (about 0.1 geometric nuclear mean free path) agrees with the number estimated from the average rates for the thick targets.

V. RESULTS WITH LIQUID HYDROGEN

The total operating time with liquid hydrogen above the chamber was 626 hours. During this time seven penetrating showers were observed which traced back to the bottom of the Dewar or to the counters. No events which appeared to come from the hydrogen were detected except for the one described in Sec. III, which cannot be classed as a penetrating shower according to our definition.

The amount of material in the bottom of the Dewar and the counters was about 0.116 geometrical nuclear mean free path (abbreviated mfp) during control 1 and 0.067 during controls 2 and 3. The number of penetrating showers which one would expect in this material on the basis of the average rate from Table I (0.08 ± 0.01 showers/hour) and the running time (104 hours with control 1 and 522 hours with controls 2 and 3), is 6. This agrees rather well with the 7 showers observed.

By measuring the curvatures of the individual tracks in those pictures taken with the field on (5 of the 7) it was found that the total momentum of the visible tracks averaged more than 3.6 Bev/c per event. Taking into account the facts that only a lower limit could be placed on the momentum of many of the tracks in each event, that some tracks would miss the chamber, and that neutral particles must also have been present, it is estimated that the average momentum of the initiating particles must have been at least 6 Bev/c. This estimate is consistent with that of Butler, Rosser, and Barker who concluded that the average energy of the penetrating showers they observed was at least 7 Bev. It is probable that the minimum value for p_m deduced in Sec. IV from the proton spectrum (4 Bev/c) is low by a factor of $1\frac{1}{2}$ or 2.

If the cross section for the production of penetrating showers in hydrogen were 6×10^{-26} cm^2/nucleus, i.e., geometrical, 3 g/cm^2 would be a little more than 0.1 mfp. This corresponds to about 43 cm of hydrogen and this figure was taken as the limit beyond which it is impracticable to attempt to trace tracks seen in the chamber. The number of nuclear interactions in material which is 0.1 mfp or less in thickness is directly proportional to the thickness and the time. To compare the hydrogen with other materials, therefore, the time integral of the amount of hydrogen below the 43-cm mark in the Dewar was found graphically for each separate run, and these were added. The total was 50.9 mfp hours. The corresponding total for the material in the bottom of the Dewars was about the same, 47.1 mfp hr. The geometries were not the same since the hydrogen was further from the chamber but it can be said that the angular spread of the particles in the showers observed from the Dewar bottom was such that they would have been observed and recognized as penetrating showers if they had occurred higher up in the Dewar. In addition, the fact that the number of penetrating showers in thin targets is no greater than that expected on the basis of the number found in thick targets (in the cases of carbon and aluminum, the tops of the targets were more than 35 cm above the top of the chamber) indicates that very few showers would have been missed if they had occurred in the hydrogen.

It should further be pointed out that a number of nuclear events, some of which may be as energetic as a penetrating shower, must occur in heavy elements which are not recognized as being of nuclear character, but which would be so recognized if they occurred in hydrogen. There is, for instance, a group of events consisting of one penetrating particle accompanied by 3 or more minimum ionization tracks, all of which trace back approximately to a point in the interior of the target. Some of these would be penetrating showers if more than one of the tracks happened to go toward the lead plate, rather than out of the chamber. In fact, this particular type of event appears to follow the $A^{\frac{1}{3}}$ cross section law. The frequency is about $\frac{3}{4}$ times the frequency of penetrating showers in the case of lead, carbon, aluminum, and Dewar bottom, in thick or thin targets. Although from these facts it would appear that a large percentage of these events must of nuclear character, it is probably not safe to count them as such in heavy materials since some of them at least must be μ-meson knock-on showers. In the case of hydrogen, however, events of this kind would be unambiguous since the probability of a knock-on shower in hydrogen (only 0.0005 radiation length per cm) is negligible.

It can be concluded that if multiple production played a prominent role in the majority of sea-level penetrating showers, probably produced at energies of 6 Bev or more, at least 7 should have been seen issuing from the hydrogen during the course of this experiment.

While there is not enough information available to make an accurate calculation, it is possible to utilize

the nucleon spectrum at sea level to make an estimate of the minimum number of penetrating showers which should be observed if the cross section for their production is assumed to have a given dependence on the momentum of the incident particle. To make such an estimate, it will be assumed that the variation of the mfp for the production of penetrating showers with the incident momentum can be approximated by a step function.

$$\lambda(p<p_m)=\infty\,, \quad \lambda(p\geq p_m)=\text{constant}.$$

The angular distribution of the penetrating secondaries from a nucleon-nucleon collision is unknown, but it has been shown that the more energetic particles which would be likely to trip the lower counter tray (*b*, Fig. 1) are emitted in the direction of the incident nucleon.[4] If one then finds the number of nucleons which would pass in a straight line through a given layer of hydrogen, through the lead plate in the well-lighted part of the chamber, and through the lower counter tray, this might be considered a lower limit to the number of possible shower producing nucleons. To estimate the minimum number of showers expected the number which would be formed in a differential layer of hydrogen 43 cm above the top of the chamber by nucleons collimated as described above, and with the mfp given above is found and it is assumed that this same number would be formed and observed in all lower layers of equal thickness. It is apparent that this is a lower limit to the number of showers which should be observed since the solid angle over which primary protons are accepted is higher for lower layers. Assuming the proton spectrum (doubled to take neutrons into account) and zenith angle dependence given by Mylroi and Wilson can be extrapolated to somewhat higher momenta than those for which it has been verified, the minimum number of showers which should be seen is

$$n_0=7.28\times10^{26}p_m^{-1.8}\sigma\int xdt(1-\cos^6\theta_m),$$

where $\int xdt$ is the time integral of the amount of hydrogen expressed in mfp hr, and θ_m is the half-angle of the cone which has the top layer of hydrogen (that at 43 cm up) as a base and whose apex is in the lead plate of the chamber. In this equation the detection efficiency is taken at 100 percent. The fact that a penetrating shower is defined to consist of three or more particles which enter the chamber, at least two of which are penetrating, makes it very unlikely that it would fail to actuate the counter control. Substituting the values of θ_m and the integral, $\int xdt$,

$$n_0=67.5\sigma_r p_m^{-1.8},$$

where σ_r is the cross section expressed in units of the geometrical cross section, and p_m is in Bev/c, as before. Since no showers were observed, n_0 is probably a fraction, but its value is unknown. From this equation one can, however, see that if the cross section were geometric ($\sigma_r=1$) at $p_m=6$ Bev/c, an average of at least three penetrating showers should have been seen in the operating time of this experiment. The statistical probability that none would have occurred in the period (assuming a Poisson distribution for the number of showers seen in a given interval if the average number is three) is 5 percent. It should be stressed that p_m is a lower limit here and that the cross section for penetrating showers in hydrogen may well be low at momenta very much higher than this. This result is consistent with the conclusion based on the number of penetrating showers which occurred in the bottom of the Dewar and the rates at which showers occurred in carbon, aluminum, and lead, that at least seven penetrating showers should have been observed in hydrogen if the cross section for their production were geometric. The conclusion that multiple production has a small cross section compared to geometric at nucleon momenta of about 6 Bev/c agrees with current theories on meson production,[25,31] and with other experiments. In a high altitude counter experiment using liquid hydrogen, Vidale and Schein[17] found evidence that multiple meson production should be expected only at energies well in excess of 10 Bev. Using nuclear emulsions, Lord and Schein[32] found indications from the latitude effect that the average multiplicity when a proton strikes a carbon nucleus at 8 Bev is less than 4. Rollosson's counter work is also in agreement with this result.[33]

VI. CONCLUSION

The majority of sea-level penetrating showers are initiated by particles of about the same average momentum in carbon, aluminum, and lead, since the frequency of the showers follows an $A^{\frac{1}{3}}$ law. This average momentum, under the conditions of the experiment described here is 6 Bev/c or higher.

From the fact that no penetrating showers were observed in hydrogen, it may be concluded that multiple production of several mesons is very improbable at the energies of these showers and that the majority of sea level penetrating showers in heavier materials should be attributed mainly to plural production.

The author wishes to express his sincere thanks to Professor Marcel Schein for very helpful discussions and advice on all the aspects of this problem. It is also a pleasure to acknowledge the advice of Professor Earl Long on the design of the liquid hydrogen container and manifold, for making a Dewar available for this work, and for cooperation in testing it and supplying liquid hydrogen. In addition, he wishes to thank Mr. Richard Plano and Mr. Robert Glasser for their assistance.

[31] W. Heisenberg (private communication to Marcel Schein); W. Heitler, Revs. Modern Phys. **21**, 113 (1949).
[32] J. J. Lord and Marcel Schein (private communication).
[33] G. W. Rollosson, Phys. Rev. **87**, 71 (1952).

Grain Density in Nuclear Emulsions

LAURIE M. BROWN*
Institute for Advanced Study, Princeton, New Jersey
(Received January 2, 1953)

A simple model of a nuclear track emulsion is discussed in which it is assumed that a grain is made developable only if a charged particle loses in the grain an energy greater than some threshold value η. It is estimated that a particle of minimum ionization loses, on the average, an energy of order of magnitude η in traversing the diameter of a grain and, therefore, that fluctuations in the energy loss are important. This has as a consequence that the shape of the curve of grain density *versus* energy and, in particular, the percentage relativistic increase of grain density may be sensitive to small variations of η.

IN recent years a number of observations have been reported concerning the magnitude of the relativistic increase of grain density in nuclear track emulsions. While the experimental situation is far from clear, it would appear that previous attempts to reconcile these observations with the theory of ionization losses have not been entirely successful. It is the purpose of this note to suggest that the discrepancy may be due to the mechanism by which fast particles make grains developable and to offer a simple model for such a mechanism; namely, an increased role is attributed to fluctuations in the energy loss.

The Bristol group[1] in 1949 selected at random, from a single Kodak NT4 plate exposed under a 10 cm thickness of lead at 11 000 feet, 25 tracks longer than one mm and attributed to fast electrons and mesons. They found a sharp distribution of grain density with a mean of 22.5 grains/100μ and a full width at half-maximum of 2 grains/100μ. Nonuniformity of development with depth gave variations along single tracks from 23.5 grains/100μ at the air surface of the emulsion to 21.5 at the glass. In addition, part of the width was ascribed to fading and to other instrumental errors. Their results, therefore, were consistent with no relativistic increase of grain density.

Subsequent observations made with Ilford G5 plates have confirmed these results in the extreme relativistic region. Thus Corson and Keck[2] found that electrons of 10 Mev and 180 Mev gave the same grain density within a statistical error of ± 2 percent and Occhialini[3] concluded that electrons of energies ranging from 7.5 Mev to 500 Mev gave the same grain density within a total experimental uncertainty of ± 10 percent. However, the most recent reports[4–9] while reaffirming these conclusions (e.g., Morrish finds 0 ± 0.25 percent for the increase from $E/mc^2 = 20$ to 1000), have also claimed to find an increase of from 5 percent to 10 percent in the range E/mc^2 from 3.5 to 10 or 20. Table I summarizes their results expressed as $(g_{pl} - g_{min})/g_{pl}$ in percent, where g_{pl} is the plateau value of grain density for $E/mc^2 > 20$ and g_{min} is the lowest observed value of the grain density.

On the theoretical side the Bethe-Bloch ionization loss theory has been corrected for polarization effects, important in condensed materials in the range of E/mc^2 we are considering, by Fermi,[10] Wick,[11] Halpern and Hall,[12] A. Bohr,[13] and Huybrechts and Schönberg.[14] The Bethe-Bloch theory has been found experimentally to hold[15,16] in gases (as it should) for E/mc^2 up to 100. The theories of the polarization effect predict a relativistic increase in ionization loss many times larger than the observed relative increase in grain density. A considerable advance in interpretation of this discrepancy has been made by Messel and Ritson[17] who have pointed out that the average energy loss is not directly responsible for the grain density since secondary electrons of sufficiently high energy (δ-rays) will leave the grain with most of their energy. They have proposed, there-

TABLE I. Summary of experimental information concerning the relativistic increase of grain density.

Observer	E/m	$\frac{g_{pl}-g_{min}}{g_{min}}$	Observed g_{pl} (grains/100μ)
4	3.5 to 20	8 ± 2	31.7 and 35.7
5	6–12 to 20–1000	4.8 ± 2	not given
6	7 to 60	8 ± 2.5	36.6
8[a]	3.5 to 10	~ 8	various
9	≥ 3	12^{+4}_{-3}	21.2

[a] Including reference 7 and L. Voyvodic (to be published).

* National Science Foundation Post-Doctoral Fellow on leave-of-absence from Northwestern University for the year 1952–1953.

[1] Brown, Camerini, Fowler, Muirhead, Powell, and Ritson, Nature **163**, 47 (1949).
[2] D. R. Corson and M. R. Keck, Phys. Rev. **79**, 209 (1950).
[3] G. P. S. Occhialini, *Como Congress* [Nuovo cimento Supplement **6**, 377 (1949)].
[4] E. Pickup and L. Voyvodic, Phys. Rev. **80**, 89 (1950).
[5] A. Morrish, Phil. Mag. **43**, 533 (1952).
[6] I. B. MacDiarmid, Phys. Rev. **84**, 851 (1951).
[7] Dansyz, Lock, and Yekutieli, Nature **169**, 364 (1952).
[8] Daniel, Davies, Mulvey, and Pekeris, Phil. Mag. **43**, 753 (1952).
[9] M. M. Shapiro and B. Stiller, Phys. Rev. **87**, 682 (1952).
[10] E. Fermi, Phys. Rev. **57**, 485 (1940).
[11] G. C. Wick, Nuovo cimento **1**, 302 (1943).
[12] O. Halpern and H. Hall, Phys. Rev. **73**, 477 (1948).
[13] A. Bohr, Kgl. Danske Videnskab. Selskab, Mat.-fys. Medd. **24**, No. 19 (1948).
[14] M. Huybrechts and M. Schönberg, Nuovo cimento **IX**, 764 (1952).
[15] R. S. Carter and W. L. Whittemore, Phys. Rev. **87**, 494 (1952).
[16] J. E. Kuperian, Jr., and E. D. Palmatier, Phys. Rev. **85**, 1043 (1952).
[17] H. Messel and D. M. Ritson, Phil. Mag. **41**, 1129 (1950).

fore, to replace the "maximum energy transfer" in the theories of Fermi, etc., by a fixed quantity equal to the mean energy left in a grain by a δ-ray. This fixed energy has been taken quite reasonably as 5 kev, and the resulting "probable" energy loss is insensitive to this particular choice. With this modification, the ionization loss saturates for E/mc^2 between 50 and 100 (depending on the particular theory used) at a value about 15 percent above the minimum value of the energy loss.

The effect, then, that we propose to discuss is a trough in the experimental grain density *vs* energy curve $\frac{1}{3}$ to $\frac{2}{3}$ as deep and 3 to 10 times as narrow as the corresponding trough in the theoretical curve of "probable" ionization loss *vs* energy. Since our purpose is to point out certain qualitative features of the process by which grains are made developable by fast particles, we introduce a simplified model of the photographic plate.

First, we assume that a grain will become developable, in a given plate under given chemical development, if, and only if, a minimum energy η ev is released in the grain by the impinging particle. Secondly, we assume that the grains are spheres of AgBr of diameter a microns (μ) distributed at random. Since the specific volume of AgBr in the standard nuclear track plates is 0.455, the number of grains touched by a track is $0.455/\frac{2}{3}a=0.682/a$ per μ, $\frac{2}{3}a$ being the mean chord. This should be equal to the observed maximum grain density g_{max} in the plate unless some of the grains are insensitive.

If we consider, say, a proton of velocity v with average rate of energy loss in AgBr$=k(\beta)$ ev/μ, where $\beta=v/c$, then this leaves in the grain, on traversing a chord of length l microns, energy kl ev. Since the fraction of chords traversed of length greater than l is $P(l)=1-l^2/a^2$, the observed grain density should be

$$g=g_{max}[1-(\eta^2/k^2a^2)], \tag{1}$$

if $ka>\eta$ and zero if $ka<\eta$. This, however,neglects fluctuations in the energy loss which may safely be done, to first approximation, *providing* $ka\gg\eta$ but not otherwise.

The question of the magnitude of η thus becomes of primary importance for the interpretation of the relation between energy loss and grain density in nuclear track plates. The minimum value k_{min} of $k(E)$ is about 900 ev/μ (the "probable" ionization loss of Messel and Ritson is somewhat less) so $k_{min}a$ is about 200 ev. Now it would appear that η for a plate sensitive to minimum ionization is just of this order of magnitude. For example, Webb[18] estimates that for an Eastman NTB plate sensitive to protons of energy up to 50 kev, the threshold sensitivity is about 1100 ev. But such a proton loses energy at a rate just five times k_{min}. Webb also notes that about forty light quanta (i.e., about 100 ev) are required to make a grain developable and that grains are much less sensitive to ionization produced by fast particles than that produced by light because of the failure of the reciprocity law for short times. Furthermore, values of η obtained by fitting (1) to the curves for low energy protons agree with this estimate.

We see that the grain density produced by minimum ionization particles must be ascribed in large measure to fluctuations in the energy loss. This holds *a fortiori* if we consider the "probable" ionization loss rather than the mean as responsible for grain density.

We now consider fluctuations of a very special type; namely, we ask for the number of secondary electrons n_E having an energy greater than E, produced in a collision with a fast particle. The Rutherford formula gives (using $Z/A=0.436$ for AgBr):

$$n_E=43.4/\beta^2E \text{ per micron of AgBr}, \tag{2}$$

E being measured in ev. If we put $\beta=1$, $E=200$ ev, we get $n_E=0.22$/micron. Since the specific volume of AgBr is 0.455, this means that fluctuations of this type alone would account for almost half of the grains observed beyond the minimum of ionization. Note that this probability *decreases* about 6 percent from the ionization minimum.

Of course, it is improper to extend the Rutherford formula to secondaries of energy so low as this in elements of medium atomic number, but N. Bohr[19] has shown that it is proper to consider about half of the ionization loss as resulting from the "free" collisions, to which this formula is applicable while the remainder is the result of "resonance" effects obeying a more complicated distribution law for energy losses in single collisions, the latter depending on the ionization probabilities and energy level structure of AgBr. Detailed calculation is complicated by the fact that the mean ionization energy and η are of the same order of magnitude.

We would like to suggest, therefore, (a) that the quantity of interest in comparing the grain density with the energy loss of high energy particles is neither the mean energy loss nor the "probable" energy loss, but rather the probability of a loss $E>\eta$ in traversing a thickness such that $k(\beta)\gtrsim\eta$, (b). that it is to be expected that the "free" collisions play a relatively larger role in this process than in the average or "probable" ionization loss processes, (c) that the *shape* of the grain density *vs* energy curve is very sensitive to ka/η in plates responsive to minimum ionization so that one may expect larger or smaller relativistic increases correlated with the plateau grain density.

In particular, if (c) is true, then one should not average the curves corresponding to different values of g_{pl}, even in the same plate, since they may have

[18] J. H. Webb, Phys. Rev. **74**, 511 (1948).

[19] N. Bohr, Kgl. Danske Videnskab. Selskab, Mat.-fys. Medd. **18**, No. 8 (1948).

different shapes. In this connection it may be noted that in Fig. 2 of the article of Pickup and Voyvodic,[4] grain density curves are given for two plates in which g_{pl} had average values of 31.7 and 35.7 grains/100μ. The two curves have been normalized to the same plateau value, but one of them is considerably flatter than the other. It is also of interest to note that Occhialini[3] reports that for $k(\beta)$ between $4k_{\min}$ and $2k_{\min}$ the grain density decreases only half as fast as the ionization loss.

PHYSICAL REVIEW VOLUME 90, NUMBER 1 APRIL 1, 1953

Remarks on the Theory of Fusion and Condensation

ARNOLD J. F. SIEGERT
Department of Physics, Northwestern University, Evanston, Illinois
(Received December 18, 1952)

We have re-examined the relation between the thermodynamic functions and the energy level density ρ of a substance consisting of N interacting particles for a class of hypothetical but (in the case $1 \ll N \ll 10^{23}$) not unreasonable functions ρ defined by certain regularity conditions. We have shown that the specific features of ρ which lead to condensation—in the sense of a discontinuous change of the most probable volume—under a volume independent force per unit area can yield partition functions which, in the condensation region, are smooth and of a shape similar to the van der Waals function. This is not a contradiction since for a substance under a volume independent force, the results of the conventional *ad hoc* re-interpretation of the van der Waals curve can be proved directly from the canonical ensemble, without the *ad hoc* assumptions.

1.

THE difficulties encountered by attempts to calculate the partition function of a system consisting of a large number of interacting particles for all values of temperature and volume are well known. It has never been proved, for instance, that, in the limit of infinite number of particles at finite density, the partition function Q of a substance approaches the three analytic parts seemingly required for the explanation of condensation. It seemed of interest, therefore, to re-examine the relation between the thermodynamic behavior and the density of energy levels $\rho(E, V)$ (V = volume, E = energy) of a—macroscopically speaking—very small amount of substance, i.e., of a substance consisting of N interacting particles for which $1 \ll N \ll 10^{23}$.

We have, for this purpose, considered a class of hypothetical, but not unreasonable, functions $\rho(E, V)$, defined by certain regularity conditions. We have shown that a function of this class can yield fusion and condensation (in the sense of a discontinuous change of the most probable energy and volume) and that the specific features of $\rho(E, V)$ which lead to these transitions need not be "pathological." The case of fusion at fixed volume was included, although our description is essentially the same as the double tangent construction given by Seitz,[1] in order to emphasize the distinction necessary for finite N between the thermodynamic quantities and the corresponding functionals of $\rho(E, V)$ with which they are piecewise identical.

In Secs. 3 and 4 we have examined the behavior of a substance under a volume independent force per unit area, realized, e.g., by a piston of finite weight with vacuum above the piston. While our treatment is similar to the double tangent construction of thermodynamics[2] it leads to an unorthodox result. We find, directly from the consideration of the canonical ensemble, that features of $\rho(E, V)$ which can be responsible for condensation, can nevertheless yield a smooth curve similar to the van der Waals curve for $kT\partial \log Q/\partial V$. This is not a contradiction, since we can show that, if the function $kT\partial \log Q/\partial V$ has the shape of the van der Waals curve, it is not to be identified with the pressure for all values of the volume and that the results of the usual *ad hoc* re-interpretation of the van der Waals type curve can be justified, directly from the canonical ensemble, without the conventional *ad hoc* assumptions. We do not claim that $N^{-1} \log Q$ does not—(in the limit of infinite N and finite density) approach a piecewise analytic function, but that condensation (in the limited sense defined above) can occur for values of N and V for which this limit has not yet been reached. In a later paper we will show that this type of condensation does not necessarily occur if a volume dependent force acts on the system, but that the partition function of a macroscopic system built up of a large number of systems of the type discussed here consists practically of the three analytic parts required for condensation in the usual sense.

To avoid considerations extraneous to our problem we will limit the discussion to a range of energies $E \geq E_0$

[1] F. Seitz, *Modern Theory of Solids* (McGraw-Hill Book Company, Inc., New York, 1940), p. 489. We do not assume the "actual curve" in Fig. 16 to be correct for $N \to \infty$.

[2] J. C. Slater, *Introduction to Chemical Physics* (McGraw-Hill Book Company, Inc., New York, 1939), p. 179.

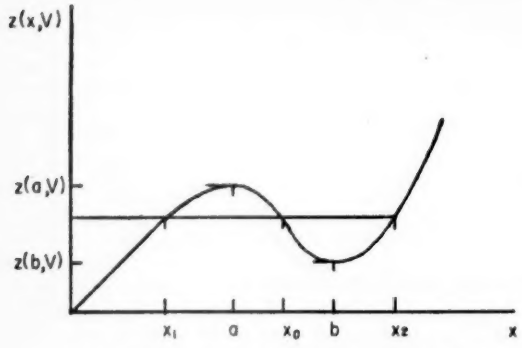

FIG. 1. Assumed shape of $z(x, V)$ as function of x.

and temperatures $T \gtrsim T_0$, for which the partition function is given with sufficient accuracy as an ordinary integral,

$$Q(\beta, V) = \int_0^\infty e^{-\beta E} \rho(E, V) dE, \tag{1.1}$$

and for which the density of energy levels $\rho(E, V)$ can be defined by the phase space volume, and for which corrected Boltzmann counting takes account of the identity of the atoms. We will chose for T_0 a temperature such that, at T_0 in the volumes under consideration, all but a negligible fraction of the atoms form a solid, which obeys the Dulong-Petit law, and we will choose the energy scale such that $E_0 = 3NkT_0$, where N is the number of atoms and k the Boltzmann constant.

The following regularity conditions are imposed on $\rho(E, V)$ over a limited range of the variables: We define the function $y(x, V)$ by

$$y(x, V) = (3N)^{-1} \log(E\rho(E, V)), \tag{1.2}$$

where

$$x = \log(E/E_0). \tag{1.3}$$

We assume that $y(x, V)$ and all its derivatives are of order zero or unity (or $\log N$, but not N or $N^{\frac{1}{3}}$). We will show in Sec. 2, for the case of fixed volume, that even with these regularity conditions a phase transition occurs if $\partial^2 y/\partial x^2 > \partial y/\partial x$ over a finite interval of the variable x.

2.

The probability that a system enclosed in a fixed volume V and in thermal equilibrium at temperature T has an energy between E and $E+dE$ is

$$w(\beta, V|E)dE = Q^{-1}(\beta, V)\rho(E, V)e^{-\beta E}dE = Q^{-1}(\beta, V) \exp\{-\beta E_0 e^x + 3Ny(x, V)\}dx. \tag{2.1}$$

The stationary points of the exponent are the roots of the equation

$$-\beta E_0 e^x + 3Ny_x = 0, \tag{2.2}$$

or

$$z(x, V) \equiv x - \log y_x = \log(T/T_0), \tag{2.3}$$

where the subscript x denotes partial differentiation with respect to x. In the neighborhood of a stationary point x_s we expand the exponent and obtain

$$-\beta E_0 e^x + 3Ny(x, V) = [-\beta E_0 e^x + 3Ny(x, V)]_s - (3N/2)(x-x_s)^2[y_x - y_{xx}]_s + \cdots, \tag{2.4}$$

where the subscript s at the brackets indicates that the function is taken at x_s. The probability function (2.1) has thus a very sharp maximum at x_s, if

$$0 < [y_x - y_{xx}]_s \sim N^\alpha, \tag{2.5}$$

with $\alpha > -1$. If there is only one maximum, the thermodynamic functions are obtained in terms of y and its derivatives as follows:

$$Q_s(\beta, V) = (2\pi/3N[y_x - y_{xx}]_s)^{\frac{1}{2}} \cdot \exp[-\beta E_0 e^x + 3Ny]_s; \tag{2.6}$$

Helmholtz free energy;

$$F_s(\beta, V) = -\beta^{-1} \log Q_s = 3N\beta^{-1}[y_x - y]_s - \tfrac{1}{2}\beta^{-1} \log(2\pi/3N[y_x - y_{xx}]_s); \tag{2.7}$$

entropy;

$$S_s(\beta, V) = 3Nk[y]_s; \tag{2.8}$$

specific heat at constant volume;

$$c_s(\beta, V) = 3Nk[y_x^2/(y_x - y_{xx})]_s. \tag{2.9}$$

The energy is given by Eq. (2.2) taken at x_s. The term of order $\log N$ has been omitted in Eqs. (2.8), but was left in Eq. (2.7) because this formally simplifies a later equation. The mean square energy fluctuation kT^2c_s is obtained correctly from Eqs. (2.1), (2.4), and (2.9).

Suppose, however, that there is a finite interval $a \leqslant x \leqslant b$, where $y_x - y_{xx} < 0$, while y_x remains positive. Then $z(x, V)$ has the shape indicated in Fig. 1, and there are three roots x_1, x_0, x_2 of Eq. (2.3) for any value of T between T_a and T_b, where $T_a = T_0 \exp z(a, V)$ and $T_b = T_0 \exp z(b, V)$ and where $z(a, V)$ and $z(b, V)$ are the maximum and minimum of $z(x, V)$. Since

$$z_x = (y_x - y_{xx})/y_x, \tag{2.10}$$

the root x_0 corresponds to a minimum of $w(\beta, V|E)$ and is to be disregarded,[3] but the roots x_1 and x_2 correspond to sharp maxima of $w(\beta, V|E)$. We, therefore, write in this case, using Eq. (2.1) and Eq. (2.4),

$$w(\beta, V|E)dE = Q^{-1}(\beta, V) \sum_{s=1,2} Q_s(\beta, V) \times G(x - x_s; (3N[y_x - y_{xx}]_s)^{-\frac{1}{2}})dx, \tag{2.11}$$

where

$$G(\xi; \sigma) \equiv (2\pi\sigma^2)^{-\frac{1}{2}} \exp(-\xi^2/2\sigma^2), \tag{2.12}$$

and where $Q_s(\beta, V)$ is defined by Eq. (2.6), and $Q(\beta, V)$ is obtained as

$$Q(\beta, V) = \sum_{s=1,2} Q_s(\beta, V). \tag{2.13}$$

Formally, therefore, the system is found with prob-

[3] This also guarantees non-negative specific heat.

ability Q_1/Q within a very narrow region of energies near $E_0e^{x_1}$ and with probability Q_2/Q near $E_0e^{x_2}$, over the whole range of temperatures $T_a<T<T_b$. Actually, however, these probabilities are extremely close to zero or unity, except for a very narrow temperature interval, since

$$Q_1/Q_2=\exp\{3N([y-y_x]_1-[y-y_x]_2)+O(\log N)\} \quad (2.14)$$

is practically zero or infinite, depending on the sign of the exponent. Since, furthermore,

$$Q_1/Q_2=\exp\{-\beta[F_1(\beta, V)-F_2(\beta, V)]\}, \quad (2.15)$$

the system is practically with certainty in the energy region corresponding to that probability maximum, for which the Helmholtz free energy computed formally from Eq. (2.7) yields the lower value. The thermodynamic functions are thus given by Eqs. (2.2) and (2.6)–(2.9) computed at that root of (2.2) which yields the lower free energy $F_a(\beta, V)$, except for the very narrow temperature interval, in which F_1-F_2 is of order kT. They are piecewise equal to y or combinations of its derivatives and are, therefore, only piece-wise analytic. Since a finite interval of x values is thus discarded, the regularity restrictions imposed on y do not produce continuity of thermodynamic functions across the transition point.

The fluctuation of the energy very close to the transition point can be written as a sum of two terms of which one is due to the widths of the two peaks, and one is due to the presence of two peaks:

$$\langle(E-\bar{E})^2\rangle_{Av}=kT^2Q^{-1}(Q_1c_1+Q_2c_2)+(E_1-E_2)^2Q^{-2}Q_1Q_2. \quad (2.16)$$

This agrees with the result obtained from the general formula

$$\langle(E-\bar{E})^2\rangle_{Av}=-\partial\bar{E}/\partial\beta. \quad (2.17)$$

The second term in Eq. (2.16) represents the well-known large fluctuations at the transition point. If the system is brought to an energy between E_1 and E_2, it no longer has an exactly defined temperature.

To make our assumptions physically plausible we will now show that if the regularity conditions for $y(x, V)$ are granted, the existence of a transition with latent heat conversely necessitates a change of sign of y_x-y_{xx}. Suppose that there is a transition at temperature T_m which brings the system from the energy $E_0e^{x_1}$ to the energy $E_0e^{x_2}$. Since the free energy of the system is continuous through the transition, we find, using Eq. (2.7)

$$3N\beta^{-1}\{[y_x-y]_{x_2+0}-[y_x-y]_{x_1-0}\}=0 \quad (2.18)$$

and, therefore,

$$\int_{x_1-0}^{x_2+0}(y_{xx}-y_x)dx=0. \quad (2.19)$$

This shows that $y_{xx}-y_x$ either changes sign or is equal to zero throughout the range of integration. If the specific heat is finite either at $x_1=0$ or at $x_2=0$ the second alternative is excluded because of Eq. (2.9) and the continuity of $y_{xx}-y_x$.

In order to see whether the regularity conditions imposed on $y(x, V)$ are reasonable, we note that $y(x, V)$ is known near $x=0$ and for large x, since in these regions it can be identified with the entropy (measured in units $3Nk$) of the solid and ideal gas, respectively. Near $x=0$, we thus have, using Eqs. (1.3), (2.8), (2.2), and the expression for the entropy and energy of a solid,[4]

$$y(x, V)=x+4/3+\log(T_0/\Theta), \quad (2.20)$$

where Θ is the Debye temperature of the solid, and where the zero-point of the energy scale is chosen to be the minimum potential energy U_0 of the system. The energy of the ideal gas on the same energy scale is

$$E=\tfrac{3}{2}NkT+|U_0|, \quad (2.21)$$

and we get for values of x such that $E_0e^x\gg|U_0|$, from the entropy of the ideal gas,[5]

$$y(x, V)=\frac{x}{2}+\frac{1}{2}\log\left(1-\frac{|U_0|}{E_0}e^{-x}\right)+\tfrac{5}{6}+\tfrac{1}{2}\log 2\pi+\tfrac{1}{3}\log(V/N\lambda_0^3), \quad (2.22)$$

where

$$\lambda_0=h/(2mkT_0)^{\frac{1}{2}},$$

and m is the mass of the particles. Thus, there is certainly the possibility of interpolating with a smooth function $y(x, V)$ over the gap between the regions of validity of Eqs. (2.20) and (2.22) if the gap is sufficiently wide. To show an example where this is the case, we choose a volume V such that the substance can be considered as an ideal gas only at temperatures exceeding $2T_1$, where T_1 is the boiling temperature of the substance at atmospheric pressure. The validity of Eq. (2.22) is then limited to values $x>x_1$, where

$$x_1=\log\{(\tfrac{3}{2}Nk\cdot 2T_1+|U_0|)/E_0\}. \quad (2.23)$$

To obtain an estimate of x_1, we substitute for $|U_0|$ the heat of sublimation L, which is roughly given by Trouton's rule[6] as

$$L\cong 11NkT_1, \quad (2.24)$$

so that

$$|U_0|/E_0\cong(11/3)(T_1/T_0), \quad (2.25)$$

$$x_1=\log[(14/11)(|U_0|/E_0)], \quad (2.26)$$

and

$$\frac{1}{2}\log\left(1-\frac{|U_0|}{E_0}e^{-x_1}\right)\cong -0.8. \quad (2.27)$$

There is no necessity, on this basis, for the shape of

[4] See J. E. Mayer and M. G. Mayer, *Statistical Mechanics* (John Wiley and Sons, Inc., New York, 1940), Eqs. (11.39) and (11.41).

[5] See reference 4, Eq. (13.52).

[6] See reference 1, page 3.

$y(x, V)$ to be more complicated than an $\int$-shaped monotonic increase from the low values of the solid to the high values of the gas. If there is an interval of values x for which $y_x - y_{xx} < 0$ it has to be located at values of x below the point of maximum slope and will, therefore, cause a transition between two states of the substance, whose entropies are both appreciably smaller than the entropy of the substance as an ideal gas. The transition treated above should, therefore, be interpreted as a transition from a state in which solid and some gas are present to a state in which liquid and some gas are present. We must not expect to find a boiling point for a substance enclosed in a fixed volume, and we will, therefore, consider next the case of a substance under fixed pressure.

3.

We consider the substance enclosed in a cylinder of cross section A by a piston of mass M, with a vacuum above the piston so that the piston exerts a force $PA \equiv Mg$ on the substance. We consider the system consisting of the substance and the piston, whose coordinate and momentum are V/A and p, respectively. The probability $w(P, \beta | p, V, E)dpdVdE$ of finding the substance in an energy state between E and $E+dE$ and the piston in a phase space element $dpd(V/A)$ is

$$w(P, \beta | p, V, E)dpdVdE = Q_t^{-1} \exp\{-\beta[PV + p^2/2M + E]\} \times h^{-1}dpd(V/A)\rho(E, V)dE, \quad (3.1)$$

where Q_t is the partition function of the total system defined by

$$\int_0^\infty dV \int_{-\infty}^\infty dp \int_0^\infty dE w(P, \beta | p, V, E) = 1. \quad (3.2)$$

The probability function $W(P, \beta | V, E)$ for volume and energy of the substance is, therefore,

$$\begin{aligned} W(P, \beta | V, E)dVdE &= Q_t^{-1}(2\pi M/\beta)^{\frac{1}{2}}(hA)^{-1} \exp\{-\beta[PV+E]\} \times \rho(E, V)dEdV \\ &= Q_t^{-1}(2\pi M/\beta)^{\frac{1}{2}}(hA)^{-1} \exp\{-\beta[PV + E_0e^x] + 3Ny(x, V)\}dxdV. \end{aligned} \quad (3.3)$$

The stationary points x_s, V_s of the exponent are defined by

$$[-\beta E_0 e^x + 3Ny_x]_s = 0, \quad (3.4)$$

$$[-\beta P + 3Ny_V]_s = 0, \quad (3.5)$$

where the subscripts x, V denote partial differential quotients and the subscript s at the square brackets indicates that the quantity is the brackets is to be evaluated at $x = x_s$, $V = V_s$. Denoting by g_s the Gibbs free energy formally calculated at x_s, V_s,

$$g_s \equiv [PV + E_0e^x - 3N\beta^{-1}y]_s, \quad (3.6)$$

we expand the exponent near the stationary point:

$$\begin{aligned} -\beta(PV + E_0e^x) + 3Ny &= -\beta g_s + \tfrac{1}{2}(x-x_s)^2[-\beta E_0 e^x + 3Ny_{xx}]_s \\ &\quad + (x-x_s)(V-V_s)3N[y_{xV}]_s \\ &\quad + \frac{3N}{2}(V-V_s)^2[y_{VV}]_s \\ &= -\beta g_s - \frac{3N}{2}\{(x-x_s - (V-V_s) \times [y_{xV}/(y_x - y_{xx})]_s)^2[y_x - y_{xx}]_s \\ &\quad - (V-V_s)^2[y_{VV} + y_{xV}^2/(y_x - y_{xx})]_s\}. \end{aligned} \quad (3.7)$$

The probability function $W(P, \beta | V, E)$ thus has sharp maxima at those stationary points x_s, V_s, for which

$$0 < [y_x - y_{xx}]_s \sim N^\alpha \quad (3.8)$$

and

$$0 < -[y_{VV} + y_{xV}^2/(y_x - y_{xx})]_s \sim N^{\alpha'}, \quad (3.9)$$

with $\alpha, \alpha' > -1$. The probability function can thus be written in the form

$$W(P, \beta | V, E) = \sum_s{}' a_s e^{-\beta g_s} G_s(x, V) / \sum_s{}' a_s e^{-\beta g_s}, \quad (3.10)$$

where $G_s(x, V)$ is a very narrow normalized Gaussian centered on x_s, V_s and the factors a_s are slowly varying compared with $e^{-\beta g_s}$, since βg_s is of order N. The summation extends over points x_s, V_s defined by Eqs. (3.4), (3.5), (3.8), and (3.9). Except for very narrow regions of β, P values, the factors $a_s e^{-\beta g_s}/\sum_s{}' a_s e^{-\beta g_s}$ are zero for all points x_s, V_s but the one (x_m, V_m) with the smallest value of g_s, so that

$$W(P, \beta | V, E) = G_m(x, V). \quad (3.11)$$

The energy and volume of the substance as functions of β and P thus follow one solution of Eqs. (3.4), (3.5), (3.8), and (3.9) until another solution of these equations and inequalities yields a smaller value of the Gibbs free energy. The transition occurs at values of (β, P) for which the Gibbs free energies computed at the two competing maxima is equal. This guarantees the validity of the Clausius-Clapeyron equation for the transition. The inequalities (3.8) and (3.9) can be written in a simpler form. We consider x_s, obtained from Eq. (3.4), as a function of β and V_s, and V_s, obtained from Eq. (3.5), as a function of β and P. Differentiating Eq. (3.5), with respect to P at fixed β, we obtain

$$-\beta + 3N\left\{[y_{xV}]_s \frac{\partial x_s}{\partial V_s}\frac{\partial V_s}{\partial P} + y_{VV}\frac{\partial V_s}{\partial P}\right\} = 0. \quad (3.12)$$

Differentiating Eq. (3.4) with respect to V_s at fixed β, we obtain

$$-\beta E_0 e^{x_s}\partial x_s/\partial V_s + 3N\{[y_{xx}]_s \partial x_s/\partial V_s + [y_{xV}]_s\} = 0, \quad (3.13)$$

and, using Eq. (3.4),

$$-[y_x-y_{xx}]_s\partial x_s/dV_s+[y_{xV}]_s=0. \quad (3.14)$$

Substituting Eq. (3.14) in Eq. (3.12), we get

$$[y_{xV}^2/(y_x-y_{xx})+y_{VV}]_s=\beta(3N\partial V_s/\partial P)^{-1}. \quad (3.15)$$

Next we consider the energy $E_s=E_0e^{x_s}$, computed formally from Eq. (3.4) as a function of β and V_s, and obtain by differentiating Eq. (3.4)

$$-\beta E_0e^{x_s}\partial x_s/\partial\beta-E_0e^{x_s}+3N[y_{xx}]_s\partial x_s/\partial\beta=0, \quad (3.16)$$

or

$$3N[y_{xx}-y_x]_s\partial x_s/\partial\beta=E_0e^{x_s}, \quad (3.17)$$

and

$$[y_x-y_{xx}]_s=-E_0e^{x_s}(3N\partial x_s/\partial\beta)^{-1}$$

$$=-(E_0e^{x_s})^2\Big/\left(3N\frac{\partial}{\partial\beta}(E_0e^{x_s})\right). \quad (3.18)$$

The inequalities (3.8) and (3.9), therefore, mean simply, that a stationary point x_s, V_s is a maximum only if the energy and volume, computed formally at this stationary point, change in the physically acceptable direction with changes of temperature and pressure, respectively.

4.

In the preceding sections, it was shown that $y(x, V)$ could be a smooth function and yet lead to piecewise analytic functions for the thermodynamic functions. We will now show that if $\partial^2\log Q/\partial V^2>0$ for a finite interval of values V the results of the *ad hoc* re-interpretation conventionally applied to the van der Waals isotherm are justified. Since our considerations are limited to submacroscopic systems, the assumption of the above inequality is not in conflict with the stability theorem of van Hove.[7] The condensation phenomenon which we shall demonstrate here is a discontinuous change of the most probable volume as function of the force acting on the system and is dependent on the assumption of a volume independent force. We consider the function

$$p(\beta, V)=3N\beta^{-1}[\partial y(x, V)/\partial V]_{x=x_s(\beta,V)}$$

$$\equiv\beta^{-1}\partial\log Q/\partial V, \quad (4.1)$$

where $x_s(\beta, V)$ is obtained from Eq. (3.4) and where in line with the preceding discussion of the shape of $y(x, V)$ we have assumed that $x_s(\beta, V)$ is a unique root of this equation. It was shown in Sec. 3 that the pressure P coincides with the function $p(\beta, V_s)$ piecewise in such a way that the volume is that root of

$$P=p(\beta, V_s) \quad (4.2)$$

which yields the lowest Gibbs potential, after excluding all roots for which $(\partial p/\partial V)_\beta>0$. Suppose we have two roots of Eq. (4.2), at V_1 and V_2, for which $\partial p/\partial V<0$. The phase transition occurs when the Gibbs potentials calculated formally at both roots are equal, i.e., when

$$3N\beta^{-1}y(x(\beta, V_1), V_1)-E_0e^{x(\beta,V_1)}-PV_1$$

$$=3N\beta^{-1}y(x(\beta, V_2), V_2)-E_0e^{x(\beta,V_2)}-PV_2. \quad (4.3)$$

On the other hand, we have for the area between the curve $p(\beta, V)$ and the constant P the expression

$$\int_{V_1}^{V_2}[p(\beta, V)-P]dV$$

$$=3N\beta^{-1}\int_{V_1}^{V_2}\left(\frac{\partial y}{\partial V}\right)_{x=x_s(\beta,V)}dV-P(V_2-V_1). \quad (4.4)$$

The first term can be written as

$$\int_{V_1}^{V_2}\left[\frac{dy(x_s(\beta, V), V)}{dV}-\left(\frac{\partial y}{\partial x}\right)_{x=x_s(\beta,V)}\cdot\frac{\partial x_s}{\partial V}\right]dV$$

$$=y(x_s(\beta, V_2), V_2)-y(x_s(\beta, V_1), V_1)$$

$$-\frac{\beta E_0}{3N}\int_{V_1}^{V_2}e^{x_s}\frac{\partial x_s}{\partial V}dV, \quad (4.5)$$

and the area becomes

$$\int_{V_1}^{V_2}[p(\beta, V)-P]dV$$

$$=3N\beta^{-1}\{y(x_s(\beta, V_2), V_2)-y(x_s(\beta, V_1), V_1)\}$$

$$-\{E_0e^{x(\beta,V_2)}-E_0e^{x(\beta,V_1)}\}-P(V_2-V_1), \quad (4.6)$$

which is indeed the difference of the Gibbs potentials.

If, therefore, the smooth van der Waals curve is interpreted as an approximation for $p(\beta, V)$, qualitatively valid for submacroscopic systems, there is no *ad hoc* assumption needed to obtain condensation in the limited sense of a discontinuous change of the most probable volume under a volume independent force.*

We would like to thank Professor G. E. Uhlenbeck for a very helpful discussion, and Dr. M. Peshkin and Dr. J. M. Luttinger for valuable comments, and the Graduate School of Northwestern University for a grant covering travel expenses for a trip to Ann Arbor, Michigan.

[7] L. van Hove, Physica **15**, 951 (1949).

* *Note added in proof:*—We found since that S. Katsura and H. Fujita, Prog. Theoret. Phys. **5**, 997 (1950), have used a similar approach with fixed volume and stochastic number of particles.

The Thermal Neutron Capture Cross Sections of Pa^{231} and Pa^{232}

R. ELSON,* P. A. SELLERS, AND E. R. JOHN
Argonne National Laboratory, Lemont, Illinois
(Received December 3, 1952)

The neutron capture cross section of Pa^{231} has been determined to be 293 barns, the largest uncertainty in this determination being due to the uncertainty in the half-life of U^{232} and being of the order of 15 percent. The neutron capture cross section of Pa^{232} was determined to be about $40\left(\begin{smallmatrix}+40\\-20\end{smallmatrix}\right)$ barns.

THE cross section of Pa^{231} for capture of pile neutrons has been determined by the measurement of the U^{232} formed by the beta-decay of the Pa^{232} initially formed. Previous values obtained either as above or by direct measurement of the Pa^{232} have ranged from 140 to 230 barns.[1]

A two-milligram sample of Pa^{231} was irradiated in the Hanford pile along with 4.52 μg of Np^{237} as a flux monitor. The amount of Pu^{238} formed was determined radiometrically. The total neutron flux was then calculated from the amount of Pu^{238} formed and using the following constants: Np^{237} half-life, 2.20×10^6 years;[2] Pu^{238} half-life, 92 years;[3] and the capture cross section of Np^{237}, 172 barns.[4] After the sample had cooled sufficiently for essentially all of the Pa^{232} to decay (16 half-lives), the sample was dissolved in $10M$ HNO_3 containing a little HF. An aliquot of this mixture was alpha-counted and pulse analyzed for U^{232} at this stage. The fluoride was removed by fuming with perchloric acid, and the uranium was isolated by exhaustive extraction with double volumes of ether from a solution $1M$ in HNO_3 and saturated with NH_4NO_3. There was less than 1 percent by activity of the original U^{232} left in the aqueous solution, as determined by pulse analysis. The uranium was re-extracted into water, and an aliquot was plated and its rate of alpha-emission determined. As pulse analysis showed this sample to be $\sim$95 percent U^{232}, the weight could be determined. This value checked that obtained from the assay of the original solution. Assuming that all of the Pa^{232} had decayed to U^{232} and using a value for the half-life of U^{232} of 70 years,[5] a value of the capture cross section for Pa^{231} was determined as 293 barns. The largest uncertainty in this determination is due to the uncertainty in the half-life of U^{232} and is of the order of 15 percent.

An estimate of the capture cross section for the second-order reaction, $Pa^{232}(n,\gamma)Pa^{233}$, was made. After the uranium was removed from the original dissolver solution, the protactinium in this solution was purified by extraction into di-isopropyl ketone from a solution $6N$ in HNO_3 and further purified by extraction from a $10N$ HNO_3 solution with thenoyltrifluoroacetone in benzene.

An attempt to resolve the G-M activity of the protactinium fraction failed, and the amount of Pa^{233} present was estimated by following the decay of the sample. As the counting efficiency was not known, this was determined by counting a purified sample of Pa^{233} under the same conditions and estimating its weight by following the increase in fissionability due to the U^{233} daughter. With due corrections for the counting efficiency, Pa^{231} blank, and other long-lived GM activity, an estimate could be made of the Pa^{233} formed. Assuming a constant flux during the irradiation, a value is estimated for the Pa^{232} capture cross section of $40\left(\begin{smallmatrix}+40\\-20\end{smallmatrix}\right)$ barns.

* Now at California Research and Development Company, Livermore, California.

[1] Clinton Laboratories Report CL-RWS-20, 1946 (unpublished); A. H. Jaffey and Q. Van Winkle, Argonne National Laboratory, Report ANL-4283, 1949 (unpublished); recalculated from data in a report by Elson, Van Winkle, Bentley, and Ghiorso [Argonne National Laboratory Report CF-3795, 1947 (unpublished)].

[2] L. B. Magnusson and T. J. LaChapelle, J. Am. Chem. Soc. **70**, 34 (1948).

[3] Seaborg, James, and Ghiorso, The Transuranium Elements: Research Papers (McGraw-Hill Book Company, New York, Inc., 1948), p. 226, National Nuclear Energy Series, Plutonium Project Record, Vol. 14B, Div. IV.

[4] A. H. Jaffey and L. B. Magnusson. Argonne National Laboratory Report ANL-4030, 1947 (unpublished).

[5] James, Florin, Hopkins, and Ghiorso, reference 3, Paper No. 22.8.

Low Frequency Resonances in the Spectra of Diatomic Molecules*

R. E. Coté† and P. Kusch
Columbia University, New York, New York

(Received December 22, 1952)

The molecular beam magnetic resonance method has been used in the study of some previously unobserved resonances in NaF, NaCl, NaBr, NaI, and KBr. The frequency and intensity distribution within the resonance spectra have been studied at zero external field and the dependence of both the frequency and the shape of the resonance spectra on external magnetic field has been determined. At zero field these resonances fall in the frequency range from 0 to 157 kc and occur because of a quadrupole interaction and from a cosine interaction between I and J. At sufficiently high field, the frequency of the maxima of the resonances is $2\epsilon_I\mu_0 H/h$. The lines are ascribed to a transition between the levels $F=J+\frac{1}{2}$ and $F=J-\frac{1}{2}$. In most respects the lines fulfill theoretical predictions; the frequencies of the lines at zero magnetic field, however, deviate considerably from those predicted from other data.

INTRODUCTION

BOTH the molecular beam magnetic and electric resonance methods have been used[1–5] in a study of the internal interactions within a diatomic molecule and of the interaction of the molecule with externally applied fields. The present paper reports the application of the molecular beam magnetic resonance method to the observation of certain previously unobserved lines in the spectra of several diatomic molecules and presents a theoretical analysis of these lines.

Feld and Lamb[6] have given an analysis of the effect of a nuclear quadrupole moment on the energy levels of a diatomic molecule in a $^1\Sigma$ state in a magnetic field. They discuss spectra due to transitions, $\Delta m_I=\pm 1$, $\Delta m_J=0$, at high fields and $\Delta F=\pm 1$ at low or zero fields. Since, in general, a large number of vibrational and rotational states is occupied, the spectrum is very rich in lines. In the most common cases it is not possible to observe individual lines and an important element of the theory is the statistical analysis of the density of the lines in the spectrum. Although FL consider the case in which one of the nuclei has a spin, I_2, of 0 they state that the results are valid for the more general case in which both nuclei may have quadrupole moments. The injection into the theory, of a cosine coupling of the nuclear spin to the molecular angular momentum was shown by Nierenberg and Ramsey,[1] to explain the otherwise anomalous widths of the fluorine resonances in LiF and CsF.

To simplify the presentation of relevant theory and since the present experiments deal only with molecules which contain a nucleus for which $I_1=\frac{3}{2}$, we shall limit our discussion to that case. For our purposes a line will be defined as the envelope of the unresolved components of a spectral distribution.

The analysis proposed by FL, of the spectrum of the simple molecule (I_2 is 0, the rotational angular momentum of the molecule, J, is large, and the cosine coupling of I and J is negligible) in zero external field predicts the appearance of a single line whose frequency is determined solely by the magnitude of the quadrupole interaction and whose width is determined by the resolution properties of the apparatus. Certain lines, observed for the alkali halides by NR, had approximately the correct frequency as determined from high field observations on the same molecules, but their widths and shapes could not be ascribed to the resolution properties of the apparatus. The extension of the theory as given by NR includes an $\mathbf{I}\cdot\mathbf{J}$ term in the Hamiltonian; the calculation is carried to terms in $1/J$ and therefore considers the effect of finite values of J. Three lines are predicted in the weak field spectrum arising from the transitions $F=J+\frac{3}{2}\leftrightarrow F=J+\frac{1}{2}$, $F=J-\frac{1}{2}\leftrightarrow F=J-\frac{3}{2}$, and $F=J+\frac{1}{2}\leftrightarrow F=J-\frac{1}{2}$. The first two of these form a close doublet, the separation of whose components is determined by the magnitude of the coefficient of the $\mathbf{I}\cdot\mathbf{J}$ interaction term. Zeiger and Bolef[5] observed this splitting in the zero field lines of Cl^{35} in $TlCl^{35}$. They have analyzed the shape of the envelope of the spectrum with the inclusion of all the known interactions and the effects of a finite J. Large residual differences between the calculated shapes after an adjustment of constants, and the observed spectra are attributed to a variation with vibrational and rotational quantum numbers of the gradient of the electric field at the nucleus.

The third line resulting from the transition $F=J+\frac{1}{2}\leftrightarrow F=J-\frac{1}{2}$ has not been observed previously although it has been discussed by Ramsey.[7] Observations of this previously unobserved line are presented for the first time in the present paper. As will be shown, the frequencies of the components of the line at zero field

* This research was supported in part by the U. S. Office of Naval Research. Submitted by R. E. Coté in partial fulfillment of the requirements for the degree of Doctor of Philosophy in the Faculty of Pure Science, Columbia University.

† Present address: Pratt and Whitney Aircraft Corporation, East Hartford, Connecticut.

[1] W. A. Nierenberg and N. F. Ramsey, Phys. Rev. **72**, 1075 (1947), hereafter referred to as NR.

[2] J. W. Trischka, Phys. Rev. **74**, 718 (1948).

[3] L. Grabner and V. Hughes, Phys. Rev. **79**, 819 (1950).

[4] Carlson, Lee, and Fabricand, Phys. Rev. **85**, 784 (1952).

[5] H. J. Zeiger and D. I. Bolef, Phys. Rev. **85**, 788 (1952).

[6] B. T. Feld and W. E. Lamb, Jr., Phys. Rev. **67**, 15 (1945), hereafter referred to as FL.

[7] N. F. Ramsey, Phys. Rev. **74**, 286 (1948).

depend on the quadrupole interaction through terms in $1/J$ and on the cosine interaction through terms in J. At fields which are somewhat greater than zero, but far less than the field at which the interaction energy of the nucleus with the applied field is comparable to the energy of interaction of the nuclear quadrupole moment with the gradient of the electric field at the nucleus, the intensity maximum of the line is found at about twice the usual nuclear resonance frequency, $g_I\mu_0 H/h$.

THEORY

The Hamiltonian which determines the energy levels of a diatomic molecule in a magnetic field is:

$$\mathcal{H}=-\frac{eqQ[3(\mathbf{I}\cdot\mathbf{J})^2+\frac{3}{2}(\mathbf{I}\cdot\mathbf{J})-I(I+1)J(J+1)]}{2I(2I-1)(2J+3)(2J-1)}+c\mathbf{I}\cdot\mathbf{J}+g_I\mu_0\mathbf{I}\cdot\mathbf{H}+g_J\mu_0\mathbf{J}\cdot\mathbf{H}. \quad (1)$$

This expression does not include any interactions involving the second nucleus within the molecule. The first term is the electric quadrupole interaction energy and is expressed in the notation of Bardeen and Townes[8] in which q is the gradient of the electric field at the nucleus. The second term is the cosine coupling between the nuclear magnetic moment and the rotational angular momentum. The third term is the interaction between the nuclear magnetic moment and the external field. The fourth term is the interaction between the molecular rotational magnetic moment and the external field.

For the analysis of the present experimental results, it is not necessary to consider the terms in the Hamiltonian which describes the interaction of the other nucleus with J. The most probable value of J is in the neighborhood of 50 and the energy levels of the entire system are described, to a very exact degree of approximation, as the sum of the energies obtained by considering the interaction of each nucleus separately with the molecular rotation. The neglection of the interaction of the second nucleus with J can be formally justified by the procedure discussed by Bardeen and Townes[8] when the quadrupole interaction of the second nucleus is small compared to that of the first nucleus.

Consider the case in which the interaction with the external field is small compared with the quadrupole interaction energy. This case is best represented in the F, m_F representation. F is the total angular momentum of the molecule and m_F is its projection along the direction of the external field. In this representation the first and second terms are diagonal. The matrix elements are given by Condon and Shortley:[9]

$$(J+\tfrac{1}{2}, m_F|\mathcal{H}|J+\tfrac{1}{2}, m_F)=eqQ[1+3/(2J+3)]/8+\tfrac{1}{2}cJ+g_J\mu_0 Hm_F+(g_I-g_J)\mu_0 Hm_F/2F, \quad (2a)$$

$$(J-\tfrac{1}{2}, m_F|\mathcal{H}|J-\tfrac{1}{2}, m_F)=eqQ[1-3/(2J-1)]/8-\tfrac{1}{2}cJ+g_J\mu_0 Hm_F-(g_I-g_J)\mu_0 Hm_F/2F, \quad (2b)$$

$$(J\pm\tfrac{1}{2}, m_F|\mathcal{H}|J\mp\tfrac{1}{2}, m_F)=(g_I-g_J)\mu_0 H[1-(m_F/F)^2]^{1/2}. \quad (2c)$$

Since the states $J\pm\frac{3}{2}$ are separated from the $J\pm\frac{1}{2}$ states by an energy difference large compared with the energy difference between $J+\frac{1}{2}$ and $J-\frac{1}{2}$ at weak fields, the four by four matrix will approximately factor. If the two by two matrix involving the $J\pm\frac{1}{2}$ states is diagonalized the following is obtained, without any further approximations:

$$E(J\pm\tfrac{1}{2})=\tfrac{1}{2}[b(2+\alpha-\beta)+2g_J\mu_0 Hm_F]\pm\tfrac{1}{2}[b^2(2+\alpha-\beta)^2-4b^2(1+\alpha)(1-\beta)+2b(\alpha+\beta)(kz+cJ)+4k^2(1-3z^2/4)+2kcJz+c^2J^2]^{\frac{1}{2}}, \quad (3)$$

where $\alpha=3/(2J+3)$, $\beta=3/(2J-1)$, $k=(g_I-g_J)\mu_0 H$, $b=eqQ/8$, and $z=m_F/F$. After some simplification and the retention of terms through $1/J$ (3) becomes:

$$E(J\pm\tfrac{1}{2})=b+g_J\mu_0 Hm_F\pm\tfrac{1}{2}[(3b/J+cJ)^2+2kz(3b/J+cJ)+4k^2(1-3z^2/4)]^{\frac{1}{2}}. \quad (4)$$

The selection rules for the perturbation due to the oscillating magnetic field are $\Delta F=0, \pm1$ and $\Delta m_F\pm1$. The frequencies of the components due to the transitions $\Delta F=0$ are zero through terms in $1/J$, except for the term $g_J\mu_0 H$ which is zero at zero field and small at intermediate fields. The moment change in the strong fields in the deflecting magnets would be $g_J\mu_0$ for these transitions and they would not be observable.

The transitions $\Delta F=\pm1$ lead to the following frequencies:

$$f=W(J\pm\tfrac{1}{2}, m_F\pm1)-W(J\mp\tfrac{1}{2}, m_F)/h=\pm[f_0^2+2\nu f_0 z+4\nu^2(1-3z^2/4)]^{\frac{1}{2}},$$
$$f_0=(3b/J+cJ)/h, \quad \nu=k/h, \quad (5)$$

where both k and ν are negative when g_I is negative, as for all nuclei considered in this paper. The term f_0 may itself be negative. Evidently, only the absolute value of f is of interest. The difference between $m\pm1$ and m has been neglected since it leads, in all cases of interest, to terms which are small compared with the main terms. It is seen at once that f_0 is the frequency of the components of the line at zero field. The expression for f_0 agrees with that of NR.

[8] J. Bardeen and C. H. Townes, Phys. Rev. 73, 97 (1948).

[9] E. U. Condon and G. H. Shortley, *Theory of Atomic Spectra* (Cambridge University Press, Cambridge, 1935), pp. 63, 64, 67. The greatest contribution to the energy occurs through the term in eqQ for all cases of interest here. The matrix elements involving this term are, therefore, exact. Since cJ is of the same order as eqQ/J for the molecules here considered and for rotational states of large population, terms involving c and J to a lesser power than the first are ignored. The interaction energies of the nuclear and rotational magnetic moments with the applied magnetic field are less than the interaction energy of the quadrupole moment with the gradient of the electric field at the nucleus for all magnetic fields here considered. Terms involving g_I and g_J and also F to the order $1/F^2$ are, therefore, ignored.

Equation (5) reduces to:

$$f_H = |2\nu(1-3z^2/4)^{\frac{1}{2}}| \tag{6}$$

at magnetic fields for which $|2\nu| \gg |f_0|$. Since the values of f_0 reported in the paper do not exceed 160 kc and since 2ν increases at the rate of somewhat more than 2 kc/gauss, the expression (6) gives an adequate representation of the line components at very moderate fields. Expression (5) differs from that of Ramsey[7] in the terms involving the $\mathbf{I}\cdot\mathbf{J}$ interaction constant and g_J.

Consider the zero field line whose components have a frequency $f_0=(3b/J+cJ)/h$. The line shape, of course, depends on the population of the various J states. The intensity at a particular frequency is determined by the product of the "density function," $|dJ/df|$ and by the population of the J states which contribute to a particular frequency interval. The intensity then is:

$$\text{Int} \propto |dJ/df| J \exp(-\alpha^2 J^2), \tag{7}$$

where

$$\alpha^2 = h^2/8\pi^2 IkT,$$

in which I is the moment of inertia of the molecule and T the temperature of the oven. Then

$$\text{Int} \propto J^3 \exp(-\alpha^2 J^2)/|cJ^2-3b|. \tag{8}$$

TABLE I. The temperature, internuclear distance, most probable value of J, and α^2 for certain alkali halides.

Molecule	T(°K)	r_e(A)	$\alpha^2\times10^4$	$\bar{J}$
NaF	1250	2.1	4.58	33
NaCl	1025	2.51	2.65	43
NaBr	1000	2.64	1.92	51
NaI	975	2.90	1.49	58
KBr	1000	2.94	1.05	69

This expression, of course, does not give the intensity in terms of the experimentally observed quantity, f_0, but only in terms of J. If c has the same sign as b it is apparent that a maximum of intensity will occur at $J=(3b/c)^{\frac{1}{2}}$ and that this intensity will occur at the frequency $f_{\min}=(12bc)^{\frac{1}{2}}/h$. At all frequencies other than $f_{\min}$, two values of J contribute to the intensity. These two values are related by $J_1J_2=3b/c$. If $f_{\min}$ occurs at a value of J for which the population is very low, as, for example, when $b\to0$ or $c\to0$, the total integrated intensity within the maximum defined by $cJ^2=3b$ is very small and an analytic maximum may occur. In the limiting case, $c=0$, $f_0=3b/Jh$ and the maximum intensity occurs at $J=\sqrt{3}\bar{J}$ corresponding to $f=\sqrt{3}b/\bar{J}h$, where $\bar{J}$ is the most probable value of J. When $b=0$, $f_0=cJ/h$ and the maximum intensity occurs at $J=\bar{J}$ and $f=c\bar{J}/h$. The general condition which determines the analytic maximum is found by differentiation of (8) with respect to f.

$$J^2=\{6\alpha^2b+c\pm[(6\alpha^2b+c)^2-72\alpha^2bc]^{\frac{1}{2}}\}/4\alpha^2c. \tag{9}$$

Since J^2 must be real and positive the condition that must be fulfilled for the occurrence of an analytic maximum for the intensity as a function of J is that $(6\alpha^2b+c)^2 \geq 72\alpha^2bc$. From a study of this inequality the following conclusions can be drawn.

1. If $0.01685 < b\alpha^2/c < 1.65$ there is only one maximum, determined by $J=(3b/c)^{\frac{1}{2}}$.

2. If $b\alpha^2/c=0.01685$ or 1.65 two maxima exist, but they coincide.

3. For values of b, c, and α not satisfying 1 and 2, two maxima occur, one for $J=(3b/c)^{\frac{1}{2}}$ and the other for the value of J determined by the root of (9).

When two maxima of intensity occur, two values of J contribute to the intensity at any frequency. We have, in the preceeding analysis, neglected one of these values; however, the maximum is not much affected, since one set of J values, of very low population, gives a monotonically varying intensity while the other, of higher population gives rise to the maximum.

When c has a sign opposite to that of b, there is a single maximum of intensity for a value of J given by (9). The sign to be taken is that which makes J positive. The value of $(3b/J+cJ)/h$ may take on both positive and negative values. Evidently, since the absolute value of f is observed, the addition of the intensity arising for a negative f and a positive f may seriously modify the position of the intensity maximum as determined from (9).

In Table I are given the values of the quantities α^2 and $\bar{J}$ appropriate to the molecules studied in this work. The temperatures of the ovens from which the molecules were evaporated are also given in the table. The internuclear distances of all the molecules except NaF are obtained[10] from electron diffraction data while that of NaF is estimated by Wick.[11] In Table II are given values of the quadrupole and dipole interaction

TABLE II. Magnitude and sign of eqQ/h and c/h. The columns A, B, and C refer, respectively, to the reference for the magnitude of eqQ/h, the sign of eqQ/h, and the magnitude of c/h. Where no reference is given the results are from the present work. The symbols HF and ZF refer to results at high field and zero field of the magnetic resonance method. The symbol ER refers to results of the electric resonance method.

Molecule	Resonance	$8b/h$ eqQ/h (Mc)	A	B	c/h (kc)	C
NaF	Na^{23}HF	−8.12	13	13		
	ZF	−8.40	5		1	5
NaCl	Na^{23}ZF	−5.67			0.37	
	HF	−5.40	1	13		
	ZF	−5.608	5		1	5
NaBr	Na^{23}HF	−4.68	1	13		
	ZF	−4.88			0.67	
NaI	Na^{23}HF	−3.88	1	13		
	ZF	−3.96			0.69	
KBr	Br^{79}ER		15		≤2	15
	$v=0$	+10.24				
	$v=1$	+11.22				
	$v=2$	+12.20				
	Br^{81}ER					
	$v=0$	+8.553			≤2	

[10] Maxwell, Hendricks, and Mosley, Phys. Rev. **52**, 968 (1937).
[11] G. C. Wick, Phys. Rev. **73**, 51 (1948).

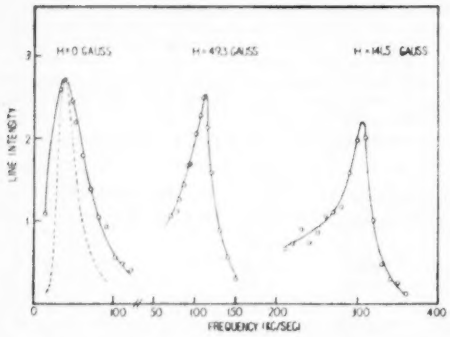

FIG. 1. Nuclear resonance spectra, $(J+\frac{1}{2})\leftrightarrow(J-\frac{1}{2})$, of Na^{23} in NaCl at several magnetic fields. The dotted curve is a theoretical curve using the values: $b/h=-709$ kc and $c/h=-0.16$ kc.

constants obtained from observations on various kinds of spectra with the exception of the spectrum arising from the transition $(J+\frac{1}{2})\leftrightarrow(J-\frac{1}{2})$ here considered. The data include the results of the present observations on the transitions $(J\pm\frac{3}{2})\leftrightarrow(J\pm\frac{1}{2})$. It is evident from a calculation involving the data of Tables I and II that an analytic maximum in the intensity distribution for the line $(J+\frac{1}{2})\leftrightarrow(J-\frac{1}{2})$ cannot occur in any of the resonances here observed if b/h and c/h have the same sign and for a considerable range of c/h around that given in Table II.

APPARATUS AND METHOD

The apparatus is the same as that used in previous experiments on molecular beams. The relevant characteristics of the apparatus are described in earlier papers.[12,13] The only modification was the addition of a re-entrant cavity, mounted on a flexible bellows. The cavity could be inserted into the gap of the C magnet, immediately adjacent to the hairpin which produced the rf field. The magnetic field could then be measured during the course of a run by use of a conventional flipcoil. The flipcoil was used during most of the experiments to measure the fields and was always used to determine the zero field condition. In several experiments a double oven mount previously described[14] was used and the field was calibrated by use of the Li^7 resonance in LiCl. The F^{19} resonance in NaF was used for this purpose when the Na^{23} resonance in this molecule was studied.

EXPERIMENTAL DATA

A. NaCl

Figure 1 shows the observed $(J+\frac{1}{2})\leftrightarrow(J-\frac{1}{2})$ line due to the sodium nucleus in NaCl at fields which vary from zero to one sufficiently high so that the frequency of the maximum and the line shape are only trivially affected by terms containing b and c. Of particular interest is the frequency of the maximum at zero field, $f_0=37$ kc, whose width at half-intensity is 54 kc.

Figure 2 shows the $(J\pm\frac{3}{2})\leftrightarrow(J\pm\frac{1}{2})$ line due to the sodium nucleus in NaCl at zero field. The present data shows more structure for this resonance than was previously observed by NR and by Zeiger and Bolef.[5]

The $(J\pm\frac{3}{2})\leftrightarrow(J\pm\frac{1}{2})$ line, in the absence of $\mathbf{I}\cdot\mathbf{J}$ interaction and any variation of b with J and v should occur at a frequency $f=2b/h$. The addition of the $\mathbf{I}\cdot\mathbf{J}$ interaction splits the line giving a doublet of separation $2c\bar{J}/h$, symmetrical about the frequency $2b/h$.

Zeiger and Bolef observed only the splitting, indicated by dd in Fig. 2, and attributed this to the $\mathbf{I}\cdot\mathbf{J}$ interaction. The value of ~1 kc is given for c/h. If the $\mathbf{I}\cdot\mathbf{J}$ splitting is assumed to give rise to the two maxima (dd in Fig. 2) the results of the present experiment give the same value for the separation $2c\bar{J}/h$, but the additional structure complicates the interpretation of the curve. It is equally possible to assume that the two maxima d', d', in Fig. 2 correspond to the $\mathbf{I}\cdot\mathbf{J}$ splitting and that the approximate repetition of the pattern corresponds to a marked variation of b with v. In fact, if we follow the notation of Zeiger and Bolef the observed curve can be fitted quite satisfactorily by the following constants:

$$b/h=-709\text{ kc},\quad |c\bar{J}/h|=16\text{ kc},\quad \bar{J}=43,\quad \gamma=0.25,$$
$$|c/h|=0.37\text{ kc},\quad P=+85\text{ kc},$$

where $\gamma=eq^{(J)}Q/2\sqrt{2}\alpha c$, $P=eq^{(v)}Q/4h$, and $q=q^{(v)}+q^{(J)}J(J+1)+q^{(v)}(v+\frac{1}{2})$. The sign of b/h is obtained from the measurements of Logan, Coté, and Kusch,[13] and cannot be determined from an analysis of the line $(J\pm\frac{3}{2})\leftrightarrow(J\pm\frac{1}{2})$. The sign of c/h cannot be determined from an analysis of this line but can be inferred from the position of the line $(J+\frac{1}{2})\leftrightarrow(J-\frac{1}{2})$. It is evident from a comparison of the observed curve with that calculated that a better fit could be obtained by considering in addition to the variation of q with J and v a marked decrease of the quantity c/h with vibrational

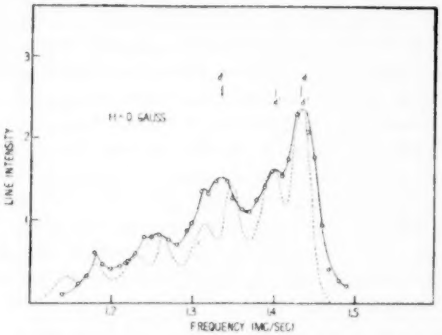

FIG. 2. Nuclear resonance spectrum of Na^{23} in NaCl arising from transitions $(J\pm\frac{3}{2})\leftrightarrow(J\pm\frac{1}{2})$. The dotted curve is a theoretical curve calculated from the following values: $b/h=-709$ kc, $c\bar{J}/h=16$ kc, $\bar{J}=43$, $\gamma=0.25$, $P=+85$ kc, and $c/h=0.37$ kc.

[12] H. Taub and P. Kusch, Phys. Rev. **75**, 1481 (1949).
[13] Logan, Coté, and Kusch, Phys. Rev. **86**, 280 (1952).
[14] P. Kusch and H. M. Foley, Phys. Rev. **74**, 250 (1948).

quantum number. As will be shown, the present interpretation yields a value of c more nearly in accord with that required to interpret the $(J+\frac{1}{2})\leftrightarrow(J-\frac{1}{2})$ line than does that of Zeiger and Bolef.

The $(J+\frac{1}{2})\leftrightarrow(J-\frac{1}{2})$ line shows shapes which are qualitatively the same as those which would be expected on the basis of the earlier discussion, both in the presence of an external field and at zero field.

At zero field where the line shape and position is sensitive to the values of b and c, it is necessary to consider both possible signs of c, since the sign is previously undetermined. From the analysis of Zeiger and Bolef and assuming a negative sign for c, $c/h=-1.0$ kc, and $f_0=92$ kc. If the present analysis of the spectrum arising from $(J\pm\frac{3}{2})\leftrightarrow(J\pm\frac{1}{2})$ is used and a negative sign is assumed for c, $c/h=-0.37$ kc and $f_0=56$ kc. In order to obtain the observed value of $f_0=37$ kc it is necessary that $c/h=-0.16$ kc.

The theoretical line shape has been calculated assuming a value of $c=-0.16$ kc and appears as the dotted curve in Fig. 1. To avoid the infinities which occur in Eq. (8), $|dJ/df|$ has been read, for a finite interval df, from a graph in which f is plotted as a function of J. These quantities when multiplied by the Boltzmann function give the intensity distribution, uncorrected for the resolution properties of the apparatus.

This uncorrected curve has been modified by a numerical integration over the usual resonance function where a resolution half-width of 5 kc has been assumed. The intensity has been adjusted to give coincidence of the peaks at the maximum. The general features of the calculated and observed curves are similar, though the observed width at half-intensity, 54 kc is considerably greater than the calculated width of 28 kc.

It is instructive to examine the case when c is positive. In Fig. 3 the intensity as calculated from Eq. (8) for $b/h=-709$ kc and several values of c, is plotted as a function of f in the dotted curves. The solid curves indicate the intensity as summed for positive and negative f. No resolution function has been applied since the structures are broad as compared to the resolution half-width. It is evident that no positive value of c will give a resonance curve of the appropriate width and at the appropriate frequency. The curve for $c=0$ has a shape similar to the observed shape. The maximum occurs at about 28 kc and the width is 32 kc, still less than the observed width. It is evident that a small positive value of c will further reduce the calculated value of f_0 and increase the calculated width.

It is probable that the more satisfactory explanation of the zero field line occurs for an analysis which gives the experimentally observed position of the line rather than the experimentally observed width for the line. Several factors will serve to increase the line width from that here calculated; among these are a variation of b with both J and v and a possible variation of c with J and v. In view of the uncertainties which occur

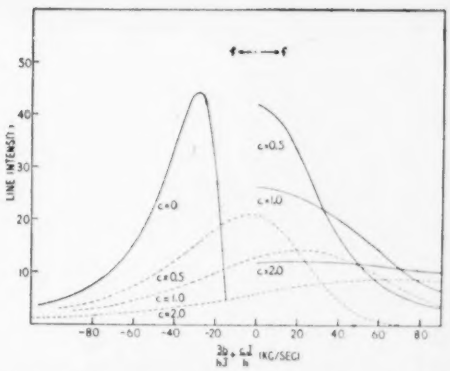

FIG. 3. Calculated line shapes for the $(J+\frac{1}{2})\leftrightarrow(J-\frac{1}{2})$ line of Na^{23} in NaCl for several positive values of c using $b/h=-709$ kc. The solid curves indicate the intensity as summed for positive and negative f.

in other analyses which purport to determine the magnitude of c/h, it might appear that a value, of at least as great a validity as previous ones, is $c/h=-0.16$ kc. However, since equally serious inconsistencies arise in the cases of other molecules where the interpretation of the $(J\pm\frac{3}{2})\leftrightarrow(J\pm\frac{1}{2})$ resonance is not ambiguous, it cannot be asserted that $c/h=-0.16$ kc for Na in NaCl.

A little analysis shows that the variation of b with J and v as given by our analysis of the line $(J\pm\frac{3}{2})\leftrightarrow(J\pm\frac{1}{2})$ will not significantly shift the line maximum. It is, however, possible to assume a variation of c with J which would shift the maximum rather considerably. If this variation were of such a nature that, for J states of high population, the Hamiltonian of the interaction is of the form $c'\mathbf{I}\cdot\mathbf{J}/J$, the observed splitting in the $(J\pm\frac{3}{2})\leftrightarrow(J\pm\frac{1}{2})$ line is $2c'$. The zero field line, $(J+\frac{1}{2})\leftrightarrow(J-\frac{1}{2})$ then has the frequency $f_0=(3b/J+c')/h$. From an analysis of the line $(J\pm\frac{3}{2})\leftrightarrow(J\pm\frac{1}{2})$, $|c'|=16$ kc. The intensity distribution is exactly as shown for the case $c=0$ in Fig. 3 except that the frequency scale is shifted. If $c'=-16$ kc, the maximum occurs at 44 kc. While no other evidence exists to indicate the validity of the analysis it is apparent that a detailed fit of experimental data to a calculated position cannot be made without further knowledge of the variation of c with J and v.

Figure 4 shows the frequency variation of the resonance as a function of magnetic field. The line whose slope is $2g(Na^{23})\mu_0/h$ is drawn for reference. The good agreement justifies the assumption that the resonance is due to the sodium nucleus and indicates that the line is, indeed, the spectroscopic structure which the theory has assumed.

B. NaBr

The lines observed in NaBr and attributed to the $(J+\frac{1}{2})\leftrightarrow(J-\frac{1}{2})$ transition of Na are similar to those observed in NaCl except at zero field. No maximum was observed for this resonance at zero field. It is to be

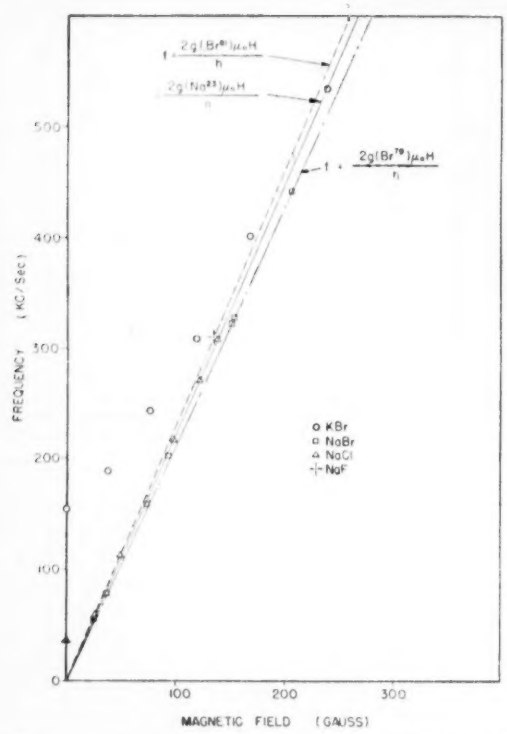

FIG. 4. The experimental data which show the variation of the intensity maximum with magnetic field for the Na^{23} resonance in NaCl, NaBr, and NaF and for the Br^{79} and Br^{81} resonances in KBr. The lines whose slopes are $2g(Br^{79})\mu_0$, $2g(Br^{81})\mu_0$ and $2g(Na^{23})\mu_0$ are shown for reference.

noted that the lines when measured at fields sufficiently greater than zero to bring them into a manageable range of frequency were sharp. For example, when the resonance maximum occurred at 52 kc, the curve had a width of 26 kc.

The g_I's of the component nuclei, Na^{23}, Br^{79}, Br^{81}, are so nearly the same that the error in field measurement precludes an identification of the nucleus responsible for the observed resonances by a measurement of the slope of the frequency *versus* field curve. However, the line does not show a splitting at fields for which a splitting greater than the observed line width should occur if the bromine nuclei are responsible for the resonance. Hence the resonance is unambiguously ascribed to the sodium nucleus.

The $(J\pm\frac{3}{2})\leftrightarrow(J\pm\frac{1}{2})$ lines of Na in NaBr are shown in Fig. 5. The lines are identified with Na since the quadrupole interaction determined from these lines is in substantial agreement with that derived from high field data where the assignment of the structure to Na is unambiguous. The splitting shown in Fig. 5 has not

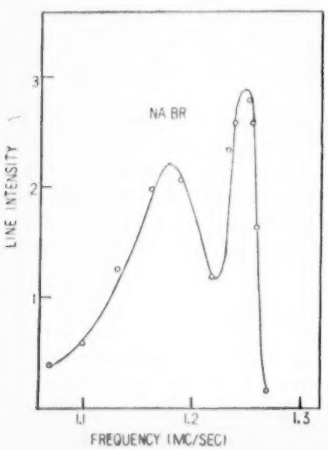

FIG. 5. Nuclear resonance spectrum of Na in NaBr arising from transitions $(J\pm\frac{3}{2})\leftrightarrow(J\pm\frac{1}{2})$ at zero field.

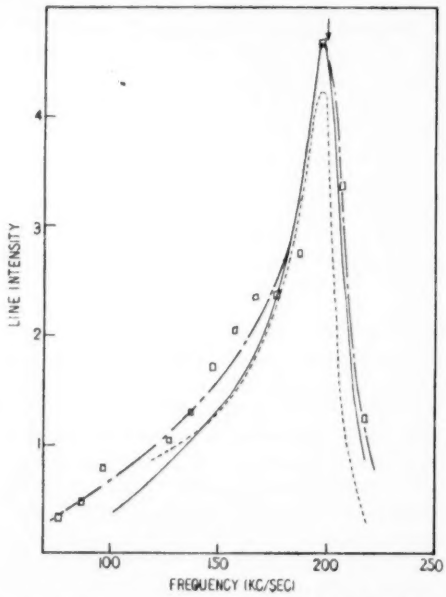

FIG. 6. Nuclear resonance spectrum of Na in NaBr arising from transitions $(J+\frac{1}{2})\leftrightarrow(J-\frac{1}{2})$ at 178 gauss. The dashed curve is the observed curve. The solid curve is a theoretical curve using the values: $b/h=-585$ kc and $c/h=0.67$ kc. The dotted curve is calculated from $f=2\nu(1-3\varepsilon^2/4)^{\frac{1}{2}}$.

previously been observed. Values of $eqQ/h=-4.88$ Mc/sec ($b=-610$ kc) and $c/h=0.67$ kc/sec are obtained from this curve on the assumption that the splitting is due to the $\mathbf{I}\cdot\mathbf{J}$ interaction. The sign of b is obtained from other evidence.[13] If c is negative, the line $(J+\frac{1}{2})\leftrightarrow(J-\frac{1}{2})$ is sharp and is expected to occur at 70 kc. If c is positive, however, the maximum occurs at about 18 kc if both positive and negative frequencies are considered. When the intensities associated with equal positive and negative frequencies are added, a single broad maximum, decreasing in intensity from zero frequency, is predicted. Neither calculation fits the observed data; the first because the line is in the wrong position and the second because the calculated line width is excessive.

In spite of the difficulties which occur in the analysis of the lines $(J+\frac{1}{2})\leftrightarrow(J-\frac{1}{2})$, at zero field, excellent agreement between the experimentally observed resonance and that calculated is obtained for the observation at "high" field where $2\nu \gg f_0$. The dashed curve in Fig. 6 is the resonance curve of Na in NaBr at a field of 178 gauss. The curve drawn as a solid line is calculated under the assumption that $b/h=-585$ kc and $c/h=+0.67$ kc. Figure 6 is the result of numerical integration. The frequencies as obtained from (5) are plotted as a function of z for several values of J. Values of dz/df are taken from the curves for each J and multiplied by the Boltzmann function to give a quantity proportional to the intensity. The transition probability is very nearly a constant and its variation is ignored. The usual resolution function for a half-width of 5 kc has been applied to give the final intensities in Fig. 6.

The dotted curve shows the intensity distribution at the same field when the high field expression (6) is used. The two curves show that the effect of the constants b and c on the shape and position of the line is very small. The small shift of the maximum in Fig. 6 from $2g_I\mu_0 H/h$ arises from the resolution effects in a highly unsymmetrical line. The agreement between the observed and calculated curves is satisfactory and indicates the general validity of the analysis of the line at high field. The resonance has been observed at fields as high as 1400 gauss where it has lost its characteristic shape and is very broad. The characteristic shape is still evident at a field of 500 gauss ($f\sim 1090$ kc) where the width is 170 kc.

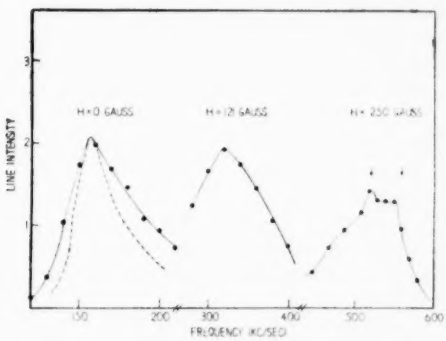

FIG. 7. Nuclear resonance spectra, $(J+\frac{1}{2})\leftrightarrow(J-\frac{1}{2})$, of Br^{79} and Br^{81} in NaBr at several magnetic fields. The dotted curve is a theoretical curve using the values: $b(79)/h=+1670$ kc, $b(81)/h=+1400$ kc, $c(79)/h=+1.21$ kc and $c(81)/h=+1.30$ kc.

The term in g_J has been neglected in all the calculations. To the precision with which the field was measured, g_J is, indeed, negligible.

C. KBr

Typical resonance curves for the line $(J+\frac{1}{2})\leftrightarrow(J-\frac{1}{2})$ for Br^{79} and Br^{81} in KBr are shown in Fig. 7. The splitting due to the two isotopes begins to be apparent in the line of highest frequency. The arrows indicate the frequencies $2g_{79}\mu_0 H/h$ and $2g_{81}\mu_0 H/h$. Both the splitting and the frequency of the line at sufficiently high fields attribute the line, unambiguously, to the Br isotopes rather than K.

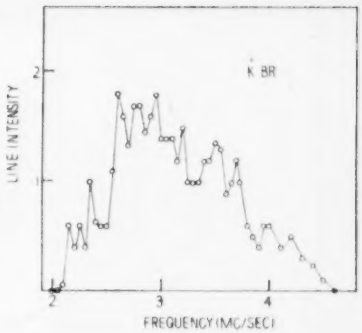

FIG. 8. Nuclear resonance spectrum of Br^{79} and Br^{81} in KBr arising from transitions $(J\pm\frac{1}{2})\leftrightarrow(J\pm\frac{1}{2})$ at zero field.

A resonance curve (Fig. 8) has been observed in KBr with a frequency around 3 Mc. Recent experiments by Fabricand, Carlson, and Lee[15] have produced the data of Table II on the quadrupole interaction of Br in KBr. The quadrupole interaction shows a large change with vibrational state and it should be noted that it is low with respect to any values which might be ascribed to the eqQ's on the basis of Fig. 8. It must be realized, however, that the results of the electrical resonance method are for the $J=0$ state while the most probable J for the present experiment is about 70. A meaningful analysis of the bromine resonance in Fig. 8 appears to be impossible.

The ratio of the quadrupole moments of the bromine isotopes is known[16] to be $Q_{79}/Q_{81}=1.194$ and the ratio of the g_I values[17] to be $g_{81}/g_{79}=1.078$.

To satisfy the known ratios of the b's and c's, to describe approximately the resonance of Fig. 8, and to give a good fit to the data on the $(J+\frac{1}{2})\leftrightarrow(J-\frac{1}{2})$ line at zero field, the following constants have been found: $c_{79}/h=+1.21$ kc, $c_{81}/h=+1.30$ kc, $b_{79}/h=+1670$ kc, $b_{81}/h=+1400$ kc.

The dotted curve shown for zero field in Fig. 7 indicates an agreement in the frequency of the maximum and the shape of the line. The excessive width of the observed line is not unexpected in view of the large variation of b with J and v. In view of the inconsistencies which arise for the case of the Na resonances $(J\pm\frac{3}{2})\leftrightarrow(J\pm\frac{1}{2})$ and $(J+\frac{1}{2})\leftrightarrow(J-\frac{1}{2})$, the given b's and c's are not to be construed as highly meaningful quantities.

D. NaF

The $(J+\frac{1}{2})\leftrightarrow(J-\frac{1}{2})$ resonance due to Na^{23} in NaF was identified by its frequency at a fixed value of magnetic field. The line had the same general shape as

[15] Fabricand, Carlson, and Lee (private communication).
[16] C. H. Townes, J. Chem. Phys. **17**, 782 (1949).
[17] J. R. Zimmerman and D. Williams, Phys. Rev. **76**, 350 (1949).

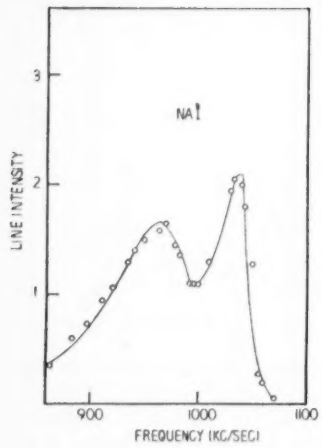

FIG. 9. Nuclear resonance spectrum of Na^{23} in NaI arising from transitions $(J\pm\frac{3}{2})\leftrightarrow(J\pm\frac{1}{2})$ at zero field.

that of the lines previously discussed. Unfortunately, the zero field $(J+\frac{1}{2})\leftrightarrow(J-\frac{1}{2})$ line was obscured by a very broad F^{19} resonance.

E. NaI

The $(J\pm\frac{3}{2})\leftrightarrow(J\pm\frac{1}{2})$ resonance of Na in NaI at zero field is shown in Fig. 9. The resonance, unresolved into two components, has been observed[1] previously. From this resonance it is found that $eqQ/h=-3.96$ Mc/sec, where the negative sign is known from other evidence,[18] and that $|c/h|=0.69$ kc. A line has been observed at zero field and attributed to the $(J+\frac{1}{2})\leftrightarrow(J-\frac{1}{2})$ resonance of Na by an observation of the frequency of this line at fields where $2\nu\gg f_0$. The line has the characteristic shape observed for Na in NaCl and for Br in KBr, i.e., a drop in intensity on the low frequency side of the maximum and a slower drop in intensity on the high frequency side. This appearance is characteristic of a c of the same sign as b when c is not extremely small. The observed value of f_0 is 36 kc which then leads to a c of -0.23 kc. The observed width is 50 kc. The discrepancy between the data obtained from the two zero field resonances is notable. In all cases the value of c obtained from the $(J+\frac{1}{2})\leftrightarrow(J-\frac{1}{2})$ line is less than that obtained from the $(J\pm\frac{3}{2})\leftrightarrow(J\pm\frac{1}{2})$ line.

DISCUSSION

In each of the diatomic molecules which has been studied except NaF, a single resonance, attributable to the transition $(J+\frac{1}{2})\leftrightarrow(J-\frac{1}{2})$ has been observed. For the Cl nucleus in NaCl and especially for the K nucleus in KBr, the nuclear g value is so small that a transition results in a small moment change and hence leads to a resonance of low intensity. A careful search under optimum experimental conditions might yield a resonance of Cl in NaCl. No resonance due to Br or I in the sodium halides has been observed in any of the several kinds of spectra observed by molecular beams methods. It may be assumed that the internal interactions, principally the quadrupole interaction, are very large and that the spectrum, therefore, is so broad that the intensity at any frequency is very small. Large internal interactions would also prevent the observation of the $(J+\frac{1}{2})\leftrightarrow(J-\frac{1}{2})$ lines for Br and I in NaBr and NaI. It is interesting to note that in the case of NaF, where the nuclear moments of both nuclei are fairly large and where the internal interactions are not large, resonances have been observed for both Na and F, even though they cannot be analyzed separately.

Several lines of evidence have been developed on the internal interactions of the alkali halides. The electrical resonance method gives unambiguous results but only for states with a very low J value. The magnetic resonance method at high magnetic field gives the quadrupole interaction energy for a statistical distribution in J as does a measurement of the transition $(J\pm\frac{3}{2})\leftrightarrow(J\pm\frac{1}{2})$ at zero field. The results of the magnetic resonance method at high and low fields are in excellent agreement and may, therefore, be assumed to give a reliable value of the quadrupole interaction energy. The line $(J\pm\frac{3}{2})\leftrightarrow(J\pm\frac{1}{2})$ gives, as well, a value for the internal dipole interaction for the most probable value of J. Finally, the line $(J+\frac{1}{2})\leftrightarrow(J-\frac{1}{2})$ at zero field gives a frequency dependent on both the quadrupole and dipole interaction energies. On the assumption that the quadrupole interaction constant is correctly determined by other lines of evidence, the value of c/h as determined from the $(J+\frac{1}{2})\leftrightarrow(J-\frac{1}{2})$ line on the basis of present theory is in marked disagreement with that determined from the $(J\pm\frac{3}{2})\leftrightarrow(J\pm\frac{1}{2})$ line. A satisfactory explanation of the discrepancy may require a more refined theoretical treatment, the inclusion of additional interaction terms and a knowledge of the variation with J and v of terms here assumed to be constant.

We wish to express our thanks to Mr. Ralph Logan and Mr. Stefan Ochs for assistance in the experimental work. Professor H. M. Foley has given much assistance in the theoretical interpretation of the results.

Capacitance Effects in Thin Conductive Films*

J. N. HUMPHREY, FRANCES L. LUMMIS, AND W. W. SCANLON
United States Naval Ordnance Laboratory, White Oak, Maryland

(Received December 18, 1952)

The frequency dependence of the resistance of thin films of lead sulfide and tellurium is analyzed in terms of distributed capacitance and intercrystallite capacitance. It is shown that for some films of either material the observed behavior can be explained in terms of distributed capacitance alone, but that others require a combination of the two types of capacitance. An expected correlation between photoconductivity and the presence of intercrystallite capacitance was not found in these experiments.

I. INTRODUCTION

IT has been shown by Chasmar[1] that the impedance of thin semiconducting films (PbS and PbSe) can be represented by an equivalent parallel *RC* circuit, in which the resistance component decreases with increasing frequency. He attributed this decrease to the capacitative shunting of the contact resistance between adjacent crystallites. His measurements were submitted as indirect evidence in support of a theory of photoconductivity proposed by Sosnowski, Starkiewics, and Simpson,[2] who suggested that contacts between *p*- and *n*-type crystallites might give rise to the photoconductivity observed in these films.

Because of the microcrystalline nature of this type of film, Chasmar suggested that it could be represented by an equivalent electrical circuit whose elements are the intercrystallite resistance and capacitance, and the internal resistance of the crystallites. Measurements of the contact resistance between the crystallites and a quantitative explanation of the attendant frequency dependence could be used to evaluate the Sosnowski hypothesis.

A study of the resistance and capacitance of tellurium and lead sulfide films was made by the present authors,[3] in which a partially successful quantitative explanation of the frequency dependence of the resistance was obtained. The behavior of some of the films studied could be explained by this model or by an extension which included a variation of intercrystallite capacitance from point to point within a given film. For other films the model was inadequate. Accordingly, a brief review of the experimental procedure used previously is given below.

Resistance measurements were made with Boonton *Q*-meters, types 160-A and 170-A, at frequencies up to 200 mc/sec. The films studied included commercial photoconductive PbS, and tellurium films in Dewar-type cells. The cells were supported by a cylindrical phenolic holder suspended above the *Q*-meter. It was established that losses due to the holder and to the coolant in the cell were negligible. After studying the resistance of a cell as a function of frequency and temperature the film was removed either chemically or by evaporation and the resistance-frequency behavior of the glass blank was obtained. In this way the actual film resistance could be calculated as a function of frequency and temperature.

Rittner and Grace[4] have found evidence that the frequency dependence of resistance in photoconductive lead sulfide films is due to distributed capacitance rather than to a capacitative shunting between crystallites. They applied a calculation by Howe[5] which predicted a decrease in the resistance of a homogeneous resistor at high frequencies. Measurements of the resistance

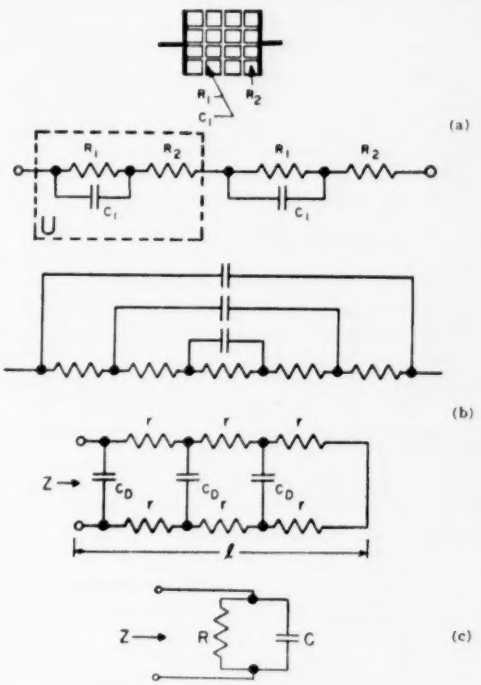

FIG. 1. Equivalent electrical circuits representing a thin microcrystalline film: (a) considering only intercrystallite capacitance; (b) considering only distributed capacitance; (c) parallel representation of either of the above cases.

* Presented at the 312th Meeting of the American Physical Society in Columbus, Ohio, March, 1952 [Phys. Rev. **86**, 660 (1952)].

[1] R. P. Chasmar, Nature **161**, 281 (1948).

[2] Sosnowski, Starkiewics, and Simpson, Nature **158**, 28 (1946); and Nature **159**, 818 (1947).

[3] Humphrey, Lummis, and Scanlon (unpublished).

[4] E. S. Rittner and F. Grace, Phys. Rev. **86**, 955 (1952).

[5] G. W. O. Howe, Wireless Engr. **12**, 291 (1935); **12**, 413 (1935); **17**, 471 (1940).

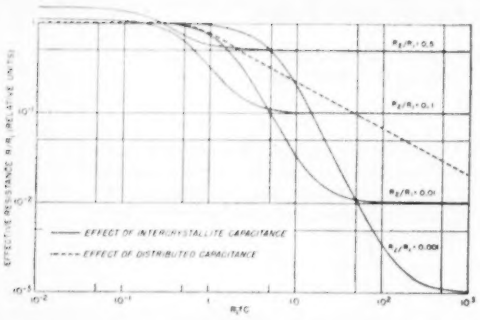

FIG. 2. Theoretical frequency dependence of resistance of thin microcrystalline films.

of three films of various types were made as a function of frequency and temperature, and the results were found to agree with the predicted behavior.

The present paper will interpret further our previous data[3] obtained for tellurium and lead sulfide in terms of intercrystallite and distributed capacitances.

II. INTERCRYSTALLITE CAPACITANCE

The equivalent circuit proposed by Chasmar is shown in Fig. 1(a), where the contact resistance between crystallites is represented as R_1, the capacitance between crystallite faces by C_1, and the internal resistance of each crystallite by R_2. This can be further simplified to Fig. 1(c), a parallel combination of a resistance and a capacitance, the value of each being a function of frequency. For a rectangular film of length L, width W, and unit thickness, the resistance is given by

$$R=\frac{L}{W}\left[\frac{(R_1+R_2)^2+R_2^2R_1^2\omega^2C_1^2}{R_1+R_2+R_2R_1^2\omega^2C_1^2}\right]. \tag{1}$$

It is convenient to express the resistance as R/R_1 with the dimensionless quantity R_1fC_1 as the independent variable and R_2/R_1 as a parameter. Four members of such a family of curves are shown in Fig. 2. There are two important characteristics of these curves to be noted:

(1) At frequencies higher than the knee frequency a nearly straight section occurs having a slope which may be as steep as -2, depending only on the ratio R_2/R_1.

(2) At higher frequencies a foot is reached where the resistance approaches a constant minimum value. These characteristics can be used to indicate the presence of intercrystallite capacitance.

III. DISTRIBUTED CAPACITANCE

The distributed capacitance is illustrated by the first circuit of Fig. 1(b) as the capacitance existing between resistor elements symmetrically displaced on each side of the center of the resistor. This capacitance gives rise to a nonuniform charge distribution lengthwise of the resistor due to current flow.

To relate the high frequency resistance to the distributed capacitance, Howe calculates the capacitance per unit length by assuming a density of charge proportional to the distance from the center. He then treats the resistor as a short-circuited transmission line, obtaining the impedance in the form:

$$Z=Z_0\tanh \alpha l, \tag{2}$$

where $Z_0=(R_1/j\omega c l)^{\frac{1}{2}}$, $\alpha=(j\omega cR_1/l)^{\frac{1}{2}}$, $c=$capacitance per unit length of line, $r=R_1/l=$dc resistance per unit length of line, $2l=$length of resistor, and $C_D=lc=$total distributed capacitance.

This impedance can also be represented by a resistor and a capacitor in parallel, the value of each being a function of frequency:

$$1/R=\mathrm{Re}(1/Z), \quad \omega C=\mathrm{Im}(1/Z). \tag{3}$$

The variation of the resistance with frequency is shown by the dashed curve in Fig. 2. A graphical identification of the position of the knee is given by the relation:

$$\text{When } R_1fC_D=1 \quad \text{then} \quad R/R_1=0.75. \tag{4}$$

Note the difference between this curve and those of the intercrystallite model. The slope for the distributed capacitance model has a maximum value only slightly steeper than $-\frac{1}{2}$. At higher frequencies the slope becomes constant with a value of $-\frac{1}{2}$. It does not subsequently flatten out.

The value of the capacitance per unit length c is obtained from the geometry of the resistor, and for the proportions found in the film discussed here it is given approximately by

$$c=0.35(K_e+1)W/L \ \mu\mu\text{f/cm},$$

TABLE I. Geometry and parameters of tellurium and lead sulfide films.

Film	Dimensions (cm) L	W	Temp. °C	Resistance (ohms) R_1	R_2	Capacitance ($\mu\mu$f) C_D—distributed by geometry	C_D—distributed from resistance data	C_1—intercrystallite from resistance data
Te No. 62	0.04	0.4	25°	1.3×10^5	···	0.3±0.1	0.5±0.1	···
			−78°	9.5×10^5	···			
			−185°	1.2×10^7	···			
Te No. 70	0.7	1.7	25°	3.5×10^6	3.6×10^4	0.5±0.2	0.5±0.1	0.5
			−185°	2.8×10^7	4.7×10^4	0.5±0.2	0.3±0.1	0.2
PbS	0.25	1.0	25°	1.9×10^6	5.0×10^3	0.7±0.3	0.6±0.1	0.5

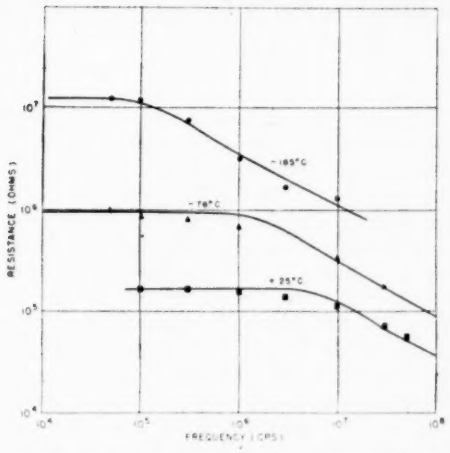

FIG. 3. Resistance *vs* frequency data for evaporated tellurium cell No. 62. $T=25°C$, $-78°C$, and $-185°C$.

where W/L is width/length of the film, and K_e, the effective value of the dielectric constant, is between 1 and K depending on the thickness of the supporting glass.

IV. TEMPERATURE DEPENDENCE

An examination of the temperature dependence of the ac resistance provides a further means for distinguishing between the two models described above. The distributed capacitance depends on the over-all geometry of the film which is relatively temperature insensitive. The intercrystallite capacitance, however, depends upon the width of the gap between adjacent crystallites. This gap width depends upon the differential expansion of the substrate and film. Furthermore the coefficient of expansion of the substrate is much less than that of the film, and the size of a crystallite is much greater than the gap between crystallites. Thus variation of the temperature of the film will cause a marked change in the width of this gap, and a corresponding change in the value of the capacitance. The ratio R_2/R_1 may also be expected to change markedly with temperature. Therefore if intercrystallite capacitance is important R/R_1 *vs* R_1f should depend upon the temperature, while it should be relatively temperature independent if only distributed capacitance is present.

V. RESULTS AND DISCUSSION

The geometry, conditions of measurement, and characteristics of a group of the films we have measured are given in Table I and Figs. 3 through 6. The resistance-frequency data for tellurium cell No. 62, shown in Fig. 3, is completely explained by the distributed capacitance model at all temperatures studied. The constancy of the distributed capacitance with temperature is shown by the fitting of all points to a single curve in Fig. 4, where R/R_1 is plotted against R_1f. This

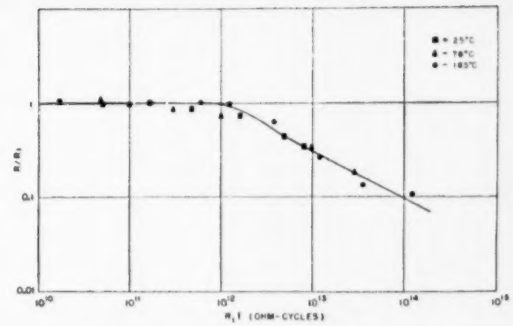

FIG. 4. Data of Fig. 3 replotted to test adequacy of distributed capacitance model (R/R_1 *vs* R_1f).

also indicates the absence of any significant contribution from intercrystallite capacitance, as described in Sec. IV.

The behavior of this film agrees in all particulars with that reported by Rittner and Grace. It is to be noted, however, that this and all other tellurium films discussed here were very weakly photoconductive, while the PbS cells (ours and those studied by Rittner) were moderately or strongly photoconductive.

The data for another tellurium film, No. 70, at 25°C and $-185°C$, are plotted as R/R_1 *vs* R_1f in Fig. 5 to test for the presence of intercrystallite capacitance by the method of Sec. IV. Since the results are temperature dependent, intercrystallite capacitance must be present. A combination of the two models will therefore be considered.

One can combine the two models into one equivalent circuit by replacing the constant resistance per unit length r in the distributed capacitance model [Fig. 1(b)] by the unit network U of Fig. 1(a), which contains R_1, R_2, and C_1 based on the crystallite model. These three parameters and C_D are then considered as constants whose values must be determined by a process of curve fitting. Rather than to express the impedance of this composite network analytically we have used a point-by-point method of making the computation.

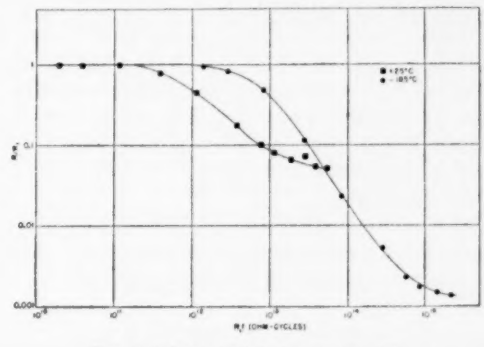

FIG. 5. R/R_1 *vs* R_1f for Te film No. 70. $T=25°C$ and $-185°C$.

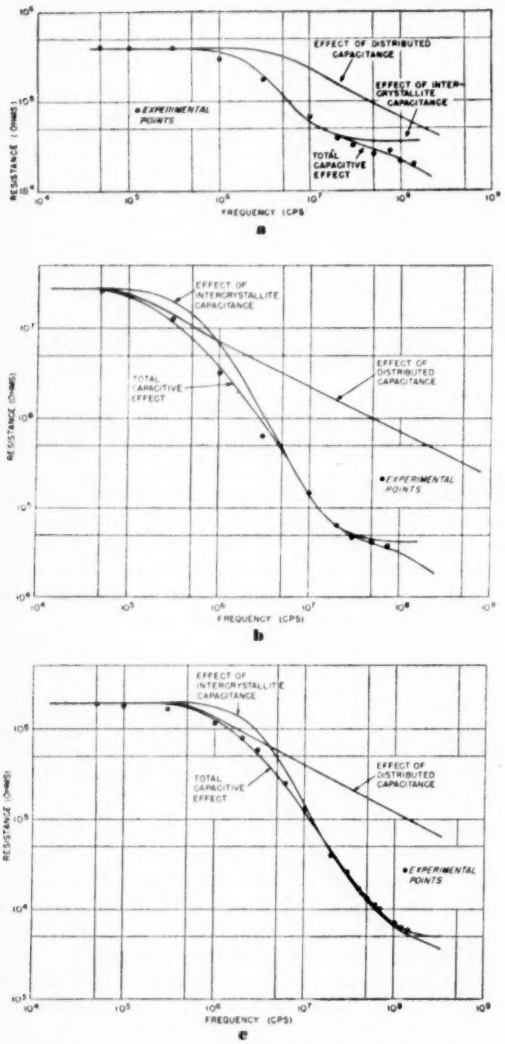

FIG. 6. Resistance *vs* frequency data together with fitted curve calculated by combining both distributed and intercrystallite capacitance effects: (a) Te film No. 70, $T=25°C$; (b) Te film No. 70, $T=-185°C$; (c) Pbs film, $T=25°C$.

This is accomplished at each frequency f by first computing the effective resistance per unit length by means of Eq. (1), based on intercrystallite capacitance, and then inserting this value of $R(f)$ in Eqs. (2) and (3). The resulting resistance R is the value to be compared with the measured value.

The evaluation of the parameters R_2/R_1, C_1, and C_D requires successive approximations in most cases. In the first approximation R_2 is the resistance at the foot of the curve and R_1+R_2 is the dc resistance. The value of R_2/R_1 determines which one from the family of curves of Eq. (1) will give the dependence due to the intercrystallite capacitance. The vertical scale of the curve is established by the dc resistance, while the horizontal scale is established by the frequency at which the knee occurs. From the horizontal scale and R_1 one can calculate C_1. (Note that the adjustment of scales is simplified by the use of the logarithmic plot: the theoretical curve of Fig. 2 need merely be translated horizontally and vertically to fit the scale of the data.) Finally the value of C_D is calculated from Eq. (4) in terms of the frequency at which the measured resistance begins to deviate from the value indicated by the intercrystallite capacitance model.

The resistance *vs* frequency data for tellurium cell No. 70 and for a photoconductive PbS cell are shown in Fig. 6. In addition to the experimental points are curves showing the variation of resistance due to intercrystallite capacitance, to distributed capacitance, and finally to both types of capacitance simultaneously. Satisfactory agreement between the data and this combined curve is obtained in all cases. It will be seen that the inclusion of distributed capacitance does not modify the intercrystallite model curve of Fig. 6 in the frequency range from 5×10^6 cps to 3×10^7 cps. This is due to the progressive decrease of the value of $R(f)$ which must be inserted in Eq. (2). If $\omega R(f)$ decreases with increasing frequency (as it does in this case) the importance of the distributed capacitance correction decreases. Then, when $R(f)$ becomes more nearly constant, the value of $\omega R(f)$ again increases with frequency, and the correction becomes more important. This effect also exists in Fig. 6(a) where it makes the choice of C_D less straightforward, but successive approximations yield a satisfactory fit to the data.

VI. SUMMARY

We have shown that the frequency dependence of the resistance of a thin conducting film can be explained in general in terms of distributed capacitance and intercrystallite capacitance. In some samples the distributed capacitance alone appears to give satisfactory agreement with experiment. In other samples satisfactory agreement can be obtained only by including the effects of both types of capacitance. We have further shown that photoconductivity can exist either with or without intercrystallite capacitance effects detectable by resistance-frequency-temperature measurements.

We wish to acknowledge a number of valuable discussions with Drs. R. L. Petritz, R. J. Maurer, P. H. Miller, Jr., and K. Lark-Horovitz. We are also indebted to Dr. E. S. Rittner for sending us a prepublication copy of his article.[4]

Studies of Compounds for Superconductivity*†

W. T. ZIEGLER AND R. A. YOUNG
Georgia Institute of Technology, Atlanta, Georgia
(Received October 6, 1952)

A number of metal carbides, borides, nitrides, and a hydride, in the form of powders, have been examined for superconductivity down to 1.8°K using a magnetic method. The substances tested were TiC, VC, ZrC, TaC, WC, ZrB_2, NbB_2, TaB_2, WB, MoB, TiB_x, ThB_2, LaN, CeN, NbN, and $LaH_{2.45}$. All specimens were characterized by x-ray diffraction methods and, in most instances, by chemical analysis. Of these substances only NbN gave evidence for superconductivity. The results for NbN are in general agreement with the work of others. The results for TiC and VC are in agreement with those found by Meissner *et al.*, using an electrical resistance method, while those for TaB_2, NbB_2, WC, and WB are in agreement with observations made by Matthias and Hulm using a magnetic method. On the other hand, ZrC, TaC, WC, and "zirconium boride" had previously been observed to exhibit superconductivity above 1.8°K by the electrical resistance method. The results for WC and MoB have recently been confirmed by Matthias and Hulm. The substances ThB_2, LaN, CeN, and $LaH_{2.45}$ had not previously been examined for superconductivity.

Particle size measurements were made on the carbide and boride powders. The particles were large enough that magnetic field penetration effects should have caused no difficulty, if a penetration depth of 1×10^{-5} cm, observed for pure metal, is assumed to apply to the present compounds.

The failure to observe superconductivity in the substances ZrC, TaC, WC, and MoB in the present study is discussed in terms of a postulated physical distribution of superconducting impurities of undetermined composition which are assumed to account for the superconductivity observed in these compounds by other investigators.

INTRODUCTION

THE occurrence of superconductivity in binary compounds containing a metal and a nonmetal has been known for more than twenty years as a result of the extensive work of Meissner and his co-workers.[1–3] A survey of the literature has shown that in many instances the occurrence of superconductivity in compounds has been observed by studying the change of electrical resistance with temperature. In all instances in which superconductivity was observed by this means, the electrical resistance of the substance was found to decrease with temperature from room temperature to the transition temperature in the manner characteristic of metals.[4,5] Most of the compounds found to exhibit superconductivity are binary compounds between superconducting metals and boron, carbon, or nitrogen. On the other hand, the carbides of tungsten and the carbides, a boride, and two nitrides of molybdenum also show superconducting behavior, even though the pure metals do not become superconducting at the lowest temperature tried (<1°K).

The difficulty of preparing these compounds in pure form has presented the possibility that the observed superconductivity may arise from superconducting filaments (either of the parent metal or a compound) present in the specimen rather than from the bulk specimen itself. This doubt has suggested the re-examination of these substances by means of magnetic methods, since, as Shoenberg has pointed out,[6] these methods should yield information concerning the behavior of the entire volume of the specimen, rather than of possible superconducting filaments.

Relatively little work has been published on the magnetic transition into superconductivity in compounds and in certain metals which are difficult to purify. Titanium specimens of various purities have been reported to have transition temperatures ranging from 1.13° to 1.77°[2,7,8] when examined by the electrical resistance method, whereas other specimens of titanium of high purity, examined by magnetic methods, have either failed to exhibit superconductivity down to 1°K[9] or exhibited superconductivity only at much lower temperatures (0.53°K).[10] A similar situation has been reported for uranium.[6,11]

Recently Matthias and Hulm,[5] in an extensive survey of the occurrence of superconductivity in compounds examined by the magnetic method, have confirmed the occurrence of superconductivity in a number of compounds in which it has previously been observed using the electrical resistance test, but failed to find the effect in WC in which it had previously been observed by the resistance method.

Studies have been in progress in this laboratory for some time to re-examine by a magnetic induction method a number of compounds previously examined for superconductivity by the electrical resistance method. A number of compounds not previously tested for superconductivity are also being studied. The present paper deals with the results of studies made on fifteen metal carbides, borides, nitrides, and a hydride.

* Carried out with the assistance of the U. S. Office of Naval Research.

† Based on a paper presented at the International Conference on Low Temperature Physics, Oxford, England, August 22–28 (1951).

[1] W. Meissner and H. Franz, Z. Physik **65**, 30 (1930).
[2] Meissner, Franz, and Westerhoff, Ann. Physik (5) **13**, 555 (1932).
[3] Meissner, Franz, and Westerhoff, Z. Physik **75**, 521 (1932).
[4] W. T. Ziegler, Research Engr. **IX**, No. 1, 15 (1947).
[5] B. T. Matthias and J. K. Hulm, Phys. Rev. **87**, 799 (1952).
[6] D. Shoenberg, Nature **159**, 303 (1947).
[7] W. Meissner, Z. Physik **60**, 181 (1930).
[8] W. J. de Haas and P. M. van Alphen, Proc. Acad. Sci. Amsterdam **34**, 70 (1931).
[9] D. Shoenberg, Proc. Cambridge Phil. Soc. **36**, 84 (1940).
[10] J. G. Daunt and C. V. Heer, Phys. Rev. **76**, 715 (1949).
[11] B. B. Goodman and D. Shoenberg, Nature **165**, 441 (1950).

TABLE I. Composition of carbides.

Metal	Calculated x in MC_x	Major constituent	X-ray diffraction analysis: Lattice	Reference	Minor constituents
Titanium	0.948	TiC	NaCl	12	Ti (?)[a] TaC (?)
Vanadium	0.820	VC	NaCl	12, 13	V
Zirconium	0.860	ZrC	NaCl	12	Nb and/or Ta Zr (?)
Tantalum	0.980	TaC	NaCl	12	None
Tungsten	0.989	WC	Hexagonal	14	None identified[b]

[a] A question mark (?) implies a few lines corresponding to structure of this substance present.
[b] W_2C absent.

The compounds studied were: TiC, VC, ZrC, WC, TaC, ZrB_2, NbB_2, TaB_2, WB, MoB, ThB_2, TiB_x, LaN, CeN, NbN, and $LaH_{2.45}$. The formulas given are descriptive rather than exact in that they correspond, in general, to the major constituents as identified by x-ray diffraction.

All materials were in the form of rather fine powders. They were examined by x-ray powder diffraction techniques using copper $K\alpha$ radiation. The diffraction patterns obtained were analyzed with the aid of published data. Partial chemical analyses were also available for all compounds. Detailed analyses of the materials have been included in order to characterize the materials studied as completely as possible.

Particle size measurements were made on the carbide and boride powders.

DESCRIPTION OF COMPOUNDS

A. Metal Carbides

The carbides were obtained through the courtesy of Dr. F. H. Horn, Research Laboratory, General Electric Company. They were prepared by the Carboloy Company, Inc., which provided the analyses from which the compositions in column 2 of Table I were calculated. Table I summarizes the x-ray diffraction results obtained.[12–14] In each instance the major constituent was identified by comparison with the data given in the reference cited. From a consideration of the chemical analyses and x-ray diffraction results it was concluded that none of the specimens contained more than a trace of free metal. The tantalum carbide sample appeared to be essentially pure TaC. The occurrence of faint lines in the diffraction patterns of the other carbides indicated the presence of small amounts of impurities. Both vanadium carbide and zirconium carbide deviated appreciably from the simple stoichiometric formula MC.

B. Metal Borides

The metal borides, obtained from Cooper Metallurgical Associates, Cleveland, Ohio, were made by direct combination at high temperatures between the powdered metal and elemental boron, both of high purity. All specimens were rather finely divided dark gray powders. Table II summarizes the results of the chemical and x-ray diffraction analyses.[15–17] The chemical analyses were supplied with the specimens.

The diffraction pattern from the thorium boride powder contained 69 lines. Of these the 19 strongest lines could be assigned to a face-centered cubic structure having an a_0 of 5.58 ± 0.01A. On the basis of the chemical analysis this structure has tentatively been assigned to ThB_2. A trace of thorium metal was present. Of the remaining lines a few were medium faint, the rest being faint or weaker. Many of these remaining lines could be accounted for by the presence of a small amount of ThB_6, using the lattice parameter ($a_0=4.32$A) given by Stackelberg and Neumann.[18] However, several of the lines expected to be strongest (as judged by comparison with the published data[18] for CaB_6) were absent.

The x-ray diffraction pattern of the titanium boride was compared with the very detailed study of Ehrlich[16] who investigated the structure of the TiB_x system over the range $0\leqq x\leqq 3$. Detailed comparison of the 23 lines obtained for this material with the work of Ehrlich indicated that the strongest lines corresponded very closely with the pattern given by Ehrlich for TiB_x where x ranged from 2 to 2.5, with a somewhat less satisfactory fit for x over the entire range 1 to 2.5. There was no evidence for free titanium.

C. Metal Nitrides and Hydride

The lanthanum and cerium nitrides were made by direct combination at 800–900°C between the rare-earth metal filings and nitrogen at one atmosphere pressure. A more detailed description of preparation and proper-

TABLE II. Composition of borides.

Metal	Calculated x in MB_x	Major constituent	X-ray diffraction analysis: Lattice	Reference	Minor constituents
Molybdenum	0.99	MoB	Tetragonal	15	Mo_2B Mo
Tungsten	1.03	WB	Tetragonal	15	None
Thorium	2.04	Not identified	Face-centered cubic		Th ThB_6 (?)[a]
Titanium	0.99	TiB_x $x=2$–2.5		16	None identified
Niobium	1.94	NbB_2	Hexagonal	17	Nb
Zirconium	2.35	ZrB_2	Hexagonal	17	None identified
Tantalum	1.75	TaB_2	Hexagonal	17	None identified

[a] A question mark implies that a few lines corresponding to the structure of this substance were present.

[12] J. T. Norton and A. L. Mowry, J. Metals **1**, No. 2, 133 (1949).
[13] W. Dawihl and W. Rix, Z. anorg. u. allgem. Chem. **244**, 191 (1940).
[14] K. Becker, Z. Physik **51**, 481 (1928).
[15] R. Kiessling, Acta. Chem. Scand. **4**, 209 (1950).
[16] P. Ehrlich, Z. anorg. Chem. **259**, 1 (1949).
[17] Norton, Blumenthal, and Sindeband, J. Metals **1**, No. 10, 749 (1949).
[18] M. v. Stackelberg and F. Neumann, Z. physik. Chem. **19B**, 314 (1932).

ties of these materials is given in another place.[19] The nitrides examined had the approximate formula $LaN_{0.97}$ (Cooper 2, Expt. 26), $LaN_{0.94}$ (Spedding 1, Expt. 29), and $CeN_{0.87}$.

The niobium nitride[20] was prepared by heating niobium metal powder (Fansteel, 99.9 percent Nb) for 4 to 4½ hours at 1500°C in pure dry nitrogen. X-ray examination showed it to be primarily NbN with $a_0 = 4.37 \pm 0.01$ *kx*-units.[21] A trace of Nb and/or Ta metal appeared to be present. A large number of faint to very faint lines could not be identified. These lines did not fit the pattern for Nb_2N reported by Brauer.[22]

The lanthanum hydride was prepared by direct combination between lanthanum metal filings and pure dry hydrogen gas at 210–290°C. The method used was similar to that employed for the nitride. The product examined for superconductivity had the composition $LaH_{2.45}$. Muthmann and Kraft[23] and Rossi,[24] using a similar method, have reported similar products having the approximate formulas LaH_3 and $LaH_{2.4}$, respectively. The hydride had an fcc lattice with $a_0 = 5.625 \pm 0.007$ *kx* units in good agreement with the value of 5.62–3 *kx* units reported by Rossi.[24]

EXPERIMENTAL METHOD

The cryostat and measuring apparatus used was similar to that described by Horn and Ziegler.[21] The apparatus, the temperature scale and the magnetic method employed to detect superconductivity have been described elsewhere.[25] Briefly, the apparatus consisted of a heavy walled copper vessel in which liquid helium was produced by the Simon expansion method. From the main helium reservoir was suspended the experimental chamber, into which helium could be condensed at will by bringing low pressure helium into contact with the main helium reservoir. The copper experimental chamber consisted of two parts, an upper section to which the thermometers were attached, and a lower section in which the specimens to be tested for superconductivity were located and on the outside of which the coils for detecting superconductivity were wound.

The temperature of the experimental chamber was measured by means of a helium gas thermometer of the type described by Mendelssohn,[26] except that the helium pressure was measured both by a Bourdon gauge and a capillary mercury manometer. The thermometer was calibrated by using the boiling points of hydrogen and helium and the triple point of hydrogen as fixed points. Gas imperfection was taken into account by making use of the virial coefficients given by Keesom.[27] The absolute accuracy of the temperature scale is believed to be about 0.05° in the range below 5°K, 0.1° in the range 5–7°K and 14–20°K, and a few tenths of a degree in the range between 7° and 14°K.

A constantan resistance thermometer, having a sensitivity of 0.01–0.02°, also was used to follow the temperature changes of the experimental chamber.

The magnetic system used for detecting superconductivity essentially measured the change in inductance produced when the specimen became superconducting. This change in inductance was measured as a galvanometer deflection produced when the primary circuit was momentarily energized. The circuits were so arranged that the galvanometer deflection could be reduced to zero at will by the suitable adjustment of a compensating inductance.

The powdered samples were generally mounted in a 7 mm o.d. Pyrex glass tube, partly open at the top end, and were in direct contact with the helium. In a few instances (TiC, VC, $LaH_{2.45}$, CeN, and LaN), the measurements were made on samples in Pyrex capsules sealed at room temperature under 20 cm Hg pressure of helium. The samples had weights varying from 0.7 to 2.5 g, and usually had a length of 20–22 mm and a diameter of 4.5–4.9 mm.

TABLE III. Superconductivity of metal carbides.

Carbide	Major constituent	Transition temp.[a] and range, °K: This research	Lit.	Method[c]
$TiC_{0.95}$	TiC	(1.8)[b]	1.1 (?)	R[d]
			(1.31)	R[e]
$VC_{0.82}$	VC	(1.8)	(1.33)	R[d]
$ZrC_{0.86}$	ZrC	(1.8)	3.7	R[e]
			3.3–4.1	
$TaC_{0.98}$	TaC	(1.8)	9.3, 9.2–9.4	R[d]
			7.6–9.5	R[e]
$WC_{0.99}$	WC	(1.8)	3.4, 2.5–4.0	R[d]
			(1.28)	M[f]

[a] Temperature corresponding to 50 percent of total resistance change in transition.
[b] Temperature in parentheses means substance not superconducting down to this temperature.
[c] R = electrical resistance method; M = magnetic method.
[d] See reference 1.
[e] See reference 3.
[f] See reference 5.

EXPERIMENTAL RESULTS

The experimental results for the various compounds tested are summarized in Tables III and IV, together with the results of other investigators.[1,3,5,28,29] In these tables the major constituent given is that found by

[19] R. A. Young and W. T. Ziegler, J. Am. Chem. Soc. **74**, 5251 (1952).
[20] This material was prepared by Dr. F. H. Horn, General Electric Co., Schenectady, N. Y., as part of a cooperative study on Nb-Ta alloys and their nitrides.
[21] F. H. Horn and W. T. Ziegler, J. Am. Chem. Soc. **69**, 2762 (1947).
[22] G. Brauer, Z. Elektrochem. **46**, 397 (1940).
[23] W. Muthmann and K. Kraft, Ann. Chem., Justus Liebigs **325**, 266 (1902).
[24] A. Rossi, Nature **133**, 174 (1934).
[25] W. T. Ziegler and R. A. Young, J. Am. Chem. Soc. March, 1953.
[26] K. Mendelssohn, Z. Physik **73**, 482 (1931).
[27] W. H. Keesom, Helium (Elsevier Publishing Company, New York, 1942), p. 49.
[28] J. K. Hulm and B. T. Matthias, Phys. Rev. **82**, 273 (1951).
[29] Aschermann, Friederich, Justi, and Kramer, Physik. Z. **42**, 349 (1941).

TABLE IV. Superconductivity of metal borides.

Boride	Major constituent	Transition temp. and range, °K This research	Lit.	Method
$MoB_{0.99}$	MoB	(1.74)	(1.28)	M^a
$WB_{1.03}$	WB	(1.77)	(1.28)	M^a
$ThB_{2.04}$	ThB_2	(1.77)		
$TiB_{0.99}$	$TiB_{2-2.5}$	(1.8)	(1.26)	R^b
			(1.28)	M^c
$NbB_{1.94}$	NbB_2	(1.8)	(1.27)	M^d
			(9.5)	R^e
$ZrB_{2.35}$	ZrB_2	(1.8)	3.1, 2.9–3.3	R^f
$TaB_{1.75}$	TaB_2	(1.8)	(1.28)	$M^{b,d}$

[a] See reference 5.
[b] See reference 3.
[c] For TiB_2, see reference 5.
[d] See reference 28.
[e] See reference 29.
[f] For "zirconium boride," see reference 3.

x-ray diffraction analysis, while the formula given in the first column of each table is that derived from chemical analysis.

The observations of superconductivity in NbN is in general agreement with the results previously found by both the electrical resistance[21,29,30] and magnetic induction[21,31] methods. The transition was spread out over the range 16.8° to 14.8°K with the midpoint of the transition at 16.0°K. The sensitivity of the magnetic detection system was such that the NbN specimen gave a total galvanometer deflection of 4.2 cm in passing from the normal to the superconducting state. On the basis of this and other measurements, it was estimated that the occurrence of superconductivity could have been detected in a volume corresponding to 5–10 percent of the volume of the samples used.

The failure to observe superconductivity in TiC and VC is in agreement with the electrical resistance measurements of Meissner *et al.*[1,3] while the absence of superconductivity in ZrC, TaC, and WC is in disagreement with the observations of these investigators. Matthias and Hulm,[5] using a magnetic method, also found no evidence of superconductivity in WC down to 1.28°K. These investigators also reported that MoB and WB failed to become superconducting down to 1.28°K, in agreement with the results of the present work.

The failure to observe superconductivity in NbB_2 and TaB_2 is in agreement with the magnetic studies of Hulm and Matthias.[28] These investigators have also reported TiB_2 not to be a superconductor down to 1.28°K.[5] We observed a similar result for a boride having the approximate composition $TiB_{2-2.5}$. Meissner *et al.*[3] observed no transition by the resistance method down to 1.26°K in a titanium boride specimen of unstated composition. No transition was observed in ZrB_2, whereas Meissner *et al.*,[3] using the resistance method, have reported a transition near 3.1°K in "zirconium boride."

[30] R. M. Milton, Chem. Revs. **39**, 419 (1946).
[31] Cook, Zemansky, and Boorse, Phys. Rev. **79**, 1021 (1950).

Thorium boride, lanthanum and cerium nitrides, and lanthanum hydride were found not to be superconductors down to 1.8°K. These substances have not previously been examined for superconductivity.

The failure to observe superconductivity in the lanthanum nitrides and hydride is interesting since the transition temperatures of the two lanthanum metal specimens used to prepare the nitrides had previously been found to be 3.1° (Cooper 2) and 5.2° (Spedding 1) while that used to prepare the hydride had a transition temperature of 3.5° (Cooper 3).[25] The cerium metal from which the nitride was prepared was not superconducting down to 1.8°K.[32]

DISCUSSION OF RESULTS

Several reasons for the failure to observe superconductivity in those compounds in which it had been observed by others suggested themselves. One was that the apparatus was not functioning properly, possibly due to thermal nonequilibrium. However, the detection of superconductivity in bulk specimens of lanthanum, lead, and tin metals, lanthanum filings and powdered NbN with the apparatus seemed to exclude this possibility.

The measurements on LaN, CeN, $LaH_{2.45}$, TiC, and VC were made on samples sealed in capsules under 20 cm Hg helium pressure at room temperature. The possibility that the helium gas was adsorbed at low temperatures, thus resulting in poor heat transfer, is not entirely excluded. However, experiments with lanthanum metal filings sealed under similar conditions showed no significant hysteresis in the transition at 4°K. In general, specimens were kept below 4.2°K for as long as an hour, and below the lambda-point (2.19°K) for periods ranging from 3 to 18 minutes.

The apparatus was further checked by studying a tin powder which consisted of spheres having a size range of approximately 15 to 50 microns.[33] The powder was free-flowing, and it had a yellowish appearance indicating the presence of some oxide on the surface of the tin particles. Tests of this powder gave a magnetic transition into superconductivity over the range 3.63° to 3.49°K. This is somewhat lower than the generally accepted transition temperature (3.7°K) for bulk tin. However, the calculated maximum field generated by the measuring primary was 27 oersteds, which could be expected to produce a lowering as great as 0.15°.

In order to obtain some information on the possible magnitude of field penetration effects, the particle size distribution of the carbide and boride powders was determined by measuring microscopically the linear dimensions of 100 particles which had been suitably dispersed on a glass slide. The appearance of the particles of all powders examined could best be described

[32] Cerium is apparently not a superconductor down to 0.25°K. See B. B. Goodman, Nature **167**, 111 (1951).
[33] This material was obtained through the courtesy of Dr. M. C. Steele of the Naval Research Laboratory, Washington, D. C.

as roughly spherical. The particle size distribution observed is expressed in Table V in terms of the median diameter, d_g, and the geometric standard deviation, σ_g.[34] Calculations show that at least 50 percent of the total volume of all boride and carbide powders consisted of particles having diameters greater than one micron. It will be noted that the MoB, ZrC, and WC specimens consisted of relatively large particles. Electron-microscopic examination of the TaC powder showed that it contained a considerable fraction below one micron in size. Microscopic examination of the NbN powder showed that it was considerably coarser than the carbide and boride powders, at least 50 percent of all particles having a diameter greater than 15 microns.

The field penetration depth in powders of alloy systems such as the carbides and borides has apparently not been investigated. If one takes for the penetration depth the rough value of 1×10^{-5} cm observed in metals,[35] it would appear that the values of d_g for all substances studied was sufficiently large so that field penetration would not be expected to play a significant role in the present measurements.

The disagreement between the results of the present work and those of Meissner and co-workers[1,3] regarding the occurrence of superconductivity in TaC, WC, and ZrC might be explained, as Shoenberg[6,9] has suggested for titanium and uranium, by assuming the presence of superconducting filaments in Meissner's specimens of these carbides. Another possibility is that the transition temperatures of our carbide specimens were lowered by strain to a temperature below that reached in our experiments (1.8°).[36]

Hudson,[37] using the magnetic induction method, has made an interesting study of two Sn–Ge "alloys" containing 2.3 and 9.3 atomic percent of tin, respectively, in which the tin was concentrated along the grain boundaries. These materials gave a rather broad diamagnetic transition beginning at 4°K. Hudson attributed this behavior to the presence of superconducting filaments of tin. Calculations by him indicated that approximately 50 percent of the volume of the alloy of lower tin content and the entire volume of the alloy of higher tin content participated in the magnetic transition.

In view of these observations of Hudson on the Sn–Ge alloys, it would appear that the precise physical structure of the "superconducting filaments" might be an important variable. Thus, if the filaments are thread-like, superconductivity might be observed electrically but not magnetically. On the other hand, if the superconducting filaments possess a sponge-like structure,[38] with the bulk material in the holes of the sponge, as in the Ge–Sn alloy experiments of Hudson, then both an electrical and a magnetic transition might be observed. The physical structure of such filamentous inclusions might be expected to depend considerably on the method of preparation of the compound and the nature of the impurity.

TABLE V. Particle size measurements.

Borides			Carbides		
Substance	d_g[a] microns	σ_g[b]	Substance	d_g microns	σ_g
NbB_2	0.8	2.0	TaC	0.8	1.6
ThB_2	1.1	1.4	TiC	1.3	1.9
WB	1.2	1.4	VC	1.6	2.1
TaB_2	1.4	1.5	ZrC	2.1	2.4
TiB_x	1.5	1.6	WC	2.6	2.7
ZrB_2	1.5	2.1			
MoB	1.7	1.9			

[a] d_g = median diameter.
[b] σ_g = geometric standard deviation.

The disagreement between the earlier magnetic results of Hulm and Matthias[28] and the present work regarding the superconductivity of MoB appears to have been due to some such sponge-like distribution of a superconducting inclusion (Mo_2B).[5] A similar explanation has been advanced[39–41] to account for the conflicting magnetic observations of Darby *et al.*[42] and Hudson[39,40] regarding the superconductivity of PbS.[43]

The possibility that superconductivity in many compounds may be due to rather specific amounts of trace impurities, distributed in a homogeneous manner through the bulk material, which makes possible a superconducting state has not been exluded.

The authors are indebted to F. W. Lafond, J. T. Roberts, Jr., G. Cook, and M. T. Gordon for assistance in carrying out the low temperature measurements, to Dr. W. M. Spicer for the spectrographic analyses, to C. Orr and Dr. J. M. DallaValle for assistance in the particle size measurements, and to L. A. Woodward for making the electron microscopic study of TaC. The help and interest of Dr. F. H. Horn, General Electric Company, in providing the carbides and preparing the niobium nitride are greatly appreciated.

[34] J. M. DallaValle, *Micromeritics: The Technology of Fine Particles* (Pitman Publishing Company, New York, 1948), Chapter 3.
[35] F. London, *Superfluids* (John Wiley and Sons, Inc., New York, 1950), Vol. I, pp. 46, 89.
[36] The crystallite size may be a more important factor than the particle size in determining the effects of field penetration. The lines of the x-ray diffraction pattern for TaC were all quite diffuse indicating a small crystallite size; on the other hand, those for WC and ZrC were quite sharp.
[37] R. P. Hudson, Phys. Rev. **79**, 883 (1950).
[38] K. Mendelssohn, Proc. Roy. Soc. (London) **A152**, 36 (1935).
[39] R. P. Hudson, *Proc. NBS Semicentennial Symposium on Low Temperature Physics*, Natl. Bur. Standards, Washington, D. C. March 27–29, 1951 [National Bureau of Standards Circular 519 (1952), p. 61].
[40] R. P. Hudson, Proc. Phys. Soc. (London) **A64**, 751 (1951).
[41] Hatton, Rollin, and Seymour, Proc. Phys. Soc. (London) **A64**, 667 (1951).
[42] Darby, Hatton, and Rollin, Proc. Phys. Soc. (London) **A63**, 1181 (1950).
[43] This explanation came to our attention after the presentation of our paper at the Oxford Conference.

Studies of Atomic Self-Consistent Fields. I. Calculation of Slater Functions*

PER-OLOV LÖWDIN
Department of Physics, University of Chicago, Chicago, Illinois, and Institute of Mechanics and Mathematical Physics, University of Uppsala, Uppsala, Sweden

(Received December 19, 1952)

A refined technique is described for approximating the numerically given radial part of atomic wave functions associated with self-consistent fields with exchange by means of Slater's analytical functions obtained by replacing each exponential in a hydrogen-like wave function by the sum of one, two, three, or more exponentials. Exponents and coefficients of these exponentials are calculated for the $3p$-function of Cl^-, corresponding to an accuracy of 0.0015 for the normalized radial part, and, with slightly less accuracy, for all the functions of two closed-shell ions, F^- (without exchange) and Na^+, and for some neutral first-row atoms, $C(^1D)$, $N(^2P)$, and $O(^1S)$. The interpolation problem is discussed, and a new interpolation rule for the coefficients is stated, which gives excellent agreement (0.001) in the examples chosen, namely the $1s$-functions of the He-like ions and the $2p$-functions of Na^+, Mg^{+2}, and Si^{+4}.

IN the quantum-mechanical treatment of many-electron atoms, the total antisymmetric wave functions describing the different atomic states are usually approximated by the sum of one, two, three or more determinants[1] of one-electron wave functions, each being a product of an atomic orbital (AO) and a spin function. The atomic orbitals are determined from the basic Schrödinger equation for the atom by means of the variation principle[2] as products of radial parts and spherical harmonics, and the best expressions for the former are obtained *numerically* by step-by-step integration of the Hartree-Fock equations by using the self-consistent-field technique developed by Hartree.[3]

For some purposes, it has been found desirable to use also *analytic* forms of these atomic orbitals. Here we will not discuss the question whether it is better to base applications of the atomic theory on the analytical wave functions rather than on the numerical tables. It has often been said that the analytic expressions would be better for use, e.g., in the theory of molecules and crystals, but our experience is that it is often just as convenient to use numerical computations as analytical calculations and that many times the former are simpler and quicker. However, considering the fact that many physicists are more accustomed to analytical work than to numerical computations, we think that both methods should be developed simultaneously without giving priority to anyone of them. This series of papers will be devoted to a study of the atomic self-consistent fields with exchange, and various problems will be discussed both from the analytical and the numerical points of view.

Analytic expressions for the radial wave functions can be derived in two ways, either directly by fixing parameters in given analytic functions, for instance, of the hydrogen-like type by means of the variation principle as described by Zener[4] and others,[5] or indirectly by approximating the numerically given Hartree-Fock functions in some way analytically, as was proposed by Slater.[6] Except for the simplest cases, the former method leads to rather formidable calculations, whereas the latter is simple but based on the assumption that the self-consistent-field functions are given in advance. An investigation of the accuracy of these analytic atomic orbitals shows that the Zener and Morse-Young-Haurwitz functions[4,5] containing only a few exponentials represent rather poor approximations of the self-consistent fields[7] and hence also of the true charge distributions,[8] and that the deviations are appreciable, particularly at large distances. The last fact is of essential importance in the theory of molecules and crystals, and the simplest way of obtaining good analytical orbitals for applications in this field seems therefore to be to use Slater's approach.[6] Part I of this series of papers will be devoted to a study of a refinement of Slater's method, giving analytic atomic wave functions with almost the same accuracy as the numerical functions themselves.

I. CALCULATION OF SLATER-FUNCTIONS

An atomic orbital with the quantum numbers n, l, m is the product of a radial wave function $f_{nl}(r)/r$ and a

* This work was assisted in part by the U. S. Office of Naval Research under contract with the University of Chicago, in part by the Swedish Natural Science Research Council, and in part by the Elizabeth Thompson Science Fund.

[1] J. C. Slater, Phys. Rev. **34**, 1293 (1929).

[2] J. C. Slater, Phys. Rev. **35**, 210 (1930), and V. Fock, Z. Physik **61**, 126 (1930).

[3] For an excellent survey of this field, see D. R. Hartree, Rep. Prog. Phys. **11**, 113 (1946).

[4] V. Guillemin and C. Zener, Z. Physik **61**, 199 (1930); C. Zener, Phys. Rev. **36**, 51 (1930); J. C. Slater, Phys. Rev. **36**, 57 (1930).

[5] Extensive tables have been given by Morse, Young, and Haurwitz, Phys. Rev. **48**, 948 (1935); for improvements and corrections, see also L. Goldberg and A. M. Clogston, Phys. Rev. **56**, 696 (1939), and W. E. Duncanson and C. A. Coulson, Proc. Roy. Soc. (Edinburgh) **62**, 37 (1944).

[6] J. C. Slater, Phys. Rev. **42**, 33 (1932); F. W. Brown, Phys. Rev. **44**, 214 (1933).

[7] Only in a few cases have Zener-type functions been used as starting functions for self-consistent-field calculations; see, e.g., V. Fock and M. J. Petrashen, Physik. Z. Sowjetunion **6**, 368 (1934); **8**, 359 (1935).

[8] H. Bethe, Z. Physik **55**, 431 (1929); **57**, 815 (1929), has given a survey of different approximations of the charge distribution of He and He-like ions in comparison to the "true" distributions given by Hylleraas.

normalized spherical harmonic $Y_{lm}(\theta, \varphi)$. The best expressions for the functions $f_{nl}(r)$ are now given numerically for many atoms and ions by Hartree and Hartree, Fock, and others.[8] In order to express $f_{nl}(r)$ analytically, we will now slightly generalize Slater's original idea[9] and try to approximate these tables by functions obtained by replacing each exponential in the corresponding hydrogen-like functions by a sum of one, two, three or more exponentials. For the lowest functions, this gives the following expansions:

$$
\begin{aligned}
&f_{1s}(r)=r\textstyle\sum_k A_k \exp(-a_k r),\\
&f_{2s}(r)=r\textstyle\sum_k A_k \exp(-a_k r)-r^2\sum_k B_k \exp(-b_k r),\\
&f_{2p}(r)=r^2\textstyle\sum_k B_k \exp(-b_k r),\\
&f_{3s}(r)=r\textstyle\sum_k A_k \exp(-a_k r)-r^2\sum_k B_k \exp(-b_k r)\\
&\qquad\qquad +r^3\textstyle\sum_k C_k \exp(-c_k r),\\
&f_{3p}(r)=r^2\textstyle\sum_k B_k \exp(-b_k r)-r^3\sum_k C_k \exp(-c_k r),\\
&\cdots\text{etc.}
\end{aligned}
\qquad (1)
$$

where the exponents a_k, b_k, $\cdots$ and the coefficients A_k, B_k, $\cdots$ may be different for each orbital. We will here determine the values of these parameters by a numerical method, which is a simple development of the graphical method described by Slater.[6]

The exponentials involved in the expansions (1) may be calculated by means of a method of successive approximations[10] going inwards from $r\approx\infty$ to $r=0$. The computations are based on the fact that in the outer region ($r\approx\infty$) only a single exponential is important, in the next inner region two terms are important, in the following region three terms, etc. The numerically given function $f(r)$, divided by the highest power r^p of r according to (1), is considered in equidistant points; a *quotient series* is then formed for the outer region by successive divisions, and from this series a trial exponential function is determined as a geometrical series. This function is now subtracted from $f(r)/r^p$, and the difference is investigated in the next inner region, where a new quotient series is formed, giving a new trial exponential function. This second function is now subtracted from $f(r)/r^p$, and the outer region is considered a second time with a still better result for the first term, etc. In most cases, this process is quite straightforward, and special care must be taken only in regions where the power of r has to be changed according to (1).

We note that here the quotient series have taken the place of Slater's logarithmic graphs. The success of the method depends partly on the fact that these quotient series and the trial exponentials, i.e., the geometrical series, can be computed so quickly by means of the modern electric desk machines.

A few words may be said about the fixing of the first trial functions for each region. It is easily seen that if a function g_n is the sum of two geometric series,

$$g_n=ak_1^n+bk_2^n, \qquad (2)$$

of which the first is dominating, then the quotient g_{n+1}/g_n is slowly varying according to the formula

$$g_{n+1}/g_n=k_1-(b/a)(k_1-k_2)(k_2/k_1)^n+\cdots. \qquad (3)$$

From the quotient series, considered in a region where g_n still has enough significant figures, it is therefore possible to get an approximate value of k_1 and estimates of k_2 and bk_2^n/ak_1^n, of which the latter are usually too rough to be of real value for determining an *initial* term ak_1^n somewhere in the first geometrical series. After fixing a suitable value of k_1, we form instead the auxiliary function

$$h_n=k_1g_n-g_{n+1}\approx bk_2^n(k_1-k_2) \qquad (4)$$

and its quotient series h_{n+1}/h_n, from which we get a much better estimate of k_2, bk_2^n, and finally of $ak_1^n=g_n-bk_2^n$. After choosing a specific initial term of the first geometric series, we can then form our first trial exponential by repeated multiplication with constant factors, different for the various interval lengths. The method of successive approximations, as described above, is now started.

The accuracy of the analytic self-consistent-field (SCF) functions obtained by Slater's graphical method may be illustrated by his own example for Rb^+ in Table I; even if the maximum error is of the order 45×10^{-3}, the approximation is certainly good for many applications. The analytic SCF-functions, calculated from Slater's exponents[6] for other atoms of the periodic system, have also errors of about the same order of magnitude. In treating F, F^-, and Ne, Brown[6] reports errors of the order 20×10^{-3}.

In our investigation of the alkali chlorides,[11] we needed the $3p$-function of Cl^- with exchange, given numerically by Hartree and Hartree,[12] with a very high accuracy and most of the technique described in this

TABLE I. Survey of the maximum errors in different intervals in the analytic SCF-functions for Rb^+ (without exchange) given by Slater (reference 6) as an example of the accuracy of his graphical method.

r-interval	Maximum error in units of 10^{-3}		
	Rb^+_{1s}	Rb^+_{2s}	Rb^+_{2p}
0.00			
	14	−41	−9
0.04			
	−30	±17	−46
0.20			
	−15	±28	14
0.50			
	2	25	−31
1.00			
		14	5

[9] According to Slater (reference 6) only the exponential multiplied with the highest power in r should eventually be replaced by a sum of exponentials, but our generalization is obvious.

[10] A preliminary report of this method was given at the Shelter Island Conference, 1951.

[11] P. O. Löwdin, *A Theoretical Investigation into some Properties of Ionic Crystals* (Almqvist and Wiksells, Uppsala, 1948), thesis.

[12] D. R. Hartree and W. Hartree, Proc. Roy. Soc. (London) **A156**, 45 (1936).

TABLE II. Exponents and coefficients in an analytic SCF-function of the form (1) for $Cl^-(3p)$ with exchange (reference 12). Maximum error $= 1.5\times10^{-3}$.

AO	$k=$	1	2	3	$k=$	1	2	3
$Cl^-(3p)$	b_k	4.2435	8.4758	22.314	c_k	0.92426	1.6658	2.9859
	B_k	9.0441	26.493	2.49	C_k	0.07099	1.3955	8.4236

TABLE III. Exponents and coefficients in analytic SCF-functions of the form (1) for F^- without exchange (reference 13) and for Na^+ with exchange according to Fock and Petrashen (reference 14). For maximum errors, see Table IV.

AO	$k=$	1	2	$k=$	1	2	3	4
$F^-(1s)$	a_k	8.1890	12.187					
	A_k	40.285	9.5770					
$F^-(2s)$	a_k	7.1485	···	b_k	1.6465	2.7178	4.1211	···
	A_k	11.755	···	B_k	1.3054	8.7816	6.6845	···
$F^-(2p)$				b_k	0.64417	1.4357	3.0759	5.9696
				B_k	0.080948	1.3016	8.6449	7.0549
$Na^+(1s)$	a_k	8.1093	11.577					
	A_k	12.835	57.640					
$Na^+(2s)$	a_k	9.1285	···	b_k	2.3650	3.9031	···	
	A_k	16.895	···	B_k	3.6178	25.462	···	
$Na^+(2p)$				b_k	2.3718	3.8934	6.5076	
				B_k	5.1958	14.024	18.128	

paper was actually developed for the investigation of this function. Our final result is given in Table II, and, by using six exponentials (three in the C-group and three in the B-group), we could obtain a fit as good as 1.5×10^{-3}, i.e., the analytic SCF-function had about the same accuracy as the numerical function itself. With slightly less accuracy, we treated then two other closed-shell ions in the same way, namely, F^- without exchange[13] and Na^+ with exchange.[14] The results in a somewhat improved form are condensed in Table III and the maximum errors for different intervals in Table IV. In tabulating the errors, we are always giving the quantity $(f_{\text{analytical}}-f_{\text{numerical}})$ for the normalized functions in units of 10^{-3}.

TABLE IV. Maximum errors of the analytic SCF-functions for F^- and Na^+ in Table III, in units of 10^{-3}.

r-interval	F^-_{1s}	F^-_{2s}	F^-_{2p}	r-interval	Na^+_{1s}	Na^+_{2s}	Na^+_{2p}
0.00				0.0			
	1	8	0		±7	3	−5
0.08				0.2			
	−1	±10	1		8	±1	−1
0.3				0.4			
	−1	−10	−5		−3	±2	2
0.6				1.0			
	1	4	±1			2	−1
1.2				2.0			
		−1	−1			±1	0
3.0							
		0	±1				
6.0							
		0	1				
10.0							
			−1				

[13] D. R. Hartree, Proc. Roy. Soc. (London) **A151**, 96 (1935).
[14] V. Fock and M. Petrashen, Physik. Z. Sowjetunion **6**, 368 (1934). The slightly improved tables for Na^+ given by D. R. Hartree and W. Hartree, Proc. Roy. Soc. (London) **A193**, 299 (1948), were not available in Uppsala at the time of these first calculations.

In the theory of molecules, some first row atoms are of particular importance, and we have therefore tried to obtain analytic SCF-functions for neutral carbon (^1D-state), neutral nitrogen (^2P-state), and neutral oxygen (^1S-state), all given numerically with exchange by different authors.[15] The results are condensed in Table V, and the maximum errors are given in Table VI. We note that all the functions in Tables III and V are of orthodox Slater-type,[6] having only their highest-power exponential developed in a sum. The accuracy is essentially higher than in Slater's original functions, but this improvement is gained by adding at least one more exponential, which will again increase the work in the applications.

As was already pointed out by Slater,[6] all these expansions are not uniquely determined at all, and the exponents and the coefficients may vary over considerable ranges. A drastic example of this phenomenon is obtained by comparing our $2p$-function for carbon (^1D)

TABLE V. Exponents and coefficients in analytic SCF-functions of the form (1) for neutral carbon (reference 15), ^1D ($\beta=0.04$), for neutral nitrogen (reference 15), ^2P state ($\beta=0$), and for neutral oxygen (reference 15), ^1S state ($\beta=0$), all with exchange. For maximum errors, see Table VI.

State	AO	$k=$	1	2	$k=$	1	2	3
^1D	C(1s)	a_k	4.9840	7.0411				
		A_k	14.881	12.811				
	C(2s)	a_k	3.9471	···	b_k	1.4784	2.8493	7.7990
		A_k	5.9095	···	B_k	2.5829	5.2230	4.5676
	C(2p)				b_k	1.0789	2.1444	5.9216
					B_k	0.87935	3.3336	2.1226
^2P	N(1s)	a_k	6.2736	10.920				
		A_k	28.744	6.8632				
	N(2s)	a_k	4.1749	···	b_k	1.7123	3.4424	8.8037
		A_k	7.8400	···	B_k	3.5175	11.832	8.4171
	N(2p)				b_k	1.2210	2.4466	5.6236
					B_k	1.0755	5.2350	3.4611
^1S	O(1s)	a_k	7.2052	12.523				
		A_k	35.267	8.6933				
	O(2s)	a_k	5.9096	···	b_k	1.9764	3.6744	13.931
		A_k	9.8450	···	B_k	4.9049	11.246	5.5364
	O(2p)				b_k	1.3632	2.7487	5.9169
					B_k	1.3284	7.3218	6.0887

in Table V with the $2p$-function in Table VII given previously by Mulliken and others;[16] it is impossible to see directly that these functions with essentially different parameters approximate the same numerical function, but this is actually the case. The respective errors may be found in Table VI, and a closer investigation shows that the two error functions have opposite signs almost everywhere. In general, the order of magnitude and the sign of the errors will determine how much the different parameters in the functions (1) may vary.

The different *states* of a specific electronic configuration of an atom (or ion) may be characterized by Slater's[17] parameter β, and Hartree and others[15] have found by experience that the corresponding radial

[15] C: A. Jucys, Proc. Roy. Soc. (London) **A173**, 59 (1939). N: D. R. Hartree and W. Hartree, Proc. Roy. Soc. (London) **A193**, 299 (1948). O: Hartree, Hartree, and Swirles, Trans. Roy. Soc. (London) **A238**, 229 (1939).
[16] Mulliken, Rieke, Orloff, and Orloff, J. Chem. Phys. **17**, 1248 (1949); the function in their Eq. (76) is transformed to our form (1).
[17] J. C. Slater, Phys. Rev. **34**, 1293 (1929).

functions $f_{nl}(r)$ vary almost linearly in this parameter. In order to investigate whether this simple linearity in β could be transferred, e.g., to the coefficients in the analytic SCF-functions, we have treated neutral oxygen in two of its states, namely the ^1S-state ($\beta=0$) and the ^3P-state ($\beta=-0.6$). As may be seen from a comparison between Tables V and VII, the preliminary result was negative, and the problem is therefore still under investigation.

II. INTERPOLATION OF SLATER-FUNCTIONS

The purpose of the original Slater-functions[6] was not only to describe numerically given SCF-functions analytically, but even to permit interpolations to atoms for which these self-consistent fields had not yet been prepared. This interpolation was based on the rule that the exponents should vary linearly for similar electron configurations and different atomic numbers. The coefficients in the last group were interpolated by means of an auxiliary "intermediate" exponent, also varying linearly, which gave the ratio between the

TABLE VI. Maximum errors of the analytic SCF-functions for C, N, and O given in Tables V and VII, in units of 10^{-3}.

r-interval	^1D			Mulliken	r-interval	^2P			^1S			^2P
	C_{1s}	C_{2s}	C_{2p}	C_{2p}		N_{1s}	N_{2s}	N_{2p}	O_{1s}	O_{2s}	O_{2p}	O_{2p}
0.0					0.0							
0.2	6	4	3	−3	0.04	8	−2	0	12	−1	0	0
0.8	±3	8	±3	12	0.2	8	−2	1	10	1	3	±1
2.4	3	−4	3	±8	0.5	±4	2	2	±4	−12	4	±1
4.0	0	−4	±1	±3	1.2	±2	±4	±3	±2	±6	±3	−6
8.0		4	−2	2	4.0	−1	±6	±3	−1	−9	±2	±6
			−2	2	7.0		2	1		2	−3	±2
								−1			−1	0

coefficients; the absolute values were then determined by the normality and orthogonality conditions.

The interpolation problem can, of course, be treated rigorously by investigating the effect of variations of the atomic number Z in the basic Hartree-Fock equations,[18] but, with the present mathematical methods, the error margins seem to be too large to render really useful results. For the moment, it seems therefore to be better to work intuitively by using the hypothesis that the SCF-functions are closely analogous to the hydrogen-like functions, but that they just have more general exponents replacing the atomic number Z. The interpolation rule for the exponents seems very plausible from this point of view,[19] but, in order to obtain full accuracy also in the interpolated functions, we must modify the interpolation rule for the coefficients.

[18] Compare also D. R. Hartree and W. Hartree, Proc. Roy. Soc. (London) **A166**, 450 (1938), and reference 3.

[19] Compare also the exponents in the analytic wave functions for Be-like atoms and ions, calculated directly from the variational principle by V. Fock and M. Petrashen, Physik. Z. Sowjetunion **8**, 359 (1935), Table IV.

TABLE VII. Exponents and coefficients in an analytic $2p$-function of the form (1) for the ^3P-state of neutral oxygen (reference 15), and in Mulliken's (reference 16) $2p$-function for the ^1D-state of neutral carbon (reference 15).

State	AO	$k=$	1	2	3
^3P	$O(2p)$	b_k	1.4107	2.8500	6.5935
		B_k	1.4384	8.3557	4.7562
^1D	$C(2p)$	b_k	0.898	1.416	2.694
Mulliken:		B_k	0.2727	1.427	3.576

Let us consider the simplest SCF-functions, namely the $1s$-functions of the He-like ions, which we will express in the following form:

$$f_{1s}(r)=A_1 r\exp(-a_1 r)+A_2 r\exp(-a_2 r). \qquad (4a)$$

The numerical functions for $Li^+(Z=3)$ and $C^{+4}(Z=6)$ are given by Fock and Petrashen[20] and by Jucys,[15] respectively, and the corresponding values of our parameters in (4a) are condensed in Table VIII; the maximum errors are in both cases below 1.0×10^{-3}. By using these data, we will then try to make interpolations and extrapolations in the series of the He-like ions.

The exponents a_1 and a_2 are easily determined as linear functions of Z from the fixed values for $Z=3$ and $Z=6$. For the coefficients A_1 and A_2, the normalization condition for f_{1s} gives one relation, but, in order to carry out the interpolation, we need one more equation for them. However, we note that, for a pure hydrogen-like $1s$-function, we would have the relations

$$f_{1s}(r)=2Z^{\frac{1}{2}}r\exp(-Zr), \quad [f_{1s}(r)/2r]_{r=0}^{\frac{1}{2}}=Z, \qquad (5)$$

and, according to our analogy rule, the last relation indicates that, also for the SCF-functions, the quantity

$$K_{1s}=[f_{1s}(r)/2r]_{r=0}^{\frac{1}{2}} \qquad (6)$$

will vary linearly with Z. We have tested this rule on some numerical SCF-functions calculated by Hartree and others,[3] and the results in Table IX show that the "linearity rule" holds with excellent accuracy. Similar quantities K_{2s}, K_{2p}, K_{3s}, $\cdots$ may be constructed also for the $2s$-, $2p$-, $3s$-, $\cdots$ functions, and a closer investigation shows that they are approximately linear in Z, too. Complete results also for the higher functions will be given in a later paper in this series. We note that all these quantities are important in the calculations of self-consistent fields with exchange, since they char-

TABLE VIII. Analytic SCF-functions of the form (1) for $Li^+(1s)$ and for $C^{+4}(1s)$; the maximum error is below 1.0×10^{-3}.

AO	$k=$	1	2
$Li^+(1s)$	a_k	2.4346	4.4250
	A_k	6.6641	2.5618
$C^{+4}(1s)$	a_k	5.4523	9.5935
	A_k	23.919	4.0324

[20] V. Fock and M. Petrashen, Physik. Z. Sowjetunion **8**, 547 (1935).

TABLE IX. The auxiliary quantity $K_{1s}=(f_{1s}(r)/2r)_{r=0}^{2/3}$ for some 1s-functions belonging to self-consistent fields with exchange.[3]

Z	Atom	K_{1s}	Z	Atom	K_{1s}
6	C	5.760	17	Cl^-	16.70
7	N	6.757	18	Ar	17.69
8	O	7.751	19	K^+	18.70
			20	Ca^{+2}	19.69
11	Na^+	10.73			
14	Si^{+4}	13.73			

acterize the behavior of the normalized wave functions in the neighborhood of the point $r=0$.

If the K_{1s}-rule is applied also to the He-series, we get a second relation for the coefficients A_1 and A_2, which then may be determined. The results of the interpolation are condensed in Table X, and it may be of some interest to test its accuracy. The 1s-function for Be^{+2} is numerically given by Hartree and Hartree,[21] and a comparison shows that our analytic functions reproduces the numerical table with full accuracy. We may suppose that the same will be true also for B^{+3}. In the extrapolations, the accuracy can certainly not be so high, but we note that our analytic function will give the same charge distribution for He as was once numerically given by Hartree.[22] Even for H^- our analytic function is comparatively good, since it gives a much better fit to Hylleraas's charge distribution[8] than the best hydrogen-like wave function.

The calculations involved in the application of the K_{1s}-rule are somewhat clumsy, and we have therefore tried to derive a simpler interpolation rule for the coefficients, which could be generalized also to functions containing more exponentials. Using the analogy principle, we will make the assumption that each coefficient A_k as a function of Z has the form

$$A_k(Z)=\kappa_k\{a_k(Z)\}^{p_k}, \tag{7}$$

where the parameters κ_k and p_k are independent of Z. This means that $\log_{10}A_k$ is a *linear* function of $\log_{10}a_k$:

$$\log_{10}A_k(Z)=\log_{10}\kappa_k+p_k\log_{10}a_k(Z), \tag{8}$$

TABLE X. Interpolated and extrapolated SCF-functions of the form (1) for some He-like ions, obtained by using the linearity of the quantity K_{1s}. The star * indicates the given quantities, taken from Table VIII.

Z	Atom	K_{1s}	a_1	a_2	A_1	A_2
1	H^-	0.7505	0.4228	0.9794	0.30025	1.0001
2	He	1.7608	1.4287	2.7022	2.7626	1.9104
3	Li^+	2.7711*	2.4346*	4.4250*	6.6641*	2.5618*
4	Be^{+2}	3.7814	3.4405	6.1478	11.601	3.1057
5	B^{+3}	4.7917	4.4464	7.8706	17.387	3.5909
6	C^{+4}	5.8021*	5.4523*	9.5935*	23.919*	4.0324*
7	N^{+5}	6.8124	6.4582	11.316	31.101	4.4604
8	O^{+6}	7.8227	7.4641	13.039	38.897	4.8621
Difference:		1.0103	1.0059	1.7228		

[21] D. R. Hartree and W. Hartree, Proc. Roy. Soc. (London) **A149**, 210 (1935).
[22] D. R. Hartree, Proc. Cambridge Phil. Soc. **24**, 111 (1928).

TABLE XI. Coefficients in interpolated and extrapolated SCF-functions for some He-like ions. The exponents are the same as in Table X, but, this time, the coefficients are obtained by using the simple rule (8). The star * indicates given quantities, taken from Table VIII.

		Unnormalized coefficients		Normalized coefficients	
Z	Atom	A_1	A_2	A_1	A_2
1	H^-	0.41560	1.0585	0.3385	0.8622
2	He	2.8631	1.9269	2.7772	1.8691
3	Li^+	6.6641*	2.5618*	6.6641	2.5618
4	Be^{+2}	11.529	3.1064	11.593	3.1236
5	B^{+3}	17.312	3.5905	17.382	3.6049
6	C^{+4}	23.919*	4.0324*	23.919	4.0324
7	N^{+5}	31.281	4.4422	31.117	4.4189
8	O^{+6}	39.349	4.8271	38.930	4.7759
		$\kappa=$ 1.6265	1.0713		
		$p=$ 1.5850	0.5862		

and the coefficients A_k are therefore easily determined, e.g., by using divided differences. However, these preliminary values of the coefficients A_k are usually not representing a function which is fully normalized, and, in the last step of the interpolation, they should therefore be given revised values by using the normalization condition.

The results of the application of the rule (8) to the He-series are given in Table XI, and we note that, for the interpolated ions Be^{+2} and B^{+3}, the coefficients are practically the same as in Table X.

The interpolation rule (8) may be directly generalized also to the other groups of coefficients $(B, C, \cdots)$. As another example, let us consider the $2p$-functions of some Ne-like ions. The functions for $Na^+(Z=11)$ and $Si^{+4}(Z=14)$ are numerically given by Hartree and others,[23] and our parameters for the corresponding analytic functions (1) are listed in Table XII and the maximum error (0.002) in Table XIII. From these fixed data, the interpolations for $Mg^{+2}(Z=12)$ and $Al^{+3}(Z=13)$ were carried out by using the simple rule (8) and the normalization condition. Our analytic $2p$-function for Mg^{+2} may be checked against the SCF-function given numerically by Yost,[24] which is almost fully reproduced with an error below 0.0016; it is somewhat surprising that the error in the interpolated function is even lower than in one of the fixed functions (Na^+), see Table XIII.

The net result of our investigation seems to be that it is possible to interpolate analytic SCF-functions with about the same accuracy as in the fixed functions by using Slater's rule for the exponents and the simple rule (8) and the normalization condition for the coefficients. The results already obtained are somewhat encouraging, and further work on this problem is now in progress.

[23] Na^+: D. R. Hartree and W. Hartree, Proc. Roy. Soc. (London) **A193**, 299 (1948). Si^{+4}: Hartree, Hartree, and Manning, Phys. Rev. **60**, 857 (1941).
[24] W. J. Yost, Phys. Rev. **58**, 557 (1940).

TABLE XII. Analytic SCF-functions for $Na^+(2p)$ and $Si^{+4}(2p)$ with exchange calculated from the numerical tables (reference 23), and interpolated functions for $Mg^{+2}(2p)$ and $Al^{+3}(2p)$ with the coefficients determined by the simple rule (8). For maximum errors, see Table XIII.

					Unnormalized coefficients			Normalized coefficients		
Z	Atom	b_1	b_2	b_3	B_1	B_2	B_3	B_1	B_2	B_3
11	Na^+	2.1880	3.7288	6.8864				3.6164	15.660	18.729
12	Mg^{+2}	2.7226	4.4808	7.9907	6.9728	22.590	21.156	7.0360	22.795	21.348
13	Al^{+3}	3.2572	5.2327	9.0950	11.952	30.781	23.524	12.043	31.016	23.704
14	Si^{+4}	3.7918	5.9847	10.1993				18.870	40.231	25.840
Diff:		0.5346	0.7520	1.1043						
					$\kappa =$ 0.34400	1.1348	3.8533			
					$p =$ 3.0046	1.9943	0.81944			

CONCLUSIONS

In the theory of molecules and crystals, which is based on the use of atomic orbitals in one or other form, the SCF-functions take a selected and most important place, since they represent the *best* one-electron AO which are available. The problem of calculating analytic SCF-functions has become particularly important during the last few years, since most of the extensive molecular tables under preparation in Chicago under Mulliken, in Oxford under Coulson, and in Tokyo under Kotani, are based on the use of single exponential functions.[25] In order to make all these tables applicable even to the best atomic orbitals, it would be desirable to have the exponents and the coefficients in the analytic functions (1) calculated for all self-consistent-fields which are numerically available, and to carry out interpolations to atoms which have not yet been treated by the Hartree-Fock technique.[26] In addition to the best fits, it would also be of interest to have fairly accurate analytic SCF-functions containing as few exponentials as possible.

By the generalized Slater method described in this paper, it is possible to calculate analytic SCF-functions from the numerically given tables with any desired accuracy, but, even if the technique is simple, the computations are still time-consuming and rather tedious. It is felt that, if the periodic system should be investigated on a large-scale basis in order to obtain analytic SCF-functions having errors of the order of magnitude (0.001–0.002) examplified in Tables II, VIII, and XIII, then it would be worthwhile to re-examine the basic method for further improvements, if possible. Work on this program is now in progress, and the results will be reported in a later paper in this series.

[25] Molecular tables for particular atoms may also be prepared directly from the numerically given SCF-functions; see, e.g., reference 11, Method I.

[26] It seems probable that the interpolated analytic functions would give very good initial functions for self-consistent-field calculations.

The author is greatly indebted to *Fil.Mag.* L. F. Ljungström, Uppsala, who kindly assisted in the computations on the sodium and the fluorine ions when this work was started, to the Swedish Natural Science Research Council for a grant, which made these calculations possible, and to Professor I. Waller for many forms of valuable support.

The work on the first-row atoms was started on the initiative of Professor R. S. Mulliken, Chicago, and I would like to express my sincere gratitude to him for many valuable discussions and for the great hospitality I enjoyed during my stay in Chicago. I would also like to thank Mr. Tracy J. Kinyon for his valuable assistance in carrying out the calculations on neutral carbon, nitrogen, and oxygen.

Finally, I would like to thank *Fil.Kand.* K. Appel, leader of our computational group, for his skilful cooperation in performing the computations in connection with the interpolation problem, the Elizabeth Thompson Science Fund for financial aid, and Professor J. C. Slater for his kind interest and valuable support of my work.

TABLE XIII. Maximum errors of the analytic SCF-functions given in Table XII in units of 10^{-3}; note that Mg^{+2} is interpolated between Na^+ and Si^{+4}.

r-interval	$Na^+{}_{2p}$	$Mg^{+2}{}_{2p}$	$Si^{+4}{}_{2p}$
0			
	−0.6	−0.7	−0.9
0.04			
	2.0	1.6	1.1
0.20			
	−2.1	−1.3	0.7
0.50			
	2.1	±1.1	−0.9
1.2			
	−2.1	±1.4	−0.8
4.0			
	−0.6	±0.4	
6.0			

Color Centers and Trapped Charge in KCl and KBr

DAVID DUTTON*† AND ROBERT MAURER
Department of Physics, University of Illinois, Urbana, Illinois
(Received December 15, 1952)

Potassium chloride and bromide crystals have been irradiated with x-rays at −183°C and the behavior of the V_1, F, and F' optical absorption bands observed during subsequent warming to room temperature. The thermal bleaching of the V_1-band is accompanied by a decrease in the F-band, the appearance of free charge within the crystal, and luminescence. The data indicate that positive holes are released from traps during this process.

INTRODUCTION

V-CENTERS in x-rayed alkali halide crystals have recently been the subject of a number of investigations.[1–7] Many of the color centers formed by irradiation at low temperature are unstable at room temperature or below: the V_1-band,[2] for example, formed in KBr by x-raying at −180°C, is bleached by warming to −140°, and cannot be formed at the higher temperature.[3] The V_1-band may also be bleached by illuminating with light in the V_1-band; in either case the F-band is partially bleached at the same time.[2] Several of the V-bands have been interpreted as due to positive holes trapped at such lattice defects as positive-ion vacancies or aggregates of vacancies.[1,2,7] The V_1-band, according to Seitz,[7] may be the simple analog of the F-center, a positive hole trapped by a single positive ion vacancy. Seitz has suggested that the thermal instability of V_1-centers may, in view of the very low temperature at which it occurs, be due to ionic diffusion and combination with F-centers, rather than thermal dissociation into holes and positive ion vacancies.

The experiments to be described indicate that free charge is released within the crystal during the thermal bleaching of the V_1-band. The behavior of the F-band during this process provides strong evidence that the released charge consists of holes. Some preliminary results for KCl were previously reported;[8] this paper describes further work on KBr and improved measurements on KCl.

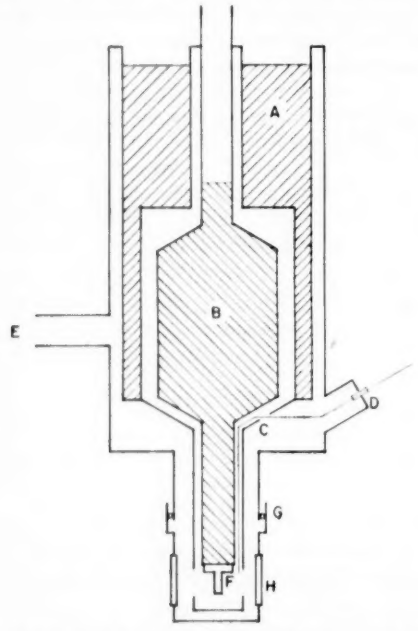

FIG. 1. Cryostat. A and B, liquid nitrogen reservoirs; C, radiation shield; D, electrical lead; E, pumping line; F, crystal holder; G, rotating O-ring seal; H, crystal quartz windows.

EXPERIMENTAL PROCEDURE

Pieces of KCl and KBr about 1.5×8×20 mm were cleaved from commercial (Harshaw) crystals and mounted in a holder which permitted a dc field of the order of 1000 volts/cm to be applied along the 8-mm dimension and allowed light to be transmitted along the 1.5-mm dimension. The holder, F, was attached to the inner vessel of the cryostat shown in Fig. 1, but was insulated from it by a 0.003-inch film of polystyrene (a compromise between the requirements of good electrical insulation and good thermal contact). A radiation shield, C, at the temperature of the outer Dewar vessel surrounded the crystal except for small windows to admit light and x-rays. The external vacuum jacket was equipped with a cap which could be rotated about an O-ring seal, G, to bring either a beryllium window (1 mm thick) or a pair of crystal quartz windows, H, into alignment with the crystal. The temperature of the crystal was measured directly by a copper-constantan couple cemented in a small hole drilled in the crystal. With liquid nitrogen in both inner and outer vessels, A and B, the equilibrium temperature of the

* Present address: Ecole Normale Superieure, Paris, France.
† Based on a thesis submitted to the University of Illinois in partial fulfillment of requirements for the degree of Doctor of Philosophy.
[1] J. Alexander and E. E. Schneider, Nature **164**, 653 (1949).
[2] Casler, Pringsheim, and Yuster, J. Chem. Phys. **18**, 887, 1564 (1950).
[3] H. Dorendorf, Z. Physik **129**, 317 (1951).
[4] Delbecq, Pringsheim, and Yuster, J. Chem. Phys. **19**, 574 (1951).
[5] W. Martienssen, Z. Physik **136**, 488 (1952).
[6] W. H. Duerig and J. J. Markham, to be published.
[7] F. Seitz, Phys. Rev. **79**, 529 (1950).
[8] Dutton, Heller, and Maurer, Phys. Rev. **84**, 363 (1951).

crystal was −183°C. By introducing an electric heater into the inner vessel the crystal could be warmed at a rate of about 5°C per minute.

The electric field was supplied by dry cells. Currents were measured with a commercial electrometer of the vibrating-reed type (Applied Physics Corporation), connected as a voltage amplifier across a 10^{10}-ohm Victoreen resistor. The noise level was about 10^{-14} amp, the chief source of disturbance apparently being thermal stresses in the crystal and insulators while the system was being warmed. Runs on unirradiated crystals were frequently made to check on spurious effects, and care was taken to establish reproducibility of interesting events. Polarization effects were negligible, owing to the small quantities of charge collected and the very small range of the charge carriers.

The source of x-rays was a beryllium-windowed, molybdenum-target tube operated at 50 kv and 20 ma. The crystals were exposed for 1 to 2 hours at about 2 inches from the tube window.

Electrical measurements were made as follows. The crystal was first irradiated with x-rays in the dark at −183°C and its absorption spectrum determined. Then an electric field was applied and the crystal warmed to room temperature, while current and temperature were recorded automatically as functions of time. The crystal was then cooled again to −183° and its optical absorption remeasured.

Luminescence was observed by a similar procedure,

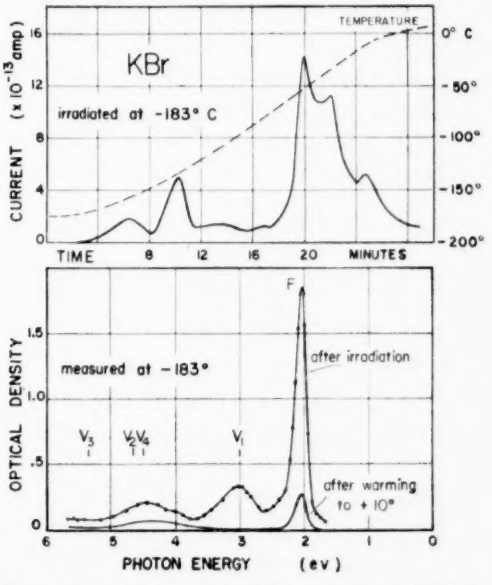

FIG. 2. Upper part: Current and temperature as functions of time as a KBr crystal is warmed with a dc field of 950 volts/cm applied, after irradiation with x-rays for 1 hour at −183°C. Lower part: The absorption spectrum of the crystal before and after warming. The indicated positions of V-bands are after Dorendorf (reference 3).

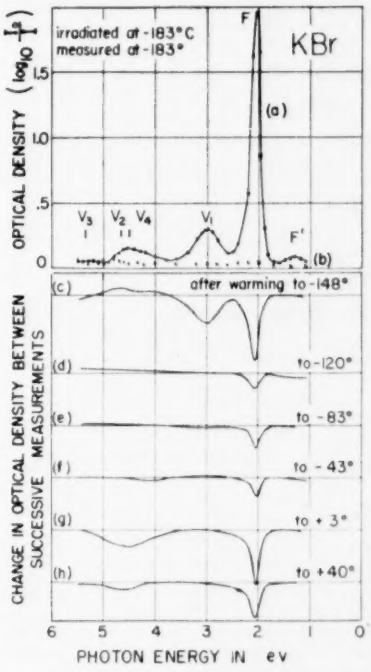

FIG. 3. (a) Absorption spectrum of KBr crystal after irradiation; (c) Change in absorption after warming momentarily to −148°C; (d)–(g) Further changes in absorption as crystal is warmed to the temperatures indicated; (h) Further change in absorption after crystal has been held at +40° for two hours; (b) Absorption spectrum at completion of the run. All curves measured at −183°. Rates of warming and cooling were approximately 5°/min.

using as detector a cesium-antimony photocell with very small dark current.

To establish correlation between certain peaks in the current-time curves obtained in this way (Figs. 2 and 5) and changes in the absorption spectrum, two methods were used. The first, applied to KCl, was to observe the V_1-band continuously while the crystal was warmed, using a low level of illumination, and to note that bleaching of the band was simultaneous with the appearance of a current peak. The second, applied to both materials, was to measure the absorption of the irradiated crystal, first at the low irradiation temperature, and again at the same low temperature after the crystal had been warmed momentarily to some higher temperature T which corresponded roughly with a current peak; a succession of such measurements were made after a single irradiation. (This resembles the pulse-annealing technique except for the very slow rates of warming and cooling, 5° to 10° per minute.)

Optical measurements were made with a Leiss double monochromator equipped with Quarzglas prisms (unfortunately not useful below 2400A), using a hydrogen discharge lamp as source and a cesium-antimony cell as detector in the ultraviolet and a

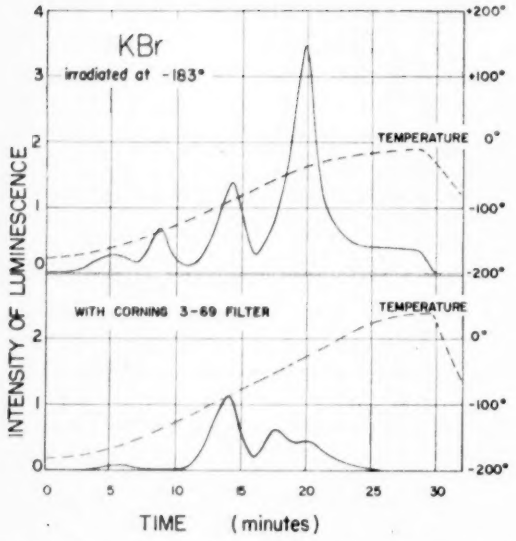

FIG. 4. Glow curves in KBr. The unit of intensity corresponds roughly to 10^9 quanta per second total emission. The upper curve was measured by a cesium-antimony cell sensitive to wave lengths below 6500A; the lower curve was measured under similar conditions but through a filter which transmits wavelengths above 5500A. The large peak at 20 minutes in the upper curve is resolved into two peaks when the filter is introduced.

tungsten lamp and dark-current-balanced cesium-silver oxide cells in the visible and near infrared. The absorption is expressed in terms of optical transmission before and after irradiation rather than in terms of the absorption constant, since the coloration varies with depth due to strong absorption of the x-rays. The penetration depth for beryllium-filtered 50-kv molybdenum radiation, as measured by Duerig and Markham,[6] is of the order of 0.05 to 0.1 mm.

RESULTS

Examples of the data are given in Figs. 2–7. The results, summarized in Table I, are as follows: (1) The V_1-band is bleached, with the release of charge and luminescence, at $-158°$ in KBr and $-145°$ in KCl. (2) Partial bleaching of the F-band occurs at the same time, in so far as can be determined. In KCl, warmed to $-160°$, the F-band had not begun to bleach appreciably, but bleaching had occured after warming to $-100°$. (3) Current and luminescence peaks at $-130°$ in KBr and $-68°$ in KCl are due to thermal ionization of F'-centers. The corresponding effect in NaCl was observed by Gudden and Pohl[9] at $+90°$. These are the temperatures at which the "thermally increased range" of photoelectrons from F-centers begins,[10] and the largest decrease in the F'-band occurs in the present experiments (Figs. 3 and 6). (4) Luminescent glow peaks unaccompanied by an observable release of charge occur at $-88°$ in KBr and at $-36°$ in KCl. No change occurs in the absorption spectrum, at least in the limited region under observation, except a decrease in the F-band. (5) Of the additional current peaks observed in KBr, one (at $-27°$) may be associated with the disappearance of the V_4-band.[3]

The spectral composition of the luminescence in KBr was examined by taking a series of glow curves under the same conditions of excitation but with various sharp-cut-off filters in front of the detector. These measurements showed that the glow peaks have different spectra, but were inadequate to establish any definite pattern of behavior. The peak associated with V_1-centers, presumably due to the recombination of holes, is transmitted well by a filter which cuts off below 5000A, while the glow peak associated with disappearance of F'-centers, is practically extinguished by a filter which cuts off below 3800A; the peak at $-27°$C, which seems to be associated with the disappearance of V_4-centers, has a much smaller component at wave lengths above 5000A than the luminescence accompanying the disappearance of V_1-centers. The luminescent yield is small and is estimated as one quantum per 10^4 to 10^5 centers destroyed. Sharma[11] has reported similar glow curves obtained with potassium iodide.

Of the KCl luminescence, only the phosphorescence at $-183°$C after x-ray irradiation was examined in this way. Of this radiation, 70 percent was transmitted by Corning filter 9–53 (cutoff about 3000A) and 6 percent by filter 0–52 (cutoff about 3800A).

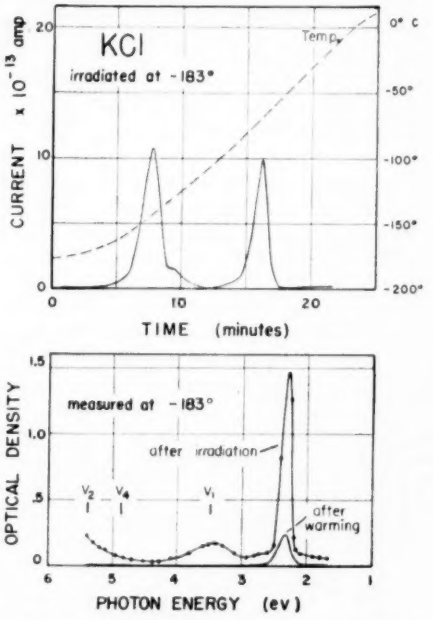

FIG. 5. Similar to Fig. 2, for KCl. The field in this case was 680 volts/cm.

[9] B. Gudden and R. W. Pohl, Z. Physik **31**, 651 (1925).
[10] G. Glaser, Gött. Nachr. **3**, 31 (1937).
[11] J. Sharma, Phys. Rev. **85**, 692 (1952).

A relation originally derived by Smakula[12] and given in somewhat simpler forms by Mollwo and Roos[13] may be used to compute the concentration of color centers from the height and half-width of the absorption band. Using the numerical constants appropriate to KCl, the number of color centers per unit area is

$$\frac{N}{A}=\left(\frac{1}{f}\times 2.44\times 10^{16} HD\right)\ \text{cm}^{-2}, \qquad (1)$$

where H is the width of the absorption band at half-maximum, in electron volts, D is the optical density $=\log_{10}(I_0/I)$, and f is the oscillator strength of the transition. f has been measured chemically for the F-band in KCl by Kleinschrod,[14] who found $f=0.81$ in this case. Oscillator strengths have not been determined for other materials and other absorption bands. Estimates of the numbers of color centers involved, with the assumption that $f=1$ and the data of Figs. 3 and 6, are given in Table II.

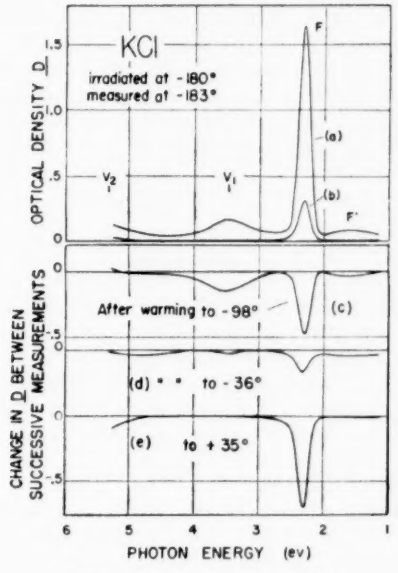

FIG. 6. Similar to Fig. 3, for KCl.

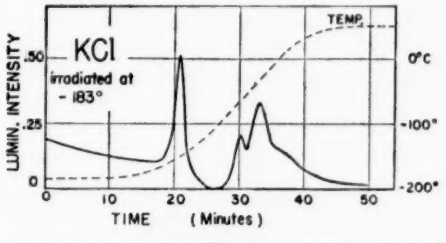

FIG. 7. Glow curve in KCl. The observation began 15 minutes after removal from the x-ray beam. The phosphorescence at −183° has a decay time of about 9 minutes.

[12] A. Smakula, Z. Physik **59**, 603 (1930).
[13] E. Mollwo and W. Roos, Gött. Nachr. **1**, 107 (1934).
[14] F. Kleinschrod, Ann. phys. **27**, 97 (1936).

TABLE I. The temperatures at which current maxima were observed on warming of crystals irradiated with x-rays at −183°C. The rate of heating was 5°C per minute. Temperatures listed are mean values from several observations, variation among individual runs was of the order of ±3°C. Trap depths are calculated from $E=1.08kT$ ln$s$. ** denotes a glow peak unaccompanied by a current peak.

	Temperature of current peak (°C)	Principal change in optical absorption	Spectral character of luminescence	Trap depth (ev)
		KBr		
	−158	V_1-band	(λ>5000A)	0.23
	−130	F'-band	(λ<3800A)	0.29
**	−88	?	(λ>5000A)	0.38
	−48	?	?	0.46
	−27	V_4-band	(λ>5000A)	0.50
		KCl		
	−145	V_1-band	?	0.26
	−68	F'-band	?	0.42
**	−36	?	?	0.49

A comparison of the total number of color centers destroyed with the total charge collected is given in Table III. If N charge carriers are released, and each drifts an average distance w in the direction of the field before it is trapped, the total charge measured will be

$$Q=New/d, \qquad (2)$$

where d is the separation of the electrodes. Assuming the presence of one type of trap, w can be written

$$w=\mu E\tau=\mu E\frac{1}{C_t\sigma_t v}, \qquad (3)$$

where τ = mean free time, E = electric field, C_t = density of traps, σ_t = trap cross section, v = thermal velocity $=10^7$ cm/sec, and μ = mobility. A small volume element $dxdydz$ which has a density n of centers able to release charge carriers and a density C_t of traps will contribute to the total charge an amount

$$dQ=\frac{eE\mu}{d\sigma_t v}\frac{n}{C_t}dxdydz. \qquad (4)$$

TABLE II. Concentration of color centers in crystals irradiated with x-rays at −183°C and change in concentration observed during warming of crystals. The numbers listed in columns 3, 4, and 5 are the quantity (Nf/A) calculated from Eq. (1) with $f=1$.

Absorption band	Half-width H(ev)	Initial number of color centers (cm^{-2})	Number bleached (Curve C, Figs. 3 and 6) (cm^{-2})	Number bleached (Curve G, Fig. 3) (cm^{-2})
		KBr		
F	0.18	8.6×10^{15}	2.2×10^{15}	2.0×10^{15}
V_1	0.6	4.0×10^{15}	3.2×10^{15}	
V_4	~1			3.0×10^{15}
		KCl		
F	0.20	8.0×10^{15}	2.2×10^{15}	
V_1	0.7	2.7×10^{15}	2.5×10^{15}	

If we assume that (1) the traps are F-centers and (2) the ratio of F-centers to V-centers is the same at different levels of coloration, the integration of the above expression reduces to the choice of an effective volume V in which there is sufficient density of color centers so that we may expect these assumptions to hold. A reasonable choice is the area of the irradiated crystal multiplied by the penetration depth of the x-rays, which gives $V=0.01$ cm^3. With these assumptions we may estimate the quantity.

$$\frac{\mu}{\sigma_t}=Q\frac{C_t}{Nv_1}\frac{dv}{eE}, \tag{5}$$

and such estimates are given in Table III. Some results by Glaser[10] for photoelectrons from F-centers are included for comparison.

The method described by Randall and Wilkins[15] was used to compute trap depths for the various glow peaks. The rate of thermal ionization of charge from the original traps is taken as

$$R=se^{-E/kT}, \tag{6}$$

and the trap depth E is related to the temperature T^* of maximum glow by

$$E=kT\ \ln s\left\{1+\frac{\ln(kT^{*2}/\beta E)}{\ln s}\right\}, \tag{7}$$

where β is the warming rate. In our case this becomes

$$E=1.08kT^*\ \ln s. \tag{8}$$

The frequency factor s was taken as $10^{9.5}$ sec^{-1}, the value obtained from glow curves in Tl-activated KCl by Bunger and Flechsig.[16] The temperatures of maximum luminescence are, within experimental error, the same as the corresponding temperatures of maximum current, as one would expect for the case in which the lifetime of the electrons or holes in their original traps is very long compared to the lifetime in the conduction band.

One further point of interest is the very low thermal ionization energy of the V_1-center, compared to the energy of the optical transition. A qualitative argument can be given[8] to the effect that the ratio of optical to thermal energies should be greater for trapped holes than for trapped electrons, but it does not appear that a ratio as large as 10 can be accounted for in this way. In a recent paper Kubo[17] has suggested that a small apparent trap depth may result from the fact that the crystal is not in thermal equilibrium; however, V_1-centers cannot be produced in KBr by irradiating at $-140°$ under conditions of thermal equilibrium, and the ionization of F'-centers is observed at the expected temperature. The V_4-band and an ultraviolet band, observed by Duerig and Markham[6] in crystals x-rayed at 5°K, which is bleached by warming to 78°K, seem to be other instances of small thermal excitation energies.

TABLE III. Data which permit a calculation of μ/σ, the ratio of mobility of the charged particles to the trapping cross section. Glaser (reference 10) found $\mu/\sigma=6\times10^{14}$ volt^{-1} sec^{-1} for photoelectrons from F-centers in x-rayed KCl at $-120°$C. Mott and Gurney (reference 17) estimate σ for the F-center to be 10^{-14}–10^{-15} cm^{-2}.

Material	Current peak (°C)	Total no. of V_1-centers	Total charge measured Q (coulombs)	Average density of F-centers C_F (cm^{-3})	Average value of w/E (cm^2-volt^{-1})	μ/σ (volt^{-1} sec^{-1})
KBr	−158	4×10^{15}	4×10^{-11}	9×10^{17}	3×10^{-11}	3×10^{14}
KCl	−145	3×10^{15}	9×10^{-12}	8×10^{17}	1×10^{-11}	1×10^{14}

CONCLUSION

The thermal bleaching of the V_1 absorption band is due to thermal ionization of the centers. Since the number of F-centers which disappear when the V_1 band is bleached is approximately the same as the number of V_1-centers which disappear it is concluded that holes are released from V_1-centers and migrate to the F-centers where recombination of the free holes and trapped electrons occurs.

The cryostat used in this work was designed by Professor Dillon Mapother. The cesium-antimony photocell was supplied by Dr. Leroy Apker of the General Electric Company. The authors are indebted to Professors F. Seitz and W. Heller for helpful discussions of the work, which was supported in part by the U. S. Office of Naval Research, Department of the Navy.

[15] J. T. Randall and M. H. F. Wilkins, Proc. Roy. Soc. (London) **A184**, 365 (1945).

[16] W. Bunger and W. Flechsig, Z. Physik **67**, 42 (1931).

[17] R. Kubo, Phys. Rev. **86**, 929 (1952).

The Generalization of the WKB Method to Radial Wave Equations

R. H. Good, Jr.
Department of Physics, University of California, Berkeley, California
(Received December 15, 1952)

There are two difficulties which arise in connection with the usual generalizations of the WKB method to the Schrödinger and Dirac radial wave equations. One difficulty is that, in deriving the approximations, the Dirac radial equation, the Schrödinger radial equation, and the one-dimensional Schrödinger equation are treated nonuniformly so that the approximate solutions are not simply related to each other in the same way that the original equations are. The other difficulty is that the Dirac radial WKB approximation cannot be applied to a certain type of bound state. In this paper it is shown that these difficulties can be avoided by using as the basis for the WKB method, instead of the customary exponential function, the functions which arise in solving the free-particle problem. In the radial problems these are Bessel functions of order integer-plus-one-half. As well as avoiding the difficulties mentioned above, this technique has the following additional advantages. In the radial problems connection formulas across the turning points are not required. The eigenvalue condition for the bound states arises from a comparison of asymptotic expressions in such a way that one would expect the approximate eigenvalues to be close to the exact ones. For a free particle the approximate wave functions become identical with the exact wave functions, so the accuracy of the approximation increases with increasing energy. On the other hand, the approximations based on Bessel functions have the disadvantages that they are clumsier to apply than the usual approximations and that they give especially poor results near the turning points.

I. INTRODUCTION

THE problem which will be discussed here is that of finding WKB-type approximations to the solutions of the Dirac and Schrödinger radial wave equations. A resumé of the differential equations which are involved and of the usual WKB approximations to their solutions will be given first.

The Dirac radial wave equations arise in discussing the motion of a Dirac particle in a spherically symmetric potential field, and may be written as follows:

$$\begin{aligned}&\frac{W-V(r)+mc^2}{\hbar c}u-\frac{d}{dr}v+\frac{l+1}{r}v=0,\\&\frac{W-V(r)-mc^2}{\hbar c}v+\frac{d}{dr}u+\frac{l+1}{r}u=0.\end{aligned}\tag{1}$$

Here u and v are the small and large components of the wave function of the particle, W is its total energy, $V(r)$ is the potential, and l is a quantum number which may be any positive or negative integer, including zero, except -1. The Schrödinger radial wave equation arises in the corresponding discussion of a Schrödinger particle, and is directly connected with the Dirac radial equations in the following way. If the small component u is eliminated from the Dirac equations, the result is

$$v''+\frac{V'(r)}{W-V(r)+mc^2}v'+\left[\frac{p^2(r)}{\hbar^2}-\frac{l(l+1)}{r^2}-\frac{V'(r)}{W-V(r)+mc^2}\frac{l+1}{r}\right]v=0,\tag{2}$$

where $p(r)$ is the local relativistic momentum:

$$p^2(r)=c^{-2}[W-V(r)]^2-m^2c^2.\tag{3}$$

In the nonrelativistic limit, which is obtained formally by taking the limit as c becomes indefinitely large, Eq. (2) reduces to the Schrödinger radial wave equation

$$v''+\left[\frac{p^2(r)}{\hbar^2}-\frac{l(l+1)}{r^2}\right]v=0,\tag{4}$$

where now

$$p^2(r)=2m[E-V(r)],\tag{5}$$

and E is the surplus over the rest energy. In taking this nonrelativistic limit the range of the quantum number l is unchanged. However, in discussing solutions of Eq. (4) the negative integer values of l may be disregarded since the equation is unchanged when l is replaced by $-(l+1)$. This corresponds physically to the twofold spin degeneracy in the nonrelativistic limit.

The WKB method is useful in approximating solutions of the one-dimensional Schrödinger equation,

$$v''+\hbar^{-2}p^2(x)v=0.\tag{6}$$

The derivation of the basic formulas[1,2] may be summarized as follows:

(a) Substitute $v=\exp[i\hbar^{-1}\beta(x)]$. This transforms Eq. (6) into

$$\beta'^2-i\hbar\beta''-p^2=0.\tag{7}$$

(b) Suppose $\hbar$ is small. Write

$$\beta(x)=\beta_0(x)+\hbar\beta_1(x)+\hbar^2\beta_2(x)+\cdots,\tag{8}$$

and solve only as far as the first two terms. The result is

$$v\cong p^{-\frac{1}{2}}\exp\left[\pm i\hbar^{-1}\int p(x)dx\right].\tag{9}$$

[1] Leonard I. Schiff, *Quantum Mechanics* (McGraw-Hill Book Company, Inc., New York, 1949), first edition, p. 178.
[2] Edwin C. Kemble, *The Fundamental Principles of Quantum Mechanics* (McGraw-Hill Book Company, Inc., New York, 1937), first edition, p. 90.

(c) Derive connection formulas between the approximate solutions in regions where $p(x)$ is real and the approximate solutions in regions where $p(x)$ is pure imaginary.

The customary way of applying the WKB approximation to the Schrödinger radial wave equation is to introduce

$$\frac{p_{\text{eff}}^2(r)}{\hbar^2}=\frac{p^2(r)}{\hbar^2}-\frac{l(l+1)}{r^2}, \tag{10}$$

so that, in terms of this effective momentum, the radial problem becomes similar to the one-dimensional problem and formula (9) may be applied directly. This technique gives useful results if one also replaces $l(l+1)$ by $(l+\frac{1}{2})^2$.[3] This substitution has been justified by Langer.[4] A generalization of the WKB method to the Dirac radial wave equations (1) has been given by Bessey and Uhlenbeck.[5] By analogy with the WKB treatment of the one-dimensional Dirac problem as developed by Pauli,[6] they introduced the expansions:

$$\begin{aligned}u&=[A_0(r)+\hbar A_1(r)+\cdots]\exp[i\hbar^{-1}\gamma(r)],\\ v&=[B_0(r)+\hbar B_1(r)+\cdots]\exp[i\hbar^{-1}\gamma(r)],\end{aligned} \tag{11}$$

and solved for small $\hbar$ to the zero order only. During the process of solving they treated $(l+1)$ formally as if it were of the order of $\hbar^{-1}$. This is an *ad hoc* assumption, though it is compatible with the idea of an approximation valid in the range of classical mechanics where $l\hbar$ is of the order of 1 erg-sec. The comparable assumption made in the usual treatment of the Schrödinger radial wave equation is that $(l+\frac{1}{2})$ is of the order of $\hbar^{-1}$—this assumption is equivalent to introducing the effective momentum and replacing $l(l+1)$ by $(l+\frac{1}{2})^2$as outlined above. Bessey and Uhlenbeck obtain the results:

$$\begin{aligned}u&\cong-\frac{|l+1|}{l+1}\left(\frac{\psi}{\delta'}\right)^{\frac{1}{2}}\\ &\quad\times\exp\left\{\pm i\left[\delta-\frac{l+1}{2}\int_{r_1}^{r}\left(1+\frac{\rho\psi'}{\psi}\right)\frac{d\rho}{\rho^2\delta'}\right]\right\},\\ v&\cong\left(\frac{\phi}{\delta'}\right)^{\frac{1}{2}}\exp\left\{\pm i\left[\delta+\frac{l+1}{2}\int_{r_1}^{r}\left(1+\frac{\rho\phi'}{\phi}\right)\frac{d\rho}{\rho^2\delta'}\right]\right\},\end{aligned} \tag{12}$$

where

$$\begin{aligned}\phi(r)&=W-V(r)+mc^2,\\ \psi(r)&=W-V(r)-mc^2,\\ \delta(r)&=\int_{r_1}^{r}\left[\frac{\psi\phi}{\hbar^2c^2}-\frac{(l+1)^2}{\rho^2}\right]^{\frac{1}{2}}d\rho\\ &=\int_{r_1}^{r}[\hbar^{-2}\rho^2p^2(\rho)-(l+1)^2]^{\frac{1}{2}}\frac{d\rho}{\rho},\end{aligned} \tag{13}$$

and r_1 is a root of $[\hbar^{-2}r^2p^2(r)-(l+1)^2]$. Zwann's method[7] yields the usual connection formulas between the approximate solutions on the opposite sides of r_1. In the case of a bound particle and when there are only two roots of $[\hbar^{-2}r^2p^2-(l+1)^2]$, the eigenvalue condition may be written in the form

$$\begin{aligned}&\oint[\hbar^{-2}\rho^2p^2-(l+1)^2]^{\frac{1}{2}}\frac{d\rho}{\rho}\\ &\quad+\frac{l+1}{2}\oint\frac{1+\rho\phi'/\phi}{[\hbar^{-2}\rho^2p^2-(l+1)^2]^{\frac{1}{2}}}\frac{d\rho}{\rho}\\ &\quad=(n_r+\tfrac{1}{2})2\pi,\quad n_r=0,\,1,\,2,\,\cdots,\end{aligned} \tag{14}$$

where the integration is to be taken in the complex plane around the branch cut joining the zeros of the radicand. One finds this condition in the usual way by matching, in the region where $[\hbar^{-2}r^2p^2-(l+1)^2]>0$, those two approximate solutions which connect with integrable approximate solutions in the regions where $[\hbar^{-2}r^2p^2-(l+1)^2]<0$. The Bessey-Uhlenbeck approximation gives good results in several respects, especially in the region far from the origin.

In the present paper a WKB-type treatment of the radial equations will be presented which is different from the treatments outlined above. The first motivation for seeking this different approximation is a difficulty which arises in applying the Bessey-Uhlenbeck approximation to the bound states of the hydrogen-like atom. If one applies the eigenvalue condition (14) to the case where $V(r)=-Ze^2/r$, the result is the Sommerfeld-Dirac fine structure formula:

$$\begin{aligned}W=mc^2\Bigg\{1+\alpha^2Z^2\Bigg[n_r+\frac{1}{2}-\frac{1}{2}\frac{l+1}{|l+1|}\\ +[(l+1)^2-\alpha^2Z^2]^{-\frac{1}{2}}\Bigg]^2\Bigg\}^{-\frac{1}{2}},\end{aligned} \tag{15}$$

where $\alpha=e^2/\hbar c$. However, when $n_r=0$ and $l+1>0$, one sees that

$$W=mc^2[1-\alpha^2Z^2(l+1)^{-2}]^{\frac{1}{2}}, \tag{16}$$

and consequently

$$\hbar^{-2}r^2p^2-(l+1)^2=-\left[\frac{\alpha Z}{l+1}\frac{mcr}{\hbar}+\frac{(l+1)W}{mc^2}\right]^2, \tag{17}$$

so that for these levels there is no region where $[\hbar^{-2}r^2p^2-(l+1)^2]>0$ and the derivation of the eigenvalue condition (14) is not valid. The second motivation for looking for another approximation is that the above three approximation techniques give nonuniform results, in spite of the simple connections between the

[3] L. A. Young and G. E. Uhlenbeck, Phys. Rev. **36**, 1154 (1930).
[4] R. E. Langer, Phys. Rev. **51**, 669 (1937).
[5] R. J. Bessey, thesis, University of Michigan (1942) (unpublished).
[6] W. Pauli, Helv. Phys. Acta **5**, 179 (1932).
[7] See reference 2, p. 95.

original equations. That is, since

$$\begin{bmatrix}\text{Dirac}\\ \text{radial}\\ \text{Eq. (2)}\end{bmatrix}\xrightarrow[c\to\infty]{}\begin{bmatrix}\text{Schrödinger}\\ \text{radial}\\ \text{Eq. (4)}\end{bmatrix}\xrightarrow[l(l+1)=0]{}\begin{bmatrix}\text{Schrödinger}\\ \text{one-dimensional}\\ \text{Eq. (6)}\end{bmatrix},$$

one would expect an analogous connection between the approximate solutions. No such connection exists between the approximations outlined above.

The central idea in the approximation discussed below is to use, in the first step of the derivation, rather than always the exponential function, the function which arises in solving the problem of the free particle. In the one-dimensional case this is still the exponential function, but in the radial problems the exponential is replaced by Bessel functions of half-integer order. This permits the approximate solutions to be identical with the exact solutions in the case where the potential field is zero, and so one is assured that the approximation will be increasingly good with higher energy. The second step in developing the approximation, analogous to step (b) in the one-dimensional derivation, is to make an expansion for small $\hbar$. The quantity $(l+1)$ is treated formally as if it were of order $\hbar^{-1}$ and, perhaps as a consequence, the Dirac radial approximation becomes similar to the approximation of Bessey and Uhlenbeck in the region near the origin and in the region far from the origin. An interesting feature of the approximation is that connection formulas are not required in discussing the radial equations so that the analog of step (c) does not arise. The difficulty with the bound states in a Coulomb field may be resolved. The eigenvalue condition (14) arises from a comparison of asymptotic developments in such a way that one would expect the approximate eigenvalues to be close to the exact eigenvalues. The derivations for the Schrödinger and Dirac radial equations are strictly parallel to each other, and there is also a weaker parallel with the one-dimensional derivation. The approximation gives especially poor results near the turning points. In Sec. II the details of the method will be given for the Schrödinger radial equation. In Sec. III the parallel development for the Dirac radial problem is outlined. Section IV contains a general discussion and details of the accuracy of the WKB method in evaluating the function $F(Z, W)$ which occurs in the theory of β-decay.

II. TREATMENT OF THE SCHRÖDINGER RADIAL EQUATION

The unnormalized free-particle solutions of the Schrödinger radial wave equation (4) are

$$v(V=0)=\left(\frac{pr}{\hbar}\right)^{\frac{1}{2}}J_{\pm(l+\frac{1}{2})}\left(\frac{pr}{\hbar}\right), \tag{18}$$

where J indicates the usual Bessel function. Therefore, as the first step in developing an approximation, one may make the substitution

$$v=T(r)J_{\pm(l+\frac{1}{2})}(S(r)), \tag{19}$$

where $T(r)$ and $S(r)$ are functions which have yet to be chosen. (The same $T(r)$ and $S(r)$ will be used for both Bessel functions so that, by choosing the proper linear combinations, approximate solutions based on the Hankel functions may be obtained. These are more appropriate in problems involving incoming and outgoing waves.) By differentiating and applying the differential equation which the Bessel function satisfies, it is found that

$$v''+\left[\frac{p^2}{\hbar^2}-\frac{l(l+1)}{r^2}\right]v=\left[2\frac{T'}{T}+\frac{S''}{S'}-\frac{S'}{S}\right]TS'J'(S)+\left[\frac{T''}{T}-S'^2+(l+\tfrac{1}{2})^2\frac{S'^2}{S^2}+\frac{p^2}{\hbar^2}-\frac{l(l+1)}{r^2}\right]v. \tag{20}$$

To make matters parallel to the one-dimensional derivation, the first term on the right should disappear. This can be arranged by making the choice

$$T=(S/S')^{\frac{1}{2}}, \tag{21}$$

and then the problem reduces to finding a solution of the equation

$$\frac{T''}{T}-S'^2+(l+\tfrac{1}{2})^2\frac{S'^2}{S^2}+\frac{p^2}{\hbar^2}-\frac{l(l+1)}{r^2}=0. \tag{22}$$

The derivation this far corresponds to part (a) of the one-dimensional WKB derivation and Eq. (22) is analogous to Eq. (7).

The next step is to find a solution of Eq. (22) for small $\hbar$. As suggested by the one-dimensional derivation, it will be assumed that S is of the order of $\hbar^{-1}$. Also $(l+1)$ will be treated formally as if it were of order $\hbar^{-1}$. Grouping the terms of orders $\hbar^{-2}$ and $\hbar^{-1}$ and discarding the rest, one obtains

$$\left[S'^2-(l+1)^2\frac{S'^2}{S^2}\right]+(l+1)\frac{S'^2}{S^2}=\left[\frac{p^2}{\hbar^2}-\frac{(l+1)^2}{r^2}\right]+\frac{l+1}{r^2}, \tag{23}$$

and on taking the square root and integrating the result is

$$\int_{S_0}^{S}[\sigma^2-(l+1)^2]^{\frac{1}{2}}\frac{d\sigma}{\sigma}+\frac{l+1}{2}\int_{S_0}^{S}\frac{1}{[\sigma^2-(l+1)^2]^{\frac{1}{2}}}\frac{d\sigma}{\sigma}=\int_{r_0}^{r}[\hbar^{-2}\rho^2p^2-(l+1)^2]^{\frac{1}{2}}\frac{d\rho}{\rho}+\frac{l+1}{2}\int_{r_0}^{r}\frac{1}{[\hbar^{-2}\rho^2p^2-(l+1)^2]^{\frac{1}{2}}}\frac{d\rho}{\rho}. \tag{24}$$

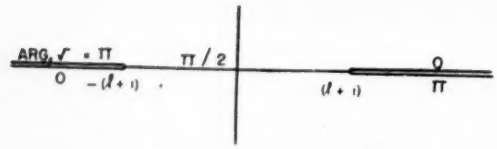

FIG. 1. The σ-plane for $[\sigma^2-(l+1)^2]^{\frac{1}{2}}$.

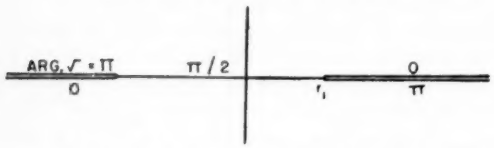

FIG. 2. The ρ-plane for $[\hbar^{-2}\rho^2p^2-(l+1)^2]^{\frac{1}{2}}$ (unbound particle).

FIG. 3. The ρ-plane for $[\hbar^{-2}\rho^2p^2-(l+1)^2]^{\frac{1}{2}}$ (bound particle).

This will be abbreviated to

$$\int_{S_0}^{S} f(\sigma)d\sigma = \int_{r_0}^{r} g(\rho)d\rho. \tag{25}$$

Usually $[\hbar^{-2}r^2p^2-(l+1)^2]$ has two positive roots, r_1 and r_2, when the particle is bound, and one positive, r_1, and one negative root when it is unbound. These are the only cases which will be discussed here. Because of the analogy with the classical problem, the positive roots will be called turning points. Later in the development it is convenient to think of the variables as complex. The branches of the square root functions which will be used are indicated in Figs. 1, 2, and 3.

For an unbound particle, from the similarities of Figs. 1 and 2, one is led to associate $S=(l+1)$ with $r=r_1$. This assignment permits $S(r)$ to be a real function over most of its range, giving then real approximate solutions over that part of its range. (The exact solutions will be real over the whole range since Eq. (4) is real.) This fixes the integration limits in Eq. (25) and determines the function $S(r)$. For an unbound particle then,

$$\psi \cong (S/S')^{\frac{1}{2}}J_{\pm(l+\frac{1}{2})}(S), \tag{26}$$

where S is defined implicitly by

$$\int_{l+1}^{S} f(\sigma)d\sigma = \int_{r_1}^{r} g(\rho)d\rho. \tag{27}$$

The Bessel function of positive index gives the approximate solution which is regular at the origin and the other gives the approximate solution which becomes infinite at the origin. As given by Eq. (27) it is seen that $S(r)$ ranges between zero and infinity as r ranges between zero and infinity. Connection formulas across the branch point r_1 are not required. However in general there is a range of r near the turning point where Eq. (27) has no real solution S for real r. This is easily seen by making a qualitative plot of the two integrals in Eq. (27), as shown in Fig. 4. From this it is seen that, unless fortuitously the heights of the two maxima are the same, there will be a region where no real function $S(r)$ exists. In many problems this difficulty will be confined to the neighborhood of the turning points and everywhere else Eq. (27) will define a real $S(r)$.

For a bound particle, from a comparison of Figs. 1 and 3, it is clear that the problem must be divided into two parts in order to obtain a real function $S(r)$. Accordingly for a bound particle one will write

$$\psi \cong c_A(S_A/S_A')^{\frac{1}{2}}J_{l+\frac{1}{2}}(S_A), \quad \text{when} \quad 0<r<r_2, \tag{28}$$

$$\psi \cong c_B(S_B/S_B')^{\frac{1}{2}}J_{l+\frac{1}{2}}(S_B), \quad \text{when} \quad r_1<r<\infty, \tag{29}$$

where c_A, c_B are constants and S_A, S_B are defined by

$$\int_{l+1}^{S_A} f(\sigma)d\sigma = \int_{r_1}^{r} g(\rho)d\rho, \tag{30}$$

$$\int_{-(l+1)}^{S_B} f(\sigma)d\sigma = \int_{r_2}^{r} g(\rho)d\rho. \tag{31}$$

With these assignments one may verify that the approximate wave function will be zero at the origin and at infinity. (As r becomes large, S_B becomes small and remains negative.) The eigenvalue condition will result by matching these two representations in a region where both are valid. It will be supposed that such a region exists in the first quadrant of the complex plane, far from the real axis. Performing the σ-integration, it is easily seen that in this region $|S(r)|$ will be large and that

$$S_A \cong (l+\tfrac{1}{2})\frac{\pi}{2} + \int_{r_1}^{r} g(\rho)d\rho, \tag{32}$$

$$S_B \cong -(l+\tfrac{1}{2})\frac{\pi}{2} + \int_{r_2}^{r} g(\rho)d\rho. \tag{33}$$

For large $|S(r)|$ the asymptotic form of the Bessel function will also be valid:

$$\psi \cong c(2/\pi)^{\frac{1}{2}}(1/S')^{\frac{1}{2}}\cos\left[S-(l+\tfrac{1}{2})\frac{\pi}{2}-\frac{\pi}{4}\right]. \tag{34}$$

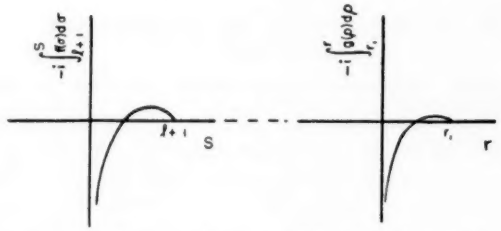

FIG. 4. Discussion of the function $S(r)$ when the turning points are separate.

From this it is seen immediately that the eigenvalue condition is

$$\int_{r_1}^{r_2} g(\rho)d\rho=(n_r+\tfrac{1}{2})\pi, \quad n_r=0, 1, 2, \cdots, \tag{35}$$

while the constants are related by

$$c_A/c_B=(-1)^{n_r+l+1}. \tag{36}$$

The procedure of the preceding paragraph does not apply in the special case when the turning points r_1 and r_2 coincide, for then the ρ-integrals diverge at the lower limits. A discussion of the case where $[\hbar^{-2}r^2p^2-(l+1)^2]^{\frac{1}{2}}$ has a double zero at a point r_{12} may be made as follows. Evidently one may write approximate solutions for the regions $r<r_{12}$ and $r_{12}<r$ analogous to Eqs. (28) and (29) above—the only difficulty is in deciding on the integration constants to be used in formulas (30) and (31). Again making a qualitative plot of the integrals involved for the region of small r (Fig. 5) one is prompted to choose the integration constant so that the two maxima correspond, as shown. Specifically this means choosing the root of $f(S)$ to correspond to the root of $g(r)$. Let r_3 be the point which then corresponds to $S_A=(l+1)$. Also let r_4 be the point (not yet specified) which corresponds to $S_B=-(l+1)$ in the other part of the approximate solution. Just as in the preceding paragraph, the condition for a match of the two functions is

$$\int_{r_3}^{r_4} g(\rho)d\rho=(n_r+\tfrac{1}{2})\pi, \quad n_r=0, 1, 2, \cdots; \tag{37}$$

but now this condition has two aspects, for the integral will in general be a complex number. The real axis will be chosen for an integration path except for a small half-circle over r_{12}. Then evidently the integration on the real axis implies that

$$\mathrm{P}\int_{r_3}^{r_4} ig(\rho)d\rho=0, \tag{38}$$

where the integration is to be taken entirely along the real axis, taking the Cauchy principal value of the integration across the pole of $g(\rho)$ at r_{12}. This condition locates r_4 unambiguously. The other aspect of the matching condition is that the integration over the upper half of the pole be $(n_r+\frac{1}{2})\pi$. Having assumed above that the radicand had only a double zero, the pole will be of order 1 and the eigenvalue condition may be written in the form

$$\oint g(\rho)d\rho=(n_r+\tfrac{1}{2})2\pi, \quad n_r=0, 1, 2\cdots, \tag{39}$$

where the integration is to be taken clockwise around the singularity. It is seen immediately that Eq. (35) may also be written in this form, taking the integration

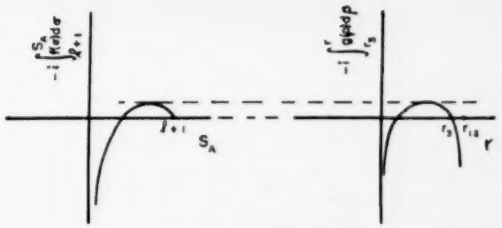

FIG. 5. Discussion of the function $S(r)$ when the turning points coincide.

entirely around the branch cut. In this way the two eigenvalue conditions may be put on the same footing.

III. TREATMENT OF THE DIRAC RADIAL EQUATION

The Dirac radial equation may be treated in the same way as the Schrödinger radial equation above. The developments are so similar that only the major results will be listed here. Using again the abbreviations

$$\phi=W-V+mc^2, \quad \psi=W-V-mc^2, \tag{40}$$

Eq. (2) may be written as

$$v''-\frac{\phi'}{\phi}v'+\left[\frac{p^2}{\hbar^2}-\frac{l(l+1)}{r^2}+\frac{\phi'}{\phi}\frac{l+1}{r}\right]v=0. \tag{41}$$

The free particle solutions of this are

$$v(V=0)=(pr/\hbar)^{\frac{1}{2}}J_{\pm(l+\frac{1}{2})}(pr/\hbar). \tag{42}$$

This leads to the approximate solutions

$$v\cong(\phi S/S')^{\frac{1}{2}}J_{\pm(l+\frac{1}{2})}(S), \tag{43}$$

where S is defined implicitly by

$$\int_{s_0}^{S}[\sigma^2-(l+1)^2]^{\frac{1}{2}}\frac{d\sigma}{\sigma}+\frac{l+1}{2}\int_{s_0}^{S}\frac{1}{[\sigma^2-(l+1)^2]^{\frac{1}{2}}}\frac{d\sigma}{\sigma}$$
$$=\int_{r_0}^{r}[\hbar^{-2}\rho^2p^2-(l+1)^2]^{\frac{1}{2}}\frac{d\rho}{\rho}$$
$$+\frac{l+1}{2}\int_{r_0}^{r}\frac{1+\rho\phi'/\phi}{[\hbar^{-2}\rho^2p^2-(l+1)^2]^{\frac{1}{2}}}\frac{d\rho}{\rho}, \tag{44}$$

which will be abbreviated to

$$\int_{s_0}^{S}f(\sigma)d\sigma=\int_{r_0}^{r}k(\rho)d\rho. \tag{45}$$

The integration constants may be chosen in exactly the same way as before. Again there will be a region near every turning point where no real function $S(r)$ exists. The eigenvalue condition which is obtained is

$$\oint k(\rho)d\rho=(n_r+\tfrac{1}{2})2\pi, \quad n_r=0, 1, 2, \cdots, \tag{46}$$

the same as Eq. (14). This of course gives only the large component v of the wave function. The corresponding approximation for the small component, except for a constant factor, may be inferred from the symmetry of Eqs. (1). The appropriate factor may also be found if it may be assumed that far from the turning points the potential becomes zero, since in such a region the approximate solutions satisfy Eqs. (1) exactly. The complete approximate solution, for an unbound particle for example, is

$$\begin{aligned} u &\cong \mp(\psi R/R')^{\frac{1}{2}} J_{\pm(l+\frac{1}{2})}(R), \\ v &\cong (\phi S/S')^{\frac{1}{2}} J_{\pm(l+\frac{1}{2})}(S), \end{aligned} \tag{47}$$

where R is defined by

$$\begin{aligned} \int_{|l+1|}^{R} [\sigma^2-(l+1)^2]^{\frac{1}{2}} \frac{d\sigma}{\sigma} - \frac{l+1}{2} \int_{|l+1|}^{R} \frac{1}{[\sigma^2-(l+1)^2]^{\frac{1}{2}}} \frac{d\sigma}{\sigma} \\ = \int_{r_1}^{r} [\hbar^{-2}\rho^2 p^2-(l+1)^2]^{\frac{1}{2}} \frac{d\rho}{\rho} \\ - \frac{l+1}{2} \int_{r_1}^{r} \frac{1+\rho\psi'/\psi}{[\hbar^{-2}\rho^2 p^2-(l+1)^2]^{\frac{1}{2}}} \frac{d\rho}{\rho}, \end{aligned} \tag{48}$$

S is defined by

$$\int_{|l+1|}^{S} f(\sigma) d\sigma = \int_{r_1}^{r} k(\rho) d\rho, \tag{49}$$

and r_1 is the positive root of $[\hbar^{-2}r^2p^2-(l+1)^2]$. In verifying that approximate solutions of this type satisfy Eqs. (1) exactly in a region of zero potential far from the turning points, one uses the asymptotic forms of the Bessel functions and approximate expressions like Eq. (32) for S and R and also makes use of the fact that

$$\begin{aligned} \frac{l+1}{2} \int_{r_1}^{\infty} \frac{2+\rho\phi'/\phi+\rho\psi'/\psi}{[\hbar^{-2}\rho^2 p^2-(l+1)^2]^{\frac{1}{2}}} \frac{d\rho}{\rho} \\ = \frac{l+1}{|l+1|} \arctan\left(\frac{\hbar^{-2}\rho^2 p^2-(l+1)^2}{(l+1)^2}\right)^{\frac{1}{2}} \Bigg|_{r_1}^{\infty} \\ = \frac{l+1}{|l+1|} \frac{\pi}{2}. \end{aligned} \tag{50}$$

IV. DISCUSSION

Since ϕ becomes constant in the nonrelativistic limit, one sees immediately that the Schrödinger radial approximation is the nonrelativistic limit of the Dirac radial approximation. Also for the value $(l+1)=0$, the approximate Schrödinger radial wave function, as given by Eqs. (19), (21), and (24), becomes

$$v \cong (2/\pi)^{\frac{1}{2}} (1/S')^{\frac{1}{2}} \begin{matrix} \cos \\ \sin \end{matrix} S, \tag{51}$$

$$\int_{S_0}^{S} d\sigma = \frac{1}{\hbar} \int_{r_0}^{r} p(\rho) d\rho, \tag{52}$$

and this may be identified with the approximate one-dimensional wave function (9). It is interesting to note that this correspondence occurs for $l=-1$, the only integer which does not arise in the radial problem. In finding Eq. (52) from Eq. (24) the secondary terms drop out. From this it is seen that these radial WKB approximations are one order higher in $\hbar$ than the familiar one-dimensional WKB approximation. Also when $(l+1)=0$ is introduced into Eq. (24) the branch points in the σ-integrand drop out, but not those in the ρ-integrand. This is the qualitative difference between the one-dimensional and the radial approximations and indicates why connection formulas are required in one case but not in the other.

One may perhaps expect the approximation to be increasingly good far from the turning points. Since the eigenvalue conditions result from matching the wave functions far from the turning points, it is indicated that this approximation will be especially good for the eigenvalues themselves. This conjecture is reinforced by the fact that the eigenvalue condition is independent of the choice of the integration constants in Eqs. (30) and (31). (Of course the points which correspond to $S_A=(l+1)$ and $S_B=-(l+1)$ will have to fulfill a condition like Eq. (38).)

It is easily seen that for a free particle the above approximations to the radial wave functions become identical with the exact wave functions. From this one may expect the approximation to improve with increasing energy or $|l|$, for then the problem approaches the free particle problem. One may also easily verify that the approximations give the correct r-dependences at the origin both when the potential is regular there and when it has a simple pole. Far from the turning points the above approximations to the Dirac wave functions become similar to the approximations of Bessey and Uhlenbeck; the two predict the same exponential factors, but with slightly different coefficients.

In a subsequent paper it is planned to use the WKB approximation to investigate some aspects of Fermi's theory of β-decay. In this theory the following function is of primary interest:

$$F(Z, W) = \left[\frac{g_0^2+f_{-2}^2}{p_\infty^2(1+s)}\right]_\rho. \tag{53}$$

Here units have been chosen so that $m=c=\hbar=1$; $g_0=r^{-1}v(l=0)$ and $f_{-2}=r^{-1}u(l=-2)$ for energy W in the continuum, normalized to one particle in a sphere of large radius, with the radius subsequently put equal

to one; $p_\infty=(W^2-1)^{\frac{1}{2}}$ and $s=(1-\alpha^2Z^2)^{\frac{1}{2}}$. The subscript ρ indicates that the wave functions are to be evaluated at the nuclear radius ρ and that only the first term in an expansion for small ρ is to be retained. Before $F(Z, W)$ is known the potential $V(r)$ to be used in calculating the radial wave functions must be assigned. Ordinarily the Coulomb potential $V=-\alpha Z/r$ is used, but in discussing some of the finer points in the theory slightly different potentials arise. In treating these finer points it is appropriate to use the WKB method because it gives approximate wave functions in an arbitrary potential. However, since the error in the approximation to the wave functions is not known, one must justify using the WKB approximation by comparing it with the exact result in a typical case. This has been done, using the Coulomb potential as the typical case; an outline of the results is given below. The approximation based on the Bessel functions does not give good results. This might have been anticipated because $F(Z, W)$ involves wave functions of low l in the region where $V(r)$ has a pole, where they will be qualitatively different from the free-particle wave functions. However, the Bessey-Uhlenbeck approximation, which may be applied here because it only gives difficulty in the bound states, reproduces $F(Z, W)$ very well. The reason for this is not understood, especially since the Bessey-Uhlenbeck approximation gives poor results for the first term in an expansion about the origin of certain of the low-l free-particle functions, while, of course, the approximation based on the Bessel functions gives the exact answer. Some of the details of the comparison between the exact and approximate calculations of $F(Z, W)$ for the case of a Coulomb field $V=-\alpha Z/r$ are as follows.

The exact calculation gives the result[8]

$$F_{\text{exact}}(Z, W) = 4(2p_\infty\rho)^{2s-2}e^{\pi\alpha ZW/p_\infty}\frac{|\Gamma(s+i\alpha ZW/p_\infty)|^2}{\Gamma^2(2s+1)}. \quad (54)$$

The Bessey-Uhlenbeck approximation gives the result

$$F_{\text{WKB}}(Z, W)=\frac{4(2p_\infty\rho)^{2s-2}e^{\pi\alpha ZW/p_\infty}}{(2s)^{4s+1}}\left[1+\left(\frac{\alpha Z}{p_\infty}\right)^2\right]^{s-\frac{1}{2}} \times\exp\left[2s-\frac{2\alpha ZW}{p_\infty}\sin^{-1}\frac{\alpha ZW}{(p_\infty^2+\alpha^2Z^2)^{\frac{1}{2}}}\right]. \quad (55)$$

Since

$$\frac{F_{\text{WKB}}(Z, W)}{F_{\text{WKB}}(-Z, W)}=e^{2\pi\alpha ZW/p_\infty}=\frac{F_{\text{exact}}(Z, W)}{F_{\text{exact}}(-Z, W)}, \quad (56)$$

only a comparison for $Z>0$ is necessary to decide on the relative merit of the approximation. Such a comparison is given in Fig. 6 for values of Z and W of interest in β-theory. It is seen that for $W>1.1$, which corresponds to an electron kinetic energy of more than 0.05 Mev, the error introduced by using the WKB approximation is less than eight percent.

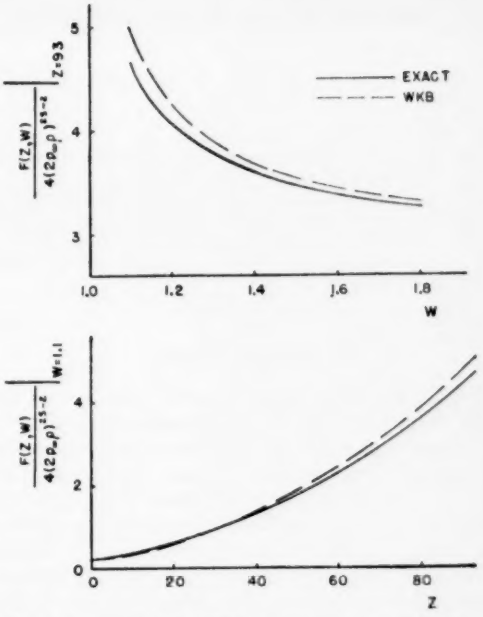

FIG. 6. Accuracy of the WKB approximation to $F(Z, W)$.

In discussing methods of evaluating $F_{\text{exact}}(Z, W)$ Hall[9] pointed out that the Stirling approximation for $\Gamma(z)$,

$$\Gamma(z)\cong(2\pi)^{\frac{1}{2}}e^{-z}z^{z-\frac{1}{2}}, \quad (57)$$

though valid only for large $|z|$, is still fairly good for $|z|\sim1$. If this is used to approximate the gamma-functions in $F_{\text{exact}}(Z, W)$, there results

$$F_{\text{exact}}(Z, W)\cong F_{\text{WKB}}(Z, W)\left[e^2\left(\frac{2s}{2s+1}\right)^{4s+1}\right]. \quad (58)$$

For $92>Z>0$, the factor in the square brackets ranges between 0.96 and 0.98 so the Bessey-Uhlenbeck approximation leads essentially to the Stirling approximation of the exact result. If $F(Z, W)$ is calculated using the approximation based on the Bessel functions, the result is the same as in Eq. (55) except with an added factor of $4e^{-2}\cong0.54$.

It is a pleasure to thank Professor G. E. Uhlenbeck for reading this paper before publication and making several valuable suggestions.

[8] E. J. Konopinski and G. E. Uhlenbeck, Phys. Rev. **60**, 308 (1941).

[9] H. Hall, Phys. Rev. **79**, 745 (1950).

Relative Energy Levels of Some P Shell Nuclei in Intermediate Coupling*†

EDWIN A. CROSBIE‡
University of Pittsburgh, Pittsburgh, Pennsylvania
(Received October 29, 1952)

The relative energy levels of the low states for configurations consisting of 2, 3, 4, 8, 9, and 10 nucleons in the P shell are shown for all values of the spin orbit to interaction energy ratio by means of second-order perturbation calculations in both extreme coupling schemes. The interaction potential is assumed to be a linear combination of ordinary, and space, spin, and charge exchange terms. Coulomb forces are ignored so that the charge quantum number T is a constant of the motion. Comparison is made with the first few excited states of some light nuclei. There is some evidence that the spin orbit energy is relatively more important for N^{14} than for Li^6.

I. INTRODUCTION

THE individual particle model with strong spin orbit coupling[1] has been successful in explaining the "magic numbers" of atomic nuclei and in explaining the ground state angular momenta. The success of this theory is dependent on an increase in the spin orbit parameter with atomic number. For very heavy nuclei the energy levels are described by the jj coupling scheme. For very light nuclei the observed splittings of what appear to be multiplet states indicates that the energy levels may be better explained by Russell-Saunders coupling.

The purpose of the present paper is to show the relative energy levels of light, P-shell nuclei assuming phenomenological central and spin-orbit interactions for all ratios of the spin-orbit to central interaction values. This is done by performing second-order perturbation calculations at the two coupling extremes. Hummel and Inglis[2] have studied the intermediate coupling states of Li^7 using both Wigner and Majorana interactions. The calculations given here differ essentially from those of Hummel and Inglis for this nucleus in the form assumed for the interaction.

TABLE I. Diagonal elements of the interaction energy for the jj states $(3/2)^u(1/2)^v$ for $n=u+v=2, 3, 4, 8, 9, 10$.

u	v	T	J	Energy	u	v	T	J	Energy
2	0	0	3	$5.00K$	8	2	0	1	$79.22K$
		1	0	2.87			1	0	77.35
		0	1	0.33	7	3	0	2	81.42
		1	2	0.33			0	1	80.89
1	1	0	2	5.00			1	2	78.09
		0	1	4.47			1	1	75.42
		1	2	1.67	6	4	0	3	81.42
		1	1	−1.00			1	0	79.29
0	2	0	1	2.80			0	1	76.75
		1	0	0.93			1	2	76.75
3	0	1/2	3/2	$9.51K$	8	1	1/2	1/2	$63.32K$
		1/2	7/2	7.98	7	2	1/2	3/2	66.16
		1/2	5/2	4.74			1/2	5/2	65.22
		3/2	3/2	2.23			1/2	3/2	62.26
		1/2	1/2	0.73			1/2	1/2	60.94
							3/2	3/2	59.65
4	0	0	0	$18.73K$					
		0	2	15.83	8	0	0	0	$49.90K$
		0	4	14.11	7	1	0	2	53.51
		1	3	11.34			0	1	49.89
		1	2	11.20			1	2	48.68
		0	2	7.42			1	1	47.03
		1	1	6.48					
		3	0	4.66					

II. THEORY

A. General

When a number of particles possessing spin and orbital angular momenta are allowed to interact they can in general couple their spins and orbital angular momenta in many ways to form different states. For atomic nuclei the energy differences between states arising from the same configuration can be as large as or larger than the energy differences between states arising from different configurations. Hence, a study of the relative energies of the states belonging to the lowest configuration is not expected to explain all of the low-lying levels for a given nucleus. However, for the nuclei from $A=6$ through $A=14$ one might expect the first few excited states to belong to configurations in which the P shell is partially filled.

The problem is to calculate the average value of the total energy

$$E=\sum_{ik}\tfrac{1}{2}V_{ik}+\sum_i a\mathbf{l}_i\cdot\mathbf{s}_i+\text{constant},$$

for the possible states of the P-shell configurations. In this formula V_{ik} represents the interaction between the ith and kth nucleons, $a\mathbf{l}_i\cdot\mathbf{s}_i$ represents the spin orbit energy of the ith nucleon and the summations are taken over all nucleons in the P shell. In what follows the spin orbit parameter a is treated as a constant for any given nucleus.

V_{ik} is, of course, one of the unsolved problems of nuclear physics. We shall assume

$$V_{ik}=(W+MP_x^{ik}+BP_\sigma^{ik}-HP_\tau^{ik})J(r_{ik}),$$

where P_x^{ik}, P_σ^{ik}, and P_τ^{ik} are the well-known space, spin, and charge exchange operators, respectively. Then

* This paper represents a summary of a thesis submitted in partial fulfillment of the requirements for the degree of Doctor of Philosophy at the University of Pittsburgh.

† Work done in Sarah Mellon Scaife Radiation Laboratory and assisted by the joint program of the U. S. Office of Naval Research and the U. S. Atomic Energy Commission.

‡ Now at Argonne National Laboratory, Chicago, Illinois.

[1] M. Mayer, Phys. Rev. **78**, 16 (1950).

[2] H. Hummel and D. Inglis, Phys. Rev. **81**, 910 (1951).

if $J(r_{ik})$ represents the correct triplet nucleon-nucleon force, the low energy scattering data supplies the conditions:

$$W+M+B+H=1, \quad W+M-B-H=0.6.$$

In the interest of eliminating from the final results all arbitrary constants except the spin orbit to interaction parameter ratio the assumption is made that this form of the interaction should also satisfy the saturation requirements of the nuclear force.[3] With this added condition one obtains the rather uncertain values:

$$W=-0.13, \quad M=0.93, \quad B=0.46, \quad H=-0.26.$$

B. Russell-Saunders Coupling

Assuming the spin orbit parameter to be zero the various states can be labeled by means of the total spin and orbital angular momentum quantum numbers of the protons and neutrons separately. Or, with charge independent forces, the states may be labeled by the total isotopic quantum number T, as well as the total spin S and the total angular momentum L. These constants of the motion are still not sufficient to completely specify the wave functions for all possible states. Wigner[4] has pointed out that, for the ordinary and space exchange terms of the interaction, the space part of the wave function should belong to a definite representation of the permutation group. This representation is described by means of the partition numbers $[\alpha]=[\alpha_1, \alpha_2, \cdots]$. In the presence of the spin and charge exchange terms these wave functions are very good approximations to the true wave functions.[5] (The off-diagonal elements of the interaction energy using these wave functions are multiples of K only—see below.) The labels T, S, L, and $[\alpha]$ are sufficient to specify completely the wave functions for all P-shell states except for the case of six nucleons. We shall use the notation ${}^{ab}A(\alpha)$, where $a=2T+1$, $b=2S+1$, and $A=S, P, D, \cdots$ specifies the total orbital angular momentum.

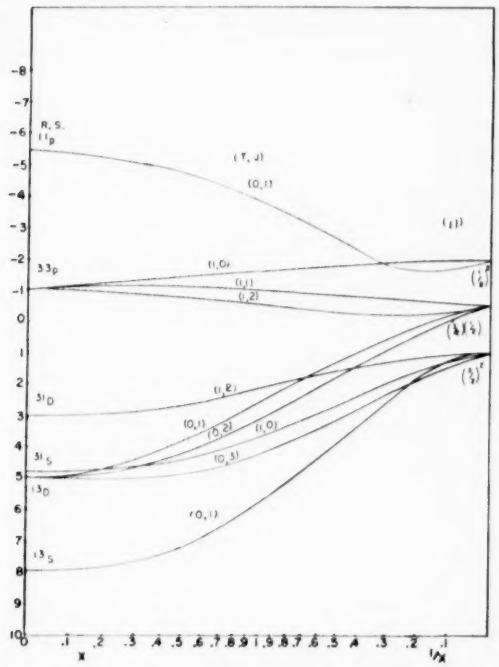

FIG. 1. $\bar{V}/K(1+\chi^2)^{\frac{1}{2}}$ vs $\chi/(1+\chi)$ for $2P$-shell nucleons. $\chi=a/K$.

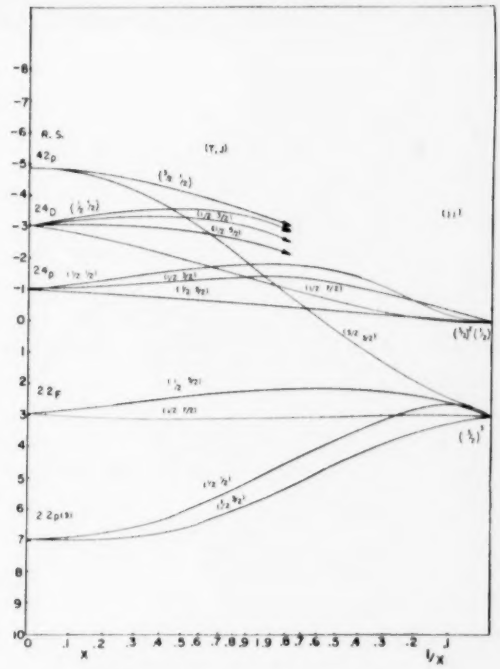

FIG. 2. $(\bar{V}-9K)/K(1+\chi^2)^{\frac{1}{2}}$ vs $\chi/(1+\chi)$ for $3P$-shell nucleons. $\chi=a/2K$.

Feenberg and Phillips[5] have calculated the interaction energies for the "low" partitions for the P-shell nuclei. Writing the three components of the single particle wave functions for P-shell nucleons in the form

$$P_{\pm 1}=(i/\sqrt{2})R(r)(x\pm iy),$$
$$P_0=R(r)z,$$

the average interaction energy appears as a linear combination,

$$\bar{V}=\omega L+\gamma K,$$

[3] L. Rosenfeld, *Nuclear Forces* (Interscience Publishers, New York, 1948), p. 217.

[4] E. Wigner, Phys. Rev. **51**, 106 (1937).

[5] E. Feenberg and M. Phillips, Phys. Rev. **51**, 597 (1937).

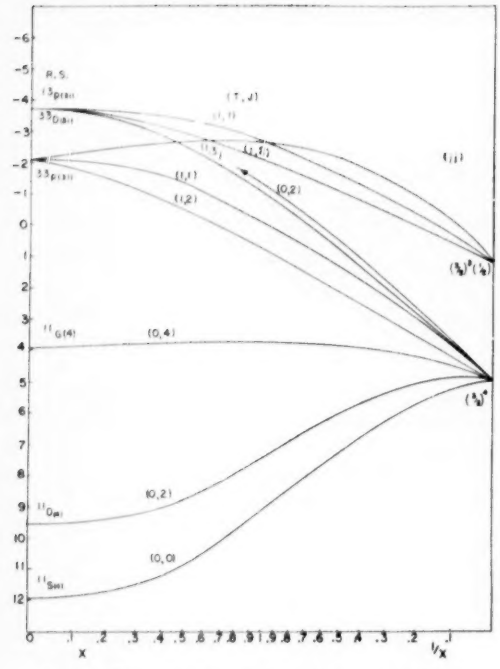

FIG. 3. $(\bar{V}-20K)/K(1+\chi^2)^{\frac{1}{2}}$ *vs* $\chi/(1+\chi)$ for $4P$-shell nucleons. $\chi=2a/5K$.

of the two integrals:

$$L=\int\cdots\int x_1^2x_2^2R^2(r_1)R^2(r_2)J(r_{12})dv_1dv_2,$$

$$K=\int\cdots\int x_1x_2y_1y_2R^2(r_1)R^2(r_2)J(r_{12})dv_1dv_2.$$

L is approximately six times K, so that the relative energy values of the Russell-Saunders multiplets can be obtained in units of K. These multiplets are split by the spin orbit energy into different states of total angular momentum $\mathbf{J}=\mathbf{L}+\mathbf{S}$.

C. *jj* Coupling

In order to take full advantage of the calculations of Feenberg and Phillips, the matrix elements of the interaction energy in the jj coupling extreme can be calculated by expressing the jj wave functions in terms of the Russell-Saunders wave functions. This transformation is readily obtained since the eigenvalues of the spin orbit matrices calculated in the Russell-Saunders limit are known. Hence, it was here necessary only to extend the calculations of Feenberg and Phillips to include all Russell-Saunders states. Table I shows the diagonal elements of the interaction energy for $L=6K$ for all jj states for 2 and 8, and for the low configuration jj states for 3, 4, 6, and 7 nucleons in the P shell.

III. INTERMEDIATE COUPLING AND DISCUSSION OF RESULTS

In order to show the transition from one coupling scheme to the other the usual practice is to plot

$$(\bar{V}-\Delta)/K(1+\chi^2)^{\frac{1}{2}}=(\bar{V}-\Delta)/ca(1+\chi^{-2})^{\frac{1}{2}}\ \ vs\ \ \chi/(1+\chi),$$

where $\chi=ca/K$. c and Δ are arbitrary constants which are chosen so that the total range and relative separation of the states are the same order of magnitude at the two extremes of the plot. For low values of a/K, one effectively plots $(\bar{V}-\Delta)/K$ *vs* χ and for low values of K/a one effectively plots $(\bar{V}-\Delta)/ca$ *vs* $1-\chi^{-1}$.

Figures 1 through 6 show the transition from Russell-Saunders to jj coupling for the low-lying levels for 2, 3, 4, 8, 9, and 10 nucleons in the P shell, respectively. The curves have been interpolated for those regions not obtainable by either second-order perturbation calculation. The Russell-Saunders perturbation calculations break down for an a/K of the order of unity. The total interaction energy for $12-n$ nucleons is the same as that for n nucleons with the addition of a constant term in K and a reversal of the sign of a. One can include the constant term in Δ so that the curves are similar for these two cases in the Russell-Saunders limit.

The first three energy levels indicated in Fig. 1 for $K/a=0.7$ show agreement with the known levels of Li^6 if $K=-1.9$ Mev. This value of K is about twice that obtained by Feenberg and Phillips by actual evaluation

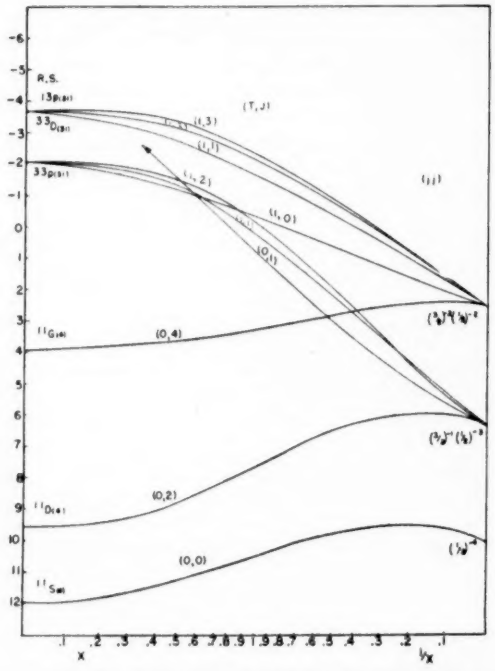

FIG. 4. $(\bar{V}-58.28K)/K(1+\chi^2)^{\frac{1}{2}}$ *vs* $\chi/(1+\chi)$ for $8P$-shell nucleons. $\chi=2a/5K$.

of the integral. The second excited state of Li^6 has $T=1$ and should correspond, in the approximation for which T is a good quantum number to the ground states of He^6 and Be^6.

The lowest states for 10 nucleons in the P shell should be those of N^{14}. The energy of the first excited (2.3-Mev) state of N^{14} is approximately the same as that of the ground states of C^{14} and O^{14} when the Coulomb energy differences are taken into account. Figure 6 shows that a value of a/K at least as large as 3 is needed to explain the first excited state of N as a charge triplet. Approximately correct relative values for the first five energy levels of N^{14} can be obtained for $a/K=5$ and $K=-0.6$ Mev. The curves are not very reliable in this region, however.

It should be noted that the relative spacings of the ^{13}D, ^{13}S, ^{31}D and ^{31}S levels depend only on the conditions,

$$W+M+B+H=1, \quad W+M-B-H=0.6.$$

Any additional conditions on these constants can only change the slopes of the curves in the jj limit. For a different reason the relative positions of the lower two multiplets in Figs. 2 and 5 and the lower three multiplets in Figs. 3 and 4 are independent of the constants W, M, B, and H. This is because the ordinary and space exchange energies are the same, and the spin and charge exchange energies are zero for these multiplets.

The lower levels shown in Fig. 2 should correspond to the energy levels of Li^7 and Be^7. Actually, the total angular momenta of the ground and first excited states of Li^7 are in agreement with the splitting of a ^{22}P level. However, the relatively large separation of the second and third excited states is not explainable by the curves in Fig. 2. In addition to this difficulty, the third excited state appears to have $J=\frac{3}{2}$.[6] It is very probable that this nucleus is better described by the Inglis model.[7] The low-lying levels of Be^8 which should correspond to the curves in Fig. 3 are also probably better described by this model.

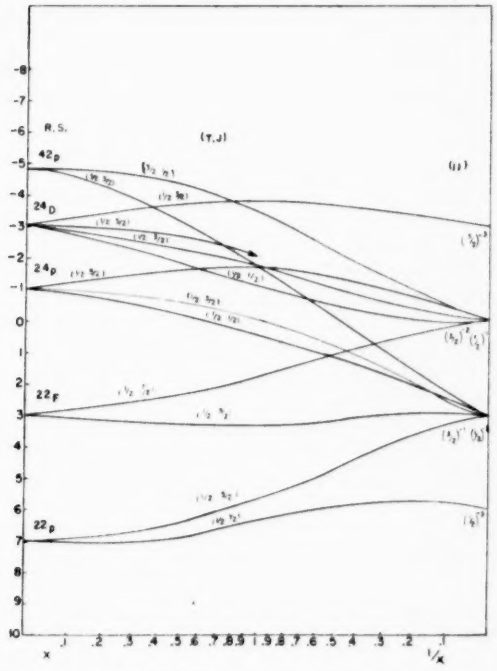

FIG. 5. $(\bar{V}-66.42K)/K(1+\chi^2)^{\frac{1}{2}}$ vs $\chi/(1+\chi)$ for 9P-shell nucleons. $\chi=a/2K$.

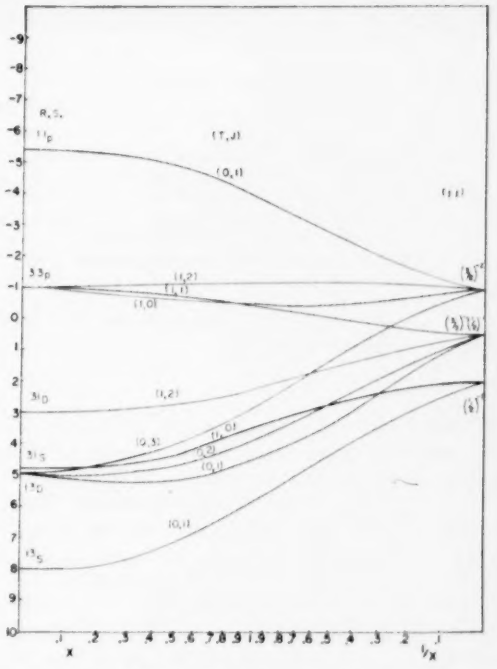

FIG. 6. $(\bar{V}-76.42K)/K(1+\chi^2)^{\frac{1}{2}}$ vs $\chi/(1+\chi)$ for 10P-shell nucleons. $\chi=a/K$.

No very definite conclusions can be obtained from Fig. 4. If one assumes K to be of the order of -1 Mev, then an a/K of the order of 3 gives the correct energy (4.5 Mev) for the first excited state of C^{12}. This places the ^{11}G level at approximately 11 Mev and causes all levels between 4.5 Mev and this value to have odd parity.

The two lower levels of C^{13} can be explained by Fig. 5 for $a/K=2.2$, $K=-1$ Mev. The splitting of the ^{22}F level would then be approximately 2 Mev, corresponding to the energy difference between the 5.4- and 3.9-Mev levels. The 3.1-Mev level of C^{13} has even parity and hence is not given by our calculations.

The author wishes to thank Dr. Philip Stehle for helpful discussions and criticism of this work. The kind interest shown by Dr. A. J. Allen is also much appreciated.

[6] M. Peshkin and A. J. F. Siegert, Phys. Rev. **87**, 735 (1952).
[7] D. Inglis, Phys. Rev. **85**, 492 (1952).

New Fine Structure in Neutral Oxygen*

LEE W. PARKER AND JOHN R. HOLMES
University of Southern California, Los Angeles, California

(Received December 19, 1952)

Untabulated fine structure in O I has been resolved in the triplet multiplets λ8446($3s\,^3S_1-3p\,^3P_{210}$), λ2884($3p\,^3P_{21}-3d'\,^3P_2$), and λ4368 ($3s\,^3S_1-4p\,^3P_{210}$). Interferometer patterns of these lines were analyzed to obtain splittings and relative intensities. Listed as a doublet, λ8446 has three components whose relative intensities allowed establishment of the $3p\,^3P_{210}$ anomalous splitting as follows: $J=1$ lies 0.559(±0.003) cm^{-1} below $J=2$, and $J=0$ lies 0.158(±0.002) cm^{-1} above $J=2$, in agreement with Edlén. λ2884, heretofore found single, has two components, separated by 0.558(±0.002) cm^{-1}. Two components of λ4368, previously considered single, were resolved and found to have a separation of 0.300(±0.001) cm^{-1}, the weaker component having the shorter wavelength. From the relative intensities it is deduced that $J=0$ lies above the degenerate $J=2$, 1 level of the state $4p\,^3P_{210}$, which, like $3p\,^3P_{210}$, is perturbed by an unobserved state in the displaced (^3D) system.

THERE are many levels of O I whose spin-orbit splittings are so small that the associated multiplet lines have remained unresolved or only partially resolved.[1] During a recent survey of isotope shift in the O I spectrum[2] new fine structure was uncovered in λλ8446, 4368, and 2884 with the use of a Fabry-Perot interferometer crossed with a large prism spectrograph. The source was a helium (2–5 mm Hg)—oxygen (about 0.1 mm Hg) mixture excited by a 10-Mc oscillator and cooled with liquid nitrogen. Plate calibrations were made for each of the three multiplets. Silvered interferometer plates were used for λ8446 and λ4368, and aluminized plates for λ2884. The density contours of the interferometer patterns were reproduced by a Zeiss microphotometer connected to a Speedomax Leeds and Northrup recorder. The fine structure splittings were determined by measuring the relative positions of pattern maxima.

λ8446:[3] Two spacers, 5 mm and 6 mm, were used to obtain interferometer patterns which show all three fine structure components clearly separated. This triplet was very strong. The background of the I-N plate used was quite clean, as Fig. 1 indicates. Because of the overlapping wings of the two strongest components, the weakest is spuriously shifted toward the nearer of its neighbors, i.e., toward the second strongest component in the 6-mm pattern. The 5-mm spacer, on the other hand, shifts the weakest component toward the strongest one. Therefore, the value for the displacement of the weakest component from the strongest, given in Table I as $^3P_2-{}^3P_0$, was obtained as a weighted average of the values obtained from the 5-mm and 6-mm traces.

λ2884: A 4-mm spacer placed the weaker component of this doublet almost exactly midway between orders. About 30 minutes were required for an exposure on a II-O plate. Molecular band background was present.

λ4368: The strength of this doublet (incompletely resolved triplet) was such that about 90 seconds were required for an exposure on a II-O plate.

RESULTS

Table I shows the splittings and relative intensities for the three transitions studied. The figures in parentheses are probable errors. Ten orders were used to obtain data for λ8446, twelve for λ2884, and twelve for λ4368. Relative intensities within a multiplet were obtained by drawing a smooth curve through each set of peaks and obtaining the average of several determinations of relative intensities in different places along the nearly flat central portions of these curves.[4] The heights, converted of course to intensities by means of the calibration, were taken with respect to the back-

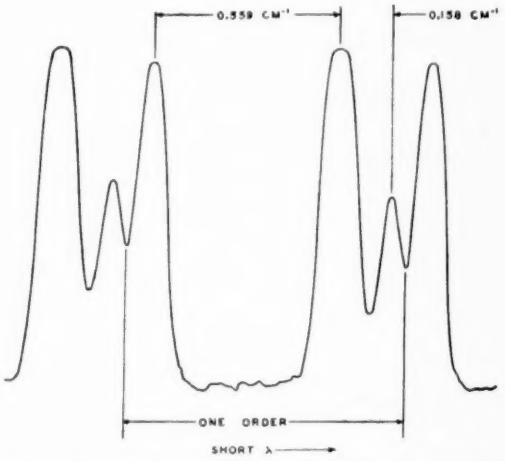

FIG. 1. Fabry-Perot fringes (6-mm spacer) showing all three components of λ8446 clearly resolved. The center of the fringe system is toward the left.

* Supported by the U. S. Office of Naval Research.

[1] B. Edlén, Kl. Svenska Vetenskapsakad. Handl., Series 3, Vol. 20, No. 10 (1943).

[2] L. W. Parker and J. R. Holmes, J. Opt. Soc. Am. 43, 103 (1953).

[3] D. O. Davis and K. W. Meissner have reported the complete structures of λλ8446, 7254, and 6046 in J. Opt. Soc. Am. 42, 871 (1952). Our measurements on λ8446 agree closely with theirs.

[4] S. Tolansky, *High Resolution Spectroscopy* (Pitman, New York, 1947), p. 270.

ground level, which was very uniform over the entire photographic plate in all cases. The values $^3P_2-{}^3P_1$ for λ8446 and $^3P_2-{}^3P_1$ for λ2884 should be equal since the same two fine structure levels are involved (Fig. 2). The error in intensity measurements is estimated to be 15 percent.

DISCUSSION

The complete anomalous structure of the $3p\,^3P$ level was inferred from its combination with $3s'\,^3D$ by Edlén with the sum rule. The corresponding complex multiplet is λ7982–95. Although the doublet structure of λ7982.41, which ends on $^3P_{20}$, was not resolved directly by Edlén, be determined the splitting $^3P_2-{}^3P_0$ (0.16 cm^{-1}) by noting that the splitting of the line pair $^3P_{20,1}-{}^3D_1$ was measurably greater than that of the pair $^3P_{1,2}-{}^3D_2$. There have remained, however, about a dozen lines involving the $3p\,^3P$ level which are incompletely resolved with respect to this level and which are expected to have splittings based on the known structure of $3p\,^3P$. Two of these are λ8446.35 and λ2883.78, the former wavelength determined by Edlén, the latter by Runge and Paschen.[5] Complete resolution of the λ8446 triplet, as well as of the λ2884 doublet, confirms the structure of $3p^3P$ proposed by Edlén. The relative intensity ratio found for the three components of λ8446, 1:0.64:0.30, was used to associate J-values of $3p\,^3P$ with individual components. This ratio deviated slightly from the theoretical ratio expected for pure Russell-Saunders coupling without configuration interactions, i.e., 1:0.60:0.20. The discrepancy may be due to an error in the relative intensity measurement since it is well known that instrumental background between orders in interferometer patterns can sometimes increase the apparent relative intensity of weak components by an order of magnitude.[6] One may examine the effect on λ2884 of band background, which is definitely present in addition to the instrumental background. In this case the relative intensity of the two components, ending on $J=2$ and $J=1$ of $3p\,^3P$, respectively, is found to be 1:0.66 whereas the theoretical ratio is 1:0.60. The corresponding ratio found for λ8446, 1:0.64, is negligibly different. There is a distinct possibility, then, that the deviation of the λ8446 relative intensity ratio from the theoretically expected ratio may be due at least in part to a perturbation effect.[7] Edlén has shown that the entire $np\,^3P$ series is perturbed by $3p'\,^3P$ in the "displaced" (^2D) system. This level, expected at a position above the ionization limit of the "normal" (^4S) system, is missing due to a strong autoionization effect in which $3p'\,^3P$ interacts with the continuum above the $np\,^3P$ series limit.[1]

TABLE I. New fine structure in O I.

Wavelength	Transition	Splittings (cm^{-1})	Intensity ratio of components
8446	$3s\,^3S_1-3p\,^3P_{210}$	$^3P_2-{}^3P_1=0.559(\pm0.003)$ $^3P_2-{}^3P_0=-0.158(\pm0.002)$	1:0.64:0.30
2884	$3p\,^3P_{21}-3d'(^3D)\,^3P_2$	$^3P_2-{}^3P_1=0.558(\pm0.002)$	1:0.66
4368	$3s\,^3S_1-4p\,^3P_{210}$	$^3P_{21}-{}^3P_0=-0.300(\pm0.001)$	1:0.26

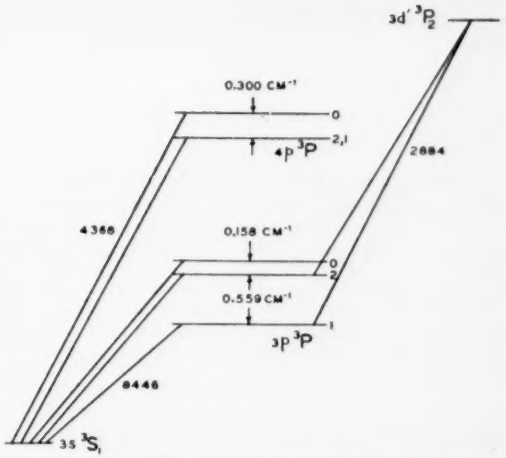

FIG. 2. Energy level diagram of states involved in the transitions studied, showing the deduced structures of $3p\,^3P_{210}$ and $4p\,^3P_{210}$. The energy scale is purposely distorted for clarity.

The structure found for λ4368 is interesting since this line originates on $4p\,^3P$ of the same perturbed series. Since only two components were resolvable, there remained the problem of deciding which two of the three levels $J=0, 1, 2$ coincide. The choice made was based on the relative intensity ratio, found to be 1:0.26. The three possibilities of coincidence were as follows: $J=0$ and $J=1$, $J=0$ and $J=2$, and $J=1$ and $J=2$, which would give relative intensity ratios 1:0.80, 1:0.50, and 1:0.125, respectively. The last possibility is most reasonable, since the presence of instrumental background would require that 0.26 be considered an upper limit. Figure 2 indicates the inferred structure of $4p\,^3P$, which is anomalous. It is to be expected that higher terms of the $np\,^3P$ series, lying closer to the perturbing level, should be even more distorted.

The same perturbation is probably responsible for the very appearance of lines such as λ7982 and λ2884, which connect terms formed by addition of the optical electron to different terms of the parent ion. Such transitions are otherwise forbidden.[8]

[5] C. Runge and F. Paschen, Ann. Phys. Chem. **61**, 641 (1897).
[6] See reference 4, p. 272.
[7] E. U. Condon and G. H. Shortley, *Theory of Atomic Spectra* (Cambridge University Press, Cambridge, 1935), pp. 218 and 367.
[8] See reference 7, p. 245.

Current Increase at Constant Amplification Factor in Steady Corona with Coaxial Cylindrical Geometry*

LEONARD B. LOEB
University of California, Berkeley, California
(Received December 5, 1952)

It has long been known that above onset of steady positive wire corona with coaxial cylindrical geometry, Townsend's relation of 1914 relating current i and over-voltage, $V-Vg$, of the form $V-Vg=Bi/V$ applies over a considerable range. This law is deduced assuming a constant potential across a zone of limited constant ionizing radius. Such assumption implies a constant Townsend amplification factor for ionization by collision, a fact just recently experimentally established by Colli, Facchini, and Gatti. The corona current i on this theory, however, increases many times despite constant amplification factor. It is shown that this occurs by slight temporary raising of the amplification factor producing a rapid proliferation of ionizing sequences over the anode surface, increasing current and space charge density, but maintaining essentially constant amplification factor. This action has a bearing on the spread of the normal glow discharge over the cathode.

SINCE 1914 the equation of Townsend[1] for corona currents with anode in coaxial cylindrical geometry above onset of steady corona has been justified experimentally within fairly wide limits of potential variation irrespective of the gas filling or corona mechanism.[2] In rough form this reads,

$$V-V_g=\frac{piA^2}{2KV}\log(A/a), \tag{1}$$

where V_g is the observed corona threshold, V the applied potential, K the reduced mobility, p the gas pressure, A and a the radii of cathode and anode cylinders, respectively, and i the current. Since space charge density n of carriers beyond the ionizing zone from anode surface at $r=a$ to $r=r_{0g}$ where ionization ceases is given by

$$n=\frac{ip\log(A/a)}{2KV}=\frac{p\log(A/a)}{2KV}\frac{dq}{dt}, \tag{2}$$

with n constant across the gap, it is clear that the overvoltage $V-V_g$ in Eq. (1) serves only to overcome and move the positive ion space charge and that the corona operates at V_g. If this is correct then the ion amplification factor

$$\exp\int_{r_{0g}}^{a}\alpha dr$$

must remain sensibly constant over the region where this law applies, for at V_g the threshold condition is

$$\gamma\exp\int_{r_{0g}}^{a}\alpha dr=1, \tag{3}$$

whether γ stands for a cathode mechanism or its equivalent in the photoelectric gas process characteristic of fast Geiger counters. While this constancy of the amplification factor has been tacitly assumed, it has not been strikingly brought home until the recent work of Colli, Facchini, and Gatti[3] who actually observed this align-constancy in A and $A+10^{-3}$ CO_2 mixture coaxial counters above corona threshold at various pressures above 200 mm. This constancy permits the use of such tubes as proportional α- and β-ray counters above background signal since the size of the short pulse produced $<10\mu$sec is clearly discernable against the slower background fluctuations.

This observation strikingly brings out an apparent paradox. For according to Eq. (1) the current i, or rate of charge production in the active zone, increases rapidly [proportional to $V(V-V_g)$], as V increases while the amplification factor is constant. Careful study shows, that the contradiction arises from assuming that the only way in which rate of ion production can increase is through change in the amplification factor. In reality ion production can be augmented, (a) by increasing the amplification factor and/or γ as well as the time rate of successive events by increasing V_g, *or*, (b) by keeping the amplification factor constant and merely increasing the number of multiplying sequences corresponding to the condition

$$\gamma\exp\int_{r_{0g}}^{a}\alpha dr=1$$

per unit area of electrode surface. Changes by mechanism (a) would involve increasing the potential for active ionization above V_g by ΔV_g and increasing r_{0g}. If the increase were of any magnitude over an extended voltage regime this would at once be detected through failure of the Townsend law and of measurements such as those of Colli, Facchini, and Gatti. It is also energetically an uneconomical mechanism for it involves increase in potential energy, and thus more degradation loss. To

* Studies underlying his have been supported by the U. S. Office of Naval Research.

[1] J. S. Townsend and P. J. Edmunds, Phil. Mag. **28**, 789 (1914); H. S. Townsend, Phil. Mag. **28**, 83 (1914); *Electricity in Gases* (Oxford University Press, London, 1915), p. 376 ff. H. F. Boulind, Phil. Mag. **18**, 909 (1934).

[2] Sven Werner, Z. Physik **90**, 356 (1934); **92**, 705 (1934); C. G. Miller and L. B. Loeb, J. Appl. Phys. **22**, 499 (1951).

[3] Colli and Facchini, and Gatti, Rev. Sci. Instr. **23**, 621 (1952).

understand the process (b), it is essential to state that the amplification factor and the quantities actually determining V_g are not the product of the ideal average experimental Townsend functions γ and

$$\exp\int_{r_{0g}}^{a}\alpha dr$$

in Eq. (3). Instead they are values somewhat larger, for at the ideal limit,[4] as Wijsman has shown, the discharge could hardly be self-sustaining, because of statistical fluctuations and here the space charges also augment interruption. Furtheremore it takes very small, (practically imperceptible on an observational scale), changes in V_g to give a quantity

$$\gamma\exp\int_{r_{0g}}^{a}\alpha dr>1.$$

Assume, for example, that such a change is produced when V is suddenly increased by a small amount ΔV above its previous value. At such an increase the first effect with a previous constant ion production dq/dt, will be to clear away space charge near the wire more rapidly than before. The active voltage in ion production, V_g, will thus instantaneously be increased by ΔV_g which may be quite small. At once

$$\gamma\exp\int_{r_{0g}}^{a}\alpha dr$$

will become greater than unity and carrier production as well as carrier densities will rise through multiplication of the number of avalanche sequences per unit surface area of anode. This will in time augment the space charge density near the temporarily extended r_{0g} and wipe out the increase ΔV_g, thus restoring the operating potential to V_g but having augmented the number of uninterrupted sequences

$$\exp\int_{r_{0g}}^{a}\alpha dr$$

per unit area of anode.

Thus space charge will be maintained despite decreased time of traverse and dq/dt, or i, will be increased. V_g and

$$\exp\int_{r_{0g}}^{a}\alpha dr$$

will however in large measure be unchanged except for a small instantaneous fluctuation, lasting perhaps some 10μsec.

On such a picture the introduction of 10^4 new electrons by an α particle track in 10^{-8} sec will cause an instantaneous increase in current for some μsec after which the excess space charge must reduce the current until it dissipates from the neighborhood of the anode. The observed current should rise to a sharp peak in a μsec and then sharply fall below its steady value eventually recovering its steady value after some 10μsec. This is just what Colli, Facchini, and Gatti[3] observed. Returning to the steady corona at V_g it is clear that the increase of current produced by proliferation of avalanche sequences per unit area of anode will continue with increasing V until the space charge density with increasing potential is reduced so that the width of the ionizing zone from a to r_{0g} irreversibly increases, or until secondary processes involving crossing times or other effects become inadequate to increase dq/dt as fast as needed. At such values of V the Townsend law begins to fail and amplification factors increase. The region over which amplification factors are constant can thus be expected to be quite extensive in potential range, as observed. There is in this explanation a vague analog to the action of the normal cathode fall in glow discharges. There however the space charge density increasing over the cathode causes a spreading of the glow over the still uncovered cathode surface by virtue of the repulsion between the various more intensive γ-conditioned unit avalanche sequences.[5] With the coaxial counter the anode wire is covered with glow over its whole surface because of the diffusive nature of the photo-ionization in the gas. Avalanches are shorter and less intense so that the space charge density is less especially with small A and rapid clearing. Increase of current can then readily occur by increase in avalanche processes per unit area of anode surface.

[4] R. A. Wijsman, Phys. Rev. **75**, 833 (1949).

[5] L. B. Loeb, J. Appl. Phys. **19**, 882 (1948); W. Finkelnburg and S. M. Segal, Phys. Rev. **83**, 582 (1951)

PHYSICAL REVIEW VOLUME 90, NUMBER 1 APRIL 1, 1953

Calculation of Peaked Angular Distributions from Legendre Polynomial Expansions and an Application to the Multiple Scattering of Charged Particles*

L. V. SPENCER
National Bureau of Standards, Washington, D. C.
(Received December 3, 1952)

A method for evaluating Fourier integrals is presented which relies upon qualitative information about the integral and which combines some of the advantages of both numerical and analytic techniques. A formula is then derived which sums slowly convergent series of Legendre polynomials by making use of a Fourier integral "small angle" approximation. A combination of the two techniques is used to sum the slowly convergent Legendre polynomial series which represents the directional distribution of multiply scattered charged particles. Comparisons with "small angle" calculations by Molière and Snyder-Scott are included.

1. INTRODUCTION

THE directional distribution of charged particles multiply scattered in a thin foil is typical of many physical problems which involve an angular distribution strongly peaked at some particular angle. In this problem as in many others the basic treatment is greatly simplified by making expansions in spherical harmonics; however the series which then represents the desired peaked angular distribution will be very slowly convergent. This slowly convergent series can be summed by making a "small angle approximation," i.e., by transforming the sum into a Fourier integral, which can usually be more easily evaluated than the sum. In the charged particle problem Molière[1] has been able to evaluate such a Fourier integral through the use of a suitable analytic representation and expansion. Snyder and Scott[2] have applied laborious standard numerical integration techniques to the same problem. The first part of this note suggests a method for making Fourier integrations which combines some of the advantages of both numerical and analytical techniques. It has flexibility in that it can be applied in a wide variety of circumstances, being not particularly dependent on a simple analytic form for the integrand. On the other hand it uses analytic expressions in making the integrations, thereby offering the advantages of quick and easy analytic manipulations. We shall illustrate this method by using it to reproduce some of the results of Snyder and Scott (Sec. 3).

The other purpose of this note is to demonstrate a method for summing Legendre polynomial series exactly, but taking advantage of a Fourier integral "approximation." We derive the basic summation formula which enables us thus to dispense with the "small angle approximation" in Sec. 4. We shall illustrate this technique also by applying it to a particular problem (Secs. 5 and 6) and comparing with the "small angle approximation" results of Molière.

Further application of these techniques will be made in a following paper which will contain a full discussion of the problem of multiple scattering of relativistic electrons in a thin foil. A comparison with experiments by Hanson *et al.*[3] will be obtained which utilizes more realistic scattering cross sections than those of Molière and Snyder-Scott.

2. DISCUSSION

In a previous paper,[4] complicated functions are represented by approximate forms which require only qualitative information reinforced by a knowledge of a few well-known parameters of the exact functions. These approximate forms have proved adequate for many purposes. For example, in reference 4 certain integrals were calculated by combining the qualitative information that an unknown factor in the integrand is smooth and single-peaked with a knowledge of a few moments of this unknown factor.

We want to apply this same idea to evaluate the Fourier integrals which appear in the Molière problem. We propose to do this by approximating the integrand with a set of terms which are chosen according to three criteria:

(a) Each term must have a known or easily determined Fourier transform.

(b) Each term must agree with the qualitative information about the integrand or its Fourier transform. Examples of this qualitative information might be smoothness and positiveness, or the known behavior of the integral or integrand for large or small values of the independent variable.

(c) The set of terms must contain constants which are chosen to fit exactly certain numbers characterizing the integrand. These numbers might be integrals, values, or derivatives of the integrand. The choice of parameters which are to be fitted may be made in such a way that the Fourier integral is given particularly accurately for a certain range of values of the independent variable.

What we are proposing is a sort of generalized nu-

* Work supported by the U. S. Office of Naval Research and the U. S. Atomic Energy Commission.
[1] G. Molière, Z. Naturforsch. **3A**, 78 (1948). *Note added in proof:*—See also a further development of the Molière technique by H. A. Bethe, Phys. Rev. **90**, 000 (1953).
[2] H. S. Snyder and W. T. Scott, Phys. Rev. **76**, 220 (1949).
[3] Hanson, Lanzl, Lyman, and Scott, Phys. Rev. **84**, 634 (1951).
[4] L. V. Spencer, Phys. Rev. **88**, 793 (1952).

merical integration technique. We wish to emphasize that the accuracy of numerical integration techniques increases rapidly with the amount of qualitative information which is utilized.

3. THE FOURIER INTEGRAL OF MOLIÈRE AND SNYDER-SCOTT

In order to obtain the (projected) angular distribution $F_1(\omega)$ of originally monodirectional charged particles multiply scattered by a thin foil, Molière and Snyder-Scott evaluate the following Fourier integral [reference 2, Eq. (8, 2)]:

$$F_1(\omega)=(2\pi)^{-1}\int_{-\infty}^{\infty}d\sigma e^{i\omega\sigma}\exp\{-A[1-L_1(\sigma)]\}, \quad (1)$$

where A is a constant, and we use the notation[5] $L_\nu(\sigma)=\sigma^\nu K_\nu(\sigma)$, K_ν being the Bessel function of the second kind with imaginary argument as given by Watson.[6] The letter ω refers to the total deflection angle divided by a scaling factor which is immaterial for our present purpose.

The available qualitative information about $F_1(\omega)$ is:

(a) $F_1(\omega)$ is a smooth, positive, single-peaked function of ω^2.

(b) $F_1(\omega)$ tends to be Gaussian for small values of ω.

(c) For large values of ω, F_1 can be calculated by expanding $\exp\{-A[1-L_1(\sigma)]\}$, i.e.,[7]

$$F_1(\omega)\rightarrow(2\pi)^{-1}\int_{-\infty}^{\infty}d\sigma e^{i\omega\sigma}AL_1(\sigma)=(A/2)(1+\omega^2)^{-\frac{1}{2}}. \quad (2)$$

Furthermore, if ω is small F_1 is essentially an integral over the function $\exp\{-A[1-L_1(\sigma)]\}$, each value of σ contributing to the result according to the magnitude of this exponential function. This suggests that for small ω accurate answers can be obtained if an approximate function is fitted to a series of *values* of this exponential function distributed over, e.g., the range $1\geqslant\exp\{-A[1-L_1(\sigma)]\}\gtrsim\frac{1}{10}$.

On the other hand, if ω is large F_1 is essentially determined by the region of small σ, as illustrated, for example, by (c). This suggests that a good approximation for large ω, which calls for an accurate representation of $\exp\{-A[1-L_1(\sigma)]\}$ for small σ, can be obtained by using *derivatives* of $\exp\{-A[1-L_1(\sigma)]\}$ evaluated at some small value of σ.

A. Approximation by Gaussians

These considerations suggest that for small ω we approximate the integrand by Gaussians:

$$\exp\{-A[1-L_1(\sigma)]\}\approx\textstyle\sum_n a_n\exp(-\alpha_n\sigma^2), \quad (3)$$

where the a_n and α_n are determined so that the approximation agrees with the exact function at values of σ distributed over a range determined by

$$1\geqslant\exp\{-A[1-L_1(\sigma)]\}\geqslant\tfrac{1}{10}.^8$$

Since Gaussians transform to Gaussians, this yields the approximation:

$$F_1(\omega)\approx\frac{1}{2\sqrt{\pi}}\sum_n a_n\alpha_n^{-\frac{1}{2}}\exp[-\omega^2/(4\alpha_n)]. \quad (4)$$

Sample calculations of this type indicate that the approximation (4) with two or three terms is accurate to within 3 percent for values of ω in the range

$$1\geqslant F_1(\omega)/F_1(0)\gtrsim 0.02.$$

In this simple calculation, no account has been taken of (c). This additional information may be introduced in two ways. We write either

$$\exp\{-A[1-L_1(\sigma)]\}\approx\textstyle\sum_n b_n\exp(-\beta_n\sigma^2)+B_0L_1(B_1\sigma), \quad (5)$$

or

$$\exp\{-A[1-L_1(\sigma)]\}\approx\{\textstyle\sum_n c_n\exp(-\gamma_n\sigma^2)\}L_1(C\sigma), \quad (6)$$

where B_0, B_1, and C are assigned values at the outset which will insure the correct asymptotic behavior. The constants b_n, β_n, c_n, and γ_n are chosen in each case so that the approximate function agrees with the exact one at values distributed over the range $1\geqslant\exp\{-A[1-L_1(\sigma)]\}\geqslant\frac{1}{10}$.[8] Of the two forms the more meaningful and more accurate is (6). Each term is the sum (6) refers to a Gaussian diffusion superimposed on a single scattering which very nearly obeys the correct differential scattering law. This form has the drawback that the angular distribution is represented by a folding integral:

$$F_1(\omega)\approx\int_{-\infty}^{\infty}d\omega'\left\{\frac{1}{2\sqrt{\pi}}\sum_n(c_n\gamma_n^{-\frac{1}{2}})\times\exp[-(\omega-\omega')^2/(4\gamma_n)]\right\}\{(C^2/2)(C^2+\omega'^2)^{-\frac{1}{2}}\}. \quad (7)$$

Fortunately, this is a practicable integration to perform numerically.

For a sample calculation of this type we chose $A=C^2=100$. Three Gaussians were used and the c_n, γ_n were determined so that the approximate function agreed with $\exp\{-A[1-L_1(\sigma)]\}$ at $\sigma^2=0$, 0.004, 0.008, 0.012, 0.016, and 0.020.[8] The resulting angular distribution obtained from expression (7) is given in the second column of Table I. It compares quite well with Snyder-Scott results for $F_1(\omega)/F_1(0)\gtrsim 0.005$. For larger values of ω, differences of $\sim$6 percent appear. If the tabulation had been continued to still larger, ω, the

[5] Compare, for example, with Eq. (A.2), G. Molière, Z. Naturforsch. **2A** (145), 1947.

[6] G. N. Watson, *Bessel Functions* (MacMillan Company, New York, 1945).

[7] See reference 6, p. 172. Also, see Campbell and Foster, *Fourier Integrals* (D. Van Nostrand Company, Inc., New York, 1948), p. 125.

[8] For an account of the fitting procedure see reference 4, Appendices B and C.

TABLE I. A comparison of Gaussian and inverse power approximations with the Snyder-Scott results for $A=100$.

ω	Snyder-Scott	Gaussian approx.	Inverse power approx.	ω	Snyder-Scott	Gaussian approx.	Inverse power approx.
	$\times 10^{-6}$	$\times 10^{-6}$	$\times 10^{-6}$		$\times 10^{-6}$	$\times 10^{-6}$	$\times 10^{-6}$
0	22850	22740		120	34.38		34.79
10	18740	18670		140	20.76		20.89
20	10780	10780		160	13.52		13.57
30	4904	4905		180	9.132		9.329
40	2041	2051	1833	200	6.691		6.699
50	888.4	887.9	836.7	220	4.973		4.976
60	430.0	428.1	423.7	240	3.798		3.800
70	236.3	233.4	237.1	260	2.968		2.969
80	140.8	137.1	144.4	280	2.364		2.364
90	93.34	89.39	94.23	300	1.913		1.914
100	63.92	60.22	64.92	330	1.430		1.430
110	45.96	43.14	46.71				

discrepancy would have increased slightly and then decreased again as $\omega\to\infty$.

B. Approximation by Inverse Powers

For large ω, F_1 tends to obey an inverse power law. The first idea which springs to mind, therefore, is to approximate by functions of the type $(K^2+\omega^2)^{-\kappa-\frac{1}{2}}$, where K and κ are constants. This form is not only an inverse power for large ω, but it is also capable of behaving like a Gaussian for small ω. Because of the Fourier relationship,[7]

$$(2\pi)^{-1}\int_{-\infty}^{\infty} d\sigma e^{i\omega\sigma}L_\kappa(K\sigma)=\frac{(2\kappa^2)^\kappa(\kappa-\frac{1}{2})!}{2\sqrt{\pi}(K^2+\omega^2)^{\kappa+\frac{1}{2}}}, \quad (8)$$

we write

$$\exp\{-A[1-L_1(\sigma)]\}\approx\sum_n k_n L_{\kappa_n}(K\sigma). \quad (9)$$

Knowledge of the exact asymptotic trend leads us to specify the constants in one term of (9) in such a way that the asymptotic trend will be given correctly, i.e., $\kappa_0=1$, $k_0=AK^{-2}$.

The function $(K^2+\omega^2)^{-\kappa-\frac{1}{2}}$ behaves like a Gaussian for $\omega^2\ll K^2$ and like an inverse power for $\omega^2\gg K^2$. Thus $\omega=K$ is a transition region between the two types of behavior. This suggests that K be identified with the abscissa of the point of inflection of the function $\log F_1(\omega)$.[9] This value for K can be determined from the simple Gaussian approximation described in A.

As discussed early in this section we want to fit the approximate function to the exact function by means of derivatives or combinations of derivatives evaluated at small σ. We make use of the relations:

$$\{S\}L_\nu(\sigma)=\left\{-\frac{1}{\sigma}\frac{d}{d\sigma}\right\}L_\nu(\sigma)=L_{\nu-1}(\sigma), \quad (10)$$

$$\{T\}L_\nu(\sigma)=\{-\tfrac{1}{2}(\sigma^2S^2-1)\}L_\nu(\sigma)=(\nu-1)L_{\nu-1}(\sigma). \quad (11)$$

If we apply to (9) the operators $\{S^3\}$, $\{TS^2+3S^3\}$, $\{T^2S+5TS^2+9S^3\}$, and $\{T^3+6T^2S+19TS^2+27S^3\}$, and if we evaluate the resulting four equations at the same small value of σ, we obtain four nonlinear equations which can be solved simultaneously.[8] This enables us to determine four constants and include two terms in the sum (9) in addition to the term giving the asymptotic trend exactly. The recurrence relations of the L_ν's enable us to calculate the desired derivatives of the left side of (9) quite readily.

Calculations of this nature have been accomplished for the case $A=100$. We chose $K=35$, which is about the value for which $(d^2/d\omega^2)\log F_1(\omega)=0$. The derivatives were all evaluated at $\sigma^2=10^{-4}$. During the solution of the set of nonlinear equations it becomes necessary to evaluate L_ν for nonintegral ν. There are series expansions which can be used for this purpose; however we preferred to obtain the desired values from graphical interpolation using the easily obtained integral[10] and half-integral L_ν's. The final results of the calculation are given in the third column of Table I. They agree well with Snyder-Scott for $\omega\gtrsim 55$. For small ω this approximation is in error by 10–20 percent.[11]

As shown by Table I, there is a considerable overlap between the Gaussian and inverse power approximations. A combination of the two yields an approximation accurate everywhere to better than 3 percent.

It should be borne in mind that the calculations described in this section represent but two of a number of ways in which the general approach described in Sec. 2 may be used to evaluate the Fourier integral (1).

The number of man hours involved in one of these calculations may be of interest. Assuming that procedural details have been ironed out, but allowing rather generously time for checking and for tabulating the final results, we estimate that either of the two types of calculation requires about 10–12 hours.

4. A SUMMATION FORMULA FOR LEGENDRE POLYNOMIALS

The actual summation of a slowly convergent Legendre polynomial series will now be discussed. We will derive a summation formula which converts a Fourier integral approximation into the exact sum. Thus, suppose we want to sum the series

$$G(\vartheta)=\sum_{l=0}^{\infty} g_l P_l(\cos\vartheta). \quad (12)$$

We let $g(l+\frac{1}{2})$ be any continuous function of $(l+\frac{1}{2})$ over the range $-\infty\leqslant(l+\frac{1}{2})\leqslant\infty$ which has the property that for positive, integral values of l, $g(l+\frac{1}{2})=g_l$. (This does not define $g(l+\frac{1}{2})$ uniquely. Each of the various functions satisfying these criteria is equally good for our purposes.) If $g(l+\frac{1}{2})$ is, e.g., an antisymmetric

[9] On semilog paper a Gaussian becomes monotonically steeper whereas an inverse power becomes monotonically flatter.

[10] Tables of the Bessel Functions $Y_0(x)$, $Y_1(x)$, $K_0(x)$, $K_1(x)$, $0\leqslant x\leqslant 1$, Natl. Bur. Stand. Applied Mathematical Series 1, February 12, 1948.

[11] In a separate calculation of this same type we have achieved an accuracy everywhere to about 7 percent. This was done by choosing K in such a way that the approximation was correct at $\omega=0$. The value of K determined in this way was slightly higher, i.e., 45 instead of 35.

function of $(l+\frac{1}{2})$ we may define a function $R(r)$ by the integral

$$R(r)=(2\pi)^{-1}\int_{-\infty}^{\infty} d(l+1)\,\sin[(l+\tfrac{1}{2})r]g(l+\tfrac{1}{2}). \quad (13)$$

We have then the reciprocal relationship,

$$g(l+\tfrac{1}{2})=\int_{-\infty}^{\infty} dr\,\sin[r(l+\tfrac{1}{2})]R(r). \quad (14)$$

If we make use of (14) together with a well-known integral expression for $P_l(\cos\vartheta)$,[12] we may rewrite (12) as follows:

$$G(\vartheta)=\frac{1}{\pi\sqrt{2}}\sum_{l=0}^{\infty}\left\{\int_{-\infty}^{\infty} dr\,\sin[r(l+\tfrac{1}{2})]R(r)\right\}\times\left\{\int_{\vartheta}^{2\pi-\vartheta} d\phi\,\sin[\phi(l+\tfrac{1}{2})](\cos\vartheta-\cos\phi)^{-\frac{1}{2}}\right\}.$$

Upon changing the order of the integrations and the summation this becomes

$$G(\vartheta)=\frac{1}{\pi\sqrt{2}}\int_{\vartheta}^{2\pi-\vartheta} d\phi(\cos\vartheta-\cos\phi)^{-\frac{1}{2}}\int_{-\infty}^{\infty} drR(r)\times\sum_{l=0}^{\infty}\sin[r(l+\tfrac{1}{2})]\sin[\phi(l+\tfrac{1}{2})].$$

The sum over l can now be performed:

$$\begin{aligned}G(\vartheta)&=\frac{1}{\sqrt{2}}\int_{\vartheta}^{2\pi-\vartheta} d\phi(\cos\vartheta-\cos\phi)^{-\frac{1}{2}}\int_{-\infty}^{\infty} drR(r)\times\sum_{m=-\infty}^{\infty}(-1)^m\delta[r-(\phi+2\pi m)]\\&=\sqrt{2}\int_{\vartheta}^{2\pi-\vartheta} d\phi(\cos\vartheta-\cos\phi)^{-\frac{1}{2}}\sum_{m=0}^{\infty}(-1)^m\times R(\phi+2\pi m).\end{aligned} \quad (15)$$

Expression (15) is the formula we wanted to derive.[13] Whenever the Legendre polynomial sequence (12) converges slowly the series in (15) converges rapidly. In the numerical illustration of Sec. 6, only the $m=0$ term is significant.

In the next section we shall present the $g(l+\frac{1}{2})$ for the Molière problem both exactly and in a very useful approximation. Both differ slightly from the form used in the ordinary "small angle approximation," and therefore the Fourier integral which we shall make use of is not quite the usual one.

TABLE II. A comparison of approximate values for $2\eta C_l$ as given by Eq. (18), with the exact values of Eq. (17). $(2\sqrt{\eta}=0.001765.)$

l	$2\eta C_l$	$1-L_1(\sigma)-\frac{1}{2}\eta L_0(\sigma)-\frac{1}{4}\eta$	$1-L_1(\sigma)$
0	0	$<10^{-12}$	2.977×10^{-6}
1	2.034×10^{-5}	2.039×10^{-5}	2.925×10^{-5}
2	5.636×10^{-5}	5.642×10^{-5}	5.877×10^{-5}
3	10.640×10^{-5}	10.655×10^{-5}	10.877×10^{-5}

5. THE SPHERICAL HARMONIC COEFFICIENTS FOR THE MOLIÈRE PROBLEM

The differential scattering cross section which leads to the Fourier integral of Molière and Snyder-Scott is $\sigma(\vartheta)=2\eta A\{1+2\eta-\cos\vartheta\}^{-2}$, where A and η are constants. The solution of the diffusion equation with this cross section, by expansion into spherical harmonics, yields the following expressions:[14]

$$\begin{aligned}&G(\vartheta)=\textstyle\sum_l g_l P_l(\cos\vartheta),\quad g_l=(l+\tfrac{1}{2})\exp(-2\eta AC_l),\\&C_l=\int_{-1}^{1} d(\cos\vartheta)[P_0-P_l(\cos\vartheta)][1+2\eta-\cos\vartheta]^{-2}.\end{aligned} \quad (16)$$

We may evaluate rather easily the integral for C_l:[15]

$$\begin{aligned}C_l&=-\frac{\partial}{\partial(2\eta)}\int_{-1}^{1} d(\cos\vartheta)\times[P_0-P_l(\cos\vartheta)][1+2\eta-\cos\vartheta]^{-1}\\&=-\frac{\partial}{\partial(2\eta)}\{2Q_0(1+2\eta)-2Q_l(1+2\eta)\}\\&=\frac{1}{2\eta(1+\eta)}\{1+l[(1+2\eta)Q_l(1+2\eta)-Q_{l-1}(1+2\eta)]\}.\end{aligned} \quad (17)$$

A very accurate approximation (for small η) which we shall use instead of (17) is

$$C_l\approx(2\eta)^{-1}\{1-L_1(\sigma)-\tfrac{1}{2}\eta L_0(\sigma)-\tfrac{1}{4}\eta\}, \quad (18)$$

where $\sigma=2\eta^{\frac{1}{2}}(l+\frac{1}{2})$. Table II compares (18) and (17) and with the "small angle approximation," i.e., $C_l\approx(2\eta)^{-1}[1-L_1(\sigma)]$, for the first four values of l. The form (18) was suggested by Lewis' Eq. (15),[14] but it is asymptotically correct as $l\to\infty$.

[12] See, for example, E. T. Whittaker and G. N. Watson, *Modern Analysis* (MacMillan Company, New York, 1946), p. 315.

[13] This formula assumes a $g(l+\frac{1}{2})$ which is antisymmetric in $(l+\frac{1}{2})$. Circumstances may arise in which it is convenient to define a $g(l+\frac{1}{2})$ which is symmetric or which contains both symmetric and antisymmetric parts. For these situations it is advantageous to make use of the formula

$$G(\vartheta)=\sqrt{2}\int_0^{\vartheta} d\phi(\cos\phi-\cos\vartheta)^{-\frac{1}{2}}\sum_{m=0}^{\infty}(-1)^m\times\{R(\phi+2\pi m)-R[(2\pi-\phi)+2\pi m]\},$$

where

$$R(r)=(2\pi)^{-1}\int_{-\infty}^{\infty} d(l+\tfrac{1}{2})\cos[(l+\tfrac{1}{2})r]g(l+\tfrac{1}{2}).$$

[14] H. W. Lewis, Phys. Rev. **78**, 527 (1950).

[15] See, e.g., reference 12, p. 320. I am indebted to Dr. C. H. Blanchard for the expression of C_l in terms of Q_l's.

TABLE III. The Legendre polynomial sum as compared with Molière's "small angle" results for $A=118.4$, $2\sqrt{\eta}=0.001765$.[a]

ϑ	Molière	Polynomial sum	ϑ	Molière	Polynomial sum
(degrees)	$\times 10^{-6}$	$\times 10^{-6}$	(degrees)	$\times 10^{-6}$	$\times 10^{-6}$
0	2850	2870	8.411	8.24	8.43
0.561	2710	2730	11.214	2.15	2.17
1.121	2320	2320	12.500	1.32	1.35
1.682	1800	1780	15.000	0.589	0.601
2.243	1270	1260	20.000	0.173	0.175
3.364	511	511	23.750	0.0843	0.0864
4.486	179	182	27.500	0.0461	0.0479
5.607	67.7	65.2	30.000	0.0322	0.0338
6.728	27.1	26.1			

[a] The tabulated quantity is actually 4η times the polynomial sum (16).

6. AN ILLUSTRATION OF THE SPHERICAL HARMONIC SUMMATION

We now want to make an application of the summation formula (15) by performing the summation (16) for specific values of A and η, corresponding to a 15.7-Mev gold foil scattering experiment of Hanson *et al.*,[3] i.e., $A=118.4$, $2\sqrt{\eta}=0.001765$.

Our first step is the evaluation of the integral

$$R(2\eta^{\frac{1}{2}}\omega)=(2\pi)^{-1}(2\eta^{\frac{1}{2}})^{-2}\int_{-\infty}^{\infty}d\sigma\,\sin(\sigma\omega)\sigma \times\exp\{-A[1-L_1(\sigma)-\tfrac{1}{2}\eta L_0(\sigma)-\tfrac{1}{4}\eta]\} \tag{19}$$
$$=-(4\eta)^{-1}\frac{\partial}{\partial\omega}(2\pi)^{-1}\int_{-\infty}^{\infty}d\sigma\,\cos(\sigma\omega) \times\exp\{-A[1-L_1(\sigma)-\tfrac{1}{2}\eta L_0(\sigma)-\tfrac{1}{4}\eta]\},$$

where $\sigma=2\eta^{\frac{1}{2}}(l+\frac{1}{2})$. This is very nearly the same calculation as that discussed in Sec. 3, since the last two terms in the exponent are very small. We make very nearly the same approximations, i.e.,

$$\exp\{-A[1-L_1(\sigma)-\tfrac{1}{2}\eta L_0(\sigma)-\tfrac{1}{4}\eta]\} \approx\{\sum_{n=1}^{3}c_n'\exp(-\gamma_n'\sigma^2)\}L_1(A^{\frac{1}{2}}\sigma) \quad\text{(small }\omega\text{)}$$

$$\exp\{-A[1-L_1(\sigma)-\tfrac{1}{2}\eta L_0(\sigma)-\tfrac{1}{4}\eta]\} \approx\sum_{n=1,2}k_n'L_{\kappa_n'}(K'\sigma)+AK'^{-2}L_1(K'\sigma) +\tfrac{1}{2}A\eta L_0(K'\sigma) \quad\text{(large }\omega\text{)},$$

where the c_n', ω_n' in the "small ω" approximation are assigned values which fit the approximation to the exact expression at six values $\sigma_j^2=\eta+0.003j$. In the "large ω" approximation the four constants k_n', κ_n' are given values which fit the approximation to the exact expression for the four combinations of derivatives mentioned in Sec. 3, part B, evaluated again at $\sigma^2=10^{-4}$. The constant K' is again given the value 35.

Since we shall make numerical integrations which involve the $R(2\sqrt{\eta}\omega)$ we tabulate the functions

$$R(2\eta^{\frac{1}{2}}\omega)\approx(4\eta)^{-1}\int_{-\infty}^{\infty}d\omega'\Big\{\frac{1}{2\sqrt{\pi}}\sum_{n=1}^{3}(c_n'\gamma_n'^{-\frac{1}{2}}) \times[2(\omega-\omega')/(4\gamma_n')]\exp[-(\omega-\omega')^2/(4\gamma_n')]\Big\} \times\{(A/2)(A+\omega'^2)^{-\frac{1}{2}}\},$$

$$R(2\eta^{\frac{1}{2}}\omega)\approx(4\eta)^{-1}(2\sqrt{\pi})^{-1}(2\omega) \Big\{\sum_{n=1,2}[k_n'(2K'^2)^{\kappa_n'}(\kappa_n'+\tfrac{1}{2})!](K'^2+\omega^2)^{-\kappa_n'-3/2} +\tfrac{3}{4}A(K'^2+\omega^2)^{-5/2}+\tfrac{1}{8}\eta A(K'^2+\omega^2)^{-3/2}\Big\}.$$

The two approximations overlap within a few percent in the region $\omega\approx 80$, as expected. Because we have taken the derivative, the two do not join quite as well as in Table I. Since we shall be integrating again this is not serious.

Finally, we evaluate the integral

$$G(\vartheta)=\sqrt{2}\int_{\vartheta}^{2\pi-\vartheta}d(2\eta^{\frac{1}{2}}\omega)[\cos\vartheta-\cos(2\eta^{\frac{1}{2}}\omega)]^{-\frac{1}{2}} \times\sum_{m=0}^{\infty}(-1)^mR[(2\eta^{\frac{1}{2}}\omega)+2\pi m].$$

Only the first term in the sum is significant and we neglect the others. This integration can be made very simply by writing

$$G(\vartheta)=2\sqrt{2}\int_{0}^{(\cos\vartheta+1)^{\frac{1}{2}}}d[\cos\vartheta-\cos(2\eta^{\frac{1}{2}}\omega)]^{\frac{1}{2}} \times\{[\sin(2\eta^{\frac{1}{2}}\omega)]^{-1}[R(2\eta^{\frac{1}{2}}\omega)+R(2\pi-2\eta^{\frac{1}{2}}\omega)]\}.$$

We plot the quantity in curly brackets against $[1-\cos(2\eta^{\frac{1}{2}}\omega)]$. For each value of $\cos\vartheta$ we then read quadratically spaced values from the graph and sum them according to a standard numerical integration formula.

Table III gives $G(\vartheta)$ calculated in this manner as compared with Molière's results obtained by Fourier inversion. The two calculations agree quite well for small angles. The oscillating discrepancy of 3 or 4 percent in the region 5° to 11° seems to be due largely to the neglect of the f^2 term in Molière's approximation. At large angles where single scattering is predominant, the exact sum is larger than the "small angle approximation" by about a factor $\sigma(\text{exact})/\sigma(\text{small angles}) \approx\frac{1}{4}\vartheta^4/(1-\cos\vartheta)^2$, which amounts to 1.047 at 30°.

Letters to the Editor

PUBLICATION of brief reports of important discoveries in physics may be secured by addressing them to this department. The closing date for this department is five weeks prior to the date of issue. No proof will be sent to the authors. The Board of Editors does not hold itself responsible for the opinions expressed by the correspondents. Communications should not exceed 600 words in length and should be submitted in duplicate

Interaction of Microwaves Propagated through a Gaseous Discharge Plasma*

L. GOLDSTEIN, J. M. ANDERSON, AND G. L. CLARK
Department of Electrical Engineering, University of Illinois, Urbana, Illinois
(Received February 16, 1953)

IT has been known for some time[1] that when two medium or low frequency radiowaves traverse a common region of the ionosphere, and one of the waves is of sufficient strength, an interaction between the two electromagnetic waves is observed. In particular, there is a measurable transfer of modulation from the stronger wave to the carrier of the weaker. Bailey and Martyn[2] proposed a theory for this phenomenon of "ionospheric cross-modulation." According to this theory, absorption of the interfering waves increases the mean energy of the electrons in the appropriate region in the ionosphere. This increased mean energy of the electrons leads to a change in the collision frequency of the electrons. As the absorption of an electromagnetic wave in a region of the ionosphere is determined by the collision frequency of the electrons in that region, the absorption of the "wanted" wave is modified by the presence of the absorbed "disturbing" wave. Bailey[3] later extended this theory by considering the effect of the earth's magnetic field. According to this more complete theory, an enhancement of transferred modulation was predicted which has since been observed experimentally.[4,5]

The purpose of this note is to report experimental observations on the interaction of two *microwave* signals which are simultaneously propagated through gaseous discharge plasmas. The frequencies f_1 and f_2 of the electromagnetic waves propagated were chosen for convenience to be 8600 and 9400 Mc/sec, respectively. The plasma, the length of which could be varied from 5½ in. to 8½ in., was produced either by continuous dc or by pulsed dc excitation. Experiments were carried out with helium, neon, argon, krypton, xenon, and hydrogen gases, and over a range of pressures from 0.2- to 20-mm Hg. The power levels of both signals were far below that which is necessary to excite or even to maintain the plasma. For convenience, these waves were propagated in a wave guide containing a gaseous discharge tube. The wave guide was of square cross section in order to permit propagation of the two signals in orthogonal polarizations in the TE_{10} mode. The observations reported here concern the interaction of these electromagnetic waves in the decaying plasma following a 1- or 2-microsecond excitation pulse. Interaction of microwaves has been observed both on the reflected and transmitted waves; however, this note deals with the observations of the transmitted signals.

Measurements were made of the transmitted signals at various times after the cessation of the excitation of the plasma. These time positions were so chosen that the temperature of the electron gas had had time to decay and approach thermal equilibrium with the gas, and so that the electron density and collision frequency had become low enough to permit transmission of f_2 with slight attenuation but high enough to absorb at least a fraction of the lower frequency signal f_1.

In these experiments the disturbing wave ($f_1 = 8600$ Mc/sec) was pulse modulated. The width of these pulses varied from 2 to 40 microseconds. The wanted continuous wave, transmitted through the decaying plasma and modulated by it, was detected through a highly selective resonant cavity. The amplified envelope was displayed on an oscilloscope. With the application of the disturbing pulsed signal this envelope was modified. The duration of this effect after the removal of the disturbing wave, as is shown in the photographs, varied as a function of the nature of the gas and its pressure, as would be expected on theoretical grounds.

Figure 1 shows the interaction of the two electromagnetic waves in a decaying plasma produced in helium at 12-mm Hg. The upper trace shows a 10-μsec pulse of the disturbing signal introduced 500 μsec after the exciting pulse. The lower trace is double, showing the envelope of the wanted wave with and without the disturbing pulse. The notched trace is the modified envelope. The absorbed peak power during the disturbing pulse is 175 milliwatts. Note that the attenuation of the wanted wave is *increased* as a result of the disturbing pulse.

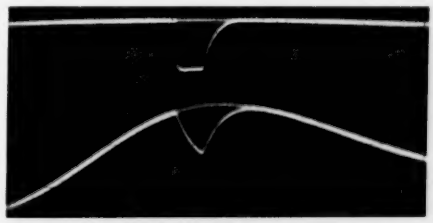

FIG. 1. Transfer of modulation to the wanted wave (lower trace) from the 10-microsecond disturbing wave pulse (upper trace) in the decaying plasma established in helium at 12 mm Hg.

Figure 2 shows the interaction in a decaying plasma excited in argon at 2.7-mm Hg. Trace No. 1 represents a pulse of the disturbing wave which is 35 μsec wide and initiates at 125 μsec after the removal of the discharge excitation pulse. Trace No. 2 is the undisturbed envelope of the wanted wave. Trace No. 3 shows the envelope of the wanted wave when the peak absorbed power from the disturbing signal is 22.5 milliwatts. Trace No. 4 is the envelope of the wanted wave when the peak absorbed power is 450 milliwatts.

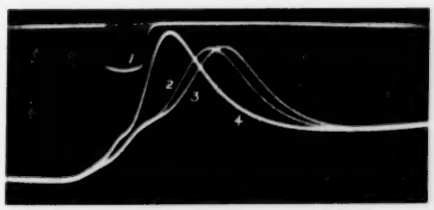

FIG. 2. Effect on the wanted wave (lower traces) in the decaying plasma established in argon at 2.7 mm Hg with the application of a 35 microsecond disturbing wave pulse. Trace 2: the undisturbed envelope of the wanted wave. Trace 3: 22.5 milliwatts absorbed in the plasma. Trace 4: 450 milliwatts absorbed in the plasma.

In contrast to Fig. 1, the result shown by trace 4 is a *decrease* in attenuation of the wanted signal during the disturbing pulse. In addition, a power dependence is observed in the shape of the traces after the disturbing pulse has been removed. For example, trace No. 3 indicates an increase in attenuation of the wanted wave shortly after the disturbing pulse, while trace No. 4 shows a decrease in attenuation of the wanted signal in the same region.

Interaction in the presence of a magnetic field.—When the disturbing wave is absorbed in the plasma at the gyro-resonance intensity of a magnetic field,[6]—here transverse to the electric vector of the disturbing wave—the interaction is observed even for low level signals for which no effect is observed in the absence

of the magnetic field. This appears to be consistent with gyro-interaction theory of radiowaves in the ionosphere.[3]

A detailed discussion of the phenomenon of interaction of electromagnetic waves in a gaseous discharge plasma will be published at a later date.

* Supported by Air Force Cambridge Research Center and Wright Air Development Center.

[1] B. D. H. Tellegen, Nature **131**, 840 (1933).
[2] V. A. Bailey and D. F. Martyn, Phil. Mag. **18**, 369 (1934).
[3] V. A. Bailey, Phil. Mag. **23**, 774 (1937).
[4] M. Cutolo, Nature **166**, 98 (1950).
[5] Bailey, Smith, Landecker, Higgs, and Hibberd, Nature **169**, 911 (1952).
[6] Goldstein, Lampert, and Heney, Phys. Rev. **83**, 1255 (1951).

Ultrasonic Attenuation Measurements in Germanium

ROHN TRUELL AND JOSEPH BRONZO
Metals Research Laboratory, Brown University, Providence, Rhode Island
(Received February 11, 1953)

ULTRASONIC attenuation (scattering and absorption) in solid materials has been studied as a function of the ultrasonic frequency and as a function of the state or condition of the material for a number of materials. In particular, it has been found that differences in the state of a semiconductor can be examined by these attenuation measurements.[1] Single crystals of germanium[2] with various histories were examined over a frequency range from 15 to 100 Mc/sec. The attenuation measurements show large differences among the germanium samples; differences caused both by heat treatment and by impurities deliberately introduced.

Figure 1 shows the attenuation as a function of frequency for four samples of germanium in the frequency range from 15 to 45 Mc/sec. The top curve, marked 1, was obtained from measure-

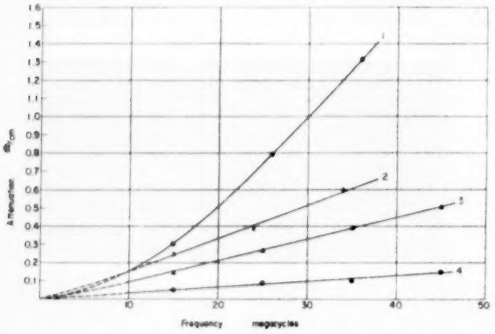

FIG. 1. Ultrasonic attenuation in germanium, as a function of frequency. Propagation normal to 100 planes.

ments on a sample of N type germanium with resistivity $\rho \simeq 0.6$ ohm cm. This sample had a lot of N type impurities deliberately introduced. Curve number 2 was obtained from measurements on a sample of P type germanium, in this case with a lot of P type impurities deliberately introduced and again with $\rho \simeq 0.6$ ohm cm. Curve number 3 was obtained from a sample of basic germanium with as small an amount of impurities as can readily be obtained. The resistivity was 12.7 ohm cm. The lowest curve, number 4, was obtained from a sample of germanium which was produced from pure germanium with $\rho = 13.2$ ohm cm and then raised in temperature to 915°C for one hour and quenched. The final germanium crystal was P type with $\rho = 0.2$ ohm cm. All of these single crystals were carefully oriented so that the propagation is normal to the 100 planes.

It is clear that above 20 Mc/sec there is a large difference among the samples as far as ultrasonic attenuation measurements are concerned. It seems reasonable that curves 1 and 2 should give rise to higher attenuation than curve 3, since the former samples should have many more defects than the latter sample. It is perhaps surprising that the pure germanium which has been heat treated to P type should have lower attenuation than the original crystal, especially since the heat treatment included quenching. It seems that this heat treatment has removed some of the "defects" from the germanium, but it is difficult to determine the nature of the "defects." It is of interest to note that while for each of the two samples with N and P type impurities the resistivity is 0.6 ohm cm, the attenuation differs by as much as a factor of two at 35 Mc/sec. Between the heat-treated sample and the N type impurity sample the attenuation differs by a factor of about ten to one at 35 Mc/sec.

The data pertaining to curve 4 is not quite as satisfactory as regards accuracy[3] as the other data for the remaining three curves, but the relative position of curve 4 with respect to the other curves is as shown.

It is believed that the attenuation measurements can be used to show relative amounts or numbers of defects present. It is desirable, of course, to separate or sort out the relative amounts of various types of defects. Measurements over a wide range of frequency and over a set of specially prepared samples may permit this separation or sorting of types of defects.

[1] H. Roderick and R. Truell, J. Appl. Phys. **23**, 267 (1952).
[2] The germanium single crystals used in this experiment were kindly supplied to us by Dr. W. P. Mason of the Bell Telephone Laboratories.
[3] These low attenuation values are at present difficult to measure.

Temporary Traps in Silicon and Germanium

J. R. HAYNES AND J. A. HORNBECK
Bell Telephone Laboratories, Murray Hill, New Jersey
(Received February 6, 1953)

EVIDENCE indicating the existence of trapping centers other than recombination centers for minority carriers in germanium and silicon has been obtained[1] from drift velocity measurements. Specifically, in p-type silicon at room temperature and n-type germanium at -80°C and lower temperatures some of the carriers appeared to suffer an additional time delay in their transit between emitter and collector. This straggle could be eliminated by increasing the ambient light falling on the semiconductor specimens. A qualitative explanation of these observations was made in terms of a simple trap model. For low external illumination some of the carriers are caught in "traps" where they sit for a time and then are ejected back into the conduction stream. High external illumination, however, creates sufficient electron-hole pairs to keep the traps filled, and no straggle is observed. By adjusting the external illumination so that a few of the carriers arriving at the collector are trapped once and the rest are not trapped at all, an estimate of the mean lifetime in a trap, τ_p, can be made.

Photoconductivity and lifetime experiments recently have furnished independent evidence for the existence of traps and have led to a quantitative empirical description of traps in a uniform crystal of 28-ohm-cm p-type silicon.[2] The basic experiment with the silicon crystal is the following. The darkened crystal is first illuminated by a light source; then the source is cut off, and the decay in photoconductivity is measured as a function of time. The decay occurs in three well-defined steps: first comes a rapid decrease in conductivity with a time constant of 20 μsec; there follows a slower decrease in conductivity which asymptotically is exponential with a final time constant of 10^{-2} sec; this is followed by a very slow decrease in conductivity with a final time constant of 260 sec.

The experiment is interpreted as follows. Illumination creates electron-hole pairs at a rate sufficient to fill two sets of volume traps, deep and shallow, and also add electrons to the conduction band. When the illumination is removed, the electrons in the conduction band recombine ($\tau_r = 20$ μsec) before the occupancy

of the traps changes appreciably. Somewhat later the shallow traps empty ($\tau \sim 10^{-2}$ sec), and this occurs before the occupancy of the deep traps changes appreciably. Finally, the deep traps empty ($\tau \sim 260$ sec). Each set of traps gives a long decay time because the average electron is trapped many times before it recombines. The photoconductivity associated with trapping comes from the additional free holes in the valence band which, due to space charge neutrality, are exactly equal in number to the number of trapped electrons.

It can be shown that the final decay time τ is related to τ_r, τ_g (the mean time an electron spends in a trap for a single trapping event), and τ_l, the mean free time an electron spends in the conduction band before trapping when most of the traps are empty. Approximately, $\tau = \tau_r \tau_g / \tau_l$. Because the time constants are so well separated, it can be shown that this formula applies to each set of traps independently.

For the shallow traps $\tau = 10^{-2}$ sec, $\tau_g = 50$ μsec, and since $\tau_r = 20$ μsec, $\tau_l = 1 \times 10^{-7}$ sec. For the deep traps τ_g cannot be measured independently, but it can be estimated from the agreement between the theory of the multiple trapping process and experiment. Thus for the deep traps, $\tau = 260$ sec, $\tau_g \simeq 1$ sec, $\tau_l \simeq 1 \times 10^{-7}$ sec. The concentration of normally empty trapping sites N can be obtained from the amplitudes of the conductivity changes. For the shallow traps $N_1 = 2 \times 10^{12}$ cm^{-3}, for the deep traps $N_2 = 9 \times 10^{12}$ cm^{-3}. If we may write $1/\tau_l = N\sigma v$, where σ is the trapping cross section and v is thermal velocity, then $\sigma_1 = 4 \times 10^{-13}$ cm^2 and $\sigma_2 \simeq 1 \times 10^{-13}$ cm^2.

From the ratios $(\tau_g/\tau_l) = (\tau/\tau_r)$, the energy ϵ of the traps below the bottom of the conduction band may be computed by using the principle of detailed balance which relates σ and τ_g. We find $\epsilon_1 = 0.57$ and $\epsilon_2 = 0.79$ ev. The Fermi level for this specimen, $\epsilon_F = 0.72$ ev.

[1] J. R. Haynes and W. Westphal, Phys. Rev. **85**, 680 (1952).
[2] Trapping effects have also been observed in n-type silicon at room temperature.

The Magnetoresistance Effect in InSb

G. L. Pearson and M. Tanenbaum
Bell Telephone Laboratories, Murray Hill, New Jersey
(Received February 11, 1953)

WELKER[1] has recently shown that the compound indium antimonide is a semiconducting material with properties akin to the fourth column elements germanium and silicon and that it has unusually high electron and hole mobilities. This letter describes the preparation of the compound in a highly purified form as well as the results of magnetoresistance measurements which verify the high electron mobility. Analysis of the data indicates that the energy surfaces in InSb are spherical in nature as contrasted with the more complicated structure proposed for germanium.

The compound was prepared by melting together stoichiometric amounts of indium and antimony metals. InSb crystallizes in the zincblende lattice[2] and melts at 523°C.[1] The starting materials and the resulting compound were purified by extensive zone-refining.[3] In this manner polycrystalline specimens of 0.03-ohm cm resistivity were obtained. The primary impurity in the final material is arsenic in concentrations of approximately 0.01 percent. By spectrographic analysis all other impurities were shown to be below 0.005 percent. The compound is stoichiometric to within 0.2 percent of antimony which is the reliability of chemical analysis. All material prepared to date has been n type at room temperature and shows a reversal to p type near 175°K.

Samples suitable for making magnetoresistance measurements were prepared as previously described.[4] With **H** perpendicular to **I**, it was found that at room temperature $\Delta\rho/\rho = 8 \times 10^{-9} H^2$ over the entire range of measurement from 0 to 13 000 gauss. For this alignment simple theory[5] predicts that

$$\mu^2 = 2.6 \times 10^{16} H^{-2} \Delta\rho/\rho,$$

where μ is the electron mobility in cm^2/volt-sec. Substitution of the experimentally determined value of $H^{-2}\,\Delta\rho/\rho$ gives an electron mobility of 15 000 cm^2/volt-sec at room temperature. Hall measurements[6] on the same sample gave a value of 23 000 cm^2/volt-sec. Welker has reported[1] Hall mobilities as high as 25 000 cm^2/volt-sec. As the temperature is lowered and the magnetic field held constant, $\Delta\rho/\rho$ reaches a maximum at 270°K and then decreases.

Figure 1 is a plot of $\Delta\rho/\rho$ for the InSb sample as a function of the angle θ between the applied field **H** and the current **I** at a fixed magnetic field of 13 000 gauss. It is seen that the effect is maximum for **H** perpendicular to **I** and approaches zero for **H** parallel to **I**. This behavior is in agreement with simple theory[5] which assumes spherical energy surfaces and is in contrast with the measurements on n-type germanium[4] where nonspherical energy surfaces have been proposed by Shockley[7] to explain the results.

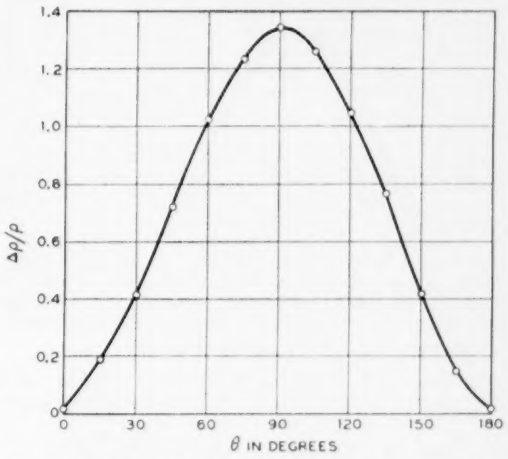

FIG. 1. Variation of $\Delta\rho/\rho$ in InSb as H is rotated through an angle θ from 0 to 180 degrees. H is 13 000 gauss and T is 300°K.

We wish to acknowledge the valuable correspondence received from H. Welker prior to the publication of his work on InSb. We wish to thank W. Shockley for his helpful discussions regarding the results reported here and W. L. Feldmann for assistance with the experimental measurements.

[1] H. Welker, Z. Naturforsch. **7a**, 744 (1952).
[2] A. Iandelli, Gazz. chim. ital. **71**, 58 (1941).
[3] W. G. Pfann, J. Metals **4**, 747 (1952).
[4] G. L. Pearson and H. Suhl, Phys. Rev. **83**, 768 (1951).
[5] A. H. Wilson, *The Theory of Metals* (Cambridge University Press, Cambridge, 1936).
[6] These measurements were performed by F. J. Morin and J. P. Maita and will be reported in detail at a later date.
[7] W. Shockley, Phys. Rev. **78**, (1950); **79**, 191 (1950).

The Continuous Layer Formation in the Atmosphere under the Influence of Solar Radiation*

H. K. Kallmann
University of California, Los Angeles, California
(Received January 12, 1953)

THE ionized layer formation in the atmosphere under the influence of a quiet sun and under the influence of a disturbed sun has been investigated. It has been found that a continuous layer formation in the ionosphere for both cases can be obtained, if account is taken of the variation with height of dissociation of molecular constituents and of the variation with height of ionization of the different constituents present at the various altitudes. By "continuous layer formation" we refer to continuous increase and decrease of the electron density with height, throughout the entire ionosphere.

Starting at the bottom of the E layer (approximately 80 km) where the effect of dissociation and ionization of the normal constituents of the atmosphere first becomes apparent, consideration has been given to three different alternatives under which an ionized layer can be formed.

Case 1.—Formation of the well-known Chapman layer.[1] A parabolic layer is formed under the influence of monochromatic radiation causing ionization (or dissociation) of a particular atmospheric constituent supposedly responsible for this layer formation. The temperature and molecular weight remain constant over the region of investigation.

Case 2.—Formation of a rather well-pronounced layer in a narrow region of altitude, a formation which is more in accordance with the findings of the radio scientists. The theory has been worked out by Nicolet[2] under the assumption that the molecular weight remains constant, and that the temperature increases with height.

Case 3.—Formation of a well-defined E layer, where the electron density increases to a maximum, then decreases with altitude to a minimum, and increases again slowly, building up for the formation of the $F1$ layer. This continuous layer formation has been found here under the assumptions that the temperature increases with altitude and, furthermore, that the molecular weight decreases with altitude. These assumptions are supported by many experimental results (see, for example, the Rocket Panel report[3] and Penndorf's[4] investigation of vertical distribution of atomic oxygen in the upper atmosphere).

The layers formed under normal conditions of the sun for all three cases are shown in Fig. 1. The calculations have been carried

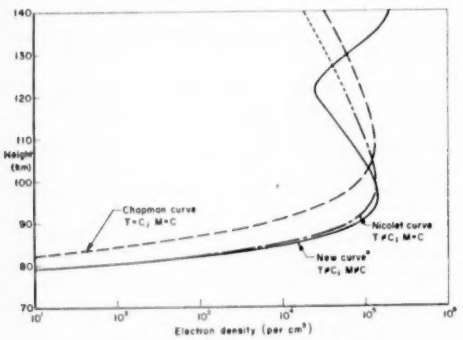

FIG. 1. Ionospheric layer formation. Quiet sun.

out on the basis of the theory developed by Chapman.[1] For Case 3, the change in molecular weight with altitude has been calculated from reference 5. It has been assumed that molecular oxygen dissociates between 80 km and 120 km, that O_2 is ionized by radiation corresponding to wavelengths of less than 972A, and that O is ionized by radiation corresponding to wavelengths of less than 910A.

A similar investigation has been made for the layer formation under the action of a disturbed sun. For a medium disturbance the increase in intensity in the corresponding wavelength region has been taken from the observed rocket results as reported by Tousey, Watanabe, and Purcell.[6] For a major disturbance, the increase in ultraviolet has been deduced from the observed increase in the visible region of the spectrum (Balmer series). Calculations have been made for all three cases. The result obtained for Case 3 only is shown here (see Fig. 2); but it should be pointed out that the decrease in height of the maximum electron density calculated for a quiet sun, becomes for a greatly disturbed sun about 19 km for the Chapman layer, about 15 km for the Nicolet layer, and about 11 km for the continuous layer (Case 3). Experimental evidence

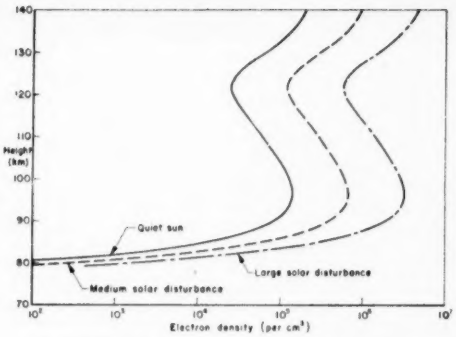

FIG. 2. Effect of disturbed sun upon the layer formation. New curves: $T \neq C$; $M \neq C$.

from radiowave investigations indicates that the change in height might be between 5 km and 10 km, depending upon the magnitude of the disturbance.

Although it is believed that the continuous layer formation, as indicated here, represents in principle the physical picture of the ionosphere better than does a discontinuous formation, the diagrams shown here present calculations only for average noontime values of electron densities which correspond to the right order of magnitude of frequencies used by the radio scientists for reflection at the E layer. It is hoped that some of the non-explainable observations in the ionosphere can be explained on the basis of this continuous layer formation process.

Work on the continuation of the electron density curve to greater altitudes is in progress. It is planned to publish a detailed account of this investigation shortly.

The author wishes to express sincere thanks to Professor Joseph Kaplan for suggesting this problem and for his very helpful interest and advice throughout this investigation.

The author is also greatly indebted to Dr. W. W. Kellogg of The Rand Corporation for many helpful discussions on the subject.

* The research was supported by the Geophysics Research Directorate, Air Force Cambridge Research Center, Cambridge, Massachusetts.

[1] S. Chapman, Proc. Phys. Soc. (London) **43**, 26 (1930).
[2] N. Nicolet, Inst. Roy. Meteorol. Belg. Mem. **19** (1945).
[3] Rocket Panel, Phys. Rev. **88**, 1027 (1952).
[4] R. Penndorf, J. Geophys. Research **54**, 7 (1949).
[5] H. K. Kallmann (to be published in the June 1953 issue of J. Geophys. Research).
[6] Tousey, Watanabe, and Purcell, Phys. Rev. **83**, 792 (1951).

The Mechanism of Phosphorescence in Crystal Phosphors

DANIEL CURIE
Laboratoire de Luminescence, Sorbonne, Paris, France
(Received December 8, 1952)

I WISH to quote here some of the results which are pointed out in my thesis[1] in a more detailed form.

Assuming a monomolecular mechanism,[2] I first deduce the statistical distribution of traps from the experimental law of decay of phosphorescence. Precise experiments are necessary. These experiments have been carried out with various conventional phosphors, ZnS(Cu) and CaS(Bi). The distributions of the lifetimes τ in the traps, for these various phosphors, calculated following Lenard's method,[3] show only a regular decrease when plotted against τ. But the statistical distributions of the depths E of the traps, deduced from the distribution of lifetimes by the well-known formula:

$$\tau^{-1} = s \exp(-E/kT),$$

(s=const) can be analyzed as a sum of several approximately

Gaussian peaks,[1,4] each of them spreading about (and possibly characterized by) a central, well-defined depth.

These discrete depths coincide with the trap-depths given by the "glow-curves" method, but this last method is not accurate enough to show the existence of distributions around these depths.

The study of the decay at different temperatures gives the same depths, and this provides a direct verification of the above fundamental formula.

This agreement between theory and experiment may be considered as a proof of the monomolecular mechanism involved. Precise experiments are indeed not consistent with the hyperbolic decay law, which is deduced, as is well known, from the assumption of a bimolecular mechanism. However, the derivation of the $1/t^2$ law implies also the assumption that there is a unique trap depth,[5] and the discrepancy may, at first sight, be attributed to this over-simplification. I have shown that for long times of decay the $1/t^2$ law should then be obtained whatever the distribution of traps may be, and so the discrepancy between the results and the bimolecular mechanism is actual.

Thus the experiments are consistent with a monomolecular decay, at least as a first approximation. This may be explained if a great number of traps are situated in the neighborhood of the activator centers. But the existence of photoconductivity and recapture implies the possibility of a more or less important bimolecular perturbation. The above results show that this perturbation is weak during the decay.

If the electrons in the conduction band have high energies, they are not stopped by the defects of the crystal, and in these conditions an approximately bimolecular mechanism is valid; this is the case if excitation or stimulation takes place, or if the electrons are accelerated by an electric field; it may also be the case during the first stage of the decay[6] (10^{-3} sec), when the electrons in the conduction band are coming out of very shallow traps. However, during the long-period phosphorescence caused by the release of electrons from deeper traps, the conduction electrons have very low energies because of the need of a thermal activation (wave mechanical calculations[7] show that these energies are less than kT). They cannot then go far from the traps, and they often fall into the next center, in agreement with an approximately monomolecular decay.

Even in this case of monomolecular decay, however, retrapping takes place if different traps are situated around the same center; the possibility of a bimolecular perturbation also involves recapture. I have studied theoretically the way in which the decay depends on this phenomenon. Analogies appear between the refilling of shallow traps by electrons escaped from deeper traps, and chains of successive radioactive disintegrations. For instance, the quick decay of the glow curves obtained when the time elapsed after the end of the excitation increased is *not* an evidence against recapture, exactly as the activity of a mixture containing comparable weights of radium and radon decreases first with the period of radon (not of radium), and this is not a proof that radium disintegration does not produce radon.

Experiments show indeed that recapture takes place during spontaneous decay[8]; but the phenomenon is found to be much more important under infrared stimulation,[9] and the better the crystallization, the more pronounced is the phenomenon, in agreement with the views expressed above.

[1] D. Curie, Thesis, Paris, March 21, 1951 [published in Ann. phys. **9**, 749 (1952)].
[2] J. T. Randall and M. H. F. Wilkins, Proc. Roy. Soc. (London) **A184**, 366 (1945). G. F. J. Garlick, *Cornell Symposium of the American Physical Society* (John Wiley and Sons, Inc., New York, 1948), p. 97.
[3] P. Lenard, *Handbuch der Experimental Physik* (J. Springer, Berlin, 1928), Part I, p. 181.
[4] D. Curie, Compt. rend. **229**, 193 (1949); and **229**, 1321 (1949). See also G. M. Nazarian, Spring Meeting, Electrochemical Society, Philadelphia, May 4–8, 1952 (unpublished).
[5] See reference 2, G. F. J. Garlick, p. 91.
[6] Pointed out by V. V. Antonov-Romanovskii; see W. Lewschin, Acta Phys. Polon. **5**, 310 (1936).
[7] D. Curie, J. phys. radium **12**, 920 (1951).
[8] J. Mattler and D. Curie, Compt. rend. **230**, 2086 (1950).
[9] G. F. J. Garlick and D. F. Mason, J. Electrochem. Soc. **96**, 90 (1949); D. Curie, Nature **166**, 70 (1950); Compt. rend. **230**, 1400 (1950).

Formation of the *D* Layer

K. Watanabe, Frederick Marmo,* and Edward C. Y. Inn
Geophysics Research Directorate, Air Force Cambridge Research Center, Air Research and Development Command, Cambridge, Massachusetts
(Received February 13, 1953)

Of the several processes suggested for the formation of the *D* layer, the following appear to have the strongest support:

$$O_2+h\nu \text{ (900–1000A, spectral region } A)\rightarrow O_2^+ + e, \qquad (A)$$

$$NO+h\nu \text{ (1100–1300A, spectral region } B)\rightarrow NO^+ + e. \qquad (B)$$

Recently, Mitra[1] has reported a detailed calculation to show that the *D* layer is produced by process *A*, which was originally proposed by Mitra, Bhar, and Ghosh.[2] On the other hand, Bates and Seaton,[3] after examining various processes, have shown that the *D* layer may very well be formed primarily by process *B*, which was suggested earlier by Nicolet.[4]

Spectroscopic data seem to show that the *D* layer cannot be produced chiefly by process *A*. As pointed out by Bates,[3] spectrograms by Hopfield[5] show that a 4-mm layer of air completely absorbs radiation in spectral region *A*. Tanaka,[6] who used higher dispersion, confirms Hopfield's results and estimates from pressures used that the windows in region *A* are about two orders of magnitude less transparent than those in region *B*.

Using a vacuum monochromator and photoelectric detection, absorption cross sections of O_2 were obtained[7] in the spectral region 1050–1900A. These data, partly reproduced in Fig. 1, show

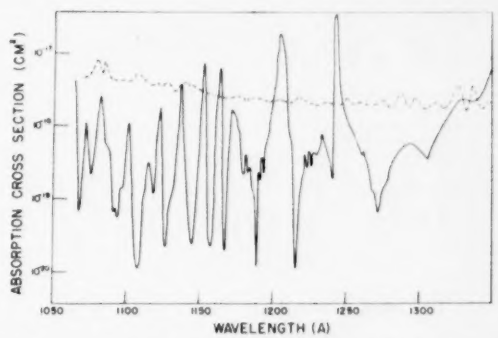

FIG. 1. The absorption cross sections of molecular oxygen (solid curve) and nitric oxide (dashed curve).

that the absorption cross sections of the oxygen windows in the region 1100–1250A are about 10^{-20} cm². Moreover, the absorption cross section for the continuum just below 1100A is about 10^{-19} cm², and should be still higher in region *A* on the basis of the data obtained by Hopfield and Tanaka. A reasonable value for air in the spectral region *A* would be 10^{-19} cm² rather than $10^{-20}-5\times10^{-22}$ which were used by Mitra.[1] If the higher value is accepted, process *A* would be placed in the lower *E* layer.

In contrast, process *B* has the very attractive feature that NO can be ionized by Lyman alpha which has now been observed[8] in the *D* layer as a strong, solar emission line. However, the concentration of atmospheric NO is not known. If the tentative estimate made by Bates[3] from a rocket spectrogram[9] is the correct order of magnitude, our absorption data for NO seem to indicate that the major part of the production of *D* layer can be attributed to process *B*.

Using NO samples (impurity less than 0.1 percent), the absorption intensity of this gas was measured[10] in the region 1070–2300A. A moderately strong absorption continuum was found in the region below 1400A. The absorption cross section is shown in Fig. 1 by the relatively flat curve, a continuum with a number of weak diffuse bands.

A preliminary photoionization experiment using a vacuum monochromator showed that the ionization current appeared

TABLE I. Absorption cross sections (in cm²) of several atmospheric gases at Lyman alpha.

Gas	Value by Preston	Our value
N_2	$<2.0 \times 10^{-22}$	$<3.0 \times 10^{-22}$
O_2	1.04×10^{-20}	1.0×10^{-20}
CO_2	7.5×10^{-20}	7.3×10^{-20}
H_2O	1.45×10^{-17}	1.44×10^{-17}
O_3		2.4×10^{-17}
CH_4		1.78×10^{-17}
NO		2.5×10^{-18}
N_2O		2.4×10^{-18}
NH_3		7.1×10^{-18}

abruptly at 1345A or 9.20 ev. Rather high yield was obtained over the entire region down to 1070A. Even with narrow slits (0.05 mm) giving a band width of 0.85A the ion current was as high as 5×10^{-11} amp (at Lyman alpha). From the light-intensity measurement based on previous thermocouple data,[11] it was found that photoionization accounted for about fifty percent of the total absorption at Lyman alpha. Thus, the ionization cross section for NO is about twenty-five times larger than the estimated value.[3]

The width and the transparency of the oxygen windows in region *B* are such that photons of required energy, particularly Lyman alpha, can penetrate deep into the *D* layer. In anticipation of the importance of Lyman alpha, absorption cross sections of several gases are listed in Table I, together with those obtained by Preston.[12]

* Also Harvard University, Cambridge, Massachusetts.
[1] A. P. Mitra, J. Geophys. Research **56**, 373 (1951).
[2] Mitra, Bhar, and Ghosh, Indian J. Phys. **12**, 455 (1939).
[3] D. R. Bates and M. J. Seaton, Proc. Phys. Soc. (London) **B63**, 129 (1950).
[4] M. Nicolet, Mem. Roy. Met. Inst. Belgium **19**, 1 (1945).
[5] J. J. Hopfield, Astrophys. J. **104**, 208 (1946).
[6] Y. Tanaka (unpublished spectrograms and private communication).
[7] Watanabe, Inn, and Zelikoff, J. Chem. Phys. (to be published).
[8] Department of Physics, University of Colorado (private communication). See Letter by W. B. Pietenpol *et al.*, this issue.
[9] Durand, Oberly, and Tousey, Astrophys. J. **109**, 1 (1949).
[10] Marmo, Zelikoff, and Tanaka, J. Opt. Soc. Am. **42**, 870 (1952).
[11] K. Watanabe and E. C. Y. Inn, J. Opt. Soc. Am. **43**, 32 (1953).
[12] W. M. Preston, Phys. Rev. **57**, 887 (1940).

Lyman Alpha-Line Photographed in the Sun's Spectrum*

W. B. PIETENPOL, W. A. RENSE, F. C. WALZ, D. S. STACEY, AND J. M. JACKSON
Department of Physics, University of Colorado, Boulder, Colorado
(Received January 26, 1953)

MEMBERS of the Physics Department of the University of Colorado at Boulder have succeeded in obtaining a picture of the sun's spectrum from an altitude of over fifty miles above the surface of the earth. By means of precision instruments sufficiently rugged to withstand high acceleration installed in the nose cone of an Aerobee rocket, a film was exposed, and the radiation from the sun in the far ultraviolet was recorded in regions heretofore not photographed. The results of this work were first reported as a post-deadline paper on January 22, 1953 at the Harvard University, Cambridge, Massachusetts meeting of the American Physical Society.

During the past three years a number of physicists at Colorado have been working on a sun-seeking device or pointing control for installation on high altitude rockets. This is an exceedingly complicated electronic and mechanical device to hold an instrument pointing at the sun during the flight of the rocket which may roll and yaw.

On December 12, 1952 an Aerobee rocket was fired from the Holloman Research and Development Center, New Mexico, carrying the University of Colorado pointing control and spectrograph. This is the first instrument of its kind which pointed directly at the sun for a considerable period. An exposure was taken for 28 seconds and a photograph of the sun's spectrum was obtained. Where previously scientists had photographed the spectrum to about 2000A, in this experiment for the first time the radiation in the far ultraviolet emitted by the hydrogen in the sun has been photographed. Much of this radiation is concentrated in a spectrum line at 1216A, namely the Lyman alpha-line. On the day of the flight the solar activity, represented by hot spots or flares, was reported by the Harvard-Colorado High Altitude Laboratory as being slightly above normal.

On the film the Lyman alpha-emission line at 1216A stands out clearly above the background density. A preliminary examination of the film indicates that the width of the line may be approximately six A and that the intensity of the Lyman alpha-emission outside of the earth's atmosphere may be of the order of 0.03 microwatt per square centimeter. A more careful analysis is being made, and the results will be reported in the near future.

The authors extend their sincere appreciation to W. E. Behring, J. P. Curtis, Russell Nidey, G. A. Stith, Barbara Todd, and other members of the Physics Department for valuable assistance. Much credit is due Dr. Marcus O'Day and Dr. Howard Edwards of the Cambridge Research Center for valuable cooperation in making this work possible.

* This research reported in this paper has been sponsored by the Geophysics Research Directorate of the Air Force Cambridge Research Center, Air Research and Development Command, under Contract W19-122 ac-9.

Helium II Film Transport Rates over Various Surfaces*

B. SMITH AND H. A. BOORSE†
Pupin Physics Laboratories, Columbia University, New York, New York
(Received February 16, 1953)

THE experimental investigation of the helium II film transport rate over various surfaces, previously reported from this laboratory,[1,2] is now being reviewed and extended. Although the present work is still in progress, a brief summary of certain results appears to merit presentation at this time, especially in view of a recent publication by Chandrasekhar.[3]

The transport rates tabulated below were obtained by means of the capacitor depth gauge method,[1,2] modified to improve the precision of the measurements. In the present arrangement, transport vessel-capacitors were constructed so that a recording potentiometer not only indicates the motion of the liquid level but also registers the time required to empty (or fill) various sections of the transport vessel. This elapsed time, when correlated with the appropriate volume and limiting perimeter, leads directly to a rate determination. Values cited in Table I are taken from smooth curves constructed in most cases from fifty or more individual rate measurements taken at temperatures between the lambda-point and just below 1°K.

TABLE I. Transport rate in cm³/sec-cm $\times 10^5$.

	1.0°	1.2°	1.4°	1.6°	1.8°	2.0°
Lucite	···	12.2	11.6	11.0	8.9	4.7
Machined nickel	···	14.8	14.6	13.8	11.3	6.8
Machined nickel[a]	13.8	13.7	13.4	12.3	9.8	5.7
Pyrex (ordinary)	···	9.6	9.5	9.1	7.4	4.4
Pyrex (precision bore)	11.8	11.6	11.2	10.3	8.3	4.9
Quartz (transparent)	10.4	10.0	9.5	8.6	7.2	4.3
Quartz (translucent)	11.2	10.7	10.0	8.6	7.7	5.0
Machined thorium[b]	···	40.9	39.1	36.1	28.5	15.5
Machined thorium[c]	···	16.5	16.2	14.6	11.5	7.1

[a] After removal from cryostat and reinstallation and measurement three months later.
[b] Averaged over entire vessel.
[c] At bottom of vessel.

The Lucite measurements previously reported were noted as tentative.[1,2] The current data (using the same beaker with a new capacitor depth gauge) duplicates neither the peak of the earlier report nor the maximum noted by Chandrasekhar.[3] Instead the results show a smooth rate-temperature variation whose absolute values are in agreement with the earlier curve omitting the peak.

Previously the absence of data for the low temperature expansion coefficient of Lucite prevented adequate correction for the contraction of this material. The present values are corrected for this effect.[4,5]

It is interesting to note that in carrying out a long series of measurements on nickel we obtained in one instance a transport rate curve characterized by a maximum of the type which has on occasion been reported not only for methyl methacrylate polymers,[3] but also for glass[6-8] and platinum.[9] However, on prior and subsequent runs a reproducibly different and more conventional rate-temperature variation was obtained. These rates, noted in the table, are substantially lower than those reported by Mendelssohn and White for a nickel beaker which had been "dipped into warm hydrochloric acid."[9] This is in general agreement with the previous observation that higher rates are obtained for etched metal surfaces.[1,2]

The results obtained for glass in this and other investigations,[7,10-12] when considered in conjunction with the known properties of glass surfaces,[13-15] suggest that a unique rate of transport over glass should not be expected.

Fused quartz (both transparent and translucent) was chosen as a source of data on vitreous materials other than glass. Data obtained by direct visual observation of transport using a clear quartz capillary were in excellent agreement with the results of electrical measurements.

Thorium fulfills the requirement of being a superconductor whose transition temperature is located in the region where the film transport rate is a slowly varying function of temperature. If there is an interaction between the film and the underlying surface which is altered by the onset of superconductivity, it might be expected to be most clearly distinguishable under such conditions. The zero-field transition temperature of our sample was determined by an induction method. The result, 1.38°K, is in good agreement with that of Shoenberg.[16] The transport data thus far obtained (on widely separate occasions) are characterized by an extreme height dependence and, in the region below about 1.4°K, by anomalously high scatter. Pending further investigation, the origin of this unusual behavior remains unexplained.

In conclusion we note that after suitable normalization at 1°K, the data cited above do not yield a universal curve for the temperature dependence of the transport rate.

* Assisted by the U. S. Office of Naval Research and Linde Air Products Company.

† Barnard College, Columbia University, New York, New York.

[1] J. G. Dash and H. A. Boorse, Phys. Rev. **82**, 851 (1951).
[2] J. G. Dash and H. A. Boorse, National Bureau of Standards Circular 519 (1952), p. 169.
[3] B. S. Chandrasekhar, Phys. Rev. **86**, 414 (1952).
[4] W. F. Giauque *et al.*, Rev. Sci. Instr. **23**, 169 (1952).
[5] H. L. Laquer and E. L. Head, Atomic Energy Commission Report AECU-2161, 1952 (unpublished).
[6] J. G. Daunt and K. Mendelssohn, Proc. Roy. Soc. (London) **A170**, 423, 439 (1939).
[7] H. A. Fairbank and C. T. Lane, Phys. Rev. **76**, 609 (1949).
[8] E. Ambler and N. Kurti, Phil. Mag. **43**, 260 (1952).
[9] K. Mendelssohn and G. K. White, Proc. Phys. Soc. (London) **A63**, 1328 (1950).
[10] Webber, Fairbank, and Lane, Phys. Rev. **76**, 609 (1949).
[11] K. R. Atkins, Proc. Roy. Soc. (London) **A203**, 240 (1950).
[12] G. J. van den Berg, Report of Proceedings of Oxford Conference, (August 1951), p. 69 (unpublished).
[13] N. K. Adam, *The Physics and Chemistry of Surfaces* (Oxford University Press, London, 1941), third edition, Chap. 5.
[14] J. W. McBain, *The Sorption of Gases and Vapours by Solids* (Routledge, London, 1932), Chap. 7 and 10.
[15] J. E. Stanworth, *The Physical Properties of Glass* (Oxford University Press, London, 1950).
[16] D. Shoenberg, Proc. Cambridge Phil. Soc. **36**, 84 (1940).

Activity Assignment to Titanium 51

WILLIAM R. HAMMOND,* D. N. KUNDU, AND M. L. POOL
Ohio State University, Columbus, Ohio

(Received February 9, 1953)

TO the isotope Ti^{51} have been attributed three activities with half-lives 2.8 minutes,[1] 6 minutes,[2] and 72 days.[3] The first[2] and last of the above three activities have been removed. During a neutron irradiation a small amount of hafnium impurity in the titanium was shown chemically to be responsible for the 72-day activity.[4] The 6-minute activity has been confirmed[5] with slow neutron irradiation but not with chemical separations. Since there are serious obstacles in rapid titanium chemical separations, it was thought that a series of cross bombardments with appropriate particles and enriched isotopes[6] would be capable of removing any doubt as to the existence of a 6-minute activity attributable to Ti^{51}.

$Ca^{48}(\alpha, n)Ti^{51}$: Calcium carbonate, enriched in isotope of mass number 48 from normal abundance of 0.15 percent to 7.49, was bombarded with 20-Mev alpha-particles from the cyclotron. Since the abundance of Ca^{40} was still very high, 89.68 percent, the 3.9-hour Sc^{43} positron activity was so intense that decay readings were necessarily made in a magnetic spectrometer. Figure 1 shows the

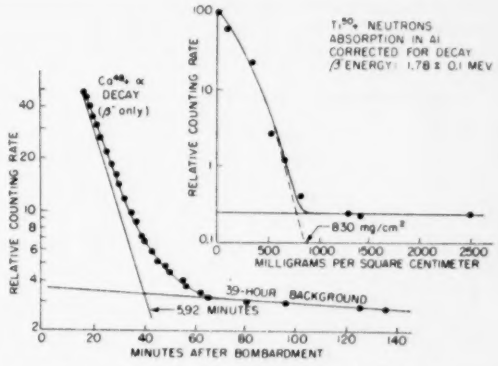
RELATIVE COUNTING RATE
MINUTES AFTER BOMBARDMENT
Ca48 α DECAY (β⁻ only)
T½ 50% NEUTRONS ABSORPTION IN Al CORRECTED FOR DECAY
β⁻ ENERGY: 1.78 ± 0.1 MEV
830 mg/cm²
MILLIGRAMS PER SQUARE CENTIMETER
39-HOUR BACKGROUND
5.92 MINUTES

FIG. 1. Decay of Ti^{51} from $Ca^{48}+\alpha$ and absorption of negatrons of Ti^{51} from $Ti^{50}+n$.

half-life to be 5.92±0.15 minutes after the 3.9-hour annihilation background activity was subtracted.

$Ti^{50}(n, \gamma)Ti^{51}$: Titanium oxide enriched in isotope of mass number 50 from normal abundance of 5.34 percent to 84.69 was irradiated with neutrons slowed down in paraffin from a proton bombardment of beryllium. A half-life of 5.89±0.15 minutes was observed. Figure 1 also shows an absorption curve. The beta-energy was found to be 1.78±0.1 Mev which compares favorably with the two previous values of 1.6 Mev[7] and 2 Mev.[2]

A gamma-ray was evident in the Ti^{51} activity, although it was not specifically investigated here. The energy has been reported as 0.320 kev.[7]

$Cr^{54}(n, \alpha)Ti^{51}$: Chromium oxide, enriched in the isotope of mass number 54 from normal abundance of 2.30 percent to 83.1, was irradiated with fast neutrons. The 6-minute activity was again clearly observed. The presence of 3.7-minute activity V^{52} prevented an accurate half-life determination.

$V^{51}(n, p)Ti^{51}$: Vanadium metal when irradiated with fast neutrons yielded the 6-minute activity and again the interfering 3.7-minute activity.

From the four types of reactions, a consistent 6-minute activity was observed with an average half-life of 5.89±0.2 minutes, negatrons of energy 1.78±0.1 Mev, and a low energy gamma-ray. A definite assignment can be made to Ti^{51}.

It is a pleasure to acknowledge the support received through the Ohio State University Development Fund.

* Major, United States Air Force. Research under auspices of U. S. Air Force Institute of Technology, Wright-Patterson Air Force Base, Dayton, Ohio.

[1] Harold Walke, Phys. Rev. **52**, 777 (1937).
[2] Seren, Friedlander, and Turke, Phys. Rev. **72**, 888 (1947).
[3] Walk, Williams, and Evans, Proc. Roy. Soc. (London) **A171**, 360 (1939).
[4] Miskel, der Mateosian, and Goldhaber, Phys. Rev. **79**, 193 (1950).
[5] E. der Mateosian and M. Goldhaber, Phys. Rev. **79**, 192 (1950).
[6] Supplied by the Y-12 Plant, Carbide and Carbon Chemicals Corporation, through the Isotopes Division, U. S. Atomic Energy Commission, Oak Ridge, Tennessee.
[7] E. Segrè and A. C. Helmholz, Revs. Modern Phys. **21**, 271 (1949).
[8] E. der Mateosian, Phys. Rev. **83**, 223 (1951).

Radioactive Decay of Y^{91}

F. I. Boley and D. S. Dunavan
Scott Laboratory, Wesleyan University, Middletown, Connecticut
(Received February 10, 1953)

THE 61-day Y^{91} decay[1,2] has been investigated using scintillation counters. The results of this investigation indicate that the decay is by negatron emission only and is unaccompanied by gamma-rays.

An analysis of the beta-spectrum yielded an end point of 1.54 ±0.05 Mev and the familiar first-forbidden shape. When the first-forbidden correction was applied to the data, the curve obtained was straight for energies above 0.5 Mev. Below this energy electron scattering began to produce large numbers of low level counts.

One of the gamma-rays reported by Langer and Price[1] was observed at 1.16±0.06 Mev, as shown in the gamma-spectrum of Fig. 1. The curve continues to rise for pulse heights below those

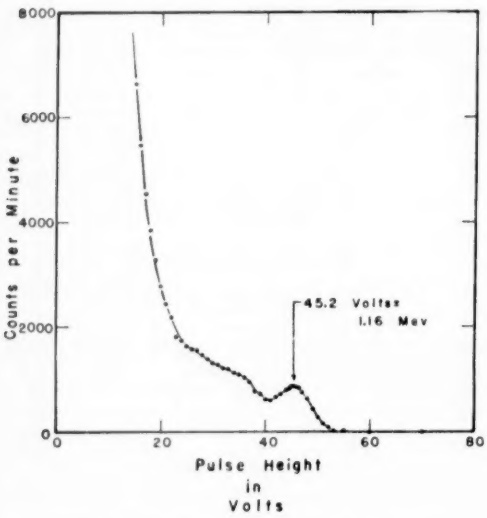

FIG. 1. Gamma-ray spectrum obtained from Y^{91} sample.

shown, and only one gamma-ray is apparent. Aluminum was used to absorb the 1.54-Mev betas.

It was not possible to detect the presence of a low energy (1.54 −1.16=0.38 Mev) beta-group by examination of the Fermi plot, owing to the large amount of electron scattering below 0.5 Mev. Experiments designed to check the possible existence of other decays in cascade with the 1.16-Mev gamma-ray were performed.

The equipment used in these experiments consisted of two independent energy-sensitive channels with provision for detecting coincidences between their output pulses. Each channel used RCA 5819 photomultipliers equipped with either anthracene or NaI(Tl) crystals depending on whether betas or gammas were to be detected. The photomultipliers were cathode followers coupled to fast amplifiers which in turn, fed Atomic Instrument Company Model 510 pulse-height analyzers. A circuit was provided for registering coincidences between the analyzer outputs.

With one of the energy-sensitive channels set to accept the 1.16-Mev gamma-rays, the other was used to scan the gamma- and the beta-spectra. No coincidences above the chance rate between the two channels were observed in either case. Apparently only one gamma-level exists and is not fed by negatron emission.

The half-lives of both the beta- and gamma-activities were measured and found to be 61±1 days and 160±30 days, respectively.

The ratio of the number of betas to gammas was determined in two ways. First, the number of beta- and gamma-transitions per unit time was obtained by taking the total number of counts in the beta- and gamma-spectra, using the scintillation spectrometer. An aluminum absorber was used to absorb the electron component when the gamma-spectrum was obtained. When account was taken of the detector efficiencies, the beta-gamma-ratio obtained was 20±4. The second method employed a Geiger counter with appropriate beta-absorbers. Making use of the Geiger counter efficiencies, the corresponding ratio was determined as 21±5. The initial ratio of the decay rates calculated on the basis of the half-lives given above was 150. The discrepancy between this ratio and the 1000 figure given by Langer and Price may be attributed to the more careful chemical purification techniques employed by them.

It therefore appears that the Y^{91} activity consists entirely of the 1.54-Mev beta-decay and that the gamma-ray at 1.16 Mev is associated with an unidentified impurity in the source.

[1] L. M. Langer and H. C. Price, Phys. Rev. **76**, 641 (1949).
[2] N. E. Ballou, *Radiochemical Studies: The Fission Products* (McGraw-Hill Book Company, Inc., 1950), National Nuclear Energy Series, Plutonium Project Record, Vol. 9, Div. IV, Paper No. 116.

Evidence for a 25.5-Day Sr−76-Sec Rb Chain†

Paul Kruger and Nathan Sugarman
Institute for Nuclear Studies, University of Chicago, Chicago, Illinois
(Received February 18, 1953)

STRONTIUM was separated from the spallation products of silver irradiated with 450-Mev protons at the University of Chicago synchrocyclotron. A nuclide of about 25-day half-life was found in the decay curve of the strontium samples. Careful analysis of the decay curves of repurified samples yielded a half-life of 25.5±0.5 days. Absorption measurements through aluminum and lead indicated beta-particles of 4.2±0.2-Mev maximum energy, and counting in a magnetic field showed these particles to be positrons.

At the time this work was done, no isotope of strontium having these radiation properties was known,[1,2] although it was later found that the nuclide had already been observed by Castner.[3] Mass number 82 was assigned on the basis of proton activation studies. The observed half-life was 25.5 days, and the radiations were shown to be positrons of 3.15±0.03-Mev maximum energy, determined by spectrometer measurements. Attempts to isolate the rubidium daughter led to half-life limits of less than a few minutes or greater than a year, despite the fact that a 6.3-hr Rb^{82} had been reported.[4] It was postulated that nuclear isomerism exists for Rb^{82}, and if the hard positron belongs to the rubidium daughter of the 25.5-day Sr^{82}, the half-life of the rubidium daughter would be of the order of 10 sec for an allowed decay.

A search was made for the radioactive rubidium daughter of the 25.5-day Sr by dissolving strontium samples and quickly removing the rubidium by precipitation. An activity was found in the rubidium samples with a half-life of 76±5 sec. A typical decay curve of separated rubidium is given in Fig. 1. The activity isolated in the rubidium fractions from four strontium samples agreed to within 25 percent with the activity of 25.5-day Sr in the strontium samples. The energy of the radiations of the rubidium activity was not measured, but it is assumed that the energetic positrons are associated with the decay of the 76-sec Rb.

A search was also made for the 6.3-hr Rb^{82}. Another strontium sample was dissolved, and the rubidium was carefully cleaned from the strontium. No evidence for the 6.3-hr Rb^{82} was observed. On the assumption of equal counting efficiencies for the 6.3-hr Rb^{82} and the 76-sec Rb, the upper limit to the branching ratio for decay of Sr^{82} to 6.3-hr Rb^{82} is 1 percent.

The existence of the 76-sec daughter of the 25.5-day Sr requires that either the mass assignment for this chain is not 82, or that nuclear isomerism exists with a highly forbidden transition be-

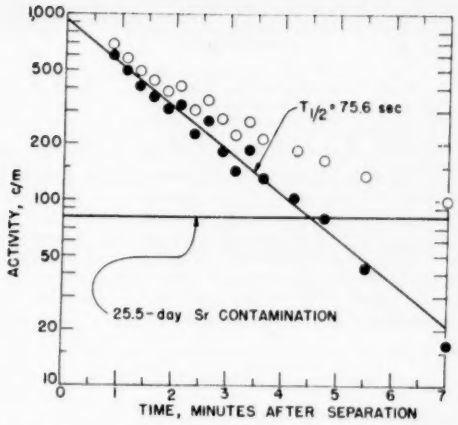

FIG. 1. Decay curve of rubidium separated from 25.5-day Sr. ○, original points; ●, activity of 25.5-day Sr contamination subtracted from original points.

tween the 6.3-hr Rb and the 25.5-day Sr, as well as between the 6.3-hr Rb and the 76-sec Rb. Although the possibility of isomerism seems quite likely because of spin considerations in the region of Rb^{82}, the recent spin assignment of 3+ and the proposed decay scheme[5] of 6.3-hr Rb^{82} make it difficult to explain the isomery of the 76-sec Rb with the 6.3-hr Rb^{82}.

* This research was supported in part by a grant from the U. S. Atomic Energy Commission.

[1] Way, Fano, Scott, and Thew, *Nuclear Data*, National Bureau of Standards Circular No. 499 (1950).
[2] G. T. Seaborg and I. Perlman, Revs. Modern Phys. **20**, 585 (1948).
[3] S. V. Castner, University of California Radiation Laboratory Unclassified Report No. 942 (1950); S. V. Castner and D. H. Templeton, Phys. Rev. **88**, 1126 (1952).
[4] D. G. Karraker and D. H. Templeton, Phys. Rev. **80**, 647 (1950).
[5] C. M. Huddleston and A. C. G. Mitchell, Phys. Rev. **88**, 1350 (1952).

The Angular Correlation of the Cascade Gamma-Rays from the Decay of Au^{198}

CARLTON D. SCHRADER, EDWARD B. NELSON, AND JAMES A. JACOBS
Department of Physics, State University of Iowa, Iowa City, Iowa
(Received February 16, 1953)

ALTHOUGH the beta-decay of Au^{198} occurs predominantly to the 0.411-Mev level in Hg^{198}, about 2 percent of the decay occurs to the 1.09-Mev level. The gamma-decay of the 1.09-Mev level occurs by cascade through the 0.411-Mev level as well as by a direct transition to the ground state.[1] Our observed angular correlation of the cascade gamma-rays determines the spin and parity of the 1.09-Mev level as 2+ in agreement with the internal conversion results of Elliott and Wolfson,[2] and the 0.68-Mev radiation has been found to be a 60 percent quadrupole, 40 percent dipole mixture.

The detectors consisted of two magnetically shielded scintillation counters using 2-in. by $1\frac{3}{4}$-in. cylindrical NaI(Tl) crystals and RCA 5819 photomultiplier tubes. Aluminum shielding was used to prevent the counting of beta-particles. Integral pulse height selection was used so that one detector counted only the 0.68-Mev gammas while the other counted both 0.411 and 0.68-Mev gammas. The bias settings were high enough so that no scattering between counters of gammas from the Au^{198} decay could be detected. The correction for accidentals was about 20 percent of the total coincidence counting rate, while the background coincidence correction was about 10 percent of the total. After these corrections the experimental curve was symmetric about 90°.

The data were fitted by the method of weighted least squares to a Legendre polynomial expansion of the form $1+A_2P_2(\cos\theta)+A_4P_4(\cos\theta)$, where $A_2=-0.261\pm0.023$ and $A_4=0.137\pm0.012$. Since the lifetime of the 0.411-Mev state is short (10^{-11} second)[3,4] compared to the time of Larmor precession, the observed correlation should be unperturbed by extra-nuclear magnetic fields.

The ground state of the even-even Hg^{198} nucleus is assumed to have zero spin and even parity. Several investigators[5,6] have found from internal conversion measurements that the 0.411-Mev radiation is pure electric quadrupole, from which it follows that the spin of the first excited state in Hg^{198} is 2. The existence of the 1.09-Mev cross-over gamma means that the spin of the second excited state cannot be zero. Also from relative intensity considerations a spin greater than three is very improbable since the cross-over gamma competes favorably with the cascade gammas.

On the assumption of a spin of 1, 2, or 3 for the second state, there is no theoretical function for pure dipole or quadrupole radiation which fits the data. Furthermore, any dipole-quadrupole mixture from a second excited state with odd integer spin would theoretically yield a coefficient $\leqslant 0$ for the $P_4(\cos\theta)$ term, while the observed coefficient is positive. Hence, the spin of the second excited state of Hg^{198} is 2. A theoretical function, corrected for finite resolution of the counters, assuming a spin of 2 and a 60 percent quadrupole, 40 percent dipole mixture for the 0.68-Mev radiation agrees best with the data, while any mixture between 65 percent Q—35 percent D and 55 percent Q—45 percent D would be statistically allowable. Full details will soon be published.

[1] P. E. Cavanagh, Phys. Rev. **82**, 791 (1951).
[2] L. G. Elliott and J. L. Wolfson, Phys. Rev. **82**, 333 (1951).
[3] P. B. Moon, Proc. Phys. Soc. (London) **A64**, 76 (1951).
[4] Bell, Graham, and Petch, Can. J. Phys. **30**, 35 (1952).
[5] M. Moon, Thesis, State University of Iowa, 1951 (unpublished).
[6] L. Simons, Phys. Rev. **86**, 570 (1952).

Spectrometer Measurement on the High Energy Positrons of Sodium 22*

BYRON T. WRIGHT
Department of Physics, University of California, Los Angeles, California
(Received December 18, 1952)

USING a small solenoidal spectrometer,[1] a measurement of the ratio R of the partial decay constant for the lower energy spectrum A to that of the higher energy spectrum B of positrons from Na^{22} was made.

The source,[2] whose strength was approximately 0.3 millicuries, was deposited on a Nylon foil whose thickness was 2.5 mg cm^{-2}. The source was 15 mm in diameter and its average thickness 2 mg cm^{-2}.

The detector was a miniature end-window Geiger counter of length 25 mm and cathode diameter 7 mm. The end of the counter formed the "energy-selecting hole" of the spectrometer. The

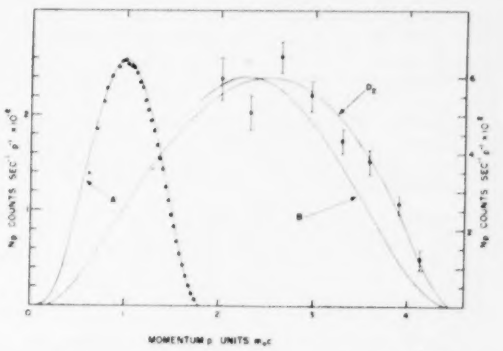

FIG. 1. Momentum plots for the two positron spectra of Na^{22}.

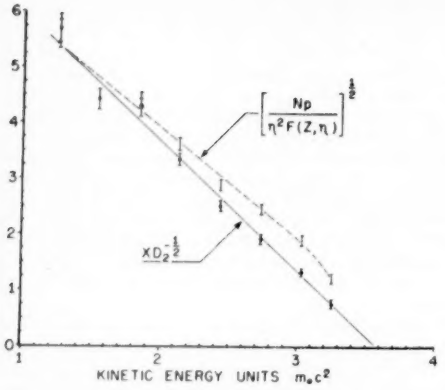

FIG. 2. Kurie plots of spectrum B.

background counting rate with no source in the spectrometer was 0.07 counts sec^{-1}. This increased to 0.09 counts sec^{-1} with the 0.3 millicurie source in position and with an aluminum plate blanking off the "angle selecting baffles" near the source. The background further increased to 0.10–0.12 counts sec^{-1} with the source in position and with a Lucite ring sufficiently thick to stop the most energetic positrons placed at the ring focus. The values quoted are for the range observed in spectrum B, points near the upper limit corresponding to the smaller background. It was by the use of such a ring absorber placed at the ring focus that a background counting rate for each of the points observed in spectrum B was determined. The most uncertain of these background rates had a standard deviation of 8 percent.

Momentum plots of the observed spectra are shown in Fig. 1. The scale of ordinates is in counts sec^{-1} per unit momentum (the momentum being measured in units m_0c). The lines A and B indicate theoretical shapes for allowed spectra. Spectrum A agrees with the theoretical shape down to 0.8 m_0c, a point well below the maximum. A Kurie plot yields an end point of 540±5 kev, in agreement with prior results.[3]

Because of the great similarity of the transitions between the ground states of $Be^{10}-B^{10}$ and $Na^{22}-Ne^{22}$, the so-called D_2 correction[4] was considered for spectrum B. The data fit the D_2 spectrum considerably better than the allowed shape B. This is indicated by Fig. 1 and shown more clearly by the Kurie plots of spectrum B in Fig. 2. The end point of spectrum B is at 1830±60 kev, a value in agreement with the sum of the energy of the gamma-ray (1277 kev)[5] of Na^{22} and the end point of spectrum A (542 kev).[3] The net counting rate for points near the peak of spectrum B was 1.5 times the background rate. The standard deviations in the net counting rates are indicated.

To obtain R we compared the areas under curves A and D_2. The result is $R=1600\pm400$. This leads, using a half-life of 2.60 years[6] for the decay via spectrum A, to a decay constant for the decay of Na^{22} to the ground state of Ne^{22} of $\geq 5.3\pm1.0\times10^{-12}$ sec^{-1}, the value being greater if a fraction of the decay of spectrum B is by orbital electron capture.

The ft value which results is $\sim10^{13}$. This is an order of magnitude less than the value based[7] on earlier experimental work[8] and about half an order less than the value based in part on a theoretical consideration.[9]

* Supported in part by the joint program of the U. S. Office of Naval Research and the U. S. Atomic Energy Commission.
[1] Byron T. Wright, Am. J. Phys. **20**, 230 (1952).
[2] Purchased from the Isotopes Division of the U. S. Atomic Energy Commission.
[3] Macklin, Lidofsky, and Wu, Phys. Rev. **78**, 318 (1950).
[4] R. E. Marshak, Phys. Rev. **75**, 513 (1949).
[5] D. E. Alburger, Phys. Rev. **76**, 435 (1949).
[6] L. J. Laslett, Phys. Rev. **76**, 858 (1949).
[7] Arnold M. Feingold, Revs. Modern Phys. **23**, 10 (1951).
[8] K. H. Morganstern and K. P. Wolf, Phys. Rev. **76**, 1261 (1949).
[9] E. Feenberg and K. C. Hammack, Phys. Rev. **75**, 1877 (1949).

Energy per Ion Pair for 5-Mev Alpha-Particles in Helium

T. E. BORTNER AND G. S. HURST
Health Physics Division, Oak Ridge National Laboratory, Oak Ridge, Tennessee
(Received February 6, 1953)

THE average number of ion pairs formed by Pu^{239} alpha-particles in helium has been measured. A parallel plate ionization chamber was filled to a pressure such that the alpha-particles (45 500 per minute) lost all of their energy in the sensitive volume. The rate of voltage change on an accurately calibrated condenser was measured by means of a potentiometer, using an ac operated electrometer[1] as a null indicator.

Our w values (electron volts per ion pair) agree well with the measurements of other investigators[2–5] for the following gases:

Gas	w (ev/ion pair) Present values	Other results	Reference
Nitrogen	36.3	36.3±0.4	2
Argon	26.4	26.4	3
Ethylene	28.0	28.2	4
Hydrogen	37.0	37.0	5

Because of the above agreement with other observers, it is believed that the self-absorption in the alpha-source is small.

With no purification grade A helium[6] taken from different tanks gave a spread for w between 31 and 43 electron volts. Two different methods of purification gave w for helium equal to 46.0±0.4 electron volts. One method of purification consisted of flowing helium over cocoanut charcoal held at liquid nitrogen temperature, the ionization being measured during flow. Stopping the flow resulted in a rapid decrease in w (increase in ionization) after a few minutes. The second method of purification involved continuous circulation of helium over metallic calcium kept at 400°C. Jesse[7] associates low values of w for helium with gas impurity. He obtained a value of 41.3 electron volts as compared with the present value of 46 electron volts.

It is interesting to note that Fano[8] based his argument that the value of w is independent of the ionization potential on a very much lower experimental value for helium, namely, 30 electron volts. His choice of comparing hydrogen and helium was unfortunate, for indeed the present results show an increase in w with the ionization potential for these gases.

[1] F. M. Glass, Nucleonics **10**, No. 2, 36 (1952).
[2] Alder, Huber, and Metzger, Helv. Phys. Acta **20**, 234 (1947).
[3] W. P. Jesse, Argonne National Laboratory Report ANL-4778 (unpublished).
[4] J. Dainty, National Research Council of Canada, Atomic Energy Project Report CRM-482, 1950 (unpublished).
[5] J. M. Valentine and S. C. Curran, Phil. Mag. **43**, 964 (1952).
[6] Grade A is the designation of helium bottled by the U. S. Bureau of Mines. This helium has a purity of 99.99 percent when bottled. This information was supplied by Dr. M. M. Deaton, Chief, Research Branch, Helium Division, Region IV (private communication).
[7] W. P. Jesse, Argonne National Laboratory Report ANL-4828 (unpublished).
[8] U. Fano, Phys. Rev. **70**, 44 (1946).

Elastic Pion-Deuteron Scattering*

E. ARASE, GERSON GOLDHABER, AND S. GOLDHABER
Columbia University, New York, New York
(Received February 13, 1953)

IT has been shown that elastic $\pi+H$ scatterings can be identified uniquely in nuclear emulsions from energy-momentum conservation.[1] This method was applied to the identification of π^-+D elastic scattering in heavy water (D_2O) loaded Ilford G5 emulsions,[2] and an angular distribution at 140 Mev was obtained.

By soaking Ilford G5 600μ emulsions at 13°C for 2 hours in heavy water, ~1 g D_2O/cm^3 of dry emulsion was introduced which is equivalent to 0.11 g of D/cm^3 of loaded emulsion. These emulsions as well as nonloaded emulsions were exposed to a total flux of $\sim3\times10^4$ mesons/cm^2 in the 140-Mev magnetically sepa-

rated π^- beam of the Nevis cyclotron. The emulsions were scanned by area and an effective path length (L_{eff}) was obtained, after correcting for a 10 percent μ-meson and electron contamination in the beam and an 85 percent scanning efficiency. Table I gives

TABLE I. Data on π^--meson interactions in D_2O loaded and nonloaded emulsions. L_{eff} is the effective path length in emulsion; $L_{D(H)}$ is the equivalent path length in pure D(H); n_s is the total number of nuclear interactions; n_D is the number of elastic π^-+D scatterings, and n_H is the number of elastic π^-+H scatterings.

	L_{eff} (meters)	L_D g/cm²	L_H g/cm²	n_s	n_D	n_H
D_2O loaded emulsion[a]	330±40	3550±500	1020±150	1000	24	4
Nonloaded emulsion	130±15	···	800±100	440	···	4

[a] In the loaded emulsion the relative H concentration is reduced by the swelling factor $K \simeq 2$.

the experimental results. π^-+D scatterings were identified by examining all one-prong scattering events according to the following three criteria:

(a) The coplanarity of the three prongs.

(b) The angular correlation between the scattered meson and the recoil prong.

(c) The correlation between the range and angle of the recoil prongs (see Fig. 1).

Carrying out such an analysis, four events could be identified as π^-+H scatterings. This is in agreement with the number of H events obtained in scanning the nonloaded emulsion which corresponds to a cross section of ~8 mb.[3] The range angle correlation of all events complying with criteria (a) and (b) are plotted in Fig. 1. Thus 24 events, of which 17 end in the emulsion, were identified as elastic π^-+D scatterings; 4 events, of which 2 end in the emulsion, as π^-+H scatterings. As the scanning efficiency decreases for events with a recoil prong shorter than 50 microns, a safe cutoff at 100 microns prong length (reduced range[4]) was taken. This corresponds to a meson scattering angle of 30°.

The experimental distribution of the scattering angle for the π^-+D elastic events is given by the histogram in Fig. 2. A strong

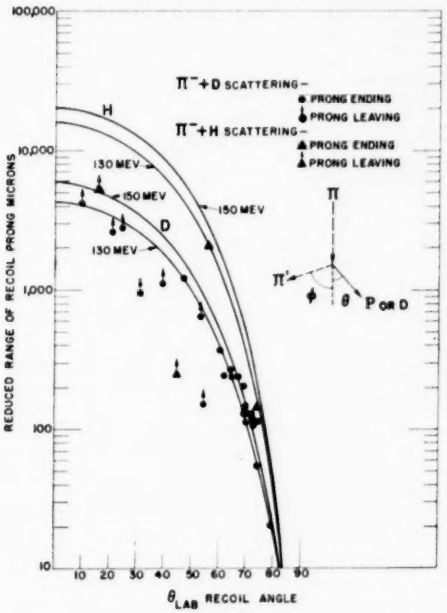

FIG. 1. The correlation between range and angle of recoil prongs for elastic π^-+D and π^-+H scattering.

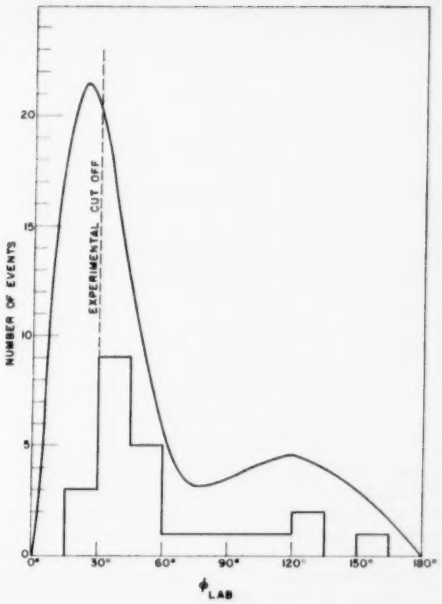

FIG. 2. The distribution in π-meson scattering angle (ϕ_{lab}) of the π^-+D elastic scattering events, at 140 Mev. The curve represents a theoretical calculation (reference 5) based on the impulse approximation.

peaking in the forward direction can be observed. For comparison, a theoretical curve expressed in terms of number of events is given. The theoretical calculation by Green[5] was carried out by an impulse approximation based on the Fermi phase shifts for single pion-nucleon scattering. The integrated cross section $\sigma(\Delta\phi_{lab})$ are $\sigma(30°-60°)=13.5\pm3.5$ mb; $\sigma(60°-180°)=6.5\pm2.5$ mb; $\sigma(30°-180°)=20\pm4.5$ mb.

Even though our statistical accuracy is small at present, there appears to be definite disagreement with the impulse approximation calculation. Namely, the experimental cross section obtained so far is considerably smaller than the calculated value, especially in the backward direction.

The comparison is discussed in detail in the accompanying letter by Green.

We wish to thank Mrs. M. Boehlert, Mr. S. Lokanathan, and Mrs. J. Bielk of the Nuclear Emulsions Group, as well as the staff of the Nevis Cyclotron Laboratories, for their assistance in this work.

* This work was supported by the joint program of the U. S. Office of Naval Research and the U. S. Atomic Energy Commission.

[1] G. Goldhaber, Phys. Rev. **89**, 1187 (1953).

[2] S. Goldhaber and G. Goldhaber, Phys. Rev. **87**, 185 (1952).

[3] This is in agreement with results obtained with a similar method by J. Orear (private communication).

[4] The reduced range R_0 is given by $R_0=(S_w/S_0)R_w$, where $S_w/S_0=0.7$ is the ratio of the stopping power of the loaded and nonloaded emulsion.

[5] T. A. Green, Phys. Rev. **90**, 161 (1953) (following Letter).

The Elastic Scattering of π-Mesons by Deuterons

THOMAS A. GREEN
Columbia University, New York, New York
(Received February 13, 1953)

BY making use of the results of Fermi's phase shift analysis[1] of the cross sections for the scattering of π-mesons by free nucleons, we have evaluated the impulse approximation expression given by Fernbach *et al.*[2] for the elastic scattering of 135-Mev

TABLE I. Calculated and experimental integrated cross sections for the elastic scattering of π-mesons by deuterons. (The angular intervals are taken in the laboratory system.)

Angular interval (deg)	Calculated cross section (mb)	Experimental cross section (mb)
0–30	29	...
30–60	25	13.5±3.5
60–180	25	6.5±2.5

π-mesons by deuterons. A comparison of our results with those obtained experimentally by Arase *et al.*[3] is given in Table I. Although the experimental statistics are such that the disagreement between the two angular distributions which is evidenced in Table I may be illusory, there is no doubt that the calculated cross section is much too large in the region where experimental data are available.

As has been pointed out by Brueckner,[4] a large error is introduced in the impulse approximation by the neglect of multiple scattering. It is not clear, however, that Brueckner's calculation, which was done for infinitely heavy scatterers and zero-range meson-nucleon forces, constitutes a valid approximation to the actual multiple scattering problem in deuterium. It does indicate at least that the inclusion of multiple scattering can be expected to improve the theoretical results considerably.

Another possibly significant source of error was introduced in the work of reference 2, where the meson-nucleon scattering matrices were evaluated for those initial and final values of the meson momentum which describe the scattering of the meson by a free nucleon at rest in the deuterium laboratory frame.[5] This involves neglecting the motion of the nucleons in deuterium in so far as it affects the values of the momentum variables in terms of which the scattering matrices are expressed. In the case of elastic scattering an additional error is introduced by the use in the scattering matrices of the final meson momentum as determined by the meson-nucleon conservation laws rather than that which follows from the conservation laws for an elastic collision of the meson with a deuteron.[6] These two approximations can change the values of the momentum variables appearing in the scattering matrices by as much as 25 percent, the changes produced by the second approximation being largest for backward scattering. In view of the rather pronounced energy dependence of the meson-nucleon scattering, we feel that some investigation of the errors introduced by the approximations just discussed should be carried out. This task is rendered difficult at present by the incomplete status of the theoretical description of meson-nucleon scattering.

[1] The following values of the phase shifts were used: $\alpha_{13}=16.1$, $\alpha_{31}=-11.1$, $\alpha_{33}=-41.8$, $\alpha_{31}=-6.1$, $\alpha_{11}=1.2$, $\alpha_{11}=5.1$ deg.
[3] Fernbach, Green, and Watson, Phys. Rev. **84**, 1084 (1951).
[3] Arase, Goldhaber, and Goldhaber (preceding Letter), Phys. Rev. **90**, 160 (1953).
[4] K. A. Brueckner, Phys. Rev. **89**, 834 (1953).
[5] See the discussion following Eq. (8) of reference 2.
[6] See Eq. (7) of reference 2.

The Spectrum of the γ-Radiation Emitted in the Reaction $n+p \rightarrow d+\gamma$

A. BRACCI, U. FACCHINI, AND A. MALVICINI
Laboratori C.I.S.E., Milan, Italy
(Received February 16, 1953)

THE energy spectrum of the γ-radiation emitted in the reaction $n+p \rightarrow d+\gamma$ has been studied by Nakagawa.[1-4] By means of the absorption curves of Compton electrons produced by the γ-rays in question, he found a line of 2.24 Mev corresponding to the energy of reaction and two lines of energy of 1.4 and 0.8 Mev, respectively, each with an intensity equaling that of the 2.24-Mev line.

The line at 2.24 Mev has been successively measured with high accuracy by Bell and Elliott,[5] who give 2.23±0.07 Mev.

The 1.4-Mev and 0.8-Mev lines indicate the existence of an excited state of the deuteron, in disagreement with theoretical expectations.[6]

The method used by Nakagawa is rather indirect, and his results are not easily interpreted. Taking account of this and of the fact that no other measurement has yet been made of the low energy spectrum of the γ-radiation in question, we thought it opportune to repeat the measurements of Nakagawa.

We have used as neutron source a beam of deuterons accelerated at 260 kv, focused on a lithium target.[7] The ion source was pulsed with ignition periods of the order of 10 μsec which repeated themselves every 150 μsec.

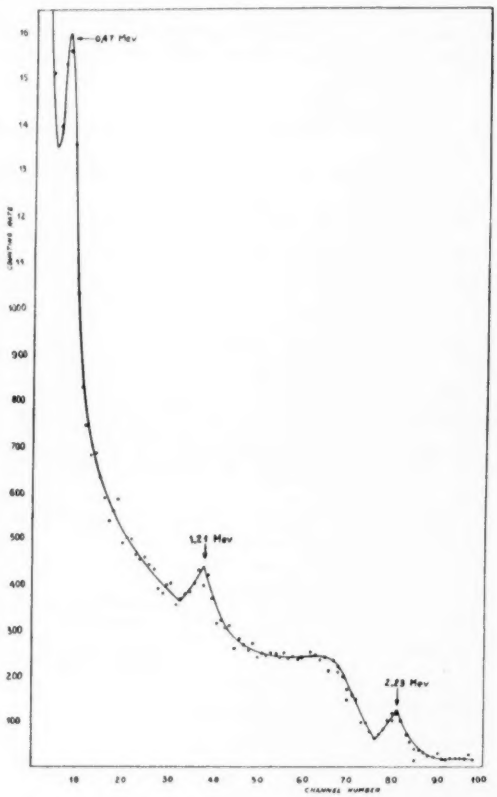

FIG. 1. Spectrum of γ-radiation from the $n+p$ reaction [NaI(Tl)].

The neutrons were slowed down in a 12-cm cube of water. The neutrons captured in the water produced the γ-rays under consideration. In front of the cube a scintillation spectrograph and an RCA 5819 photomultiplier were placed.[8] 1.3-cm cube crystals of Tl-activated NaI and 1.3-cm cube crystals of anthracene were used. The photomultiplier anode was connected across an ordinary amplification chain to a 99-channel pulse analyzer.

A block circuit intercepted the pulses from the photomultiplier for a period of 15 μsec from the starting time of the ion source.

By means of this block the pulses produced by γ-rays of the reaction $d+\mathrm{Li}$ or through the effect of fast neutrons are excluded. On the other hand, since the slow neutrons have an average life in the water of about 75 μsec, they can produce γ-rays from the reaction $n+p$ even after the blocking period.

A 2-cm screen of Pb protected the crystal and the photomultiplier laterally from the scattered radiation.

The crystal was protected from the slow neutrons by means of two absorbing layers, one of metallic Li, 1.3 cm thick, the other of powdered B_4C, 1 cm thick. In order to further reduce the slow neutron beam on the crystal, a larger water vessel was used in some measurements. In all cases the source size never had considerable influence on the γ-spectrum under consideration.[9]

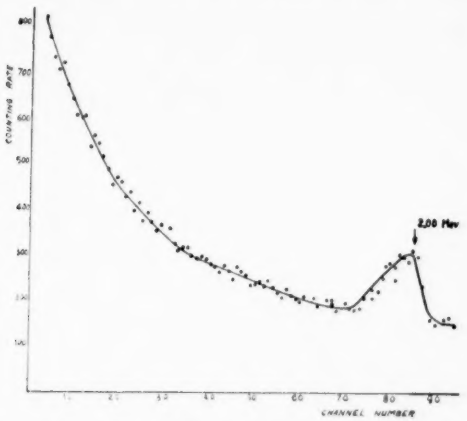

FIG. 2. Spectrum of γ-radiation from the $n+p$ reaction (anthracene).

Figures 1 and 2 represent the spectrum of the pulses obtained from the NaI and anthracene crystals, respectively.

In Fig. 1 we see the peak which is due to the photoelectric effect, the spectrum of Compton electrons with the characteristic edge at about 2 Mev, and the maximum at 1.21 Mev resulting from pair formation in the crystals, which are all produced by the 2.23-Mev γ-rays. The line at about 0.5 Mev is due to the γ-rays produced by the neutrons captured in the boron.

Part of the pulses (about one-third of the total), which is responsible for the continuous slope of the low energy spectrum, is due to the activation of iodine by slow neutrons and to the radiation from various sources, which can be observed even if the target of the accelerator tube is not surrounded by water.

In Fig. 2 we see only the spectrum of Compton electrons, because with anthracene only this effect has a high cross section. In these results there is no evidence of the lines observed by Nakagawa.

In order to ensure the sensibility of our measurement, we studied the effect of two sources of Na^{22} and of Cs^{137} which provided γ-rays of 0.69 Mev and 1.28 Mev. These sources were placed alternately in a fixed position in order to obtain a known intensity on the crystal.

From the observation of the peaks of these γ-rays superimposed on the studied spectra, we can conclude that in the neutron-proton capture spectrum no line with an intensity over 20 percent of the main line at 2.23 Mev exists in the range of energy from 0.7 to 2.23 Mev.

We wish to thank Professor G. Bolla and Professor P. Caldirola for their stimulating discussions and Dr. E. Gatti, Dr. E. Germagnoli, and Dr. G. Perona for their collaboration.

[1] Hornyak, Lauritsen, Morrison, and Fowler, Revs. Modern Phys. **22**, 291 (1950).
[2] Nakagawa, Sumoto, and Arai, Proc. Imp. Acad. (Tokyo) **19**, 373 (1947).
[3] S. Nakagawa, J. Sci. Research Inst. Tokyo **43**, No. 1185 (1948).
[4] S. Nakagawa, J. Sci. Research Inst. Tokyo **43**, No. 1196 (1949).
[5] R. E. Bell and L. C. Elliott, Phys. Rev. **79**, 282 (1950).
[6] J. M. Blatt and V. F. Weisskopf, *Theoretical Nuclear Physics* (John Wiley and Sons, Inc., New York, 1952).
[7] Gatti, Perona, and Persano, Nuovo cimento **10**, 80 (1953).
[8] Bracci, Facchini, and Malvicini, Nuovo cimento **9**, 1237 (1952).
[9] A detailed description of the experimental equipment will be published in the Nuovo cimento.

Levels in N^{14} from the $C^{13}(p,\gamma)N^{14}$ Reaction

D. HICKS, T. HUSAIN, L. G. SANDERS, AND L. E. BEGHIAN
Clarendon Laboratory, Oxford, England
(Received January 30, 1953)

PROTON capture by C^{13} exhibits a well-known resonance at 554 kev. We have bombarded an enriched C^{13} target (60 percent C^{13}, 200 $\mu g/cm^2$) deposited on copper with protons of energy 554 kev and examined the resultant gamma-radiation with a scintillation pair spectrometer similar to that described by Johanssen.[1]

Gamma-ray lines of the following energies and intensities were observed, the intensities being referred to the well-known 8.06-Mev ground state transition as 100 percent.

5.1 $\pm$0.2 Mev$\sim$ 4 percent
4.45$\pm$0.1 Mev$\sim$18 percent
3.05$\pm$0.1 Mev$\sim$15 percent
2.75$\pm$0.1 Mev$\sim$10 percent
2.35$\pm$0.1 Mev$\sim$25 percent

The region below 2 Mev was not investigated. Energy calibrations were made with RdTh (2.62-Mev), Po-Be (4.47-Mev) sources and with the 8.06-Mev radiation to the ground state. Over the period of measurement the energy calibration of the spectrometer was stable to better than 1 percent.

The intensity of the 2.35-Mev line is difficult to estimate accurately, since 2.45-Mev gamma-rays from the reaction $C^{12}(p,\gamma)N^{13}$ were present in greater intensity, and the resolution of the instrument was not sufficient to separate these lines completely. A rough estimate of the relative intensities of the two components was made as follows. Two measurements of the intensity of the radiation in this energy region were made, one with beam energy on the C^{13} resonance and the other 25 kev below. Since these energies are both well clear of the $C^{13}(p,\gamma)N^{14}$ resonance at 456 kev, one would not expect the yield from this reaction to alter appreciably. However the yield from the $C^{13}(p,\gamma)N^{14}$ reaction falls by a factor 0.42 at the off-resonance energy. From these two measurements the relative intensities of the two components could be estimated.

The 5.1, 3.05, 2.75, and 2.35-Mev lines can be fitted into the level scheme for N^{14} described by Ajzenberg and Lauritsen[2] (see Fig. 1). The transition from level A (0^-, 1^-) to level B is probably $E1$ since this is consistent with the observed intensity relative to

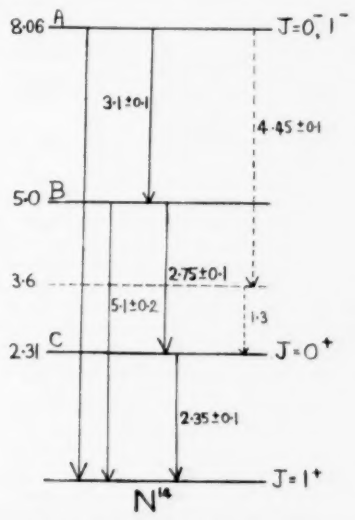

FIG. 1. Decay scheme for $C^{13}(p,\gamma)N^{14}$.

the ground state transition. Hence level B would have + parity and spin 1 or 2. However the transition from level A to level $C(0^+)$ is completely absent. This transition would have to be either $E1$ ($1^- \rightarrow 0^+$) in which case it would compete both with the ground state and $A \rightarrow B$ transitions or be completely forbidden ($0^- \rightarrow 0^+$). It seems likely, therefore, that the spin of level A is in fact 0^-, in which case that of level B would be 1^+.

The 4.45-Mev line has not been previously observed and cannot be made to fit into the scheme unless a further level is introduced at 3.6 Mev which decays to the ground state by a cascade via level C (this has been indicated by dotted lines in the diagram). To make certain that this line was not due to a target impurity two measurements were made of its intensity relative to the 8.06-Mev line at the on- and off-resonance beam energies. The relative intensity remained unchanged within statistical error, showing that the line is associated with the $C^{13}(p, \gamma)N^{14}$ reaction.

We wish to thank Dr. H. Halban for his advice and interest in this work; Professor Lord Cherwell for extending the facilities of his laboratory; Dr. W. B. Mims for his advice and help in constructing the spectrometer; A. M. Woodbury, R. B. Day, and A. V. Tollestrup of the Kellogg Radiation Laboratory for communicating their unpublished results; and Dr. H. Dawton of Atomic Energy Research Establishments, Harwell, for supplying the C^{13} target.

[1] S. Johannsen, Phil. Mag. **43**, 249 (1952).
[2] F. Ajzenberg and T. Lauritsen, Revs. Modern Phys. **24**, 231 (1952).

The (γ, α) Reaction of B^{11} and B^{10}

K. Locher and P. Stoll
Federal Institute of Technology, Zurich, Switzerland
(Received December 29, 1952)

In addition to the 3-particle reaction of B^{11} and B^{10},[1] the following (γ, α) processes can be initiated with the γ-radiation of lithium (17.6; 14.8; 12.3 Mev):

$$B^{11}(\gamma, \alpha)Li^7, \quad Q = 8.667, \tag{1a}$$
$$B^{10}(\gamma, \alpha)Li^6, \quad Q = 4.453. \tag{2a}$$

Beside these transitions to the ground state of Li^7 and Li^6, there also exist transitions to excited levels, which then decay with γ-emission.

$$B^{11}(\gamma, \alpha)Li^{7*}, \quad Li^{7*} \rightarrow \gamma + Li^7, \tag{1b}$$
$$B^{10}(\gamma, \alpha)Li^{6*}, \quad Li^{6*} \rightarrow \gamma + Li^6. \tag{2b}$$

The excited levels (E^* values) cannot be determined directly as in the case of the 3-particle reaction; the assignment of the events to the E^* values is only possible with help of a detailed knowledge of the incident γ-ray spectrum.

Boron-loaded Kodak NTla plates of 400μ thickness have been exposed to Li γ-radiation, until an average number of 675 stars per cm² of the reaction $C^{12}(\gamma, 3\alpha)$ were produced. The Amidol temperature development was carried out at pH = 5.5. By this process the single charged particles disappeared, and a good discrimination between alpha and Li recoils was obtained. With help of alpha-track lengths and the known energy-range relation[2] a new lithium energy-range diagram can be plotted, as shown in Fig. 1. The values for Li^6 are theoretically about 5 percent lower than those of Li^7; therefore the two curves cannot be separated experimentally. The experimental diagram agrees well with the theoretical one, computed starting from the proton energy-range relation.[3]

In order to separate the events of B^{11} and B^{10}, the momentum balance-criterion and the knowledge of the incident γ-ray spectrum are applied. An emulsion loaded with pure B^{11} isotope was used to confirm the results of the separation. The cross sections of both reactions are related to the carbon disintegration $C^{12}(\gamma, 3\alpha)$ cross section, which we have determined[4] as 1.75×10^{-28} cm² for Li γ-radiation. The analysis is indicated in Fig. 2.

In the energy range of Li γ-radiation, the probability of the (γ, α) process on B^{10} is ten times greater than on B^{11} as can be seen from Table I. The large cross section of the reaction B^{10}

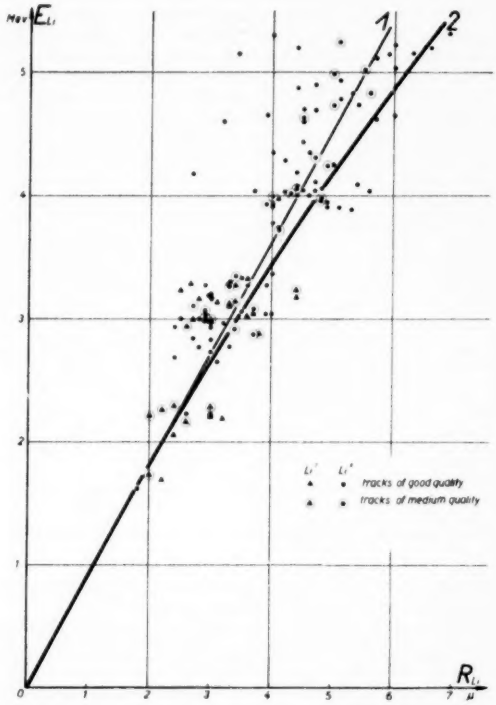

FIG. 1. Range-energy curve for Li^6 and Li^7. Curve 1, averaged curve from the experimental points. Curve 2, corrected for "photographic straggling."

$(\gamma, \alpha)Li^6$ for $E_\gamma = 12$ Mev permits a very accurate measurement of the 12.3-Mev γ-line. The transitions involved in this experiment are indicated in Fig. 3.

The selection rules give the only criterion to explain the different probabilities of transitions to the respective states of Li^6 and Li^7. The small cross section of the reaction $B^{11}(\gamma, \alpha)Li^7$ for $E_\gamma = 17.6$ and 14.8 Mev can only be understood by postulating dipole-absorption in this energy range, according to the model of Levinger and Bethe.[5] Only p wave emission of alpha-particles is possible. An analogous discussion is valid for the transition to the ground state of the (γ, α) process on B^{11}.

TABLE I. Cross sections of the (γ, α) reactions on B^{10} and B^{11}. σ^*: summed cross section for $E_\gamma = 17.6$ and 14.8 Mev for both ground state and 0.478-Mev level of Li^7. σ_T: total cross section for $E_\gamma = 12.3$, 14.8, and 17.6 Mev for ground-state transitions.

Reaction	Q_{Mev}	E_{Mev}^*	Cross sections (cm²)	Cross-section ratio for the 3 lines of the lithium γ-rays
$B^{11}(\gamma, \alpha)Li^7$	8.667	0	$\sigma^* = 0.18 \pm 0.09 \times 10^{-28}$	
$B^{11}(\gamma, \alpha)Li^{7*}$		0.478	$\sigma_{14.8} = 0.30 \times 10^{-28}$ $\sigma_{17.6} = 0.12 \times 10^{-28}$	$\sigma_{14.8}/\sigma_{17.6} = 2.6$
$B^{10}(\gamma, \alpha)Li^6$	4.453	0	$\sigma_T = 2.1 \pm 1 \times 10^{-28}$ $\sigma_{12.3} = 11.9 \times 10^{-28}$ $\sigma_{14.8} = 1.6 \times 10^{-28}$ $\sigma_{17.6} = 0.3 \times 10^{-28}$	$\sigma_{17.6} : \sigma_{14.8} : \sigma_{12.3}$ $= 1 : 5.5 : 14.5$

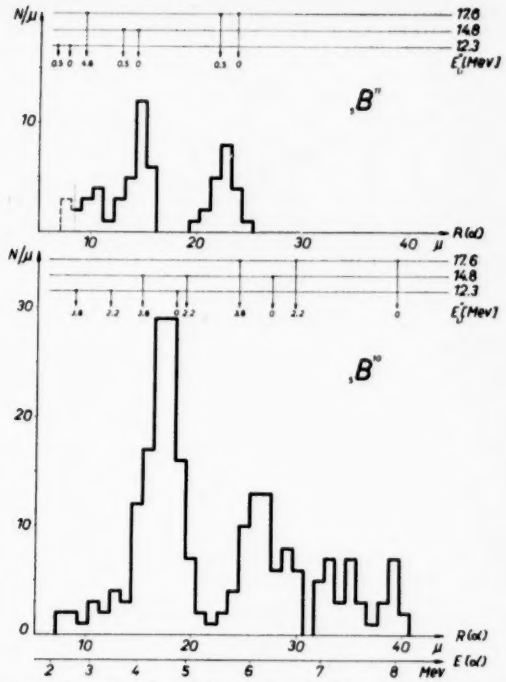

FIG. 2. Range distributions for the reactions: $B^{11}(\gamma, \alpha)Li^7$ and $B^{11}(\gamma, \alpha)Li^{7*}$ ($Li^{7*} \rightarrow \gamma + Li^7$), $B^{10}(\gamma, \alpha)Li^8$ and $B^{10}(\gamma, \alpha)Li^{6*}$ ($Li^{6*} \rightarrow \gamma + Li^6$). Only tracks with $|p| \leq 0.35$ unit are considered. p = momentum unbalance vector. (By definition: 1 p unit = momentum of a 1-Mev alpha-particle.)

The three different probabilities of the alpha-transition can be understood by assuming mainly dipole absorption of 17.6- and 14.8-Mev quanta, changing to quadrupole absorption for 12.3 Mev. The most probable transition (s wave) is initiated by 12.3-Mev γ-rays, while transitions according to higher quantum-energies are only possible as p waves.

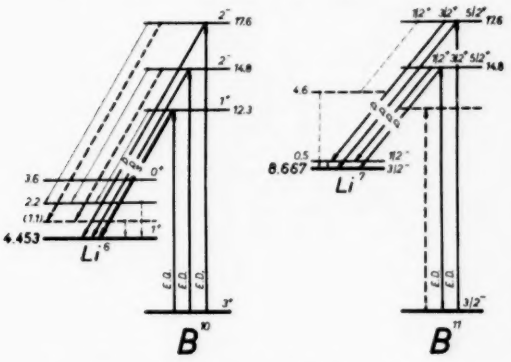

FIG. 3. Decay scheme for the (γ, α) reaction on B^{11} and B^{10}.

The measurements confirm the calculations of Levinger and Bethe.[5] The distribution of angles between emitted alpha-particle and incident γ-ray should furnish further information.

[1] O. Rochat and P. Stoll, Helv. Phys. Acta **25**, 451 (1952).
[2] J. Rotblat, Nature **167**, 550 (1951).
[3] Richards, Johnson, Ajzenberg, and Laubenstein, Phys. Rev. **83**, 994 (1951).
[4] Glättli, Seippel, and Stoll, Helv. Phys. Acta **25**, 491 (1952).
[5] J. S. Levinger and H. A. Bethe, Phys. Rev. **78**, 115 (1950).

The Existence of Positronium Chloride

LENNART SIMONS
University of Helsinki, Helsinki, Finland
(Received February 16, 1953)

A POSITRON passing through chlorine gas may, upon striking a chlorine molecule,[1] form a complex consisting of a neutral chlorine atom (Cl), an electron (e^-) and a positron (e^+). The combinations $(Cle^-)e^+$ and $Cl(e^-e^+)$ then suggest themselves, where the two particles in the parentheses would be more closely bound to one another than to the third.

It is possible to treat mathematically the system $(Cle^-)e^+$ quite accurately, as even in its ground state the positron proves to be relatively far away from the (Cle^-) group (mean distance about 1.7A). A Hartree-Fock field[2] has been assumed for the Cl^- ion. Sets of radial parts, $\Psi_0(r)$ and $\Psi_\infty(r)$, of the wave functions were calculated for different energies E so as to be finite for $r=0$ and to vanish for $r=\infty$. For a fixed value of the logarithmic derivative the corresponding values of r were determined. Relations $f(r, E)=0$ and $g(r, E)=0$ were then derived for the functions Ψ_0 and Ψ_∞, respectively, and the eigenvalues were found from the intersections of these curves.

The earlier computation[3] for the quantum number $l=0$ has now been completed for the whole spectrum. The values of $-E$ obtained by the above method for the different energy levels are given in Table I with an accuracy of about one percent.

The values of $-E$ not found in the table can be calculated by the formula

$$E \approx -1/[2(n+\alpha)^2],$$

where $\alpha \approx 1$, for $l=0$ and $\alpha \approx 0$ for $l \geq 1$.

The method has also been tried on sodium and in agreement with Jastrow;[4] the Prokofjew[5] field gives very accurate values for the energy levels of the valency electron of the sodium atom.

If the system $Cl(e^-e^+)$ has a smaller energy than the system $(Cle^-)e^+$, it is possible for the latter to be transformed into the former in a rather short time by the positron catching one of the M electrons. In this case,

$$\epsilon + A < E - B,$$

where $-\epsilon$ is the binding energy of positronium to the chlorine atom, $-A$ is the binding energy of the positronium atom (e^-e^+), $-E$ is the binding energy of e^+ to (Cle^-) and B the electron affinity of the chlorine atom, here taken equal to 3.76 ev. The binding energy of positronium to chlorine is then greater than 0.73 ev when $A=-0.25$ and $E=-0.138$ Hartree units. Consequently, if the probability of formation of $Cl(e^-e^+)$ is large, the system must be dynamically stable. Further consideration of different cases where annihilation is not taken into account also leads to the conclusion that positronium chloride is stable.

When annihilation is taken into consideration, we get according to Dirac[6] and Wheeler[1] the following mean annihilation probability per unit time for different spin constellations:

$$l = \pi c \left(\frac{e^2}{mc^2}\right)^2 \int \rho \Psi^2 dV,$$

where ρ is the electron density and Ψ the normalized eigenfunction of the positron. The integration is taken over the whole space. In this case a mean life $\tau = 1/l = 5 \times 10^{-9}$ sec is obtained for the system $(Cle^-)e^+$ when the positron is in its normal state and ρ is evaluated according to the Hartree-Fock-field. But if the probability of antiparallel spins is only 1:4, as in the case of positronium,

TABLE I. Spectrum of Positronium Chloride.

l \ n	1	2	3	4	5	6	7	8	9
0	0.138	0.060	0.033	0.021	0.014				
1		0.097	0.046	0.027	0.0175	0.0125	0.0095	0.0074	0.0058
2			0.054	0.031	0.0195	0.0138			
3				0.0312	0.0198	0.0139	0.0100	0.0077	

τ has to be divided by four. On the other hand, the mean life of the system $Cl(e^-e^+)$ should be of the same order of magnitude as that of positronium, i.e., 10^{-10} sec. However, inasmuch as the time necessary for the emission of light is of the order of 10^{-8} sec and as the probability of annihilation and of catching an M electron is small in the higher states of the system $(Cle^-)e^+$, the conclusion must be made that the spectrum given in Table I is to be expected.

A more detailed account of this work will be presented in *Societas Scientiarum Fennica Commentationes Physico-Mathematicae* in the near future.

[1] J. A. Wheeler, Ann. N. Y. Acad. Sci. **48**, 219 (1946).
[2] D. R. and W. Hartree, Proc. Roy. Soc. (London) **A156**, 45 (1936).
[3] L. Simons, Soc. Scient. Fennica Commentationes Phys.-Math. **14**, 9 (1949).
[4] R. Jastrow, Phys. Rev. **73**, 60 (1948).
[5] W. K. Prokofjew, Z. Physik **58**, 255 (1929).
[6] P. A. M. Dirac, Proc. Cambridge Phil. Soc. **26**, 361 (1930).

The Formation of a Compound Nucleus in Neutron Reactions*

HERMAN FESHBACH, CHARLES E. PORTER, AND VICTOR F. WEISSKOPF
Department of Physics and Laboratory for Nuclear Science and Engineering, Massachusetts Institute of Technology, Cambridge, Massachusetts
(Received February 18, 1953)

IN the theory of nuclear reactions with particles of moderate energy (<50 Mev), one generally makes the following assumption: The incident particle, upon entering the target nucleus, immediately forms a compound nucleus in which its motion is completely integrated into a complicated collective motion of the entire system. There are some reasons to doubt the validity of this assumption. The success of the shell model of nuclear structure suggests that nucleons do not interact very strongly with each other when moving inside the nucleus. The motion is rather like that of an independent particle in a potential well. Recent measurements by Barschall[1] and co-workers of the total cross sections for neutrons on various nuclei as a function of energy have brought some new evidence corroborating the latter point of view.

A theory for total neutron cross sections was developed by Feshbach and Weisskopf[2] under the assumption that the incident neutron and the target nucleus immediately form a compound nucleus. The resulting total cross sections decrease *monotonically* with increasing energy,

$$\begin{aligned} \sigma_t &\approx 4\pi/(kK) \quad (\lambda \gg R) \\ &\approx 2\pi(R+\lambda)^2 \quad (\lambda \ll R). \end{aligned} \tag{1}$$

Here $k=\lambda^{-1}$ is the wave number of the incident neutron; $K \approx 10^{13}$ cm^{-1} is the wave number of the neutron in the interior of the nucleus; and R is the nuclear radius. These results are at variance with the experiments which are shown in a three-dimensional plot in the upper part of Fig. 1.

The regular maxima and minima exhibited by the experimental results seem to indicate an interference of the incident wave with an outgoing one, suggesting that the neutron wave is not completely absorbed into collective motion in one passage through the nucleus. We therefore have recalculated the total neutron cross section with the following model. The nucleus is replaced by a potential well with a complex potential,

$$\begin{aligned} V(r) &= -V_0(1+i\zeta) \quad \text{for} \quad r<R \\ &= 0 \quad \text{for} \quad r>R, \end{aligned} \tag{2}$$

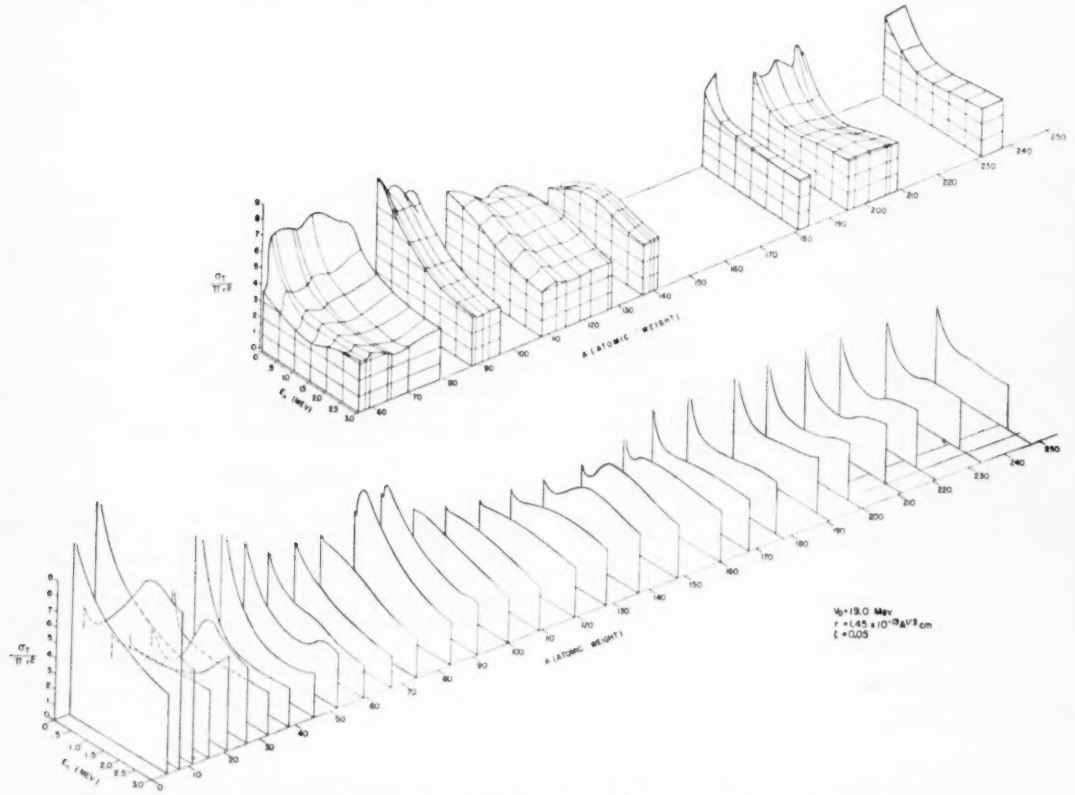

FIG. 1. Total neutron cross section as a function of energy and atomic number. Upper profile: experimental results (reference 1). Lower profile: theoretical results with the constants as indicated.

where V_0 is a real number giving the depth of the well, and ζ is a parameter which indicates an "absorption" for neutrons within nuclear matter. This absorption is introduced in order to describe the formation of the compound nucleus. The distance l in nuclear matter, within which the neutron intensity is reduced by this absorption by $(1/e)$, is given by $(\zeta K)^{-1}$. If (R/l) is small, part of the neutron wave emerges from the nucleus and causes interference with the incoming beam. If $\zeta \gg (KR)^{-1}$, no neutron wave emerges, and the results are equivalent to those of Feshbach and Weisskopf, quoted above.

The calculation of the total cross section arising from the potential of Eq. (2) is a straightforward problem of wave theory, and the results are shown in the lower half of Fig. 1 for the following choices of constants: $V_0=19$ Mev, $R=1.45\times10^{-13}A^{\frac{1}{3}}$ cm, $\zeta=0.05$. It is evident that this simple model reproduces all the main features of the experimental results. If this agreement is not fortuitous, we must conclude that in the energy range considered the neutron penetrates a distance l of about 2×10^{-13} cm into nuclear matter before it is incorporated into a collective compound motion.

It should be mentioned that the experimental curves are averaged over many narrow resonances which the simple model employed here will not predict. They are resonances of the compound system which is formed after "absorption" of the neutrons. The relatively large value of l given above does not preclude the existence of such resonances. A more elaborate theory which also includes these resonances has been developed and will be submitted for publication in the near future.

* This work was assisted by the joint program of the U. S. Office of Naval Research and the U. S. Atomic Energy Commission.

[1] Miller, Adair, Bockelman, and Darden, Phys. Rev. **88**, 83 (1952); H. H. Barschall, Phys. Rev. **86**, 431 (1952).

[2] H. Feshbach and V. F. Weisskopf, Phys. Rev. **76**, 1550 (1949).

Direct Experimental Evidence for the Existence of a Heavy Positive V Particle*

C. M. York, R. B. Leighton, and E. K. Bjornerud
California Institute of Technology, Pasadena, California
(Received February 9, 1953)

VARIOUS workers have shown[1,2] that some, if not all, charged V particles observed in cloud-chamber experiments can be identified with the K particles[3] (κ- and χ-mesons) found in nuclear emulsions. Direct mass measurements have been made on primary V particles of both signs of charge. These measurements have in all cases given values, somewhat lighter than a proton mass, which are entirely consistent with the known masses of K particles. The question arises, therefore, as to whether charged V particles exist whose mass is considerably greater than that of a K particle, and which perhaps decay into a nucleon and π-meson, in a manner analogous to the decay of the neutral V_1^0 particles.

Alford and Leighton[4] have suggested that the observed charged V particles may be of two or more types, of quite different lifetimes. This suggestion was based upon an observation of the distribution of the decay points of the particles in their cloud chamber. The upper chamber appeared to favor the detection of a relatively long-lived particle (i.e., $\tau\sim10^{-9}$ sec) formed in the lead blocks above the chamber, while the lower chamber seemed to show a number of particles of relatively short life ($\tau\sim10^{-10}$ sec) formed in the lead plate between the chambers.

Additional data have been obtained with the same apparatus, and an analysis has been made, based upon this apparent difference in sensitivity of the two chambers. In this way there was found a striking charge asymmetry between the charged V particles produced in the lead plate and those produced elsewhere (mainly in the lead blocks above the chamber). This is indicated in Table I.

A rough calculation reveals that, if the relative population of positive and negative V particles in the two chambers is actually the same, the statistical probability of observing the above charge asymmetry, or a greater one, is about 0.007. This result thus tends to substantiate the conclusions drawn on the basis of the distribution of the observed decay points, but it should, of course, be emphasized that the number of events is still comparatively small.

A possible interpretation of these asymmetries in terms of a mixture of long-lived and short-lived V particles might be made as follows: Because the lead blocks above the chamber are rather far away from the illuminated region, the V particles observed to decay in the upper chamber are predominantly of the long-lived type. From the charge asymmetry of this fairly pure sample of particles, we may tentatively conclude that they are produced with a negative excess of about two to one. On the other hand,

TABLE I. Classification of charged V particles according to place of origin and sign of charge.

Origin \ Sign	Positive	Negative	Total
Above plate	8	18	26
In plate	18	9	27
Total	26	27	

TABLE II. Measured data pertaining to two positive V particles with heavy charged secondary particles.

Case	Sign	P_{pri} (Mev/c)	I_{pri} (×min)	M_{pri} (m_e)	P_{sec} (Mev/c)	I_{sec} (×min)	M_{sec} (m_e)	θ	P_T (Mev/c)
1	+	−	3–7	−	360±60	3–7	1300–2300	20°	125±25
2	+	−	2–4	−	520±75	2–4	1300–2200	18°	160±40

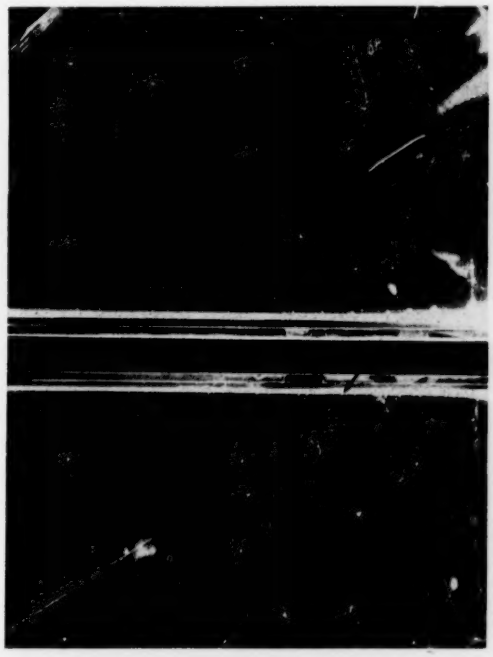

FIG. 1. Cloud-chamber photograph showing a charged V particle originating in an interaction in the lead plate and decaying into a heavy secondary particle. The V particle travels diagonally downward toward the left from the interaction and decays after having traversed only a short distance in the chamber. The heavy secondary particle proceeds almost in the same direction as the V particle. Both the primary and secondary particles are heavily ionizing.

those charged V particles originating in the plate, which is quite near the illuminated region, are a mixture of the long- and short-lived particles. From the marked positive excess of this group we may conclude that the short-lived particle is predominantly (if not always) positive.

A more direct indication that the charged V particles are composed of both (long-lived) K particles and (presumably short-lived) heavier particles is given by measurements on two positive V particles with origins in the lead plate. These proved to be of special interest because the mass of the charged secondary particle was in each case much greater than that of a π-meson. The pertinent data for these two events are contained in Table II, and a photograph of the first case is reproduced in Fig. 1. In both cases the primary track was to short to permit a momentum measurement, but is heavily ionizing. The secondary particles have masses lying in the range 1300–2300 m_e and are consistent with the mass of a proton.[5] The possibility that these events might be interpreted as the scattering of protons is ruled out by the high transverse momentum P_T of the decay and the absence of a recoil nucleus at the decay point. It is natural to suggest that this new decay follows the scheme

$$V_1^+ \rightarrow P + \pi^0 + (Q \sim 40 \text{ Mev}),$$

which is a charged counterpart of the well-known neutral V particle decay scheme: $V_1^0 \rightarrow P + \pi^- + (Q = 35 \text{ Mev})$.[6,7] It is to be noted that the observed transverse momenta are consistent with the most probable values to be expected from this decay scheme.

One would naturally expect that an alternate mode of decay of this heavy V particle might be $V_1^+ \rightarrow N + \pi^+ + (Q \sim 35 \text{ Mev})$, and indeed one can deduce, using the above arguments, that about 12 of the positive particles from the lead plate should be of this type. However, without accurate estimates of the masses of the primary particles it would be difficult to distinguish this type of decay from that of a K particle in any individual case.

* Supported in part by the joint program of the U. S. Office of Naval Research and the U. S. Atomic Energy Commission.

[1] R. B. Leighton and S. D. Wanlass, Phys. Rev. **86**, 426 (1952).
[2] Armenteros, Barker, Butler, Cachon, and York, Phil. Mag. **43**, 597 (1952).
[3] D. H. Perkins, Proceedings of the Third Annual Rochester Conference on High Energy Physics, December 1952 (unpublished).
[4] W. L. Alford and R. B. Leighton (to be published).
[5] The masses M were estimated from momentum P and ionization I as described in reference 6.
[6] Armenteros, Barker, Butler, and Cachon, Phil. Mag. **42**, 1113 (1951).
[7] Leighton, Wanlass, and Anderson, Phys. Rev. **89**, 148 (1953).

Meteorites as Cosmic-Ray Meters

S. F. SINGER
Office of Naval Research, United States Embassy, London, England
(Received January 17, 1953)

THE production of helium in iron meteorites by cosmic rays[1] has been treated quantitatively in a recent publication.[2] In addition, a method was described there for separating the contributions from cosmic rays and from radioactivity (uranium and thorium) to the total helium content of the meteorite; namely, it has been calculated that the cosmic-ray produced helium consists of ~30 percent He^3 isotope.[2] The He^3 is produced mainly in evaporations of the iron nuclei, both directly and through beta-decay from tritium.

The actual presence of He^3 in iron meteorites has now been established experimentally;[3] hence, it becomes possible to apply corrections to previously determined "ages"[4] (time since last solidification) by subtracting the cosmic-ray produced helium. One may also be able to place limits on the times of break up of the parent bodies and the dates of creation of the meteorites.[5]

It has also been pointed out[2] that this accumulating property of He^3, in effect, allows one to consider the meteorite as a kind of cosmic-ray meter which integrates the cosmic-ray flux it encounters over its path from the time it becomes exposed to cosmic rays to the time of its fall on earth. On the basis of certain assumptions,[2] it may thus be possible to gain information about the prehistoric cosmic-ray intensity.

The integrating-meter properties of meteorites are, of course, due to the fact that both He^3 and He^4 are stable. One may, however, also consider the possibility of using a radioactive species produced by cosmic rays as an indicator of the (essentially present-day) cosmic-ray intensity existing in the region from which the meteorite came.

Tritium nuclei are released in considerable quantities during evaporations of iron nuclei. Their rate of production (near the surface of a large meteorite) is calculated to be $\sim 2.5 \times 10^6$ tritons per g of meteorite material per year under the same conditions as before.[2] With a constant rate of production secular equilibrium is soon established; after several half-lives the tritium content becomes $\sim 5 \times 10^6$ atoms/g.

In a freshly fallen meteorite the tritium activity should be within range of detection. Immediately after fall the activity per g in the region of maximum tritium production (2–15 cm from the "pre-atmospheric"[6] surface) should be ~0.01 counts/sec; this activity decreases by only 5.8 percent every year. Should the cosmic-ray intensity experienced by the meteorite in the years just preceding its fall be different from the intensity near the earth, the *measured* activity would differ from the expected value in the same manner.

It may not be necessary to rely on an absolute measurement, since, in addition to calculating the activity expected, one could actually calibrate it to the cosmic-ray intensity near the earth. With successive flights in high altitude balloons one can easily achieve an exposure of 0.1 year for a 10^3 g mass of iron; it should then contain $\sim 2.5 \times 10^7$ atoms of cosmic-ray produced tritium.

[1] C. A. Bauer, Phys. Rev. **72**, 354 (1947); **74**, 225, 501 (1948).
[2] S. F. Singer, Nature **170**, 728 (1952).
[3] Paneth, Reasbeck, and Mayne, Geochim. et Cosmochim. Acta **2**, 300 (1952).
[4] Arrol, Jacobi, and Paneth, Nature **149**, 235 (1942).
[5] S. F. Singer, Astrophys. J. (to be published).
[6] That is, before any part of the surface is removed by ablation in the earth's atmosphere.

Orbital Effect in Neutron-Electron Magnetic Scattering*

W. H. KLEINER
Lincoln Laboratory, Massachusetts Institute of Technology, Cambridge, Massachusetts
(Received February 5, 1953)

THE spin-spin part ($\mathcal{H}_{SS}$) of the neutron-electron magnetic interaction has been considered in some detail in the literature,[1] while the spin-orbit part ($\mathcal{H}_{SL}$) associated with the interaction between the neutron magnetic moment and a moving electron has not. It is worth while to consider both of these in detail from the viewpoint of exploiting the scattering of thermal neutrons from magnetic materials as a tool for investigating the electronic structure of matter.

The magnetic Hamiltonian is

$$\mathcal{H}_{SS} + \mathcal{H}_{SL} = -\boldsymbol{\mu}_n \cdot \mathbf{H}^{(S)} - \boldsymbol{\mu}_n \cdot \mathbf{H}^{(L)}, \tag{1}$$

in which $\boldsymbol{\mu}_n = g_n(m/M_p)\beta \mathbf{s}_n$ is the neutron magnetic moment, and the magnetic field at the neutron generated by electrons of the scatterer is given by

$$\mathbf{H}^{(S)} = \sum_j \{-\boldsymbol{\nabla}_j \times [\boldsymbol{\mu}_j \times (\boldsymbol{\nabla}_j r_{nj}^{-1})]\}, \tag{2}$$

$$\mathbf{H}^{(L)} = \frac{e}{mc} \sum_j (\boldsymbol{\nabla}_j r_{nj}^{-1}) \times \mathbf{p}_j, \tag{3}$$

where $\boldsymbol{\mu}_j = -2\beta \mathbf{s}_j$ is the magnetic moment, $\mathbf{r}_j$ the position, $\mathbf{p}_j$ the momentum, and $\mathbf{s}_j$ the spin angular momentum (in units of $\hbar$) of the jth electron, the summation being over all electrons; $\mathbf{r}_n$ is the position, $\mathbf{s}_n$ the spin, and $g_n = -3.83$ the g factor of the neutron; m/M_p is the electron-proton mass ratio; $\beta = e\hbar/2mc$ is the Bohr magneton; $r_{nj} = |\mathbf{r}_n - \mathbf{r}_j|$. These expressions for $\mathcal{H}_{SS}$ and

$\mathcal{H}_{SL}$ were obtained by transcribing the nonrelativistic form of the Breit fine structure Hamiltonian[2] for the electromagnetic interaction between two electrons to apply to the interaction between a neutron and an electron, neglecting a term in the neutron momentum $\mathbf{p}_n$, smaller by a factor $\sim m/M_p$ than the electron momentum term in Eq. (3). Equation (2), when expanded, includes besides the usual dipolar energy a δ-function term necessary to obtain agreement with experiment.[3] Both Eqs. (2) and (3) may be derived in an elementary way from classical electromagnetic theory.

Consider the differential scattering cross section in center-of-mass coordinates in Born approximation for the scattering of a monochromatic beam of neutrons by a molecule or small crystal. The Born approximation is expected to be valid here for scatterers of linear dimensions less than about 20A independent of neutron wavelength but may well be valid for much larger scatterers. The matrix elements of Eq. (1) involved are between wave functions of the system neutron plus scatterer with no interaction. When integration is carried out over the neutron space and spin coordinates, and an average over initial neutron spin states is performed, the differential cross section may be written

$$\sigma(\omega)=\left(R\frac{g_n e^2}{2mc^2}\right)^2\Sigma_b\frac{k_b}{k_a}\{[\mathbf{I}-\mathbf{e}_{ba}\mathbf{e}_{ba}]:[\mathbf{P}_{ab}{}^S\mathbf{P}_{ba}{}^S - i(\mathbf{P}_{ab}{}^S\mathbf{P}_{ba}{}^L+\mathbf{P}_{ab}{}^L\mathbf{P}_{ba}{}^S)]-\mathbf{P}_{ab}{}^L\cdot\mathbf{P}_{ba}{}^L\}, \quad (4)$$

corresponding to an unpolarized incident beam. In Eq. (4) we have used the abbreviation

$$\mathbf{P}_{ba}=\int\psi_b{}^*\mathbf{P}(\mathbf{K}_{ba})\psi_a d\tau \quad (5)$$

for matrix elements of the operators

$$\mathbf{P}^{(S)}(\mathbf{K})=\Sigma_j e^{i\mathbf{K}\cdot\mathbf{r}_j}\mathbf{s}_j, \quad (6)$$

$$\mathbf{P}^{(L)}(\mathbf{K})=\Sigma_j e^{i\mathbf{K}\cdot\mathbf{r}_j}K^{-2}\mathbf{K}\times(\mathbf{p}_j/\hbar), \quad (7)$$

with respect to wave functions ψ of the scatterer. The subscripts a and b refer, respectively, to initial and final states; R is the ratio of the reduced mass to the proton mass; $\mathbf{k}$ is the neutron wave vector, $\mathbf{K}_{ba}=\mathbf{k}_a-\mathbf{k}_b=K_{ba}\mathbf{e}_{ba}$; $\mathbf{I}$ is the unit dyadic; k_a and k_b are related by conservation of energy.

Equation (4), or analogous expressions for cases in which the incident neutron beam is polarized and/or the scattered beam is analyzed, should be useful for testing electronic wave functions of a magnetic scatterer, especially in regions frequented by valence electrons. Assuming that any bound-state electronic eigenfunction of the scatterer can be expressed as a linear combination of antisymmetrized products of orthonormal one-electron orbitals ϕ, e.g., molecular or crystal orbitals, the electronic part of the matrix elements (5) is expressible as a linear combination of one-electron matrix elements of the types

$$(\phi'|e^{i\mathbf{K}\cdot\mathbf{r}}|\phi) \quad \text{and} \quad (\phi'|e^{i\mathbf{K}\cdot\mathbf{r}}\nabla|\phi). \quad (8,9)$$

The ϕ's are commonly approximated as a linear combination of orthonormal atomic orbitals[4] $u_{nl}(r)Y_l{}^m(\theta,\varphi)\chi^{m_s}(\sigma)$, in which case (5) is ultimately expressible as a linear combination of matrix elements (8, 9) in which the ϕ's are atomic orbitals about the same center. These can be evaluated quite generally except for radial integrals:

$$(n'l'm'm_s'|e^{i\mathbf{K}\cdot\mathbf{r}}\mathbf{s}|nlmm_s)=(m_s'|\mathbf{s}|m_s)\times\int_0^\infty u_{n'l'}(l'm'|e^{i\mathbf{K}\cdot\mathbf{r}}|lm)u_{nl}r^2dr,$$

$$(n'l'm'm_s'|e^{i\mathbf{K}\cdot\mathbf{r}}\nabla|nlmm_s)=\delta(m_sm_s')\times\int_0^\infty u_{n'l'}(l'm'|e^{i\mathbf{K}\cdot\mathbf{r}}\nabla|lm)u_{nl}r^2dr,$$

in which the angular matrix elements $(l'm'|e^{i\mathbf{K}\cdot\mathbf{r}}|lm)$ and $(l'm'|e^{i\mathbf{K}\cdot\mathbf{r}}\nabla|lm)$ involve linear combinations of spherical Bessel functions $j_p(Kr)$ with coefficients depending on the direction of $\mathbf{K}$ times 1, $1/r$, or $\partial/\partial r$; tables of these matrix elements for l', $l\leqslant 3$ will be published elsewhere.

For free atomic scatters closed shells yield no contribution to Eq. (4) and, if spin interactions are neglected in the atomic Hamiltonian, neither do the cross terms in Eq. (4).

* The research in this document was supported jointly by the Army, Navy, and Air Force under contract with the Massachusetts Institute of Technology.

[1] For example, O. Halpern and M. H. Johnson, Phys. Rev. **55**, 898 (1939); G. T. Trammel, Bull. Am. Phys. Soc. **28**, No. 1, 26 (1953).
[2] G. Breit, Phys. Rev. **34**, 553 (1929).
[3] Shull, Wollan, and Strauser, Phys. Rev. **81**, 483 (1951).
[4] See, for example, E. U. Condon and G. H. Shortley, *The Theory of Atomic Spectra* (Cambridge University Press, Cambridge, 1951).

Total Cross Sections for 400-Mev Neutrons*

V. Alexander Nedzel
Institute for Nuclear Studies, University of Chicago, Chicago, Illinois
(Received February 9, 1953)

THOUGH the present program of total neutron cross-section measurements at this laboratory has not yet been completed, it was thought of interest to report the preliminary results already available.

The experiment consists of good geometry transmission measurements in the well-collimated neutron beam of the University of Chicago synchrocyclotron. A novel threshold detector is used to define a narrower energy spread of the effective neutron beam than is available directly from the cyclotron. This detector is a counter telescope, consisting of two scintillation counters and a Čerenkov counter,[1] set to observe recoil protons scattered from polyethylene in the neutron beam. The average effective energy of the neutron beam is estimated to be about 400 Mev.

The hydrogen cross section was determined by measuring the attenuations of the neutron beam by samples of graphite, benzene, and cyclohexane containing the same thicknesses of carbon. This technique conveniently permits measuring the effect of different amounts of hydrogen in approximately the same geometry.

The cross sections that have been determined are as follows, in barns:

Hydrogen	$0.033_6 \pm 0.001$
Carbon	0.298 ± 0.003
Copper	1.190 ± 0.015
Cadmium	1.84 ± 0.03
Lead	2.88 ± 0.04
Thorium	3.23 ± 0.05
Uranium	3.26 ± 0.05

The errors shown are statistical errors of counting and the values given are to be regarded as tentative pending a more complete study of possible systematic errors in the measurement, and a more accurate determination of the neutron energy spectrum.

* Assisted by the joint program of the U. S. Office of Naval Research and the U. S. Atomic Energy Commission.
[1] John Marshall, Phys. Rev. **86**, 685 (1952).

Comparison of Gamma-Ray Reflections from the (550) and (310) Planes of Quartz

Harry C. Hoyt, Joseph J. Murray, and Jesse W. M. DuMond
California Institute of Technology, Pasadena, California
(Received February 6, 1953)

MEASUREMENTS with the curved crystal focusing gamma-ray spectrometer[1-3] to date have been made using a thin lamina of quartz cut so that the (310) planes are perpendicular to the faces of the lamina. Although the (310) planes are the most convenient for establishing a link between the region of x-radiation and the region of gamma-radiation, the use of these reflecting planes places rather severe limitations on the precision of the instrument in the energy region above 500 kev. These limitations are as follows: (1) The Bragg angle for selective reflection varies as E^{-1}, and for first-order reflections is less than 20 minutes of arc for 1-Mev gamma-radiation. An accuracy of better than 1 or

2 parts in 1000 at angles of less than one degree cannot be obtained with the mechanical arrangement of the present instrument. (2) The resolving power, $\Delta\lambda/\lambda$, is poor at high energies. (3) The reflecting power of the curved crystal lamina varies as $E^{-2.4}$ and is of the order of 4×10^{-4} for 1-Mev gamma-radiation. (4) At the small angles involved, the scattering of the direct beam (i.e., the radiation passing through the crystal without undergoing selective reflection) in the collimator which separates direct and reflected beams becomes excessive and obscures all but the strongest gamma-ray lines.

Replacing the (310) crystal with another crystal having a smaller grating spacing should alleviate all of the difficulties, except the third, to some extent. However, now that it is possible to obtain much higher neutron flux densities for irradiations, the problems of low reflecting power can be overcome. Several different sets of reflecting planes can be used for this purpose, as long as the grating spacing is less than that of the (310) planes. Of the different sets of planes available to us at this time, the (550) planes seem to be the best choice. From x-ray work it is known that the reflecting power is not too low, and it is easily calculated that the grating spacing of these planes is 1/2.40192 that of the (310) planes.

A very strong source of Au^{198} (412-kev gamma-radiation) was used to compare the reflections from two different curved quartz crystal laminae, one of which was cut with the (310) planes normal to the large faces and the other cut with the (110) planes normal to the large faces. Both crystals were 2 mm thick and were optically flat in the unstressed state. After preliminary tests indicated that reflection from the (550) planes was possible, a Hartmann-type test[1] was performed in order to determine the position of best focus of the bent lamina. The width of this "best focus" was found to be 0.08 mm. The source was then placed at this point and a pair of profiles corresponding to reflections from opposite sides of the (550) planes was obtained. A similar pair of profiles was made using the (310) crystal. Comparison of these two pairs of profiles gives a check on the ratio of the grating spacings for the two sets of planes, and also gives (after decay corrections) the ratio of the reflecting powers for the 412-kev gamma-radiation. The value obtained for the grating spacing ratio was $d_{(550)}/d_{(310)} = 1/(2.4014\pm0.0017)$, which agrees with the calculated value given previously. The height of the profile peak above background was taken as proportional to the reflecting power of the crystal for the radiation studied. Comparison of the profiles then showed that the reflections from the (550) crystal were 1/15.6 as intense as those from the (310) crystal.

The use of the (550) planes of quartz as well as the (310) planes will extend the range of the curved crystal spectrometer to about 4 Mev, and will materially increase the precision possible in the 1 to 2-Mev region. Since both sets of planes are parallel to the optic axis of the quartz, and since each set of (310) planes has a set of (550) planes turned only 16°6′ away from it, it should be possible to make use of both sets of planes in a single crystal lamina.

[1] Jesse W. M. DuMond, Rev. Sci. Instr. **18**, 626 (1947).
[2] DuMond, Lind, and Watson, Phys. Rev. **75**, 1226 (1949).
[3] Muller, Hoyt, Klein, and DuMond, Phys. Rev. **88**, 775 (1952).
[4] Lind, West, and DuMond, Phys. Rev. **77**, 475 (1950).

THE AMERICAN INSTITUTE OF PHYSICS

INCORPORATED

57 East 55 Street, New York 22, N.Y.

MEMBER SOCIETIES:

American Physical Society
Earle K. Plyler, *Secretary*, Columbia University, New York 27, New York.

Optical Society of America
Arthur C. Hardy, *Secretary*, Massachusetts Institute of Technology, Cambridge 39, Massachusetts.

Acoustical Society of America
Wallace Waterfall, *Secretary*, 57 East 55th Street, New York 22, New York.

Society of Rheology
G. J. Dienes, *Secretary*, Brookhaven National Laboratory, Upton, Long Island, New York.

American Association of Physics Teachers
R. F. Paton, *Secretary*, University of Illinois, Urbana, Illinois.

AFFILIATED SOCIETIES:

American Crystallographic Association
American Society for Metals
Electron Microscopy Society of America
Physical Society of Pittsburgh
Physics Club of Chicago
Physics Club of Philadelphia
Cleveland Physics Society
Physics Club of the Lehigh Valley
Sigma Pi Sigma

ASSOCIATES:

Over seventy-five leading industrial corporations and other institutions which contribute to the support of the Institute.

JOURNALS:

The Physical Review
S. A. Goudsmit, *Editor*, Brookhaven National Laboratory, Upton, Long Island, New York.

Reviews of Modern Physics
J. W. Buchta, *Editor*, University of Minnesota, Minneapolis, Minnesota.

Journal of the Optical Society of America
Wallace R. Brode, *Editor*, National Bureau of Standards, Washington 25, D. C.

The Journal of the Acoustical Society of America
Floyd A. Firestone, *Editor*, 57 East 55th Street, New York 22, New York.

American Journal of Physics
Thomas H. Osgood, *Editor*, Michigan State College, East Lansing, Michigan.

The Review of Scientific Instruments
Gaylord P. Harnwell, *Editor*, Physical Measurements Laboratory of Physics, University of Pennsylvania, Philadelphia, Pennsylvania.

The Journal of Chemical Physics
Clyde A. Hutchison, Jr., *Editor*, Institute for Nuclear Studies, University of Chicago, Chicago 37, Illinois.

Journal of Applied Physics
Elmer Hoyemeyer, *Editor*, Case Institute of Technology, Cleveland 6, Ohio.

Physics Today
Gaylord P. Harnwell, *Editorial Director*; Robert B. Davis, *Managing Editor*, American Institute of Physics, 57 East 55 Street, New York 22, New York.

Committee on Finance
Gaylord P. Harnwell, *Chairman*
Wallace Waterfall, *Secretary*
Carlos J. Romualdi, *Treasurer*
Karl K. Darrow

CORPORATION BOARD
Lloyd V. Berkner
Lee A. DuBridge
Karl K. Darrow
S. A. Goudsmit
Gaylord P. Harnwell
Elmer L. Hoffman
Frederick V. Hunt
Francis R. Lunn
Henry A. Barton
C. C. Lauritsen
William F. Meggers
Philip M. Morse
Robert O'Brien
George B. Pegram
I. I. Rabi
Frank Spedding
Raymond Sloan
William Shockley
Richard M. Sutton
J. H. Van Vleck
Mark W. Zemansky

Committee on Printing
Malcolm Low

ADMINISTRATIVE STAFF
Henry A. Barton, *Director*
Wallace Waterfall, *Secretary*
Theodore Vermeulen, *Advertising Manager*
Byron T. Bryans, *Publication Manager*
Betty H. Goudsmit, *Assistant Secretary*
Marie E. Neverman, *Circulation Manager*
Lawrence Berne, *Assistant Treasurer*

THE American Institute of Physics was founded in 1931 as a federation of leading societies in the field of Physics. It combines into one operating agency those functions on behalf of physics which can best be done by the Societies jointly. Its purpose is the advancement and diffusion of physics and its applications to human welfare. To this end it publishes for each of the Societies the nine journals listed on this page; promotes unity and effectiveness of effort among all who are interested in physics; renders numerous direct services to physicists and to the public; and cooperates with government agencies, national associations, educational institutions, technical laboratories, and others in such manner as to realize the opportunities and fulfill the responsibilities of physics as an important and constructive human activity.

CONTENTS

THE PHYSICAL REVIEW SECOND SERIES, VOLUME 90, NO. 1 APRIL 1, 1953

Hyperfine Structure of the $3p^2P_{\frac{1}{2}}$ State of Al^{27} . . . . . HIN LEW AND GÜNTER WESSEL 1
Radiative Correction for the Collision Loss of Heavy Particles . . . . . V. Z. JANKUS 4
Radiations of Pu^{243} . . . . . D. W. ENGELKEMEIR, P. R. FIELDS, AND J. R. HUIZENGA 6
Effects of Radioactive Disintegrations on Inner Electrons of the Atom . . . . . J. S. LEVINGER 11
Alpha-Particle Induced Phosphorescence of Silver-Activated Sodium Chloride . . . . . C. E. MANDEVILLE AND H. O. ALBRECHT 25
First Excited States of Even-Even Nuclei . . . . . KENNETH W. FORD 29
Cosmic-Ray Neutron Production in Elements as a Function of Latitude and Altitude . . . . . J. A. SIMPSON AND R. B. UBETZ 44
Excitation of Molecular Rotation-Vibration by Electron Impact . . . . . PHILIP M. MORSE 51
Magnetic Structure Transitions . . . . . J. SAMUEL SMART 55
Effect of Temperature on the Duration of the $^1P_1$ Metastable Level of Neon . . . . . F. A. GRANT AND A. D. KRUMBEIN 59
Photodisintegration of the Deuteron . . . . . LAMEK HULTHÉN AND BENGT C. H. NAGEL 62
Electronic Transitions in the Luminescence of Zinc Sulfide Phosphors . . . . . RICHARD H. BUBE 70
Zeeman Effect in the Spectra of Tellurium . . . . . J. B. GREEN AND R. A. LORING 80
Effects of Departure from the Single Particle Model on Nuclear Magnetic Moments . . . A. DE-SHALIT 83
Search for Penetrating Showers from Hydrogen at Sea Level Using a Cloud Chamber . ALBERT B. WEAVER 86
Grain Density in Nuclear Emulsions . . . . . LAURIE M. BROWN 95
Remarks on the Theory of Fusion and Condensation . . . . . ARNOLD J. F. SIEGERT 97
Thermal Neutron Capture Cross Sections of Pa^{231} and Pa^{233} . . R. ELSON, P. A. SELLERS, AND E. R. JOHN 102
Low Frequency Resonances in the Spectra of Diatomic Molecules . . . . . R. E. COTÉ AND P. KUSCH 103
Capacitance Effects in Thin Conductive Films . J. N. HUMPHREY, FRANCES L. LUMMIS, AND W. W. SCANLON 111
Studies of Compounds for Superconductivity . . . . . W. T. ZIEGLER AND R. A. YOUNG 115
Studies of Atomic Self-Consistent Fields. I. Calculation of Slater Functions . . . . . PER-OLOV LÖWDIN 120
Color Centers and Trapped Charge in KCl and KBr . . . . . DAVID DUTTON AND ROBERT MAURER 126
Generalization of the WKB Method to Radial Wave Equations . . . . . R. H. GOOD, JR. 131
Relative Energy Levels of Some *P* Shell Nuclei in Intermediate Coupling . . . . . EDWIN A. CROSBIE 138
New Fine Structure in Neutral Oxygen . . . . . LEE W. PARKER AND JOHN R. HOLMES 142
Current Increase at Constant Amplification Factor in Steady Corona with Coaxial Cylindrical Geometry . . . . . LEONARD B. LOEB 144
Calculation of Peaked Angular Distributions from Legendre Polynomial Expansions and an Application to the Multiple Scattering of Charged Particles . . . . . L. V. SPENCER 146

Letters to the Editor:

Interaction of Microwaves Propagated through a Gaseous Discharge Plasma . . . . . L. GOLDSTEIN, J. M. ANDERSON, AND G. L. CLARK 151
Ultrasonic Attenuation Measurements in Germanium . . . . . ROBIN TRUELL AND JOSEPH BRONES 152
Temporary Traps in Silicon and Germanium . . . . . J. R. HAYNES AND J. A. HORNBECK 152
Magnetoresistance Effect in InSb . . . . . G. L. PEARSON AND M. TANENBAUM 153
Continuous Layer Formation in the Atmosphere under the Influence of Solar Radiation . . . . H. K. KALLMANN 153
Mechanism of Phosphorescence in Crystal Phosphors . . . . . DANIEL CURIE 154
Formation of the *D*-Layer . . . . . K. WATANABE, FREDERICK MARMO, AND EDWARD C. Y. INN 155
Lyman Alpha-Line Photographed in the Sun's Spectrum . . . . . W. B. FIEBENPOL, W. A. REINER, F. C. WALZ, D. S. STACEY, AND J. M. JACKSON 156
Helium II Film Transport Rates over Various Surfaces . . . . . B. SMITH AND H. A. BOORSE 156
Activity Assignment to Titanium 51 . . . . . WILLIAM R. HAMMOND, D. N. KUNDU, AND M. L. POOL 157
Radioactive Decay of Y^{91} . . . . . F. I. BOLEY AND D. S. DUNAVAN 158
Evidence for a 25.5-Day Sr $-$76-Sec Rb Chain . . . . . PAUL KRUGER AND NATHAN SUGARMAN 158
Angular Correlation of the Cascade Gamma-Rays from the Decay of Au^{198} . . . . . CARLTON D. SCHRADER, EDWARD B. NELSON, AND JAMES A. JACOBS 159
Spectrometer Measurement on the High Energy Positrons of Sodium 22 . . . . . BYRON T. WRIGHT 159
Energy per Ion Pair for 5-Mev Alpha-Particles in Helium . . . . . T. E. BORTNER AND G. S. HURST 160
Elastic Pion-Deuteron Scattering . . . . . E. ARARE, GERSON GOLDHABER, AND S. GOLDHABER 160
Elastic Scattering of Pi-Mesons by Deuterons . . . . . THOMAS A. GREEN 161
Spectrum of the Gamma-Radiation Emitted in the Reaction $n+p \rightarrow d+\gamma$ . . . . . A. BRACCI, U. FACCHINI, AND A. MALVICINI 162
Levels in F^{19} from the $C^{13}(p,\gamma)F^{14}$ Reaction . . . . . D. HICKS, T. HUSAIN, L. G. SANDERS, AND L. E. BEGHIAN 163
(γ,α) Reaction of B^{11} and B^{10} . . . . . K. LOCHER AND P. STOLL 164
Existence of Positronium Chloride . . . . . LENNART SIMONS 165
Formation of a Compound Nucleus in Neutron Reactions . . . . . HERMAN FESHBACH, CHARLES E. PORTER, AND VICTOR F. WEISSKOPF 166
Direct Experimental Evidence for the Existence of a Heavy Positive *V*-Particle . . . . . C. M. YORK, R. B. LEIGHTON, AND E. K. BJORNERUD 167
Meteorites as Cosmic-Ray Meters . . . . . S. F. SINGER 168
Orbital Effect in Neutron-Electron Magnetic Scattering . . . . . W. H. KLEINER 168
Total Cross Sections for 400-Mev Neutrons . . . . . V. ALEXANDER NEDZEL 169
Comparison of Gamma-Ray Reflections from the (550) and (310) Planes of Quartz . . . . . HARRY C. HOYT, JOSEPH J. MURRAY, AND JESSE W. M. DUMOND 169

LANCASTER PRESS, INC., LANCASTER, PA.